ΕΘΝΙΚΟ ΜΕΤΣΟΒΙΟ ΠΟΛΥΤΕΧΝΕΙΟ

ΣΧΟΛΗ ΧΗΜΙΚΩΝ ΜΗΧΑΝΙΚΩΝ

ΤΟΜΕΑΣ ΙΙΙ: ΕΠΙΣΤΗΜΗΣ ΚΑΙ ΤΕΧΝΙΚΗΣ ΤΩΝ ΥΛΙΚΩΝ

ΔΙΔΑΚΤΟΡΙΚΗ ΔΙΑΤΡΙΒΗ

ΑΝΑΠΤΥΞΗ ΚΑΙ ΜΕΛΕΤΗ ΙΔΙΟΤΗΤΩΝ ΠΡΟΗΓΜΕΝΩΝ ΝΑΝΟΔΟΜΩΝ ΚΑΙ ΕΠΙΚΑΛΥΨΕΩΝ ΜΕ ΕΜΦΑΣΗ ΣΤΙΣ ΝΑΝΟΜΗΧΑΝΙΚΕΣ ΙΔΙΟΤΗΤΕΣ

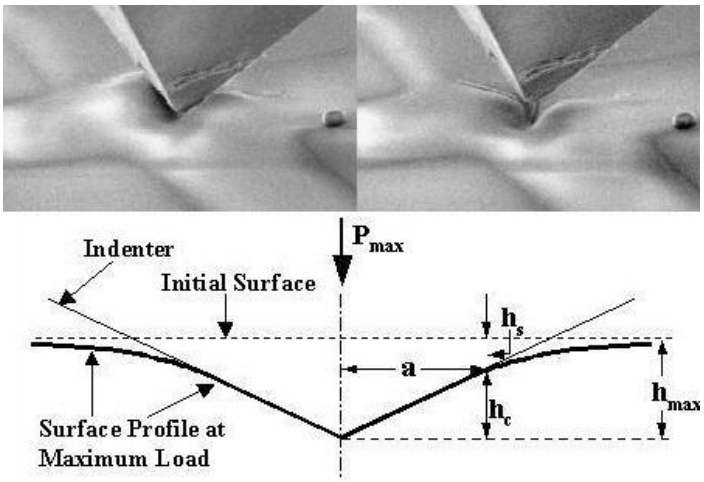

ΗΛΙΑΣ ΚΟΥΜΟΥΛΟΣ

MSc Χημικός Μηχανικός ΕΜΠ

Επίβλεψη:Κ.Α. Χαριτίδης

Καθηγητής ΕΜΠ

Αθήνα 2015

ΜΕΛΗ 3ΜΕΛΟΥΣ ΣΥΜΒΟΥΛΕΥΤΙΚΗΣ ΕΠΙΤΡΟΠΗΣ

Χαριτίδης Κ., Καθ. ΕΜΠ (επιβλέπων)

Χρυσουλάκης Ι., Ομ. Καθ. ΕΜΠ

Τσετσέκου Α., Αναπ. Καθ. ΕΜΠ

ΜΕΛΗ 7ΜΕΛΟΥΣ ΕΞΕΤΑΣΤΙΚΗΣ ΕΠΙΤΡΟΠΗΣ

Μανωλάκος Δ., Καθ. ΕΜΠ

Παντελής Δ., Καθ. ΕΜΠ

Χριστοφόρου Ε., Καθ. ΕΜΠ

Χρυσουλάκης Ι., Ομ. Καθ. ΕΜΠ

Χαριτίδης Κ., Καθ. ΕΜΠ (επιβλέπων)

Τσετσέκου Α., Αναπ. Καθ. ΕΜΠ

Μπακόλας Α., Επικ. Καθ. ΕΜΠ

«Η έγκριση της Διδακτορικής Διατριβής από την Ανώτατη Σχολή Χημικών Μηχανικών του ΕΜΠ, δεν υποδηλώνει αποδοχή των απόψεων του συγγραφέα» (Νόμος 5343/32, αρθρ. 202)

"Τι΄ αυτό είσαι ασυγχώρητος, ω άνθρωπε, οποιοσδήποτε κι αν είσαι που κρίνεις. Γιατί όποτε κρίνεις, καταδικάζεις τον εαυτό σου. Γιατί κάνεις τα ίδια με αυτά που κρίνεις."

Επιστολές Παύλου προς Ρωμαίους 2:1-2

Αφιερώνεται στους κοντινούς μου ανθρώπους και στο στήριγμά μου..

Η παρούσα διδακτορική διατριβή (ΔΔ) πραγματοποιήθηκε στην εργαστηριακή Μονάδα Νανομηχανικής & Νανοτεχνολογίας, στον Τομέα ΙΙΙ της Σχολής Χημικών Μηχανικών του Εθνικού Μετσοβίου Πολυτεχνείου κατά το διάστημα 2009-2014, με τίτλο "ΑΝΑΠΤΥΞΗ ΚΑΙ ΜΕΛΕΤΗ ΙΔΙΟΤΗΤΩΝ ΠΡΟΗΓΜΕΝΩΝ ΝΑΝΟΔΟΜΩΝ ΚΑΙ ΕΠΙΚΑΛΥΨΕΩΝ ΜΕ ΕΜΦΑΣΗ ΣΤΙΣ ΝΑΝΟΜΗΧΑΝΙΚΕΣ ΙΔΙΟΤΗΤΕΣ ".

Οφείλω ένα μεγάλο ευχαριστώ στον επιβλέποντα κ. Χαριτίδη Κων/νο, Καθηγητή της Σχολής Χημικών Μηχανικών ΕΜΠ, για την ανάθεση της ΔΔ, την αμέριστη και συνεχή βοήθεια και καθοδήγηση που μου έδωσε κατά την διάρκεια αυτής καθώς και τις για κοινές βλέψεις, προβληματισμούς και προσοδοφόρες (και μη, το ίδιο σημαντικές) προσπάθειες για εξέλιξη.

Ιδιαίτερα θέλω να ευχαριστήσω τα μέλη της 3μελούς συμβουλευτικής επιτροπής Χρυσουλάκη Ιωάννη, Ομ. Καθ. ΕΜΠ και Τσετσέκου Αθηνά, Αναπ. Καθ. ΕΜΠ για την πολύτιμη βοήθειά τους και την καθοδήγηση.

Οφείλω επίσης να ευχαριστήσω μέλη ΔΕΠ και κύριους ερευνητές (Ι. Ζιώμα, Α. Μπουντουβή, Δ. Παντελή, Ε. Χριστοφόρου, Α. Τσετσέκου, Α. Παπαθανασίου, Π. Ταραντίλη, Μ. Κομπίτσα, Β. Νικολάκη) τους ΥΔ και προπτυχιακούς/μεταπτυχιακούς φοιτητές (Μ. Κυρίτση, Π. Διαμαντόπουλο, Β. Παντελεάκου, Σ. Καραλή, Σ. Βασιλάκο, Θ. Παρούση, Π. Ελένη, Ν. Δανιόλο, Β. Αντωνακάκη, Α. Ηλιοπούλου, Δ. Παπαγεωργίου)που συνεργαστήκαμε κατά τη διάρκεια της ΔΔ. Σίγουρα ξεχνάω κάποιους..

Πως θα μπορούσα να ξεχάσω τους βασικούς συνοδοιπόρους της ομάδας για την δημιουργία ευχάριστου κλίματος κατά την διάρκεια των σπουδών μου.

Τέλος, ευχαριστώ όλα τα υπόλοιπα νέα μέλη της ομάδας Νανομηχανικής & Νανοτεχνολογίας και της Σχολής Χημικών Μηχανικών, και φυσικά την οικογένειά μου που με στηρίζει στις επιλογές μου με υπομονή.

Αθήνα, Μάϊος 2015

Ηλίας Κούμουλος

Δημοσιεύσεις σε διεθνή περιοδικά και συνέδρια με κριτές που προέκυψαν από την παρούσα διατριβή:

1. E.P. Koumoulos, M. Giorcelli, P. Jagadale, A. Tagliaferro, C.A. Charitidis, Evaluation of mechanical integrity of epoxy-nanodiamonds composites via nanoindentation, Composites Part B (2015), in press
2. E.P. Koumoulos, M. Giorcelli, P. Jagadale, A. Tagliaferro C.A. Charitidis, Carbon nanotube/ polymer nanocomposites: a study on mechanical integrity through nanoindentation,Polymer Composites (2015), in press, DOI: 10.1002/pc.23049
3. C.A. Charitidis, E.P. Koumoulos, D.A. Dragatogiannis, Nanotribological behavior of carbon based thin films: friction and lubricity mechanisms at the atomic level,Special Issue "Nanotribology and Atomic Mechanisms of Friction", Lubricants (2013) 1(2), 22-47
4. C.A.Charitidis, E.P. Koumoulos, M. Giorcelli, S. Musso, P. Jagadale, A. Tagliaferro, Nanomechanical and tribological properties of carbon nanotube/polyvinyl butyral composites, Journal of Polymer Composites, 2013, 34(11), 1950–1960
5. P. N. Eleni, M. K. Krokida, G. L. Polyzois, C. A. Charitidis, E. P. Koumoulos, V. P. Tsikourkitoudi, I. Ziomas, Mechanical behaviour of PDMS silicone elastomer after outdoor weathering in two different weathering locations,Journal of Polymer Degradation and Stability 96 470-476 (2011)
6. C.A. Charitidis, E. P. Koumoulos, V.P. Tsikourkitoudi, S.P. Vasilakos, P.A. Tarantili,Adhesive forces and time dependent behaviour (creep and loading rate effects) on nanomechanical properties of polydimethylsiloxane (PDMS), Journal of Nanostructured Polymers and Nanocomposites, 7:1 32-42 (2011).
7. E.P. Koumoulos, V.P. Tsikourkitoudi, C.A. Charitidis, P.N. Eleni, M.K. Krokida, I.C. Ziomas, Nanomechanical properties of physically-aged Polydimethylsiloxane, Proceedings of the 6th International Conference on Modification Degradation and Stabilization of Polymers 5-9 September 2010, Athens, Greece, Publisher: MoDeSt Hellenic Organizing Committee, Editors: Constantine D. Papaspyrides, Stamatina N. Vouyiouka
   ISBN: 978-960-99362-0-0
8. I.A. Kartsonakis, E.P. Koumoulos, C.A.Charitidis, G. Kordas, Hybrid organic-inorganic coatings including nanocontainers for corrosion protection of magnesium alloy ZK30, Journal of Nanoparticle Research, Volume 15, Issue 8, 1871 (2013)
9. I.A. Kartsonakis, E.P. Koumoulos, G.S. Pappas, A.C. Balaskas, C.A.Charitidis, G.C. Kordas, Hybrid organic-inorganic multilayer coatings including nanocontainers for corrosion protection of metal alloys, Journal of Corrosion Science, 57 (2012) 56–66
10. I.A. Kartsonakis, A.C. Balaskas, E.P. Koumoulos, C.A.Charitidis, G.C. Kordas,ORMOSIL-Epoxy Coatings with Ceramic Nanocontainers for Corrosion Protection of Magnesium Alloys ZK10, Progress in Organic Coatings, 76 (2–3) 2013
11. I.A. Kartsonakis, A.C. Balaskas, E.P. Koumoulos, C.A.Charitidis, G.C. Kordas,Evaluation of corrosion resistance of magnesium alloy ZK10 coated with hybrid organic–inorganic film including containers, Corrosion Science, 65, (2012), 481-493
12. I.A. Kartsonakis, A.C. Balaskas, E.P. Koumoulos, C.A.Charitidis, G.C. Kordas,Incorporation of ceramic nanocontainers into epoxy coatings for the corrosion protection of hot dip galvanized steel,Journal of Corrosion Science, 57 (2012) 30–41
13. E.P. Koumoulos, V.P. Tsikourkitoudi, I.A. Kartsonakis, V. Markakis, N. Papadopoulos, E. Hristoforou, C.A. Charitidis, Synthesis, structural and nanomechanical properties of cobalt based thin films, International Journal of Structural Integrity (2015), 6 (2)
14. Elias P. Koumoulos, Vassileios Markakis, Vasiliki P. Tsikourkitoudi, Costas A. Charitidis, Nikolaos Papadopoulos, Evangelos Hristoforou, Tribological characterization of chemical vapor deposited Co and Co3O4 thin films for sensing reliability in engineering applications, Tribology International, 82, Part A, 2015, 89–94 (2014)
15. M. Kandyla, C. Chatzimanolis-Moustakas, E.P. Koumoulos, C. Charitidis, M. Kompitsas, Nanocomposite NiO:Au hydrogen sensors with high sensitivity and low operating temperature, Materials Research Bulletin Volume 49, January 2014, Pages 552–559
16. V.P. Tsikourkitoudi, E.P. Koumoulos, N. Papadopoulos, C.A. Charitidis, Growth, Structural and Mechanical Characterization and Reliability of Chemical Vapor Deposited Co and Co3O4 Thin Films as Candidate Materials for Sensing Applications, Key Engineering Materials 495, pp. 108-111 (2012).
17. V.P. Tsikourkitoudi, E.P. Koumoulos, N. Papadopoulos, E. Hristoforou, C.A. Charitidis, Growth, Structural and Mechanical Characterization and Reliability of Chemical Vapor Deposited Co and Co3O4 Thin Films as Candidate Materials for Sensing Applications, Journal Of Optoelectronics and Advanced Materials, 14(1), pp. 169-175 (2012).
18. D.A. Dragatogiannis, E. Koumoulos, K. Ellinas, A. Tserepi, E. Gogolides, C.A. Charitidis, Nanoscale Mechanical and Tribological Properties of Plasma Nanotextured COP Surfaces with Hydrophobic Coatings, Plasma Processes and Polymers, (2015), in press
19. Elias P. Koumoulos, Costas A. Charitidis, Dimitrios P Papageorgiou, Athanasios G Papathanasiou, Andreas G Boudouvis, Nanomechanical and Nanotribological Properties of Hydrophobic Fluorocarbon Dielectric Coating on Tetraethoxysilane for Electrowetting Applications, Journal of Surface and Coatings Technology, 206, pp. 3823–3831 (2012)
20. Dimitrios P. Papageorgiou, Elias P. Koumoulos, Costas A. Charitidis, Andreas G. Boudouvis, Athanasios G. Papathanasiou, Evaluating the robustness of top coatings comprising plasma-deposited fluorocarbons in electrowetting systems, Journal of Adhesion Science and Technology (2012), 26 (12-17), pp. 2001-2015
21. C.A.Charitidis, E.P. Koumoulos, V. Nikolakis, D.A.Dragatogiannis, Structural & Nanomechanical Properties of a Zeolite Membrane measured using Nanoindentation, Journal of Thin Solid Films, 526, 2012, 168–175

Δημοσιεύσεις σε συνέδρια που προέκυψαν από την παρούσα διατριβή:

1. E.P. Koumoulos, A. Darivaki, C.A. Charitidis, CNTs/polymer nanocomposites for antifouling activity: surface properties and perspectives, 10th Panhellenic Conference on Chemical Engineering (2015)
2. T. Parousis, D. Perivoliotis, E. P. Koumoulos, C.A. Charitidis, Evaluation of MWCNTs/PDMS composite coating for antifouling applications, European Coatings CONGRESS 2015, 20-21 April 2015 Nuremberg/Germany
3. E.P. Koumoulos, C.A. Charitidis, Nanoindentation analysis of composite engineering materials, Eurofillers 2013, Slovakia (2013)
4. E.P. Koumoulos, C.A. Charitidis, Nanomechanical properties of engineering nanostructures, XXIX Panhellenic Conference on Solid State Physics and Materials Science (2013)
5. C.A. Charitidis, E. P. Koumoulos, Duracosys 2010, Nanomechanical Properties and Nanoscale Deformation of PDMS nanocomposites, 9th International Conference on Durability of Composite Systems (2010),
6. E. P. Koumoulos, V. P. Tsikourkitoudi, C. A. Charitidis, P. N. Eleni, M. K. Krokida, I. Ziomas, Investigation of the Nanomechanical Properties of Physically-aged Polydimethylsiloxane (PDMS), XXVI Panhellenic Conference on Solid State Physics and Materials Science (2010)
7. C.A. Charitidis, E.P. Koumoulos, Nanoindentation of Nanocomposites Polydimethylsiloxane Elastomers, 6th International Conference on Nanosciences & Nanotechnologies (2009)
8. E.P.Koumoulos, C.A.Charitidis, S.P.Vasilakos, P.A.Tarantili ,Nanomechanical Properies of PDMS nanocomposites, 7th Panhellenic Conference on Chemical Engineering (2009)
9. I.A.Kartsonakis, A.C.Balaskas, E.P.Koumoulos, C.A.Charitidis, G.Kordas, Corrosion resistance of magnesium alloy ZK10 coated with hybrid organic-inorganic film including containersEurocorr 2012, The European Corrosion Congress 2012, 9-13 September, Istanbul – Turkey
10. Costas Charitidis, Ioannis Kartsonakis (Presenter), Evangelia Karaxi, Elias Koumoulos, Irini Kanellopoulou, Antonis Karantonis, Self-healing microcomposites for corrosion protection of hot dip galvanized steel, EUROCORR 2015, Graz/Austria, September 2015.
11. C.A. Charitidis, V.P. Tsikourkitoudi, E.P. Koumoulos, I.A. Kartsonakis, N. Papadopoulos, E. Hristoforou, Synthesis, structural and nanomechanical properties of cobalt based thin films, ICEAF III. 3rd International Conference of Engineering Against Failure. 26-28 June, 2013 - Kos island.
12. V. P. Tsikourkitoudi, E.P. Koumoulos, I.A. Kartsonakis, C.A. Charitidis, Structural investigation and mechanical integrity of metal and metal oxide thin films for sensing applications: A comparative study through nanoindentation, 9th International Conference on Nanosciences & Nanotechnologies(2012)
13. V.P. Tsikourkitoudi, E.P. Koumoulos, N. Papadopoulos, E. Hristoforou, C.A. Charitidis, Tribological characterization of chemical vapor deposited Co and Co3O4 thin films for sensing reliability in engineering applications, 20th International Conference on Soft Magnetic Materials (SMM-20) (2011)
14. V.P. Tsikourkitoudi, E.P. Koumoulos, N. Papadopoulos, C.A. Charitidis, Growth, Structural and Mechanical Characterization and Reliability of Chemical Vapor Deposited Co and Co3O4 Thin Films as Candidate Materials for Sensing Applications, International Conference on Materials and Applications for Sensors and Transducers (IC-MAST) (2011)
15. Elias P. Koumoulos, D.A. Dragatogiannis, K. Ellinas, A. Tserepi, E. Gogolides, C.A. Charitidis, Nanomechanical and tribological properties of plasma nanotextured surfaces for "smart" microfluidic devices, International Middle East Plasma Science (IMEPS), Antalya, Turkey April 23 – 25, 2014
16. Aspasia Iliopoulou, Elias P. Koumoulos, Dimitrios P. Papageorgiou, Athanasios G. Papathanasiou, Costas A. Charitidis, Adhesion strength of hydrophobic dielectric coatings for electrowetting applications, 8th Panhellenic Conference on Chemical Engineering (2011)
17. C.A.Charitidis, M. Kyritsi, E.P. Koumoulos, V. Nikolakis. Synthesis, Structural & Nanomechanical Properties of Zeolite Membrane, XXVII Panhellenic Conference on Solid State Physics and Materials Science, Synthesis (2011)

Συνεργασίες που προέκυψαν από την παρούσα διατριβή/χρηματοδοτούμενη έρευνα:

-Εργαστήριο Μεταλλογνωσίας, Τομέας Μεταλλουργίας και Τεχνολογίας Υλικών, Σχολή Μηχ. Μεταλλείων – Μεταλλειολόγων, Ε. Χριστοφόρου, Καθ. ΕΜΠ

-Τομέας Ανάλυσης, Σχεδιασμού και Ανάπτυξης Διεργασιών και Συστημάτων,Σχολή Χημικών Μηχανικών Ε.Μ.Π., Α. Μπουντουβής, Καθ. ΕΜΠ-Α. Παπαθανασίου. Επικ. Καθ. ΕΜΠ

-Εργαστήριο Πολυμερών, Σχολή Χημικών Μηχανικών Ε.Μ.Π., Τομέας Σύνθεσης και Ανάπτυξης Βιομηχανικών Διαδικασιών, Π. Ταραντίλη, Επικ. Καθ. ΕΜΠ

- Εργαστήριο Σχεδιασμού & Ανάλυσης Διεργασιών, Σχολή Χημικών Μηχανικών Ε.Μ.Π., Ι. Ζιώμας, Καθ. ΕΜΠ, Μ. Κροκίδα, Αναπ. Καθ. ΕΜΠ

-Theoretical and Physical Chemistry Institute, National Hellenic Research Foundation, Δρ. Μιχάλης Κομπίτσας, Ερευν. Α'

-Ίδρυμα Τεχνολογίας και Έρευνας (ΙΤΕ), Ινστιτούτο Επιστημών Χημικής Μηχανικής (ΙΕΧΜΗ), Δρ. Β. Νικολάκης, Ερευν. Α'

-Carbon Group, Politecnico di Torino, Italy, Prof. A. Tagliaferro

-Slovak Academy of Sciences, Polymer Intistute, Dr. Igor Krupa

Οργανολογία που χρησιμοποιήθηκε στην παρούσα διατριβή:

Nanoindenter - Nanoscratch

Scanning Probe Microscopy (SPM)

Scanning Electron Microscopy (SEM)

Thermal Chemical Vapor Deposition (T-CVD)

X-Ray Diffractometer (XRD)

Differential Scanning Calorimetry (DSC)

Fourier Transformed InfraRed Spectroscopy (FTIR)

Metallographic analysis – optical microscope

Περίληψη

Η παρούσα διδακτορική διατριβή (ΔΔ) πραγματεύεται την ανάπτυξη και μελέτη προηγμένων νανοδομών και επικαλύψεων με έμφαση στις νανομηχανικές ιδιότητες μέσω της τεχνικής της νανοδιείσδυσης (nanoindentation), προκειμένου:
1) να υπολογίζονται με ακρίβεια οι τιμές σκληρότητας και οι μηχανικές ιδιότητες υλικών, όπως τα λεπτά υμένια, όπου ο υπολογισμός της επιφάνειας του αποτυπώματος είναι αδύνατος λόγω μεγέθους με τις κλασσικές τεχνικές
2) να αποτιμηθούν ιδιότητες όπως παραμόρφωση, ερπυσμός, μηχανισμοί αποδόμησης, διασπορά προσθέτων σε μήτρα, πρόσφυση, δομή
Σκοπός ήταν ο κατάλληλος σχεδιασμός πειραμάτων και πρωτοκόλλων ώστε η συγκεκριμένη τεχνική να μπορεί να συμβάλλει σημαντικά (αν όχι να αποφανθεί) στην απόφαση για τη λειτουργικότητα και την αξιοπιστία των υλικών στις εφαρμογές για τις οποίες προορίζονται (σημαντικότητα όρου "τεχνολογικές ιδιότητες, engineering properties").
Το αποτέλεσμα αποτυπώνεται σε καμπύλες φόρτισης-αποφόρτισης, από τις οποίες προκύπτουν πληροφορίες για τις μηχανικές ιδιότητες του υλικού που εξετάζεται, όπως το μέτρο ελαστικότητας και η σκληρότητα. Τα φορτία που επιτυγχάνονται πλέον είναι της τάξεως των nN.
Τις δύο τελευταίες δεκαετίες η ανάπτυξη τεχνολογίας καταγραφής φορτίων και μετατοπίσεων κατά τη διάρκεια της σκληρομέτρησης με υψηλή ακρίβεια οδήγησε στη χρήση των πειραμάτων στη νανοκλίμακα. Συγκεκριμένα στις μέρες μας έχει επιτευχθεί χρήση φορτίων nN και ανίχνευση μετατοπίσεων της ακίδας - διεισδύτη με διακριτική ικανότητα ~0.04 nm, καθιστώντας τη νανοδιείσδυση κυρίαρχη μέθοδο προσδιορισμού των νανομηχανικών ιδιοτήτων υλικών, όπως λεπτά υμένια, επικαλύψεις και διατάξεις με πάχος μερικές δεκάδες nm. Επίσης με την χρήση αισθητήρα εφαπτομενικής δύναμης δύναται να διενεργούνται πειράματα εγχάραξης (scratch testing) στην επιφάνεια δοκιμίων με αποτέλεσμα τον προσδιορισμό των τριβολογικών τους ιδιοτήτων.
Στη βιβλιογραφία, ενώ οι νανομηχανικές ιδιότητες αναφέρονται ευρέως σε πληθώρα υλικών, δεν συσχετίζονται άμεσα με το πεδίο εφαρμογής αφήνοντας έτσι κενό στον καθορισμό τους ως κατάλληλα ή μη. Επιπλέον, ο υπολογισμός μέτρου ελαστικότητας ή/και σκληρότητας τοπικά -στην περιοχή λίγων nm- (όπως η όποια εφαρμογή το απαιτεί) καθιστά τη χρήση συμβατικών μεθόδων (π.χ. εφελκυσμός, μικροσκληρότητα) αδύνατη.
Με τη χρήση της συγκεκριμένης τεχνικής, σε συνδυασμό με τις τεχνικές Scanning Probe Microscopy (SPM), Scanning Electron Microscopy (SEM), Thermal Chemical Vapor Deposition (T-CVD), X-Ray Diffractometer (XRD), Differential Scanning Calorimetry (DSC), Fourier Transformed InfraRed Spectroscopy (FTIR), Metallographic analysis – optical microscope αποτιμήθηκαν χαρακτηριστικές ομάδες υλικών, που χαρακτηρίζονται ως τεχνολογικά. Συγκεκριμένα, μελετήθηκαν πολυμερή και νανοσύνθετα πολυμερή (PDMS, PDMS με νανοσωματίδια μοντμοριλλονίτη, εποξειδική μήτρα με νανοσωλήνες άνθρακα), πολυστρωματικές δομές (Teflon, FC), λεπτά υμένια μετάλλων και οξειδίων τους (Co, Co3O4) και κεραμικά (ζεόλιθος) που προορίζονται για βιοεφαρμογές, αντιδιάβρωση, μικροηλεκτρονική, αισθητήρες και μοριακά κόσκινα, αντίστοιχα.
Συγκεκριμένα, οι μετρήσεις νανοδιείσδυσης στα πολυμερικά και νανοσύνθετα ανέδειξαν τους μηχανισμούς αποδόμησης κατά τη μέτρηση, δίνοντας ταυτόχρονα πληροφορία για τη διασπορά των νανοσωματιδίων και τη μέγιστη συγκέντρωση πέρα από την οποία φθίνει η μηχανική απόκριση του υλικού. Αποδείχθηκε ότι η νανοδιείσδυση μπορεί να χρησιμοποιηθεί αξιόπιστα ως εργαλείο αποτίμησης νανομηχανικών ιδιοτήτων, καθώς ποσοτικοποιούνται φαινόμενα όπως η ιξωδοελαστικότητα, η πρόσφυση της ακίδας στο δείγμα, η διεπιφάνεια μήτρας-νανοσωλήνων και χρονοεξαρτημένη συμπεριφορά. Ειδικότερα για τις αντιδιαβρωτικές επικαλύψεις, καθορίστηκε η κρίσιμη συγκέντρωση πέρα από την οποία φθίνει η μηχανική ακεραιότητα του υλικού, καθιστώντας το ακατάλληλο για εφαρμογή. Ταυτόχρονα, καθορίστηκε ο μηχανισμός αποδόμησης κατά την εγχάραξη. Σχετικά με τα

λεπτά υμένια κοβαλτίου και οξειδίου του, η τεχνική έδωσε τις απαραίτητες κατευθύνσεις για την αξιοπιστία των υλικών. Ειδικότερα, το οξείδιο του κοβαλτίου αποδείχθηκε ως καταλληλότερο, με αυξημένες μηχανικές και τριβολογικές ιδιότητες (αντίσταση σε φθορά). Μετρώντας την πολυστρωματική δομή, αποκαλύφθηκε η μετάβαση από προηγούμενο σε επόμενο στρώμα (βάσει ιδιοτήτων) αλλά και η αλληλεπίδραση τους. Ελέγχθηκε η πρόσφυση και αποτιμήθηκε η λειτουργία τους ως υλικά ηλεκτροδιαβροχής. Τέλος, υπολογίστηκαν οι νανομηχανικές ιδιότητες του ζεόλιθου φωγιασίτη, δίνοντας σημαντικά δεδομένα για την απόκριση του υλικού, χρησιμοποιώντας σύγκριση πειραμάτων ερπυσμού.

Abstract

This doctoral thesis addresses nanostructures and advanced coatings with emphasis on nanomechanical properties through nanoindentation, in order:
1) for the hardness and the mechanical properties of materials to be calculated more accurately, (such as thin films, where the exact knowledge of imprint area and calculation is difficult due to size)
2) to evaluate properties such as deformation, creep, time dependent properties, deformation mechanisms, dispersion, adhesion, structure
The aim was the proper design of experiments and protocols that this technique can contribute significantly (if not to rule) decisions on the functionality and reliability of materials in applications for which they are intended (using the term "technological/ engineering properties").
The result is reflected in load-unload curves of the material being tested, and properties such as modulus and toughness are extracted.
Over the last two decades, the development of technology and recording load shifts during indentation with high accuracy led to the use of experiments at the nanoscale. Specifically, nowadays this is achived using nN and load displacement detection pin - penetrating with a resolution of ~ 0.04 nm, making the nanoindentation a dominant method of determining the nanomechanical properties of substances, such as thin films, coatings and devices with a thickness of several tens of nm. Using nanoindentation, it is possible to assess the determination of the hardness, the modulus and the elastic / plastic response of materials. Also using tangential force, scratch tests are performed so as to determine tribological properties.
In literature, while nanomechanical properties arewidely reported in a variety of materials, these are not directly related to the application field, leaving a knowledge gap whether these materials are finally suitable or not. Furthermore, the calculation of modulus and / or hardness locally (as as many applications require) makes the use of conventional methods (e.g. tension, microhardness) rather inapplicable.
By use of this technique, coupled with the techniques of Scanning Probe Microscopy (SPM), Scanning Electron Microscopy (SEM), Thermal Chemical Vapor Deposition (T-CVD), X-Ray Diffractometer (XRD), Differential Scanning Calorimetry (DSC), Fourier Transformed InfraRed Spectroscopy (FTIR), Metallographic analysis - optical microscope engineering materials are technologically characterized. Polymers and polymer nanocomposites (PDMS, PDMS with montmorillonite nanoparticles, epoxy matrix with carbon nanotubes), multilayer thin film structures (Teflon, FC), thin films of metals and their oxides (Co, Co_3O_4) and ceramic (zeolite) for bioapplications, anticorrosion, microelectronics, sensors and molecular sieves, respectively.
Specifically, nanoindentation measurements of the polymeric nanocomposites revealed the deformation mechanisms during testing, also giving information about the dispersion of nanoparticles and the maximum concentration (percolation threshold) beyond which the

mechanical integrity of the material deteriorates. It turned out that nanoindentation can be not only a reliable mechanical properties valuation tool, but also a useful mean of quantifying phenomena such as viscoelasticity, adhesion of the tip in the sample, nanotube-matrix interface and timedependent behavior. Especially for anti-corrosive coatings, the critical concentration is determined, above which the mechanical integrity of the material deteriorates, making it unsuitable for final application. For thin films of cobalt and cobalt oxide, the technique gave the necessary guidelines for the reliability of the materials. Specifically, the cobalt oxide was proved to be suitable, with increased mechanical and tribological properties (wear resistance). Regarding the multilayer structure, the transition from the previous to next layer (based on properties) was revealed, indicating the influence of each other. Finally, we calculated the nanomechanical properties of zeolite faujasite, giving relevant data for the response of the material, using a comparison of creep experiments.

Table of Contents

Κεφάλαιο 1. Νανοσκληρομέτρηση

1.1 Γενικά – βασικές αρχές

Οι διάφορες τεχνικές μέτρησης σκληρότητας βασίζονται σε συγκεκριμένους κανόνες διεξαγωγής μετρήσεων (όπως Vickers, Knoop, Brinell και Rockwell). Εκτός από την τελευταία όλες οι υπόλοιπες ορίζουν τη σκληρότητα ως το λόγο φορτίου F που εφαρμόζεται προς την επιφάνεια του αποτυπώματος A. Η επιφάνεια του αποτυπώματος συνήθως υπολογίζεται μέσω οπτικής μικροσκοπίας ενώ η τιμή της σκληρότητας που προκύπτει βασίζεται στο αποτύπωμα που δημιουργείται. Το μειονέκτημα που προκύπτει έγκειται στο ποσοστό ακριβούς μέτρησης της επιφάνειας του αποτυπώματος.[1][2][3]

Μία νέα τεχνική βασισμένη στην ανίχνευση του βάθους διείσδυσης του εντυπωτή (Nanoindentation) αναπτύχθηκε προκειμένου να υπολογίζονται με μεγαλύτερη ακρίβεια οι τιμές σκληρότητας και οι μηχανικές ιδιότητες υλικών, όπως τα λεπτά υμένια, όπου ο υπολογισμός επιφάνειας αποτυπώματος είναι δύσκολος. Η βασική αρχή της τεχνικής αυτής είναι η εφαρμογή φορτίου στο δείγμα (μέσω ενός εντυπωτή) και παράλληλη καταγραφή της μετατόπισης που προκαλείται σε αυτό. Το αποτέλεσμα αποτυπώνεται σε καμπύλες φόρτισης-αποφόρτισης, από τις οποίες προκύπτουν πληροφορίες για τις μηχανικές ιδιότητες του υλικού που εξετάζεται, όπως το μέτρο ελαστικότητας και η σκληρότητα. Τα φορτία που επιτυγχάνονται πλέον είναι της τάξεως των nN. Σύμφωνα με την τεχνική αυτή, το βάθος και η δύναμη καταγράφονται ταυτόχρονα σε έναν κύκλο φόρτισης-αποφόρτισης.

1.2 Ιδιότητες – Μοντέλο

Η επιφάνεια που χρησιμοποιείται για τον προσδιορισμό της σκληρότητας υπολογίζεται από το βάθος επαφής [4][5][6].

[1] T. Chudoba, Measurement of Hardness and Young's Modulus by Nanoindentation, in Book Nanostructured Coatings, Albano Cavaleiro and Jeff Th. M. De Hosson (Editors), Springer, New York, pp.216-260, (2006).
[2] B. Bhushan (Ed.), Nanotribology and Nanomechanics: An Introduction, Springer, Berlin, (2005).
[3] Metals Handbook, Vol. 8: Mechanical Testing and Evaluation, ASM International, (2000)
[4] B. Poon, A Critical Appraisal of Nanoindentation woth Application to Elastic-Plastic and Soft Materials, PhD Thesis, California Institute of Technology, California, (2009).
[5] Κ.Α. Χαριτίδης, Νανοδομές και Νανοϋλικά: Σύνθεση, Ιδιότητες και Εφαρμογές, Εκδόσεις ΕΜΠ, Αθήνα, σσ.107-142, (2007).
[6] L. Hay and G.M. Pharr, Instrumented Indentation Testing, in Metals Handbook, Vol. 8: Mechanical Testing and Evaluation, ASM International, pp.232-243, (2000).

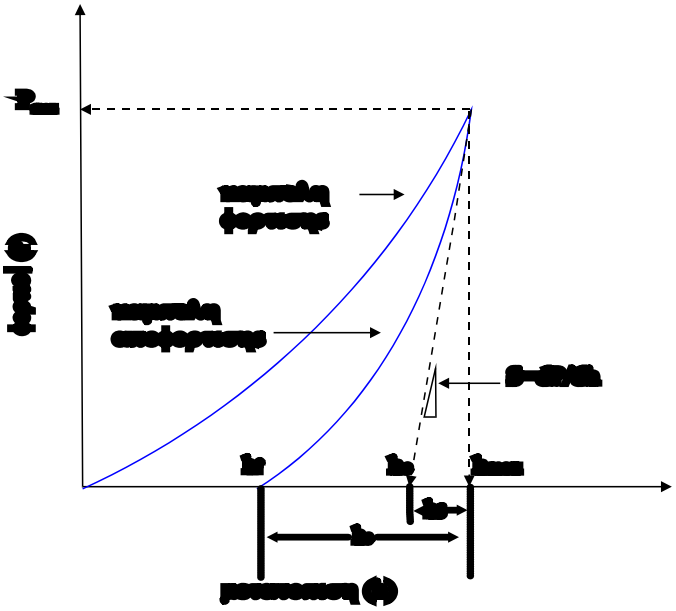

Σχήμα 1.1: Καμπύλη φόρτισης-αποφόρτισης σε συμβατικό πείραμα νανοσκληρομέτρησης.

Στις καμπύλες φόρτισης – αποφόρτισης διακρίνουμε τα ακόλουθα κρίσιμα μεγέθη:

$\boldsymbol{h_{max}}$: Μέγιστο βάθος διείσδυσης της ακίδας του εντυπωτή

$\boldsymbol{P_{max}}$: Μέγιστο εφαρμοζόμενο φορτίο

$\boldsymbol{h_f}$: Τελικό παραμένον βάθος διείσδυσης στο υλικό μετά την αποφόρτιση

$\boldsymbol{h_c}$: Βάθος επαφής υλικού και ακίδας διείσδυσης μετά την αποφόρτιση

$\boldsymbol{h_e}$: Ελαστική μετατόπιση της επιφάνειας του δείγματος κατά την αποφόρτιση

$\boldsymbol{h_s}$: Ελαστική μετατόπιση της επιφάνειας του δείγματος δίχως επαφή με την ακίδα

Αρχικά υπολογίζεται η ποσότητα S [Stiffness (ακαμψία)] από την γραμμική περιοχή της καμπύλης αποφόρτισης, όπως φαίνεται στο σχήμα 1.1, σύμφωνα με την εξίσωση 1.1.

$$S = \frac{dP}{dh} \tag{1.1}$$

και είναι η κλίση του γραμμικού τμήματος της καμπύλης αποφόρτισης.

Η σκληρότητα υπολογίζεται από την σχέση:

$$H = \frac{P_{\max}}{A} \tag{1.2}$$

όπου $\boldsymbol{A}$: η επιφάνεια επαφής.

Η επιφάνεια επαφής A είναι μια συνάρτηση της μορφής: $A = f(h_c)$.

Σύμφωνα με την παραπάνω τεχνική, η επιφάνεια αποτυπώματος του εντυπωτή υπολογίζεται μέσω της γεωμετρίας του εντυπωτή, αν θεωρηθεί ότι αυτή είναι ιδανική. Στην

πραγματικότητα όμως, οι αποκλίσεις της ακίδας από την ιδανική γεωμετρία είναι σημαντικές και γίνονται σημαντικότερες με τη μείωση του βάθους διείσδυσης. Επίσης, στην ανάλυση των δεδομένων πρέπει να ληφθούν υπόψη τόσο οι πλαστικές όσο και οι ελαστικές ιδιότητες του υλικού και της ακίδας. Η πλαστικότητα εκφράζεται από το εμβαδό που περικλείει η καμπύλη φόρτισης-αποφόρτισης και είναι το ποσό της ενέργειας που παραμένει στο προς μέτρηση υλικό μετά τη διαδικασία της νανοδιείσδυσης-νανοσκληρομέτρησης.

Με άλλα λόγια η πλαστικότητα σχετίζεται με το έργο που δαπανάται για την πλαστική παραμόρφωση σε σχέση με το συνολικό έργο που δαπανάται σε έναν κύκλο φόρτισης – αποφόρτισης (βλ. σχήμα 1.2) [43]:

$$\delta_{\mathrm{A}} = \frac{A_p}{A_t} = 1 - \frac{A_e}{A_t} \tag{1.3}$$

Η εξίσωση 1.3 υποθέτει ότι η ενέργεια καταναλώνεται μόνο για την παραμόρφωση του δείγματος, ενώ στην πραγματικότητα παραμορφώνεται και ο εντυπωτής.

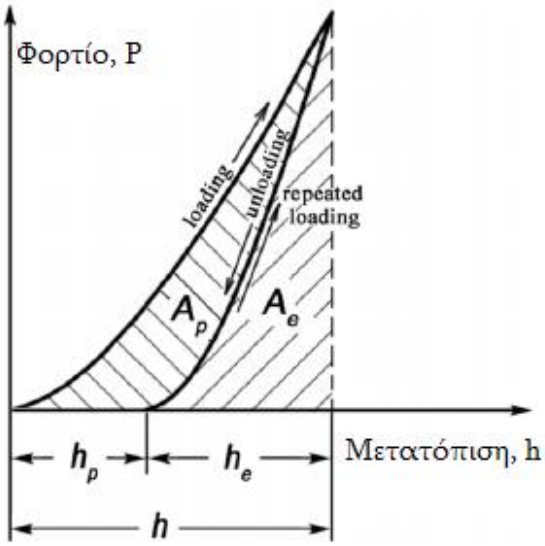

Σχήμα 1.2: Υπολογισμός του έργου ελαστικής και πλαστικής παραμόρφωσης.

Πλέον ευρέως χρησιμοποιείται η μέθοδος Oliver-Pharr για τον προσδιορισμό της σκληρότητας και του μέτρου ελαστικότητας, η οποία έχει καθιερωθεί από το 1992 και ενσωματώθηκε στο πρότυπο ISO 14577:2002 για τις νανοσκληρομετρήσεις [7][8][9].

[7] T. Chudoba, Measurement of Hardness and Young's Modulus by Nanoindentation, in Book Nanostructured Coatings, Albano Cavaleiro and Jeff Th. M. De Hosson (Editors), Springer, New York, pp.216-260, (2006).
[8] B. Bhushan (Ed.), Nanotribology and Nanomechanics: An Introduction, Springer, Berlin, (2005)

1.2.1 Μέθοδος Oliver-Pharr για εντυπωτές αξονικής συμμετρίας

<u>Πλήρως ελαστική θεώρηση</u>

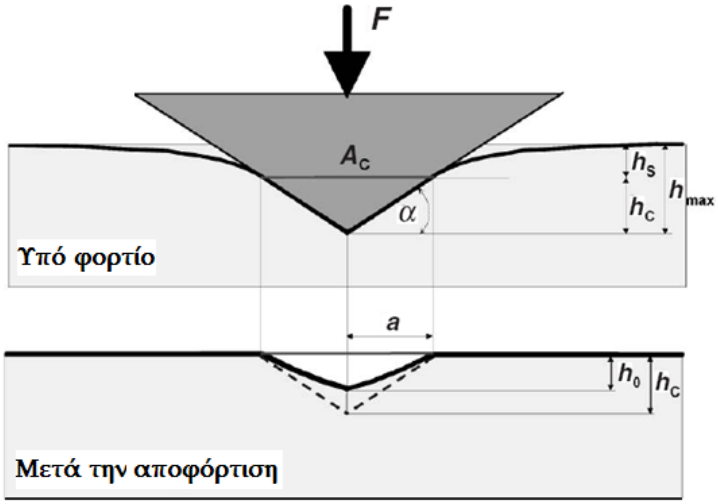

Σχήμα 1.3: Μέγιστη φόρτιση (πάνω) και αποφόρτιση (κάτω) κατά την διείσδυση με κωνικό ή πυραμιδικό εντυπωτή (μοντέλο Oliver-Pharr).

Μέσω της μετατόπισης της επιφάνειας του δείγματος κατά την διείσδυση, h, μετράται η παραμόρφωση (deformation) που προκύπτει στο δείγμα. Προκειμένου να υπολογιστεί η μέγιστη μετατόπιση, h_{max}, πρέπει να συνυπολογιστεί και η παραμόρφωση του εντυπωτή. Θεωρώντας άκαμπτο εντυπωτή (rigidindenter), η μέγιστη μετατόπιση προκύπτει ως άθροισμα τη ελαστικής και πλαστικής μετατόπισης. Προκειμένου να επανακτηθεί η συμβατότητα της παραδοσιακής σκληρότητας με αυτή που μετρήθηκε από το πείραμα νανοδιείσδυσης, χρειάζεται να προσδιοριστεί η επιφάνεια του αποτυπώματος μετά την αποφόρτιση. Για το λόγο αυτό γίνονται οι εξής παραδοχές [9][10][11][12][37,38,41]:

- Η επιφάνεια επαφής υπό μέγιστη φόρτιση και η επιφάνεια αποτυπώματος μετά την αποφόρτιση είναι ίσες, δηλαδή δεν υπάρχει ελαστικη αποκατάσταση στο επίπεδο επαφής ($h_c = h_0$, σχήμα 1.3) και η διάμετρος του αποτυπώματος δεν αλλάζει με την αφαίρεση του φορτίου.

[9] B. Poon, A Critical Appraisal of Nanoindentation woth Application to Elastic-Plastic and Soft Materials, PhD Thesis, California Institute of Technology, California, (2009).
[10] T. Chudoba, Measurement of Hardness and Young's Modulus by Nanoindentation, in Book Nanostructured Coatings, Albano Cavaleiro and Jeff Th. M. De Hosson (Editors), Springer, New York, pp.216-260, (2006).
[11] B. Bhushan (Ed.), Nanotribology and Nanomechanics: An Introduction, Springer, Berlin, (2005).
[12] Κ.Α. Χαριτίδης, Νανοδομές και Νανοϋλικά: Σύνθεση, Ιδιότητες και Εφαρμογές, Εκδόσεις ΕΜΠ, Αθήνα, σσ.107-142, (2007).

- Οι πλαστικές και ελαστικές παραμορφώσεις δεν επηρεάζονται μεταξύ τους. Η ελαστική παραμόρφωση πάνω από την περιοχή επαφής είναι η ίδια ανεξάρτητα από την πλαστική παραμόρφωση. Επίσης, το μέτρο Young είναι το ίδιο τόσο για τις παραμορφωμένες όσο και για τις μη παραμορφωμένες περιοχές του υλικού.
- Η τραχύτητα της επιφάνειας, τα φαινόμενα συσσώρευσης (pile-upeffects) και μη αναστρέψιμης (πλαστικής) βύθισης (sink-ineffects) θεωρούνται αμελητέα.
- Ο εντυπωτής είναι άκαμπτος.

Σύμφωνα με την πρώτη παραδοχή, αν είναι γνωστό το σχήμα του εντυπωτή, η παραμένουσα επιφάνεια του αποτυπώματος μπορεί να υπολογιστεί από το βάθος διείσδυσης του εντυπωτή υπό μέγιστο φορτίο, h_c (με την προϋπόθεση ότι μπορούμε να υπολογίσουμε την παραμόρφωση πάνω από την περιοχή επαφής (ελαστική), h_s) [13][14][15].

Ο Sheddon στηριζόμενος σε μοντέλα των Hertz[16] και Boussinesq[17], προσπάθησε να εξάγει μία σχέση μεταξύ φορτίου P και μετατόπισης h για άκαμπτο εντυπωτή με αξονική συμμετρία που ωθείται σε ένα ελαστικό υλικό, προκειμένου να προσδιορίσει το ποσοστό ελαστικής παραμόρφωσης του υλικού. Ο μόνος περιορισμός που έθεσε ήταν ο εντυπωτής να περιγράφεται ως στερεό εκ περιστροφής μιας ομαλής συνάρτησης. Βασική παραδοχή στη θεώρηση του Sheddon αποτελεί η εξής: η περιοχή επαφής είναι αρκετά μικρή σε σχέση με τις διαστάσεις των υλικών, ώστε οι τάσεις που αναπτύσσονται στην περιοχή αυτή δεν είναι ισχυρά εξαρτώμενες από το ακριβές σχήμα των σωμάτων ή τον τρόπο τρόπο που υποστηρίζονται (elastic half - spaces).

Σύμφωνα με τα παραπάνω, προκύπτουν οι γενικευμένες σχέσεις του Sheddon για κύλινδρο ακτίνας α και κώνο γωνίας φ αντίστοιχα:

$$P = \frac{4\mu\alpha}{1-\nu} h \qquad (1.4)$$

$$P = \frac{4\mu \cot\phi}{\pi(1-\nu)} h^2 \qquad (1.5)$$

όπου, μ: το μέτρο διάτμησης (shearmodulus) και ν : ο λόγος του Poisson

[13] B. Bhushan (Ed.), Nanotribology and Nanomechanics: An Introduction, Springer, Berlin, (2005).
[14] M. F. Doerner and W. D. Nix, A method for interpreting the data from depth sensing indentation instruments, Journal of Materials Research, Vol.1, pp. 601–609, (1986).
[15] W. C. Oliver and G. M. Pharr, An improved technique for determining hardness and elastic modulus using load and displacement sensing indentation experiments, Journal of Materials Research, Vol.7, pp.1564–1583, (1992).
[16] K.L. Johnson, Contact Mechanics, Cambridge University Press, Cambridge, pp. 11-104, (1985).
[17] I.N. Sneddon, The Relation between Load and Penetration in the Axisymmetric Boussinesq Problem for a Punch of Arbitrary Profile, International Journal of Engineering Science, Vol.3, pp. 47-57, (1995).

Προκειμένου να προσδιοριστεί ο λόγος της ελαστικής παραμόρφωσης (πάνω από την περιοχή επαφής) προς την συνολική ελαστική παραμόρφωση, χρησιμοποιούμε τις αντίστοιχες αναλυτικές σχέσεις του Sheddon. Για κώνο 1819[37,45]:

$$w(r) = \left(\frac{\pi}{2} - \frac{r}{\alpha} \right) \alpha \tan a, r \le a \tag{1.6}$$

$$w(x) = \frac{-2h}{\pi\alpha} \left(\alpha \sin^{-1}(\frac{a}{\rho}) - r + \sqrt{r^2 - \alpha^2} \right), r > a \tag{1.7}$$

Όπου, ***r***: η αξονική θέση (r=0 στο κέντρο της επαφής) και ***α*** : η ακτίνα της επαφής

Από τις παραπάνω εξισώσεις προκύπτει τελικά ότι :

$$h_s / h_{\max,e} = 1 - 2\pi \tag{1.8}$$

Από την παραπάνω σχέση προκύπτει, ότι για ένα στερεό εκ περιστροφής για το οποίο είναι γνωστές οι αναλυτικές σχέσεις από τη θεωρία ελαστικής επαφής και άρα ο λόγος , το βάθος επαφής μπορεί να υπολογιστεί από την παρακάτω σχεση, λαμβάνοντας υπόψη ότι $h_{\max} = h_{\max,e} + h_0$:

$$h_c = h_{\max}(1 - X) + Xh_0 \tag{1.9}$$

Με προσαρμογή των δεδομένων της καμπύλης αποφόρτισης μπορεί να προσδιοριστεί η ακαμψία, S (stiffness). Η πρώτη παράγωγος dP / dh στο καλείται ακαμψία της επαφής (contactstiffness, S). Οι Oliver και Pharr έδειξαν ότι διαφορίζοντας τις αναλυτικές σχέσεις φορτίου– μετατόπισης του Sneddon για εντυπωτές με σχήμα στερεού εκ περιστροφής μπορεί να προσδιοριστεί το μέτρο ελαστικότητας, εάν είναι γνωστή η επιφάνεια επαφής, μέσω της σχέσης[20]:

$$S = \frac{2}{\sqrt{\pi}} \sqrt{\mathrm{A}_c} \frac{E}{(1 - \nu^2)} \tag{1.10}$$

Η παραπάνω σχέση προέκυψε σύμφωνα με την παραδοχή ότι ο εντυπωτής είναι άκαμπτος. Στην πραγματικότητα, ο εντυπωτής παραμορφώνεται ελαστικά. Η ενσωμάτωση

[18] T. Chudoba, Measurement of Hardness and Young's Modulus by Nanoindentation, in Book Nanostructured Coatings, Albano Cavaleiro and Jeff Th. M. De Hosson (Editors), Springer, New York, pp.216-260, (2006).
[19] W. C. Oliver and G. M. Pharr, An improved technique for determining hardness and elastic modulus using load and displacement sensing indentation experiments, Journal of Materials Research, Vol.7, pp.1564–1583, (1992).
[20] G. M. Pharr, W. C. Oliver, and F. R. Brotzen, On the generality of the relationship between contact stiffness, contact area, and elastic modulus during indentation, Journal of Materials Research, Vol.7, pp. 613–618, (1992).

της παραμόρφωσης του εντυπωτή στο μοντελο γίνεται με βάση τη γενική σχέση από τη θεωρία ελαστικότηταςπου δίνει το λόγο των παραμορφώσεων στην διεύθυνση εφαρμογής της δύναμης δύο σωμάτων αυθαίρετου σχήματος των οποίων η επιφάνεια επαφής είναι κάθετη στη διεύθυνση της δύναμης[21]:

$$\frac{w_i}{w_s} = \frac{(1-\nu_i^2)E_s}{(1-\nu_s^2)E_i} \tag{1.11}$$

όπου $\boldsymbol{\nu}$: ο λόγος Poisson

$\boldsymbol{E}$: το μέτρο Young

i, s: δείκτες για τον εντυπωτή και το δείγμα αντίστοιχα

Με βάση αυτή τη σχέση ορίζεται το <u>σύνθετο μέτρο ελαστικότητας</u> <u>E_r</u>(reducedmodulus)[22][23] :

$$\frac{1}{E_r} = \frac{(1-\nu_i^2)}{E_i} + \frac{(1-\nu_s^2)}{E_s} \tag{1.12}$$

και η εξίσωση 1.10 τροποποιείται αντίστοιχα [24][25][26]:

$$S = \frac{2}{\sqrt{\pi}}\sqrt{\mathrm{A}_c}E_r \tag{1.13}$$

Οι Oliver και Pharr πρότειναν τη χρησιμοποίηση του παράγοντα ε για τον προσδιορισμό του βάθους διείσδυσης. Συγκεκριμένα, παρατήρησαν ότι για εντυπωτές με σχέση φορτίου – μετατόπισης του τύπου $P = ah^m$, όπως κωνικοί ή κυλινδρικοί ισχύει[27]:

$$\frac{P}{S} = \frac{P}{(dP/dh)} = \frac{ah^m}{amh^{m-1}} = \frac{h}{m} \tag{1.14}$$

Η σχέση (1.14) αφορά μόνο τις ελαστικές παραμορφώσεις άρα:

[21] T. Chudoba, Measurement of Hardness and Young's Modulus by Nanoindentation, in Book Nanostructured Coatings, Albano Cavaleiro and Jeff Th. M. De Hosson (Editors), Springer, New York, pp.216-260, (2006).
[22] Metals Handbook, Vol. 8: Mechanical Testing and Evaluation, ASM International, (2000)
[23] L. Hay and G.M. Pharr, Instrumented Indentation Testing, in Metals Handbook, Vol. 8: Mechanical Testing and Evaluation, ASM International, pp.232-243, (2000).
[24] B. Bhushan (Ed.), Nanotribology and Nanomechanics: An Introduction, Springer, Berlin, (2005).
[25] B. Poon, A Critical Appraisal of Nanoindentation woth Application to Elastic-Plastic and Soft Materials, PhD Thesis, California Institute of Technology, California, (2009).
[26] Κ.Α. Χαριτίδης, Νανοδομές και Νανοϋλικά: Σύνθεση, Ιδιότητες και Εφαρμογές, Εκδόσεις ΕΜΠ, Αθήνα, σσ.107-142, (2007).
[27] W. C. Oliver and G. M. Pharr, An improved technique for determining hardness and elastic modulus using load and displacement sensing indentation experiments, Journal of Materials Research, Vol.7, pp.1564–1583, (1992).

$$\frac{P_{\max}}{S_{\max}} = \frac{h_{\max,e}}{m} \tag{1.15}$$

Ορίζοντας τον παράγοντα **ε** ως[28]:

$$\varepsilon = m \cdot \left(\frac{h_s}{h_{\max,e}} \right) \tag{1.16}$$

προκύπτει η σχέση:

$$h_c = h_{\max} - \varepsilon \frac{P_{\max}}{S_{\max}} \tag{1.17}$$

<u>Ελαστοπλαστική θεώρηση</u>

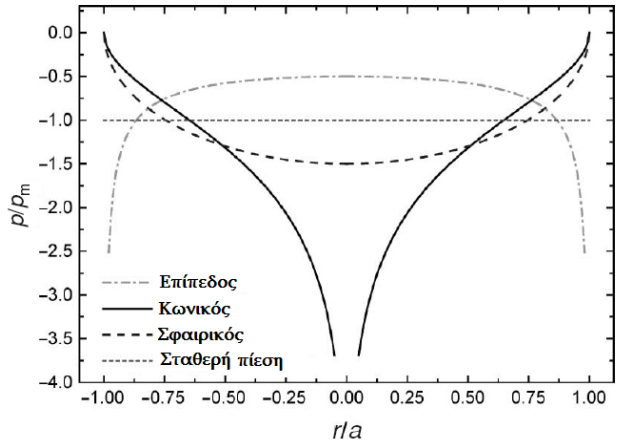

Σχήμα 1.4:Κατανομή της πίεσης (p_m) στην περιοχή της επαφής ακτίνας α για πλήρως ελαστική επαφή.

Παρατηρώντας το σχήμα 1.4, προκύπτει ότι για κωνικό εντυπωτή η πίεση στο κέντρο της επαφής γίνεται άπειρη. Το ίδιο ισχύει στα άκρα για εντυπωτή επίπεδο. Σε τόσο υψηλές πιέσεις όλα τα υλικά υπόκεινται σε πλαστική παραμόρφωση και επομένως σημαντική μείωση της πίεσης. Οι Oliver και Pharr έχουν δείξει ότι η καμπύλη αποφόρτισης για ελαστοπλαστικές διεισδύσεις μπορεί να περιγραφεί από μια συνάρτηση της μορφής[293031]:

[28] W. C. Oliver and G. M. Pharr, An improved technique for determining hardness and elastic modulus using load and displacement sensing indentation experiments, Journal of Materials Research, Vol.7, pp.1564–1583, (1992).
[29] T. Chudoba, Measurement of Hardness and Young's Modulus by Nanoindentation, in Book Nanostructured Coatings, Albano Cavaleiro and Jeff Th. M. De Hosson (Editors), Springer, New York, pp.216-260, (2006).

(1.18)

$$P = K(h - h_0)^m$$

Για εντυπωτές γεωμετρίας Berkovich οι πειραματικές τιμές που βρέθηκαν για τον εκθέτη m είναι 1,2-1,6, ενώ η καλύτερη τιμή για τον παράγοντα ε ήταν 0,75 ο οποίος προκύπτει για m=1,5. Ο εκθέτης m αντιστοιχεί σε σφαιρικό εντυπωτή και όχι σε πυραμιδικό (m=2). Ο λόγος που συμβαίνει έγκειται στην αλλαγή κατανομής πίεσης λόγω πλαστικής παραμόρφωσης. Παρότι χρησιμοποιήθηκε πυραμιδικός εντυπωτής, η κατανομή της πίεσης προσεγγίζει αυτή ενός σφαιρικού εντυπωτή.Συνεπώς, η ελαστοπλαστική θεώρηση απαιτεί τροποποίηση του παράγοντα ε για τον υπολογισμό του πραγματικού βάθους επαφής από την εξίσωση 1.17. Το πρότυπο ISO 14577 προτείνει τιμή 0.75 για διεισδύσεις με Vickers και Berkovich, όμως αυτή είναι μια προσέγγιση και, ανάλογα με το υλικό, οι αποκλίσεις μπορεί να είναι σημαντικές[32][33]. Οι Woirgardetal. πρότειναν μία συνάρτηση υπολογισμού του ε που εξαρτάται μόνο από τον εκθέτη της σχέσης (1.18) [34][35]:

$$\varepsilon(m) = m\left[1 - \frac{2(m-1)\Gamma\left(\frac{m}{2(m-1)}\right)}{\sqrt{\pi}\Gamma\left(\frac{1}{2(m-1)}\right)}\right] \qquad (1.19)$$

1.2.2 Μέθοδος Oliver-Pharr για εντυπωτές μη αξονικής συμμετρίας

Στα περισσότερα πειράματα νανοσκληρομέτρησης χρησιμοποιούνται εντυπωτές μη αξονικής συμμετρίας. Ενώ αρχικά χρησιμοποιήθηκε πολύ ο εντυπωτής τύπου Vickers (πυραμίδα με τέσσερα επίπεδα που δεν συγκλίνουν σε ένα σημείο), πλεόν επικρατεί η χρήση εντυπωτή τύπου Berkovich (τριγωνική πυραμίδα), όπου η αιχμηρή ακίδα κατασκευάζεται πιο εύκολα (μικρότερη καμπυλότητα). Επίσης,η Berkovich έχει τον ίδιο λόγο επιφάνειας προς βάθος διείσδυσης με τη Vickers, καθιστώντας έτσι τα αποτελέσματα, στο μέτρο του δυνατού, συγκρίσιμα με αυτά της Vickers[36][37][38][39].

---

[30] M. F. Doerner and W. D. Nix, A method for interpreting the data from depth sensing indentation instruments, Journal of Materials Research, Vol.1, pp. 601–609, (1986).
[31] A. Bolshakov, W.C. Oliver and G.M. Pharr, An explanation for the shape of nanoindentation unloading curves based on finite element simulation, Fall meeting of the Materials Research Society (MRS), Boston, MA (United States), (28 Nov - 9 Dec 2001).
[32] B. Bhushan (Ed.), Nanotribology and Nanomechanics: An Introduction, Springer, Berlin, (2005).
[33] B. Poon, A Critical Appraisal of Nanoindentation woth Application to Elastic-Plastic and Soft Materials, PhD Thesis, California Institute of Technology, California, (2009)
[34] J. Woirgard, J.-C. Dargenton, An alternative method for penetration depth determination in nanoindentation measurements, Journal of Materials Research, Vol.12, pp.2455-2458, (1996).
[35] M. Martin, M. Troyon, Fundamental relations used in nanoindentation: Critical examination based on experimental measurements, Journal of Materials Research, Vol.17, p.2227, (2002).
[36] T. Chudoba, Measurement of Hardness and Young's Modulus by Nanoindentation, in Book Nanostructured Coatings, Albano Cavaleiro and Jeff Th. M. De Hosson (Editors), Springer, New York, pp.216-260, (2006).

Η ισχύς της μεθόδου Oliver–Pharr για εντυπωτές μη αξονικής συμμετρίας δεν έχει αποδειχθεί μαθηματικά. Ωστόσο, έχουν γίνει πολλές προσπάθειες προσαρμογής της μέσω κλασσικών μεθόδων αριθμητικής ανάλυσης και, πιο πρόσφατα, πεπερασμένων στοιχείων (FEM), για πλήρως ελαστική επαφή. Από τις πρώτες και πιο γνωστές μελέτες, ήταν αυτή του King[40], ο οποίος κατέληξε μέσω αριθμητικής ανάλυσης στην προσαρμογή της σχέσης (1.13) μέσω μιας σταθεράς β εξαρτώμενης από τη γεωμετρία του εντυπωτή:

$$S = \frac{2}{\sqrt{\pi}} \beta \sqrt{\mathrm{A}_c} E_r \qquad (1.20)$$

Όπου, β = 1.000 για κυκλική επιφάνεια επαφής

β = 1.034 για τριγωνική επιφάνεια επαφής

β = 1.012 για τετραγωνική επιφάνεια επαφής

Με μια παρόμοια ανάλυση, ο Bilodaeu βρήκε μια προσεγγιστική λύση για πυραμιδικούς εντυπωτές [41]. Οι Vlassak και Nix ακολουθώντας μια παρόμοια μέθοδο με αυτήν του King, αλλά με ανισοτροπική θεώρηση του δείγματος, βρήκαν ότι το μέτρο ελαστικότητας που υπολογίζεται με τριγωνικό εντυπωτή είναι 5-6% υψηλότερο από το αντίστοιχο για εντυπωτές με αξονική συμμετρία και μεταβάλλεται ελάχιστα με τον προσανατολισμό του εγχαράκτη στο επίπεδο διείσδυσης [42]. Οι Giannakopoulosetal. σύγκριναν τα αποτελέσματα για την ακαμψία μέσω μιας πολύ ακριβούς FE ανάλυσης για Berkovich με αυτά της εξίσωσης 1.19 του King και βρήκαν ότι η απόκλιση κυμαίνεται μέχρι 5% [43]. Οι Gao και Wu απέδειξαν ότι η ακαμψία επαφής ενός στρωματικού υλικού δεν εξαρτάται ισχυρά από το σχήμα της κάθετης τομής του εντυπωτή, εάν αυτό δεν αποκλίνει πολύ από κύκλο[44] . Ο Hendrix έχει προσδιορίσει την τιμή του β θεωρώντας σταθερό προφίλ πίεσης επαφής για τριγωνική και τετραγωνική επαφή [45].

---

[37] B. Bhushan (Ed.), Nanotribology and Nanomechanics: An Introduction, Springer, Berlin, (2005).
[38] B. Poon, A Critical Appraisal of Nanoindentation woth Application to Elastic-Plastic and Soft Materials, PhD Thesis, California Institute of Technology, California, (2009).
[39] L. Hay and G.M. Pharr, Instrumented Indentation Testing, in Metals Handbook, Vol. 8: Mechanical Testing and Evaluation, ASM International, pp.232-243, (2000).
[40] R. B. King, Elastic analysis of some punch problems for a layered medium, International Journal of Solids Structure, Vol.23, No 12, pp.1657–1664, (1987).
[41] G. G. Bilodeau, Regular pyramid punch problem, Journal of Applied Mechanics, Vol.59, pp. 519–523, (1992).
[42] J.J. Vlassak and W.D. Nix, Measuring the Elastic Properties of Anisotropic Materials by Means of Indentation Experiments, Journal of the Mechanics and Physics of Solids, Vol.42, p. 1223, (1994).
[43] A.E. Giannakopoulos, P.L. Larsson, E. Soderlund, et al., Analysis of Berkovich Indentation, International Journal of Solids Structure, Vol.33, pp.221-248, (1996).
[44] H. Gao and T.W. Wu, A note on the elastic contact stiffness of a layered medium, Journal of Materials Research, Vol.8, pp. 3229–3233, (1993).
[45] M. T. Hendrix, The use of shape correction factors for elastic indentation measurements, Journal of Materials Research, Vol.10, pp. 255–258, (1995).

Πίνακας 1.1: Τιμές του διορθωτικού παράγοντα μη αξονικής συμμετρίας για τριγωνικό σχήμα κάθετης τομής εντυπωτή.

Μέθοδος	Τιμή β	Εντυπωτές	Αναφορά
Αναλυτικά, Ελαστική θεώρηση	1.034	Flat Punch (επίπεδος)	**56**
FEM, Ελαστοπλαστική θεώρηση	1.055	Πυραμιδικός (Berkovich)	**62**
FEM, Ελαστοπλαστική θεώρηση	1.136	Πυραμιδικός (Berkovich)	**60**
Αναλυτικά, Ελαστική θεώρηση	1.141	Πυραμιδικός	**58**
Αναλυτικά, Ελαστική Ανισοτροπική θεώρηση	1.058	Flat Punch (επίπεδος)	**59**
Σταθερή πίεση στην περιοχή επαφής	1.0226	-	**61**

Όπως φαίνεται από τον πίνακα 1.1, η μικρότερη διόρθωση προκύπτει από τη θεώρηση σταθερής πίεσης του Hendrix. Όπως, όμως, προαναφέρθηκε, οι άπειρες πιέσεις στην ακίδα θα μειωθούν από την πλαστική παραμόρφωση, άρα αυτή είναι η πιθανότερη κατανομή της πίεσης. Για αυτό το λόγο, στο πρότυπο ISO 14577 προτείνεται να μη χρησιμοποιείται διόρθωση για Berkovich εντυπωτές (β=1). Στην πραγματικότητα, είναι πιθανές αποκλίσεις από την τιμή 1 για υλικά υψηλής ελαστικότητας, με μικρή πλαστική ζώνη, όμως το σφάλμα που υπεισέρχεται είναι μικρότερο του 5%.

Κεφάλαιο 2. Πέρα από τη..νανοσκληρομέτρηση

2.1 Διορθώσεις – Βελτιώσεις της μεθόδου Oliver-Pharr

2.1.1 Επιφάνεια Επαφής – καμπυλότητας ακίδας

Για τον υπολογισμό τιμών των νανομηχανικών ιδιοτήτων με το μοντέλο Oliver-Pharr είναι σημαντικός ο υπολογισμός της ακριβούς τιμής της επιφάνειας επαφής της ακίδας με το προς εξέταση υλικό. Ιδανικά η επιφάνεια αυτή προσδιορίζεται μέσω γεωμετρικών σχέσεων σχετικών με τη γεωμετρία του εντυπωτή. Στην πραγματικότητα, κανένας εντυπωτής δεν είναι ιδανικός, δηλαδή δεν έχει ιδανικά αιχμηρό άκρο. Οι περισσότεροι εντυπωτές έχουν καμπυλότητα ακίδας 50 nm έως και μερικά εκατοντάδες nm. Το πρότυπο ISO 14577 θέτει τα 200 nm ως άνω όριο για μετρήσεις στη νανοκλίμακα. Το βασικό πρόβλημα που προκύπτει είναι ότι με τη χρήση του εντυπωτή λόγω φθοράς η καμπυλότητα δεν είναι σταθερή αλλά αυξάνεται. Για τον υπολογισμό της καμπυλότητας υπάρχουν δύο μέθοδοι: α) άμεση μέτρηση μέσω μικροσκοπίου ατομικών δυνάμεων (AFM) και β) έμμεση μέτρηση υπολογίζοντας τη συνάρτηση μέσω διεισδύσεων σε ισοτροπικό υλικό γνωστού μέτρου ελαστικότητας. Στην παρούσα διπλωματική εργασία εφαρμόστηκε η δεύτερη μέθοδος (και συγκεκριμένα αυτή των Oliver-Pharr)[46][47]. Πρόσφατα, προτάθηκε από τον Oliver[48] και βελτιώθηκε από τους Troyonetal. μια εναλλακτική μέθοδος υπολογισμού του μέτρου ελαστικότητας που δεν απαιτεί τον υπολογισμό της επιφάνειας επαφής. Η μέθοδος αυτή βασίζεται στην ακαμψία τόσο από την καμπύλη φόρτισης όσο και από την καμπύλη αποφόρτισης (two-slopemethod).

[46] M. F. Doerner and W. D. Nix, A method for interpreting the data from depth sensing indentation instruments, Journal of Materials Research, Vol.1, pp. 601–609, (1986)..
[47] M. Martin, M. Troyon, Fundamental relations used in nanoindentation: Critical examination based on experimental measurements, Journal of Materials Research, Vol.17, p.2227, (2002).
[48] Y. V. Milman, B. A. Galanov and S. I. Chugunova, Plasticity Characteristic Obtained Through Hardness Measurement, Acta Mater., Vol.41, No.9, pp. 2523-2532, (1993).

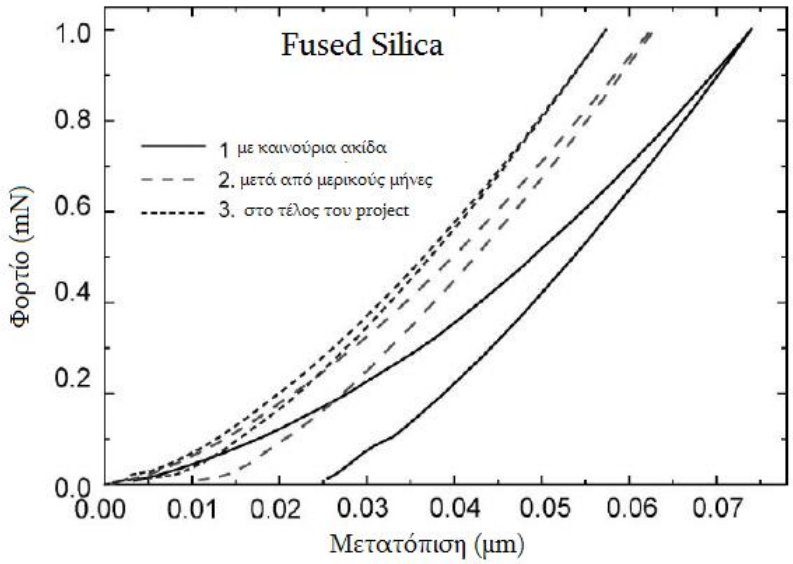

Σχήμα 2.1: Επίδραση της φθοράς (αύξηση της καμπυλότητας) της ακίδας του εντυπωτή.

Η καμπυλότητα της ακίδας έχει συσχετιστεί με τη μετάβαση από την πλήρως ελαστική στην ελαστοπλαστική συμπεριφορά. Όσο πιο αιχμηρή είναι άκρη της ακίδας τόσο πιο γρήγορα (σε μικρότερα φορτία) θα εμφανιστεί η μετάβαση. Το φαινόμενο αποδίδεται στη μεγαλύτερη συγκέντρωση τάσεων, η οποία ευνοεί την έναρξη της πλαστικής ροής[49].
Οι ακίδες ανάλογα με την γεωμετρία τους διακρίνονται σε αιχμηρές (π.χ. Berkovich, Vickers, Knoop κτλ.) και σφαιρικές. Συγκεκριμένα στην παρακάτω εικόνα φαίνονται οι γεωμετρίες για ακίδα Berkovich και σφαιροκωνική [50].

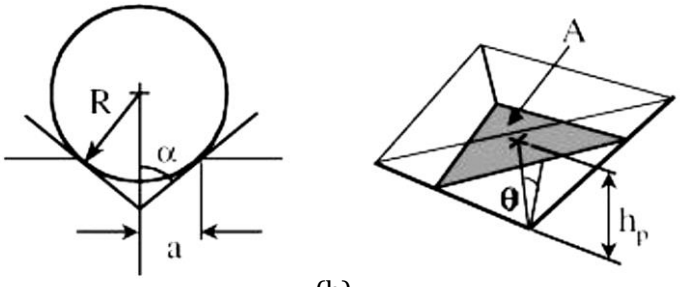

(a) (b)

Σχήμα2.2: Γεωμετρικές παράμετροι για ακίδα (a) Berkovich και (b) conospherical

[49]K.L. Johnson, Contact Mechanics, Cambridge University Press, Cambridge, pp. 11-104, (1985).
[50] Moseson A. J.: "Spherical Nanoindentation: Insights & Improvements, Including Stress-Strain Curves & Effective Zero Point Determination" Thesis, Drexel University, 2007

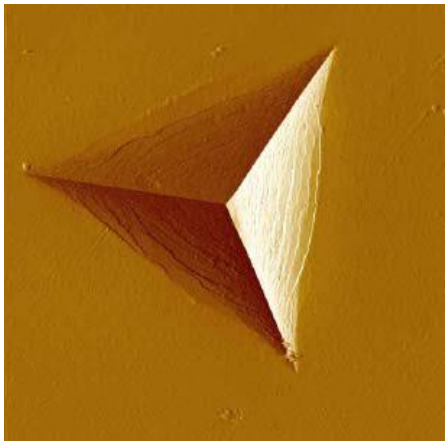

Σχήμα2.3: Το αποτύπωμα μιας ακίδας Berkovich

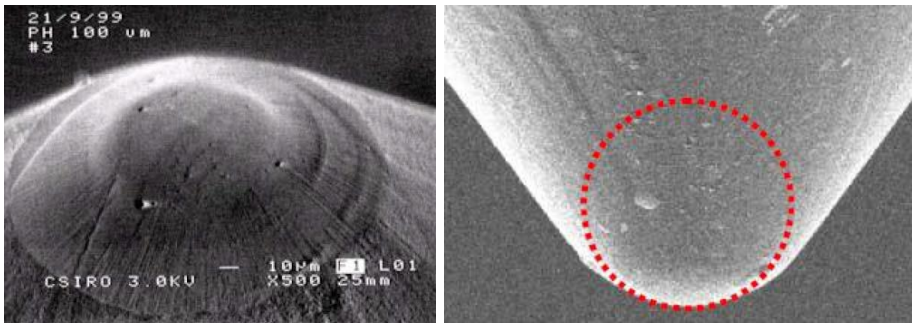

Σχήμα2.4: Conospherical ακίδα.

Σε μια αιχμηρή ακίδα, ο λόγος της ακτίνας της επιφάνειας επαφής προς το βάθος διείσδυσης (ή αντίστοιχα ο λόγος της διαμέτρου της επιφάνειας επαφής προς το βάθος διείσδυσης $d_1/\delta_1 \approx d_2/\delta_2$), παραμένει σταθερός με την αύξηση του εφαρμοζόμενου φορτίου. Αυτές οι ακίδες έχουν την ιδιότητα της «Γεωμετρικής ομοιότητας». Έτσι η τιμή της σκληρότητας καθίσταται ανεξάρτητη από το εφαρμοζόμενο φορτίο. Στις σφαιρικές ακίδες η ακτίνα της επιφάνειας επαφής αυξάνει ταχύτερα σε σχέση με το βάθος διείσδυσης, καθώς το φορτίο αυξάνει ($a_1/\delta_1 \neq a_2/\delta_2$), οπότε και η τιμή της σκληρότητας μεταβάλλεται ανάλογα με το εφαρμοζόμενο φορτίο [51].

[51] Fischer-Cripps A. C.: "Introduction to Contact Mechanics" © 2000 Springer- Verlag New York, Inc.

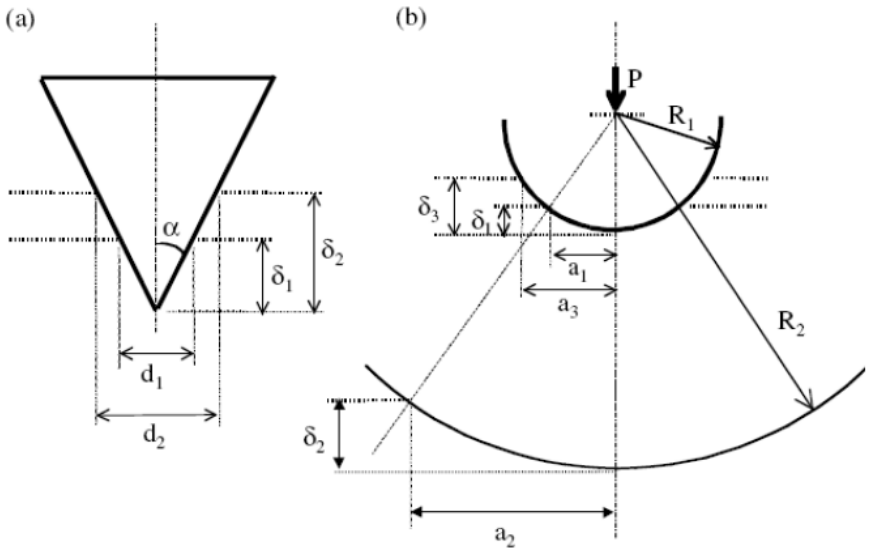

Σχήμα2.5: Γεωμετρική ομοιότητα για (a) αιχμηρή (πυραμιδική ή κωνική) ακίδα (b) σφαιρική ακίδα

Η πλαστική παραμόρφωση στην περίπτωση της αιχμηρής ακίδας αρχίζει, σε θεωρητική πάντα βάση, την στιγμή της επαφής της ακίδας με το δείγμα. Με αυτό τον τρόπο, μπορεί να μετρηθεί η σκληρότητα για τα λεπτά υμένια, πριν η ακίδα φτάσει στην διεπιφάνεια ή το υπόστρωμα.

Οι σφαιρικές ακίδες στην ιδανική περίπτωση, παραμορφώνουν ελαστικά το δείγμα όταν έρχονται σε επαφή με αυτό, ενώ στη συνέχεια με την αύξηση του εφαρμοζόμενου φορτίου λαμβάνει χώρα η ομαλή μετάβαση από ελαστική σε ελαστική-πλαστική παραμόρφωση, και στην συνέχεια ακολουθεί η τέλεια πλαστική περιοχή παραμόρφωσης. Η ιδιότητα αυτή χρησιμεύει ιδιαίτερα στην μελέτη μαλακών δειγμάτων. Οι σχέσεις που συνδέουν το φορτίο με την μετατόπιση για αιχμηρή ακίδα και σφαιρική ακίδα αντίστοιχα είναι οι εξής:

$$P = \frac{2}{\pi(1-\nu^2)\tan\varphi} Eh^2 \qquad (2.1)$$

$$P = \frac{4\sqrt{R}}{3(1-\nu^2)} Eh^{3/2} \qquad (2.2)$$

Οι αντίστοιχες σχέσεις για τις επιφάνειες επαφής για αιχμηρή και σφαιρική ακίδα είναι:

$$A = 3\sqrt{3}h_p^2 \tan\theta \qquad (2.3)$$

$$A = 2\pi R h_p \qquad (2.4)$$

Επομένως για τις αντίστοιχες σκληρότητες θα ισχύει:

$$H = \frac{P}{A} = \sigma\tau\alpha\theta. \quad (2.5)$$

$$H = \sigma\tau\alpha\theta.\cdot h_p^{1/2} \quad (2.6)$$

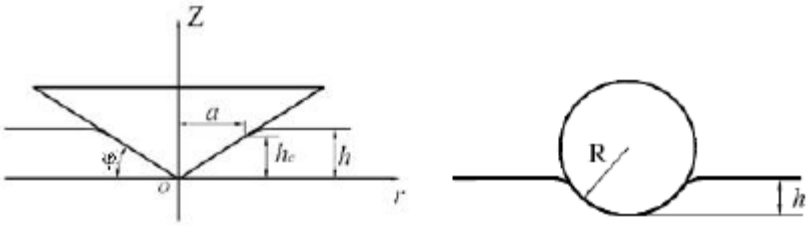

Σχήμα2.6: Γεωμετρικά χαρακτηριστικά για (a) αιχμηρή (πυραμιδική ή κωνική) και (b) σφαιρική ακίδα

Η μορφή της γραφικής παράστασης $H=H(h_p)$ για σφαιρική ακίδα, δεν έχει άνω όριο κι αυτό μπορεί να αποδειχθεί διερευνώντας τα ακρότατα της συνάρτησης, μέσω της παραγώγου:

$$\frac{dH}{dh} = \frac{d(\sigma\tau\alpha\theta.\cdot h_p^{1/2})}{dh} = \frac{1}{2h^{1/2}} \Rightarrow \frac{dH}{dh} \neq 0 \Rightarrow \Delta\text{εν παρουσιάζει μέγιστο} \quad (2.7)$$

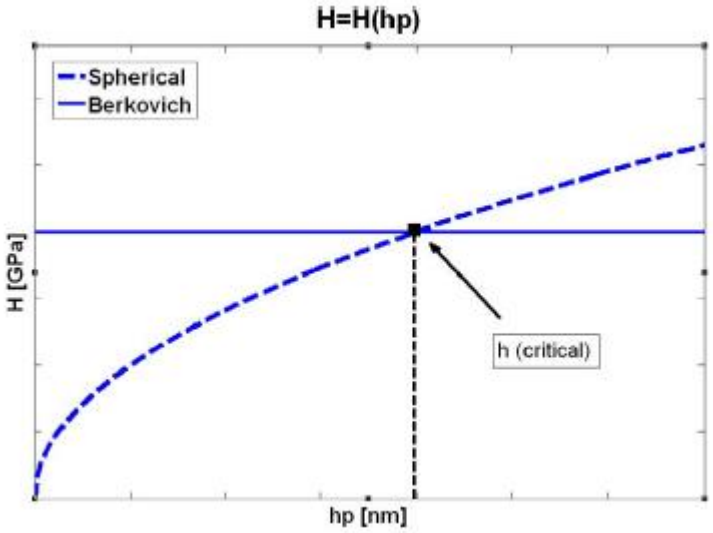

Εικόνα 2.7: Διάγραμμα που δείχνει την μεταβολή στην τιμή της σκληρότητας που υπολογίζεται με βάση τις πειραματικές μετρήσεις αιχμηρής και σφαιρικής ακίδας

Εξισώνοντας τις σχέσεις που δίνουν την σκληρότητα για αιχμηρή και σφαιρική ακίδα, είναι δυνατόν να προσδιοριστεί θεωρητικά η τιμή της μετατόπισης h (critical) στην

οποία θεωρείται ότι ξεκινάει η περιοχή της τέλειας πλαστικής ζώνης παραμόρφωσης για σφαιρική ακίδα.

$$h_{critical} = \frac{R}{3}\cos^2\varphi\cos^2\theta \qquad (2.8)$$

Οι παράμετροι R, και φ και θ εξαρτώνται από τα γεωμετρικά χαρακτηριστικά της σφαιρικής και αιχμηρής ακίδας αντίστοιχα [52].

2.1.2 Ακτινική παραμόρφωση

Η διάμετρος επαφής θεωρείται προσεγγιστικά ότι δεν αλλάζει μετά την αποφόρτιση. Αυτή η παραδοχή ισχύει με ικανοποιητική ακρίβεια για μαλακά υλικά. Για υλικά με μεγάλο μέτρο ελαστικότητας η ελαστική επαναφορά μπορεί να συνοδεύεται από σημαντική αλλαγή στην ακτίνα επαφής.

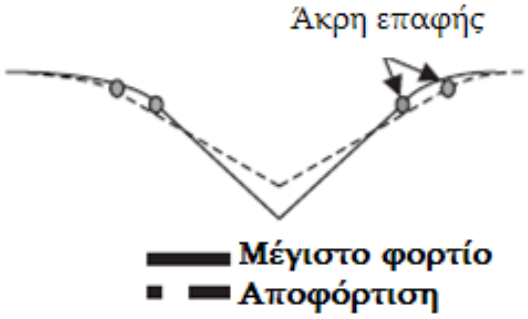

Σχήμα 2.8: Μεταβολή της επιφάνειας επαφής μετά την αποφόρτιση.

Για εντυπωτές αξονικής συμμετρίας η ακτινική παραμόρφωση υπολογίζεται αναλυτικά βάσει των σχέσεων από τη θεωρία της ελαστικότητας [53]. Οι Bolshakovetal.[54] έδειξαν ότι χρειάζεται διόρθωση, καθώς το σχήμα της επιφάνειας επαφής σε κάθετη τομή ως προς την επιφάνεια του δείγματος δεν είναι γραμμικό, αλλά τοξοειδές. Το φαινόμενο αυτό είναι πιο έντονο για αιχμηρούς εντυπωτές και εξαρτάται από τον λόγο Poisson του υλικού. Οι Hayetal. [55]πρότειναν έναν διορθωτικό παράγοντα y για την συνάρτηση της γωνίας κεντρικού άξονα του εντυπωτή και του λόγου Poisson του υλικού. Στις περισσότερες περιπτώσεις νανοσκληρομετρήσεων, ο λόγος Poisson δεν είναι γνωστός ή αν

[52] Fischer-Cripps A. C.: "Introduction to Contact Mechanics" © 2000 Springer- Verlag New York, Inc
[53] Y.V. Milman, Plasticity Characteristic Obtained by Indentation, Journal of Physics D: Applied Physics, Vol.41, p.074013, (2008).
[54]A. Bolshakov, W.C. Oliver and G.M. Pharr, An explanation for the shape of nanoindentation unloading curves based on finite element simulation, Fall meeting of the Materials Research Society (MRS), Boston, MA (United States), (28 Nov - 9 Dec 2001).
[55]J.C. Hay and G.M. Pharr, Critical issues in measuring the mechanical properties of hard films on soft substrates by nanoindentation techniques, Fall meeting of the Materials Research Society, Boston, MA (United States), (1-5 Dec 1997).

είναι, η ακρίβειά του είναι αμφίβολη. Για να ισχύει η διόρθωση αυτή, ο παράγοντας y θα πρέπει να ληφθεί υπόψη κατά τον προσδιορισμό της συνάρτησης $A_c = f(h_c)$ (areafunctionmethod). Σε περίπτωση που δεν εφαρμόζεται η διόρθωση, το μέγεθος του σφάλματος θα εξαρτάται από τη διαφορά του λόγου Poisson του μετρούμενου δείγματος και του πρότυπου υλικού που χρησιμοποιείται για τον υπολογισμό της συνάρτησης επιφάνειας επαφής[56].

2.2 Ακαμψία ακίδας

Για υλικά όπως πολύ σκληρές επικαλύψεις η ακαμψία της ακίδας μπορεί να είναι συγκρίσιμη με την ακαμψία του μετρούμενου υλικού, εισάγοντας σφάλματα στη μετρούμενη μετατόπιση. Έτσι, προκειμένου να ληφθούν αξιόπιστες μετρήσεις θα πρέπει να προσδιοριστεί η ακαμψία της ακίδας. Χρησιμοποιώντας το αντίστροφο μέγεθος της ακαμψίας (*compliance*) [57]:

$$C_t = C_f + C_s \qquad (2.9)$$

όπου ***f, s, t*** : οι δείκτες για την ακίδα, το πρότυπο δείγμα και το συνολικό αντίστροφο της ακαμψίας αντίστοιχα

2.3 Θερμική Μετατόπιση (ThermalDrift)

Γενικά, οι μετρήσεις μήκους επηρεάζονται από τη θερμική διαστολή του οργάνου και του δείγματος που λαμβάνει χώρα κατά τη διάρκεια της μέτρησης. Για το λόγο αυτό κρίνεται απαραίτητη η παρουσία συντελεστή διόρθωσης για τη θερμική μετατόπιση. Οι τυπικοί χρόνοι διάρκειας μιας μέτρησης νανοεγχάραξης (φόρτιση, αποφόρτιση, χρόνος σταθεροποίησης -holdingtime- στο μέγιστο φορτίο) κυμαίνονται από 30 ως 300 s. Σε αυτό το χρόνο το βάθος δε θα πρέπει να μεταβάλλεται πάνω από 1 nm εξαιτίας θερμικών φαινομένων. Αυτό σημαίνει ότι η θερμοκρασία στο χώρο κατά το χρόνο διεξαγωγής της μέτρησης δε θα πρέπει να μεταβάλλεται πάνω από 1 mK, κάτι που δεν είναι εφικτό για κανένα ανοιχτό σύστημα. Έτσι, συνήθως το όργανο υπολογίζει την μετατόπιση που οφείλεται σε θερμικά φαινόμενα κατά τη διάρκεια του πειράματος [58][59][60].

[56] M. F. Doerner and W. D. Nix, A method for interpreting the data from depth sensing indentation instruments, Journal of Materials Research, Vol.1, pp. 601–609, (1986).
[57] Κ.Α. Χαριτίδης "Νανοδομές και Νανοϋλικά: Σύνθεση, Ιδιότητες και Εφαρμογές" Εκδόσεις ΕΜΠ, Αθήνα, 2007, σσ.107-142
[58] T. Chudoba in "Measurement of Hardness and Young's Modulus by Nanoindentation, in Book Nanostructured Coatings", Albano Cavaleiro and Jeff Th. M. De Hosson (Editors), Springer, New York, 2006, pp.216-260

2.4 Μηδενικό Σημείο (ZeroPoint)

Η μέτρηση της μετατόπισης ξεκινάει από το σημείο πρώτης επαφής του εντυπωτή με το δείγμα. Ο καθορισμός αυτού του σημείου επηρεάζει όλη την καμπύλη φορτίου–μετατόπισης. Η σωστή ανίχνευση της επιφάνειας του δείγματος δεν είναι εύκολη, ειδικά στην νανοκλίμακα. Οι μέθοδοι που χρησιμοποιούνται γενικά είναι δύο: Στην πρώτη, φορτίο και βάθος καταγράφονται και το πρώτο σημείο επαφής καθορίζεται από την πρώτη αύξηση της δύναμης. Το σκαλοπάτι αυτό πρέπει να είναι αρκετά μικρό ώστε η αβεβαιότητα προσδιορισμού του σημείου μηδέν να είναι ικανοποιητικά μικρή. Σε αντίθετη περίπτωση, χρειάζεται μια κατάλληλη προεκβολή των δεδομένων. Η δεύτερη μέθοδος ανιχνεύει την επιφάνεια στο σημείο που η ελάχιστη δυνατή δύναμη επαφής υπερβαίνεται και από αυτό το σημείο αρχίζει η καταγραφή. Πολλές φορές μπορεί να ανιχνεύεται η επιφάνεια πολύ νωρίς, λόγω τραχύτητας ή ταλαντώσεων, οπότε απαιτείται μετατόπιση της καμπύλης προς τα αριστερά [61][62].

2.5 Το φαινόμενο pop-in

Στη βιβλιογραφία αναφέρονται φαινόμενα που σχετίζονται με τη νανοσληρομέτρηση όπως το indentation size effect και το φαινόμενο pop-in. Το φαινόμενο pop-in είναι η απότομη αύξηση της μετατόπισης χωρίς αύξηση του φορτίου κατά τη φάση της φόρτισης του πειράματος της νανο-σκληρομέτρησης και παρατηρείται ως ασυνέχεια στο διάγραμμα φόρτισης-αποφόρτισης (Σχήμα 2.9). Οι εμφάνιση του φαινομένου pop-in επηρεάζει τις μετρήσεις των μηχανικών ιδιοτήτων.

[59] L.Hay and G.Pharr in "Instrumented Indentation Testing", in Metals Handbook, Vol. 8: Mechanical Testing and Evaluation" ASM International, 2000, pp.232-243
[60] B. Poon in "A Critical Appraisal of Nanoindentation woth Application to Elastic-Plastic and Soft Material" PhD Thesis, California Institute of Technology, California, 2009.
[61] T. Chudoba in "Measurement of Hardness and Young's Modulus by Nanoindentation, in Book Nanostructured Coatings", Albano Cavaleiro and Jeff Th. M. De Hosson (Editors), Springer, New York, 2006, pp.216-260
[62] L.Hay and G.Pharr in "Instrumented Indentation Testing", in Metals Handbook, Vol. 8: Mechanical Testing and Evaluation" ASM International, 2000, pp.232-243.

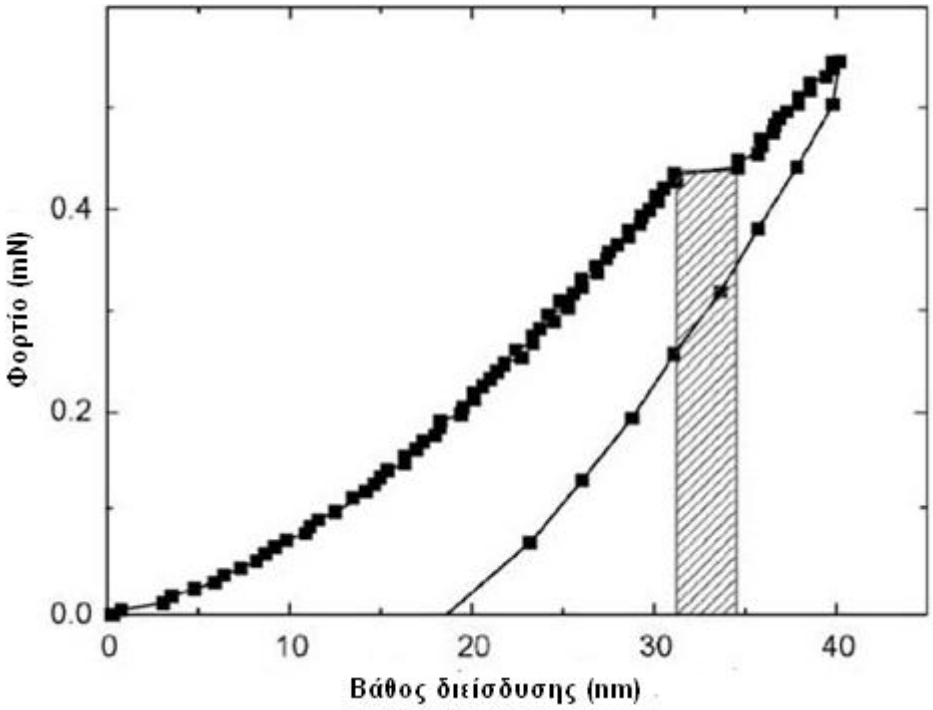

Σχήμα 2.9: Φαινόμενο popin σε διάγραμμα δύναμης-βάθους διείσδυσης κατά τη νανο-σκληρομέτρηση [63]

Αν και το φαινόμενο pop-in παρουσιάζεται σε αρκετά υλικά, ακόμα δεν είναι γνωστός ο μηχανισμός εμφάνισης και εξέλιξής του. Το φαινόμενο popin παρέχει σημαντικές πληροφορίες για το συσχετισμό των μηχανικών ιδιοτήτων με τα μικροδομικά χαρακτηριστικά του προς έλεγχο υλικού (π.χ. με την πλαστική πυρηνοποίηση κατά τη νανοσκληρομέτρηση). Η κοινά αποδεκτή ερμηνεία για την περίπτωση των μετάλλων, χωρίς την ύπαρξη διαταραχών (dislocations), συσχετίζει το πρώτο pop-in (στο χαμηλότερο φορτίο διείσδυσης) με την θεωρητική δύναμη διάτμησης του υλικού και την ομογενή πυρηνοποίηση των διαταραχών. Στη βιβλιογραφία έχει αναφερθεί αξιοσημείωτη μείωση στο φορτίο όπου εμφανίζεται το πρώτο pop-in για νανοδιεισδύσεις στην περιοχή γύρω από τα όρια κόκκων , η οποία σχετίζεται με το φαινόμενο αυτό. Αυτή η ερμηνεία ισχύει τόσο για υλικά όγκου όσο και για λεπτά υμένια. Με τον τρόπο αυτό διαχωρίζεται η περιοχή της πλήρως ελαστικής περιοχής σε χαμηλά φορτία από την ελαστο-πλαστική περιοχή σε υψηλότερα φορτία.

Η εμφάνιση του φαινομένου pop-in σχετίζεται με την κατεργασία που έχει υποστεί η επιφάνεια του υλικού. Στις περισσότερες περιπτώσεις παρατηρείται μετά από

[63] C.A.Charitidis, Local mechanical properties and nanoscale deformation of aluminum and magnesium lightweight alloys, Int. J. Surface science and engineering, accepted for publication (2010)

ενεργοποίηση της επιφάνειας (π.χ. λείανση, φθορά, electropolishing, κλπ), αφού η ενεργοποίηση της επιφάνειας (π.χ. μηχανική λείανση) προκαλεί μια ζώνη παραμόρφωσης στο επιφανειακό στρώμα. Μετά από σύγκριση μετρήσεων στο ίδιο υλικό με ή χωρίς λείανση έχει παρατηρηθεί το φαινόμενο εντονότερο στο υλικό που έχει υποστεί λείανση, γεγονός που αποδίδεται στη μεγαλύτερη πυκνότητα διαταραχών (Σχήμα 2.10). Στην περίπτωση αυτή, το pop-in συνδέεται με την ύπαρξη ατελειών (π.χ. διαταραχές) πριν την εμφάνιση του φαινομένου και ενεργοποίηση τους και όχι σε πυρηνοποίηση διαταραχών. Στη βιβλιογραφία έχει αναφερθεί το φαινόμενο αυτό σε υλικά όπως οι ημιαγωγοί [64]. Οι *Gerberichetal.*[65] θεωρούν ότι οι διαταραχές στα υλικά δημιουργούνται πριν το pop-in και το φαινόμενο αυτό αποδεικνύει την αποτυχία του παθητικού προστατευτικού υμενίου οξειδίου στην επιφάνεια του υλικού. Οι *Mann* και *Pethica*[66] θεωρούν ότι το φαινόμενο pop-in υποδεικνύει την πυρηνοποίηση διαταραχών.

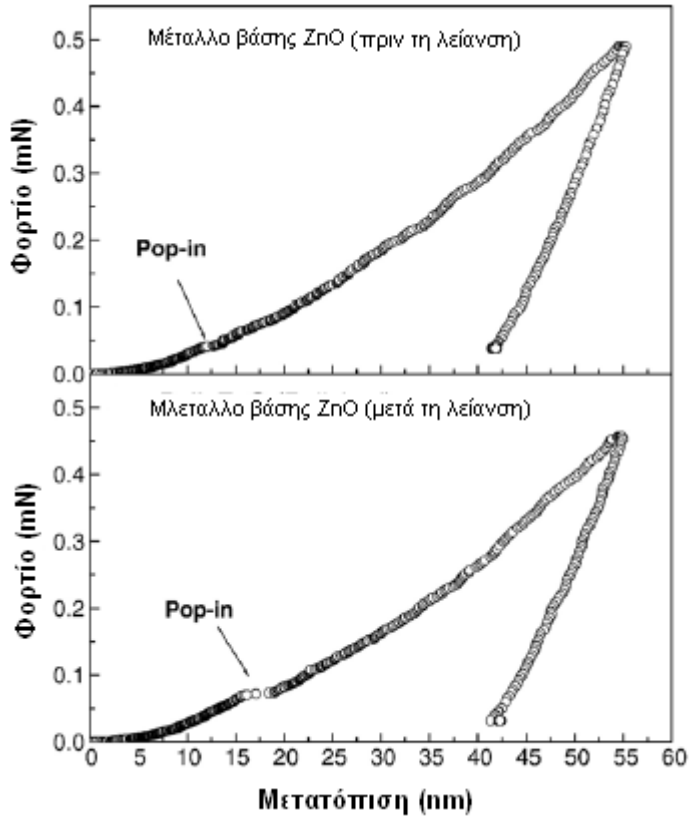

Σχήμα 2.10: Εμφάνιση popin σε υλικό όγκου ZnO με και χωρίς λείανση [67]

Σε εργασίες για τη μηχανική παραμόρφωση υποστρώματος μονοκρυσταλλικού ZnO παρατηρήθηκαν πολλαπλές ασυνέχειες- pop-ins (μετρήσεις με χρήση σφαιρικού

[64] Y.V. Milman, B.A. Galanov and S.I. Chugunova, Plasticity Characteristic Obtained Through Hardness Measurement, Acta Metallurgica et Materiallia, Vol.41, No.9, 1993, pp. 2523-2532.
[65] W.W. Gerberich, J.C. Nelson, E.T. Lilleodden, P. Anderson, J.T. Wyrobek, Acta Mater. 44 (9) (1996), p.3585–3598
[66] A.B. Mann, J.B. Pethica, Langmuir 12 (19) (1996), p.4583–4586
[67] Y.V. Milman, B.A. Galanov and S.I. Chugunova, Plasticity Characteristic Obtained Through Hardness Measurement, Acta Metallurgica et Materiallia, Vol.41, No.9, 1993, pp. 2523-2532.

εγχαράκτη) κατά το πείραμα της νανοσκληρομέτρησης και αποδόθηκαν σε έναρξη διαταραχών. Σε αυτές τις περιπτώσεις (οι οποίες επηρεάζονται από το βάθος διείσδυσης) μια απότομη αύξηση στη μετατόπιση μπορεί να λάβει χώρα σε συγκεκριμένο φορτίο. Σε πολλά πειράματα νανοσκληρομέτρησης τέλος έχει παρατηρηθεί η εμφάνιση διαρροής (yielding) στη νανοκλίμακα η οποία φαίνεται να ελέγχεται από την ομογενή πυρηνοποίηση διαταραχών σε μικρό όγκο του υλικού που υποβάλλεται σε τάση κοντά στη θεωρητική (Yieldstress).

2.6 Επίδραση του υποστρώματος στη νανοδιείσδυση

Ο ακριβής προσδιορισμός των μηχανικών ιδιοτήτων των λεπτών υμενίων με πείραμα νανοδιείσδυσης αποτελεί μία αρκετά δύσκολή υπόθεση, εξαιτίας κυρίως της επίδρασης του υποστρώματος, πάνω στο οποίο έχει αναπτυχθεί το λεπτό υμένιο. Πρακτικός κανόνας αναφέρει ότι διείσδυση της ακίδας σε βάθος μεγαλύτερο από το 10% του πάχους του λεπτού υμενίου προσδιορίζει τις μηχανικές ιδιότητες του συστήματος λεπτό υμένιο /υπόστρωμα και όχι μόνο του λεπτού υμενίου που είναι και το ζητούμενο.

2.7 Indentation Size Effect (ISE)

Αναμένεται τα πειράματα νανοδιείσδυσης ομογενών και ισότροπων υλικών να παρουσιάζουν ίδιες τιμές σκληρότητας και ελαστικότητας αλλά παρατηρείται ότι για διάφορους λόγους οι τιμές αυτές διαφέρουν ανάλογα με το βάθος διείσδυσης. Πολλά υλικά εμφανίζουν indentationsizeeffect κατά το οποίο η σκληρότητα μειώνεται καθώς το βάθος διείσδυσης ή το φορτίο αυξάνεται (σχήμα 2.11). Το ISE παρατηρείται πολλές φορές λόγο της ύπαρξης λεπτών υμενίων οξειδίων με διαφορετικές μηχανικές ιδιότητες. Επίσης η τριβή μεταξύ της ακίδας και του δείγματος αλλά και η γεωμετρία της ακίδας ειδικά σε πολύ μικρά βάθη προκαλούν συχνά ISE[68][69].

[68] Vasarla Nagendra Sekhar (B.Tech, NIT, India), "Nanomechanical characterization of BD 9low-k) thin films and Cu/BD multilayered satcks", National University of Singapore, 2006
[69] Sahin O., Uzun O., Kolemen U.and Ucar N., "Dynamic hardness and reduced modulus determination on the (001) face of β-Sn single crystals by a depth sensing indentation technique", 2007

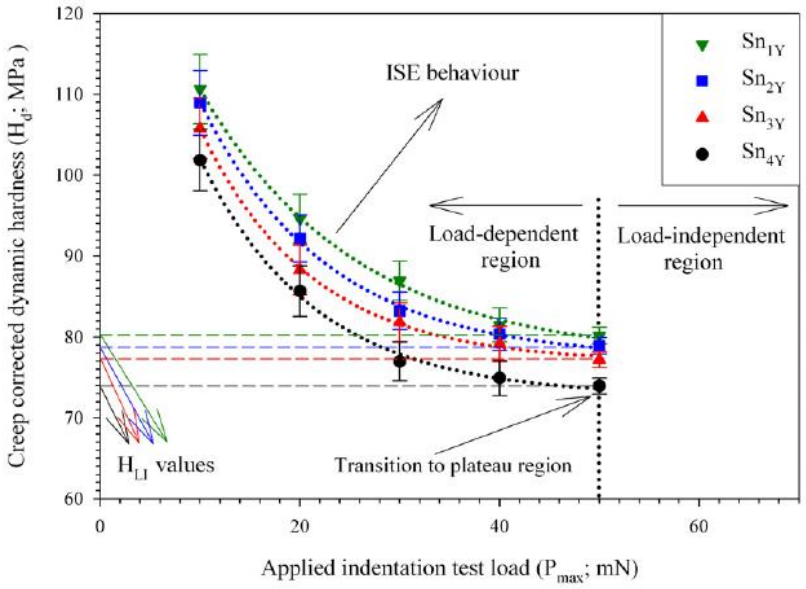

Σχήμα 2.11: Διάγραμμα στο οποίο απεικονίζεται το φαινόμενο ISE

2.8 Φαινόμενο Συσσώρευσης (Pile-upEffect)

Στη μέθοδο Oliver-Pharr για τον προσδιορισμό του βάθους επαφής συνυπολογίζεται η ελαστική βύθιση της επιφάνειας γύρω από την περιοχή επαφής (sink-in) αλλά δεν λαμβάνεται υπόψη το αντίθετο φαινόμενο, δηλαδή η συσσώρευση υλικού (pile-up). Από το σχήμα 2.12 φαίνεται ότι το βάθος επαφής είναι μεγαλύτερο από το μέγιστο βάθος που μετράται, οδηγώντας σε σφάλματα στον υπολογισμό των μηχανικών ιδιοτήτων. Οι Marx και Balke περιέγραψαν το φαινόμενο φορμαλιστικά με τον παράγοντα δ[70]:

$$h_c = \sqrt{\delta} h_{\max}, \qquad \delta<1: \text{sink-in}, \quad \delta>1: \text{pile-up} \tag{2.10}$$

[70]V. Marx and H. Balke, A Critical Investigation of the Unloading Behavior of Sharp Indentation, Acta Metallurgica, Vol.45, No.9, pp.3791-3800, (1997).

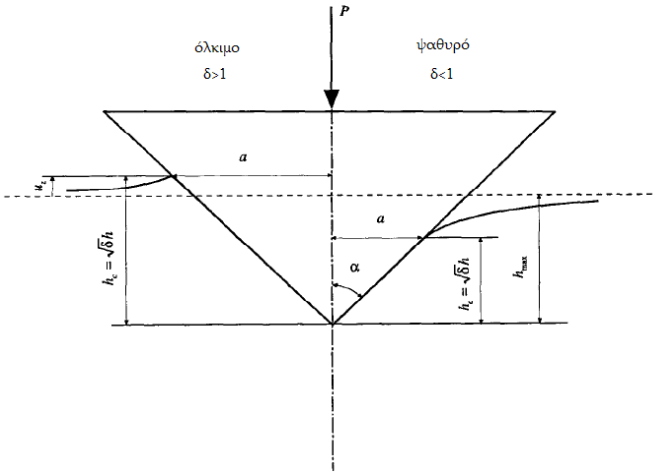

Σχήμα 2.12: Επίδραση των φαινομένων βύθισης και συσσώρευσης στο βάθος επαφής.

Το φαινόμενο της συσσώρευσης αναμένεται να είναι σημαντικό σε μαλακά, όλκιμα υλικά. Σε σκληρά, ψαθυρά υλικά η βύθιση είναι η επικρατούσα συμπεριφορά. Οι Oliver και Pharr μελέτησαν πρόσφατα την αξιοπιστία της μεθόδου τους σε σχέση με τα φαινόμενα συσσώρευσης, χρησιμοποιώντας ως κριτήριο το λόγο h_f/h_{max}. Βρήκαν ότι η μέθοδος προβλέπει με πολύ ακρίβεια τις ιδιότητες για υλικά με $h_f/h_{max} < 0.7$ και για υλικά που ενδοτραχύνονται μετά την διείσδυση[71]. Για μεγαλύτερες τιμές του λόγου, τα φαινόμενα συσσώρευσης γίνονται σημαντικά και η ακρίβεια μειώνεται. Ειδικά για διεισδύσεις με ακίδες Berkovich, ο Larsson μέσω υπολογισμών FE (πεπερασμένων στοιχείων) βρήκε ότι η παραμόρφωση που προκαλείται τείνει να δίνει συσσωρεύσεις στα μέσα των πλευρών και βυθίσεις στις γωνίες, οπότε αλληλοαναιρούνται συνολικά.

Ο Fisher-Cripps (2002) παρατήρησε αυτή την συμπεριφορά στο αλουμίνιο, όπου η τιμή του μέτρου ελαστικότητας ήταν πολύ μικρότερη από την αναμενόμενη [72]. Το 2005 οι Raretal. παρατήρησαν ότι το ίδιο υλικό μπορεί να παρουσιάσει και sink-in και pile-up κατά την διάρκεια της διείσδυσης [73]. Για μεγάλο χρόνο ερπυσμού, ο μηχανισμός αποδόμησης ενδέχεται να εναλλάσσεται μεταξύ pile-up και sink-in (αρχικά ελαστικά με sink-in σε πλαστικά με plasticpile-up). Το 2008 οι Mandaletal. έδειξαν ότι ο χρόνος αναμονής ερπυσμού δεν επηρεάζει το pile-up/sink-in του κράματος αλουμινίου [74] .

Επίσης σκληρά υλικά με υψηλό λόγο H/Er εμφανίζουν sink-in, ενώ πιο μαλακά υλικά με χαμηλότερο λόγο εμφανίζουν pile-up. Σύμφωνα με την βιβλιογραφία, όταν

[71]W. C. Oliver and G. M. Pharr, An improved technique for determining hardness and elastic modulus using load and displacement sensing indentation experiments, Journal of Materials Research, Vol.7, pp.1564–1583, (1992).
[72] Fischer-Cripps, A.C.,: "Nanoindentation", Springer-Verlag, New York, 2002
[73] Rar A., Sohn S., Oliver W.C., Goldsby D.L., Tullis T.E., Pharr G.M.,: "On the measurement of creep by nanoindentation with continuous stiffness techniques", MRS, Boston, MA, USA, 2005
[74] Mandal, S., Kose, S., Frank, A., Elmustafa, A.A.: "A numerical study on pile-up in nanoindentation creep". Int. J. Surf. Sci. Eng., 2, 41-51, 2008

ο λόγος h_c/h τείνει στην μονάδα τότε ο μηχανισμός αποδόμησης διακατέχεται κυρίως από το φαινόμενο pile-up, ενώ όταν τείνει στο μηδέν το υλικό παρουσιάζει πιο ελαστική παραμόρφωση και στον μηχανισμό αποδόμησης κυριαρχεί το sink-in[75][76].

2.9 Ερπυσμός

Ερπυσμός είναι το φαινόμενο κατά το οποίο παρατηρείται συνεχής αύξηση των παραμορφώσεων συναρτήσει του χρόνου υπό την επίδραση σταθερής τάσεως, υπό σταθερή θερμοκρασία.

Η μέθοδος της νανοδιείσδυσης με ερπυσμό παρέχει πληροφορίες για περιορισμένη περιοχή και είναι μέθοδος που χρησιμοποιείται πολύ στη μελέτη λεπτών υμενίων. Τα πολύ καλά ελεγχόμενα εφαρμοζόμενα φορτία μπορούν να παρέχουν πληροφορίες για υλικά με πολύ χαμηλά ποσοστά ερπυσμού. Παρέχει επίσης κρίσιμες πληροφορίες για υλικά που έχουν μετρηθεί με την παραδοσιακή μέθοδο σε κλίμακα μάκρο και σε περιπτώσεις που οι ιδιότητες ερπυσμού πρέπει να αξιολογηθούν σε τοπικό επίπεδο. Μονοαξονικά τεστ ερπυσμού μπορούν να γίνουν σε μια προκαθορισμένη ποσότητα υλικού με μονοαξονική κατανομή τάσεων, κάτι που δεν μπορεί να γίνει στην νανοσκληρομέτρηση με ερπυσμό. Γενικά υπάρχουν πολλά μειονεκτήματα που συνδέονται με τις μαθηματικές αρχές και την φυσική ερμηνεία της νανοδιείσδυσης με ερπυσμό. Το φαινόμενο του ερπυσμού μπορεί να παρατηρηθεί σε όλα σχεδόν τα μεταλλικά υλικά, ακόμα και σε θερμοκρασία η οποία είναι πολύ χαμηλότερη από την μισή της θερμοκρασίας τήξης του μετάλλου, πάνω από την οποία αναμένεται οι διαδικασίες διάχυσης να είναι σημαντικές[77] . Είναι επίσης γνωστό ότι οι μηχανικές ιδιότητες που εξάγονται από μία κλασική δοκιμή εφελκυσμού σε θερμοκρασία δωματίου είναι χρονικά ανεξάρτητες. Δοκιμές νανοδιείσδυσης έχουν αρκετά σημαντικά πλεονεκτήματα έναντι των συμβατικών δοκιμών σε εφελκυσμό, ιδιαίτερα για την παραμόρφωση ερπυσμού [78]. Στην νανοδιείσδυση ο ερπυσμός ξεχωρίζει από εκείνων των συμβατών δοκιμών στο ότι ο όγκος που συμμετέχει επεκτείνεται κατά την διάρκεια του ερπυσμού. Στην περίπτωση μιας συμβατικής δοκιμής το υλικό που συμμετέχει είναι περιορισμένο στο μήκος του μετρητή του δείγματος. Οι μεταβλητές τάσης που υπολογίζονται με την νανοδιείσδυση δεν είναι ίσες με εκείνες που υπολογίζονται από τις συμβατικές δοκιμές. Οι μηχανισμοί παραμόρφωσης είναι διαφορετικοί στο ότι η κίνηση εξάρθρωσης (dislocationmotion) και/ή ατομική διάχυση είναι οι κύριοι μηχανισμοί

[75] Hill, R., Storakers, B., Zdunek, A.B.,: "A theoretical study of the Brinell hardness test", Proceed. Royal Soc. Lond., Series A (Mathem.Phys. Sci.), 423, 301–330, 1989.
[76] Hertz, H., Miscellaneous Papers by H. Hertz, Macmillan, 1896
[77] Mayo M.J., Nix W.D., Acta Metall. Pb. 36 (1988) 2183-2192.
[78] Lucas B.N., Oliver W.C., Metall. Mater. Trans. A 30 (1999) 601-610.

παραμόρφωσης για κρυσταλλικά υλικά [79], ενώ το διατμητικό banding είναι ο μηχανισμός παραμόρφωσης στα υαλώδη μεταλλικά κράματα[80].

Ο ερπυσμός κατά την νανοδιείσδυση αποτελείται από δύο στάδια, το transient (primarycreep) και το steadystate (secondarycreep)[81]. Ύστερα από μια γρήγορη , μείωση της μετατόπισης, ο ρυθμός παραμόρφωσης μειώνεται γρήγορα (transientcreepstage), και σταδιακά προσεγγίζει μια σταθερή τιμή καθώς μπαίνει στο δεύτερο στάδιο. Οι μεταβλητές τάσεων στο δεύτερο στάδιο μπορούν να υπολογιστούν από συνεχείς δοκιμές διείσδυσης[82]. Σε ένα πείραμα νανοδιείσδυσης με ερπυσμό, η ακίδα εισχωρεί στην επιφάνεια με έναν συγκεκριμένο ρυθμό μέχρι μια καθορισμένη τιμή φορτίου ή μετατόπισης και στην συνέχεια, ενώ το φορτίο παραμένει σταθερό η ακίδα συνεχίζει να εισχωρεί στην επιφάνεια και το υλικό κάτω από την ακίδα συνεχίζει να παραμορφώνεται στον χρόνο. Μέσα στο δείγμα λαμβάνει χώρα ερπυσμός κατά την διάρκεια του χρόνου αναμονής και εκδηλώνεται σαν αλλαγή του βάθους διείσδυσης ενώ το φορτίο παραμένει σταθερό. Θεωρείται ότι στο υλικό κάτω από την ακίδα δημιουργείται ένα χημικό δυναμικό που οδηγεί σε θερμικά ενεργοποιημένη διάχυση ατόμων που μετακινούνται από κάτω από την ακίδα προς την επιφάνεια και κατά μήκος της διεπιφάνειας μεταξύ της ακίδας και του δείγματος, ακόμα και υπό ελαστική επαφή.

2.10 Ο λόγος της σκληρότητας προς το μέτρο ελαστικότητας, H/E*

Ο λόγος της σκληρότητας προς το μέτρο ελαστικότητας, H/E*,παρουσιάζει σημαντικό ενδιαφέρον στην τριβολογία. Ο λόγος αυτός πολλαπλασιασμένος με ένα γεωμετρικό παράγοντα δίνει τον «δείκτη πλαστικότητας» (plasticity index) ο οποίος περιγράφει τις ιδιότητες παραμόρφωσης τραχειών επιφανειών. Η συσχέτιση αυτή παρέχει μία εναλλακτική μέθοδο για την μέτρηση του λόγου H/E^* στην μικρο- και νανο- κλίμακα για μέταλλα και κεραμικά[83]. Θεωρίες σχετικές με τη διάβρωση υποστηρίζουν ότι οι τιμές λόγου σκληρότητας-σύνθετου μέτρου ελαστικότητας των υλικών καθορίζουν την αντίσταση στη διάβρωση των επιφανειών των υλικών. Υπάρχουν σκληρά υλικά (μέταλλα), τα οποία παρουσιάζουν μεγάλες τιμές σκληρότητας και μέτρου ελαστικότητας ταυτόχρονα με εξαιρετική αντοχή στη φθορά. Από την άλλη, έχει παρατηρηθεί ότι μαλακά υλικά (ελαστομερή κυρίως), τα οποία παρουσιάζουν ταυτόχρονα χαμηλές τιμές σκληρότητας και μέτρου ελαστικότητας και παρουσιάζουν εξίσου εξαιρετική αντοχή στη διάβρωση. Πειραματικά, έχει βρεθεί συσχετισμός ανάμεσα στην αντίσταση σε φθορά των επιφανειών

[79] Li W.B., Warren R., Acta Metall. 41 (1993) 3065-3069
[80] Li H., Ngan A.H.W., J. Mater. Res. 19 (2004) 513-522
[81] Cao Z.Q., Zhang X., Scr. Mater. 56 (2007) 249-252.
[82] Pelletier H., Krier J., Cornet A., Mille P., J. Th. Sol. Fil. 379 (2000) 147–155.
[83] J.F. Archard in "Contact and rubbing of flat surfaces" J. Appl. Phys. 24 (1953), p.981.

των υλικών και στον λόγο H/E*, ωστόσο ακόμα δεν έχει μαθηματικά αποδειχθεί η σχέση μεταξύ μέτρου ελαστικότητας και αντίστασης στη φθορά [84][85]. Οι *Lancaster*[86] και *Spur* και *Newsome*[87]υποστηρίζουν ότι η αντίσταση στη φθορά αυξάνεται με αύξηση του μέτρου ελαστικότητας, διότι τέτοια υλικά συνήθως παρουσιάζουν και υψηλές τιμές σκληρότητας.

Κατά τη διαδικασία διείσδυσης του εντυπωτή στο μέγιστο βάθος διείσδυσης στο εξεταζόμενο υλικό, το έργο που έχει ο εντυπωτής, W_{tot}, μεταφέρεται στο υλικό που εξετάζεται. Το έργο αυτό προκαλεί ελαστοπλαστική παραμόρφωση. Αντίστοιχα, κατά τη διαδικασία αποφόρτισης μεταφέρεται έργο, W_u, από το εξεταζόμενο υλικό στον εντυπωτή (αυτό είναι το έργο που ήδη έχει αποθηκευτεί στο υλικό κια αποδεσμεύεται σταδιακά με μείωση του φορτίου κατά την διαδικασία αποφόρτισης). Οι *Cheng* και *Cheng*[88][89][90] βρήκαν μία συσχέτιση μεταξύ του λόγου του έργου που μεταφέρεται από το υλικό στον εντυπωτή προς το έργο που μεταφέρεται από τον εντυπωτή στο υλικό $(W_{tot}-W_u)/W_{tot}$ (για μία ολοκληρωμένη διαδικασία φόρτισης-αποφόρτισης) και του λόγου σκληρότητας προς το σύνθετο μέτρο ελαστικότητας (H/E*). Από την μελέτη τους, προκύπτει ότι ο λόγος (H/E*) και $(W_{tot}-W_u)/W_{tot}$ παρουσιάζουν γραμμική εξάρτηση κια μάλιστα είναι αντιστρόφως ανάλογοι. Συμπερασματικά, ο λόγος H/E* θα μπορούσε να προκύψει από μετρήσεις των έργων W_{tot} και W_u, τα οποία μπορούν να υπολογιστούν από απλές μαθηματικές ολοκληρώσεις βασισμένες σε μετρήσεις φορτίου-μετατόπισης.

Βρέθηκε ότι μία αξιοσημείωτη σχέση υπάρχει μεταξύ του έργου που παραμένει στο υλικό προς το συνολικό έργο για μία πλήρη διαδικασία φόρτισης-αποφόρτισης, $(W_{tot}-W_u)/W_{tot}$, και του όρου *H/E** [83], η οποία δίνεται παρακάτω:

$$\frac{H}{E^*} = \Pi_\theta \frac{(W_{tot} - W_u)}{W_{tot}} \qquad (2.11)$$

[84] T.L. Oberle, J. Met. 3 (1951) 438–439
[85] Greenwood, J.A. and Williamson, J.B. in "Contact of nominally flat surfaces" Proceedings of the Royal Society of London. Series A, Mathematical and Physical Sciences, Vol. 295, No. 1442, pp.300-319.
[86] J.K. Lancaster in "The relationship between the wear of carbon brush materials and their elastic moduli" Br. J. Appl. Phys. 14 (1963), p.497
[87] R.T. Spurr and T.P. Newcombe in "The friction and wear of various materials sliding against unlubricated surfaces of different types and degrees of roughness" Proceedings of the Conference on Lubrication and Wear Institution of Mechanical Engineers, London, UK, 1957, Inst. Mech. Eng. (1957), p.269
[88] Cheng,Y.-T. and Cheng, C.-M. (1998) 'Relationships between hardness, elastic modulus, and the work of indentation', Appl. Phys. Lett., Vol. 73, No. 5, pp.614-616.
[89] Cheng,Y.-T. and Cheng, C.-M. (1999) 'Can stress-strain relationships be determined from indentation curves using conical and pyramidal indenters?', Mater. Res. Rapid Commun., Vol. 14, No. 9, pp.3493-3496.
[90] Cheng,Y.-T. and Cheng, C.-M. (2000) 'What is indentation hardness?', Surf. Coat.Techn., Vol. 133-134, pp.417-424.

Ο όρος E* συμβολίζει το σύνθετο μέτρο ελαστικότητας, το οποίο συνδέεται με το μέτρο ελαστικότητας (Young) με τον παρακάτω τύπο [91] (βλ.αναλυτικά σχέση 10):

$$E^{*}=E/(1-\nu^{2}) \quad (2.12)$$

όπου ν: λόγος Poisson δείγματος

Ο δείκτης , θ, υποδηλώνει μία πιθανή εξάρτηση από την γεωμετρία της ακίδας (από την γωνία του κεντρικού άξονα της ακίδας). Συγκεκριμένα, το σχήμα 2.13 δείχνει ότι για δεδομένη γεωμετρία ακίδας Berkovich υπάρχει μία προσεγγιστική γραμμική σχέση μεταξύ του H/E^{*} και $(W_{tot}-W_{u})/W_{tot}$. Επομένως, η τιμή H/E* μπορεί να εξαχθεί από την μέτρηση του και W_u του W_{tot} , τα οποία μπορούν να υπολογιστούν από απλή μαθηματική ολοκλήρωση βασισμένη σε μετρήσεις φορτίου και μετατόπισης.

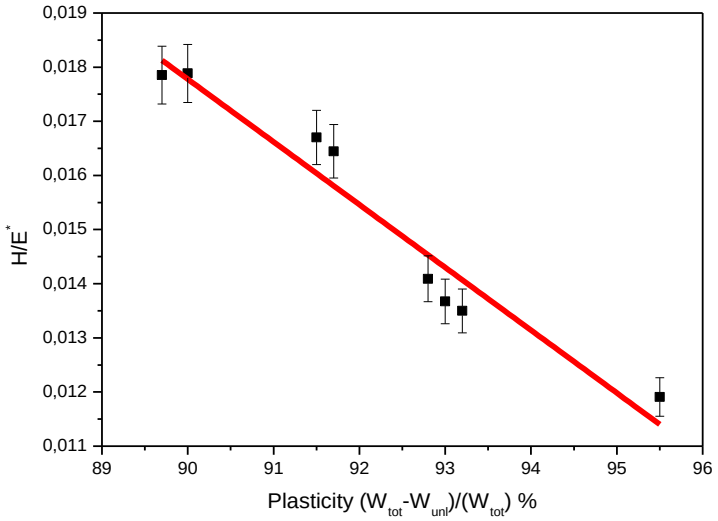

Σχήμα 2.13:Προσεγγιστική γραμμική σχέση μεταξύ του H/E^{*} και $(W_{tot}-W_{u})/W_{tot}$.

2.11 Πρόσφυση (Adhesion) - ***Υδροφιλικότητα - Υδροφοβικότητα επιφανειών***

Έχει αναφερθεί στη βιβλιογραφία σημαντική μεταβολή των επιφανειακών ιδιοτήτων που προκύπτουν από την κατεργασία στην επιφάνεια υλικού. Στην περίπτωση των πολυμερών η επίδραση του οξυγόνου, της UV ακτινοβολίας και της κατεργασίας με όζον επιφέρει

[91] T.L. Oberle, J. Met. 3 (1951) 438–439.

αλλαγές στην επιφανειακή δομή οι οποίες εξαρτώνται από τον χρόνο κατεργασίας και τη φύση του πολυμερούς. Με τη μέθοδο της νανοσκληρομέτρησης σε συνδυασμό με τη μέθοδο γωνίας επαφής είναι δυνατή η μελέτη επίδρασης της επιφανειακής κατεργασίας στις περιπτώσεις υδροφιλικότητας / υδροφοβικότητας (πολικά μόρια στην επιφάνεια, διαφοροποίηση νανο-τραχύτητας, επιφανειακή ενέργεια). Η επιλογή κατάλληλης ακίδας (π.χ. τύπου Berkovich ή ακίδα siliconnitride – Si_3N_4)για το σύστημα νανοσκληρομέτρησης κρίνεται απαραίτητη καθώς οι ιδιότητες της (π.χ. ποσοστό υδροφιλικότητας, ηλεκτροστατικές δυνάμεις) έχει επίδραση στις δυνάμεις πρόσφυσης (adhesiveforces) που αναπτύσσονται λίγο πριν την επαφή της ακίδας με την επιφάνεια του δείγματος (σχήμα 2.14). Οι μετρούμενες δυνάμεις πρόσφυσης αποτελούν σαφή ένδειξη της υδροφιλικότητας της επιφάνειας του δείγματος (σχήματα 2.15). Η μείωση της επιφάνειας μεταξύ της καμπύλης φόρτισης και της καμπύλης αποφόρτισης (σχήμα 2.16) υποδηλώνει μετάβαση από υδρόφιλη σε υδρόφοβη κατάσταση [9293].

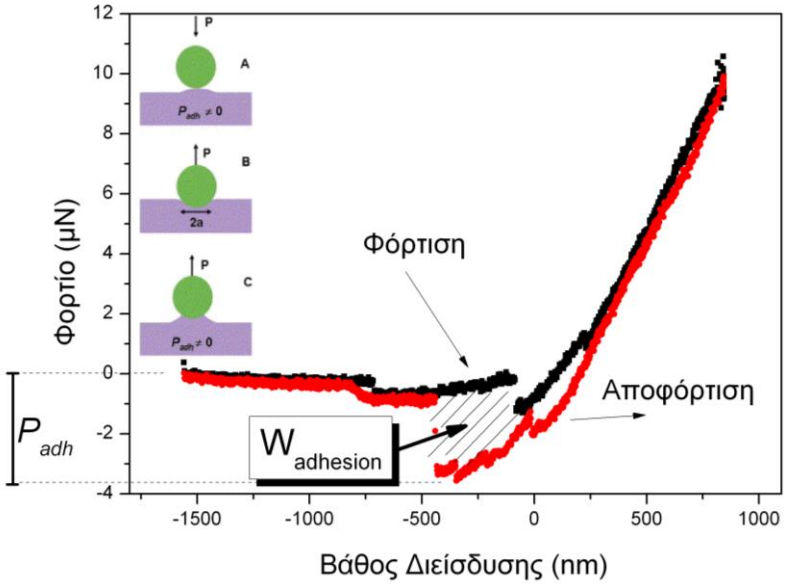

Σχήμα 2.14. Καμπύλη φόρτισης–αποφόρτισης νανοσκληρομέτρησης. Το συνολικό έργο της ενέργειας λίγο πριν την επαφή αποτυπώνεται με το γραμμοσκιασμένο τμήμα [94].

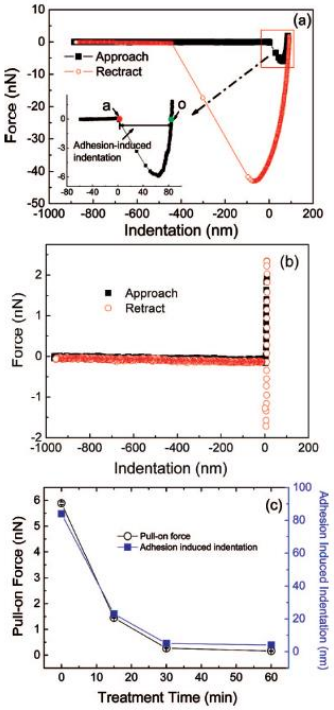

Σχήμα 2.15. Μετρήσεις νανοσκληρομέτρησης με ακίδα Si_3N_4 σε a)untreated και b) UV treatedPDMS δειγμάτων [95].

[92] M. Meincken, T.A.Berhane, P.E.Mallon, Tracking the hydrophobicity recovery of PDMS compounds using the adhesive force determined by AFM force distance measurements, Polymer 46 (2005) 203-208
[93]M.Brogly, O.Noel, H.Awada, G.Castelein, J.Shultz, A nanoscale study of the adhesive contact, C.R.Chimie 9 (2006) 99-110.
[94] C.Charitidis, Nanoscale deformation and nanomechanical properties of Polydimethylsiloxane (PDMS), submitted for publication to Industrial & Engineering Chemistry Research (2010).
[95] J.Song, D.Tranchida, G.J.Vancso, Contact Mechanics of UV/Ozone-Treated PDMS by AFM and JKR Testing : Mechanical Performance from Nano-to Micrometer Length Scales, Macromolecules 2008,41,6757-6762.

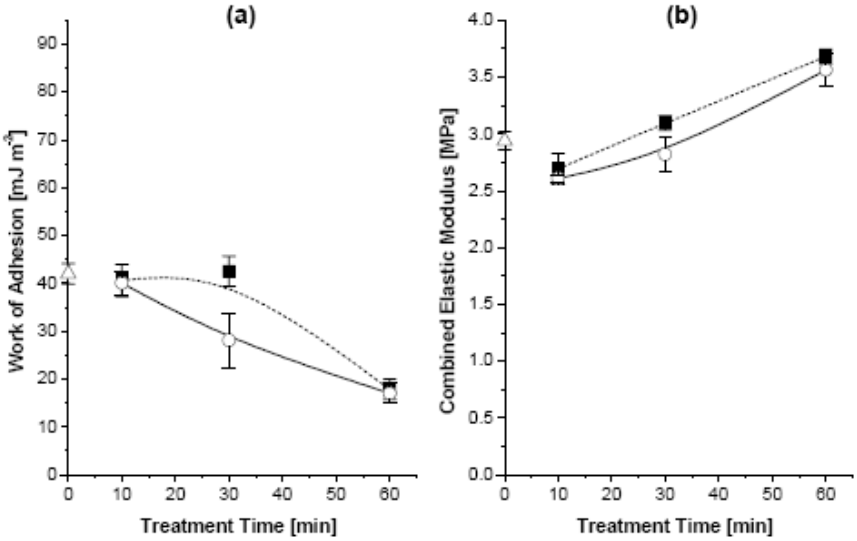

Σχήμα 2.16.(a) $W_{adhesion}$ και (b) σύνθετο μέτρο ελαστικότητας δείγματος PDMSSylgard 170 μετά από έκθεση για 10–60 λεπτά σε περιβάλλον UV/ozone. (Δ) χωρίς έκθεση, (■) αμέσως μετά την έκθεση, (○) 8 ημέρες μετά την έκθεση.

Η εναλλαγή της φύσης της επιφάνειας γίνεται αισθητή από την διαφοροποίηση των $W_{adhesion}$, E_r[96].

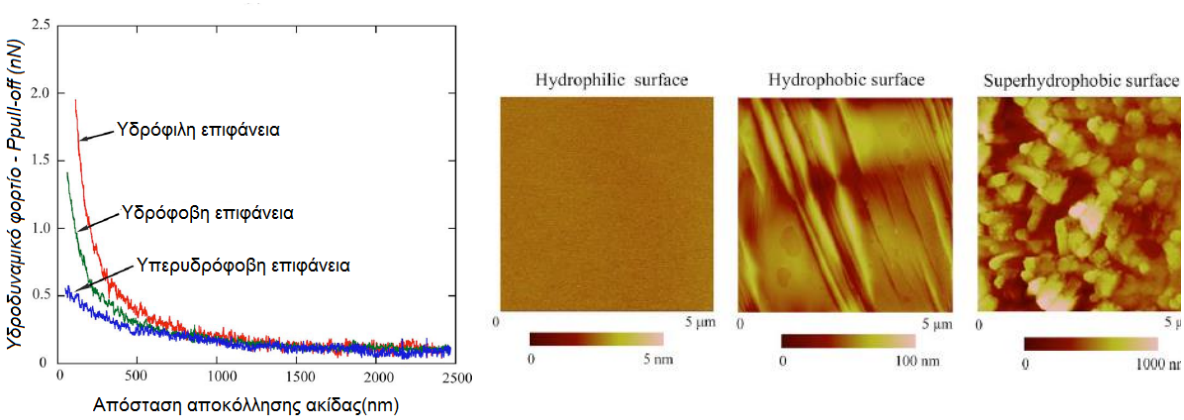

Σχήμα 2.17. Συσχέτιση φορτίου αποκόλλησης με την απόσταση αποκόλλησης και απεικόνιση για 3 τύπους επιφανειών (υδρόφιλη, υδρόφοβη, υπερυδρόφοβη) [97].

Οι *Songetal.* προσάρμοσαν τα δεδομένα τους μέσω του μοντέλου JKR στην εξίσωση [98]:

[96] A.Oláh, H.Hillborg, G.J.Vancso, Hydrophobic recovery of UV/ozone treated poly(dimethylsiloxane): adhesion studies by contact mechanics and mechanism of surface modification, Applied surface science, 2005, 239, 3-4, pp. 410-423.
[97]Y.Wang, B.Bhushan, A.Maali, Atomic force microscopy measurement of boundary slip on hydrophilic, hydrophobic, and superhydrophobic surfaces, J.Vac.Sci.Technol. A 27(4), 2009 754-760.
[98] C.Charitidis, Nanoscale deformation and nanomechanical properties of Polydimethylsiloxane (PDMS), submitted for publication to Industrial & Engineering Chemistry Research (2010).

$$a^3 = \frac{R}{E_r}\left[P + 3\pi R W_{adhesion} + \left(6\pi R P W_{adhesion} + \left(3\pi R P W_{adhesion} \right)^2 \right)^{1/2} \right] \quad (2.13)$$

Όπου α η ημιγωνία της ακίδας, R η καμπυλότητα της ακίδας (tipradius), P το φορτίο, $W_{adhesion}$ το έργο και E_r το σύνθετο μέτρο ελαστικότητας. Στη μελέτη των *Sirghi, Rossi* τροποποιείται το συμβατικό μοντέλο των Oliver-Pharr συνυπολογίζοντας το $W_{adhesion}$ και θεωρώντας το συνολικό φορτίο ως άθροισμα ελαστικών και ηλεκτροστατικών δυνάμεων, καταλήγοντας στην εξίσωση [99]:

$$P(h) = a(h - h_f)^2 - b(h - h_f), \qquad \text{όπου} \quad a = \frac{2E\tan a}{(1-\nu^2)\pi}, b = \frac{8W_{adhesion}\tan a}{\pi \cos a} \quad (2.14)$$

Και h το βάθος διείσδυσης, h_f το βάθος της παραμένουσας παραμόρφωσης. Το μαθηματικό μοντέλο DMT συνδέει το φορτίο αποκόλλησης ($P_{Pull\text{-}off} = P_{adhesion}$) με το $W_{adhesion}$μέσω της εξίσωσης[100] :

$$P_{adhesion} = -2\pi R W_{adhesion} \quad (2.15)$$

[99]L.Sirghi, F.Rossi, Adhesion and elasticity in nanoscale indentation, Applied Physics Letter 89, 243118 (2006).
[100] A.Oláh, H.Hillborg, G.J.Vancso, Hydrophobic recovery of UV/ozone treated poly(dimethylsiloxane): adhesion studies by contact mechanics and mechanism of surface modification, Applied surface science, 2005, 239, 3-4, pp. 410-423.

Κεφάλαιο 3. Νανοεγχάραξη (Scratchtest)

Η δοκιμή της εγχάραξης (Σχήμα 3.1) είναι ακριβής, ευαίσθητη και εφαρμόζεται τόσο για τον προσδιορισμό της πρόσφυσης επικάλυψης-υποστρώματος, όσο και για τον υπολογισμό της τριβής των υλικών. Μειονεκτεί στο ότι δε μπορεί εύκολα να μοντελοποιηθεί μαθηματικά, ωστόσο αποτελεί μια εξαιρετική τεχνική για τη σύγκριση των τριβολογικών ιδιοτήτων υμενίων και επικαλύψεων. Τα αποτελέσματα της μεθόδου αυτής εξαρτώνται τόσο από το υλικό, τη γεωμετρία και την επιφάνεια του εγχαράκτη όσο και από τις ιδιότητες του εξεταζόμενου σώματος (πχ. σκληρότητα), τη γεωμετρία του ακόμη και από τη σχετική υγρασία της ατμόσφαιρας κατά τη διεξαγωγή του πειράματος.

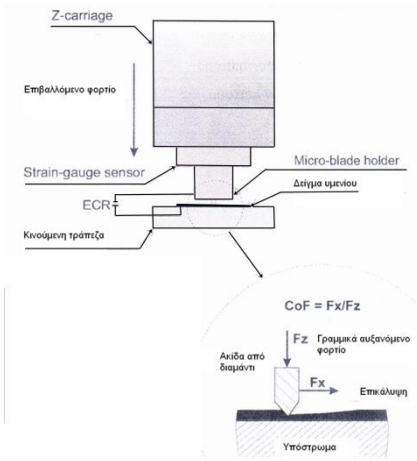

Σχήμα 3.1: Scratch tester.

Η διαμήκης εγχάραξη (Scratch Test, ST) αποτελεί πειραματική διαδικασία κατά την οποία ο εγχαράκτης εφαρμόζει κάθετο φορτίο PN, σταθερό ή αυξανόμενο, στην επιφάνεια υλικού, το οποίο κινείται κάτω από τον εγχαράκτη. Στο Σχ. 3.1 παρουσιάζεται σχηματική αναπαράσταση του ST [101][102]. Με το ST είναι δυνατή η μελέτη των τρόπων παραμόρφωσης των υλικών και ο χαρακτηρισμός της συνοχής, την προσκόλλησης των λεπτών υμενίων με το υπόστρωμα, στην περίπτωση και της μέτρησης του συντελεστή τριβής (μ), η οποία επιτυγχάνεται με μέτρηση των πλευρικών δυνάμεων (Lateral Force Measurements, LFM) που δέχεται ο εγχαράκτης. [103][104]. Τα πειράματα διαμήκους εγχάραξης που παρουσιάζονται σε αυτήτ ητν μελέτη πραγματοποιήθηκαν στην διάταξη Nano Indenter XP, η οποία υποστηρίζει και μετρήσεις LFM.

[101] C. Charitidis, S. Logothetidis, M. Gioti, Surf. Coat. Tech., 125 (2000) 201-206.
[102] T.W. Scharf, J.A. Barnard, Thin Solid Films 308/309 (1997) 340.
[103] C. Charitidis, S. Logothetidis, M. Gioti, Surf. Coat. Tech., 125 (2000) 201-206.
[104] Fischer-Cripps A.C., Materials and Engineering, 385.(2004), 74.

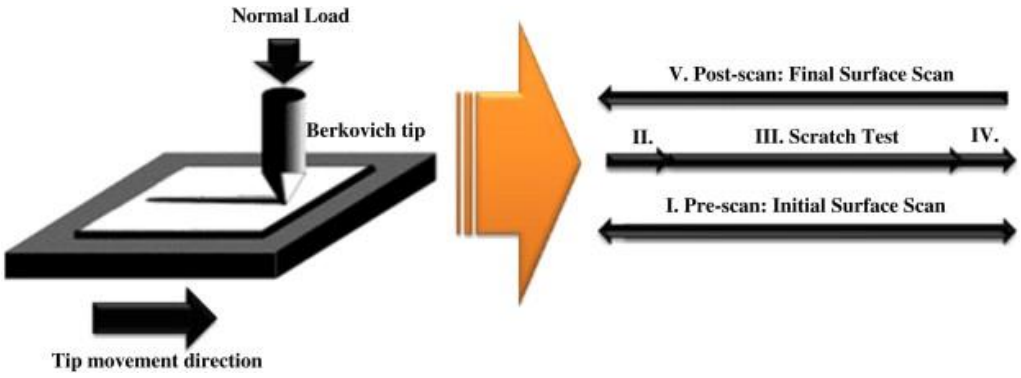

Σχήμα 3.2 Σχηματική απεικόνιση πειράματος διαμήκους νανοεγχάραξης [105]

Συγκεκριμένα ένα πείραμα ST αποτελείται από τα ακόλουθα τμήματα (Σχ. 3.2):

α) Προσέγγιση της επιφάνειας του δείγματος

β) Τμήμα (1) - Pre-Scratch Scan: κατά το τμήμα αυτό ο εγχαράκτης σαρώνει την επιφάνεια του δείγματος ασκώντας σε αυτή ιδιαίτερα χαμηλό φορτίο (P= 0,020 mN), με σκοπό την «ανάγνωση» του προφίλ της επιφάνειας του δείγματος, κατά μήκος της περιοχής (στο Σχ.3.2 αυτό είναι 700 μm) όπου θα πραγματοποιηθεί η διαμήκης εγχάραξη

γ) Τμήματα (2), (3), (4) - Scratch Scan: Το τμήμα (2) έχει μήκος 100 μm και εκτελείται με φορτίο 0,020 mN. Ακολουθεί το τμήμα (3) κατά το οποίο πραγματοποιείται η διαμήκης εγχάραξη με αυξανόμενο ή σταθερό κάθετα εφαρμοζόμενο φορτίο από τον εγχαράκτη στο δείγμα, της οποίας το μήκος (Στο Σχ. 3.2 το μήκος είναι 500 μm) και το τελικό φορτίο επιλέγονται από τον χρήστη. Στη συνέχεια το φορτίο αποσύρεται από τον εγχαράκτη και εκτελείται το τμήμα (4) με εφαρμοζόμενο φορτίο P= 0,020 mN

δ) Τμήματα (5) και (6) - Post Scratch Scan: ο εγχαράκτης σαρώνει την επιφάνεια με χαμηλό εφαρμοζόμενο φορτίο (P= 0,020 μN) όπου πραγματοποιήθηκε η διαμήκης εγχάραξη, με σκοπό την ανάγνωση της παραμόρφωσης που προκλήθηκε.

Όταν τα φορτία που ασκούνται στον εγχαράκτη είναι από 50 μN έως 10-20 mN εφαρμόζεται η τεχνική της νανοεγχάραξης, ενώ από 10-20 mN έως 5-10 N η τεχνική της μικροεγχάραξης και για φορτία πάνω από 5-10 N έως τα 100 N η τεχνική της μακροεγχάραξης. Στο Σχήμα 3.38, δίνονται παραδείγματα επικαλύψεων και υμενίων που έχουν υποβληθεί σε δοκιμή εγχάραξης.

[105] Elias P. Koumoulos, Costas A. Charitidis, Dimitrios P Papageorgiou, Athanasios G Papathanasiou, Andreas G Boudouvis, Nanomechanical and Nanotribological Properties of Hydrophobic Fluorocarbon Dielectric Coating on Tetraethoxysilane for Electrowetting Applications, Journal of Surface and Coatings Technology, 206, pp. 3823–3831 (2012)

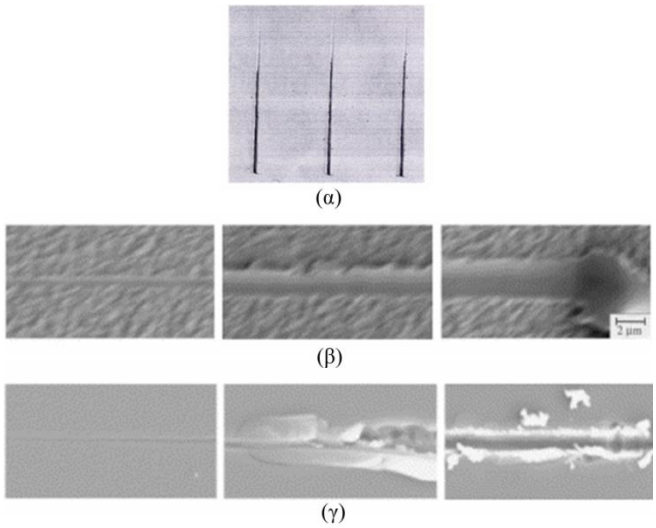

Σχήμα 3.3: α) Πείραμα εγχάραξης μαγνητικού δίσκου με επικάλυψη DLC. Το πάχος του DLC κυμαινόταν από 3 έως 10 nm. Η ταχύτητα ολίσθησης ήταν 10 mm/s και το φορτίο αυξανόταν γραμμικά από 2 mN έως 2 N. Οι τρεις εγχαράξεις επιβεβαιώνουν την επαναληψιμότητα της μεθόδου. β) Πείραμα εγχάραξης υμενίου SiO_2. γ) Πείραμα εγχάραξης υμενίου Au.

Ένα τυπικό πείραμα νανοεγχάραξης πραγματοποιείται σε τρία κύρια στάδια (Σχήμα 3).

Στο Σχήμα 3.4 παρουσιάζονται 3-D εγχαράξεις.

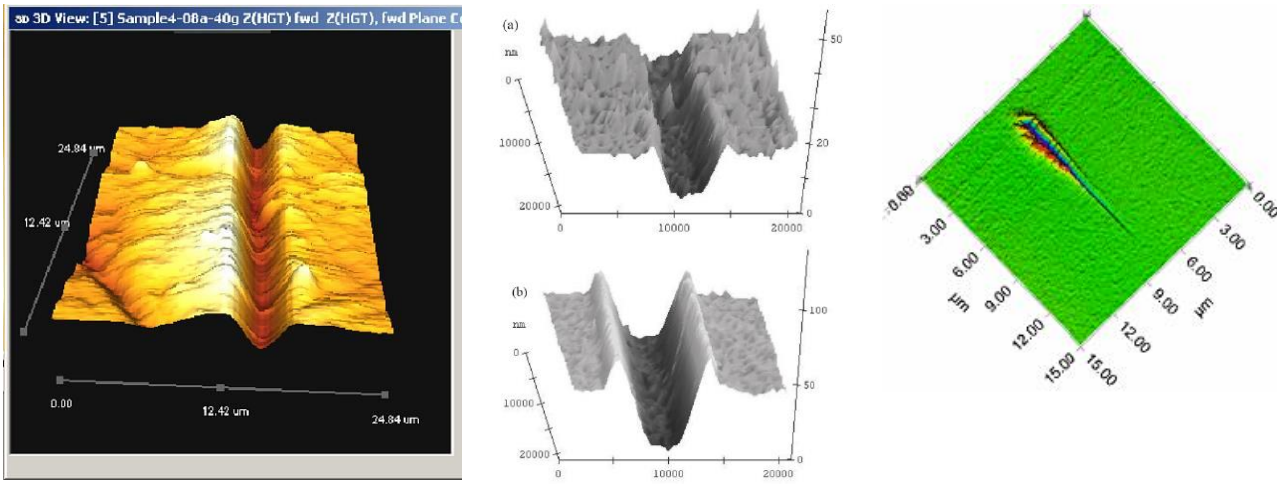

Σχήμα 3.4 3-D απεικόνιση επιφανειών, όπου είναι φανερή η πλαστική παραμόρφωση μετά από πείραμα νανοεγχάραξης.

Το πραγματικό βάθος διείσδυσης του νανοεγχαράκτη στο δείγμα εκτιμάται συγκρίνοντας το βάθος διείσδυσης του νανοεγχαράκτη κατά την διάρκεια του πειράματος, με την θέση (το ύψος) της αρχικής επιφάνειας σε κάθε θέση κατά μήκος της διαδρομής πραγματοποίησης της νανοεγχάραξης. Η αρχική μορφολογία της επιφάνειας λαμβάνεται σχηματίζοντας το προφίλ της επιφάνειας με την επιβολή ενός πολύ μικρού φορτίου κατά

μήκος της διαδρομής όπου πρόκειται να πραγματοποιηθεί η νανοεγχάραξη. Η τραχύτητα και η κλίση της επιφάνειας κατά την αρχική σάρωση, λαμβάνονται υπόψη στον υπολογισμό του βάθους διείσδυσης του νανοεγχαράκτη. Η μελέτη με νανοεγχάραξη θα δώσει πληροφορίες για την αντοχή των δειγμάτων σε εγχάραξη καθώς και θα εξεταστεί η πρόσφυσή τους στο υπόστρωμα που έχουν αναπτυχθεί και ο συντελεστής τριβής. Οι παράμετροι της μέτρησης είναι το επιβαλλόμενο φορτίο, ο ρυθμός φόρτισης, η έκταση της νανοεγχάραξης και η ταχύτητα της νανοεγχάραξης (για σταθερή θερμοκρασία και υγρασία κατά το πείραμα).

Το πεδίο που επιτρέπει την πληροφόρηση και μελέτη των φαινομένων που συμβαίνουν στην ατομική κλίμακα και των βασικών ιδιοτήτων των επιφανειών που βρίσκονται σε κίνηση καλείται μοριακή τριβολογία ή νανοτριβολογία. Μέσω της νανοτριβολογίας επιτυγχάνεται η μελέτη των διεπιφανειακών φαινομένων σε μικρο/νανοδομές (MEMS, NEMS) και σε άλλες βιομηχανικές εφαρμογές. Επομένως, προσδιορίζονται με μεγάλη ακρίβεια οι επιφανειακές αλληλεπιδράσεις των υλικών και συστημάτων. Πέρα όμως από τα μικρο-συστήματα και νανο-διατάξεις δύνανται να μελετηθούν και μακροδομές προσφέροντας σημαντικές πληροφορίες για τα διεπιφανειακά φαινόμενα, ώστε να γεφυρωθεί το χάσμα μεταξύ επιστήμης και μηχανικής.

Συγκρίνοντας τις τεχνικές της μακροτριβολογίας με τη μικρο/νανοτριβολογία διαπιστώνεται ότι στη μακροτριβολογία, λόγω των μεγάλων φορτίων, η φθορά που προκαλείται στο προς μελέτη υλικό είναι αναπόφευκτη και προτιμάται κυρίως για τη μελέτη υλικών όγκου. Αντίθετα, με τη μικρο/ νανοτριβολογική μελέτη των υλικών, λόγω των μικρών επιβαλλόμενων φορτίων (μ§ ή mg ή μN) και μικρής μάζας του υλικού επαφής (ακίδας, μg) με το προς μελέτη υλικό, δεν παρατηρείται φθορά στο υλικό, καθώς αλληλεπιδρούν μερικές μόνο ατομικές στοιβάδες, άρα μελετώνται κυρίως τα χαρακτηριστικά και οι ιδιότητες της επιφάνειας. Τα εξαρτήματα που χρησιμοποιούνται στις μικρο/νανοδομές είναι πολύ ελαφριά και λειτουργούν κάτω από μικρά φορτία. Επομένως, η τριβή και η φθορά (στη νανοκλίμακα) κάτω από μικρά φορτία εξαρτώνται σημαντικά από τις αλληλεπιδράσεις της επιφάνειας (μερικές ατομικές στοιβάδες). Τα πλεονεκτήματα που παρουσιάζει η νανοτριβολογία σχετίζονται με τον ακριβή ορισμό της τριβής στην ατομική κλίμακα διότι:

1. Ορίζεται με μεγαλύτερη ακρίβεια η μικρή επιφάνεια επαφής ακίδας και δείγματος σε σχέση με τα συμβατικά τριβολογικά πειράματα (Σχήμα 3.5)
2. Πραγματοποιείται πιο εύκολα σύγκριση με τα αποτελέσματα των ατομικών προσομοιώσεων, που στηρίζονται στη γεωμετρία των ατόμων.

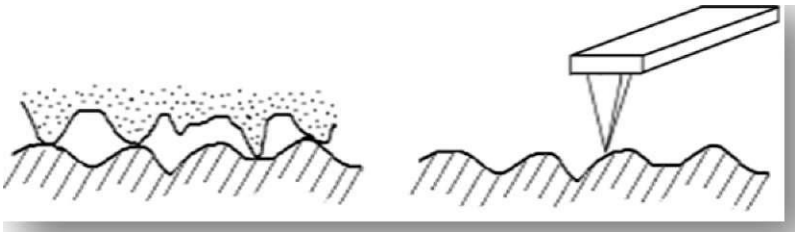

Σχήμα 3.5 Συγκριτική αναπαράσταση της επιφάνειας επαφής σε τριβολογικό πείραμα και σε πείραμα νανοτριβολογίας.

Κατά τα πειράματα νανοτριβολογίας όμως παρατηρείται φθορά σε ατομική κλίμακα στην επιφάνεια του προς μελέτη υλικού. Η φθορά κατά την οποία οι μηχανισμοί κίνησης αποκολλούν άτομα (ιοντικά ζευγάρια) από τις αρχικές τους θέσεις καλείται ρυθμός ατομικής φθοράς. Η ατομική φθορά χωρίζεται σε δυο κατηγορίες:

Φθορά Συνάφειας (adhesive wear), η οποία αναφέρεται στις περιπτώσεις κατά τις οποίες οι κάθετες δυνάμεις (van der Waals) είναι κυρίαρχες και τα άτομα μεταφέρονται από τη μια επιφάνεια στην άλλη.

Φθορά Τριβής (abrasive wear), η οποία αναφέρεται στις περιπτώσεις κατά τις οποίες οι διατμητικές δυνάμεις είναι κυρίαρχες, οδηγώντας στη μετακίνηση των ατόμων σε διπλανές θέσεις από την αρχική τους, δηλαδή δεν παρατηρείται μεταπήδηση των ατόμων από τη μια επιφάνεια στην άλλη.

Γενικά οι δοκιμές νανοεγχάραξης χρησιμοποιούνται με επιτυχία για τον προσδιορισμό των κύριων παραμέτρων της αντίστασης σε φθορά των επιφανειών των υλικών. Οι δοκιμές εγχάραξης φαίνονται χρήσιμες για το χαρακτηρισμό των πολυμερικών υλικών κάτω από έναν αριθμό συνθηκών επαφής. Λαμβάνονται διαφορετικά αποτελέσματα όταν μεταβάλλεται η γεωμετρία της ακίδας, η ταχύτητα ολίσθησης, η θερμοκρασία και το κάθετο επιβαλλόμενο φορτίο. Η χρήση διαφορετικής γεωμετρίας ακίδα είναι συνήθως απαραίτητη για να χαρακτηρισθεί καλύτερα η έναρξη του φαινομένου θραύσης για ένα υλικό.

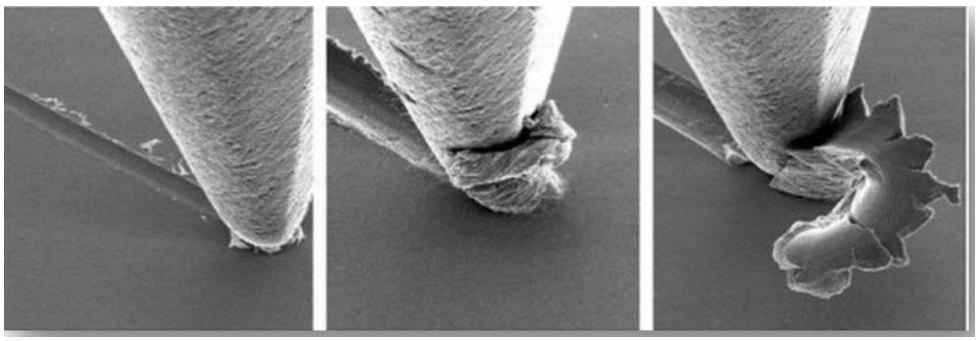

Σχήμα 3.6 Σχηματική αναπαράσταση πειράματος νανοεγχάραξης.

Κεφάλαιο 4. Νανοδομές

Οι νανοδομές κατηγοριοποιούνται με βάση παραμέτρους όπως προέλευση, χημική σύσταση, δομή/μορφή, επιφανειακή κατάσταση κ.λ.π. όπως φαίνεται στο Σχήμα 4.1.

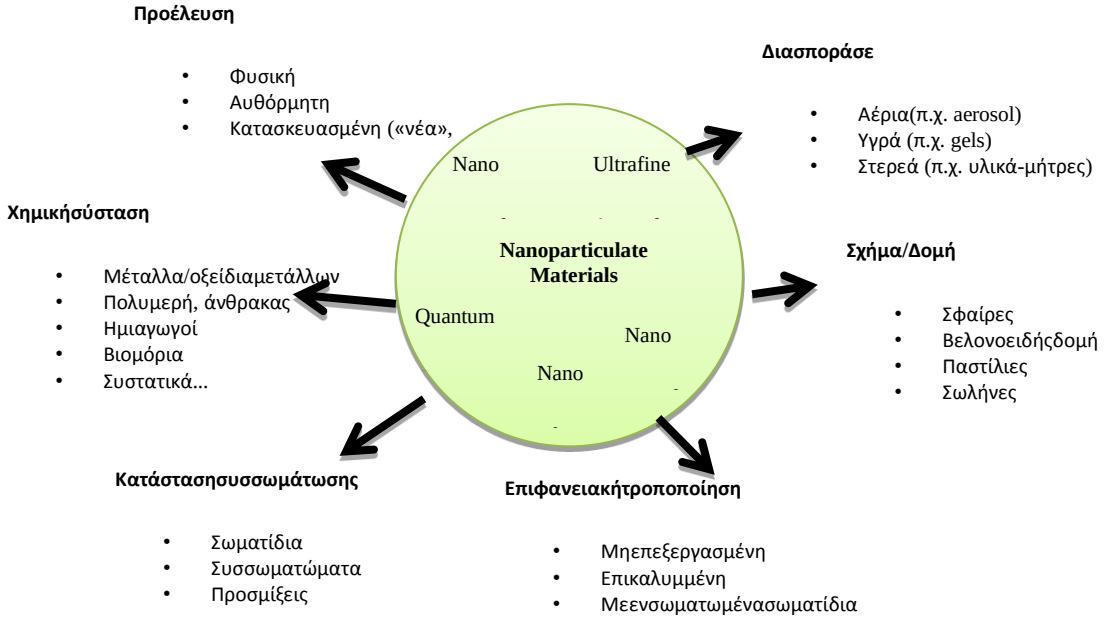

Σχήμα 4.1: Κατηγοριοποίηση νανοδομών με βάση διαφορετικές παραμέτρους (προέλευση, χημική σύσταση, δομή/μορφή, επιφανειακή τροποποίηση, κλπ).

Μια κατηγοριοποίηση των νανοδομών, με βάση τη φύση τους και όχι τις διαστάσεις τους, είναι η ακόλουθη:

- Οργανικές: οργανικοί νανοκρύσταλλοι (organicnanocrystals), πολυμερικά λεπτά υμένια (polymerthinfilms), υπερμοριακές δομές (supramolecularstructures).
- Μη οργανικές: μεταλλικά κραματικά συμπλέγματα, συμπλέγματα από άνθρακα, νανοσωλήνες άνθρακα, ημιαγώγιμοι νανοκρύσταλλοι (semiconductornanocrystals), κβαντικές τελείες (quantumdots), κβαντικά πηγάδια (quantumwells) και καλώδια (wires).
- Βιολογικές: φεριτίνη, DNA, μικύλλια (micelles), κολλοειδή σωματίδια και κυψελίδες (vesicles).
- Νανοδομές και υβριδικές δομές (nanocomposites and hybrid structures).

- Ιεραρχικές κατασκευές: τροποποιημένες νανοκρυσταλλικές συστοιχίες χρυσού ή αργύρου (functionalized gold or silver nanocrystal arrays, photonic crystals – opals and inverse opals.)

Αν επιλεχθεί ως παράμετρος κατηγοριοποίησης η διάσταση της νανοδομής, προκύπτουν οι παρακάτω κατηγορίες:

- Νανοδομές μηδενικών διαστάσεων
- Μονοδιάστατες νανοδομές
- Διδιάστατες νανοδομές

4.1 Μέταλλα – κράματα

Τα σύνθετα μεταλλικών μητρών κατέχουν την πρώτη θέση σε ονομαστική εφελκυστική αντοχή. Επίσης παρουσιάζουν εξαιρετικές ιδιότητες σε ορισμένα χαρακτηριστικά όπως το πολύ υψηλό σημείο τήξης και η μεγάλη ολκιμότητα. Η διαφορά τους με τα σύνθετα πολυμερικών μητρών (PMC) είναι ότι τα MMC είναι βαρύτερα. Οι συνηθέστερες μεταλλικές μήτρες είναι από αργίλιο ή τιτάνιο, ενώ το μέσο πλήρωσης/ενίσχυσης των MMC μπορεί να αποτελείται από ίνες ποικίλων μεγεθών ή από κόκκους. Πρόσφατα, μερικοί από τους παραγωγούς αυτοκινήτων έχουν εισάγει εξαρτήματα μηχανών τα οποία αποτελούνται από μια μήτρα ενός κράματος αλουμινίου ενισχυμένου με ίνες οξειδίου του αλουμινίου και άνθρακα. Αυτό το MMC είναι χαμηλού βάρους και αντιστέκεται στη φθορά και στις θερμικές παραμορφώσεις. Δομικού χαρακτήρα αεροναυπηγικές εφαρμογές εμπεριέχουν προηγμένα σύνθετα υλικά τα οποία αποτελούνται από μεταλλική μήτρα κράματος αλουμινίου. Οι ίνες βορίου χρησιμοποιούνται ως ενίσχυση για το διαστημικό λεωφορείο (SpaceShuttleOrbiter) και οι συνεχείς ίνες γραφίτη για το τηλεσκόπιο Hubble.

4.2 Νανοσύνθετα

4.2.1 Πολυμερική μήτρα με νανοσωλήνες άνθρακα

Πολυμερές ονομάζεται μια ουσία που δομείται από μόρια, τα οποία σχηματίζονται με πολλαπλή επανάληψη στοιχειωδών δομικών μονάδων και τα οποία είναι τόσο μεγάλα, ώστε οι ιδιότητες τους να μην αλλάζουν με την προσθήκη ή αφαίρεση μιας ή λίγων μονάδων. Η στερεή φάση στα πολυμερή μπορεί να είναι κρυσταλλική ή άμορφη. Με βάση τις θερμομηχανικές τους ιδιότητες τα πολυμερή μπορούν να ταξινομηθούν σε θερμοπλαστικά, θερμοσκληρυνόμενα και ελαστομερή [106].

[106]Π.Α. Ταραντίλη, Σημειώσεις του μαθήματος 'Μηχανική Πολυμερών', Εκδ. Ε.Μ.Π., Αθήνα 2009.

Σύνθετα υλικά, είναι τα υλικά, τα οποία μακροσκοπικά αποτελούνται από δύο ή περισσότερα χημικά ευδιάκριτα συστατικά μέρη που έχουν μια συγκεκριμένη διαχωριστική επιφάνεια μεταξύ τους. Το ένα, από τα συστατικά μέρη, χαρακτηρίζεται ως συστατικό ενίσχυσης και προσδίδει στο σύνθετο βελτιωμένες μηχανικές, κυρίως, ιδιότητες. Το δεύτερο συστατικό καλείται μήτρα, είναι συνήθως χαμηλής πυκνότητας και η συμμετοχή του στο σύνθετο εξασφαλίζει τη μέγιστη δυνατή εκμετάλλευση των ιδιοτήτων της ενίσχυσης. Γενικά, ένα σύνθετο υλικό αποτελείται από την ενίσχυση (ίνες, μόρια, σωματίδια και υλικά πληρώσεως) που ενσωματώνεται σε μια μήτρα (πολυμερή σώματα, μέταλλα, ή κεραμικά υλικά) [107].

Νανοσύνθετο πολυμερές ονομάζεται το πολυμερές, που στη μήτρα του έχει διεσπαρμένα ως μέσο ενίσχυσης νανοσωματίδια, δηλαδή σωματίδια τα οποία έχουν την μία τουλάχιστον διάστασή τους στην νανοκλίμακα (1 έως 100nm), που του προσδίδουν μοναδικές ιδιότητες ή ενισχύουν τις ήδη υπάρχουσες. Στην παρούσα εργασία θα αναφερθούμε σε νανοσύνθετα πολυμερή στα οποία το μέσο ενίσχυσης θα είναι νανοσωλήνες άνθρακα [108].

Η ενσωμάτωση των CNTs σε μια πολυμερή μήτρα παρέχει στα υλικά εντυπωσιακά αυξανόμενη δυσκαμψία και αντοχή. Παραδείγματος χάριν, προσθέτοντας έως 7% κατά βάρος (μετά παρατηρείται μείωση των μηχανικών ιδιοτήτων) MWCNTs στις συνθετικές μεμβράνες PMMA/MWCNT οδηγούμαστε σε αύξηση του μέτρου ελαστικότητας μέχρι 30% [109]. Έχει παρατηρηθεί (Biercuketal.) ότι η σκληρότητα του υλικού (Vickers) αυξάνει πάνω από 3,5 φορές κατά την προσθήκη 2% κατά βάρος SWCNTs σε εποξική ρητίνη [110]**.** Συνοπτικά, οι μηχανικές ιδιότητες τυπικών σύνθετων υλικών ενισχυμένων με νανοσωλήνες παρουσιάζονται στον παρακάτω πίνακα 4.1:

Πίνακας 4.1Οι τυπικές μηχανικές ιδιότητες των συνθέτων ενισχυμένων με CNTs[111]

[107]Α. Μοροπούλου, Π. Βασιλείου, Ι. Σιμιτζής, Λ. Ζουμπουλάκης, Επιστήμη και Τεχνική Υλικών, Εκδ. Ε.Μ.Π., Αθήνα 2010.
[108] Polymer nanocomposites , Processing , characterization and applications , Joseph H Koo , Mc Graw Hill ,2006
[109] M. Meyyappan e.a., Carbon Nanotubes Science and Applications, CRC Press
[110]M. J. Biercuk, M. C.Liaguno, M.Radosavljevic, J. K. Hyun and A. T. Johnson.
Carbon nanotube composites for thermal management.Phys.Lett. 80 (2002) 2767
[111] Jihua Gou, Bob Minaie, Ben Wang, Zhiyong Liang, Chuck Zhang. Computational
and experimental study of interfacial bonding of single-walled nanotube reinforced
composites. Computational Materials Science 31 (2004) 225–236

Selected mechanical properties of CNT/polymer composites

CNT	Matrix	Conc. (%)	Loading	Modulus	Yield stress	Strength	Tough-ness	Max. strain	ISS (Mpa)
MWNT	None	100	Tensile[a]	910 GPa		150 GPa			
MWNT	None	100	Tensile[b]	270–950 GPa		11–200 GPa		12%	
MWNT	PAN	1.8 vol.%	Tensile	+36%	+46%	+31%	+80%		
SWNT	PVA	60 wt.%	Tensile	80 GPa		1.8 GPa	570 J/g	~100%	
MWNT	PS	5 wt.%	DMA (25 °C)	+49% (aligned) + 10% (random)					
MWNT	PE–B[c]		AFM[c]						47 MPa
MWNT	UHMWPE	1 wt.%	Tensile	+25%	+48%	+25%	+150%	+60 to +140%	
SWNT	PAN	4 wt.%	AFM[d]	~ +100%					
CNF	PMMA	5 wt.%	Tensile	+50%		+200%[e]		−37.5%	
MWNT	PMEMA	1 wt.%	DMA	+200%					

(+/−) indicates an enhancement/diminishment from the neat matrix. Recently reported mechanical property enhancements for various CNT/polymer composites are presented with additional information on the method used to collect the data. Experimentally measured values of MWNT mechanical properties are also presented.

[a] In situ TEM tensile testing of individual MWNTs via a micro-fabricated device.
[b] In situ SEM tensile testing of individual MWNTs via dual AFM tips.
[c] In situ AFM pull-out of individual MWNT from PE–B film.
[d] Moduli measured using an AFM nanoindentation technique.
[e] Compressive strength via loop test.

Η προσθήκη CNTs θα μπορούσε να αυξήσει τη θερμοκρασία υαλώδους μετάπτωσης, την θερμοκρασία τήξη και τις θερμοκρασίες αποσύνθεσης της πολυμερούς μήτρας λόγω του περιορισμού που επιβάλουν στα πολυμερή τμήματα και τις αλυσίδες. Αποτέλεσμα αυτού είναι η βελτίωση της θερμικής αντοχής των πολυμερών σύνθετων. Ως παράδειγμα αναφέρεται ότι, προσθέτοντας 1% κατά βάρος CNTs στις εποξικές ρητίνες, αυξάνεται η θερμοκρασία υαλώδους μετάπτωσης από 63 σε 88 ^{o}C. Ομοίως, με 1% κατά βάρος SWCNTs, η θερμοκρασία μετάβασης γυαλιού του PMMA αυξάνεται κατά 40^{o}C. Επίσης, η ενσωμάτωση CNTs θα μπορούσε να βελτιώσει την θερμική αγωγιμότητα των πολυμερών σύνθετων λόγω της άριστης θερμικής αγωγιμότητας των CNTs, όπως φαίνεται και στο σχήμα 4.2 . Αυτό προσφέρει μια ευκαιρία για το πολυμερές σώμα το οποίο ενισχύεται με CNTs για χρήσεις ως πίνακες κυκλωμάτων, διακόπτες, θερμικά υλικά διεπαφών, δεξαμενές θερμότητας, κ.α. [112][113]

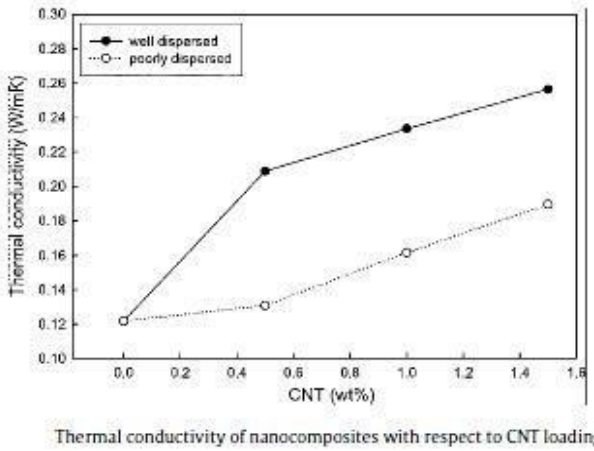

Thermal conductivity of nanocomposites with respect to CNT loading.

Σχήμα 4.2Συγκριτική καμπύλη θερμικής αγωγιμότητας για καλά διεσπαρμένους και ασθενώς διεσπαρμένους νανοσωλήνες σε πολυμερική μήτρα [114]

[112] Nanomaterials Handbook , edited by Yuri Gogotsi , CRC Press Taylor and Francis group , 2006
[113] http://www.pa.msu.edu/cmp/csc/ntproperties
[114] http://www.pa.msu.edu/cmp/csc/ntproperties

Η πιο σημαντική εμπορική εφαρμογή των νανοσωλήνων άνθρακα είναι η χρήση τους ως ηλεκτρικά αγώγιμα συστατικά στα σύνθετα πολυμερή. Η ηλεκτρική αγωγιμότητα αυξάνεται σημαντικά με την προσθήκη νανοσωλήνων όπως φαίνεται στο σχήμα 4.3 που ακολουθεί [115].

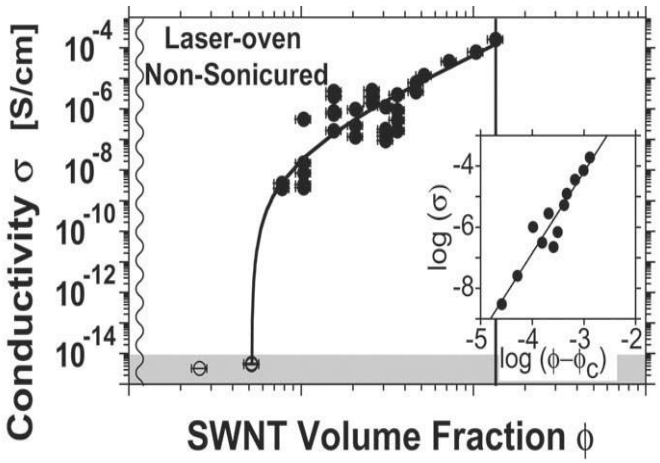

Σχήμα 4.3Καμπύλη ηλεκτρικής αγωγιμότητας συναρτήσει περιεκτηκότητας SWCNTs[116]

Τα σύνθετα πολυμερή με νανοσωλήνες άνθρακα λόγω των μοναδικών ιδιοτήτων τους έχουν τη δυνατότητα να χρησιμοποιηθούν σε εφαρμογές ευρείας κλίμακας. Έτσι μπορούν να χρησιμοποιηθούν στον αεροδιαστημικό τομέα λόγω της υψηλής τους αντοχής αλλά και λόγω της μικρής τους πυκνότητας, στον στρατιωτικό τομέας για την κατασκευή ισχυρότερων και ελαφρύτερων θωρακίσεων όπως κρανών και υφασμάτων, στα αθλητικά προϊόντα υψηλής απόδοσης (ισχυρότερα και ελαφρύτερα, μπαστούνια γκολφ, ρακέτες αντισφαίρισης, πλαίσια ποδηλάτων), καθώς και στον ηλεκτρονικό τομέα (καλώδια από νανοσωλήνες) λόγω των εξαιρετικών ιδιοτήτων τους. Επιπλέον, η ενσωμάτωση νανοσωλήνων άνθρακα σε ένα πολυμερές, το κάνουν βιοσυμβατό, με αποτέλεσμα να μπορεί να χρησιμοποιηθεί σε μοσχεύματα, αλλά και για την κατασκευή ιατρικών εργαλείων.

Μια από τις σημαντικότερες εφαρμογές (που θα ασχοληθούμε και στην παρούσα εργασία) αυτές είναι να λειτουργούν ως επικαλύψεις σε επιφάνειες. Επειδή οι νανοσωλήνες άνθρακα έχουν εξαιρετικές μηχανικές ιδιότητες, τα πολυμερικά νανοσύθετα τους μπορούν να λειτουργήσουν σαν προστατευτικές επικαλύψεις σε επιφάνειες. Χαρακτηριστική είναι η χρήση αυτής της εφαρμογής στην αυτοκινητοβιομηχανία και ιδιαίτερα στα αγωνιστικά αυτοκίνητα, τα οποία διαθέτουν επιφάνειες τους επικαλυμμένες με πολυμερικά νανοσύνθετα νανοσωλήνων άνθρακα, ως προστασία, για να αντέχουν τις υψηλές πιέσεις που δέχεται το όχημα κατά την κίνηση του. Επιπλέον, μπορούν να χρησιμοποιηθούν στη

[115] http://students.chem.tue.nl/ifp03/introduction.html
[116] http://students.chem.tue.nl/ifp03/introduction.html

βιοχημεία ως μεμβράνες για μοριακούς διαχωρισμούς ή για την ανάπτυξη οστεϊκών κυττάρων [117][118].

Το πολυαιθυλένιο πολύ υψηλού μοριακού βάρους (UHMWPE) είναι ένα ιδιαίτερα μοναδικό πολυμερές λόγω των εξαιρετικών τριβολογικών ιδιοτήτων του (υψηλή αντίσταση σε φθορά τριβής , χαμηλός συντελεστής τριβής). Το πρόβλημα όμως που εμφανίζεται με το UHMWPE είναι ότι δεν αντέχει πολύ φορτίο, καθώς και ότι είναι θερμικά ασταθές. Για αυτό το λόγω προστίθενται σε αυτό νανοσωλήνες άνθρακα πολλαπλών τοιχωμάτων, οι οποίοι έχουν υψηλή θερμοχωρητικότητα και υψηλό μέτρο ελαστικότητας, ώστε να ενισχυθούν ακόμα περισσότερο οι μηχανικές και τριβολογικές του ιδιότητες του UHMWPE και παράλληλα να ξεπεραστούν τα προβλήματα που εμφανίζονται. Το UHMWPE χρησιμοποιείται ως υλικό επικαλύψεων σε μικροηλεκτρονικά συστήματα ως προστατευτικό διάβρωσης, αλλά και σε επικαλύψεις σε εμφυτεύματα στον ανθρώπινο οργανισμό λόγω της καλής του βιοσυμβατότητας.

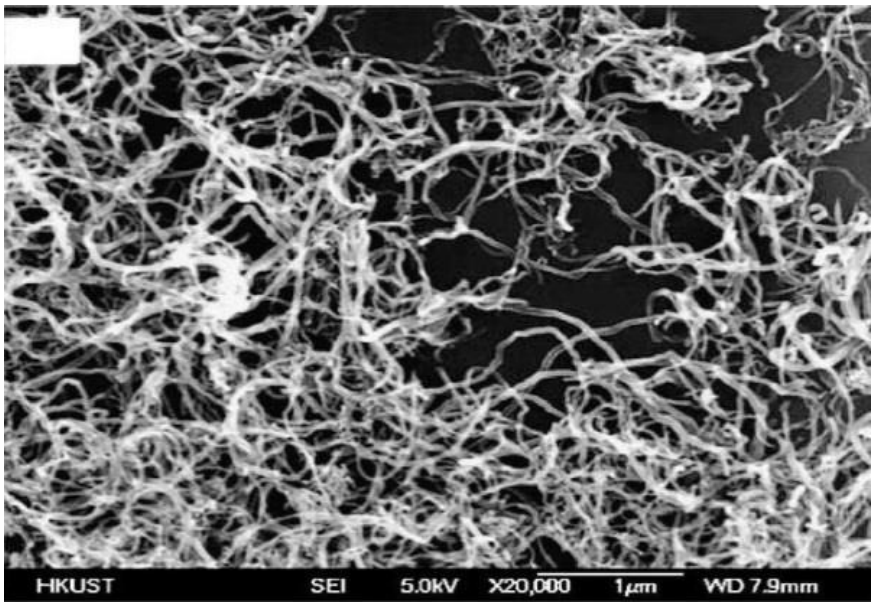

Σχήμα 4.4Νανοσωλήνες άνθρακα πολλαπλών τοιχωμάτων , όπως φαίνονται από ηλεκτρονικό μικροσκόπιο[119]

Οι μετρήσεις που πραγματοποίησε οι Bakshietal. των μηχανικών ιδιοτήτων έγιναν με το σύστημα HysitronTriboindenter, χρησιμοποιώντας ακίδα τύπου Berkovich. Το φορτίο που ασκήθηκε στο δείγμα ασκήθηκε με ρυθμό 25 N/sec φτάνοντας σε ένα μέγιστο 250 N , όπου έμεινε για 10 sec και μετά μειώθηκε στα 0 N με ρυθμό μείωσης πάλι 25 N/sec . Στο σχήμα

[117] Polymer nanocomposites , Processing , characterization and applications , Joseph H Koo , Mc Graw Hill ,2006
[118] Nanomaterials Handbook , edited by Yuri Gogotsi , CRC Press Taylor and Francis group , 2006
[119] Bin Zhang , Ruo Wen Fu, Ming Qiu Zhang , Xian Ming Dong,Pei Liang Lan, Jie Shan Qiu ,Preparation and characterization of gas-sensitive composites from
multi-walled carbon nanotubes/polystyrene, Sensors and Actuators B 109 (2005) 323–328

4.5 είναι οι καμπύλες φορτίου φόρτισης – αποφόρτισης για το καθαρό πολυμερές και για το νανοσύνθετο.

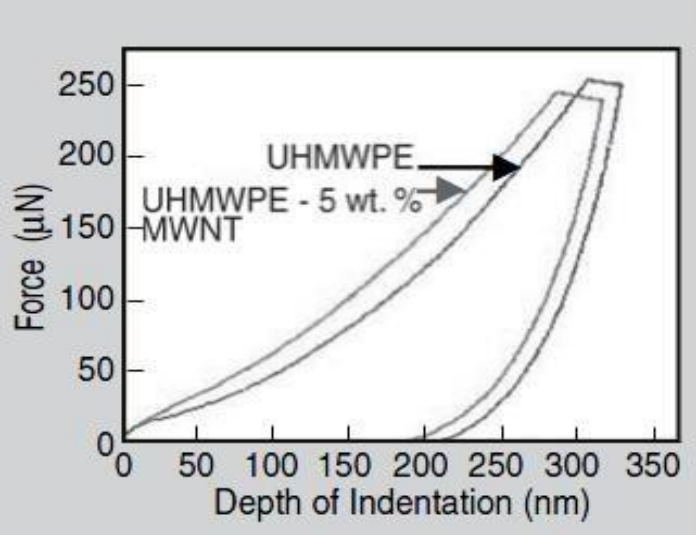

Σχήμα 4.5 Καμπύλη φόρτισης-αποφόρτισης για καθαρό πολυμερές και νανοσύνθετο[120]

Η σκληρότητα P και το μέτρο E μετρήθηκαν με τη μέθοδο Oliver και Pharr. Το μέτρο ελαστικότητας των επικαλύψεων υπολογίστηκε λαμβάνοντας ότι το μέτρο ελαστικότητας και το μέτρο Poisson του εγχαράκτη είναι ίσα με 1141 GPa και 0,07, αντίστοιχα. Παρατηρήθηκε ότι με την προσθήκη των νανοσωλήνων 5% , το μέτρο ελαστικότητας αυξήθηκε κατά 10% ενώ η σκληρότητα κατά 12%. Στο σχήμα 4.5 παρατίθενται συγκριτικά τα αποτελέσματα. Επίσης μετρήθηκε και η πλαστικότητα του δείγματος μέσω του δείκτη πλαστικότητας που είναι ο λόγος του εμβαδού κάτω από την καμπύλη για το κομμάτι φόρτισης – αποφόρτισης, προς το εμβαδόν κάτω από το τμήμα της καμπύλης όπου γίνεται ασκείται σταθερό το φορτίο. Για ένα απόλυτα πλαστικό υλικό αυτός ο δείκτης ισούται με 1, ενώ για τα ιξωδοελαστικά υλικά είναι μεταξύ 0 και 1. Από τις μετρήσεις προέκυψε ότι ο δείκτης πλαστικότητας του νανοσυνθέτου είναι 0,71 ενώ του πολυμερούς 0,70. Συνεπώς η προσθήκη των νανοσωλήνων πολλαπλών τοιχωμάτων δεν αύξησε σημαντικά την πλαστικότητα του πολυμερούς .

Πίνακας 4.2: Αποτελέσματα πειράματος[121]

[120] S.R. Bakshi, K. Balani, T. Laha, J. Tercero, and A. Agarwal , The Nanomechanical and Nanoscratch Properties of MWNTReinforced Ultrahigh-Molecular-Weight Polyethylene Coatings ,Research Summary , JOM 2007

[121] S.R. Bakshi, K. Balani, T. Laha, J. Tercero, and A. Agarwal , The Nanomechanical and Nanoscratch Properties of MWNTReinforced Ultrahigh-Molecular-Weight Polyethylene Coatings ,Research Summary , JOM 2007

Coating	Elastic Modulus (GPa)	Hardness (MPa)	Plasticity Index
UHMWPE	2.02 ± 0.10	104 ± 14	0.70
UHMWPE–5 wt.% MWNT	2.23 ± 0.17	116 ± 14	0.71

Η νανοεγχάραξη πραγματοποιήθηκε με το ίδιο σύστημα και την ίδια ακίδα Berkovich. Η ακίδα αρχικά μετακινήθηκε κατά 5 μm ως το σημείο ηρεμίας της, ενώ έπειτα ασκήθηκε γραμμικά αυξανόμενο φορτίο από 0 μN στα 200 μN, μετακινώντας παράλληλα την ακίδα κατά 10 μm σε μια θέση που βρίσκεται 5 μm πίσω από τη θέση ηρεμίας. Αυτή η απόσταση καλύφθηκε σε 30 sec. Στο τέλος του scratchtest το φορτίο μειώθηκε στα 0 μN μέσα σε 2 sec.

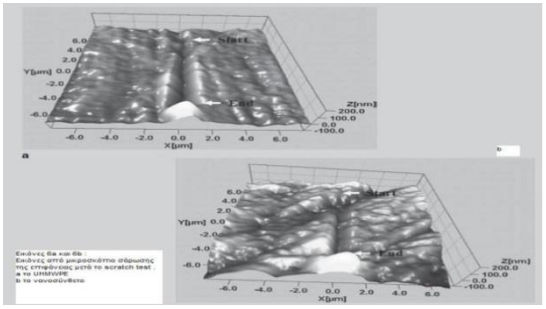

Σχήμα 4.6 Εικόνες από το μικροσκόπιο σάρωσης μετά το πέρας του scratchtesting[122]

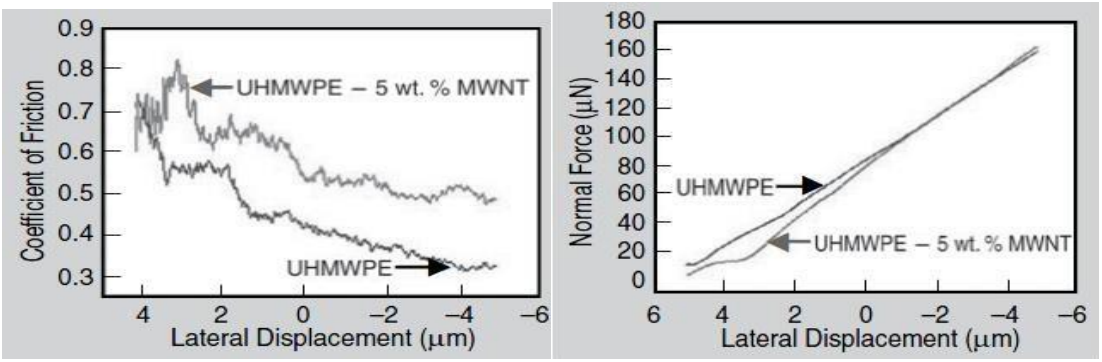

Σχήμα 4.7 Συσχέτιση συντελεστή τριβής- μετατόπισης και καμπύλη ασκούμενης δύναμης–μετατόπισης [123]

Ο συντελεστής τριβής εδώ υπολογίστηκε ως ο λόγος της πλευρικής δύναμης προς το εφαρμοζόμενο. Ο συντελεστής τριβής εξαρτάται από τη γεωμετρία της ακίδας, την επιφανειακή τραχύτητα του δείγματος και τις ιδιότητες του υλικού του δείγματος. Ο

[122] S.R. Bakshi, K. Balani, T. Laha, J. Tercero, and A. Agarwal , The Nanomechanical and Nanoscratch Properties of MWNTReinforced Ultrahigh-Molecular-Weight Polyethylene Coatings ,Research Summary , JOM 2007

[123] S.R. Bakshi, K. Balani, T. Laha, J. Tercero, and A. Agarwal , The Nanomechanical and Nanoscratch Properties of MWNTReinforced Ultrahigh-Molecular-Weight Polyethylene Coatings ,Research Summary , JOM 2007

συντελεστής τριβής λειτουργεί ως μέτρο της αντίστασης του υλικού στην εγχάραξη. Ο συντελεστής τριβής για το πολυμερές μετρήθηκε ίσος με 0,36 ± 0,03 και για το νανοσύνθετο 0,51 ± 0,02. Διαπιστώνεται μεγάλη αύξηση του συντελεστή τριβής λόγω της προσθήκης των νανοσωλήνων. Να τονιστεί ότι για τον υπολογισμό του συντελεστή τριβής χρησιμοποιήθηκαν τα δεδομένα κατά τη μετακίνηση κατά 10 μm, επειδή στο πρώτο μέρος του test οι μετρήσεις δύναμης θα επηρεάζονταν από την μορφολογία της επιφάνειας[124].

4.3 Ζεόλιθος – Μεμβράνες

Οι ζεόλιθοι συμβάλλουν σε ένα καθαρότερο, ασφαλέστερο περιβάλλον με πολλούς τρόπους. Στα απορρυπαντικά σκόνης, οι ζεόλιθοι αντικατέστησαν τα επιβλαβή φωσφορικά άλατα. Σαν στερεά οξέα, οι ζεόλιθοι μειώνουν την ανάγκη για τα διαβρωτικά υγρά οξέα. Ως οξειδοαναγωγικοί καταλύτες, μπορούν να αφαιρέσουν τους ατμοσφαιρικούς ρύπους, όπως τα αέρια μηχανών και τα CFCs που προκαλούν την μείωση του όζοντος. Χρησιμοποιούνται στο χωρισμό των επιβλαβών οργανικών ουσιών από το ύδωρ, και στην αφαίρεση των ιόντων βαριών μετάλλων, συμπεριλαμβανομένων εκείνων που παράγονται από την πυρηνική διάσπαση, από το νερό.

Ένα"μοριακό κόσκινο" είναι ένα υλικό με εκλεκτικές ιδιότητες προσρόφησης, ικανό να διαχωρίσει τα συστατικά ενός μίγματος βάσει της διαφοράς στο μοριακό μέγεθος και το σχήμα. Ο όρος μοριακά κόσκινα δόθηκε από το McBain το 1932 και περιλαμβάνει τους αργίλους, τα πορώδη γυαλιά, τους μικροπορώδεις ξυλάνθρακες, τους ενεργούς άνθρακες, κ.λ.π. Από το 1982 διάφορες νέες οικογένειες μοριακών κόσκινων βασισμένων σε $AlPO_4$ έχουν ανακαλυφθεί. Αυτά τα αλουμινοφωσφορικά, αλουμινοπυριτιο-φωσφορικά, μεταλλοαλουμινοφωσφορικά και μεταλλοαλουμινοπυριτιο-φωσφορικά συμβολίζονται ως $AlPO_4$-n, SAPO-n, MeAPO-n και MeAPSO-n,αντίστοιχα, όπου το n είναι ένας ακέραιος αριθμός που δείχνει τον τύπο δομών. Σε περισσότερα από είκοσι μοριακά κόσκινα $AlPO_4$ που παρασκευάζονται μέχρι τώρα, ορισμένα έχουν τις δομές γνωστών ζεόλιθων ενώ αλλά εμφανίζουν νέες δομές. Όταν το Si ενσωματώνεται στο πλαίσιο $AlPO_4$-n, το προϊόν είναι γνωστό ως SAPO. Τα MeAPO ή MeAPSO κόσκινα διαμορφώνονται από την ενσωμάτωση ενός ατόμου μετάλλου (Me) σε ένα πλαίσιο $AlPO_4$-n ή SAPO. Αυτά τα άτομα μετάλλων περιλαμβάνουν το Li, Be, Mg, Co, Fe, Mn, Zn, B, Ga, Fe, Ge, Ti και As. Τα περισσότερα αντικατασταθέντα $AlPO_4$-n έχουν την ίδια δομή με το $AlPO_4$-n, αλλά διαφορετικές νέες δομές βρέθηκαν μόνο στα υλικά SAPO, MeAPO και MeAPSO. Τα πλαίσια τους φέρουν ένα

[124] S.R. Bakshi, K. Balani, T. Laha, J. Tercero, and A. Agarwal , The Nanomechanical and Nanoscratch Properties of MWNTReinforced Ultrahigh-Molecular-Weight Polyethylene Coatings ,Research Summary , JOM 2007

ηλεκτρικό φορτίο, παρέχοντας ενδεχομένως μια περαιτέρω αλλαγή της καταλυτικής τους συμπεριφοράς[125].

Το πλαίσιο ενός μοριακού κόσκινου είναι βασισμένο σε ένα εκτενές τρισδιάστατο δίκτυο στο οποίο οι πολύεδρες επιφάνειες, συνήθως τετραεδρικές, συνδέονται με άτομα οξυγόνου. Το κρυσταλλικό πλαίσιο περιέχει κλωβούς και κανάλια ιδιαίτερου μεγέθους με διάμετρο 3-30 Å. Η αρχική μονάδα οικοδόμησης ενός μοριακού κόσκινου είναι η μεμονωμένη τετραεδρική μονάδα. Η τοπολογία όλων των γνωστών τύπων πλαισίου μοριακών κόσκινων μπορεί να περιγραφεί από την άποψη ενός πεπερασμένου αριθμού συγκεκριμένων συνδυασμών τετραέδρων αποκαλούμενων "δευτεροβάθμιων μονάδων οικοδόμησης" (SBU). Ένα μοριακό πλαίσιο κόσκινων αποτελείται από μόνο ένα τύπο SBU.

Η δομή και οι ιδιότητες του μοριακού κόσκινου εξαρτώνται ιδιαίτερα από:

- το φυσικό και χημικό χαρακτήρα των αντιδραστηρίων που χρησιμοποιούνται στην προετοιμασία του μίγματος αντίδρασης,
- τον τύπο κατιόντων ή οργανικού προτύπου,
- και τις συνθήκες (θερμοκρασία, πίεση και διάρκεια) της υδροθερμικής επεξεργασίας.

Τα μοριακά κόσκινα είναι εκλεκτικά, μεγάλης χωρητικότητας προσροφητικά λόγω της μεγάλης ειδικής επιφάνειας που εμφανίζουν και τις ισχυρές αλληλεπιδράσεις με τις προσροφημένες ουσίες. Τα μόρια διαφορετικού μεγέθους έχουν γενικά διαφορετικές ιδιότητες διάχυσης στο ίδιο μοριακό κόσκινο. Τα διαφορετικής πολικότητας μόρια έχουν μια διαφορετική αλληλεπίδραση στο πλαίσιο των μοριακών κόσκινων, και μπορούν έτσι να διαχωριστούν από ένα συγκεκριμένο μοριακό κόσκινο. Αυτό είναι μια από τις σημαντικότερες χρήσεις των ζεόλιθων. Ένα παράδειγμα είναι ο διαχωρισμός του N_2 και του O_2 στον αέρα με ζεόλιθο Α, λόγω της διαφορετικής πολικότητας των δύο μορίων. Η ποσότητα προσροφημένου αερίου ή υγρού εξαρτάται από την πίεση, τη θερμοκρασία, τη φύση της προσροφημένης ουσίας και το είδος του μοριακού κόσκινου. Οι παραλλαγές στη χημική σύνθεση του κόσκινου έχουν επιπτώσεις επίσης στην προσρόφηση. Τα προσροφημένα μόρια μπορούν να αφαιρεθούν με τη θέρμανση ή / και την εκκένωση. Τα μεγέθη των δαχτυλιδιών του μοριακού κόσκινου μπορούν να καθοριστούν από την προσρόφηση μορίων διαφορετικού μεγέθους. Το νερό και το άζωτο είναι δύο από τα μικρότερα μόρια που μπορούν εύκολα να διαπεράσουν σχεδόν ολόκληρες τις δομές. Αυτά τα δύο μόρια χρησιμοποιούνται για να καθορίσουν τη διαύγεια των μοριακών κόσκινων με τη σύγκριση του όγκου προσρόφησης με αυτόν ενός τυποποιημένου δείγματος[126].

[125] Van Bekkum H., Flanigen E.M. and Jansen J.C. (editors), Studies in interface science and catalysis vol 58: Introduction to zeolite science and practice, Elsevier, 1991.
[126] Van Bekkum H., Flanigen E.M. and Jansen J.C. (editors), Studies in interface science and catalysis vol 58: Introduction to zeolite science and practice, Elsevier, 1991.

Τα μοριακά κόσκινα έχουν βρει διαδεδομένες βιομηχανικές εφαρμογές ως:

- Ιδιαίτερα εκλεκτικά προσροφητικά,
- Ιονικοί εναλλάκτες και
- Καταλύτες εξαιρετικά υψηλής δραστικότητας και επιλεκτικότητας σε ένα ευρύ φάσμα αντιδράσεων.

Αυτές οι εφαρμογές περιλαμβάνουν:

- Ξήρανση ψυκτικών ουσιών,
- Αφαίρεση ατμοσφαιρικών ρύπων όπως το διοξείδιο του θείου,
- Διαχωρισμό των συστατικών του αέρα,
- Διαχωρισμό και την αποκατάσταση των κανονικών υδρογονανθράκων παραφίνης,
- Ανάκτηση ραδιενεργών ιόντων από απόβλητα και κατάλυση των αντιδράσεων υδρογονανθράκων [127].

Το ενδιαφέρον για την ανάπτυξη ζεολιθικών μεμβρανών προέκυψε γιατί η μέχρι τότε χρήση των ζεόλιθων σε μη συνεχείς διεργασίες διαχωρισμού απαιτούσε τη χρήση μεγάλου αριθμού πληρωμένων κλινών από ζεόλιθους, τη συχνή αναγέννησή τους καθώς και την κυκλική εναλλαγή παραμέτρων λειτουργίας όπως είναι η πίεση και η θερμοκρασία προκειμένου να επιτευχθούν οι διαχωρισμοί. Η χρήση ζεολιθικών μεμβρανών στις παραπάνω διεργασίες διαχωρισμού θα μπορούσε να μειώσει σημαντικά το λειτουργικό κόστος και τις ενεργειακές απαιτήσεις των διεργασιών αυτών επειδή οι μεμβράνες μπορούν να λειτουργήσουν συνεχώς, τόσο σε υψηλές πιέσεις, όσο και σε υψηλές θερμοκρασίες. Από το μεγάλο αριθμό συνθετικών ζεολιθικών δομών που έχουν αναπτυχθεί περίπου δεκαπέντε έχουν αναπτυχθεί υπό τη μορφή μεμβρανών.

Οι ζεολιθικές μεμβράνες MFI είναι εκείνες οι οποίες έχουν μελετηθεί περισσότερο επειδή μπορούν να δεχτούν μόρια με βιομηχανικό ενδιαφέρον, έχουν υψηλή θερμική και χημική σταθερότητα, παρασκευάζονται εύκολα και γρήγορα ενώ μπορεί να τροποποιηθεί κατάλληλα η χημική σύστασή τους. Οι πρώτες ζεολιθικές μεμβράνες που παρασκευάστηκαν στο εργαστήριο δεν αποτελούταν μόνο από κρυστάλλους ζεόλιθων, ήταν σύνθετες μεμβράνες και προέκυπταν από τη διασπορά μικρών ποσοστών ζεολιθικών κρυστάλλων σε πολυμερικά υμένια . Οι συγκεκριμένες μεμβράνες συνδύαζαν τις ιδιότητες των πολυμερών με τις ιδιότητες των ζεόλιθων και είχαν μελετηθεί στο διαχωρισμό μιγμάτων αερίων και μιγμάτων ατμών. Η χαμηλή όμως θερμική και χημική σταθερότητα των πολυμερικών

[127] Van Bekkum H., Flanigen E.M. and Jansen J.C. (editors), Studies in interface science and catalysis vol 58: Introduction to zeolite science and practice, Elsevier, 1991.

υλικών, έστρεψε το ερευνητικό ενδιαφέρον γύρω από την ανάπτυξη ζεολιθικών μεμβρανών υποστηριγμένων στην επιφάνεια πιο σταθερών υποστρωμάτων[128].

Οι υποστηριγμένες ζεολιθικές μεμβράνες αναπτύσσονται στην επιφάνεια πορωδών κυρίως υποστρωμάτων, των οποίων η γεωμετρία, η χημική σύσταση, οι ιδιότητες της δομής τους (μέγεθος πόρων και πορώδες) καθώς και η αρχική επεξεργασία τους μπορεί να επηρεάσουν τα χαρακτηριστικά των μεμβρανών. Τα πορώδη υποστρώματα τα οποία έχουν μελετηθεί περισσότερο προέρχονται από α- Al_2O_3, γ- Al_2O_3, TiO_2, SiC, μουλίτη ή ατσάλι. Μικρός αριθμός ερευνητικών ομάδων έχει χρησιμοποιήσει επίσης υποστρώματα από άνθρακα ή και γυαλί [129].

Κατά την επιλογή ενός υποστρώματος οι βασικές παράμετροι οι οποίες θα πρέπει πάντα να εκτιμώνται είναι η θερμική και χημική σταθερότητα σε αιωρήματα σύνθεσης των μεμβρανών καθώς και οι διαφορές μεταξύ των συντελεστών θερμικής διαστολής-συστολής του υποστρώματος και της ζεολιθικής μεμβράνης. Επιπρόσθετα, η τραχύτητα της επιφάνειας των υποστρωμάτων είναι σημαντική παράμετρος η οποία μπορεί να επηρεάσει την ποιότητα των μεμβρανών κατά τη διάρκεια του σχηματισμού τους. Οι περισσότερες ζεολιθικές μεμβράνες σύμφωνα με τη βιβλιογραφία έχουν αναπτυχθεί στην επιφάνεια επίπεδων (δισκία) ή κυλινδρικών υποστρωμάτων. Ιδιαίτερο ενδιαφέρον σήμερα έχει η ανάπτυξη ζεολιθικών μεμβρανών σε υποστρώματα που έχουν μεγάλη επιφάνεια και γεωμετρία και που μπορούν να χρησιμοποιηθούν σε βιομηχανικές εφαρμογές, όπως τα τριχοειδή και τα κυψελωτά υποστρώματα [130].

4.4 Επικαλύψεις

Οι solgel επιστρώσεις και ειδικότερα οι υβριδικές παρέχουν πολύ καλές ιδιότητες φραγμού. Ωστόσο, οι επιστρώσεις αυτές από μόνες τους δεν μπορούν να παρέχουν αρκετή προστασία από την διάβρωση καθώς στις επιστρώσεις αυτές ενδέχεται να υπάρχουν πόροι, ρωγμές και περιοχές οπού η πυκνότητα των σταυροδεσμών στο sol – gel δίκτυο είναι μικρή. Έτσι δημιουργούνται μονοπάτια που επιτρέπουν στα διαβρωτικά είδη, όπως είναι το νερό το οξυγόνο και ιόντα χλωρίου, να φτάσουν στην διεπιφάνεια επικάλυψης/μετάλλου. Ορισμένες solgel επιστρώσεις παρουσιάζουν την ικανότητα αυτοΐασης (self – healingeffect), βέβαια σε πολύ μικρότερο βαθμό σε σύγκριση με τις χρωμικές επιστρώσεις. Συνεπώς, οι solgel επιστρώσεις μπορούν να παρέχουν επαρκή προστασία μόνο εάν δεν παρουσιάζουν ατέλειες.

[128] Hennepe H., Boswerger W.B.F., Bargeman D., Mulder M.H.V., Smolders C.A., J. Membr. Sci., 89 (1994) 185. T. Bein, Chem. Mat., 8 (1996) 1636
[129] Julbe A., Stud. Surf.Sci. Catal., Vol.157 (2005) 135.
[130] Hennepe H., Boswerger W.B.F., Bargeman D., Mulder M.H.V., Smolders C.A., J. Membr. Sci., 89 (1994) 185. T. Bein, Chem. Mat., 8 (1996) 1636.

Η ενσωμάτωση και η διασπορά ανόργανων σωματιδίων, η διάμετρος των οποίων είναι συνήθως στην νανοκλίμακα, στις υβριδικές solgel επιστρώσεις, οδηγεί σε βελτίωση των ιδιοτήτων φραγμού των επιστρώσεων αυτών, καθώς οδηγεί σε επιστρώσεις με μικρότερο πορώδες και μικρότερη τάση σχηματισμού ατελειών. Ωστόσο, σημειώνεται ότι οι αντιδιαβρωτικές ιδιότητες των επιστρώσεων αυτών εξαρτώνται σε μεγάλο βαθμό από το μέγεθος των σωματιδίων. Όσο αυξάνεται η διάμετρος των σωματιδίων υποβαθμίζονται οι ιδιότητες φραγμού της επίστρωσης, λόγω των ρωγμών που σχηματίζονται σε αυτή.

Στην βελτίωση των αντιδιαβρωτικών ικανοτήτων των solgel επιστρώσεων στοχεύει και η εισαγωγή ανόργανων ή οργανικών αναστολέων διάβρωσης στην επίστρωση. Βέβαια υπάρχει μία κρίσιμη συγκέντρωση του αναστολέα, πάνω από την οποία σχηματίζονται ατέλειες στο solgel δίκτυο μειώνοντας την αντιδιαβρωτική ικανότητα της.

Με σκοπό να ελαχιστοποιηθούν αυτές οι αρνητικές επιδράσεις της προσθήκης του αναστολέα στην επίστρωση, ο αναστολέας μπορεί να εισαχθεί σε νανοδοχεία. Τα νανοδοχεία αυτά λειτουργούν σαν δεξαμενές αποθήκευσης του αναστολέα μέσα στην επίστρωση, και τον απελευθερώνουν όταν κάποια ατέλεια σχηματιστεί στην επίστρωση. Έτσι οι επιστρώσεις θα παρουσιάζουν την ικανότητα αυτοΐασης (self – healingeffect) καθώς τα νανοδοχεία θα απελευθερώνουν τον αναστολέα, όταν στην επίστρωση θα δημιουργούνται ατέλειες παρέχοντας έτσι ενεργή προστασία στο μέταλλο για μεγάλο χρονικό διάστημα.

Οι αντιδιαβρωτικές sol – gel επιστρώσεις μπορούν να αποτεθούν στα μεταλλικά υποστρώματα με ποικίλες τεχνικές. Από τις σημαντικότερες τεχνικές εναπόθεσης είναι η εναπόθεση με εμβάπτιση (dipcoating), η εναπόθεση με περιστροφή (spincoating), η εναπόθεση με ψεκασμό (spraycoating) και η ηλεκτροχημική εναπόθεση (electrodeposition). Στην παρούσα διπλωματική εργασία εξετάζεται η τεχνική dipcoating[131][132].

Η dipcoating τεχνική αποτελεί μία αρκετά διαδεδομένη τεχνική απόθεσης solgelεπιστρώσεων σε μεταλλικά υποστρώματα. Η τεχνική αυτή αποτελείται από πέντε στάδια, όπως φαίνεται και στην εικόνα 4 που ακολουθεί. Τα στάδια αυτά είναι:

[131] C. J. Brinker and G. W. Scherer, Sol – gel science: The Physics and Chemistry of Sol – gel Processing (Academic Press, Inc. : New York, 1990

[132] http://www.solgel.com/articles/nov00/mennig.htm

- Εμβάπτιση (immersion)
- Ανάσυρση (start – up)
- Εναπόθεση και αποστράγγιση (deposition and drainage)
- Αποστράγγιση (drainage)
- Εξάτμιση (evaporation)

Στην περίπτωση που το διάλυμα είναι πτητικό τότε το στάδιο της εξάτμισης συνοδεύει το στάδιο της ανάσυρσης, της εναπόθεσης και της αποστράγγισης.

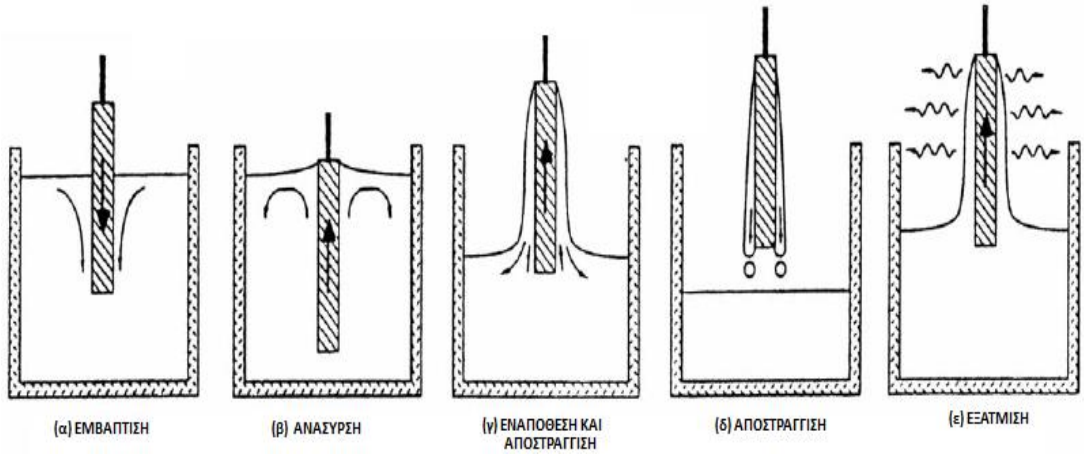

Σχήμα 4.8 Τα στάδια της dipcoating τεχνικής απόθεσης solgel επικαλύψεων [133]

Κατά το στάδιο της εμβάπτισης, η επιφάνεια που πρόκειται να επικαλυφθεί βυθίζεται στο διάλυμα, μέχρι να καλυφθεί τελείως από αυτό. Αφού παραμείνει το υπόστρωμα βυθισμένο στο διάλυμα για κάποιο χρονικό διάστημα (π.χ. 1 min) ξεκινάει το στάδιο της ανάσυρσης, κατά το οποίο το υπόστρωμα αρχίζει να ανασύρεται από το διάλυμα με σταθερή ταχύτητα μεταφέροντας μαζί του και μέρος του διαλύματος. Στο επόμενο στάδιο της απόθεσης, καθώς το υπόστρωμα απομακρύνεται από το διάλυμα μέρος του διαλύματος παραμένει πάνω σε αυτό, ενώ συντελείται μέρος της αποστράγγισης καθώς το μεγαλύτερο μέρος του διαλύματος επιστρέφει στο δοχείο στο οποίο περιέχεται. Η αποστράγγιση συνεχίζεται και ολοκληρώνεται αφού το υπόστρωμα έχει απομακρυνθεί πλήρως από το δοχείο. Τότε λαμβάνει χώρα το στάδιο της εξάτμισης, όπου διαλύτης από το μέρος διαλύματος που έχει παραμείνει πάνω στο υπόστρωμα εξατμίζεται και συνεπώς η επίστρωση μικραίνει σε όγκο και σκληραίνει.

Οι κυριότεροι παράγοντες που επηρεάζουν το πάχος του υμενίου είναι η ταχύτητα αλλά και η γωνία ανάσυρσης, το ιξώδες του διαλύματος και ο ρυθμός εξάτμισης. Σημειώνεται ότι όσο μεγαλύτερη είναι η ταχύτητα ανάσυρσης, τόσο μεγαλύτερο είναι το πάχος του υμενίου, ενώ ταυτόχρονα τόσο πιο μεγάλο είναι και το χρονικό διάστημα κατά το οποίο τα στάδια της

[133] http://www.solgel.com/articles/nov00/mennig.htm

απόθεσης και της αποστράγγισης που αλληλεπικαλύπτονται. Βασική παράμετρος που επηρεάζει το στάδιο της εξάτμισης είναι ο ρυθμός με τον οποίον απομακρύνεται ο εξατμιζόμενος διαλύτης από την επιφάνεια του υμενίου. Ο ρυθμός αυτός επηρεάζεται κυρίως από τις εξωτερικές συνθήκες που επικρατούν πάνω από το διάλυμα.

Στα βασικά πλεονεκτήματα της μεθόδου συμπεριλαμβάνονται η δυνατότητα επικάλυψης όλων των ειδών των επιφανειών, η ομοιομορφία του πάχους των επιστρώσεων αλλά και η εξοικονόμηση χρόνου και πρώτων υλών, καθώς μόνο ένα μικρό μέρος του διαλύματος χρησιμοποιείται για την επίστρωση, ενώ το υπόλοιπο παραμένει στο δοχείο και φυλάσσεται για επόμενη χρήση. Έτσι η τεχνική dipcoating είναι μία από τις πλέον διαδεδομένες τεχνικές εναπόθεσης λεπτών υμενίων.

4.5 Λεπτά υμένια

Η **φθορά (wear)** μπορεί να εμφανιστεί μέσω 4 διαφορετικών μηχανισμών: τοπική συγκόλληση ή πρόσφυση (adhesion), εκτριβή (abrasion), κόπωση (fatigue) και διάβρωση (corrosion) [134][135][136].

- *Φθορά λόγω πρόσφυσης (ή τοπικής συγκόλλησης)* εμφανίζεται όταν οι ατομικές δυνάμεις μεταξύ των υλικών δύο επιφανειών που βρίσκονται σε σχετική κίνηση είναι ισχυρότερες από τις εγγενείς ιδιότητες κάθε υλικού. Για παράδειγμα, όταν δύο επιφάνειες κινούνται η μία σε σχέση με την άλλη, εμφανίζεται σύνδεση (bonding) των τραχειών τμημάτων (asperities). Η συνεχής κίνηση αναγκάζει στη συνέχεια τους δεσμούς να σπάσουν. Κάθε φορά που σπάει ένας τέτοιος δεσμός, αποκολλούνται σωματίδια από το υλικό με τους ασθενέστερους ενδοατομικούς δεσμούς.
- *Φθορά εκτριβής* εμφανίζεται μεταξύ επιφανειών διαφορετικής σκληρότητας. Σε αυτό το μηχανισμό, τα μικροσκληρυμένα και τα τραχεία τμήματα της σκληρότερης επιφάνειας εισχωρούν στην μαλακότερη επιφάνεια και, μέσω της σχετικής κίνησής τους, αποξέουν τμήματα της δεύτερης. Η φθορά τρίτου σώματος (third-bodywear) είναι ένα είδος φθοράς εκτριβής που προκαλείται όταν μια επιφάνεια βρίσκεται σε επαφή με σκληρά σωματίδια, τα οποία μπορεί να είναι είτε το ανταγωνιστικό υλικό, είτε προϊόντα φθοράς της εν λόγω επιφάνειας με μία δεύτερη.

[134] P. Pruitt, What are the wear mechanisms and what controls them?, 'Aspects of Biomaterials' Lectures Notes, Mechanical Engineering Department, Berkley University of California, http://www.me.berkeley.edu/ME117/S06/lectures/AAOS-WEAR.pdf [πρόσβαση 29-03-09]

[135] P. Pruitt, What are the wear mechanisms and what controls them?, 'Aspects of Biomaterials' Lectures Notes, Mechanical Engineering Department, Berkley University of California, http://www.me.berkeley.edu/ME117/S06/lectures/AAOS-WEAR.pdf [πρόσβαση 29-03-09]

[136] Χρυσουλάκης Γ.Δ. και Παντελής Δ.Ι., Επιστήμη και Τεχνολογία των Μεταλλικών Υλικών, Εκδόσεις Παπασωτηρίου, Αθήνα 2003, σσ. 225-233

- Η *φθορά λόγω κόπωσης* οδηγεί σε επιφανειακή ρωγμάτωση του υλικού, εξαιτίας κυκλικών φορτίσεων.
- *Φθορά λόγω διάβρωσης* είναι μηχανισμός έμμεσης φθοράς. Στην ουσία πρόκειται για μηχανισμό εκτριβής μέσω των απελευθερωθέντων σωματιδίων, που είναι προϊόντα διάβρωσης της επιφάνειας.

Επιπλέον, ανάλογα με τον τρόπο σχετικής κίνησης των δύο υλικών σε επαφή διακρίνουμε [137]:

- ***Φθορά λόγω ολίσθησης:*** Παρατηρείται όταν οι επιφάνειες που βρίσκονται σε επαφή ολισθαίνουν η μία πάνω στην άλλη, με ή χωρίς την παρουσία αποξεστικών σωματιδίων ή λιπαντικού στη διεπιφάνεια.
- ***Φθορά λόγω κύλισης:*** Συναντάται κατά την κύλιση μιας σφαίρας ή ενός κυλίνδρου σε μια στερεά επιφάνεια.
- ***Φθορά λόγω παλινδρόμησης:*** Οφείλεται σε παλινδρομικές κινήσεις υψηλής συχνότητας και μικρής έντασης.
- ***Φθορά λόγω πρόσκρουσης:*** Προκαλεί καταστροφή της επιφάνειας λόγω πρόσκρουσης στερεών σωματιδίων, σταγόνων ή υγρών εκτοξευμάτων.
- ***Φθορά λόγω μηχανικής διάβρωσης:*** Προκαλείται στην επιφάνεια του υλικού από στερεά σωματίδια μεταφερόμενα από κάποιο ρευστό.
- ***Φθορά λόγω δόνησης:*** Προκαλείται στη διεπιφάνεια των εν επαφή υλικών όταν αυτά υποβάλλονται σε ταυτόχρονη φόρτιση παλινδρόμησης και ολίσθησης

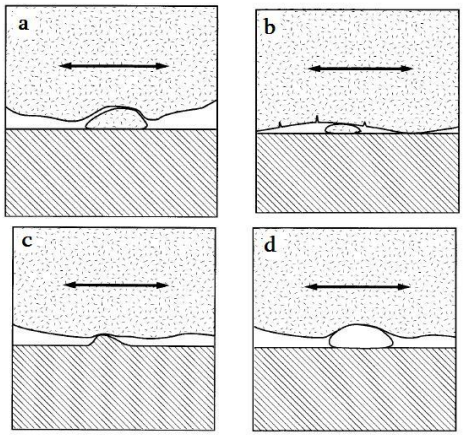

Σχήμα 4.9 Μηχανισμοί φθοράς λόγω πρόσφυσης (a), κόπωσης (b), εκτριβής (c), τρίτου σώματος (d) [138]

[137]Χρυσουλάκης Γ.Δ. και Παντελής Δ.Ι., Επιστήμη και Τεχνολογία των Μεταλλικών Υλικών, Εκδόσεις Παπασωτηρίου, Αθήνα 2003, σσ. 225-233

[138] P. Pruitt, What are the wear mechanisms and what controls them?, 'Aspects of Biomaterials' Lectures Notes, Mechanical Engineering Department, Berkley University of California, http://www.me.berkeley.edu/ME117/S06/lectures/AAOS-WEAR.pdf [πρόσβαση 29-03-09]

Η επιφάνεια ενός εξαρτήματος είναι συνήθως ο πιο σημαντικός παράγων από μηχανικής απόψεως. Κατά τη χρήση ενός οποιοδήποτε αντικειμένου, η επιφάνειά του είναι αυτή που υπόκειται σε φθορά και διάβρωση. Ο βαθμός περιπλοκότητας των τριβολογικών ιδιοτήτων των υλικών, καθώς και οι οικονομικές πτυχές της τριβής και της φθοράς των υλικών αιτιολογούν το αυξανόμενο ερευνητικό ενδιαφέρον στον τομέα αυτό. Στις βιομηχανικές χώρες περίπου το 30% όλης της παραγόμενης ενέργειας χάνεται τελικά σε απώλειες λόγω τριβών. Ειδικά στις χώρες υψηλού βαθμού βιομηχανοποίησης, οι ενεργειακές απώλειες λόγω τριβών και φθοράς βρίσκονται στο 1 με 2% του Α.Ε.Π [139].

Για αυτό το λόγο, οι έρευνες συγκεντρώνονται σε τεχνικές τροποποίησης των επιφανειών, ώστε να αυξηθεί η αντίσταση σε φθορά των υλικών. Υπάρχει ένας τρομακτικός, θα έλεγε κανείς, αριθμός μεθόδων επεξεργασίας, που καλύπτει ένα ευρύ φάσμα παχών. Η επιλογή πρέπει να είναι τέτοια ώστε η επιφανειακή επεξεργασία να μην αλλοιώνει πολύ τις ιδιότητες του υποστρώματος και να είναι κατάλληλη για τη συγκεκριμένη περίπτωση φθοράς. Για παράδειγμα, αν ένα λεπτό στρώμα μπορεί να παράσχει ικανοποιητική προστασία, δεν είναι λογικό να γίνει επικάλυψη μεγάλου πάχους [140][141].

Σε αυτό το σημείο θα πρέπει να σημειωθεί ότι η αντίσταση σε φθορά δεν είναι μία εγγενής ιδιότητα των υλικών, αλλά είναι ιδιότητα των συστημάτων, αφού το υλικό φθείρεται πάντα αλληλεπιδρώντας με κάποιο άλλο μέσο. Η σχέση του υλικού με το περιβάλλον (π.χ. λίπανση, ταχύτητα ολίσθησης) είναι αυτή που καθορίζει την αντίσταση σε φθορά του υλικού σε μία δεδομένη κατασκευή [142][143].

Κατά κανόνα, η φθορά είναι συνάρτηση δύο αντικρουόμενων ιδιοτήτων: της ολκιμότητας και της σκληρότητας. Μείωση της φθοράς μπορεί να επέλθει τροποποιώντας το επιφανειακό στρώμα ώστε να αυξηθεί η πλαστικότητά του, άρα αυξάνοντας την πλαστική παραμόρφωση που μπορεί να εμφανίσει το υλικό χωρίς αποκόλληση σωματιδίων. Τα μαλακά επιστρώματα μειώνουν αποτελεσματικά την φθορά μέσω αποκόλλησης στρωμάτων (delamination). Η αντίστασή τους, όμως, σε φθορά εκτριβής είναι πολύ μικρή. Εάν, από την άλλη πλευρά, επιλεχθεί η εφαρμογή ενός σκληρού επιστρώματος, αυτή θα συνεπάγεται την αύξηση του ορίου ελαστικότητας και τη μείωση της ολκιμότητας, συνεπώς αναμένεται μειωμένη αντίσταση σε κόπωση και σε ψαθυρή θραύση. Τα ειδικά

[139] A. Cavaleiro and J. De Hosson (Eds), Nanostructured Coatings, Springer, New York, 2006.
[140] A. Cavaleiro and J. De Hosson (Eds), Nanostructured Coatings, Springer, New York, 2006.
[141]Τριβή: Μια περιήγηση στην ιστορία και τις εφαρμογές της, Περιφερειακή Δ/νση Ιονίων Νήσων Δ/νση Δ/βάθμιας Εκπαίδευσης, Εργαστηριακό Κέντρο Φυσικών Επιστημών Κέρκυρας, http://www.dide.ker.sch.gr/ekfe/epiloges/3arthra/tribh.doc[πρόσβαση 30-05-09]
[142]Τριβή: Μια περιήγηση στην ιστορία και τις εφαρμογές της, Περιφερειακή Δ/νση Ιονίων Νήσων Δ/νση Δ/βάθμιας Εκπαίδευσης, Εργαστηριακό Κέντρο Φυσικών Επιστημών Κέρκυρας, http://www.dide.ker.sch.gr/ekfe/epiloges/3arthra/tribh.doc[πρόσβαση 30-05-09]
[143] Colin R. Gagg & Peter R. Lewis, Wear as a product failure mechanism – Overview and case studies , Engineering Failure Analysis, Vol.14, 2007, pp.1618–1640.

χαρακτηριστικά κάθε συστήματος θα καθορίσουν ποια είναι η κατάλληλη μέθοδος επιφανειακής τροποποίησης [144][145].

Σχήμα 4.10 Σχηματική αναπαράσταση ενός επιστρώματος προστασίας κατά φθοράς ολίσθησης [146]

Οι σκληρές επικαλύψεις έχουν χρησιμοποιηθεί για την προστασία υλικών, και κυρίως για την επιμήκυνση του χρόνου ζωής των εργαλείων κοπής, από την δεκαετία του 1970. Από τότε, τόσο η τεχνολογία παραγωγής τους όσο και οι ιδιότητές τους, δηλαδή η σκληρότητα, η αντίσταση σε φθορά και οξείδωση, διαρκώς βελτιώνονται. Συγκεκριμένα, οι προσπάθειες είναι στην κατεύθυνση της μείωσης της θερμοκρασίας παραγωγής/σχηματισμού του επιστρώματος, στην αύξηση της θερμικής του σταθερότητας πάνω από τους 1000 ^{o}C (άνω όριο θερμοκρασιών που αναπτύσσονται σε υψηλών ταχυτήτων εργαλεία κοπής), και στην αύξηση της σκληρότητας [147].

Όσον αφορά τη σκληρότητα, τα επιστρώματα διακρίνονται σε *σκληρά (hard)* (H<40 GPa) και *υπέρσκληρα (superhard)* (H>40 GPa). Σε αντίθεση με τη μεγάλη ποικιλία διαθέσιμων σκληρών υλικών, υπάρχουν λίγα μόνο ενδογενώς υπέρσκληρα υλικά: το διαμάντι (70-90 GPa), το νιτρίδιο του βορίου (48 GPa), ο άνθρακας DL (diamondlike) και το άμορφο νιτρίδιο του άνθρακα [148].

Τα προστατευτικά επιστρώματα έναντι φθοράς μπορούν να διακριθούν ανάλογα με τον αριθμό των συστατικών και των φάσεων από τις οποίες αποτελούνται ως εξής [149] :

1. Μονοφασικά επιστρώματα δυαδικών συστημάτων (π.χ. TiN, CrN)
2. Μονοφασικά επιστρώματα τριαδικών συστημάτων (π.χ. TiAlN)

[144] Colin R. Gagg & Peter R. Lewis, Wear as a product failure mechanism – Overview and case studies , Engineering Failure Analysis, Vol.14, 2007, pp.1618–1640.
[145] A.A. Voevodin et al., Recent Advances in Hard, Tough and Low Friction Nanocomposite Coatings, Tsinghua Science and Technology, vol.10, No 6, 2005, pp.665-679.
[146] A.A. Voevodin et al., Recent Advances in Hard, Tough and Low Friction Nanocomposite Coatings, Tsinghua Science and Technology, vol.10, No 6, 2005, pp.665-679.
[147] J. Musil, Hard and Superhard Nanocomposite Coatings, Surface and Coatings Technology, Vol.125, 2000, pp.322-330.
[148] J. Musil, Hard and Superhard Nanocomposite Coatings, Surface and Coatings Technology, Vol.125, 2000, pp.322-330.
[149] J. Patscheider et al., Structure – Performance Relations in Nanocomposite Coatings, Surface and Coatings Technology, Vol. 146-147, 2001, pp.201-208.

3. Πολυστρωματικά επιστρώματα που αποτελούνται διαδοχικά εναλλακτικά στρώματα δύο ή περισσότερων σκληρών υλικών (π.χ. TiN με VN)
4. Σύνθετα μονοστρωματικά επιστρώματα τα οποία αποτελούνται από δύο φάσεις με διακριτά όρια (π.χ. ZrN με Cu)

Τα τελευταία χρόνια έχει αναφερθεί ένας αρκετά μεγάλος αριθμός υπέρσκληρων επικαλύψεων από διάφορους ερευνητές. Αυτές οι επικαλύψεις μπορούν να κατηγοριοποιηθούν σε εκείνες στις οποίες η ενίσχυση της σκληρότητας προκύπτει από τη νανοδομή, και σε εκείνες στις οποίες η αυξημένη σκληρότητα είναι αποτέλεσμα υψηλών διαξονικών θλιπτικών τάσεων που εισάγονται στο υλικό κατά την εναπόθεση. Τα νανοδομημένα επιστρώματα μπορεί να είναι αποτελούνται από διαδοχικά νανοστρώματα ή από νανοκρυσταλλίτες. Τα υπέρσκληρα νανοδομημένα επιστρώματα πλεονεκτούν έναντι των επιστρωμάτων με υψηλές θλιπτικές τάσεις σε εφαρμογές στις οποίες απαιτείται θερμική σταθερότητα, καθώς τα πρώτα είναι σταθερά σε θερμοκρασίες έως και 1100 ^{o}C, ενώ τα δεύτερα έως και 400-500 ^{o}C[150].

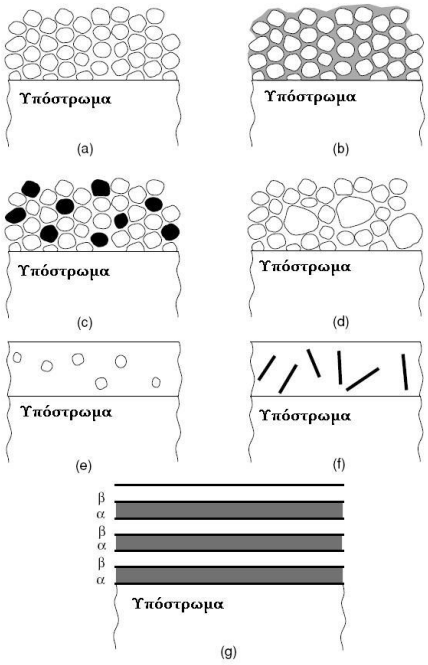

Σχήμα 4.11 Νανοδομημένες επικαλύψεις: (a) νανοκρυσταλλίτες μίας φάσης (b) νανοκρυσταλλίτες μίας φάσης που διαχωρίζονται από δεύτερη φάση (c) νανοκρυσταλλίτες δύο διαφορετικών φάσεων (d) μικροκρυσταλλίτες σε νανοκρυσταλλική μήτρα (e, f) νανοσωματιδία ή νανοίνες εντός μονοκρυσταλλικής μήτρας και (g) στρώματα νανοδιαστάσεων δύο ή περισσότερων φάσεων[151] .

[150] S. Veprek, Super- and ultrahard nanocomposite coatings: generic concept for their preparation, properties and industrial applications,Vacuum, Vo.67, 2002, pp.443-449.
[151] A. Cavaleiro and J. De Hosson (Eds), Nanostructured Coatings, Springer, New York, 2006

Τα νανοδομημένα υμένια παρουσιάζουν εξαιρετικές ιδιότητες, όπως υψηλή σκληρότητα ως υπερσκληρότητα, και τριβολογικά χαρακτηριστικά που είναι ιδιαίτερα επιθυμητά για συγκεκριμένες εφαρμογές. Οι ιδιότητές τους αυτές οφείλονται [152][153]:

- Στα *διεπιφανειακά φαινόμενα (interfaceeeffects)*, που είναι σημαντικά λόγω του μεγάλου ποσοστού ατόμων που βρίσκονται σε διεπιφάνειες (κόκκων ή/και φάσεων), στις οποίες η συμπεριφορά διαφοροποιείται από αυτήν του υλικού όγκου (bulk).
- Στα *φαινόμενα κλίμακας (nanoscaleeffects),* τα οποία εμφανίζονται καθώς πολλές θεμελιώδεις διεργασίες και φαινόμενα των στερεών λαμβάνουν χώρα σε μήκη της τάξεως των μερικών νανομέτρων.

Τα περισσότερα θεωρητικά μοντέλα για τη μελέτη των μηχανισμών παραμόρφωσης των νανοκρυσταλλικών υλικών έχουν αναπτυχθεί με βάση τις θεωρίες που ισχύουν για τα υλικά όγκου (bulk). Ωστόσο, αυτό δεν είναι απαραίτητα περιοριστικό, καθώς οι εγγενείς μηχανισμοί παραμόρφωσης είναι ίδιοι με αυτούς για τις νανοεπικαλύψεις, αφού η νανοδομή είναι αυτή που καθορίζει τους επικρατούντες μηχανισμούς, ενώ παράγοντες όπως η γεωμετρία του δείγματος, η επίδραση του υποστρώματος ή οι συνθήκες φόρτισης επηρεάζουν τα μακροσκοπικά μηχανικά χαρακτηριστικά [154][155].

Σε γενικές γραμμές, σύμφωνα με σύγχρονες μελέτες των πλαστικών διεργασιών σε νανοκρυσταλλικά υλικά, οι μηχανισμοί παραμόρφωσης που εμφανίζονται σε νανοκρυσταλλικά υλικά όγκου (bulk) είναι:

1. ολίσθηση διαταραχών (dislocationslip),

2. ολίσθηση ορίων κόκκων (grainboundaryslip),

3. ερπυσμόςδιάχυσηςορίωνκόκκων (grainboundarydiffusionalcreep),

4. ερπυσμός διάχυσης τριπλού σημείου (triplejunctiondiffusionalcreep),

5. περιστροφική παραμόρφωση μέσω κίνησης διαταραχών των ορίων των κόκκων και 6. παραμόρφωση διδυμίας από μερικές διαταραχές παραγόμενες από τα όρια των κόκκων [156][157].

Ο μηχανισμός της ολίσθησης διαταραχών κυριαρχεί στα κρυσταλλικά υλικά με μέγεθος κόκκων $d>d_c$, όπου d_c =[10-30]nm, ανάλογα με το υλικό. Στα κρυσταλλικά υλικά με μέγεθος

[152] A. Cavaleiro and J. De Hosson (Eds), Nanostructured Coatings, Springer, New York, 2006
[153] V.G. Gryaznov et al., Size Effects of Dislocation stability in Nanocrystals, Physical Review B, Vol.44, No 1, 1991, pp. 42-44
[154] R. A. Masumura, P. M. Hazzledine, and C. S. Pande,Yield stress of fine grained materials, Acta Materiala,Vol. 46, 1998, pp.4527–4534.
[155]I. A. Ovid'ko, Deformation and diffusion modes in nanocrystalline materials, International Materials Review, Vol.52, 2005, pp.65-82.
[156] R. A. Masumura, P. M. Hazzledine, and C. S. Pande,Yield stress of fine grained materials, Acta Materiala,Vol. 46, 1998, pp.4527–4534.
[157]I. A. Ovid'ko, Deformation and diffusion modes in nanocrystalline materials, International Materials Review, Vol.52, 2005, pp.65-82.

κόκκων ως μερικά δεκάδες νανόμετρα το όριο διαρροής αυξάνει με την μείωση του μεγέθους των κόκκων, δηλαδή ισχύει η σχέση Hall-Petch[158]:

$$\tau = \tau_0 + kd^{-1/2}$$

όπου τ το όριο διαρροής του πολυκρυσταλλικού υλικού , τ_0το όριο διαρροής του μονοκρυσταλλικού υλικού, και k σταθερά εξαρτώμενη από τη δομή των ορίων των κόκκων. Για $d<d_c$ όμως, προκύπτει είτε κορεσμός του ορίου διαρροής, είτε μείωσή του με περαιτέρω μείωση του d. Το τελευταίο φαινόμενο έχει σχετισθεί με τον ενεργό ρόλο των ορίων των κόκκων σε αυτά τα υλικά, που προαναφέρθηκε συμμετέχουν σε πλήθος μηχανισμών παραμορφώσεων. Η ακριβής λειτουργία των μηχανισμών αυτών δεν έχει κατανοηθεί πλήρως και είναι αντικείμενο αντικρουόμενων απόψεων. Ωστόσο, είναι δεδομένο ότι [159][160][161]:

- Με τη μείωση του μεγέθους των κόκκων ο αριθμός των διαταραχών εντός του κόκκου μειώνεται.
- Η ύπαρξη διαταραχών πλέγματος σε ένα νανοκρυσταλλικό υλικό δεν ευνοείται ενεργειακά εάν το μέγεθος των κόκκων είναι μικρότερο από μία κρίσιμη τιμή, χαρακτηριστική για κάθε υλικό. Η ενεργειακή αστάθεια σχετίζεται με τις δυνάμεις ειδώλου (imageforces) που δημιουργούνται λόγω της ελαστικής αλληλεπίδρασης της διαταραχής με τα όρια των κόκκων.

Πρόσφατα, οι Cheng et al. πρότειναν μία πολύ ενδιαφέρουσα κατηγοριοποίηση των πολυκρυσταλλικών υλικών, με βάση το ρόλο της κίνησης των διαταραχών και των ορίων των κόκκων ως γεννητόρων διαταραχών. Έτσι, τα υλικά χωρίζονται σε τέσσερις κατηγορίες [162]:

- Υλικά με μέγεθος κόκκων d μεγαλύτερο από 1 μm. Σε αυτά τα υλικά, η κίνηση διαταραχών είναι κυρίαρχη, με τους φορείς (τέλειες διαταραχές πλέγματος) να παράγονται εντός των κόκκων από πηγές όπως τύπου Frank-Read.
- Λεπτόκοκκα υλικά με μέγεθος κόκκων από 30 nm ως 1 μm. Σε αυτά τα υλικά, η ολίσθηση διαταραχών είναι κυρίαρχη με τους φορείς (τέλειες διαταραχές πλέγματος) να παράγονται από πηγές στα όρια των κόκκων.

[158] A. Lasalmonie and J. L. Strudel, Influence of grain-size on the mechanical behavior of some high-strength materials, Journal of Materials Research, Vol.21, 1986, pp.1837–1852.
[159] A. Cavaleiro and J. De Hosson (Eds), Nanostructured Coatings, Springer, New York, 2006
[160] R. A. Masumura, P. M. Hazzledine, and C. S. Pande,Yield stress of fine grained materials, Acta Materiala,Vol. 46, 1998, pp.4527–4534
[161] V.G. Gryaznov et al., Size Effects of Dislocation stability in Nanocrystals, Physical Review B, Vol.44, No 1, 1991, pp. 42-44.
[162] S. Cheng, J. A. Spencer, and W. W. Milligan, Strength and tension/ compression asymmetry in nanostructured and ultrafine-grain metals, Acta Materiala,Vol. 51, 2003, pp. 4505–4518.

- Νάνο ΙΙ υλικά με μέγεθος κόκκων 10-30 nm. Σε αυτά τα υλικά, οι κύριοι φορείς πλαστικής παραμόρφωσης είναι μερικές διαταραχές στα όρια των κόκκων. Αφού οι κινούμενες αυτές διαταραχές είναι μερικές, η κίνησή τους συνοδεύεται από δημιουργία σφαλμάτων στοίβαξης και παραμορφώσεων διδυμιών.
- Νάνο Ι υλικά με μέγεθος κόκκων μικρότερο των 10 nm. Σε αυτά τα υλικά, κυριαρχούν η ολίσθηση των ορίων των κόκκων και άλλοι μηχανισμοί παραμόρφωσης που γίνονται από τα όρια των κόκκων.

Οι νανοδομημένες πολυστρωματικές επικαλύψεις που αποτελούνται από δύο εναλλακτικές στρώσεις υλικών με περίοδο (δηλαδή με πάχος δύο διαδοχικών διαφορετικών στρωμάτων) από 5-10 nm καλούνται υπερπλέγματα. Ανάλογα με τη σύσταση τους, τα υπερπλέγματα μπορούν να διακριθούν σε [163]:

1. μεταλλικά υπερπλέγματα,
2. υπερπλέγματα νιτριδίων,
3. υπερπλέγματα καρβιδίων,
4. υπερπλέγματα οξειδίων,
5. υπερπλέγματα μετάλλου με καρβίδιο, νιτρίδιο ή οξείδιο.

Τα μεταλλικά υπερπλέγματα έχουν σχετικά χαμηλή σκληρότητα σε σχέση με αυτά των νιτριδίων και καρβιδίων, τα οποία είναι υπέρσκληρα. Για τα υπερπλέγματα οξειδίων δεν υπάρχουν αρκετά διαθέσιμα δεδομένα. Μεταξύ των επικαλύψεων της κατηγορίας 5 ξεχωρίζουν τα υπερπλέγματα νιτρίδιου/μετάλλου, γιατί ο συνδυασμός του σκληρού νιτρίδιου με το όλκιμο μέταλλο καθιστά εφικτή την αύξηση της αντοχής, διατηρώντας υψηλή σκληρότητα. Η βελτίωση της αντοχής της επικάλυψης έχει ως αποτέλεσμα βελτιωμένη πρόσφυση στο υπόστρωμα, η οποία τελευταία είναι θεμελιώδης ιδιότητα για επικαλύψεις.

Οι επικαλύψεις υπερπλεγμάτων μειονεκτούν στην δυσκολία ελέγχου της σκληρότητας του υμενίου. Συγκεκριμένα, η σκληρότητα εξαρτάται έντονα από την περίοδο του υπερπλέγματος. Έτσι, η εφαρμογή τέτοιων επικαλύψεων σε βιομηχανική κλίμακα ενέχει τον κίνδυνο μεγάλης διακύμανσης της σκληρότητας του τελικού φιλμ, αφού είναι πολύ δύσκολο να επιτευχθεί ακριβώς ίδιο πάχος για όλα τα στρώματα όλων των επικαλύψεων. Επίσης, παρόμοιες διακυμάνσεις της σκληρότητας μπορούν να προέλθουν κατά την εφαρμογή από διαχύσεις ατόμων σε γειτονικά στρώματα, αν το υμένιο βρεθεί σε υψηλές θερμοκρασίες λειτουργίας [164].

[163] J. Musil, Hard and Superhard Nanocomposite Coatings, Surface and Coatings Technology, Vol.125, 2000, pp.322-330.
[164] J. Musil, Hard and Superhard Nanocomposite Coatings, Surface and Coatings Technology, Vol.125, 2000, pp.322-330.

Νανοσύνθετα επιστρώματα συντίθενται από δύο διαφορετικά υλικά με μέγεθος κόκκων 3-10 nm. Τα νανοσύνθετα επιστρώματα μπορούν να αποτελούνται είτε από δύο νανοκρυσταλλικές φάσεις (π.χ. TiN/cBN), είτε από έναν συνδυασμό νανοκρυσταλλικής και άμορφης φάσης (π.χ. nc-TiN/a-Si_3N_4). Γενικά, ενώ η σκληρότητα των μονοφασικών υλικών μπορεί να εξηγηθεί μέσω θεμελιωδών ιδιοτήτων των υλικών, όπως η ισχύς του δεσμού και το μέτρο διάτμησης, η σκληρότητα των νανοσύνθετων υλικών είναι το αποτέλεσμα μιας σύνθετης αλληλεπίδρασης του μεγέθους των κρυσταλλιτών, του προσανατολισμού τους και του διαχωρισμού τους από τυχόν άμορφη φάση. Σχετικές μελέτες δείχνουν ότι προκειμένου να επιτευχθεί ενίσχυση της σκληρότητας, η μέση απόσταση μεταξύ δύο ορίων φάσης, δηλαδή το μέσο μέγεθος κρυσταλλιτών, θα πρέπει να είναι της τάξεως των 5 nm και η άμορφη φάση να διαχωρίζει τους κρυσταλλίτες περίπου κατά 0.5 nm[165][166][167].

[165] J. Patscheider et al., Structure – Performance Relations in Nanocomposite Coatings, Surface and Coatings Technology, Vol. 146-147, 2001, pp.201-208.
[166] A.C. Fischer-Cripps, On the Measurement of Hardness of Superhard Coatings, Surface & Coatings Technology, Vol. 200, 2006, pp.5645 – 5654.
[167] S. Veprek and S. Reiprich, A Concept for the Design of Novel Superhard Materials, Thin Solid Films, Vol.268, 1995, pp.64-71.

Κεφάλαιο 5. Υλικά και Διερεύνηση - Αποτελέσματα και Συζήτηση

5.1 Πολυμερή νανοσύνθετα με νανοσωλήνες άνθρακα (Epilox, PVB, Henkel, PDMS ρητίνη με 2 τύπους νανοσωλήνων)[168]

Οι εικόνες FE-SEM παρουσιάζονται στο σχήμα 5.1. Η σύσταση καθορίστηκε από EDX: Ni 1.87%, Fe 0.56%, 0.21 Cl και S 0.02% για τον τύπο νανοσωλήνων MW-1 και Co 1.1%, Cl 1.0%, S 0.3 %, Al 0.2 % για τον τύπο νανοσωλήνων MW-2. Αντιπροσωπευτικά γραφήματα Raman από τα δείγματα Epilox και Epilox με 7% MW-1 παρουσιάζονται στο Σχήμα 5.2. Η ρητίνη Epilox παρουσιάζει χαρακτηριστικές κορυφές που αντιστοιχούν στις εποξεικές ομάδες. Η κορυφή στα 639 cm^{-1} οφείλεται στη διάνοιξη του εποξεικού δακτυλίου - αποδόμηση. Η κορυφήστα 1002 cm^{-1}αντιστοιχεί στη τάση της ομάδας C–O–C, ενώ η δόνηση του εποξεικού δακτυλίου παρουσιάζεται στα 1112 cm^{-1}.

Το φάσμα Raman του νανοσυνθέτου περιέχει αρκετά στοιχεία που οφείλονται στους νανοσωλήνες άνθρακα. Η D κορυφή που βρίσκεται στα ~1310 cm^{-1} σχετίζεται με δομικές ατέλειες γραφίτη ή νανοσωλήνα, ενώ η G κορυφή στα ~1585 cm^{-1} αντιστοιχεί σε δονήσεις τάσεων των δεσμών sp^2 άνθρακα - άνθρακα. Η κορυφή στα ~1610 cm^{-1} είναι χαρακτηριστική των «γραφιτοειδών» υλικών, ενώ η G' κορυφή στα ~2600 cm^{-1} είναι περίπου διπλάσια της D (ενίσχυση).

1. [168]E.P. Koumoulos, M. Giorcelli, P. Jagadale, A. Tagliaferro, C.A. Charitidis, Evaluation of mechanical integrity of epoxy-nanodiamonds composites via nanoindentation, Composites Part B (2015), in press
2. E.P. Koumoulos, M. Giorcelli, P. Jagadale, A. Tagliaferro C.A. Charitidis, Carbon nanotube/ polymer nanocomposites: a study on mechanical integrity through nanoindentation,Polymer Composites (2015), in press, DOI: 10.1002/pc.23049
3. C.A. Charitidis, E.P. Koumoulos, D.A. Dragatogiannis, Nanotribological behavior of carbon based thin films: friction and lubricity mechanisms at the atomic level,Special Issue "Nanotribology and Atomic Mechanisms of Friction", Lubricants (2013) 1(2), 22-47
4. C.A.Charitidis, E.P. Koumoulos, M. Giorcelli, S. Musso, P. Jagadale, A. Tagliaferro, Nanomechanical and tribological properties of carbon nanotube/polyvinyl butyral composites, Journal of Polymer Composites, 2013, 34(11), 1950–1960
5. *E.P. Koumoulos, A. Darivaki, C.A. Charitidis, CNTs/polymer nanocomposites for antifouling activity: surface properties and perspectives, 10th Panhellenic Conference on Chemical Engineering (2015)*
6. *T. Parousis, D. Perivoliotis, E. P. Koumoulos, C.A. Charitidis, Evaluation of MWCNTs/PDMS composite coating for antifouling applications, European Coatings CONGRESS 2015, 20-21 April 2015 Nuremberg/Germany*
7. *E.P. Koumoulos, C.A. Charitidis, Nanoindentation analysis of composite engineering materials, Eurofillers 2013, Slovakia (2013)*
8. *E.P. Koumoulos, C.A. Charitidis, Nanomechanical properties of engineering nanostructures, XXIX Panhellenic Conference on Solid State Physics and Materials Science (2013)*

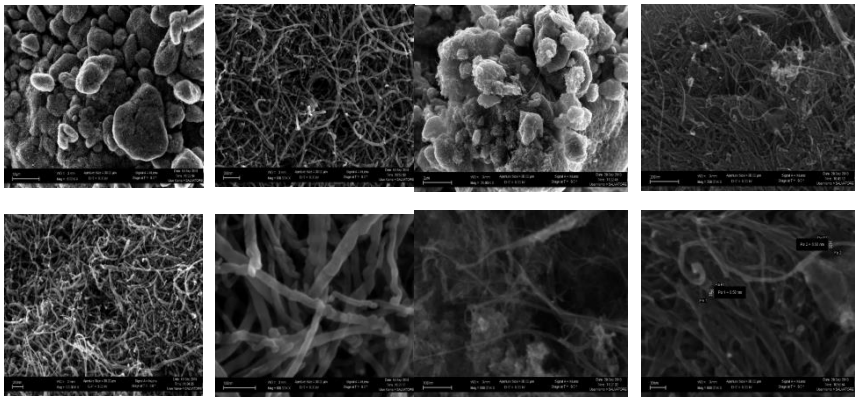

(a) (b)

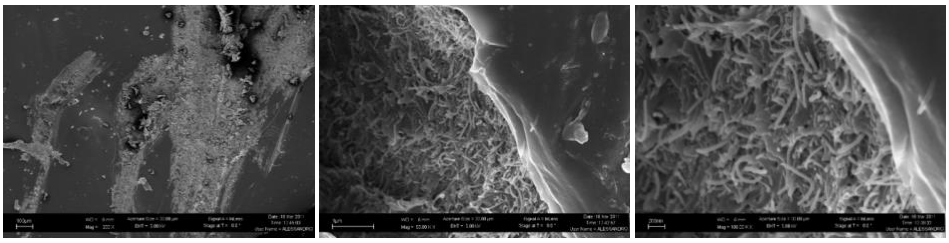

(c)

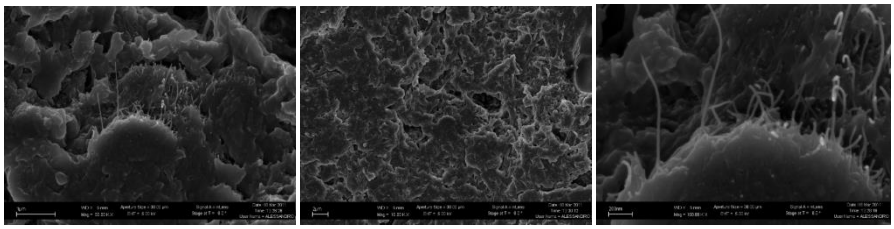

(d)

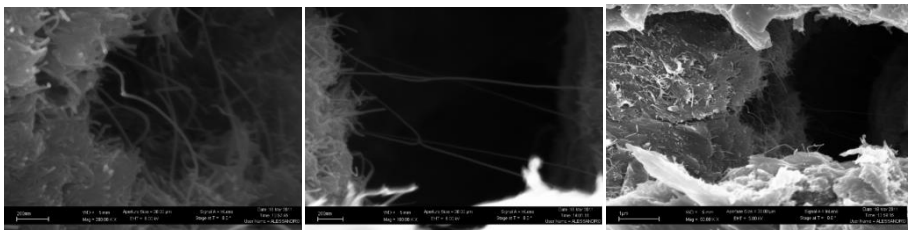

(e)

Σχήμα 5.1 ΕικόνεςFE-SEMτων (a) MW-1, (b) MW-2, (c) Epilox–7% SW-1, (d) Henkel–5% MW-2 και (e) PVB–5% MW-2.

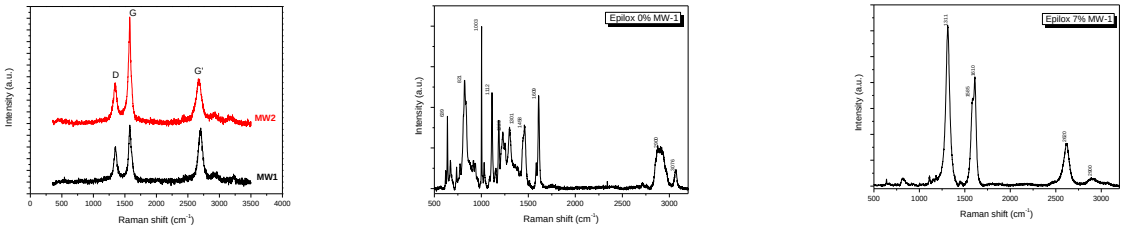

(a) (b) (c)

Σχήμα 5. 1.ΦάσματαRamantων (a) MW-1 and MW-2 πουλήφθηκανμelaser στα514nm, (b) Epilox 0% MW-1 και (c) Epilox 5% MW-1 πουλήφθηκανμelaser στα 785nm.

Η συσχέτιση (ως συνάρτηση εισόδου του πειράματος) βάθους διείσδυσης και χρόνου που χρησιμοποιήθηκε παρουσιάζεται στα σχήματα 5.3 και 5.4 παρακάτω (σχηματική τραπεζοειδής $P = P(t)$ συνάρτηση εισόδου). Στην περίπτωση του πειράματος ερπυσμού, οι χρόνοι φόρτισης και αποφόρτισης είναι ίδιοι (10 sec), ενώ ο χρόνος ερπυσμού ορίστηκε στα 100 sec (40 και 3 sec για συμβατική νανσκληρομέτρηση, αντίστοιχα).

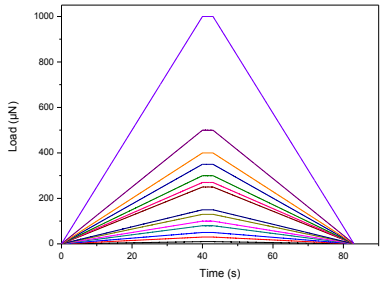

Σχήμα 5.3. Συσχέτιση (ως συνάρτηση εισόδου του πειράματος) βάθους διείσδυσης και χρόνου που χρησιμοποιήθηκε.

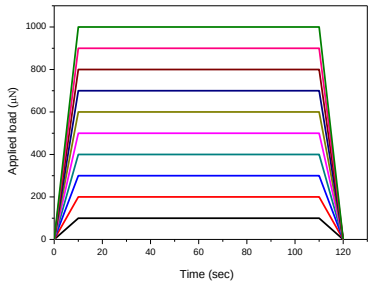

Σχήμα 5.4. Συσχέτιση (ως συνάρτηση εισόδου του πειράματος) βάθους διείσδυσης και χρόνου που χρησιμοποιήθηκε (πείραμα ερπυσμού).

Στα σχήματα 5.5- 5.9 παρουσιάζονται η σκληρότητα, το μέτρο ελαστικότητας και το εφαρμοζόμενο φορτίο συναρτήσει του βάθους διείσδυσης. Η σκληρότητα και το μέτρο ελαστικότητας του Epilox MW-1 βρέθηκε να ποικίλει στην επιφανειακή περιοχή (~0-200nm), πιθανώς λόγω καμπυλότητας της ακίδας και του Indentation Size Effect (ISE), τείνοντας σε σταθερές τιμές 0.2 και 4 GPa, αντίστοιχα. Παρόμοια συμπεριφορά προκύπτει και από τα δείγματα Henkel MW-2, PVB MW-2 και PDMS με MWCNTs και SWCNTs.

Οι λόγοι για το ευρύ φάσματων νανομηχανικών ιδιοτήτων οφείλονται πιθανώς σε συνέργεια παραγόντων, όπως βαθμωτή επιφανειακή δομή λόγω συγκέντρωσης CNTs, δυνάμειας συνοχής/ συνάφειας μεταξύ δείγματος- ακίδας κλπ. Λόγω μικρής επιφάνειας

επαφής, αναπτύσσονται υψηλές τάσεις μεταξύ ακίδας και δείγματος. Η εκτεταμένη πίεση επιτρέπει την πλαστική παραμόρφωση/ αποδόμηση, τη στιγμή που οι συμβατικές τεχνικές (π.χ. εφελκυσμός) οδηγούν σε αστοχία, σε θερμοκρασία περιβάλλοντος. Ορισμένα υλικά παρουσιάζουν ISE, το οποίο εμφανίζει αύξηση της σκληρότητας με μείωση του επιβαλλόμενου φορτίου.

Η παρουσία νανοσωλήνων στην πολυμερική μήτρα βελτιώνει τις νανομηχανικές ιδιότητες (μέχρι 3% συγκέντρωση, απο την οποία και μετά οι νανομηχανικές ιδιότητες εμφανίζουν μείωση). Έχει αναφερθεί ότι οι μηχανικές ιδιότητες επιδεινώνονται με την αύξηση της περιεκτικότητας των CNTs, μετά από ένα βέλτιστο όριο συγκέντρωσης, λόγω της έντονης παρουσίας του μηχανισμού "tube – tube slip". Παρουσιάζεται δηλαδή ολίσθηση μεταξύ μεμονωμένων CNTs, οι οποίοι έρχονται σε επαφή καθώς βρίσκονται ενωμένοι σε ένα συσσωμάτωμα. Σε συγκεντρώσεις μεγαλύτερες από την βέλτιστη συγκέντρωση, η επαφή των CNTs και η δημιουργία συσσωματωμάτων είναι εντονότερη, γεγονός που ενεργεί ως μηχανικό ελάττωμα για το σύνθετο υλικό (οι βέλτιστες συγκεντρώσεις είναι επισημασμένες με διακεκομμένη γραμμή, σχήματα 5.5-5.9).

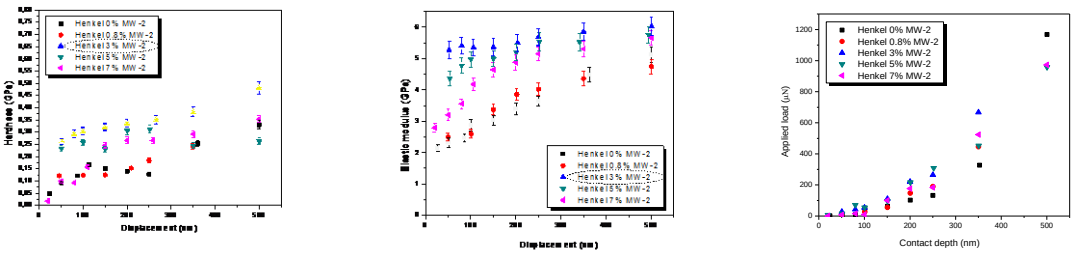

(a) (b) (c)

Σχήμα5.5. (a) Σκληρότητα, (b) μέτρο ελαστικότητας και (c) P_{max} ως προς το βάθος διείσδυσης για το δείγμα HenkelMW-2

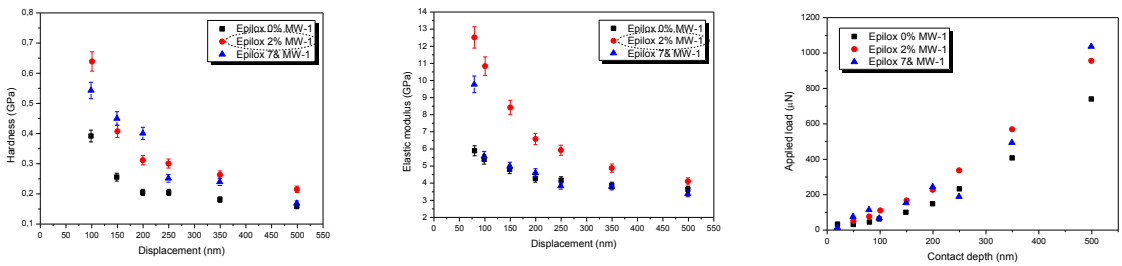

(a) (b) (c)

Σχήμα5.6. (a) Σκληρότητα, (b) μέτρο ελαστικότητας και (c) P_{max} ως προς το βάθος διείσδυσης για το δείγμαEpiloxMW-1

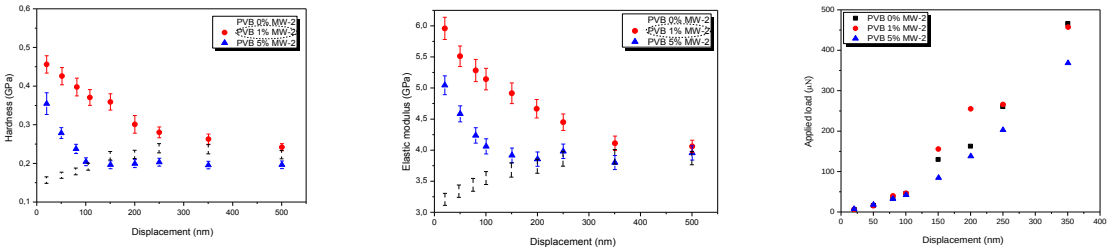

(a) (b) (c)

Σχήμα5.7. (a) Σκληρότητα, (b) μέτρο ελαστικότητας και (c) P_{max}ως προς το βάθος διείσδυσης για το δείγμαPVBMW-2.

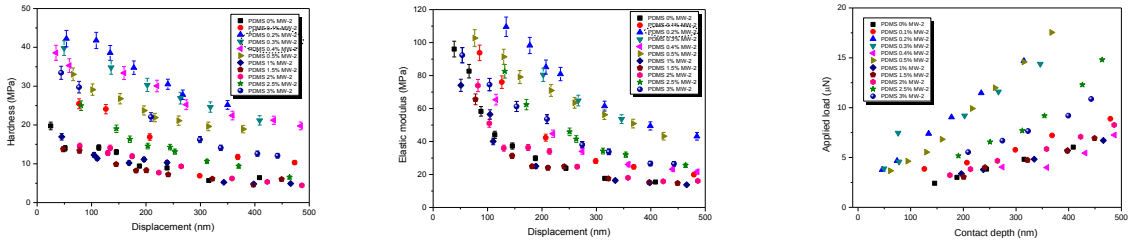

(a) (b) (c)

Σχήμα5.2. (a) Σκληρότητα, (b) μέτρο ελαστικότητας και (c) P_{max} ως προς το βάθος διείσδυσης για το δείγμα PDMS MW-2

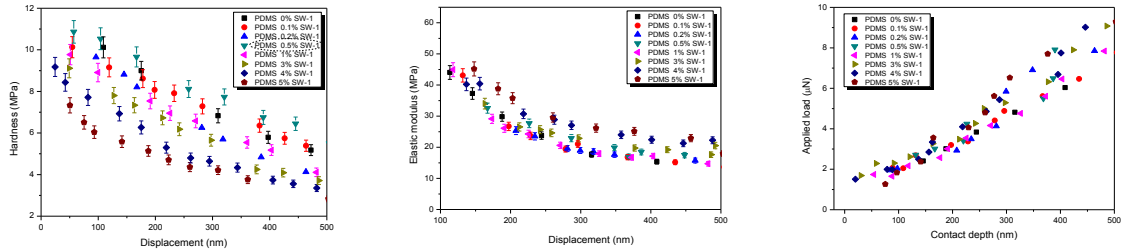

(a) (b) (c)

Σχήμα 5.3. (a) Σκληρότητα, (b) μέτρο ελαστικότητας και (c) P_{max} ως προς το βάθος διείσδυσης για το δείγμα PDMS SW-1

Από τις τιμές σκληρότητας και μέτρου ελαστικότητας είναι δυνατός ο υπολογισμός των λόγων H/E («δείκτης πλαστικότητας») και h_c/h_m που είναι ενδεικτικοί για την αντίσταση στη φθορά (wear resistance) και την ελαστική-πλαστική συμπεριφορά, αντίστοιχα. Τα σχήματα 5.10-5.15 παρέχουν πληροφορίες για την αντίσταση στη φθορά των δειγμάτων.

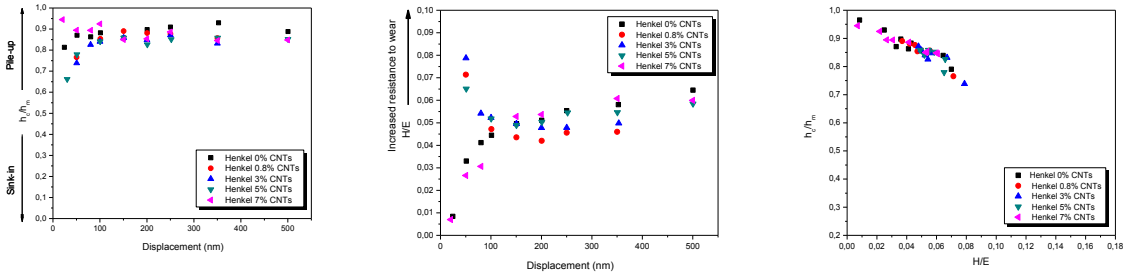

(a) (b) (c)

Σχήμα5.10.(a) Κανονικοποιημένος λόγος pile-up/sink-in(h_c/h_m) ως προς το βάθος διείσδυσης, (b) δείκτης πλαστικότητας(H/E) ως προς το βάθος διείσδυσης και (c) H/Eως προςh_c/h_mτων δειγμάτωνHenkelMW-2

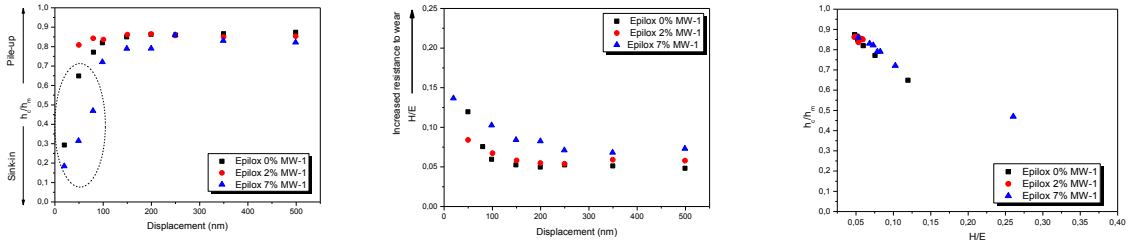

(a) (b) (c)

Σχήμα5.4. (a) Κανονικοποιημένος λόγος pile-up/sink-in (h_c/h_m) ως προς το βάθος διείσδυσης, (b) δείκτης πλαστικότητας (H/E) ως προς το βάθος διείσδυσης και (c) H/E ως προς h_c/h_m των δειγμάτων Epilox MW-1

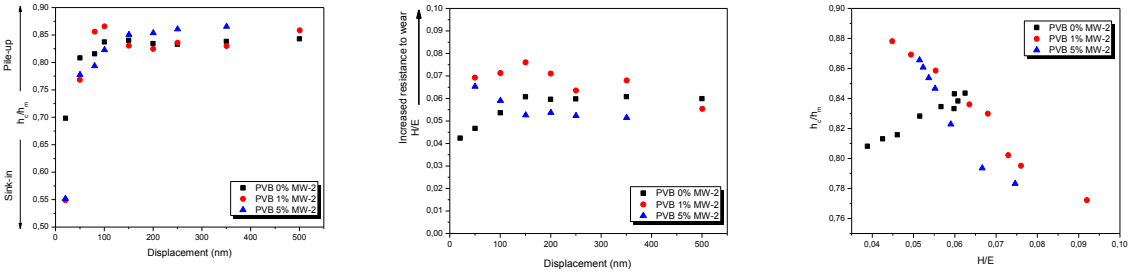

(a) (b) (c)

Σχήμα 5.5. (a) Κανονικοποιημένος λόγος pile-up/sink-in (h_c/h_m) ως προς το βάθος διείσδυσης, (b) δείκτης πλαστικότητας (H/E) ως προς το βάθος διείσδυσης και (c) H/E ως προς h_c/h_m των δειγμάτων PVB MW-2

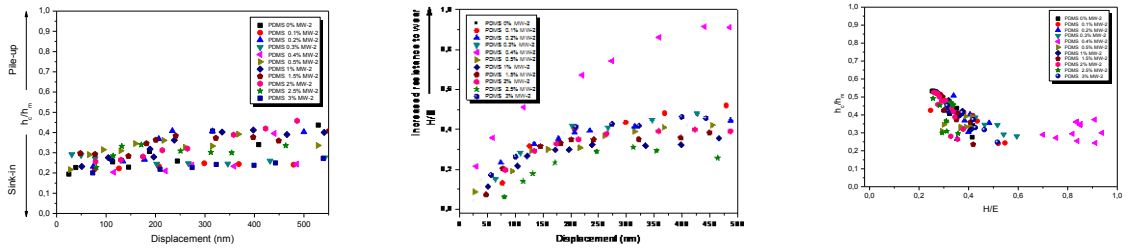

(a) (b) (c)

Σχήμα 5.6. (a) Κανονικοποιημένος λόγος pile-up/sink-in (h_c/h_m) ως προς το βάθος διείσδυσης, (b) δείκτης πλαστικότητας (H/E) ως προς το βάθος διείσδυσης και (c) H/E ως προς h_c/h_m των δειγμάτων PDMS MW-2

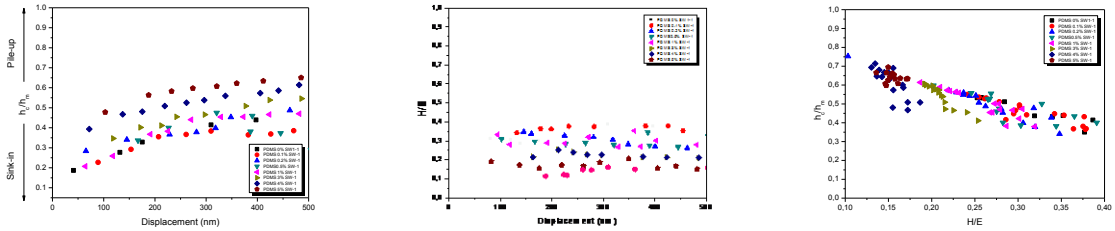

(a) (b) (c)

Σχήμα 5.7. (a) Κανονικοποιημένος λόγος pile-up/sink-in (h_c/h_m) ως προς το βάθος διείσδυσης, (b) δείκτης πλαστικότητας (H/E) ως προς το βάθος διείσδυσης και (c) H/E ως προς h_c/h_m των δειγμάτων PDMS SW-1

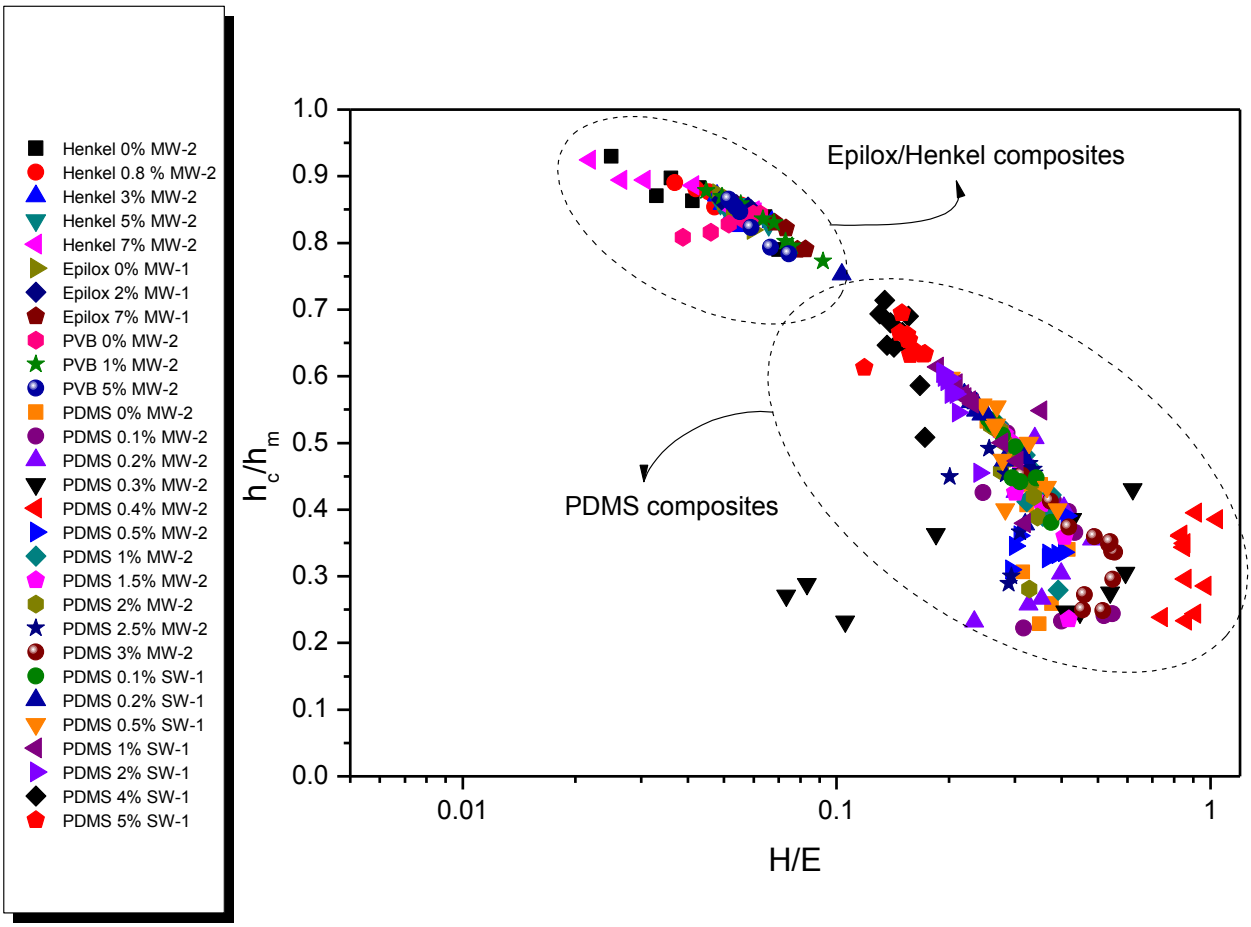

Σχήμα5.8. Δείκτης πλαστικότητας (H/E) ως προς h_c/h_m των νανοσυνθέτων

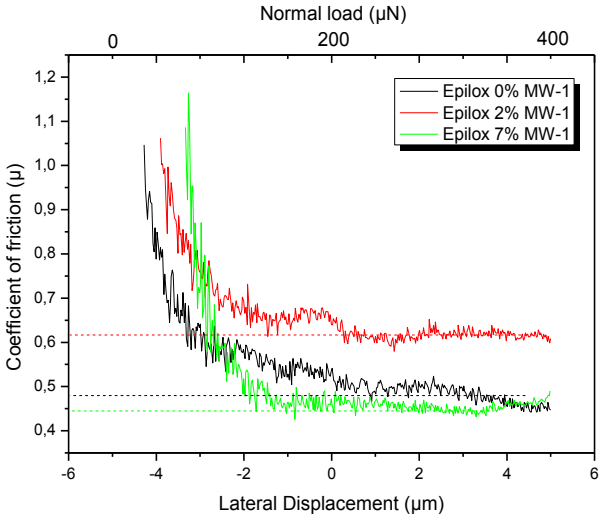

Σχήμα 5.16.Συντελεστές τριβής για τα δείγματα Epilox με νανοσωλήνες άνθρακα

Στο σχήμα 5.16 παρουσιάζεται ο συντελεστής τριβής για τα δείγματα Epilox με νανοσωλήνες άνθρακα. Ο συντελεστής τριβής (CoF) ορίζεται ως ο λόγος του μέτρου της

πλευρικής δύναμης προς το μέτρο της κάθετης δύναμης και εξαρτάται από πολλούς παράγοντες όπως οι ιδιότητες του υλικού του δείγματος, η γεωμετρία της ακίδας και η τραχύτητα της επιφάνειας. Ένα υλικό με μεγαλύτερη αντοχή στη φθορά θα επιβάλει μεγαλύτερη αντίσταση στην εγχάραξη με αποτέλεσμα η ακίδα να δεχτεί μια μεγαλύτερη πλευρική δύναμη. Τα παραπάνω δείγματα παρουσιάζουν μεγαλύτερη αντίσταση στην κίνηση της ακίδας κατά τη δοκιμή εγχάραξης. Δηλαδή, η ύπαρξη των CNTs, τόσο ομοιογενώς διασπαρμένων αλλά και σε μεγάλο ποσοστό εμποδίζουν την εγχάραξη της επιφάνειας.

Στη συνέχεια, παρουσιάζεται η εξέλιξη του ερπυσμού για σταθερό ρυθμό φόρτισης (10 μN/s) και χρόνο παραμονής (100s) στο μέγιστο επιβαλλόμενο φορτίο. Ο χρόνος παραμονής επιλέχθηκε ώστε να προσδιοριστεί το σημείο στο οποίο σταματάει η αύξηση του καταγραφόμενου βάθους διείσδυσης. Γενικά, σε δείγματα μαλακής ύλης αποφεύγονται πολύ μεγάλοι χρόνοι παραμονής (> 120 s), διότι έχει δειχθεί ότι η τοπική βαθμίδα θερμοκρασίας επηρεάζει την εξέλιξη του φαινομένου του ερπυσμού (thermal drift).

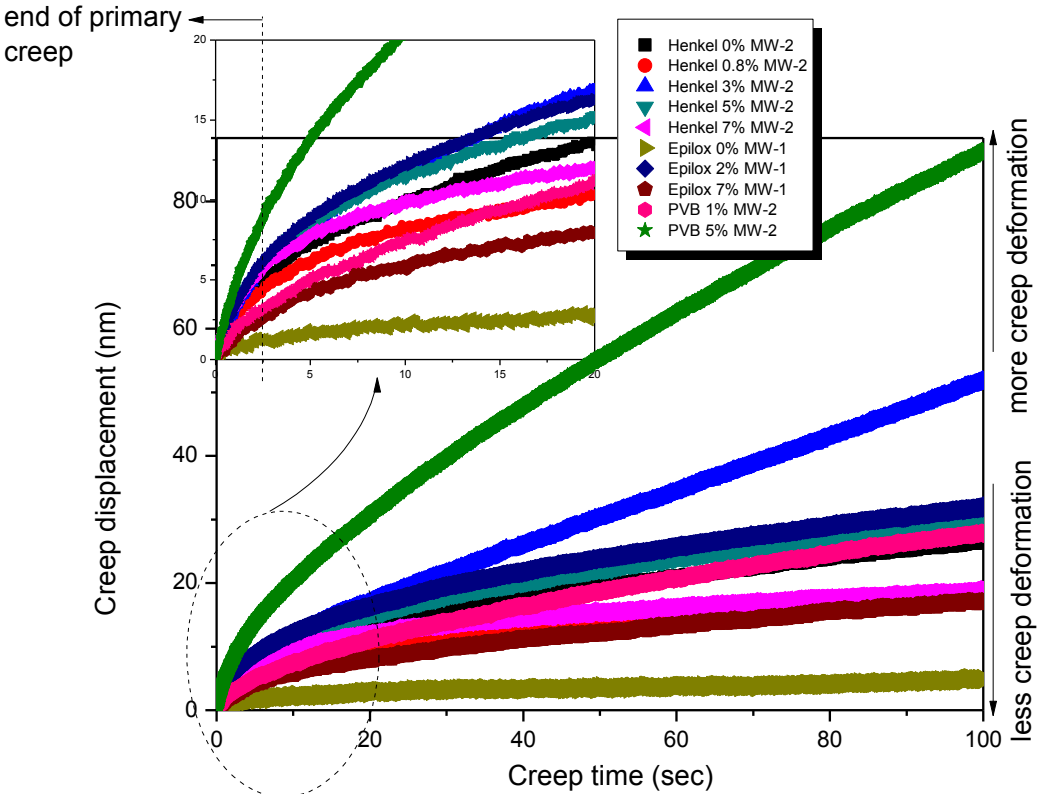

Σχήμα 5.17.Μεταβολή βάθους διείσδυσης με το χρόνο ερπυσμού (ρυθμός φόρτισης 10μN/sec) για τα δείγματα HenkelMW-2, EpiloxMW-1 καιPVBMW-2

Κατά την απομάκρυνση της ακίδας από τη δομή των δειγμάτων παρατηρείται πρόσφυση, η οποία εκφράζεται με αρνητικές τιμές φόρτισης στο σχήμα 5.18. Η υστέρηση της πρόσφυσης πιστεύεται ότι οφείλεται στη διάδοση της ενέργειας στο υλικό όγκου και στην αιχμή της

ακίδας και η ιξωδοελαστικότητα του υλικού είναι ο κυρίαρχος παράγοντας για την εμφάνισή της. Η πρόσφυση που καταγράφεται στο σχήμα 5.18 παρουσιάζει διαφορετικά αποτελέσματα για τα δείγματα με και χωρίς CNTs. Πιο συγκεκριμένα η προσθήκη των CNTs μειώνει την πρόσφυση που καταγράφεται.

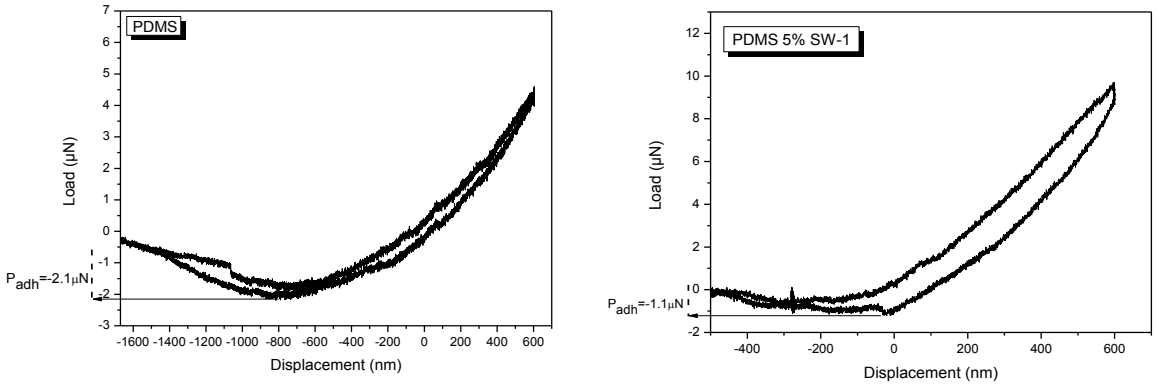

(a) (b)

Σχήμα 5.9 Καμπύλες φόρτισης-αποφόρτισης για τα δείγματα (a) PDMSκαι (b) PDMS5% SW-1

Η προσθήκη CNTs οδήγησε σε βελτίωση των νανομηχανικών ιδιοτήτων στην περίπτωση των Henkel 3% MW-2, Epilox 2% MW-1, PVB 1% MW-2 καιPDMS 0.2-0.5% MW-2 (αυξημένος λόγος (H/E) αντοχής σε φθορά στην περίπτωση των Henkel 7% MW-2, Epilox 7% MW-1, PDMS 0.4% MW-2 και PDMS 0.1% SW-1.

Τα νανοσύνθετα ενώ εμφάνισαν βελτιωμένες νανομηχανικές ιδιότητες σε σχέση με την πολυμερική μήτρα, σε όλες τις περιπτώσεις καθορίστηκε η συγκέντρωση πέρα από την οποία η επιπλέον προσθήκη νανοσωλήνων προκαλούσε μείωση των νανομηχανικών ιδιοτήτων, η μείωση του συντελεστή τριβής και η μείωση της ενέργειας πρόσφυσης, για διαφορετικό τύπο νανοσωλήνων.

5.2 Πολυμερή νανοσύνθετα με οργανικά τροποποιημένο μοντμοριλλονίτη (MMT) και επιφανειακή γήρανση[169]

9. [169]C.A.Charitidis, E.P.Koumoulos,Nanomechanical Properties and Nanoscale Deformation of PDMS nanocomposites, Plastics, Rubber and Composites (2012) 41(2) pp. 88-93
10. P. N. Eleni, M. K. Krokida, G. L. Polyzois, C. A. Charitidis, E. P. Koumoulos, V. P. Tsikourkitoudi, I. Ziomas, Mechanical behaviour of PDMS silicone elastomer after outdoor weathering in two different weathering locations,Journal of Polymer Degradation and Stability 96 470-476 (2011)
11. C.A. Charitidis, E. P. Koumoulos, V.P. Tsikourkitoudi, S.P. Vasilakos, P.A. Tarantili,Adhesive forces and time dependent behaviour (creep and loading rate effects) on nanomechanical properties of polydimethylsiloxane (PDMS), Journal of Nanostructured Polymers and Nanocomposites, 7:1 32-42 (2011).

Στόχος της εργασίας είναι η μέτρηση νανομηχανικών ιδιοτήτων σε νανοσύνθετο ελαστομερούς πολυδιμεθυλοσιλοξάνης (PDMS) και οργανικά τροποποιημένου μοντμοριλλονίτη (MMT). Το PDMS χρησιμοποιείται ευρέως σε βιοϊατρικές εφαρμογές, λόγω των εξαιρετικών ιδιοτήτων που παρουσιάζει όπως βιοσυμβατότητα, μη-τοξικότητα, χαμηλή χημική δραστικότητα, και αντίσταση στην επίδραση από το οξυγόνο, το όζον και το φως. Για την ανάλυση των μετρήσεων των νανομηχανικών ιδιοτήτων χρησιμοποιείται το μοντέλο των Oliver – Pharr. Μετρήσεις έγιναν σε δείγματα PDMS χωρίς ποσότητα (0%) νανοσωματιδίων, με περιεκτικότητα 5% και 8%, σε διάφορες δυνάμεις (2-150 μN) και παρατηρήθηκε ελαστική συμπεριφορά του υλικού. Επίσης μετρήσεις πραγματοποιήθηκαν σε κατεργασμένη επιφάνεια πολυδιμεθυλοσιλοξάνης με επιβολή UV ακτινοβολίας.

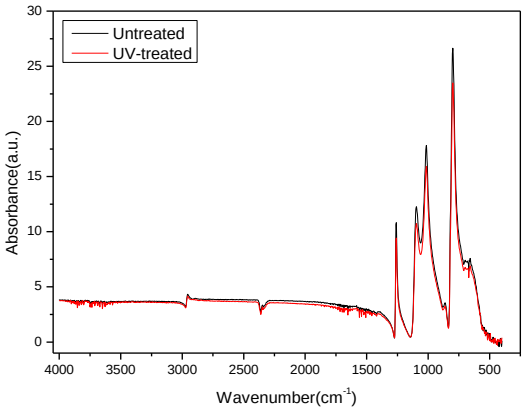

Σχήμα 5.19Φάσματα FTIRγιαταδείγματα untreatedκαιUV-treatedPDMS.

Τα φάσματα FTIR για τα δείγματα untreated και UV-treatedPDMS βρέθηκαν πανομοιότυπα, μη μπορώντας να αναδείξουν το ποσοστό επιφανειακής υποβάθμισης του υλικού, λόγω της UV ακτινοβολίας.

12. E.P. Koumoulos, V.P. Tsikourkitoudi, C.A. Charitidis, P.N. Eleni, M.K. Krokida, I.C. Ziomas, Nanomechanical properties of physically-aged Polydimethylsiloxane, Proceedings of the 6th International Conference on Modification Degradation and Stabilization of Polymers 5-9 September 2010, Athens, Greece, Publisher: MoDeSt Hellenic Organizing Committee, Editors: Constantine D. Papaspyrides, Stamatina N. Vouyiouka ISBN: 978-960-99362-0-0
13. *C.A. Charitidis, E. P. Koumoulos, Duracosys 2010, Nanomechanical Properties and Nanoscale Deformation of PDMS nanocomposites, 9th International Conference on Durability of Composite Systems (2010),*
14. *E. P. Koumoulos, V. P. Tsikourkitoudi, C. A. Charitidis, P. N. Eleni, M. K. Krokida, I. Ziomas, Investigation of the Nanomechanical Properties of Physically-aged Polydimethylsiloxane (PDMS), XXVI Panhellenic Conference on Solid State Physics and Materials Science (2010)*
15. *C.A. Charitidis, E.P. Koumoulos, Nanoindentation of Nanocomposites Polydimethylsiloxane Elastomers, 6th International Conference on Nanosciences & Nanotechnologies (2009)*
16. *E.P.Koumoulos, C.A.Charitidis, S.P.Vasilakos, P.A.Tarantili ,Nanomechanical Properies of PDMS nanocomposites, 7th Panhellenic Conference on Chemical Engineering (2009)*

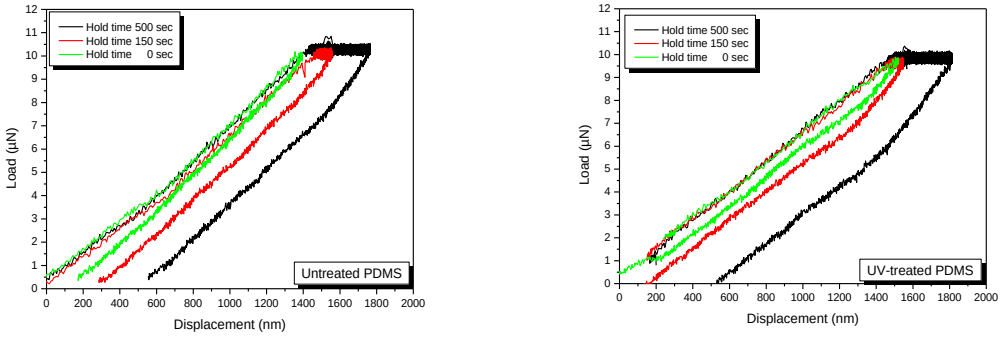

(a) (b)

Σχήμα 5.20Χαρακτηριστικές καμπύλες φορτίου διείσδυσης για τα δείγματα untreated (a) και UV-treated (b) PDMS με χρόνους ερπυσμού 0, 150 και 500 s.

Οι νανομηχανικές ιδιότητες βρέθηκαν αυξημένες στην επιφανειακή περιοχή, λόγω πιθανού σχηματισμού ζώνης silica-like, η οποία δημιουργήθηκε κατά την επεξεργασία. Η ανάλυση ερπυσμού έδειξε ότι μόνο μετά από i) ~400 s και πλέον για το untreatedPDMS και ii) ~200 s και πλέον για το UV-treatedPDMSμπορεί να αγνοηθεί το σφάλμα του λόγου *H/E*λόγω ερπυσμού (H και E επηρεάζονται εξίσου).

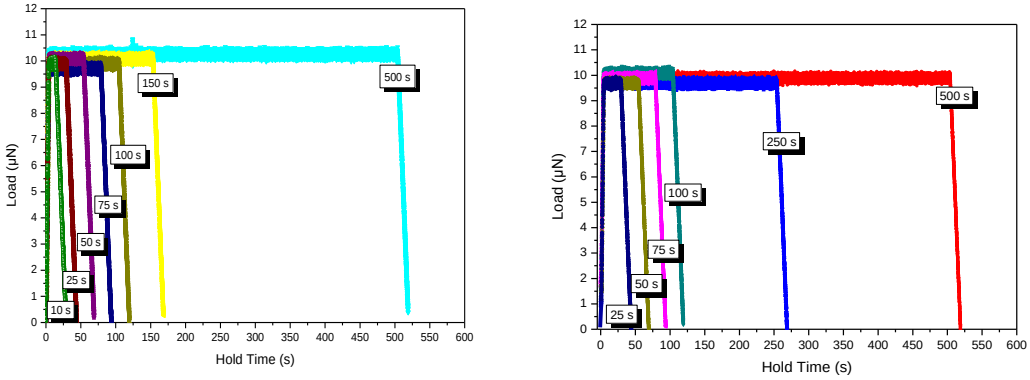

(a) (b)

Σχήμα 5.21Επιβαλλόμενο φορτίο συναρτήσει του χρόνου ερπυσμού για τα δείγματα untreated (a) και UV-treated (b) PDMS.

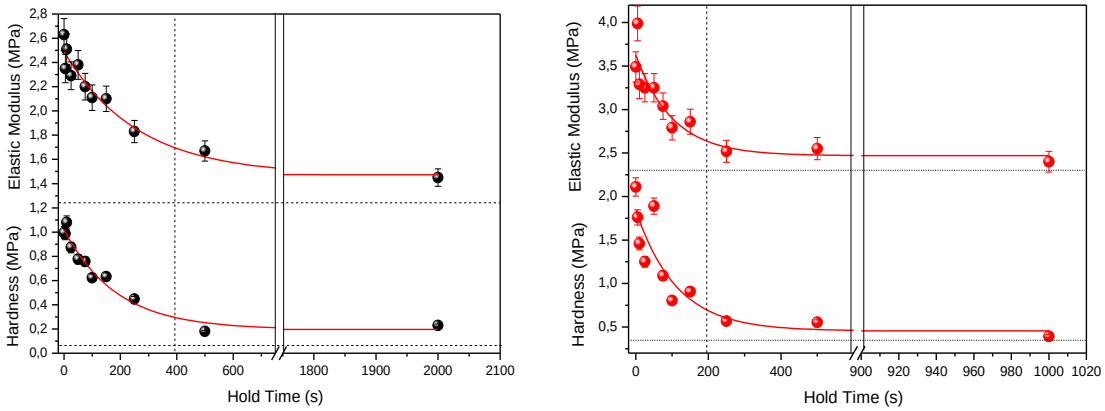

(a) (b)

Σχήμα 5.22Σκληρότητα και μέτρο ελαστικότητας συναρτήσει του χρόνου ερπυσμού για τα δείγματα untreated (a) και UV-treated (b) PDMS για 10μN επιβαλλόμενου φορτίου.

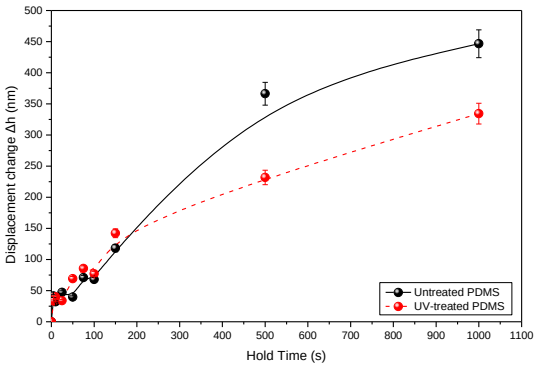

Σχήμα 5.23Μεταβολή βάθους διείσδυσης συναρτήσει του χρόνου ερπυσμού για τα δείγματα untreated (a) και UV-treated (b) PDMS.

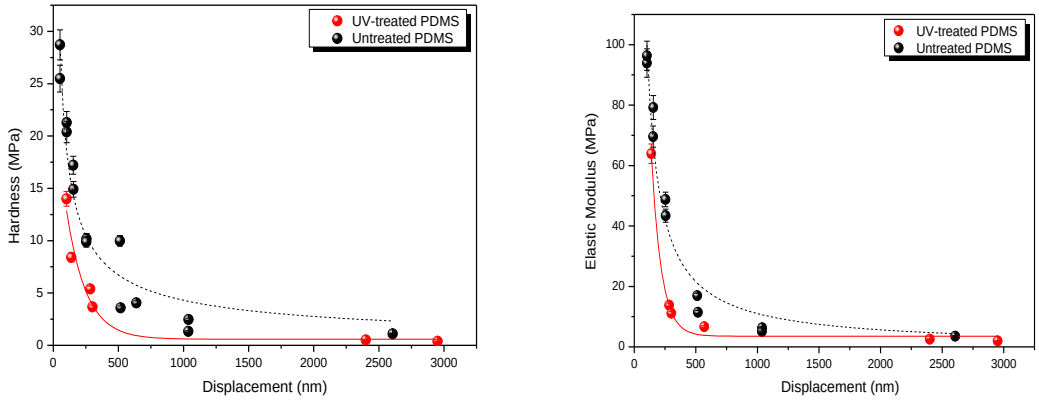

(a) (b)

Σχήμα 5.24Σύγκριση σκληρότητας και μέτρου ελαστικότητας για τα δείγματα untreated (a) και UV-treated (b) PDMS.

Η ενέργεια πρόσφυσης (adhesiveenergy) παρουσιάζει μείωση στην περίπτωση του UV-treatedPDMS, δείχνοντας ότι η ενέργεια πρόσφυσης παίζει σημαντικό ρόλο στη νανοκλίμακα (λόγω επίδρασης στην επιφάνεια επαφής).

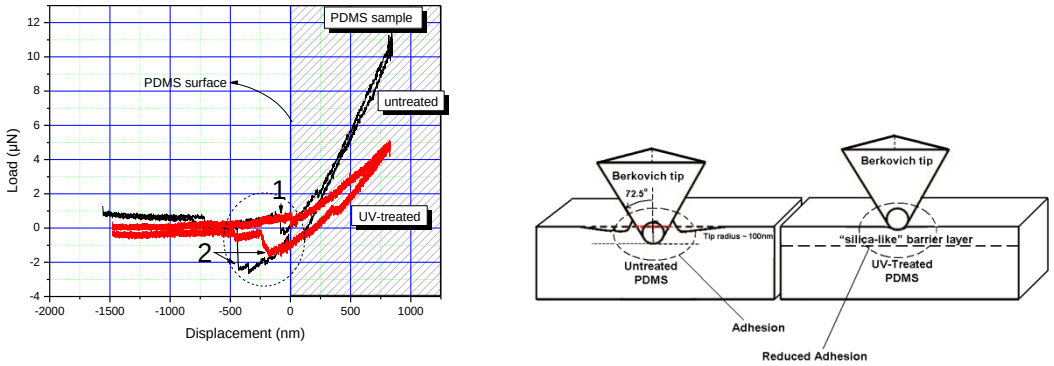

Σχήμα 5.25Καταγραφή πρόσφυσης και μηχανισμός για τα δείγματα untreated και UV-treatedPDMS.

Οι τιμές της σκληρότητας και του μέτρου ελαστικότητας είναι υψηλότερες όσο το βάθος διείσδυσης μειώνεται. Οι υψηλότερες τιμές σκληρότητας και μέτρου ελαστικότητας που εμφανίζονται στην επιφάνεια πιθανό να οφείλονται στη μεγαλύτερη πυκνότητα πλέγματος σταυροδεσμών και στην έκθεση των δειγμάτων στον ατμοσφαιρικό αέρα. Κατά τα πρώτα nm της νανοσκληρομέτρησης λαμβάνει χώρα το φαινόμενο της ολίσθησης της ακίδας στη σιλικόνη ενώ σε μεγαλύτερο βάθος η ακίδα παρασέρνει τη σιλικόνη λόγω πολύ καλής πρόσφυσης ακίδας-σιλικόνης και των αλληλεπιδράσεων μεταξύ τους, ήδη για πολύ μικρά φορτία. Η γεωμετρία της αιχμηρής ακίδας Berkovich έχει ως αποτέλεσμα τη συγκέντρωση τάσεων κυρίως κάτω από το άκρο της, οπότε η ζώνη πλαστικής παραμόρφωσης εμφανίζεται κυρίως κάτω από την επιφάνεια επαφής.

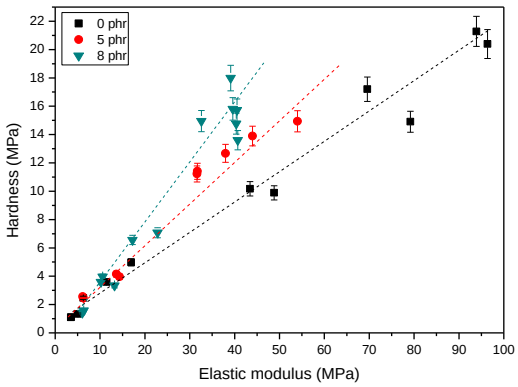

Σχήμα 5.26Καταγραφή γραμμικής σχέσης σκληρότητας με μέτρο ελαστικότητας.

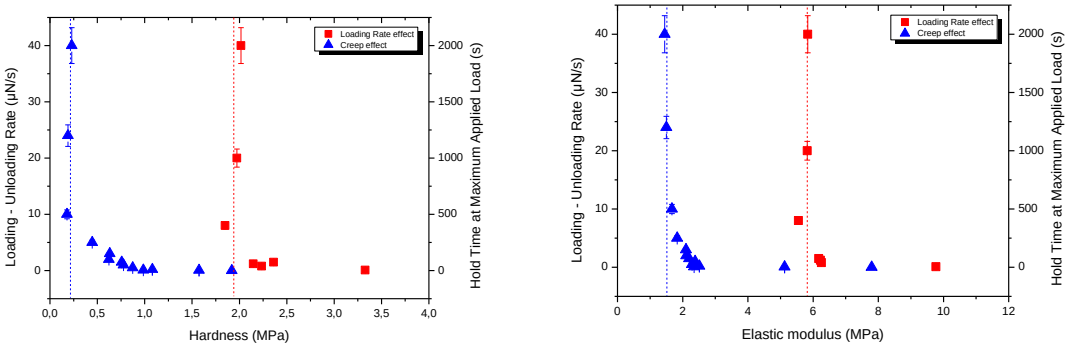

Σχήμα 5.27 Χρονοεξαρτημένες ιδιότητες: Επίδραση ρυθμού φόρτισης και χρόνου ερπυσμού σε σκληρότητα και μέτρο ελαστικότητας

Μεγαλύτερο μέτρο ελαστικότητας αντιστοιχεί στα δείγματα με μεγαλύτερο ποσοστό μέσου διασταύρωσης (μικρότερος βαθμός πολυμερισμού) και μετρήσεις σε όμοια συστήματα έδειξαν ότι το μέτρο ελαστικότητας της επιφάνειας ήταν υψηλότερο από το αντίστοιχο του κυρίως όγκου του υλικού χωρίς να καταστεί δυνατό να προσδιοριστεί το πάχος της επιφανειακής ζώνης με το υψηλότερο μέτρο ελαστικότητας. Η συμπεριφορά αυτή οφείλεται στην έκθεση του δείγματος στον ατμοσφαιρικό αέρα με αποτέλεσμα να δημιουργείται επιφανειακή ζώνη λόγω της περιεκτικότητας του αέρα σε οξυγόνο με υψηλότερο ποσοστό διασταυρώσεων-σταυροδεσμών. Σε αυτή την εργασία προσδιορίσθηκε με ακρίβεια το πάχος της επιφανειακής ζώνης που παρουσιάζει αυξημένες τιμές σκληρότητας και μέτρου ελαστικότητας.

5.3 Νανομηχανικές και νανοτριβολογικές ιδιότητες αντιδιαβρωτικών sol gel επιστρώσεων με προσθήκη αναστολέων διάβρωσης μέσω νανοφορέων[170]

Στο σχήμα 5.28 που ακολουθεί απεικονίζονται οι τιμές της σκληρότητας (H) και του μέτρου ελαστικότητας (E) συναρτήσει της μετατόπισης, για όλες τις επιστρώσεις που μελετήθηκαν.

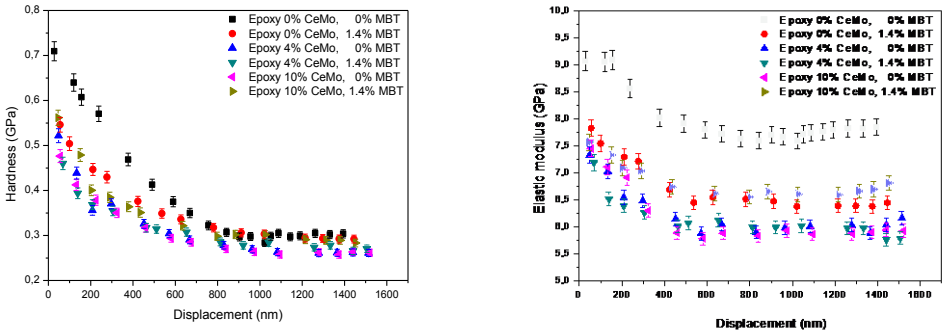

Σχήμα 5.28 Νανομηχανικές ιδιότητες (H, E) των επιστρώσεων

Η ελαστικότητα μίας επίστρωσης είναι επιθυμητό να μεταβάλλεται από τα στρώματα που βρίσκονται κοντά στην μεταλλική επιφάνεια τα οποία οφείλουν να παρουσιάζουν υψηλή τιμή μέτρου ελαστικότητας (μειωμένη ελαστική συμπεριφορά) ενώ τα εξωτερικά στρώματα χαμηλές τιμές μέτρου ελαστικότητας (αυξημένη ελαστική συμπεριφορά).

Οι πειραματικές μετρήσεις αφορούν το εξωτερικό στρώμα των επιστρώσεων καθώς το βάθος διείσδυσης είναι 3 μm ενώ το πάχος των όλων των επιστρώσεων είναι μεγαλύτερο από 20 μm όπως διαπιστώθηκε από τις φωτογραφίες SEM των επιστρώσεων. Επειδή το

17. [170]I.A. Kartsonakis, E.P. Koumoulos, C.A.Charitidis, G. Kordas, Hybrid organic-inorganic coatings including nanocontainers for corrosion protection of magnesium alloy ZK30, Journal of Nanoparticle Research, Volume 15, Issue 8, 1871 (2013)
18. I.A. Kartsonakis, E.P. Koumoulos, G.S. Pappas, A.C. Balaskas, C.A.Charitidis, G.C. Kordas, Hybrid organic-inorganic multilayer coatings including nanocontainers for corrosion protection of metal alloys, Journal of Corrosion Science, 57 (2012) 56–66
19. I.A. Kartsonakis, A.C. Balaskas, E.P. Koumoulos, C.A.Charitidis, G.C. Kordas,ORMOSIL-Epoxy Coatings with Ceramic Nanocontainers for Corrosion Protection of Magnesium Alloys ZK10, Progress in Organic Coatings, 76 (2–3) 2013
20. I.A. Kartsonakis, A.C. Balaskas, E.P. Koumoulos, C.A.Charitidis, G.C. Kordas,Evaluation of corrosion resistance of magnesium alloy ZK10 coated with hybrid organic–inorganic film including containers, Corrosion Science, 65, (2012), 481-493
21. I.A. Kartsonakis, A.C. Balaskas, E.P. Koumoulos, C.A.Charitidis, G.C. Kordas,Incorporation of ceramic nanocontainers into epoxy coatings for the corrosion protection of hot dip galvanized steel,Journal of Corrosion Science, 57 (2012) 30–41
22. *I.A.Kartsonakis, A.C.Balaskas, E.P.Koumoulos, C.A.Charitidis, G.Kordas, Corrosion resistance of magnesium alloy ZK10 coated with hybrid organic-inorganic film including containersEurocorr 2012, The European Corrosion Congress 2012, 9-13 September, Istanbul – Turkey*
23. *Costas Charitidis, Ioannis Kartsonakis (Presenter), Evangelia Karaxi, Elias Koumoulos, Irini Kanellopoulou, Antonis Karantonis, Self-healing microcomposites for corrosion protection of hot dip galvanized steel, EUROCORR 2015, Graz/Austria, September 2015.*

βάθος διείσδυσης των μετρήσεων νανοσκληρομέτρησης δεν ξεπέρασε το άνω όριο του 15-20% του συνολικού πάχους της επίστρωσης, δεν υπάρχει επίδραση του υποστρώματος (AA2024) στα αποτελέσματα. Σύμφωνα με τα παραπάνω οι επιστρώσεις με τα νανοδοχεία παρουσιάζουν βελτιωμένη συμπεριφορά όσον αφορά την ελαστικότητα. Το μέτρο ελαστικότητας των επιστρώσεων αυτών παρουσιάζει σημαντικά μικρότερες τιμές σε σύγκριση με αυτό της επίστρωσης χωρίς νανοδοχεία. Επιπλέον, για την επίστρωση με τα πληρωμένα νανοδοχεία το μέτρο ελαστικότητας παρουσιάζει τάση μείωσης καθώς το βάθος διείσδυσης (μετατόπιση) αυξάνεται αντίθετα με τις άλλες επιστρώσεις που παρουσιάζει τάση σταθεροποίησης (στην επίστρωση χωρίς νανοδοχεία) ή ελαφρά αυξητική τάση (στην επίστρωση με τα άδεια νανοδοχεία). Όσον αφορά την σκληρότητα, αυτή παρουσιάζεται ελαφρώς μειωμένη για τις επιστρώσεις με νανοδοχεία (άδεια ή γεμάτα).

Στο σχήμα 5.29, παρουσιάζεται ο λόγος H/E ως συνάρτηση της μετατόπισης για τις τρείς επιστρώσεις. Υψηλότερες τιμές του λόγου αυτού παρουσιάζει η επίστρωση με τα πληρωμένα με αναστολέα νανοδοχεία, ενώ σημαντικά μειωμένες τιμές του λόγου αυτού παρουσιάζει η επίστρωση χωρίς νανοδοχεία. Στο σχήμα 5.30 παρουσιάζεται ο συντελεστής τριβής για όλες τις επιστρώσεις. Η ενσωμάτωση των νανοδοχείων στην επίστρωση μειώνει τον συντελεστή τριβής σε όλο το μήκος της χαραγής (scratchpath). Μάλιστα οι επίστρωση με τα άδεια νανοδοχεία παρουσιάζει την μικρότερή τιμή συντελεστή τριβής. Σημειώνεται επίσης ότι στην περίπτωση της επίστρωσης με τα άδεια νανοδοχεία, η μείωση του συντελεστή τριβής έρχεται σε πλήρη συμφωνία με την εξέλιξη του λόγου H/E.

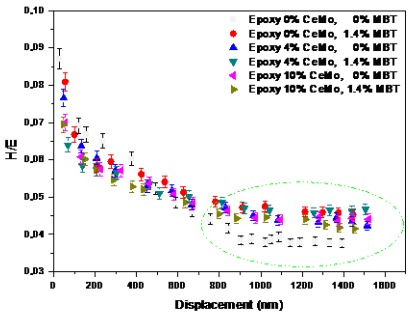

Σχήμα 5.29 Αντοχή σε φθορά (H/E) των επιστρώσεων

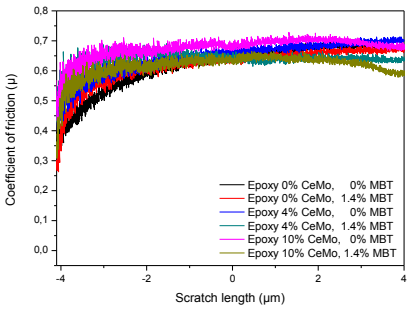

Σχήμα 5.30 Συντελεστής τριβής των επιστρώσεων

Συμπερασματικά, η προσθήκη νανοδοχείων βελτιώνει τις μηχανικές και τριβολογικές ιδιότητες των συγκεκριμένων επιστρώσεων. Μάλιστα, οι επιστρώσεις με τα πληρωμένα νανοδοχεία παρουσιάζουν καλύτερες τριβολογικές ιδιότητες. Η τελευταία παρατήρηση θα μπορούσε να αποδοθεί στην παρουσία του αναστολέα διάβρωσης. Μέρος του αναστολέα που βρίσκεται εντός των νανανοδοχείων απελευθερώνεται στο διάλυμα κατά το χρονικό

διάστημα που μεσολαβεί από την σύνθεση του διαλύματος μέχρι την εναπόθεσή του στην μεταλλική επιφάνεια. Η παρουσία του ελεύθερου αναστολέα επιδρά στις ιδιότητες της επίστρωσης. Στην συγκεκριμένη περίπτωση, όπως προκύπτει από τα πειραμάτα νανοεγχάραξης/ νανοσκληρομέτρησης η παρουσία του αναστολέα έχει ως αποτέλεσμα την βελτίωση των νανοτριβολογικών ιδιοτήτων στο εξωτερικό στρώμα της επίστρωσης.

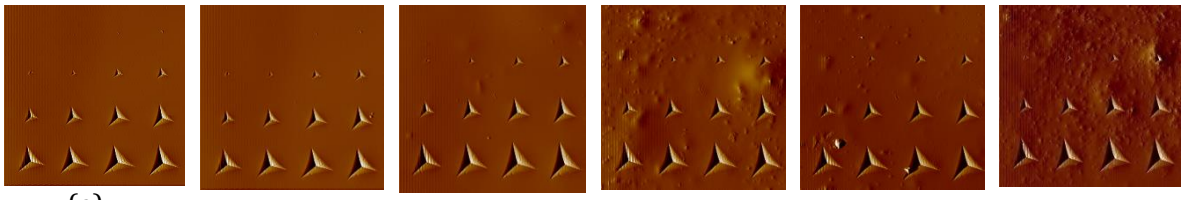

(a) (b) (c) (d) (e) (f)

Σχήμα 5.31 ΕικόνεςSPMτων εποξικών επιστρώσεων: (a) απλή επίστρωση, (b) επίστρωση με αναστολέα, (c) επίστρωση με 4% νανοδοχεία, (d) επίστρωση με 4% νανοδοχεία και αναστολέα, (e) επίστρωση με 10% νανοδοχεία και (f) επίστρωση με 10% νανοδοχεία και αναστολέα**.**

5.4 Νανομηχανικές και νανοτριβολογικές ιδιότητες λεπτών υμενίων Co_3O_4 και Co [171]

Ο λόγος Η/Ε είναι ιδιαίτερα σημαντικός στην τριβολογία, καθώς μπορεί να χρησιμοποιηθεί ως παράμετρος κατηγοριοποίησης των υλικών σε όρους φθοράς. Ο λόγος αυτός, αν

24. [171]E.P. Koumoulos, V.P. Tsikourkitoudi, I.A. Kartsonakis, V. Markakis, N. Papadopoulos, E. Hristoforou, C.A. Charitidis, Synthesis, structural and nanomechanical properties of cobalt based thin films, International Journal of Structural Integrity (2015), 6 (2)
25. Elias P. Koumoulos, Vassileios Markakis, Vasiliki P. Tsikourkitoudi, Costas A. Charitidis, Nikolaos Papadopoulos, Evangelos Hristoforou, Tribological characterization of chemical vapor deposited Co and Co3O4 thin films for sensing reliability in engineering applications, Tribology International, 82, Part A, 2015, 89–94 (2014)
26. M. Kandyla, C. Chatzimanolis-Moustakas, E.P. Koumoulos, C. Charitidis, M. Kompitsas, Nanocomposite NiO:Au hydrogen sensors with high sensitivity and low operating temperature, Materials Research Bulletin Volume 49, January 2014, Pages 552–559
27. V.P. Tsikourkitoudi, E.P. Koumoulos, N. Papadopoulos, C.A. Charitidis, Growth, Structural and Mechanical Characterization and Reliability of Chemical Vapor Deposited Co and Co3O4 Thin Films as Candidate Materials for Sensing Applications, Key Engineering Materials 495, pp. 108-111 (2012).
28. V.P. Tsikourkitoudi, E.P. Koumoulos, N. Papadopoulos, E. Hristoforou, C.A. Charitidis, Growth, Structural and Mechanical Characterization and Reliability of Chemical Vapor Deposited Co and Co3O4 Thin Films as Candidate Materials for Sensing Applications, Journal Of Optoelectronics and Advanced Materials, 14(1), pp. 169-175 (2012).
29. *C.A. Charitidis, V.P. Tsikourkitoudi, E.P. Koumoulos, I.A. Kartsonakis, N. Papadopoulos, E. Hristoforou, Synthesis, structural and nanomechanical properties of cobalt based thin films, ICEAF III. 3rd International Conference of Engineering Against Failure. 26-28 June, 2013 - Kos island.*
30. *V. P. Tsikourkitoudi, E.P. Koumoulos, I.A. Kartsonakis, C.A. Charitidis, Structural investigation and mechanical integrity of metal and metal oxide thin films for sensing applications: A comparative study through nanoindentation, 9th International Conference on Nanosciences & Nanotechnologies(2012)*
31. *V.P. Tsikourkitoudi, E.P. Koumoulos, N. Papadopoulos, E. Hristoforou, C.A. Charitidis, Tribological characterization of chemical vapor deposited Co and Co3O4 thin films for sensing reliability in engineering applications, 20th International Conference on Soft Magnetic Materials (SMM-20) (2011)*
32. *V.P. Tsikourkitoudi, E.P. Koumoulos, N. Papadopoulos, C.A. Charitidis, Growth, Structural and Mechanical Characterization and Reliability of Chemical Vapor Deposited Co and Co3O4 Thin Films as Candidate Materials for Sensing Applications, International Conference on Materials and Applications for Sensors and Transducers (IC-MAST) (2011)*

πολλαπλασιαστεί με ένα γεωμετρικό παράγοντα, ορίζει το «δείκτη πλαστικότητας», ο οποίος είναι ένα πολύτιμο μέτρο για τον καθορισμό του ορίου του ελαστικού χαρακτήρα στην επαφή επιφανειών (περιγράφει τις ιδιότητες παραμόρφωσης τραχιών επιφανειών). Το Σχήμα 5.34 παρουσιάζει το λόγο *H/E* συναρτήσει του βάθους διείσδυσης του εντυπωτή. Το λεπτό υμένιο Co_3O_4 παρουσιάζει υψηλότερη αντίσταση στη φθορά σε σύγκριση με το λεπτό υμένιο Co.

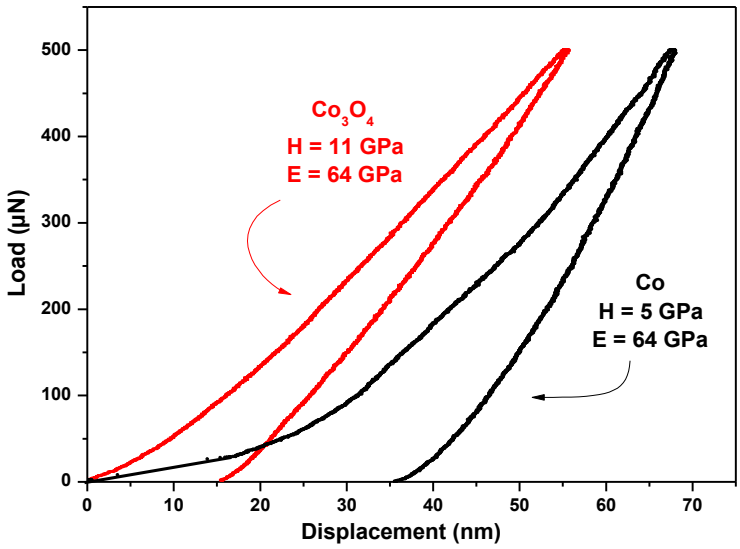

Σχήμα 5.32 Καμπύλες φόρτισης αποφόρτισης για τα λεπτά υμένια Co_3O_4 και Co.

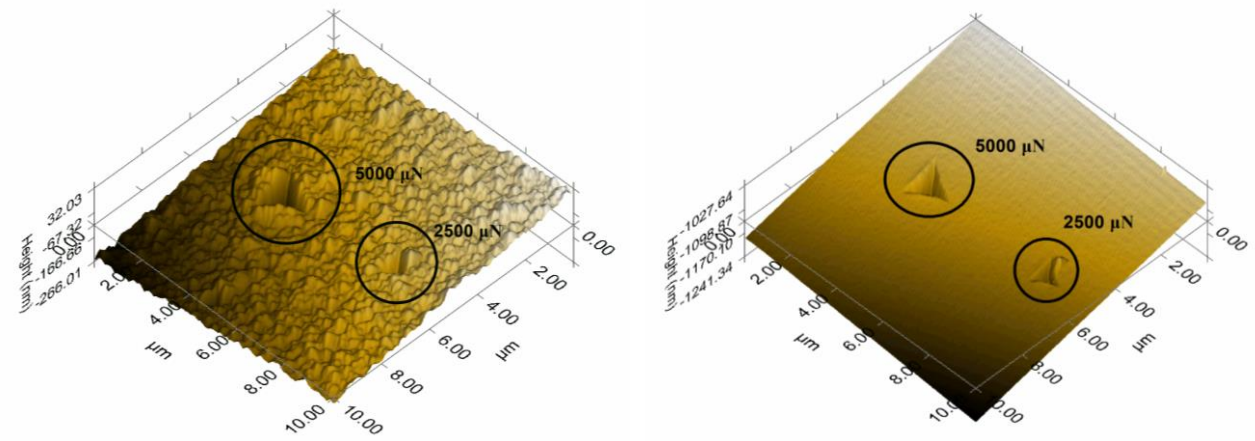

(a) (b)

Σχήμα 5.33 Εικόνες SPMγια τα λεπτά υμένια Co_3O_4 και Co.

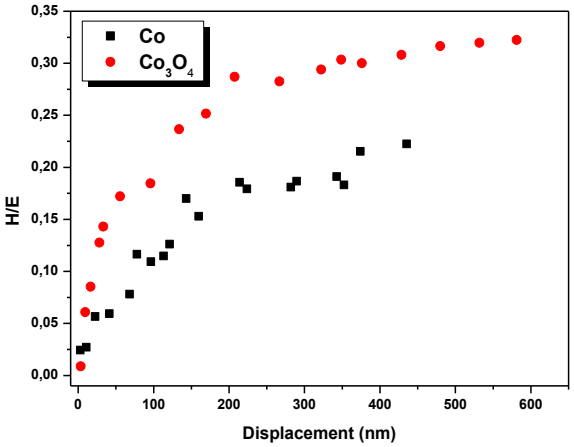

Σχήμα 5.34 Λόγος σκληρότητας προς μέτρο ελαστικότητας (αντίσταση στη φθορά) συναρτήσει του βάθους διείσδυσης του εντυπωτή για τα δυο λεπτά υμένια.

Υπολογίστηκαν, επίσης, το ολικό έργο που αναπτύσσεται από τον εντυπωτή (W_{tot}), το οποίο προκαλεί ελαστοπλαστική παραμόρφωση σε μέγιστο βάθος διείσδυσης, και το έργο που μεταφέρεται από το δείγμα στον εντυπωτή κατά τη διάρκεια της αποφόρτισης (W_u). Βρέθηκε ότι υπάρχει σχέση μεταξύ του λόγου του αναντίστρεπτου έργου προς το ολικό έργο για μια πλήρη διαδικασία φόρτισης-αποφόρτισης, $(W_{tot}-W_u)/W_{tot}$, και του λόγου σκληρότητας προς μέτρο ελαστικότητας (H/E). Η σχέση αυτή δίνεται παρακάτω (Εξ. 5.1):

$$\frac{H}{E} = \Pi_\theta \frac{\left(W_{tot} - W_u\right)}{W_{tot}}, \qquad (5.1)$$

Ο δείκτης, θ, δηλώνει πιθανή εξάρτηση από τη γωνία του εντυπωτή. Το Σχήμα 5.14 παρουσιάζει, για συγκεκριμένο εντυπωτή, τη γραμμική σχέση μεταξύ H/E και $(W_{tot}-W_u)/W_{tot}$. Τα W_u και W_{tot} μπορούν να υπολογιστούν από απλή αριθμητική ολοκλήρωση που βασίζεται σε μετρήσεις φορτίου-βάθους διείσδυσης.

Η Εξ. 5.1 παρέχει μια εναλλακτική μέθοδο για τη μέτρηση του λόγου H/E στη μικρο- και νανο- κλίμακα τόσο για μέταλλα όσο και για κεραμικά. Επιπλέον, είναι δυνατό να ληφθούν τόσο οι τιμές H όσο και οι τιμές E χρησιμοποιώντας την παραπάνω συσχέτιση σε συνδυασμό με γνωστές σχέσεις μεταξύ του E, της επιφάνειας επαφής και της κλίσης του άνω τμήματος της καμπύλης αποφόρτισης (ακαμψία).

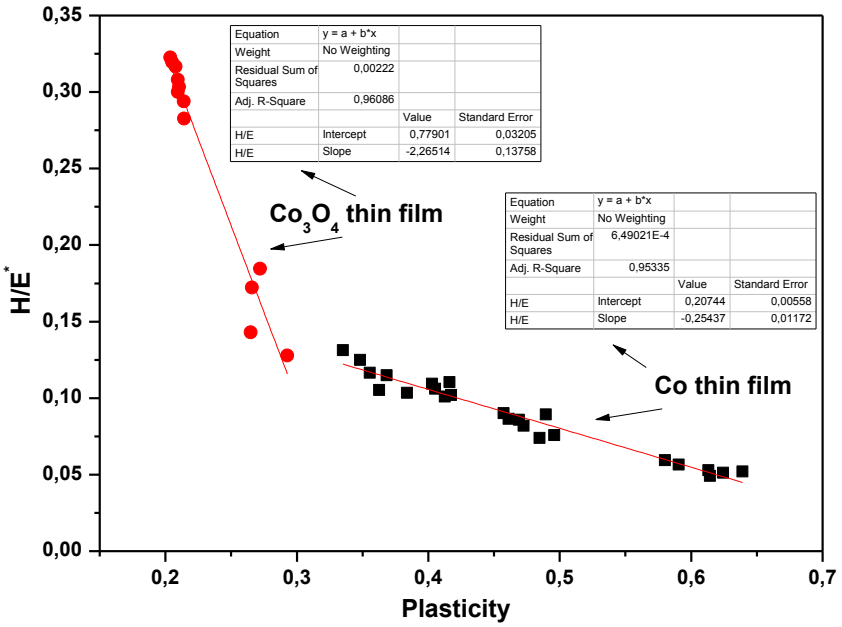

Σχήμα 5.35 Γραμμική σχέση H/E και $(W_{tot}-W_u)/W_{tot}$ για τα λεπτά υμένια Co_3O_4 και Co.

Όπως παρουσιάζεται στο Σχήμα 5.35, το λεπτό υμένιο Co_3O_4 παρουσιάζει μεγαλύτερη αντίσταση στη φθορά σε σχέση με το λεπτό υμένιο Co. Οι τριβολογικές ιδιότητες των λεπτών υμενίων και ο τρόπος παραμόρφωσής τους (ελαστική ή/και πλαστική παραμόρφωση), τα οποία είναι χαρακτηριστικά της επιφάνειας και όχι του υλικού όγκου, διερευνήθηκαν και μελετήθηκαν με την τεχνική της νανοεγχάραξης (μέτρηση πλευρικών δυνάμεων). Αρχικά, πραγματοποιήθηκε σάρωση (pre-scratch) με πολύ μικρό φορτίο (0,2 μN). Στη συνέχεια, πραγματοποιήθηκε εγχάραξη της επιφάνειας από ένα αρχικό φορτίο 0,2 μN μέχρι μια μέγιστη τιμή 500 μN στο τέλος της εγχάραξης. Η διαδρομή εγχάραξης ήταν 10 μm και η ταχύτητα της ακίδας 0,2 μm/s. Τέλος, πραγματοποιήθηκε μια ακόμα σάρωση (post-scratch) με μικρό φορτίο (2 μN). Το εφαρμοζόμενο φορτίο κατά την αρχική και τελική σάρωση ήταν πολύ μικρό για την αποφυγή καταστροφής ή μόνιμης παραμόρφωσης των υμενίων.

Στο Σχήμα 5.36, παρουσιάζεται ο συντελεστής τριβής των δυο λεπτών υμενίων συναρτήσει της διαδρομής εγχάραξης. Ο συντελεστής τριβής είναι ο λόγος των πλευρικών δυνάμεων προς τις κάθετες δυνάμεις και μπορεί να εκφραστεί ως το άθροισμα των συντελεστών τριβής πρόσφυσης και «οργώματος/ploughing».

Το λεπτό υμένιο Co_3O_4 παρουσιάζει χαμηλότερο συντελεστή τριβής σε σύγκριση με το λεπτό υμένιο Co.

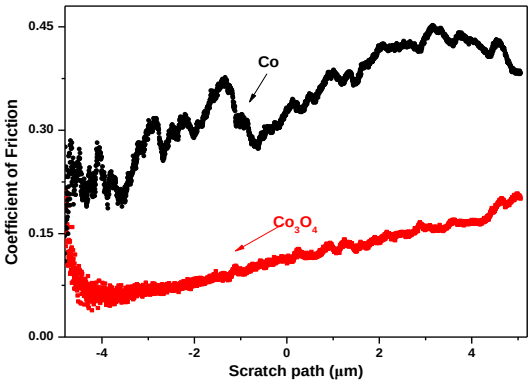

Σχήμα 5.36. Συντελεστής τριβής για τα λεπτά υμένια Co και Co_3O_4.

Οι μετρήσεις νανοεγχάραξης επιβεβαιώνουν το γεγονός ότι το λεπτό υμένιο Co_3O_4 παρουσιάζει μεγαλύτερη αντίσταση στη φθορά (χαμηλότερο συντελεστή τριβής) που παρουσιάστηκε στην προηγούμενη ενότητα.

Στο Σχήμα 5.37, παρουσιάζονται τα προφίλ βάθους διείσδυσης κατά τη νανοεγχάραξη για τα δυο λεπτά υμένια για μέγιστο εφαρμοζόμενο κάθετο φορτίο 500 μN. Η καμπύλη νανοεγχάραξης (scratch curve) αντιστοιχεί σε διείσδυση της ακίδας στο δείγμα, ενώ η καμπύλη σάρωσης με μικρό φορτίο μετά τη νανοεγχάραξη (post-scratch curve) παρουσιάζει το τελικό προφίλ της επιφάνειας μετά την εγχάραξη (δηλαδή την πλαστική παραμόρφωση του εξεταζόμενου υλικού). Η διαφορά μεταξύ των καμπυλών νανοεγχάραξης (scratch curve) και σάρωσης με μικρό φορτίο μετά τη νανοεγχάραξη (post-scratch curve) ορίζει την ελαστική επαναφορά των λεπτών υμενίων. Όπως παρουσιάζεται στο Σχήμα 5.37, η παραμόρφωση των λεπτών υμενίων είναι κυρίως πλαστική κατά μήκος της διαδρομής εγχάραξης. Όσον αφορά στο λεπτό υμένιο Co, παρατηρούνται διακυμάνσεις κατά την εγχάραξη, οι οποίες δείχνουν πιθανή θραύση του υμενίου. Η αύξηση στο βάθος διείσδυσης κατά τη διάρκεια της σάρωσης με μικρό φορτίο μετά την εγχάραξη (post-scratch) μπορεί να αποδοθεί σε καθυστερημένη ανάκτηση της παραμόφωσης του λεπτού υμενίου σε σύγκριση με το υπόστρωμα, γεγονός το οποίο προκαλεί τάσεις διάτμησης κατά μήκος της διεπιφάνειας προκαλώντας αποκόλληση τμημάτων του υμενίου. Δεν παρατηρούνται σημαντικές διακυμάνσεις στην καμπύλη εγχάραξης του λεπτού υμενίου Co_3O_4. Συνεπώς, το λεπτό υμένιο δεν αποκολλήθηκε από το υπόστρωμα κατά την εγχάραξη. Παρόλα αυτά, παρατηρείται μικρή αύξηση στο βάθος διείσδυσης της παραμόρφωσης, γεγονός που δείχνει ένα κρίσιμο φορτίο (L_{cL}= 150 μN) για την αποκόλληση του υμενίου, που προκαλείται από υψηλά θλιπτικά φορτία. Οι τιμές φορτίου που αντιστοιχούν στο σημείο όπου το λεπτό υμένιο Co_3O_4 αστοχεί κατά τη σάρωση μετά την εγχάραξη (post-scratch) είναι ίσες με 150 & 290 μN.

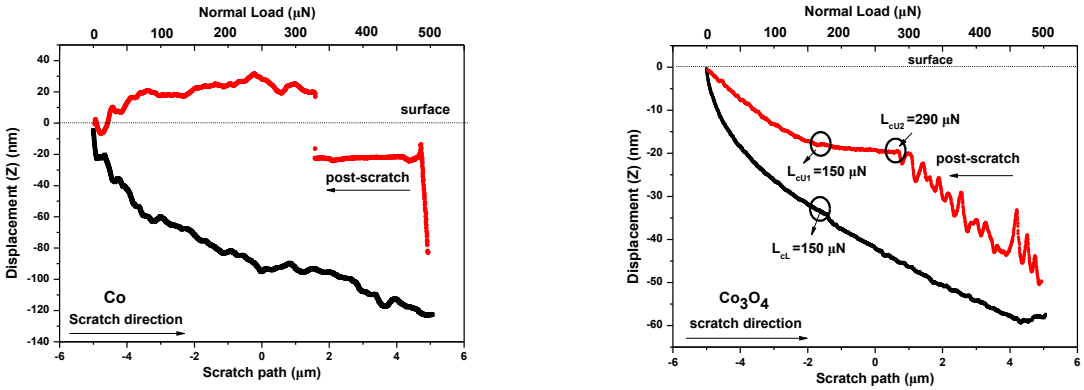

α **B**

Σχήμα 5.37. Προφίλ βάθους διείσδυσης κατά τη νανοεγχάραξη υπό μεταβαλλόμενο κάθετο φορτίο 0,2-500 μN για τα λεπτά υμένια Co (α) και Co_3O_4 (β).

5.5 Νανομηχανικές και νανοτριβολογικές ιδιότητες λεπτών υμενίων υδρόφοβων διηλεκτρικών δομών[172]

Στο παρόν πείραμα πραγματοποιήθηκαν μετρήσεις μεταξύ δύο διαφορετικών υδρόφοβων διηλεκτρικών δομών ίδιου πάχους ώστε να είναι συγκρίσιμες και να διερευνηθεί το κατά πόσο μπορεί να προσδώσει βελτιωμένες μηχανικές ιδιότητες μια πιο σύνθετη δομή επιστρώσεων. Τα δύο υμένια που εξετάζονται είναι 1. 60nmTeflon® σε οξείδιο τετρα-εθοξυ-σιλάνης (TEOS) και 2. 60nm "*σύνθετη επίστρωση*"σε TEOS. Η σύνθετη επίστρωση αποτελείται από υμένιο φθοράνθρακα FC πάχους 30 nm που δρα ενισχυτικά στην πρόσφυση των 30nmTeflon® (AF 1600) στο TEOS, με αποτέλεσμα να έχουμε μία υδρόφοβη επίστρωση δομής "*sandwich*".

33. [172] D.A. Dragatogiannis, E. Koumoulos, K. Ellinas, A. Tserepi, E. Gogolides, C.A. Charitidis, Nanoscale Mechanical and Tribological Properties of Plasma Nanotextured COP Surfaces with Hydrophobic Coatings, Plasma Processes and Polymers, (2015), in press
34. Elias P. Koumoulos, Costas A. Charitidis, Dimitrios P Papageorgiou, Athanasios G Papathanasiou, Andreas G Boudouvis, Nanomechanical and Nanotribological Properties of Hydrophobic Fluorocarbon Dielectric Coating on Tetraethoxysilane for Electrowetting Applications, Journal of Surface and Coatings Technology, 206, pp. 3823–3831 (2012)
35. Dimitrios P. Papageorgiou, Elias P. Koumoulos, Costas A. Charitidis, Andreas G. Boudouvis, Athanasios G. Papathanasiou, Evaluating the robustness of top coatings comprising plasma-deposited fluorocarbons in electrowetting systems, Journal of Adhesion Science and Technology (2012), 26 (12-17), pp. 2001-2015
36. *Elias P. Koumoulos, D.A. Dragatogiannis, K. Ellinas, A. Tserepi, E. Gogolides, C.A. Charitidis, Nanomechanical and tribological properties of plasma nanotextured surfaces for "smart" microfluidic devices, International Middle East Plasma Science (IMEPS), Antalya, Turkey April 23 – 25, 2014*
37. *Aspasia Iliopoulou, Elias P. Koumoulos, Dimitrios P. Papageorgiou, Athanasios G. Papathanasiou, Costas A. Charitidis, Adhesion strength of hydrophobic dielectric coatings for electrowetting applications, 8th Panhellenic Conference on Chemical Engineering (2011)*

Displacement	A (60nm *composite coating* on TEOS)	B (Teflon® 60nm on TEOS)
~ 35nm	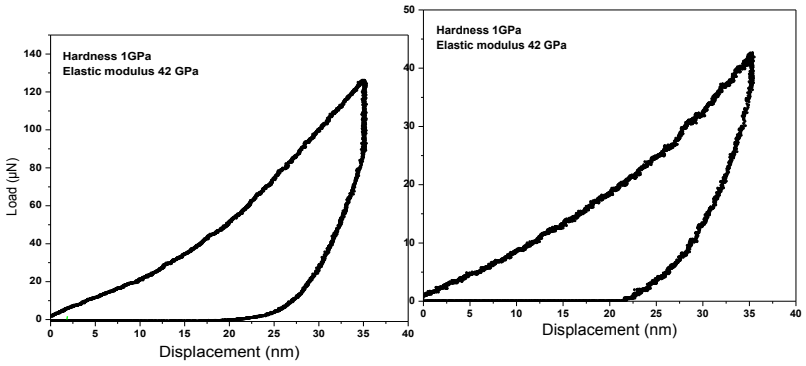	
	A_1	A_2
~ 65nm	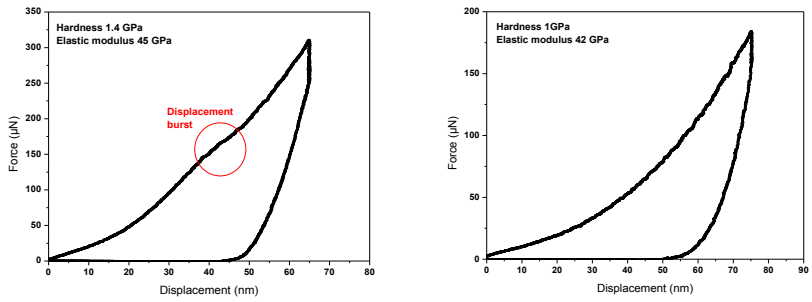	
	B_1	B_2
~ 400nm	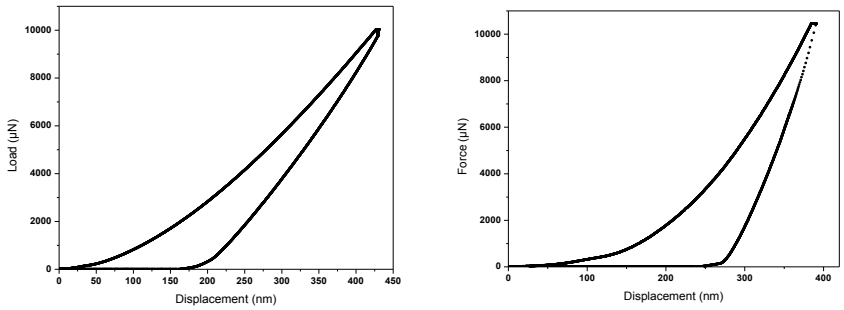	
	C_1	C_2

Τίθενται σε αντιπαραβολή οι καμπύλες φόρτισης αποφόρτισης και αποκαλύπτεται η πολύ καλύτερη αντίσταση που παρουσιάζει η σύνθετη επικάλυψη στο εφαρμοζόμενο φορτίο καθώς απαιτείται μεγαλύτερη φόρτιση προκειμένου να επιτευχθεί η ίδια μετατόπιση. Στο δεύτερο σχήμα επισημαίνεται στα 150 μN το σημείο όπου οι διατμητικές τάσεις αρχίζουν να συσσωρεύονται και να επιδρούν στη διεπιφάνεια μεταξύ φθοράνθρακα και TEOS.

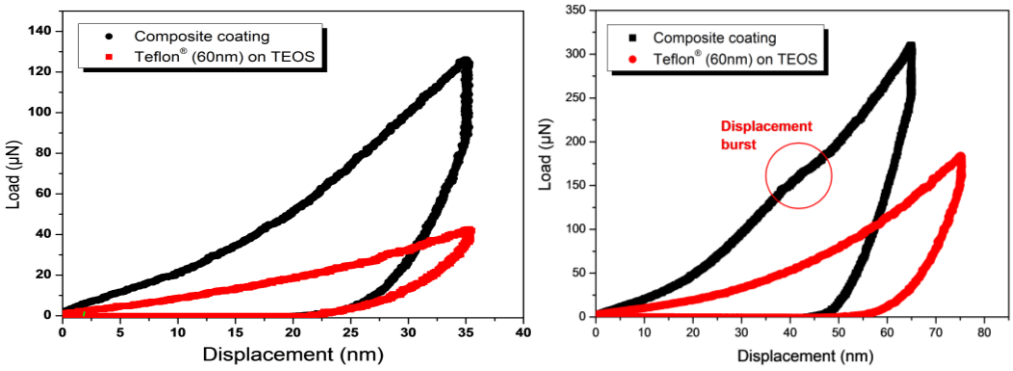

Σχήμα 5.39Συγκριτική απεικόνιση των καμπυλών φόρτισης – αποφόρτισης για τις δύο δομές για διαφορετικές μετατοπίσεις (35nm και 65nm αντίστοιχα)

Παρουσιάζονται η σκληρότητα και το μέτρο ελαστικότητας σε συνάρτηση με τη μετατόπιση.

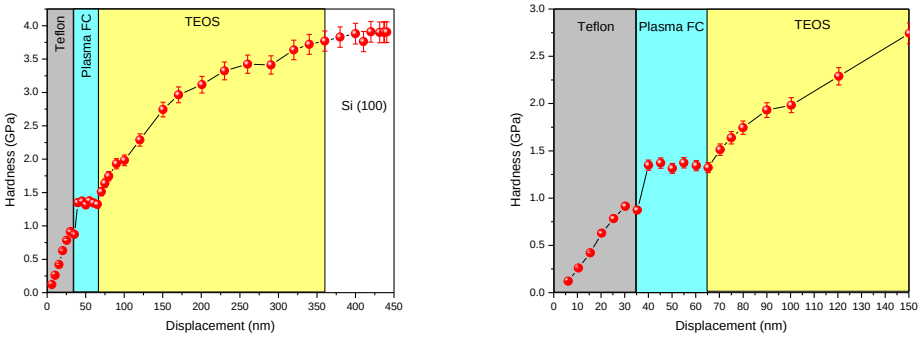

Σχήμα 5.40 Σκληρότητα συναρτήσει του βάθους διείσδυσης για το δείγμαTeflon®-plasmaFC- TEOSassembly σε υπόστρωμα Si.

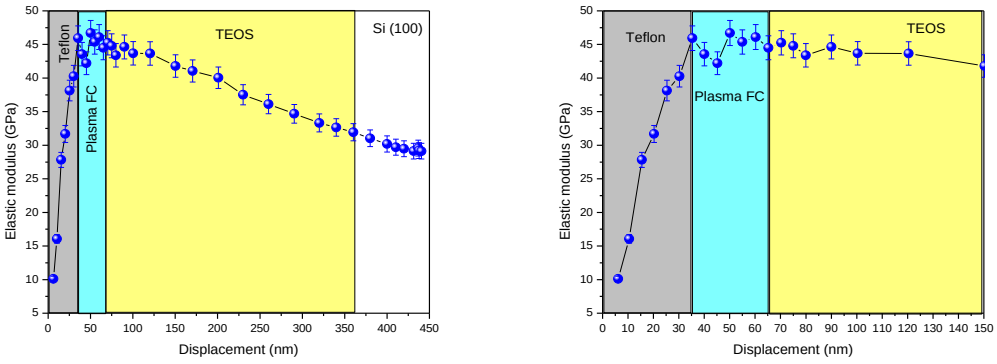

Σχήμα 5.41Μέτρο ελαστικότητας συναρτήσει του βάθους διείσδυσης για το δείγμαTeflon®-plasmaFC- TEOSassembly σε υπόστρωμα Si.

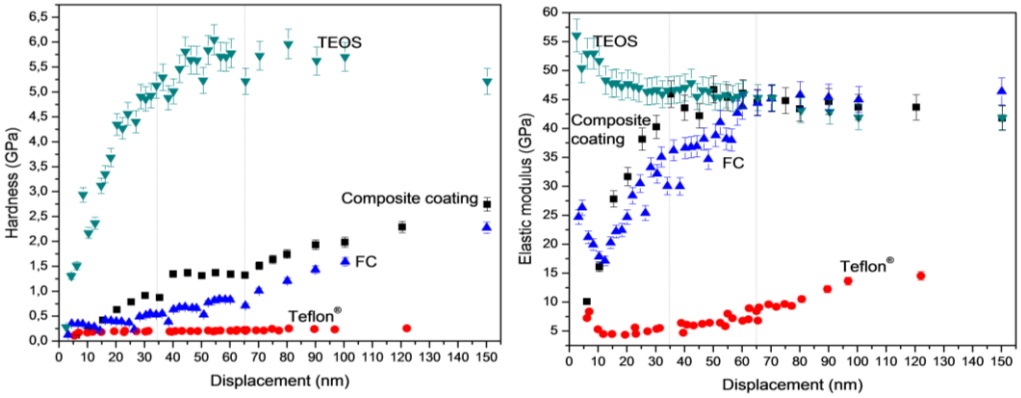

Σχήμα 5.42 Σκληρότητα και μέτρο ελαστικότητας συναρτήσει του βάθους διείσδυσης για το δείγμαTeflon®-plasmaFC- TEOSassembly και τα επιμέρους συστατικά του σε υπόστρωμα Si.

Στο σχήμα 5.43 παρουσιάζεται το αποτύπωμα νανοσκληρομέτρησης για όλα τα δείγματα. Στη σύνθετη επικάλυψη παρατηρείται μεγάλη παραμόρφωση pile-up.

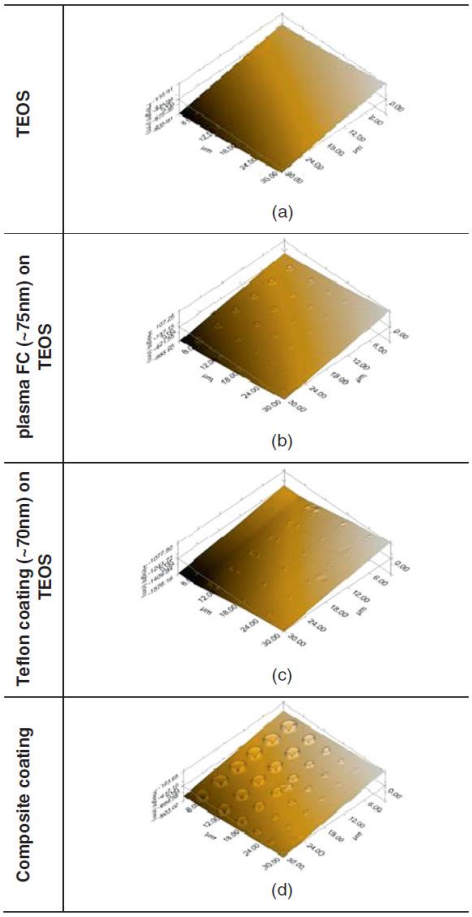

Σχήμα 5.43Εικόνες SPM για τη σύνθετη επικάλυψη αλλά και τα FC, Teflon και TEOS

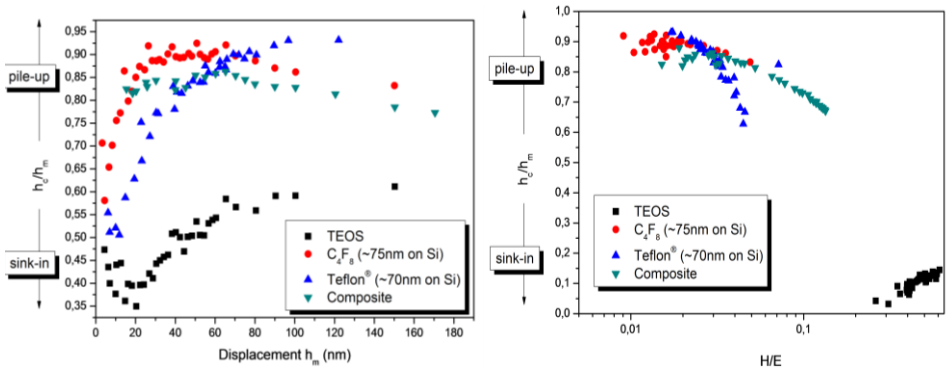

Σχήμα 5.44 Pile-up/sink-in διερεύνηση του μηχανισμού παραμόρφωσης για τη σύνθετη επικάλυψη for και για τα δείγματα FC, Teflon® και TEOS.

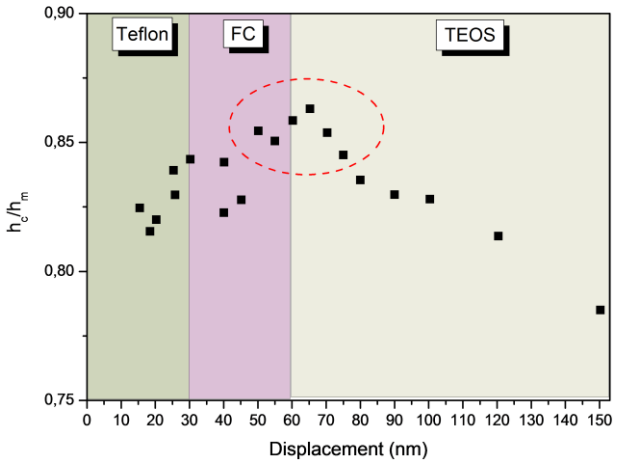

Σχήμα 5.45 Εύρεση σημείου εναλλαγής μηχανισμού παραμόρφωσης από Pile-up σε sink-in

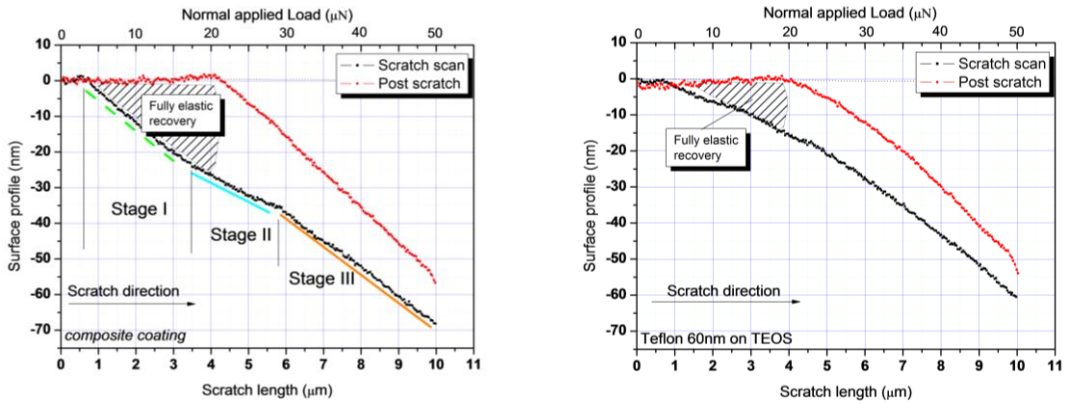

(α) (β)

Σχήμα 5.46 Nanoscratch depth profiles για τα δύο δείγματα με εφαρμογή δύναμης 50 μN.

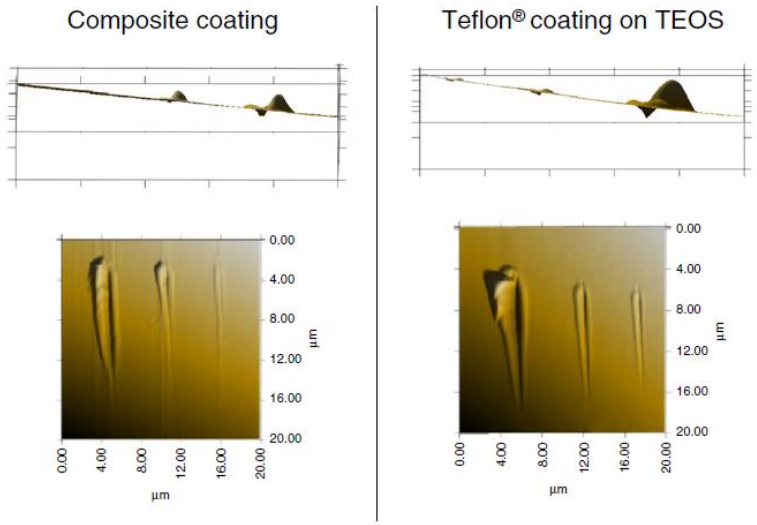

Σχήμα 5.47 Εικόνες SPM για δοκιμή νανοεγχάραξης με εφαρμοζόμενο φορτίο 50, 100 και 300μN.

Το εφαρμοζόμενο φορτίο φαίνεται στο σχήμα 5.46, καθώς και το βάθος εγχάραξης.

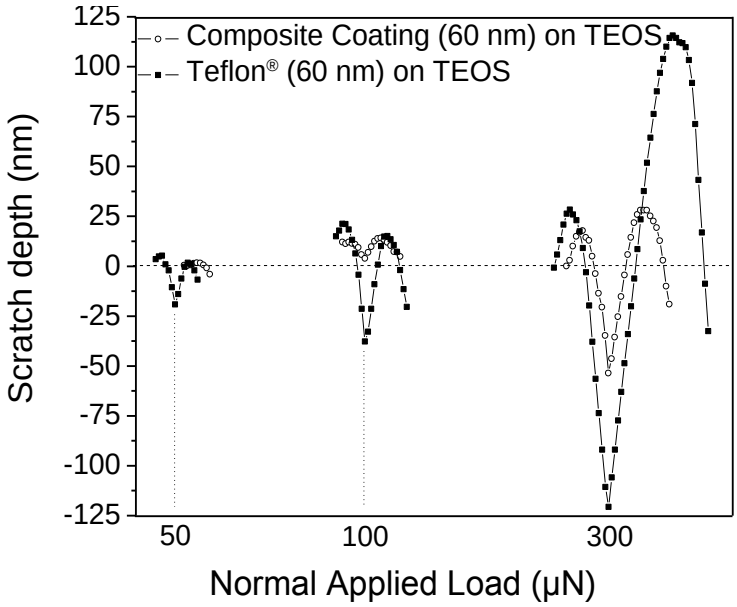

Σχήμα 5.48 Βάθος εγχάραξης συναρτήσει του εφαρμοζόμενου φορτίου, 50, 100 και 300 μN.

Το σύνθετο υμένιο που κατασκευάστηκε πληροί τις προϋποθέσεις για να ανταπεξέλθει σε εφαρμογές ηλεκτροδιαβροχής. Είναι θερμοδυναμικά ευσταθής και χημικά σταθερή δομή, μηχανικά ακέραιο και ανθεκτικό. Υπερτερεί του απλού υμενίου όσον αφορά τις μηχανικές και τριβολογικές του ιδιότητες. Από τη σύγκριση των δύο δειγμάτων προκύπτει πως για την ίδια μετατόπιση - βάθος διείσδυσης της ακίδας – το σύνθετο υμένιο επιδεικνύει μεγαλύτερη αντίσταση στο εφαρμοζόμενο φορτίο καθώς χρειάζεται αρκετά μεγαλύτερη

φόρτιση προκειμένου να έχει την ίδια μετατόπιση σε σχέση με το απλό υμένιο του Teflon στο TEOS. Η διεπιφανειακή πρόσφυση στο σύνθετο υμένιο είναι πολύ καλή αφού παρά τις αρκούντως ισχυρές διατμητικές τάσεις δεν παρατηρήθηκε καμία αλλαγή στη μορφολογία της επιφάνειας στην περιοχή της νανοδιείσδυσης. Παρατηρώντας τα προφίλ της νανοεγχάραξης είναι φανερό πως η ελαστική περιοχή του σύνθετου υμενίου είναι μεγαλύτερη και μάλιστα η χαραγή του σύνθετου υμενίου είχε διπλάσια ελαστική επαναφορά (~15nm) έναντι του απλού υμενίου (~30nm). Σχετικά με την πλαστική παραμόρφωση με εφαρμοζόμενη δύναμη 300μN στο σύνθετο υμένιο το βάθος της εγχάραξης είναι πολύ μικρότερο. Για εφαρμογή ίδιας δύναμης το απλό υμένιο υπόκειται σε εγχάραξη μεγάλου βάθους και παρουσιάζει πλαστική παραμόρφωση (accumulation) ενώ το σύνθετο υμένιο επιδεικνύει καλύτερη αντίσταση στη φθορά. Η αλλαγή της κλίσης στο διάγραμμα H/E αποκαλύπτει την «ενδυνάμωση» του σύνθετου υμενίου σε συνάρτηση με την αύξηση του βάθους διείσδυσης. Μεταξύ των δύο δειγμάτων η σύνθετη δομή παρουσιάζει βελτιωμένη δύναμη πρόσφυσης.

5.6 Νανομηχανικές και νανοτριβολογικές ιδιότητες μεμβράνης φωγιασίτη[173]

Μελετήθηκε μεμβράνη φωγιασίτη η οποία συντέθηκε πάνω σε πορώδη υπόστρωμα α-Al_2O_3 με επίπεδη γεωμετρία (δισκίο διαμέτρου 14mm, πάχους 2mm, μέσο μέγεθος πόρων 150-200nm και πορώδες 0,4) με την μέθοδο seededgrowth. Πριν την κρυστάλλωση της μεμβράνης τοποθετούνται κατάλληλα κρύσταλλοι φωγιασίτη (NaY- Aldrich) στην επιφάνεια του υποστρώματος με την τεχνική dip-casting. Η σύνθεση της μεμβράνης έγινε στους 85 ^oC χρησιμοποιώντας γέλη με σύσταση $4.17Na_2O/1.0Al_2O_3/5$TEA(τριαιθανολαμίνη)$/1.87SiO_2/460H_2O$. Η διάρκεια της σύνθεσης ήταν 120 ώρες.

Η ταυτοποίηση δομής των κρυστάλλων έγινε με XRD (BrukerD-8 ADVANCEdiffractometer εξοπλισμένο με LynxEye ανιχνευτή θέσης και μια CuKa πηγή ακτίνων X (40 kV, 40 mA)) και παρατηρήθηκε ότι ευνοήθηκε και η ανάπτυξη κρυστάλλων ζεόλιθου A (LTA). Η μορφολογία και το μέγεθος των κρυστάλλων προσδιορίστηκαν με SEM (LEO-SUPRA 35VPFieldEmissionScanningElectronMicroscope).

Στη συνέχεια πραγματοποιήθηκαν δύο σειρές μετρήσεων με την τεχνική της νανοδιείσδυσης. Κατά την πρώτη σειρά μετρήσεων πραγματοποιήθηκε φόρτιση μέχρι ένα μέγιστο φορτίο και στην συνέχεια αποφόρτιση. Από τις πειραματικές μετρήσεις

38. [173]C.A.Charitidis, E.P. Koumoulos, V. Nikolakis, D.A.Dragatogiannis, Structural & Nanomechanical Properties of a Zeolite Membrane measured using Nanoindentation, Journal of Thin Solid Films, 526, 2012, 168–175
39. *C.A.Charitidis, M. Kyritsi, E.P. Koumoulos, V. Nikolakis. Synthesis, Structural & Nanomechanical Properties of Zeolite Membrane, XXVII Panhellenic Conference on Solid State Physics and Materials Science, Synthesis (2011)*

μελετήθηκαν η χρονική εξέλιξη του εφαρμοζόμενου φορτίου, η συμπεριφορά του υλικού στο εφαρμοζόμενο φορτίο (καμπύλες φόρτισης-αποφόρτισης), οι νανομηχανικές ιδιότητες καθώς και το φαινόμενο IndentationSizeEffect (ISE). Επίσης πραγματοποιήθηκε ανάλυση των λόγων H/E_r και H^3/E_r^2 και πλαστικότητας και στην συνέχεια μελετήθηκαν οι μηχανισμοί αποδόμησης (pile-up και sink-in) κατά τη διάρκεια της νανοδιείσδυσης. Οι τιμές που υπολογίστηκαν από τα πειραματικά δεδομένα συμφωνούν με αντίστοιχες από μελέτες της βιβλιογραφίας.

Στη δεύτερη σειρά μετρήσεων, πραγματοποιήθηκε μελέτη ερπυσμού (φόρτιση για 5 s, διατήρηση σταθερού φορτίου για 35 s και αποφόρτιση για 5 s). Από τις πειραματικές μετρήσεις που προέκυψαν μελετήθηκαν η χρονική εξέλιξη του εφαρμοζόμενου φορτίου, η συμπεριφορά του υλικό στο εφαρμοζόμενο φορτίο (καμπύλες φόρτισης- αποφόρτισης), οι νανομηχανικές ιδιότητες καθώς και το φαινόμενο ISE. Επίσης πραγματοποιήθηκε ανάλυση των λόγων H/E_r και H^3/E_r^2 και στην συνέχεια οι μηχανισμοί αποδόμησης (pile-up και sink-in). Σ' αυτή την σειρά μετρήσεων μελετήθηκε και η χρονική εξέλιξη της μετατόπισης της ακίδας και τέλος έγινε μαθηματική προσέγγιση σε κάθε μία από τις καμπύλες αυτές. Οι τιμές που υπολογίστηκαν από τα πειραματικά δεδομένα συμφωνούν με αντίστοιχες από μελέτες της. Η μεμβράνη συντέθηκε σε 85°C με τη χρήση γέλης με σύσταση $4.17Na_2O/1.0Al_2O_3$/ 5TEA (τριαιθανολαμίνη) /$1.87SiO_2/460H_2O$. Η διάρκεια της σύνθεσης ήταν 120 ώρες. Επίσης ευνοείται η παράλληλη ανάπτυξη τόσο κρυστάλλων φωγιασίτη όσο και κρυστάλλων ζεόλιθου Α (LTA).

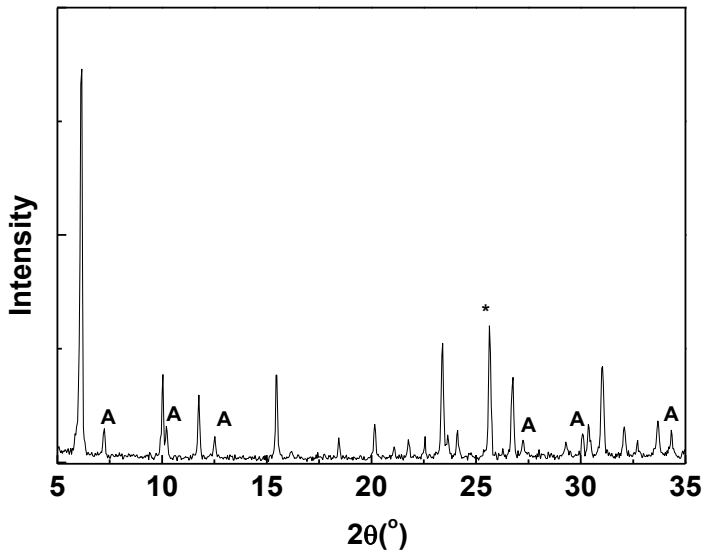

Σχήμα 5.49 Ακτινοδιάγραμμα της μεμβράνης που συντέθηκε στο εργαστήριο

Οι κορυφές που αντιστοιχούν στον LTA είναι σημειωμένες με A ενώ οι υπόλοιπες αντιστοιχούν στον φωγιασίτη. Επίσης η κορυφή στα ~25.66ºπου είναι σημειωμένη με αστερίσκο αντιστοιχεί στην αλούμινα. Ακολουθούν εικόνες SEM με τις οποίες προσδιορίζεται η μορφολογία και το μέγεθος των κρυστάλλων.

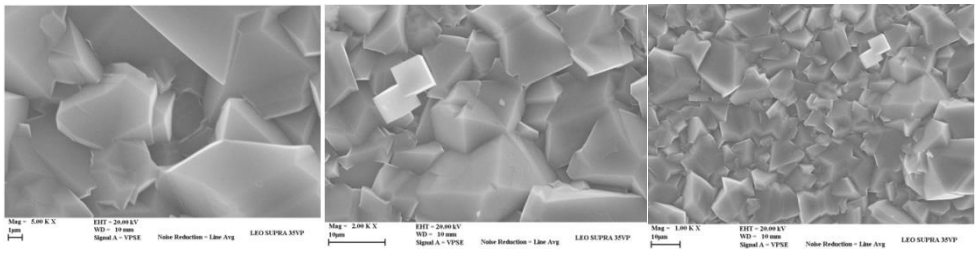

Σχήμα 5.50 Εικόνα SEM της επιφάνειας της μεμβράνης που αναπτύχθηκε πάνω σε υπόστρωμα Al_2O_3

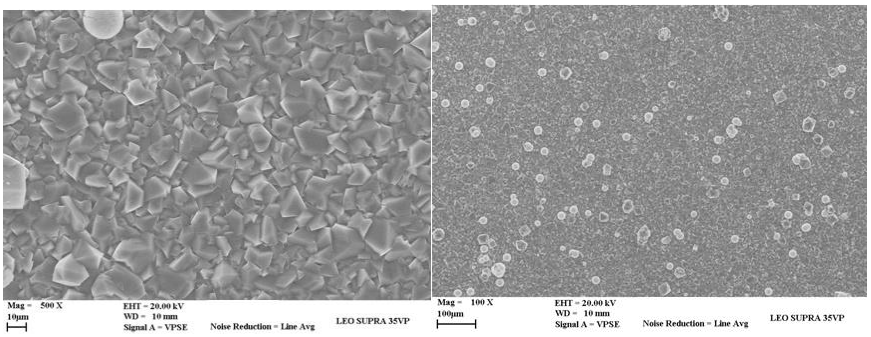

Σχήμα 5.51Εικόνα SEM της επιφάνειας της μεμβράνης που αναπτύχθηκε πάνω σε υπόστρωμα Al_2O_3

Κατά την πρώτη σειρά μετρήσεων γίνεται φόρτιση μέχρι ένα μέγιστο φορτίο και στη συνέχεια αποφόρτιση. Το μέγιστο φορτίο είναι διαφορετικό σε κάθε μέτρηση (10, 30, 50, 80, 100, 130, 150, 250, 270, 300, 350, 400, 500, 1000, 1500 μN). Ακολουθεί διάγραμμα φορτίου σε συνάρτηση με τον χρόνο στο οποίο φαίνεται η χρονική εξέλιξη του εφαρμοζόμενου φορτίου.

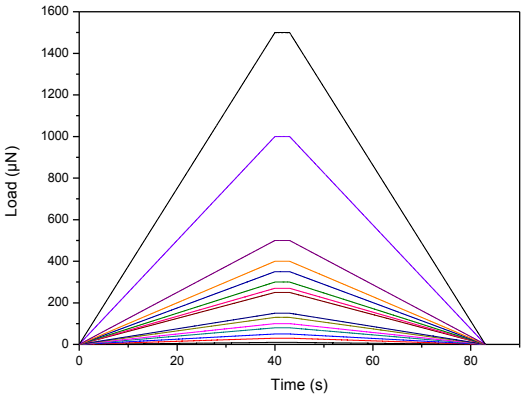

Σχήμα 5.52Χρονική εξέλιξη εφαρμοζόμενου φορτίου

Στα σχήματα 5.53, 5.54 και 5.55 παρουσιάζονται τυπικές καμπύλες φορτίου – βάθους διείσδυσης (καμπύλες φόρτισης - αποφόρτισης) για διαφορετικά μέγιστα φορτία οι οποίες μας δείχνουν πως συμπεριφέρεται το υλικό μας κατά την εφαρμογή φορτίου. Παρατηρούμε ότι οι καμπύλες φόρτισης δεν ταυτίζονται με τις καμπύλες αποφόρτισης επομένως το υλικό δεν συμπεριφέρεται ελαστικά.

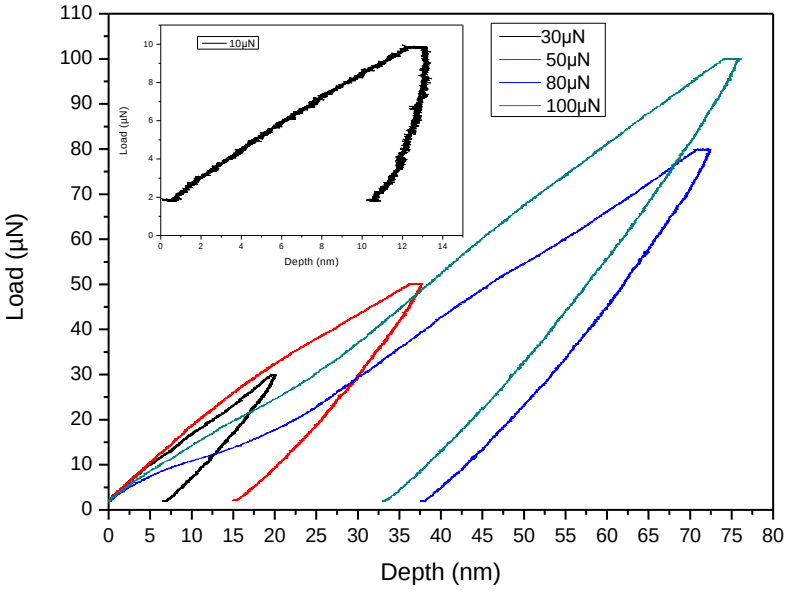

Σχήμα 5.53Καμπύλες φόρτισης - αποφόρτισης για μέγιστα φορτία 10-100 μN

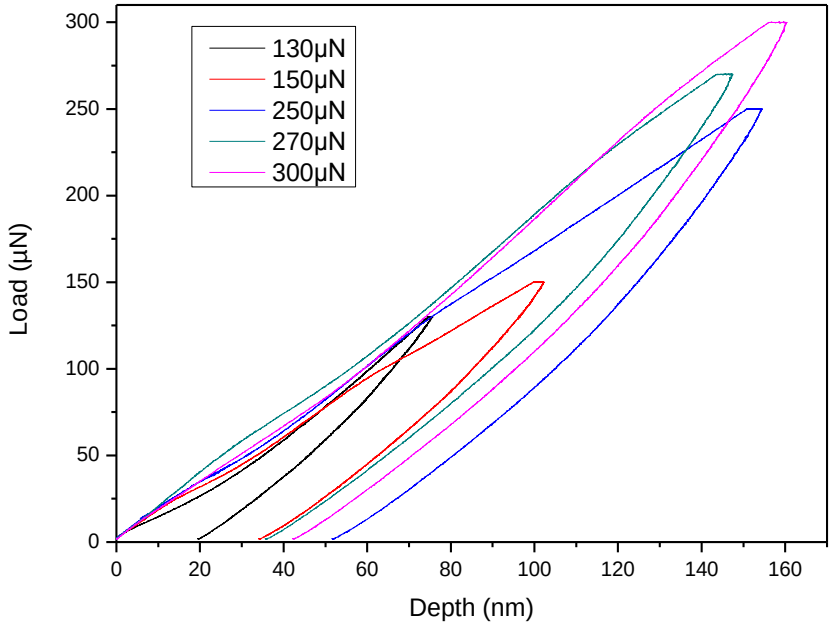

Σχήμα 5.54Καμπύλες φόρτισης - αποφόρτισης για μέγιστα φορτία 130-300 μN

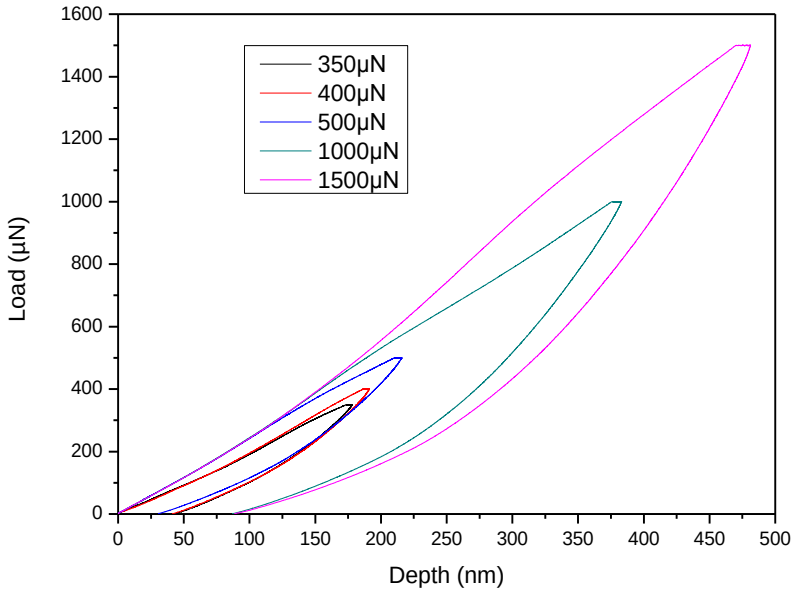

Σχήμα 5.55Καμπύλες φόρτισης - αποφόρτισης για μέγιστα φορτία 350-1500 μN

Στα σχήματα 5.56 και 5.57 παρουσιάζονται η σκληρότητα και το μέτρο ελαστικότητας σε συνάρτηση με το βάθος διείσδυσης. Όσο το βάθος διείσδυσης αυξάνεται παρατηρείται μείωση των τιμών μέτρου ελαστικότητας και σκληρότητας. Επομένως το

υλικό παρουσιάζει διαφορετικές νανομηχανικές ιδιότητες στην επιφάνεια του και σε μεγαλύτερα βάθη. Η μείωση που παρατηρείται σε μικρά βάθη διείσδυσης πιθανόν να οφείλεται στο φαινόμενο ISE καθώς επίσης και στην πιθανή ύπαρξη α-Al_2O_3 (κατά την διάρκεια σύνθεσης της μεμβράνης μέρος του υποστρώματος μπορεί να διαλυθεί και να βρεθεί στην επιφάνεια των μεμβρανών). Παρατηρείται ότι στην επιφάνεια το μέτρο ελαστικότητας και η σκληρότητα έχουν τιμές γύρω στα 12,5GPa και 2,75GPa αντίστοιχα ενώ σε μεγαλύτερα βάθη σταθεροποιούνται περίπου στα 4,5 GPa και στο 1 GPa αντίστοιχα.

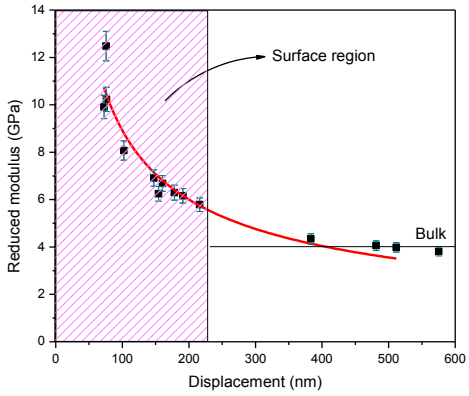

Σχήμα 5.56Καμπύλημέτρου ελαστικότητας συναρτήσει του βάθους διείσδυσης όπου με κόκκινη γραμμή επισημαίνεται η τάση

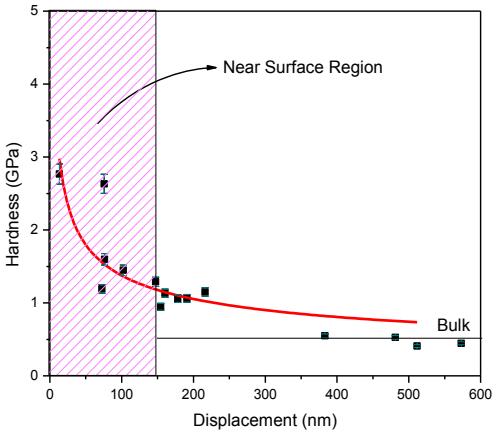

Σχήμα 5.57Καμπύλησκληρότητας συναρτήσει του βάθους διείσδυσης όπου με κόκκινη γραμμή επισημαίνεται η τάση

Από την σκληρότητα και το μέτρο ελαστικότητας υπολογίστηκαν οι λόγοι H/E_r και H^3/E_r^2. Ο λόγος H/E_r είναι δείκτης πλαστικότητας και είναι μία μέτρηση η οποία καθορίζει το όριο της ελαστικής συμπεριφοράς στην επιφάνεια επαφής. Είναι πολύ σημαντικός στην τριβολογία σαν χαρακτηριστικό των υλικών φθοράς. Υψηλός δείκτης πλαστικότητας

δείχνει μεγάλη αντοχή στην φθορά των επιστρώσεων, λεπτών υμενίων κ.λ.π.. Στα σχήματα 5.58 και 5.59 φαίνονται οι καμπύλες H/E_r και H^3/E_r^2σε συνάρτηση με το βάθος διείσδυσης.

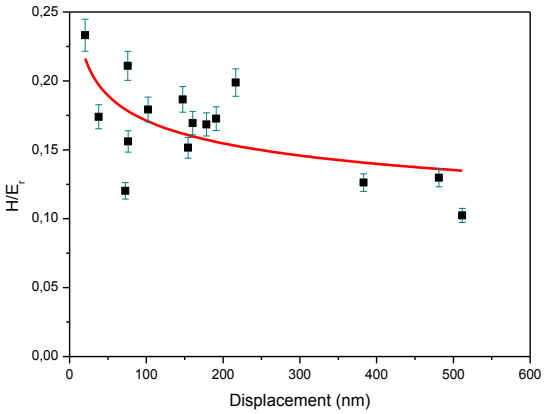

Σχήμα 5.58 Καμπύλη H/E_r σε συνάρτηση με το βάθος διείσδυσης

Παρατηρείται ότι οι λόγοι H/E_r μειώνονται καθώς αυξάνεται το βάθος διείσδυσης και περίπου μετά τα 400nm σταθεροποιούνται περίπου στο 0,13. Επομένως συμπεραίνεται ότι στην επιφάνεια του υμενίου έχουμε μεγαλύτερη αντοχή στην φθορά από ότι σε μεγαλύτερα βάθη.

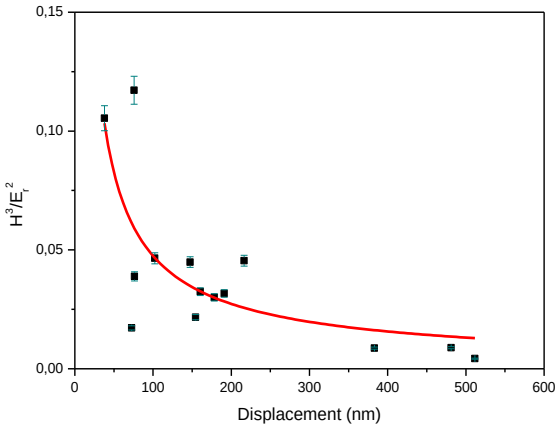

Σχήμα 5.59 Καμπύλη H^3/E_r^2 σε συνάρτηση με το βάθος διείσδυσης

Στο ίδιο συμπέρασμα καταλήγουμε και από το διάγραμμα H^3/E_r^2 σε συνάρτηση με το βάθος διείσδυσης. Και εδώ οι τιμές του λόγου H^3/E_r^2 είναι υψηλές στην περιοχή κοντά στην επιφάνεια του υμενίου, ενώ σταθεροποιούνται μετά τα 380nm γύρω στο 0,01.

Στην συνέχεια υπολογίστηκε η % πλαστικότητα του υλικού ολοκληρώνοντας την περιοχή φόρτισης – αποφόρτισης των καμπυλών φορτίου σε συνάρτηση με το βάθος διείσδυσης. Ο τύπος που χρησιμοποιήθηκε είναι ο εξής:

$$\%Πλαστικότητα = \frac{E_{between}}{E_{tot}} \cdot 100\% \qquad (Εξ. 5.2)$$

όπου:

E_{tot}: το ολοκληρωμένο εμβαδόν για 100% πλαστική συμπεριφορά του υλικού στο επιβαλλόμενο φορτίο και

$E_{between}$: το ολοκληρωμένο εμβαδόν μεταξύ καμπύλης φόρτισης και αποφόρτισης.

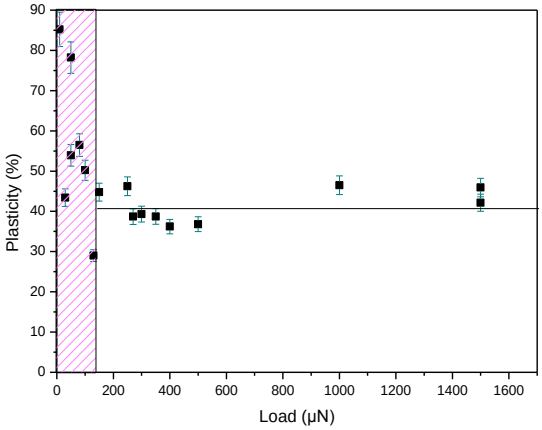

Σχήμα 5.60 Καμπύλη % πλαστικότητας σε συνάρτηση με το επιβαλλόμενο φορτίο

Από την % πλαστικότητα σε συνάρτηση με το επιβαλλόμενο φορτίο προκύπτει ότι για φορτία μικρότερα από περίπου 130μN οι τιμές μειώνονται καθώς αυξάνεται το φορτίο μέχρι να σταθεροποιηθούν γύρω στο 40% για φορτία μεγαλύτερα των 200μN.

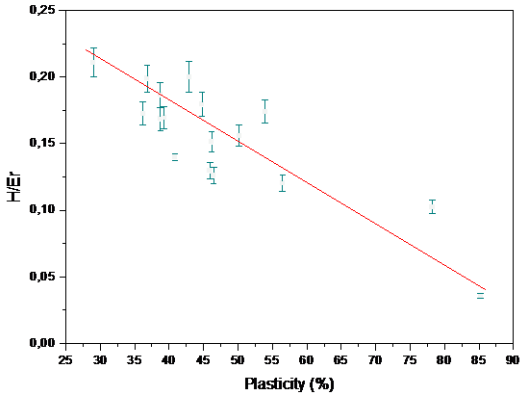

Σχήμα 5.61 Καμπύλη H/E_r σε συνάρτηση με την % πλαστικότητα

Από το παραπάνω σχήμα προκύπτει ότι για μια δεδομένη ακίδα η σχέση μεταξύ του λόγου H/E_r και της % πλαστικότητας είναι κατά προσέγγιση γραμμική, επομένως ο λόγος H/E_r μπορεί να υπολογιστεί από την μέτρηση του $E_{between}$και E_{tot} που μπορούν να

υπολογιστούν από την ολοκλήρωση των καμπυλών φόρτισης – αποφόρτισης. Ακολουθούν τα διαγράμματα h_c/h_{max} σε συνάρτηση με το h_{max} και τον λόγο H/E_r. Από το πρώτο σχήμα προκύπτει ότι για μικρά βάθη διείσδυσης οι τιμές του λόγου h_c/h_{max} απομακρύνονται από την μονάδα επομένως στον μηχανισμός αποδόμησης κυριαρχεί το sink-in ειδικά σε βάθη μικρότερα των 200nm.

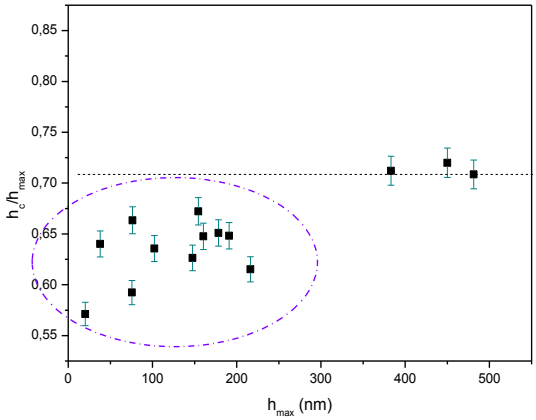

Σχήμα 5.62 Γραφική παράσταση του λόγου h_c/h_{max} σε συνάρτηση με το μέγιστο βάθος διείσδυσης

Στο ίδιο συμπέρασμα καταλήγουμε και από το σχήμα των λόγων h_c/h_{max} και H/E_r αφού οι τιμές του h_c/h_{max} απομακρύνονται από την μονάδα για μικρά βάθη διείσδυσης (ο λόγος h_c/h_{max} μειώνεται καθώς αυξάνεται ο λόγος H/E_r).

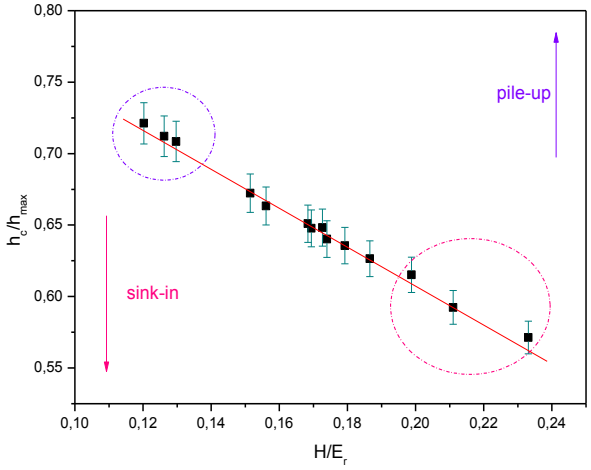

Σχήμα 5.63 Γραφική παράσταση του λόγου h_c/h_{max} σε συνάρτηση με τον λόγο H/E_r

Η σχέση των δύο λόγων h_c/h_{max} και H/E_r όπως φαίνεται από το διάγραμμα είναι γραμμική. Οι τιμές που παίρνει ο λόγος h_c/h_{max} κοντά στην επιφάνεια είναι γύρω στα 0,57

και μπορούμε να πούμε ότι ο μηχανισμός αποδόμησης που κυριαρχεί είναι το sink-in ενώ σε μεγαλύτερα βάθη φτάνει στα 0,73 και κυριαρχεί το pile-up. Κατά την δεύτερη σειρά μετρήσεων πραγματοποιήθηκε φόρτιση για 5 s, διατήρηση σταθερού φορτίου για 35 s και αποφόρτιση για 5 s. Η μέγιστη τιμή του φορτίου ήταν διαφορετική σε κάθε μέτρηση (5, 10, 20, 50, 80, 100, 150, 200, 300, 500, 700, 900, 1100, 1200, 1250, 1500 μN). Παρακάτω παρουσιάζονται οι καμπύλες φορτίου – χρόνου στις οποίες φαίνεται η χρονική εξέλιξη του εφαρμοζόμενου φορτίου.

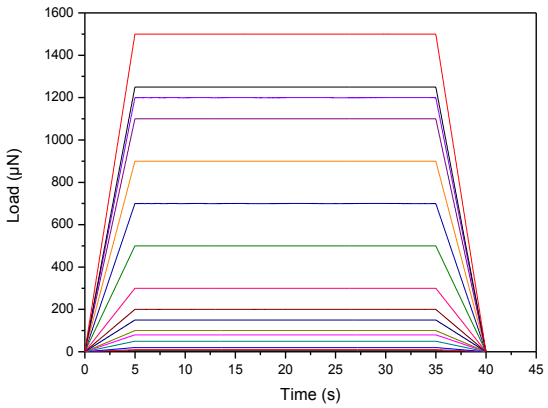

Σχήμα 5.64 Χρονική εξέλιξη εφαρμοζόμενου φορτίου

Στα σχήματα 5.65, 5.66 και 5.67 παρουσιάζονται τυπικές καμπύλες φορτίου – βάθους διείσδυσης (καμπύλες φόρτισης - αποφόρτισης) για διαφορετικά μέγιστα φορτία οι οποίες μας δείχνουν πως συμπεριφέρεται το υλικό μας κατά την εφαρμογή φορτίου. Παρατηρούμε ότι οι καμπύλες φόρτισης δεν ταυτίζονται με τις καμπύλες αποφόρτισης επομένως το υλικό μας δεν συμπεριφέρεται ελαστικά.

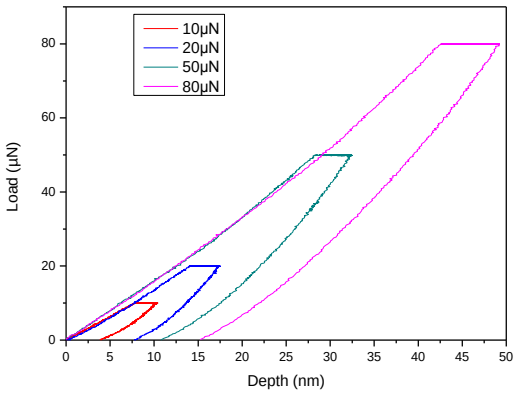

Σχήμα 5.65 Πειραματική καμπύλη φόρτισης - αποφόρτισης για μέγιστα φορτία 10-80μN

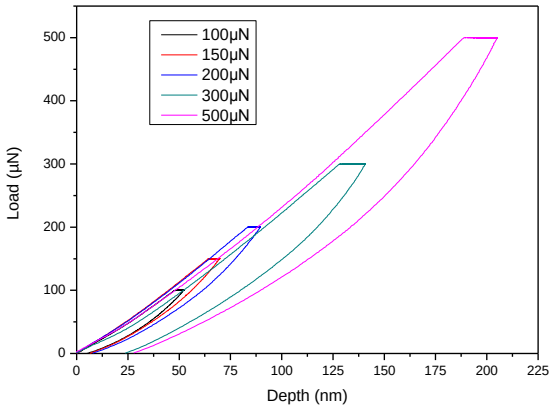

Σχήμα 5.66 Πειραματική καμπύλη φόρτισης - αποφόρτισης για μέγιστα φορτία 100-500μN

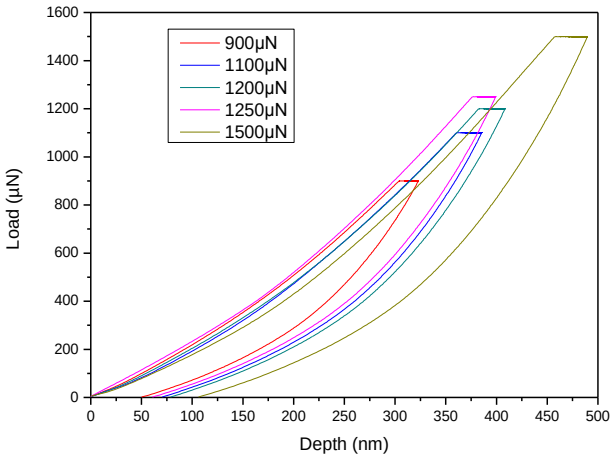

Σχήμα 5.67 Πειραματική καμπύλη φόρτισης - αποφόρτισης για μέγιστα φορτία 700-1500μN

Στα σχήματα 5.68 και 5.69 παρουσιάζονται η σκληρότητα και το μέτρο ελαστικότητας σε συνάρτηση με το βάθος διείσδυσης. Όσο το βάθος διείσδυσης αυξάνεται παρατηρείται μείωση των τιμών μέτρου ελαστικότητας και σκληρότητας. Επομένως το υλικό παρουσιάζει διαφορετικές νανομηχανικές ιδιότητες στην επιφάνεια του και σε μεγαλύτερα βάθη. Η μείωση που παρατηρείται σε μικρά βάθη διείσδυσης πιθανόν να οφείλεται στο φαινόμενο ISE καθώς επίσης και στην πιθανή ύπαρξη α-Al_2O_3 (κατά την διάρκεια σύνθεσης της μεμβράνης μέρος του υποστρώματος μπορεί να διαλυθεί και να βρεθεί στην επιφάνεια των μεμβρανών). Παρατηρείται ότι στην επιφάνεια το μέτρο ελαστικότητας και η σκληρότητα έχουν τιμές γύρω στα 60GPa και 8GPa αντίστοιχα ενώ σε μεγαλύτερα βάθη σταθεροποιούνται περίπου στα 7GPa και στο 0,8GPa αντίστοιχα.

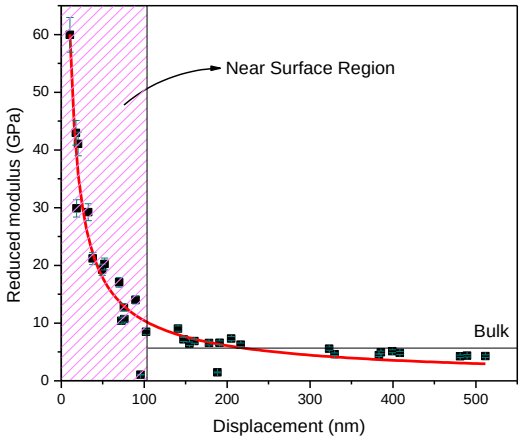

Σχήμα 5.68 Πειραματική καμπύλη μέτρου ελαστικότητας και βάθους διείσδυσης όπου με κόκκινη γραμμή επισημαίνεται η τάση

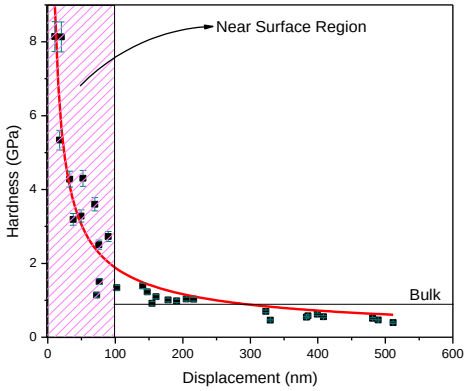

Σχήμα 5.69Πειραματική καμπύλη σκληρότητας και βάθους διείσδυσης όπου με κόκκινη γραμμή επισημαίνεται η τάση

Από την σκληρότητα και το μέτρο ελαστικότητας υπολογίστηκαν οι λόγοι H/E_r και H^3/E_r^2. Στα σχήματα 5.70 και 5.71 φαίνονται οι καμπύλες H/Er και H^3/E_r^2σε συνάρτηση με το βάθος διείσδυσης.

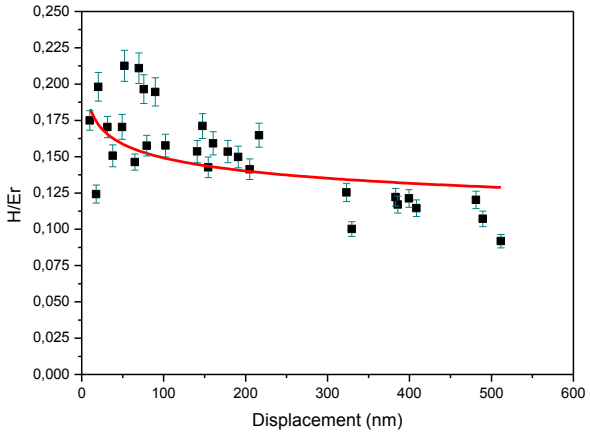

Σχήμα 5.70 Καμπύλη H/E_r σε συνάρτηση με το βάθος διείσδυσης

Παρατηρείται ότι οι λόγοι H/E_r μειώνονται καθώς αυξάνεται το βάθος διείσδυσης και περίπου μετά τα 330nm σταθεροποιούνται περίπου στο 0,12. Επομένως συμπεραίνεται ότι στην επιφάνεια του υμενίου έχουμε μεγαλύτερη αντοχή στην φθορά από ότι σε μεγαλύτερα βάθη.

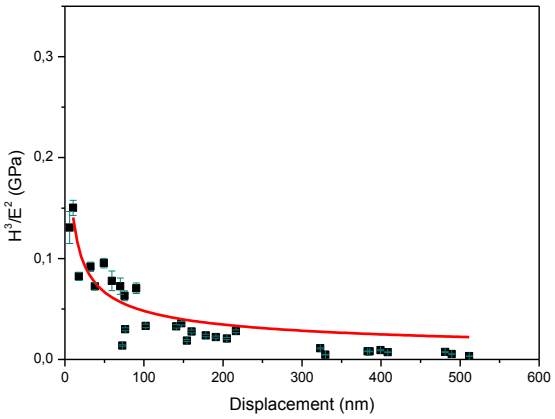

Σχήμα 5.71Καμπύλη H^3/E_r^2 σε συνάρτηση με το βάθος διείσδυσης

Στο ίδιο συμπέρασμα καταλήγουμε και από το διάγραμμα H^3/E_r^2 σε συνάρτηση με το βάθος διείσδυσης. Και εδώ οι τιμές του λόγου H^3/E_r^2 είναι υψηλές πριν τα 100nm, ενώ σταθεροποιούνται μετά τα 320nm γύρω στο 0,01. Ακολουθούν τα διαγράμματα h_c/h_{max} σε συνάρτηση με το h_{max}και τον λόγο H/E_r αντίστοιχα. Από το πρώτο σχήμα προκύπτει ότι για μικρά βάθη διείσδυσης οι τιμές του λόγου h_c/h_{max} απομακρύνονται από την μονάδα επομένως στον μηχανισμό αποδόμησης κυριαρχεί το sink-in.

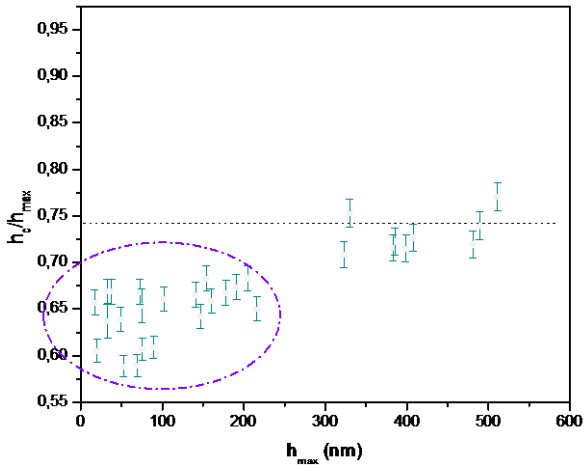

Σχήμα 5.72Καμπύλη h_c/h_{max} σε συνάρτηση με το h_{max}

Στο ίδιο συμπέρασμα καταλήγουμε και από το σχήμα των λόγων h_c/h_{max} και H/E_r αφού οι τιμές του h_c/h_{max} απομακρύνονται από την μονάδα για μικρά βάθη διείσδυσης(ο λόγος h_c/h_{max} μειώνεται καθώς αυξάνεται ο λόγος H/E_r).

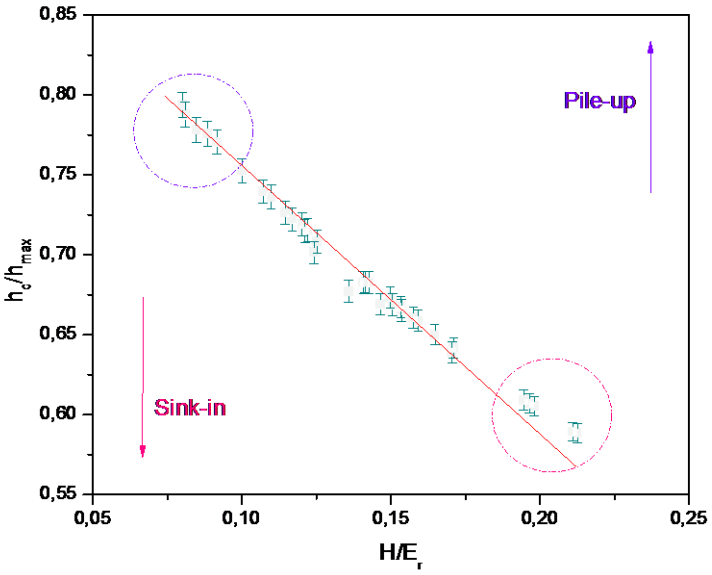

Σχήμα 5.73Καμπύλη h_c/h_{max} σε συνάρτηση με το H/E_r

Η σχέση των δύο λόγων h_c/h_{max} και H/E_r όπως φαίνεται από το διάγραμμα είναι γραμμική. Οι τιμές που παίρνει ο λόγος h_c/h_{max} κοντά στην επιφάνεια είναι γύρω στα 0,59 και μπορούμε να πούμε ότι ο μηχανισμός αποδόμησης που κυριαρχεί είναι το sin-inενώ σε μεγαλύτερα βάθη φτάνει στα 0,78 και κυριαρχεί το pile-up. Παρακάτω παρουσιάζονται τα διαγράμματα βάθους διείσδυσης τον ερπυσμό – χρόνου.

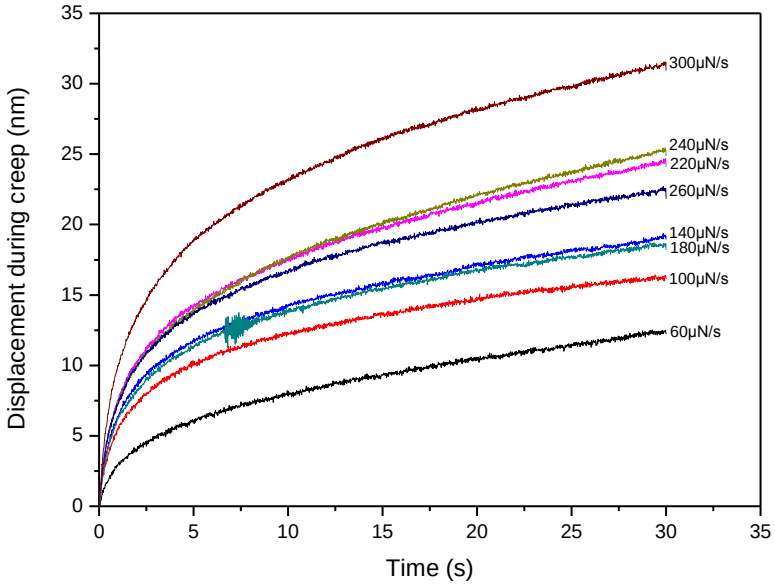

Σχήμα 5.74 Καμπύλες βάθους διείσδυσης στον ερπυσμό – χρόνου.

Από το σχήμα 5.74 παρατηρείται ότι όσο πιο μικρός είναι ο ρυθμός φόρτισης τόσο πιο μικρό είναι το πρώτο στάδιο ερπυσμού και τόσο πιο γρήγορη η γραμμικοποίηση. Αυτό μπορεί να αποδοθεί στο ότι ο ρυθμός παραμόρφωσης, κατά τον χαμηλότερο ρυθμό φόρτισης, είναι ο χαμηλότερος και ο χρόνος που χρειάζεται για να φτάσει στο μέγιστο εφαρμοζόμενο φορτίο στο οποίο θα παραμείνει είναι ο μεγαλύτερος. Επομένως παραμόρφωση ερπυσμού μπορεί να εμφανιστεί και κατά την διάρκεια του χρόνου φόρτισης και στην συνέχεια ο μετέπειτα ερπυσμός, κατά την διάρκεια του χρόνου αναμονής μειώνεται. Επίσης, η υποδομή που δημιουργείται κάτω από την ακίδα λόγω της πίεσης από την διείσδυση μπορεί να είναι διαφορετική σε διαφορετικούς ρυθμούς φόρτισης και αυτή η υποδομή θα επηρεάσει σίγουρα την συμπεριφορά ερπυσμού.Όσο το βάθος διείσδυσης αυξάνεται παρατηρείται μείωση των τιμών μέτρου ελαστικότητας και σκληρότητας. Επομένως το υλικό παρουσιάζει διαφορετικές νανομηχανικές ιδιότητες στην επιφάνεια του και σε μεγαλύτερα βάθη.Η μείωση που παρατηρείται σε μικρά βάθη διείσδυσης πιθανόν να οφείλεται στο φαινόμενο ISE καθώς επίσης και στην πιθανή ύπαρξη α-Al_2O_3 (κατά την διάρκεια σύνθεσης της μεμβράνης μέρος του υποστρώματος μπορεί να διαλυθεί και να βρεθεί στην επιφάνεια των μεμβρανών). Παρατηρείται επίσης ότι στην επιφάνεια το μέτρο ελαστικότητας και η σκληρότητα έχουν τιμές γύρω στα 12,5GPa και 2,75GPa αντίστοιχα ενώ σε μεγαλύτερα βάθη σταθεροποιούνται περίπου στα 4,5GPa και στο 1GPa αντίστοιχα. Από την μελέτη του ερπυσμού προκύπτει ότι στην επιφάνεια το μέτρο ελαστικότητας και η σκληρότητα έχουν τιμές γύρω στα 60GPa και 8GPa αντίστοιχα ενώ σε μεγαλύτερα βάθη

σταθεροποιούνται περίπου στα 7GPa και στο 0,8GPa αντίστοιχα. Ο λόγος H/E_r μειώνεται καθώς αυξάνεται το βάθος διείσδυσης και περίπου μετά τα 400nm σταθεροποιείται ~0,13, ενώ στον ερπυσμό μετά τα 330nm σταθεροποιείται ~0,12. Επομένως συμπεραίνεται ότι στην επιφάνεια του υμενίου έχουμε μεγαλύτερη αντοχή στην φθορά από ότι σε μεγαλύτερα βάθη. Στο ίδιο συμπέρασμα καταλήγουμε και από το διάγραμμα H^3/E_r^2 σε συνάρτηση με το βάθος διείσδυσης. Και εδώ οι τιμές του λόγου H^3/E_r^2 είναι υψηλές στην περιοχή κοντά στην επιφάνεια του υμενίου, ενώ σταθεροποιούνται μετά τα 380nm ~0,01.Από την % πλαστικότητα σε συνάρτηση με το επιβαλλόμενο φορτίο προκύπτει ότι για φορτία μικρότερα από περίπου 130μN οι τιμές μειώνονται καθώς αυξάνεται το φορτίο μέχρι να σταθεροποιηθούν γύρω στο 40% για φορτία μεγαλύτερα των 200μN. Για την δεδομένη ακίδα η σχέση μεταξύ του λόγου H/E_r και της % πλαστικότητας είναι κατά προσέγγιση γραμμική, επομένως ο λόγος H/E_r μπορεί να υπολογιστεί από την μέτρηση του $E_{between}$και E_{tot} που μπορούν να υπολογιστούν από την ολοκλήρωση των καμπυλών φόρτισης – αποφόρτισης. Για μικρά βάθη διείσδυσης οι τιμές του λόγου h_c/h_{max} απομακρύνονται από την μονάδα επομένως στον μηχανισμό αποδόμησης κυριαρχεί το sink-in ειδικά σε βάθη μικρότερα των 200nm. Στο ίδιο συμπέρασμα καταλήγουμε και από το σχήμα των λόγων h_c/h_{max} και H/E_r αφού οι τιμές του h_c/h_{max} απομακρύνονται από την μονάδα για μικρά βάθη διείσδυσης (ο λόγος h_c/h_{max} μειώνεται καθώς αυξάνεται ο λόγος H/E_r). Οι τιμές που παίρνει ο λόγος h_c/h_{max} κοντά στην επιφάνεια είναι γύρω στα 0,57 (0,59 από την μελέτη ερπυσμού) και μπορούμε να πούμε ότι ο μηχανισμός αποδόμησης που κυριαρχεί είναι το sink-in ενώ σε μεγαλύτερα βάθη φτάνει στα 0,73 (0,78 από την μελέτη ερπυσμού)και κυριαρχεί το pile-up. Παρατηρήθηκε επίσης από την μελέτη ερπυσμού ότι όσο πιο μικρός είναι ο ρυθμός φόρτισης τόσο πιο μικρό είναι το πρώτο στάδιο ερπυσμού και τόσο πιο γρήγορη η γραμμικοποίηση. Αυτό μπορεί να αποδοθεί στο ότι ο ρυθμός παραμόρφωσης, κατά τον χαμηλότερο ρυθμό φόρτισης, είναι ο χαμηλότερος και ο χρόνος που χρειάζεται για να φτάσει στο μέγιστο εφαρμοζόμενο φορτίο στο οποίο θα παραμείνει είναι ο μεγαλύτερος. Επομένως παραμόρφωση ερπυσμού μπορεί να εμφανιστεί και κατά την διάρκεια του χρόνου φόρτισης και στην συνέχεια ο μετέπειτα ερπυσμός κατά την διάρκεια του χρόνου αναμονής μειώνεται. Επίσης, η υποδομή που δημιουργείται κάτω από την ακίδα λόγω της πίεσης από την διείσδυση μπορεί να είναι διαφορετική σε διαφορετικούς ρυθμούς φόρτισης και αυτή η υποδομή θα επηρεάσει σίγουρα την συμπεριφορά ερπυσμού.

Κεφάλαιο 6. Συμπεράσματα

Στη παρούσα ΔΔ μελετήθηκε ο τρόπος προσέγγισης του πειράματος νανοσκληρομέτρησης ανάλογα με τη φύση, το είδος και τη γεωμετρία του υλικού, με κατεύθυνση την αξιοπιστία τω υλικών σε συνθήκες λειτουργίας.

Από τα ευρήματα της έρευνας εξήχθησαν τα παρακάτω συμπεράσματα:

-

ΗπροσθήκηCNTsοδήγησεσεβελτίωσητωννανομηχανικώνιδιοτήτωνστηνπερίπτωσητων Henkel 3% MW-2, Epilox 2% MW-1, PVB 1% MW-2 καιPDMS 0.2-0.5% MW-2 (αυξημένοςλόγος (H/E) αντοχήςσεφθοράστηνπερίπτωσητωνHenkel 7% MW-2, Epilox 7% MW-1, PDMS 0.4% MW-2 καιPDMS 0.1% SW-1. Τα νανοσύνθετα ενώ εμφάνισαν βελτιωμένες νανομηχανικές ιδιότητες σε σχέση με την πολυμερική μήτρα, σε όλες τις περιπτώσεις καθορίστηκε η συγκέντρωση πέρα από την οποία η επιπλέον προσθήκη νανοσωλήνων προκαλούσε μείωση των νανομηχανικών ιδιοτήτων, η μείωση του συντελεστή τριβής και η μείωση της ενέργειας πρόσφυσης, για διαφορετικό τύπο νανοσωλήνων. Οι μηχανικές ιδιότητες επιδεινώνονται με την αύξηση της περιεκτικότητας των CNTs, μετά από ένα βέλτιστο όριο συγκέντρωσης, λόγω της έντονης παρουσίας του μηχανισμού "tube – tube slip". Η ύπαρξη των CNTs, τόσο ομοιογενώς διασπαρμένων αλλά και σε μεγάλο ποσοστό εμποδίζουν την εγχάραξη της επιφάνειας.

- Οι νανομηχανικές ιδιότητες βρέθηκαν αυξημένες στην επιφανειακή περιοχή του PDMS, λόγω πιθανού σχηματισμού ζώνης silica-like (το πάχος της οποίας προσδιορίστηκε), η οποία δημιουργήθηκε κατά την επεξεργασία. Η συμπεριφορά αυτή οφείλεται στην έκθεση του δείγματος στον ατμοσφαιρικό αέρα με αποτέλεσμα να δημιουργείται επιφανειακή ζώνη λόγω της περιεκτικότητας του αέρα σε οξυγόνο με υψηλότερο ποσοστό διασταυρώσεων-σταυροδεσμών. Σε αυτή την εργασία προσδιορίσθηκε με ακρίβεια το πάχος της επιφανειακής ζώνης που παρουσιάζει αυξημένες τιμές σκληρότητας και μέτρου ελαστικότητας.

- Η προσθήκη νανοδοχείων βελτιώνει τις μηχανικές και τριβολογικές ιδιότητες των συγκεκριμένων επιστρώσεων. Μάλιστα, οι επιστρώσεις με τα πληρωμένα νανοδοχεία παρουσιάζουν καλύτερες τριβολογικές ιδιότητες. Η τελευταία παρατήρηση θα μπορούσε να αποδοθεί στην παρουσία του αναστολέα διάβρωσης. Μέρος του αναστολέα που βρίσκεται εντός των νανανοδοχείων απελευθερώνεται στο διάλυμα κατά το χρονικό διάστημα που μεσολαβεί από την σύνθεση του διαλύματος μέχρι την εναπόθεσή του στην μεταλλική επιφάνεια. Η παρουσία του ελεύθερου αναστολέα επιδρά στις ιδιότητες της επίστρωσης. Στην συγκεκριμένη περίπτωση, όπως προκύπτει από τα πειραμάτα νανοεγχάραξης/

νανοσκληρομέτρησης η παρουσία του αναστολέα έχει ως αποτέλεσμα την βελτίωση των νανοτριβολογικών ιδιοτήτων στο εξωτερικό στρώμα της επίστρωσης.

- Το λεπτό υμένιο Co_3O_4 παρουσιάζει αυξημένη αντίσταση στο εφαρμοζόμενο φορτίο (υψηλότερες τιμές σκληρότητας), δηλαδή απαιτούνται υψηλότερες τιμές εφαρμοζόμενου φορτίου, ώστε η ακίδα να φτάσει την ίδια τιμή βάθους διείσδυσης σε σχέση με το υμένιο Co. Το λεπτό υμένιο Co είναι πιο πλαστικό αποθηκεύει μεγαλύτερη ενέργεια μετά το τέλος της νανοδιείσδυσης. Οι καμπύλες φόρτισης-αποφόρτισης των λεπτών υμενίων Co και Co_3O_4 παρουσιάζουν τοπικές αλλαγές (ασυνέχειες) στην κλίση (pop-ins και elbows στην καμπύλη φόρτισης και αποφόρτισης, αντίστοιχα), που συνδέονται με μετασχηματισμούς φάσης. Η έναρξη της πλαστικότητας σε κάθε λεπτό υμένιο παρατηρείται στα ~10 nm. Όσο το βάθος διείσδυσης της ακίδας του εντυπωτή αυξάνεται κάτω από τα 100 nm, παρατηρείται μια μικρή αύξηση των τιμών Η λόγω της επίδρασης της παρουσίας οξειδίου στην επιφάνεια του λεπτού υμενίου και της επίδρασης της αιχμηρής ακίδας του εντυπωτή για χαμηλές τιμές βάθους διείσδυσης. Οι τιμές Ε είναι παρόμοιες για τα δυο λεπτά υμένια. Μέσω του νόμου του Meyer επιβεβαιώθηκε η εμφάνιση του φαινομένου indentationsizeeffect. Η ανάλυση φθοράς με βάση το λόγο σκληρότητας προς μέτρο ελαστικότητας (H/E) έδειξε ότι το λεπτό υμένιο Co_3O_4 παρουσιάζει υψηλότερη αντίσταση στη φθορά σε σύγκριση με το λεπτό υμένιο Co, γεγονός που επιβεβαιώθηκε και από μετρήσεις νανοεγχάραξης.

- Το σύνθετο υμένιο που κατασκευάστηκε πληρεί τις προϋποθέσεις για να ανταπεξέλθει σε εφαρμογές ηλεκτροδιαβροχής. Είναι θερμοδυναμικά ευσταθής και χημικά σταθερή δομή, μηχανικά ακέραιο και ανθεκτικό. Υπερτερεί του απλού υμενίου όσον αφορά τις μηχανικές και τριβολογικές του ιδιότητες. Από τη σύγκριση των δύο δειγμάτων προκύπτει πως για την ίδια μετατόπιση - βάθος διείσδυσης της ακίδας – το σύνθετο υμένιο επιδεικνύει μεγαλύτερη αντίσταση στο εφαρμοζόμενο φορτίο καθώς χρειάζεται αρκετά μεγαλύτερη φόρτιση προκειμένου να έχει την ίδια μετατόπιση σε σχέση με το απλό υμένιο του Teflon στο TEOS. Η διεπιφανειακή πρόσφυση στο σύνθετο υμένιο είναι πολύ καλή αφού παρά τις αρκούντως ισχυρές διατμητικές τάσεις δεν παρατηρήθηκε καμία αλλαγή στη μορφολογία της επιφάνειας στην περιοχή της νανοδιείσδυσης. Παρατηρώντας τα προφίλ της νανοεγχάραξης είναι φανερό πως η ελαστική περιοχή του σύνθετου υμενίου είναι μεγαλύτερη και μάλιστα η χαραγή του σύνθετου υμενίου είχε διπλάσια ελαστική επαναφορά (~15nm) έναντι του απλού υμενίου (~30nm). Σχετικά με την πλαστική παραμόρφωση με εφαρμοζόμενη δύναμη 300μN στο σύνθετο υμένιο το βάθος της εγχάραξης είναι πολύ μικρότερο. Για εφαρμογή ίδιας δύναμης το απλό υμένιο υπόκειται σε εγχάραξη μεγάλου βάθους και παρουσιάζει πλαστική παραμόρφωση (accumulation) ενώ το σύνθετο υμένιο επιδεικνύει καλύτερη αντίσταση στη φθορά. Η αλλαγή της κλίσης στο διάγραμμα H/E αποκαλύπτει την «ενδυνάμωση» του σύνθετου υμενίου σε συνάρτηση με

την αύξηση του βάθους διείσδυσης. Μεταξύ των δύο δειγμάτων η σύνθετη δομή παρουσιάζει βελτιωμένη δύναμη πρόσφυσης.

- Από την νανοδιείσδυση με και χωρίς ερπυσμό του φωγιασίτη, βρέθηκε πως, όσο το βάθος διείσδυσης αυξάνεται παρατηρείται μείωση των τιμών μέτρου ελαστικότητας και σκληρότητας. Επομένως το υλικό παρουσιάζει διαφορετικές νανομηχανικές ιδιότητες στην επιφάνεια του και σε μεγαλύτερα βάθη. Η μείωση που παρατηρείται σε μικρά βάθη διείσδυσης πιθανόν να οφείλεται στο φαινόμενο ISE καθώς επίσης και στην πιθανή ύπαρξη α-Al2O3 (κατά την διάρκεια σύνθεσης της μεμβράνης μέρος του υποστρώματος μπορεί να διαλυθεί και να βρεθεί στην επιφάνεια των μεμβρανών). Παρατηρείται επίσης ότι στην επιφάνεια το μέτρο ελαστικότητας και η σκληρότητα έχουν τιμές γύρω στα 12,5GPa και 2,75GPa αντίστοιχα ενώ σε μεγαλύτερα βάθη σταθεροποιούνται περίπου στα 4,5GPa και στο 1GPa αντίστοιχα. Από την μελέτη του ερπυσμού προκύπτει ότι στην επιφάνεια το μέτρο ελαστικότητας και η σκληρότητα έχουν τιμές γύρω στα 60GPa και 8GPa αντίστοιχα ενώ σε μεγαλύτερα βάθη σταθεροποιούνται περίπου στα 7GPa και στο 0,8GPa αντίστοιχα. Ο λόγος H/Er μειώνεται καθώς αυξάνεται το βάθος διείσδυσης και περίπου μετά τα 400nm σταθεροποιείται ~0,13, ενώ στον ερπυσμό μετά τα 330nm σταθεροποιείται ~0,12. Επομένως συμπεραίνεται ότι στην επιφάνεια του υμενίου έχουμε μεγαλύτερη αντοχή στην φθορά από ότι σε μεγαλύτερα βάθη. Για την δεδομένη ακίδα η σχέση μεταξύ του λόγου H/Er και της % πλαστικότητας είναι κατά προσέγγιση γραμμική, επομένως ο λόγος H/Er μπορεί να υπολογιστεί από την μέτρηση του Ebetween και Etot που μπορούν να υπολογιστούν από την ολοκλήρωση των καμπυλών φόρτισης – αποφόρτισης. Για μικρά βάθη διείσδυσης οι τιμές του λόγου hc/hmax απομακρύνονται από την μονάδα επομένως στον μηχανισμό αποδόμησης κυριαρχεί το sink-in ειδικά σε βάθη μικρότερα των 200nm. Στο ίδιο συμπέρασμα καταλήγουμε και από το σχήμα των λόγων hc/hmax και H/Er αφού οι τιμές του hc/hmax απομακρύνονται από την μονάδα για μικρά βάθη διείσδυσης (ο λόγος hc/hmax μειώνεται καθώς αυξάνεται ο λόγος H/Er). Οι τιμές που παίρνει ο λόγος hc/hmax κοντά στην επιφάνεια είναι γύρω στα 0,57 (0,59 από την μελέτη ερπυσμού) και μπορούμε να πούμε ότι ο μηχανισμός αποδόμησης που κυριαρχεί είναι το sink-in ενώ σε μεγαλύτερα βάθη φτάνει στα 0,73 (0,78 από την μελέτη ερπυσμού)και κυριαρχεί το pile-up. Παρατηρήθηκε επίσης από την μελέτη ερπυσμού ότι όσο πιο μικρός είναι ο ρυθμός φόρτισης τόσο πιο μικρό είναι το πρώτο στάδιο ερπυσμού και τόσο πιο γρήγορη η γραμμικοποίηση. Αυτό μπορεί να αποδοθεί στο ότι ο ρυθμός παραμόρφωσης, κατά τον χαμηλότερο ρυθμό φόρτισης, είναι ο χαμηλότερος και ο χρόνος που χρειάζεται για να φτάσει στο μέγιστο εφαρμοζόμενο φορτίο στο οποίο θα παραμείνει είναι ο μεγαλύτερος. Επομένως παραμόρφωση ερπυσμού μπορεί να εμφανιστεί και κατά την διάρκεια του χρόνου φόρτισης και στην συνέχεια ο μετέπειτα ερπυσμός κατά την διάρκεια του χρόνου

αναμονής μειώνεται. Επίσης, η υποδομή που δημιουργείται κάτω από την ακίδα λόγω της πίεσης από την διείσδυση μπορεί να είναι διαφορετική σε διαφορετικούς ρυθμούς φόρτισης και αυτή η υποδομή θα επηρεάσει σίγουρα την συμπεριφορά ερπυσμού.

Η παρούσα ΔΔ αποτελεί έναυσμα για μελλοντική μελέτη καθώς δημιουργήθηκαν πολλά ζητήματα τα οποία δεν ήταν δυνατό να απαντηθούν στα πλαίσια μίας ΔΔ. Συγκεκριμένα, όπως έχει ήδη αναφερθεί το ζήτημα της θερμοκρασίας λειτουργίας και θερμοκρασίας μελέτης είναι ύψιστης σημασίας για τις ιδιότητες τεχνικά προηγμένων υλικών, επομένως είναι αναγκαία η έρευνα μέσω της νανοσκληρομέτρησης με θερμοκρασιακό εύρος απο -20 έως 700 βαθμούς Κελσίου. Επίσης για την αξιοπιστία των αποτελεσμάτων υδροφιλικότητας/υδροφοβικότητας είναι σημαντικό να δοκιμαστεί η επικάλυψη τις ακίδας μ εσυγκεκριμένο υολικο (εναλλακτικά χρήση της ακίδας Si_3N_4). Θα πρέπει να μελετηθεί η επίδραση της γεωμετρίας της ακίδας, η επίδραση παραμενουσών τάσεων και η σύνδεση των αποτελεσμάτων με θεωρητικά μοντέλα.

ΒΙΟΓΡΑΦΙΚΟ ΣΗΜΕΙΩΜΑ

CurriculumVitae

EliasP. Koumoulos

Chemical Engineer

PERSONAL INFO

Surname: Koumoulos

Name: Elias

Middle Name: P.

Date of Birth: 22 July 1983

Place of Birth: Athens

Status: Married

Home Address: Perikleous Ave.,10, Holargos, Athens 15562, GR

Phone: +302106513517 (home), +302107723323 (work), +306973726846 (mobile)

E-mail:elikoum@chemeng.ntua.gr, elikoum@gmail.com

STUDIES

2009- 2013 National Technical University of Athens - School of Chemical Engineering

Doctoral Research thesis entitled «Synthesis and Study of advanced nanostructures and coatings, focusing on nanomechanical properties», Supervisor: C. A. Charitidis

2007– 2008 National Technical University of Athens - School of Chemical Engineering

Interdisciplinary MSc in Materials Science & Technology
Master Thesis topic: “Nanomechanical Properties of thin films, Study cases i) SiO_x on PET and ii) PDMS nanocomposites”, Supervisor: C. A. Charitidis

2001 – 2007 National Technical University of Athens - School of Chemical Engineering

BSc and MSc in Department of Synthesis and Development of Industrial Processes, Direction "Organic Industries"

Diploma Thesis: “Study of drug release from a D,L-polylactic acid matrix”, Supervisor: P. A. Tarantili

LANGUAGES

Mother tongue: **Greek**

Fluent: **English** (First Certificate in English (Cambridge), Palso Higher Certificate in English)

Advanced: **French** (DELF1 (Unités A1, A2, A3, A4) et Unité A5)

IT/ OPERATIVE SKILLS -

- MS-DOS, Windows 95/98/2000/NT, Windows XP, Vista,7,8
- Linux
- MS Office (Word, Excel, Powerpoint, Access), Open Office
- Sigmaplot, Origin, Mathcad
- Fortran 95/98
- Extensive experience in web development, hardware, PC support and network.

Operation of

- *Nanoindenter - Nanoscratch*
- *Scanning Probe Microscopy (SPM)*
- *Thermal Chemical Vapor Deposition (T-CVD)*
- *X-Ray Diffractometer (XRD)*
- *High Pressure Liquid Chromatography (HPLC)*
- *Differential Scanning Calorimetry (DSC)*
- *Thermogravimetric analyzer (TGA)*
- *UltraViolet-Visible Spectroscopy (UV-VIS)*
- *Metallographic analysis – optical microscope*
- *Conductivity measurements*

WORKING-ACADEMIC EXPERIENCE

February 2009 – February 2012: Academic assistant, trainee in BSc and MSc lessons in School of Chemical Engineering, Department of Materials Science and Technology:

-Metallic materials: micro/nanomechanical properties, phase identification, microstructure, SPM imaging

-Physicochemistry: Structural analysis through X-Ray technique, Conductivity measurements (electrochemistry)

-Nanostructures and Nanomaterials: Nanomechanical properties, SPM imaging

-Materials' Structure and Properties: Nanomechanical properties, SPM imaging

-Fabrication and Characterization of Nanostructures(MSc Microsystems and nanostructures)

-Structure and mechanical properties of materials (MSc Materials Science and Technology)

Supervisor assistant in 4 BSc and 4 MSc theses.

September 2007 – February 2010: Teaching at Institute of Vocational Training, Athens
Sessions: *Materials Science, Design, Machine Design, Testing Research and Standards for Gas Fuel, CAD*

July – August 2006: P.P.C. S.A. Testing Research and Standards Center (Greek Public Power Corporation), Athens, Internship - Laboratory Characterization and Analysis on Fuel-Lubricants, Environment Chemistry and Special Material, Analytical Chemistry

RESEARCH - PAPERS IN ISI JOURNALS [34]

1. **Nanoscale Mechanical and Tribological Properties of Plasma Nanotextured COP Surfaces with Hydrophobic Coatings**

   D.A. Dragatogiannis, ***E. Koumoulos***, K. Ellinas, A. Tserepi, E. Gogolides, C.A. Charitidis

   Plasma Processes and Polymers, (2015), in press

2. **Synthesis, structural and nanomechanical properties of cobalt based thin films**

   E.P. Koumoulos, V.P. Tsikourkitoudi, I.A. Kartsonakis, V. Markakis, N. Papadopoulos, E. Hristoforou, C.A. Charitidis

   International Journal of Structural Integrity (2015), 6 (2)

3. **Study of corrosion of copper in industrial cooling systems**

   I.A. Kartsonakis, ***E.P. Koumoulos***, A. Karantonis, G.Kordas, C.A. Charitidis, S. Dessypris, A. Monos

   International Journal of Structural Integrity (2015), in press

4. **Deformation mechanism during nanoindentation creep and corrosion resistance of Zn**

   D.A. Dragatogiannis, ***E.P. Koumoulos***, I.A. Kartsonakis, C.A. Charitidis

   International Journal of Structural Integrity (2015), in press

5. **Corrosion investigation and evaluation of mechanical and structural properties of powder coatings for industrial-domestic applications**

   E.P. Koumoulos, I.A. Kartsonakis, G. Kordas, G. Vlachakis, M. Vlachakis, C.A. Charitidis

   International Journal of Structural Integrity (2015), in press

6. **Mechanical properties of dissimilar friction stir welded AA5083-H111 and AA6082-T6 reinforced with SiC nanoparticles**

   D.I. Pantelis, P. N. Karakizis, N.M. Daniolos C.A. Charitidis, ***E.P. Koumoulos***, D.A. Dragatogiannis

   Materials and Manufacturing Processes (2015), in press

7. **Evaluation of mechanical integrity of epoxy-nanodiamonds composites via nanoindentation**

   E.P. Koumoulos, M. Giorcelli, P. Jagadale, A. Tagliaferro, C.A. Charitidis

   Composites Part B (2015), in press

8. **Nanomechanical Properties of Plasma-Treated Polylactic Acid for Packaging Applications,**

   E.P. Koumoulos, M. Valentin, D.A. Dragatogiannis, C.A. Charitidis, I. Krupa, I. Novak

   Plastics, Rubber and Composites (2015), in press

9. **Carbon nanotube/ polymer nanocomposites: a study on mechanical integrity through nanoindentation,**

E.P. Koumoulos, M. Giorcelli, P. Jagadale, A. Tagliaferro C.A. Charitidis

Polymer Composites (2015), in press, DOI: 10.1002/pc.23049

10. **Tribological characterization of chemical vapor deposited Co and Co_3O_4 thin films for sensing reliability in engineering applications,**

    Elias P. Koumoulos, Vassileios Markakis, Vasiliki P. Tsikourkitoudi, Costas A. Charitidis, Nikolaos Papadopoulos, Evangelos Hristoforou,

    Tribology International, 82, Part A, 2015, 89–94 (2014)

11. **Nanomechanical Properties of Amorphous FeCuNbSiB Thin Films Deposited by HiPIMS**

    Velicu, Ioana-Laura; Neagu, Maria; Costinescu, Lucian; Munteanu, Daniel; ***Koumoulos, Elias P.;*** Charitidis, Costas A.

    Sensor Letters, Volume 11, Number 10, October 2013 , pp. 1925-1930(6)

12. **Hybrid organic-inorganic coatings including nanocontainers for corrosion protection of magnesium alloy ZK30,**

    I.A. Kartsonakis, ***E.P. Koumoulos***, C.A.Charitidis, G. Kordas

    Journal of Nanoparticle Research, Volume 15, Issue 8, 1871 (2013).

13. **Nanocomposite NiO:Au hydrogen sensors with high sensitivity and low operating temperature,**

    M. Kandyla, C. Chatzimanolis-Moustakas, ***E.P. Koumoulos***, C. Charitidis, M. Kompitsas

    Materials Research Bulletin Volume 49, January 2014, Pages 552–559

14. **Nanotribological behavior of carbon based thin films: friction and lubricity mechanisms at the atomic level,**

    C.A. Charitidis, ***E.P. Koumoulos***, D.A. Dragatogiannis

    Special Issue "Nanotribology and Atomic Mechanisms of Friction", Lubricants (2013) 1(2), 22-47

15. **Nanomechanical and tribological properties of carbon nanotube/polyvinyl butyral composites,**

    C.A.Charitidis, ***E.P. Koumoulos***, M. Giorcelli, S. Musso, P. Jagadale, A. Tagliaferro, Journal of Polymer Composites, 2013, 34(11), 1950–1960

16. **Residual stress and deformation mechanism of friction stir welded aluminum alloys by nanoindentation,**

    C.A.Charitidis, D.A. Dragatogiannis, ***E.P. Koumoulos***, I. A. Kartsonakis,

    Journal of Materials and Science Engineering A, 540, 2012, 226–234

17. **Hybrid organic-inorganic multilayer coatings including nanocontainers for corrosion protection of metal alloys,**

    I.A. Kartsonakis, ***E.P. Koumoulos***, G.S. Pappas, A.C. Balaskas, C.A.Charitidis, G.C. Kordas,

    Journal of Corrosion Science, 57 (2012) 56–66

18. **Growth, Structural and Mechanical Characterization and Reliability of Chemical Vapor Deposited Co and Co_3O_4 Thin Films as Candidate Materials for Sensing Applications**,

    V.P. Tsikourkitoudi, ***E.P. Koumoulos***, N. Papadopoulos, C.A. Charitidis,

    Key Engineering Materials 495, pp. 108-111 (2012).

19. **Growth, Structural and Mechanical Characterization and Reliability of Chemical Vapor**

Deposited Co and Co_3O_4 Thin Films as Candidate Materials for Sensing Applications,

V.P. Tsikourkitoudi, ***E.P. Koumoulos***, N. Papadopoulos, E. Hristoforou, C.A. Charitidis,

Journal Of Optoelectronics and Advanced Materials, 14(1), pp. 169-175 (2012).

20. **ORMOSIL-Epoxy Coatings with Ceramic Nanocontainers for Corrosion Protection of Magnesium Alloys ZK10,**

    I.A. Kartsonakis, A.C. Balaskas, ***E.P. Koumoulos***, C.A.Charitidis, G.C. Kordas,

    Progress in Organic Coatings, 76 (2–3) 2013.

21. **Structural & Nanomechanical Properties of a Zeolite Membrane measured using Nanoindentation,**

    C.A.Charitidis, ***E.P. Koumoulos***, V. Nikolakis, D.A.Dragatogiannis,

    Journal of Thin Solid Films, 526, 2012, 168–175

22. **Studying the corrosion resistance performance of hybrid organic-inorganic coatings including containers to magnesium alloy ZK 30,**

    I.A. Kartsonakis, A.C. Balaskas, ***E.P. Koumoulos***, C.A.Charitidis, G.C. Kordas,

    submitted to Langmuir (2012).

23. **Evaluation of corrosion resistance of magnesium alloy ZK10 coated with hybrid organic–inorganic film including containers,**

    I.A. Kartsonakis, A.C. Balaskas, ***E.P. Koumoulos***, C.A.Charitidis, G.C. Kordas,

    Corrosion Science, 65, (2012), 481-493.

24. **Nanomechanical and Nanotribological Properties of Hydrophobic Fluorocarbon Dielectric Coating on Tetraethoxysilane for Electrowetting Applications,**

    Elias P. Koumoulos, Costas A. Charitidis, Dimitrios P Papageorgiou, Athanasios G Papathanasiou, Andreas G Boudouvis,

    Journal of Surface and Coatings Technology, 206, pp. 3823–3831 (2012).

25. **Determination of onset of plasticity (yielding) and comparison of local mechanical properties of friction stir welded aluminum alloys using the micro- and nano- indentation techniques,**

    Elias P. Koumoulos, Costas A. Charitidis, Nikolaos M. Daniolos, Dimitrios I. Pantelis,

    International Journal of Structural Integrity, Vol. 4 No. 1, 2013, pp. 143-158

26. **A study on time dependent properties of aluminum alloy by nanoindentation technique: variation of loading rate, maximum applied load and loading time,**

    C.A.Charitidis, D.A. Dragatogiannis, ***E.P. Koumoulos***,

    International Journal of Structural Integrity, Vol. 4 No. 1, 2013, pp. 33-54

27. **Incorporation of ceramic nanocontainers into epoxy coatings for the corrosion protection of hot dip galvanized steel**,

    I.A. Kartsonakis, A.C. Balaskas, ***E.P. Koumoulos***, C.A.Charitidis, G.C. Kordas,

    Journal of Corrosion Science, 57 (2012) 30–41

28. **Influence of accelerated ageing on nanomechanical properties, creep behavior and adhesive forces of PDMS**,

C. A. Charitidis, ***E. P. Koumoulos***, V. P. Tsikourkitoudi, D. A. Dragatogiannis, G. Lolas,

Plastics, Rubber and Composites (2012) 41(2) pp. 94-99

29. **Evaluating the robustness of top coatings comprising plasma-deposited fluorocarbons in electrowetting systems**,

    Dimitrios P. Papageorgiou, ***Elias P. Koumoulos,*** Costas A. Charitidis, Andreas G. Boudouvis, Athanasios G. Papathanasiou,

    Journal of Adhesion Science and Technology (2012), 26 (12-17), pp. 2001-2015

30. **Nanomechanical Properties of Friction Stir Welded AA6082-T6 Aluminum Alloy**,

    E. P. Koumoulos, N. Daniolos, D. Pantelis, C. A. Charitidis, Journal of Materials and Science Engineering B, 176 (2011) 1585–1589.

31. **Nanomechanical Properties and Nanoscale Deformation of PDMS nanocomposites**,

    C.A.Charitidis, ***E.P.Koumoulos***,

    Plastics, Rubber and Composites (2012) 41(2) pp. 88-93

32. **Mechanical behaviour of PDMS silicone elastomer after outdoor weathering in two different weathering locations,**

    P. N. Eleni, M. K. Krokida, G. L. Polyzois, C. A. Charitidis, ***E. P. Koumoulos***, V. P. Tsikourkitoudi, I. Ziomas,

    Journal of Polymer Degradation and Stability 96 470-476 (2011).

33. **Adhesive forces and time dependent behaviour (creep and loading rate effects) on nanomechanical properties of polydimethylsiloxane (PDMS)**,

    C.A. Charitidis, ***E. P. Koumoulos***, V.P. Tsikourkitoudi, S.P. Vasilakos, P.A. Tarantili,

    Journal of Nanostructured Polymers and Nanocomposites, 7:1 32-42 (2011).

34. **Sustained release of guaifenesin and ipriflavone from biodegradable coatings,**

    P.A. Tarantili, ***H. Koumoulos***,

    European Polymer Journal Volume 44, Issue 2, February 2008, Pages 444-452.

BOOK CHAPTERS [4]

1. **Nanomechanical properties and deformation mechanism in metals, oxides and alloys**

   E.P. Koumoulos, D.A. Dragatogiannis, C.A. Charitidis

   Title: "Nanomechanical Analysis of High Performance Materials"

   Series: Solid Mechanics and Its Applications, Vol. 203

   2014, X, 290 p. 80 illus., 40 illus. in color.

   Editor: Dr. Atul Tiwari

   Publisher: Springer

   ISBN 978-94-007-6918-2

2. **Nanomechanical properties of plasma-treated polylactic acid for packaging applications**

Proceedings of the 7th International Conference on Modification Degradation and Stabilization of

Polymers 2-6 September 2012, Prague, Czech Republic

E.P. Koumoulos, M. Valentin, D.A. Dragatogiannis, C.A. Charitidis, I. Krupa, I. Novak

Publisher: Institute of Macromolecular Chemistry Academy of Sciences of the Czech Republic

Heyrovského nám. 2 162 06 Prague 6 - Břevnov Czech Republic

ISBN 978-80-85009-75-0 this digital version

(ISBN 978-80-85009-74-3 printed version)

3. Nanomechanical properties of physically-aged Polydimethylsiloxane

Proceedings of the 6th International Conference on Modification Degradation and Stabilization of Polymers 5-9 September 2010, Athens, Greece

E.P. Koumoulos, V.P. Tsikourkitoudi, C.A. Charitidis, P.N. Eleni, M.K. Krokida, I.C. Ziomas

Publisher: MoDeSt Hellenic Organizing Committee

Editors: Constantine D. Papaspyrides, Stamatina N. Vouyiouka

ISBN: 978-960-99362-0-0

4. Drug release from biodegradable polymers

E.P.Koumoulos, P.A.Tarantili

Proceedings of the 170 Years NTUA Symposium "NTUA in Innovation of Research and Technology" 3-4 December 2007, Athens, Greece

Publisher: NTUA

Editors: Antonia Moropoulou

RESEARCH - CONFERENCES/SYMPOSIA PRESENTATIONS [54]

1. SUN-SNO-GUIDENANO Sustainable Nanotechnology Conference 2015 9-11 March 2015 in Venice, Italy

Lignin as a new sustainable precursor for carbon fiber

Stavros Anagnou, Eleni Milioni, Costas Mpalias, Ioannis Kartsonakis, ***Elias Koumoulos***, Vasilis Markakis, Costas Charitidis

2. Annual World Conference on Carbon - CARBON 2015 Dresden, July 12-17, 2015

Towards mass production of high quality multi-walled carbon nanotubes: An industrial safe-by-design and sustainable approach

Malamatenia Koklioti, Dimitrios Perivoliotis, Pravin Jagadale, Irene Cannavaro, Miroslav Slouf, Maria Omastová, Alberto Tagliaferro, ***Elias Koumoulos***, Constantinos Charitidis

3. Annual World Conference on Carbon - CARBON 2015 Dresden, July 12-17, 2015

New precursors for the development of carbon fibers: the case of lignin

S. Anagnou, E. Milioni, C. Mpalias, I.A. Kartsonakis, ***E.P. Koumoulos***, C.A. Charitidis

4. International Conference Energy and Environment in Ships, May 22 – 24, 2015, Athens

Self-Healing Nanomaterials for Protection of Metal Alloys for Marine Applications

E.K. Karaxi, I.A. Kartsonakis, A. Gondikas, ***E.P. Koumoulos***, C.A.Charitidis

5. 10th Panhellenic Conference on Chemical Engineering (2015),

CNTs/polymer nanocomposites for antifouling activity: surface properties and perspectives,

E.P. Koumoulos, A. Darivaki, C.A. Charitidis

6. 10th Panhellenic Conference on Chemical Engineering (2015),

Carbon fiber production: a step-by-step design and market analysis,

C. Balias, V. Markakis, S. Anagnou, ***E.P. Koumoulos,*** C.A. Charitidis

7. ICEAF IV. 4th International Conference of Engineering Against Failure. 24-26 June, 2015 - Skiathos island.

Evaluation of corrosion properties of dissimilar friction stir welded AA5083-H111 and AA6082-T6 reinforced with nanoadditives

I.A Kartsonakis, D. Dragatogiannis, ***E. P. Koumoulos***, A. Karantonis, C.A Charitidis

8. ICEAF IV. 4th International Conference of Engineering Against Failure. 24-26 June, 2015 - Skiathos island.

Mechanical behaviour of carbon based structures synthesized by CVD

D.K. Perivoliotis, M.A. Koklioti, ***E.P. Koumoulos***, C.A. Charitidis

9. ICEAF IV. 4th International Conference of Engineering Against Failure. 24-26 June, 2015 - Skiathos island.

Lignin as new precursors for the development of carbon fibers: co-blends and extrusion

S. Anagnou, E. Milioni, I.A. Kartsonakis, ***E.P. Koumoulos***, C.A. Charitidis

10. European Coatings CONGRESS 2015, 20-21 April 2015 Nuremberg/Germany

Evaluation of MWCNTs/PDMS composite coating for antifouling applications

T. Parousis, D. Perivoliotis, ***E. P. Koumoulos***, C.A. Charitidis

11. SAFEJOINT Industry Workshop, Greece 03-04 July 2014

Micro structural and mechanical study of AA 5083 and AA 6082 friction stir welds reinforced with SiC, TiC and CNTs

C. Charitidis, D.A. Dragatogiannis, ***E. P. Koumoulos***, D. Pantelis, P. Karakizis, N.Daniolos

12. International Middle East Plasma Science (IMEPS), Antalya, Turkey April 23 – 25, 2014

Nanomechanical and tribological properties of plasma nanotextured surfaces for "smart" microfluidic devices

Elias P. Koumoulos, D.A. Dragatogiannis, K. Ellinas, A. Tserepi, E. Gogolides, C.A. Charitidis

13. International Middle East Plasma Science (IMEPS), Antalya, Turkey April 23 – 25, 2014

Plasma treatment effect on surface properties of polylactic acid

Elias P. Koumoulos, Marian Valentin, Costas A. Charitidis, Igor Krupa

14. 5th Pan Hellenic Conference on Metallic Materials (2013)

Synthesis and characterization of surface treated aluminum alloy composites through Friction Stir Processing, with addition of micro and nano alumina

D.I. Pantelis, V. Antonakaki,P.K. Diamantopoulos, C.A.Charitidis, ***E.P. Koumoulos***

15. Eurofillers 2013, Slovakia (2013)

Nanoindentation analysis of composite engineering materials

E.P. Koumoulos, C.A. Charitidis

16. XXIX Panhellenic Conference on Solid State Physics and Materials Science (2013),

Nanomechanical properties of engineering nanostructures

E.P. Koumoulos, C.A. Charitidis

17. ICSAAM 2013, The 5th International Conference on Structural Analysis of Advanced Materials, 23 - 26 September 2013, Island of Kos, Greece

Evaluation of dissimilar aluminum alloys friction stir welding through nanoindentation

C.A Charitidis, D.K. Perivoliotis, ***E.P. Koumoulos***, I.A. Kartsonakis, D. Pantelis, N.M Daniolos, P. N. Karakizis

18. ICEAF III. 3rd International Conference of Engineering Against Failure. 26-28 June, 2013 - Kos island.

Orientation effects in nanomechanical properties of Ni: an experimental study

D.A. Dragatogiannis, ***E.P. Koumoulos***, M. Robinson, C.A. Charitidis

19. ICEAF III. 3rd International Conference of Engineering Against Failure. 26-28 June, 2013 - Kos island.

Synthesis, structural and nanomechanical properties of cobalt based thin films C.A. Charitidis, V.P. Tsikourkitoudi, ***E.P. Koumoulos***, I.A. Kartsonakis, N. Papadopoulos, E. Hristoforou

20. ICEAF III. 3rd International Conference of Engineering Against Failure. 26-28 June, 2013 - Kos island.

Nanoindentation analysis of light-weighted magnesium and aluminum alloys

C.A. Charitidis, A. Skarmoutsou, ***E.P. Koumoulos***, G. Kotsikos, D.I. Pantelis, M. Robinson, Sp. G. Pantelakis

21. ICEAF III. 3rd International Conference of Engineering Against Failure. 26-28 June, 2013 - Kos island.

Study of corrosion of copper in industrial cooling systems

I.A. Kartsonakis, ***E.P. Koumoulos***, A. Karantonis, G.Kordas, C.A. Charitidis, S. Dessypris, A. Monos

22. ICEAF III. 3rd International Conference of Engineering Against Failure. 26-28 June, 2013 - Kos island.

Corrosion investigation and evaluation of mechanical and structural properties of powder coatings for industrial-domestic applications

C.A. Charitidis, ***E.P. Koumoulos***, I.A. Kartsonakis, G. Kordas, G. Vlachakis, M. Vlachakis

23. 7th Conference on Modification, Degradation and Stabilization of Polymers (MoDeSt) (2012),

Nanomechanical properties of plasma-treated polylactic acid for packaging applications

E.P. Koumoulos, M. Valentin, D.A. Dragatogiannis, C.A. Charitidis, I. Krupa, I. Novak

24. XXVIII Panhellenic Conference on Solid State Physics and Materials Science (2012),

Human Health Risk Management in Engineered Nanomaterials,

E. Margaritis, D.A. Dragatogiannis, ***E.P. Koumoulos***, D. Diakoulaki, C.A. Charitidis

25. 9th InternationalConferenceonNanosciences&Nanotechnologies(2012),

Structural investigation and mechanical integrity of metal and metal oxide thin films for sensing applications: A comparative study through nanoindentation

V. P. Tsikourkitoudi, ***E.P. Koumoulos***, I.A. Kartsonakis, C.A. Charitidis

26. 9th InternationalConferenceonNanosciences&Nanotechnologies(2012),

Nanomechanical characterization of electrodeposited nickel containing silicon carbide nanodispersions

A. Sohrabi, A. Dolati, M. Ghorbani, V.P. Tsikourkitoudi, ***E.P. Koumoulos***, I.A. Kartsonakis, P. Stroeve, C.A. Charitidis

27. 9th InternationalConferenceonNanosciences&Nanotechnologies(2012),

Nanomechanical properties of FINEMET-type thin films deposited by HiPIMS for sensing applications

E.P. Koumoulos, I.L. Velicu, V.P. Tsikourkitoudi, C.A. Charitidis, M. Neagu, V. Tiron

28. 9th InternationalConferenceonNanosciences&Nanotechnologies(2012),

Structural and mechanical properties of 7075-T651 aluminum alloy with incorporation of Al_2O_3 nanoparticles through Friction Stir Processing

V. Antonakaki, ***E.P. Koumoulos,*** P.K. Diamantopoulos, D.I. Pantelis, C.A.Charitidis

29. Eurocorr 2012, The European Corrosion Congress 2012, 9-13 September, Istanbul – Turkey

Corrosion resistance of magnesium alloy ZK10 coated with hybrid organic-inorganic film including containers

I.A.Kartsonakis, A.C.Balaskas, ***E.P.Koumoulos***, C.A.Charitidis, G.Kordas

30. 9th InternationalConferenceonNanosciences&Nanotechnologies(2012),

Nanomechanical integrity, structural analysis and thermal stability of Cu-Al_2O_3 nanocomposites for FGM application

E. P. Koumoulos, A. Tsetsekou, C. A. Charitidis, I.A.Kartsonakis, A. Bakolas, N.M. Daniolos, K. Pietrzak

31. 4th International Symposium on Nanotechnology in Construction (NICOM 4), Agios Nikolaos, Crete, 20-22 May 2012, Special session on "Nanomaterials in Cultural Heritage,

Encapsulation of $CaCO_3$-producing bacterial strains into nanocontainers for marble self-restoration,

I.A. Kartsonakis, E.K. Efthimiadou, ***E.P. Koumoulos***, C.A.Charitidis, G.C. Kordas

32. 20th International Conference on Soft Magnetic Materials (SMM-20) (2011),

Tribological characterization of chemical vapor deposited Co and Co_3O_4 thin films for sensing reliability in engineering applications,

V.P. Tsikourkitoudi, ***E.P. Koumoulos***, N. Papadopoulos, E. Hristoforou, C.A. Charitidis

33. International Conference on Materials and Applications for Sensors and Transducers (IC-MAST) (2011),

Growth, Structural and Mechanical Characterization and Reliability of Chemical Vapor Deposited Co and Co_3O_4 Thin Films as Candidate Materials for Sensing Applications,

V.P. Tsikourkitoudi, ***E.P. Koumoulos***, N. Papadopoulos, C.A. Charitidis

34. XXVII Panhellenic Conference on Solid State Physics and Materials Science, Synthesis(2011),

Synthesis, Structural & Nanomechanical Properties of Zeolite Membrane,

C.A.Charitidis, M. Kyritsi, ***E.P. Koumoulos***, V. Nikolakis.

35. 8th Panhellenic Conference on Chemical Engineering (2011),

Nanoindentation study in metals and alloys: determination of yielding, onset of plasticity and energy absorbing/releasing events,

Costas A. Charitidis, ***Elias P. Koumoulos***

36. 8th Panhellenic Conference on Chemical Engineering (2011),

Nanoindentation Stress-Strain Curves, Finite Element Modeling and Time Dependent Properties of Aluminum Alloys,

Dimitrios A. Dragatogiannis, Costas A. Charitidis, ***Elias P. Koumoulos***

37. 8th Panhellenic Conference on Chemical Engineering(2011),

Adhesion strength of hydrophobic dielectric coatings for electrowetting applications,

Aspasia Iliopoulou, ***Elias P. Koumoulos***, Dimitrios P. Papageorgiou, Athanasios G. Papathanasiou, Costas A. Charitidis

38. ICEAF II, 2nd International Conference of "Engineering Against Fracture" (2011),

Time dependent properties of aluminum alloys by nanoindentation technique,

C.A. Charitidis, D.A. Dragatogiannis,***E.P. Koumoulos***

39. ICEAF II, 2nd International Conference of "Engineering Against Fracture" (2011),

Evaluation of mechanical properties of friction stir welded 6082 aluminum alloy using the micro- and nano- indentation techniques,

Nikolaos M. Daniolos, ***Elias P. Koumoulos***, Costas A. Charitidis, Dimitrios I. Pantelis

40. ICEAF II, 2nd International Conference of "Engineering Against Fracture" (2011),

Determination of onset on plasticity (yielding) and comparison of local mechanical properties of friction stir welded aluminum alloys AA5083 and AA6082,

Elias P. Koumoulos, Costas A. Charitidis, Nikolaos M. Daniolos, Dimitrios I. Pantelis

41. Duracosys 2010, 9th International Conference on Durability of Composite Systems (2010),

Nanomechanical Properties and Nanoscale Deformation of PDMS nanocomposites,

C.A. Charitidis,***E. P. Koumoulos***

42. XXVI Panhellenic Conference on Solid State Physics and Materials Science (2010),

Investigation of the Nanomechanical Properties of Physically-aged Polydimethylsiloxane (PDMS),

E. P. Koumoulos**,** V. P. Tsikourkitoudi, C. A. Charitidis, P. N. Eleni, M. K. Krokida, I. Ziomas

43. XXVI Panhellenic Conference on Solid State Physics and Materials Science (2010),

Nanoindentation stress–strain curves of aluminium (AA6082-T6) and magnesium (AZ31) alloys,

C. A. Charitidis, D. Dragatogiannis, ***E.P.Koumoulos***

44. XXVI Panhellenic Conference on Solid State Physics and Materials Science(2010),

Finite Element Modeling and Nanoindentation Stress - Strain curves of Monocrystalline Silicon,

D. Dragatogiannis, ***E.P. Koumoulos***, C. A. Charitidis

45. XXVI Panhellenic Conference on Solid State Physics and Materials Science(2010),

Local Nanomechanical Properties at Cross-Section of Friction Stir Welded AA6082-T6 Aluminum Alloy,

E. P. Koumoulos, C. A. Charitidis, S. Karali, P. C. Diamantopoulos, N. M. Daniolos, D. I. Pantelis

46. 7thInternationalConferenceonNanosciences&Nanotechnologies(2010),

Impact of Crystal Phase Content on the Mechanical Properties of Glass-Ceramic Materials,

P. Kavouras, C.A. Charitidis, ***E.P. Koumoulos***, Th. Kehagias

47. 7thInternationalConferenceonNanosciences&Nanotechnologies(2010),

Nanomechanical Properties of Friction Stir Welded AA6082-T6 Aluminum Alloy,

E. P. Koumoulos, N. Daniolos, D. Pantelis, C. A. Charitidis

48. 6th Conference on Modification, Degradation and Stabilization of Polymers (MoDeSt) (2010),

Nanomechanical properties of Physically-aged Polydimethylsiloxane,

E.P. Koumoulos, V.P. Tsikourkitoudi, C.A. Charitidis, P.N. Eleni, M.K. Krokida, I.C. Ziomas

49. XXV Panhellenic Conference on Solid State Physics and Materials Science (2009),

Effect of the Adhesive Forces and Time-Dependent Response of Polydimethylsiloxane Elastomer on the Nanomechanical Properties Determination by Nanoindentation,

C.A. Charitidis, ***E.P. Koumoulos***

50. 6thInternationalConferenceonNanosciences&Nanotechnologies(2009),

NanoindentationofNanocompositesPolydimethylsiloxaneElastomers,

C.A. Charitidis, ***E.P. Koumoulos***

51. 7thPanhellenic Conference on Chemical Engineering (2009),

Nanomechanical Properies of PDMS nanocomposites,

***E.P.Koumoulos*,** C.A.Charitidis, S.P.Vasilakos, P.A.Tarantili

52. 22nd European Conference on Biomaterials, Lausanne, 7-11/9/2009,

Drug release from thin, biodegradable PLA coatings,

Tarantili P.,***Koumoulos, H***.

53. 6thPanhellenic Conference on Chemical Engineering (2007),

Study of drug release from PLA coatings,

***E.P.Koumoulos*,** P.A.Tarantili, A. Andreopoulos

54. 1st Panhellenic Biomaterials Conference, 2006, Athens,

Study of prolonged drug release from polymer coatings,

***E.P.Koumoulos*,** P.A.Tarantili, A. Andreopoulos

FUNDED PROJECTS [9]

1. 1/2014-12/2017 "Fuctionalised Innovative Carbon Fibres Developed from Novel Precursors With Cost Efficiency and Tailored Properties ", Proposal acronym: FIBRALSPEC, Collaborative project (Large focused research project), THEME [FP7- NMP.2013.2.1-1 Developing new precursors, functionalisations and processing routes for carbon fibres], Budget: 6.083.991,00 (EC funded), Coordinator: C. Charitidis (NTUA)
2. 12/2013-11/2017 "Low-toxic cost-efficient environment-friendly antifouling materials", Proposal acronym: BYEFOULING, Collaborative project (Large), THEME [FP7- OCEAN 2013.3 Innovative antifouling materials for maritime applications], Budget: 7.447.584,00 (EC funded), Coordinator: C. Simon (SINTEF)
3. 1/2013-12/2015 'Enhancing structural efficiency through novel dissimilar material joining techniques', Proposal acronym: SAFEJOINT, Collaborative project (Small or medium-scale focused research project), THEME [NMP.2012.2.1-1] [Joining dissimilar materials (excluding applications specific only to healthcare)], Budget: 3.500.000,00 € (EC funded), Coordinator: G. Kotsikos (UNEW)
4. 10/2012-1/2013 Examination, diagnosis and treatment of water cooling circuit corrosion, Funded by Hellenic Telecommunications Organization (OTE S.A.), Budget: 11.500,00 € Coordinator: C. Charitidis (NTUA)
5. 2012-2015 Design and fabrication of robust super hydrophobic/hydrophilic surfaces and their application in the realization of smart microfluidic valves, Call Thales, (Code: 173), Budget: 599.424,00 € (funded by Hellenic Ministry of Education), Coordinator: A. Tserepi (NCSR D)
6. 2011-2015 'Virtual Lab Services in NTUA', Sustainable Development and Improvement of Quality of Life (ESPA 2011), Budget: 700.000,00 €, Coordinator: NTUA
7. 2010-2013 'Micro and Nanocrystalline Functionally Graded Materials for Transport Applications', Proposal acronym: MATRANS, Collaborative project (Small or medium-scale focused research project), Call identifier FP7-NMP-2008-SMALL-2, THEME 4. NMP-2008-2.5-1 Functionally graded materials for improved mechanical performance, Budget: 4.700.000,00 €, Coordinator: M. Basista (KMM-VIN)
8. 2010-2012 'Synthesis of metal and ceramic thin films (10-500nm) in 3-D substrate via Chemical Vapor Deposition techniques, Basic Research Funded Project (PEVE), NTUA, Budget: 15.000,00 €, Coordinator: C. Charitidis (NTUA)

COLLABORATIONS – INVITATIONS - PARTICIPATIONS

1. Invited by A. Allison (TWI) to present SAFEJOINT (Enhancing structural efficiency through novel dissimilar material joining techniques) project at Joining Sub-Platform General Assembly - 28 November 2013, Brussels
2. Invited by Prof. Maria Omastova in Eurofillers 2013, Bratislava, Slovakia for lecture entitled "Nanoindentation analysis of composite engineering materials" (August, 2013).
3. Invited by Prof. Igor Krupa in Polymer Institute of the Slovak Academy of Sciences, Slovakia for lecture entitled "Nanoindentation perspectives for nanostructures and polymer characterizations" (March, 2012).
4. Attending technical meetings with University of Newcastle upon Tyne (UNEW) (coordinator), Anthony, Patrick & Murta-Exportacao LDA (AP&M), Swerea Sicomp AB (SICOMP), Instituto

Tecnologico de Aragon (ITA), Construcciones y Auxiliar de Ferrocarriles, S.A. (CAF), Fraunhofer-Institut für Fertigungstechnik und angewandte Materialforschung (IFAM), Kauno Technologijos Universitetas (KTU)and partners within SAFEJOINT FP7 project consortium (Newcastle -Feb. 2013, Lagos –Jun. 2013, Zaragoza – Jan. 2014, Bremen Jan 2015)

5. Attending technical meetings with KMM-VIN, EADS, CRF, IMIM, IMSAS, TUD, UNIVPL and partners within MATRANS FP7 project consortium (Torino -Jan. 2011, Warsaw –Jul. 2011, Brussels –Feb.2012, Warsaw –Jul. 2012, Brussels Jan. 2013)
6. Politecnico di Torino, Department of Materials Science and Chemical Engineering, Italy, Prof. Alberto Tagliaferro (CNT technology)
7. National Institute of Research and Development for Technical Physics, Iasi, Romania, Prof. Maria Neagu, Dr. Ioana-Laura Velicu (Thin films technology)

AWARDS

1. Award/prize of MoDeSt Society for the work “Nanomechanical properties of plasma-treated polylactic acid for packaging applications” presented at the MoDeSt Conference held in Prague (2-6 September 2012) - Treasurer of the MoDeSt, Prof. Jean-Luc Gardette, President of the MoDeSt Society 2008-2012
2. Award/prize of Thomaidio (NTUA) for the work C.A. Charitidis, D.A. Dragatogiannis, E.P. Koumoulos, Nanoindentation stress–strain curves of aluminum (AA6082-T6) and magnesium (AZ31) alloys, XXVI Panhellenic Conference of Physics Solid State and Materials Sciences, 26-29 September 2010, (oral presentation).
3. Award/prize of Thomaidio (NTUA) for the work Investigation of the Nanomechanical Properties of Physically-aged Polydimethylsiloxane (PDMS) Proceedings of the 26th PanHellenic Conference on Solid State Physics & Materials Science, 26-29 September 2010, Ioannina, Greece, E. P. Koumoulos, V. P. Tsikourkitoudi, C. A. Charitidis, P. N. Eleni, M. K. Krokida, I. Ziomas

ΠΑΡΑΡΤΗΜΑ ΔΗΜΟΣΙΕΥΣΕΩΝ ΔΙΔΑΚΤΟΡΙΚΗΣ ΔΙΑΤΡΙΒΗΣ

Elsevier Editorial System(tm) for Composites Part B
Manuscript Draft

Manuscript Number: JCOMB-D-15-00185

Title: Evaluation of surface properties of epoxy-nanodiamonds composites

Article Type: Full Length Article

Keywords: A. Nano-structures; A. Particle-reinforcement; B. Mechanical properties; B. Surface properties; Nanoindentation

Corresponding Author: Prof. Costantinos Charitidis,

Corresponding Author's Institution: National Technical University of Athens

First Author: Elias P Koumoulos, PhD

Order of Authors: Elias P Koumoulos, PhD; Pravin Jagadale, PhD; Alberto Tagliaferro, Prof; Costantinos Charitidis

Abstract: Epoxy-matrix reinforced with nanodiamond (ND) particles, with ND content up to 5 wt%, were synthesized. Characterization of NDs by field emission scanning electron microscopy (FE- SEM) and Raman spectroscopy was conducted, while composites were characterized through contact angle, nanoindentation, nanoscratch and scanning probe microscopy.The assessed properties evaluated were hardness, elastic modulus, contact angle, deformation mechanisms, creep deformation, coefficient of friction and adhesion, namely. Results showed that even small additions of ND lead to significant enhancement in the hardness and elastic modulus of epoxy matrix, while properties of composites present a switch in behaviour after passing a concentration threshold; this threshold was identified and discussed.

Suggested Reviewers: Gerard Fernando Dr.
Professor, Sensors and Composites Group, Polymer Engineering, University of Birmingham
g.fernando@bham.ac.uk

George Kotsikos Dr.
Professor, Composite Materials Engineering, Newcastle University
george.kotsikos@newcastle.ac.uk

Geoff Gibson Dr.
Professor, Composite Materials Engineering, Newcastle University
geoff.gibson@ncl.ac.uk

Paulo Davim Dr.
Professor, Department Mechanical Engineering, University of Aveiro
pdavim@mec.ua.pt

Manish Roy Dr.
Professor, Defence Metallurgical Research Laboratory, Defence Metallurgical Research Laboratory
rmanish64@rediffmail.com

Opposed Reviewers:

Dear Editor,

Please accept my manuscript entitled "Evaluation of surface properties of epoxy-nanodiamonds composites" for publication in your Journal. This paper presents a thorough research concerning hardness, elastic modulus, contact angle, deformation mechanisms, creep deformation, coefficient of friction and adhesion, namely. Results showed that even small additions of ND lead to significant enhancement in the hardness and elastic modulus of epoxy matrix, while properties of composites present a switch in behaviour after passing a concentration threshold; this threshold was identified and discussed. These interesting results are of high impact, being worth reading in the Journal of Composites Part B: Engineering; they will most likely meet strong citation upon publication.

Thank you very much for your consideration.

Yours sincerely,

Constantinos A. Charitidis

Evaluation of surface properties of epoxy-nanodiamonds composites

Elias. P. Koumoulos[a], Pravin Jagdale[b], Alberto Tagliaferro[b], Constantinos A. Charitidis[a,*1]

[a]National Technical University of Athens, School of Chemical Engineering, 9 Heroon, Polytechnioust., Zografos, Athens, GR-157 73, Greece

[b]Politecnico di Torino, Applied Sciences and Technology Department, CorsoDucadegli Abruzzi 24, Torino, IT-10129, Italy

Abstract

Epoxy-matrix reinforced with nanodiamond (ND) particles, with ND content up to 5 wt%, were synthesized. Characterization of NDs by field emission scanning electron microscopy (FE- SEM) and Raman spectroscopy was conducted, while composites were characterized through contact angle, nanoindentation, nanoscratch and scanning probe microscopy.The assessed properties evaluated were hardness, elastic modulus, contact angle, deformation mechanisms, creep deformation, coefficient of friction and adhesion, namely. Results showed that even small additions of ND lead to significant enhancement in the hardness and elastic modulus of epoxy matrix, while properties of composites present a switch in behaviour after passing a concentration threshold; this threshold was identified and discussed.

A. Nano-structures; A. Particle-reinforcement; B. Mechanical properties; B. Surface properties; Nanoindentation

1. Introduction

Nanodiamond (ND) is a member of the carbon nanomaterials family, of which the mechanical properties and structural integrity (small diameter (5 nm on average), large and accessible

* Corresponding author at: National Technical University of Athens, School of Chemical Engineering, 9 Heroon, Polytechnioust., Zografos, Athens, GR-157 80, Greece. Tel: +30 2107724046.
E-mail address: charitidis@chemeng.ntua.gr (Constantinos A. Charitidis)

surface (300-500 m^2/g) and a rich, tailorable surface chemistry) make NDs a great candidate material for ultimate polymer matrix reinforcement [1-6]. In literature, controversial findings are reported on the mechanical behavior of polymer-ND composites; decrease in storage modulus of an epoxy-ND composite [7], slightly increased Young's modulus and hardness values for different polymers due to the addition of ND [8-9], significantly improved mechanical properties [10-12] at low ND content, high mechanical properties were recently demonstrated for polymer composites with very high ND contents [13-15]. Behler et al. [13] have recently reported a 400% increase of Young's modulus and a 200% increase of hardness by dispersing ND (20 wt%) into electro spun polyamide fibers; however, higher concentrations of ND lead to agglomeration of the powders. Dolmatov [16] have studied the effect of ND (~2 wt%) addition on the mechanical properties of rubber (particle size ~44 nm). Kurin et al. [17] reported a ~200% increment in stiffness and large enhancement in breaking strength of PVA-7wt% ND fiber coatings; yet,these composites suffer from poor ductility, which could be due to the large ND content. One way to avoid this problem is using lower filler additions, so that the properties of the polymers are preserved with moderate enhancement in mechanical properties. Furthermore, the rate of enhancement in the mechanical properties is highest when the nanofiller concentration is at the dilute limit [18]. There are very few recent studies on the effectiveness of ND in enhancing the mechanical properties, when ND concentration is less than 1 wt% [19,20]. Such discrepancies and underperformance of polymer- ND composites can be attributed to agglomeration and poor dispersion of ND, together with non-optimized polymer- ND interactions [1].

Polymer composites, consisting of additives and polymer matrices, including thermoplastics, thermosets and elastomers, are considered as an important group of relatively inexpensive materials for many engineering applications. Epoxy resin (EpR) category is one of the most common thermoset polymer categories used in the formation of polymer nanotube composites; these polymers cure when mixed with a crosslinker, a catalyzing agent or hardener. Epoxy resins have been widely used in practical applications such as adhesives, construction materials, composites, laminates and coatings owing to their excellent mechanical properties, low cost, ease of processing, good adhesion to many substrates, and good chemical resistance [21].

Mechanical properties and thermal conductivity of composites made of nanodiamond with epoxy polymer binder have been studied in a wide range of nanodiamond concentrations (0–25 vol.%); the composites with 25 vol.% nanodiamond showed an vast increase in Young's modulus (up to

470%) and hardness (up to 300%) as compared to neat epoxy, followed by significant increase in scratch resistance and thermal conductivity[14].

With a NDP content of only 0.3 wt%, the Vicker's hardness, tensile strength and tensile modulus of the NDP/epoxy nanocomposites were 24.7%, 52.7% and 54.2% higher than that of pure epoxy, respectively. The significant improvement of the mechanical properties of the NDP/epoxy nanocomposites could be attributed to the good dispersion of the NDP in the epoxy matrix and grafting of epoxy to NDP by an esterification reaction [22].

Ayatollahi et al. reported that while the addition of 0.1 wt% of ND improved the Young's modulus and tensile strength compared with those of the pure epoxy, the fracture toughness did not show any improvement. Mixed mode fracture resistance of nanocomposites was investigated, in order to study the effect of shear deformation on fracture properties of nanocomposites; results showed that as the share of shear deformation in mixed mode loading increases, the positive effect of ND particles enhances [23].

2. Experimental

2.1. Materials

Epilox T 19-36/700 (LEUNA-Harze GmbH, Germany) is a commercially modified thermoset resin mainly used for applications that requires a strong surface to surface binding. It is a colorless, low viscosity (650-750 mPa.s at 25 °C) epoxy resin with a reduced crystallization tendency having a density 1.14 cm-3. Cross linking with suitable curing agents is preferably performed at room temperature. The Epilox polymeric resin has chemical composition as follows, Bisphenol A epichlorohydrine (50-100 wt. %) and oxirane, mono-{(C12-14-alkyloxy) methyl derivatives (10-25 wt.%).

Epilox Cross linker H 10-31(LEUNA-Harze GmbH, Germany) is a liquid, colourless, low viscosity (400-600 mPa.s) modified cycloaliphatic polyamine epoxide adduct having density 1 gcm-3. It contain the chemical combination with 3-aminomethyl-3,5,5-trimethylcyclohexyl (25-50 wt. %), benzyl alcohol (25-50 wt %) and nonylphenol (< 5 wt. %). 3-aminomethyl-3,5,5-trimethylcyclohexyl is in clear liquid puriss grade having a density (0.24 g/mL at 200 C).

*Method of preparation of Epilox/NDs:*Resin, crosslinker and NDs were thoroughly mixed in specific ratio with mechanical stirring (20,000 RPM for 2 minutes); the composite mixture was then degassed in low vacuum. Before the onset of polymerisation, the polymer was set into the mould. Chemical reaction between resin and crosslinker resulted in exothermic reaction. Handling strength for these composite occurred in 24 hours (when temperature >77°F/25°C) and complete curing was achieved after 5-7 days at 25 °C. For faster curing the molds were kept in the oven at 90 °C for 1 hour or 70 °C for 4 hours. Samples were prepared with seven different ND concentrations in epoxy resin: 0.4, 0.8, 1.2, 1.6, 2.0, 2.4 and 5 wt% (END0.4 – END5).

Epoxy Resin (T 19-36/700) (63 wt %), Cross linker (H 10-31) (37 wt %) and filler NDs (0.4, 0.8, 1.2, 1.6, 2.0, 2.4 and 5 wt %) was thoroughly mixed in a specific ratio with mechanical stirring (20,000 RPM for 2 minutes). Sonication (ultrasonic frequency 37 KHz for 15 min) helped to escape entrapped bubbles in the mixture. A 20 minute degassing in the vacuum step has been subsequently undertaken in order to get rid of the trapped gas bubbles completely. Before the onset of polymerization, the polymer was set into the mold. A chemical reaction between resin and cross linker resulted in an exothermic reaction. The epoxy NDs composite specimens were molded into required shape. Handling strength of these composite occurred in 24 hours (when temperature > 77°F/25°C) and complete curing was achieved after 5-7 days at 25 °C. For faster curing the molds were kept in the oven at 90 °C for 1 hour or 70 °C for 4 hours. The defected samples (with uneven surface and surface entrapped air bubble) are avoided for analysis.

2.2. Methods

2.2.1 FE-SEM and Energy Dispersive X-ray Spectroscopy

Sample morphology was checked by a scanning field emission electron microscope (FE-SEM, Zeiss Supra 40), connected to an Energy Dispersive X-ray Spectroscopy (Oxford Inca Energy 450), used to determine the average elemental composition, in particular the presence of non-carbon elements.

2.2.2 Raman Spectroscopy

The Raman spectra were obtained using a Green laser (514 nm). The microscope used an objective lens to focus the laser beam on the sample surface, and the size of the focused laser spot on the sample has a diameter of a few micrometers. All measurements were performed at room temperature and ambient conditions.

2.2.3 Contact angle

Contact angle measurements were performed using a prototype contact angle apparatus, with a motorized stage, in isolated environment and ambient conditions, using distilled water.

2.2.4. Nanoindentation and nanoscratch testing

Nanoindentation testing was performed with HysitronTriboLab® Nanomechanical Test Instrument, which allows the application of loads from 1 μN to 30 mN and records the displacement as a function of applied loads with a high load resolution (1 nN) and a high displacement resolution (0.04 nm). The TriboLab® employed in this study is equipped with a Scanning Probe Microscope (SPM), in which a sharp probe tip moves in a raster scan pattern across a sample surface using a three-axis piezo positioner. In all nanoindentation tests a total of 10 indents are averaged to determine the mean hardness (H) and elastic modulus (E) values for statistical purposes, with a spacing of 50 μm, in a clean area environment with 45 % humidity and 23 °C ambient temperature. In order to operate under closed loop load control, feedback control option was used. All nanoindentation measurements have been performed with the standard three-sided pyramidal Berkovich probe, with an average radius of curvature of about 100 nm [24]. Nanoscratch testing is a versatile tool for analysis of the mechanical properties of thin films and bulk materials [25]. The scratch tests performed in this work included three main segments. Firstly, a pre-scratch scan under a very small load (1 μN) was carried out. Then, the indenter scrapes the sample under a certain force and a scratch was generated. The normal applied loads used in this work were 0-400 μN. The length of the scratches was 10 μm.

Based on the half-space elastic deformation theory, H and E values can be extracted from the experimental data (load displacement curves) using the Oliver-Pharr (O&P) method [26, 27]. The derived expressions for calculating the elastic modulus from indentation experiments are based on Sneddon's [28] elastic contact theory:

$$E_r = \frac{S\sqrt{\pi}}{2\beta\sqrt{A_c}} \quad (1)$$

where S is the unloading stiffness (initial slope of the unloading load-displacement curve at the maximum displacement of penetration (or peak load)), A_c is the projected contact area between the tip and the substrate and β is a constant that depends on the geometry of the indenter (β =1.167 for Berkovich tip [26, 27]). Conventional nanoindentation hardness refers to the mean contact pressure; this hardness, which is the contact hardness (H_c) is actually dependent upon the geometry of the indenter (Eq. 2-4).

$$H_c = F / A \quad (2)$$

where,

$$A(h_c) = 24,5h_c^{\,2} + a_1 h_c + a_{1/2} h_c^{\,1/2} + ... + a_{1/16} h_c^{\,1/16} \quad (3)$$

and

$$h_c = h_m - \varepsilon \frac{P_m}{S_m} \quad (4)$$

where h_m is the total penetration displacement of the indenter at peak load, P_m is the peak load at the indenter displacement h_m, and ε is an indenter geometry constant, equal to 0.75 for Berkovich indenter [26-29]. Prior to indentation, the area function of the indenter tip was calibrated in a fused silica, a standard material for this purpose [30, 31].

3. Results and discussion

3.1. Structural Characterization

3.1.1 FESEM-EDS

FESEM analysis (Fig. 1) shows that the NDs are agglomerated with having different size and shapes. The size of the crystal size varies from 20 to more than 200 nm. EDS analysis (Fig. 2) confirms the elemental analysis wt % as follows,

Element	Weight%
C (Carbon)	97.53
O (Oxygen)	2.15
Si (Silicon)	0.12
Cl (Chloride)	0.20
Total	*100.00*

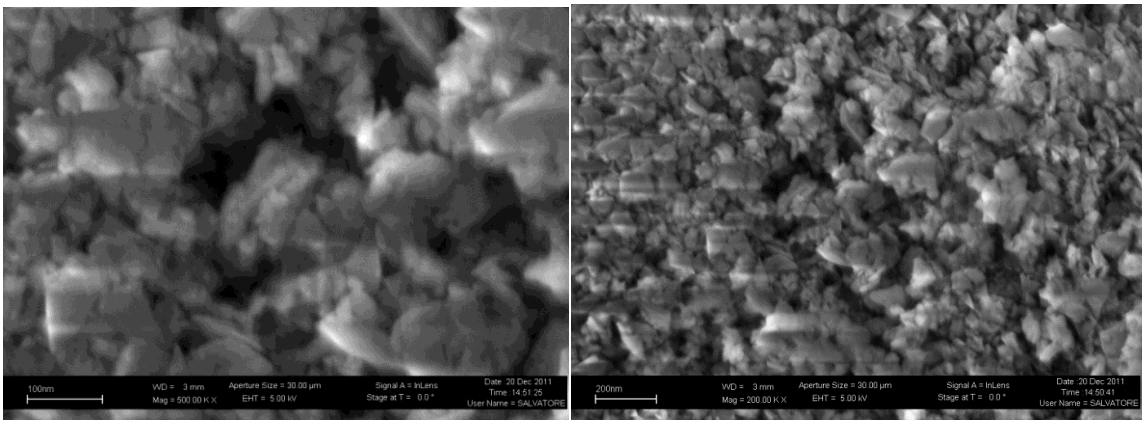

Figure 1. FESEM analysis of NDs.

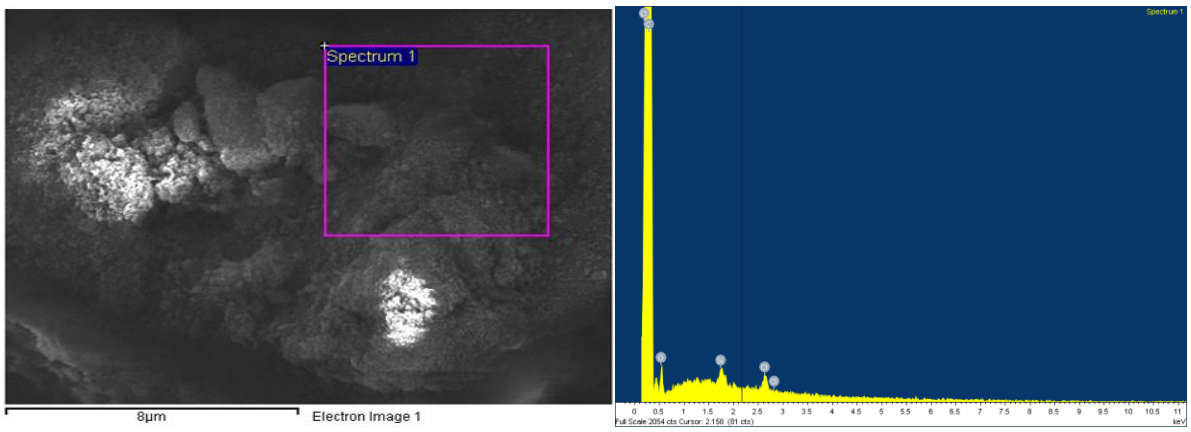

Figure 2. EDS analysis of NDs.

3.1.2 Micro Raman

Micro Raman analysis shows the sharp diamond peak at 1332 cm-1 and graphite peak at 1560 cm^{-1}. The I_D/I_G ratio is ~ 0.7.

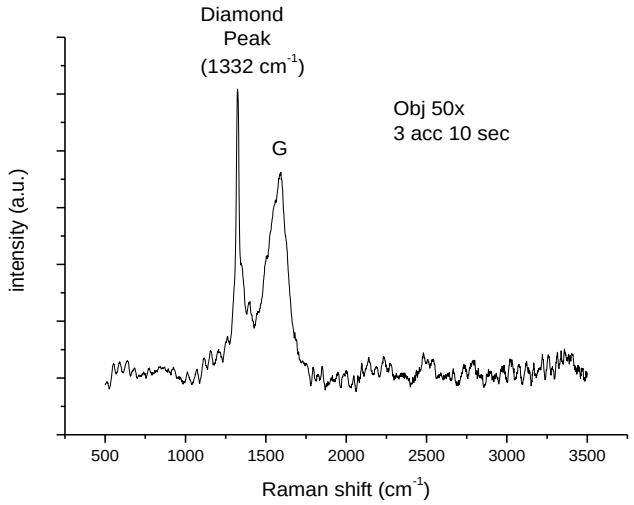

Figure 3. Micro Raman analysis of NDs.

3.2 Nanomechanical Characterization and Contact Angle

The relation (input functions) of displacement change versus time used in experiments is plotted in Figs. 4-5 below (schematic trapezoidal load-time $P = P(t)$ input function). In the case of creep experiment, loading and unloading times were identical (10 sec), while creep time was set to 100 sec (40 and 3 sec for conventional nanoindentation testing, respectively).

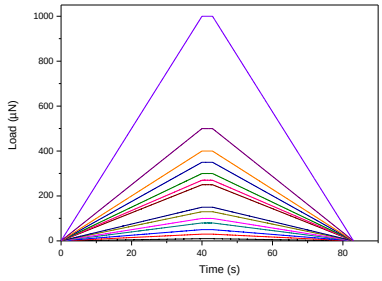

Figure 4. Load curves as a function of time

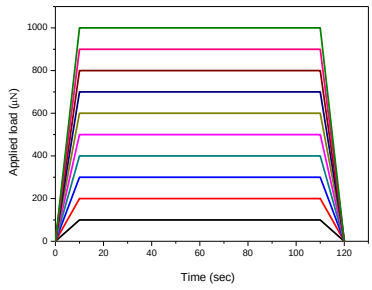

Figure 5. Applied load curves as a function of creep time

The load unload curves of END 0.4 is presented in Fig. 6, as representative of all samples. The hardness and the elastic modulus as a function of displacement for all samples are presented in Figure 7. END5 presents enhanced hardness, while elastic modulus of END0.4, END0.8 and

END1.2 is higher than the rest of concentrations. Hardness and elastic modulus of pure epoxy are 0.2 GPa and 3.5 GPa, respectively [32].

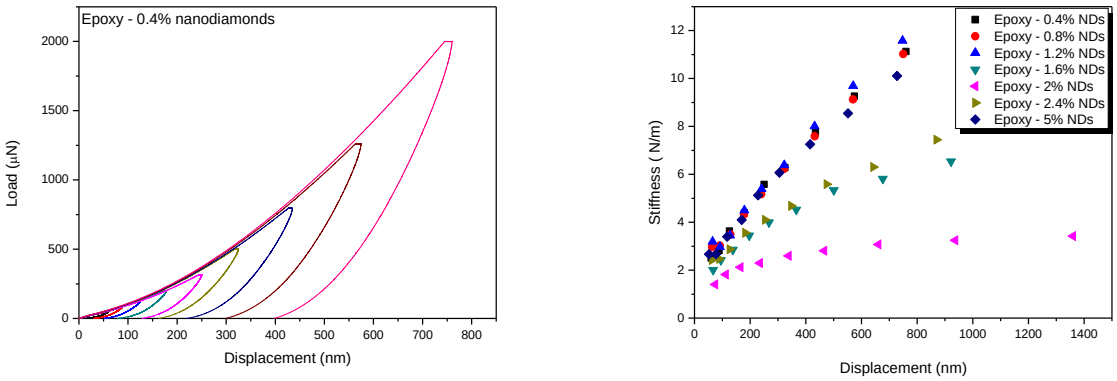

Figure 6. (a) Load – unload curves of END0.4, as a function of displacement and (b) stiffness as a function of displacement, for all samples.

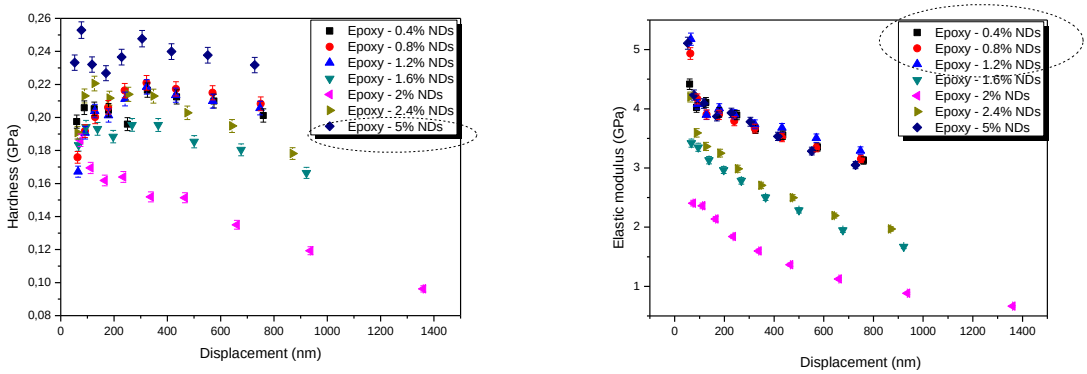

Figure 7. Hardness and the elastic modulus as a function of displacement, for all samples.

Hardness and elastic modulus values END samples were found to deviate at surface region (~0-100nm), probably due to roundness of the tip and Indentation Size Effect (ISE), tending to reach constant values. The reasons for this narrow range in hardness and modulus values obtained from these nanoindentation measurements are currently unknown, but it is likely due to a combination of factors, e.g. graded surface structure due to NDs concentration, adhesive forces between the tip and the sample etc. Due to the very low contact area between the indenter and the sample, very high stresses can be developed. The high hydrostatic pressure exerted by the surrounding material allows plastic deformation at room temperature when conventional mechanical testing only leads to fracture. It is revealed that some materials exhibit ISE, which shows an increase in

hardness with decreasing applied load [33]. Apparently, the existence of ISE may hamper the accurate measurement of hardness value, and is attributed to experimental artifact, a consequence of inadequate measurement capability or presence of oxides (if applicable) on the surface [34]. Other explanations include indenter-specimen friction [35], and changing dislocation density (for metals) for shallow indents due to the presence, for instance, of geometrically necessary dislocations [36]. The Berkovich indenter generates dislocations organised in a quite complex way during a nanoindentation test, even for very low deformations [37], making difficult the formulation for the stress field generated, even during an elastic deformation, as well as its modelling. Most of the dislocations stay generally confined around the residual imprint in a dense structure [38-40] with many dislocation interactions [41]. For polymers and polymer composites, further disussion is needed.

The contact angle measurements revealed a change in behavior of ENDs composites (Figure 8). A switch from hydrophobic to hydrophilic behaviour is evidenced, when passing the concentration threshold of 2% ND (noted in green circle) (adding NDs in the epoxy matrix increases the hydrophobicity till the value of 2%).

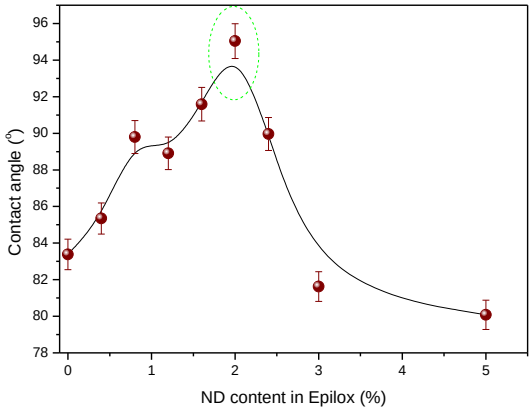

Figure 8. Contact angle as a function of ND concentration.

3.3 Wearanalysis-deformationmechanism

An important feature of indentation experiments is that the material around the contact area tends to deform upwards (pile-up) or downwards (sink-in) with respect to the indented surface plane. The occurrence of such pile-up and sink-in patterns is usually interpreted in terms of the strain-

hardening behavior of the indented material [42-45]. According to these studies the surface around indents tends to pile up against the indenter in cases where the indented sample is heavily pre-strained with only little reserves for further work-hardening or has generally a low strain-hardening potential. On the other hand, when the sample is fully annealed and has a high strain-hardening potential, the surface around indents tends to sink in [42-45]. The reason for this relationship between strain hardening behavior and displacement patterns is plausible: well-annealed soft metals which exhibit a high strain-hardening rate tend to show far off field plasticity yielding a large lateral smear out of the plastic out-of-plane displacement field. Rapid strain-hardening in the immediate vicinity of the indenter tip will cause plastic deformation to occur gradually further away from the contact region, causing the material to be displaced far away from the indentation entailing sink-in patterns. In contrast, strain-hardened materials as well as alloys and metallic glasses which exhibit a low (residual) strain-hardening rate will reveal a stronger localization of the plastic zone, creating a local pile-up instead of a sink-in displacement pattern around the indent. Good knowledge of the deformation zone around an indent is of considerable importance for nanoindentation testing because the shape of the out-of-plane displacement zone determines the actual contact area between the indenter and the specimen. Sink-in patterns reduce and pile-up patterns increase the contact area. These differences in the surface deformation mode affect the quantitative analysis of the hardness measurements. Not taking the piling-up or sinking-in into account in micro- and nanoindentation hardness tests can result in significant errors when extracting hardness values from the experimental data [42-43].

The presence of creep during nanoindentation (Fig 9.) has an effect on pile-up, which results in incorrect measurement of the material properties. Fischer-Cripps observed this behaviour, in case where the measured elastic modulus was much less than expected [46]. Rar et al. observed that the same material when allowed to creep for a long duration produced a higher value of pile-up/sink-in indicating a switch from an initial elastic sink-in to a plastic pile-up [47-48].

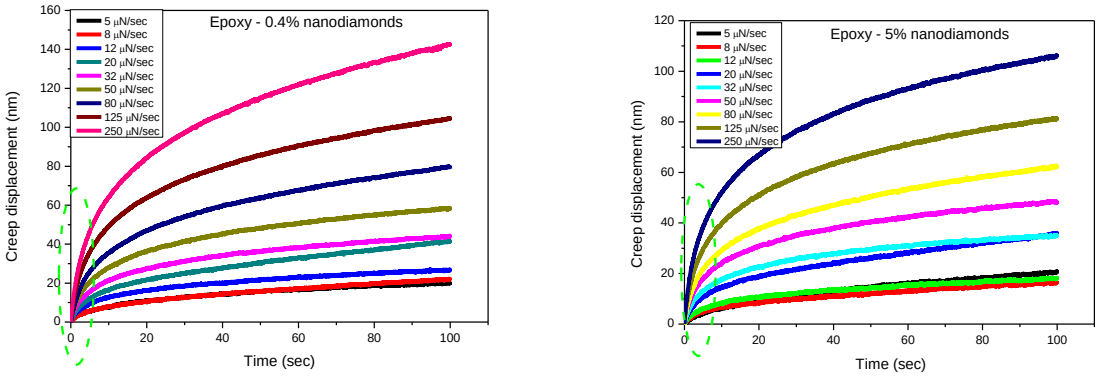

Figure 9. Creep displacement as a function of hold time for END0.4 and END5.

In Fig. 9, the penetration of the indenter tip into the sample surface (i.e. creep displacement) during the peak load holding against the holding time is presented, for two representative cases (END0.4 and END5.0). The magnitude of the total creep displacement during the peak load holding is strongly load dependent, i.e., larger peak load causes larger penetration. The creep displacement increases but at a decreasing rate, and it becomes almost linear with regard to the holding time (an initial sharp rise in creep displacement in the early part of the creep segment, followed by a region showing a smaller rate of increase in creep displacement). The general profile of these curves is similar to the strain vs. time plot obtained for the uniaxial tensile creep testing of bulk materials that exhibit power-law creep behavior [49-50]. The initial stage of the curves (noted in circle) in Fig. 9 corresponds to transient creep, and after this initial displacement, the descent of the indenter continues but the rate of descent decreases to attain a steady state value. The transient creep deformation showed a dependence upon the loading rate. As Fig. 9 denotes, a higher loading rate cause a greater primary creep deformation and leads to an increase of the total creep deformation. This behavior may be attributed to the fact that at the lowest loading rate (that obviously leads to a longer time needed to reach the final load value), a relevant creep deformation may also occur during the loading process [51]. As a consequence the creep during the holding time will decrease. Moreover the substructure formed beneath the indenter due to the indentation stress may be different at different loading strain rates, and this substructure will affect the subsequent creep behavior [52]. In Fig. 9, less creep deformation for the case of END5.0 is evident, compared with END0.4.

In Fig. 10, the normalised pile-up/sink-in height h_c/h_m and the normalized hardness H/E are plotted vs. displacement. In Fig. 10 (a), the normalised pile-up/sink-in height h_c/h_m vs. the normalized hardness is plotted. Higher stresses are expected in high H/E, hard materials, and high stress concentrations develop towards the indenter tip, whereas in case of low H/E, soft materials, the stresses are lower and are distributed more evenly across the cross-section of the material [53]. Rate sensitive materials experience less pile-up compared to rate insensitive materials due strain hardening. Cheng and Cheng reported a 22% pile-up for a work hardening exponent [54]. This is consistent with the fact that when h_c/h_m approaches 1 for small H/E, deformation is intimately dominated by pile-up [55-56]. On the other hand, when h_c/h_m approaches 0 for large H/E, it corresponds to purely elastic deformation and is apparently dominated by sink-in in a manner prescribed by Hertzian contact mechanics [57]. The composites exhibit a switch from pile-up to sink-in deformation in the H/E value of ~0.06; such behaviour is also evidenced in other polymeric materials [48].

The ratio of hardness/elastic modulus (H/E) is of significant interest in tribology. Higher stresses are expected in high H/E, hard materials, and high stress concentrations develop towards the indenter tip, whereas in the case of low H/E, soft materials, the stresses are lower and are distributed more evenly across the cross-section of the material [58-59]. The high ratio of H/E is indicative of the good wear resistance in a disparate range of materials [59-60]: ceramic, metallic and polymeric (e.g. c-BN, tool steel and nylon, respectively), which are equally effective in resisting attrition for their particular intended application. In Fig. 10 (b), the change of H/E slope reveals the strengthening of nanocomposites with increasing NDs concentration (more resistant to wear) up to 2% NDs; thereafter, increasing ND content results in lower resistance to wear.

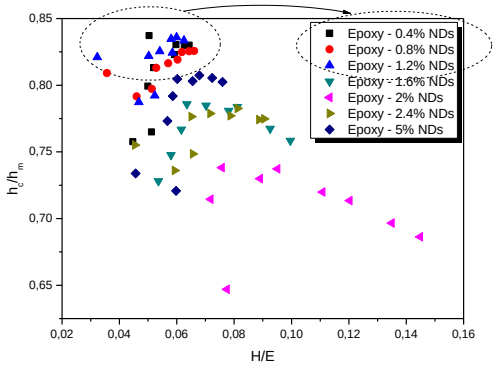

(a)

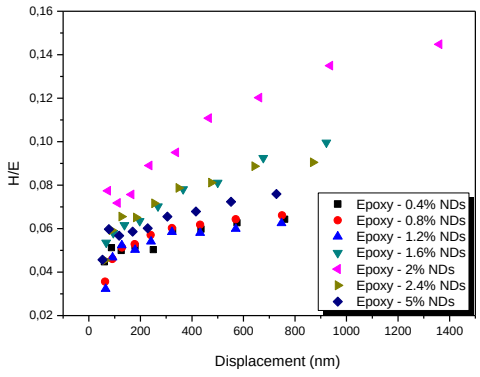

(b)

Figure 10. (a) Normalised pile-up/sink-in height hc/h m plotted vs. displacement and (b) the ratio of hardness/elastic modulus vs. displacement is plotted.

3.4 Analysis beyond nanomechanical properties

Scanning Probe Microscopy - Scratch test

As seen in the images in Figure 11, there is a buildup ahead of polymer material at one side (mostly) of the scratch path; as the indenter moves along the surface, the displaced material forms a pile-up which accumulates on the sides of the scratch. A groove is formed which is roughly of the shape of a triangular prism. For the Berkovich tip, it should be noted that the orientation of the tip with respect to the scratch direction is very important. As the indenter scratches, total volume swiped by the indenter will depend on the projected area of the indenter along the scratch axis. These buildups are found on the same side of all scratches we created, which leads us to believe that the composites were plastically deformed (buildup is most likely an accumulation of compressed materials). When the scratch tip ploughs through the material ahead of it, the material will be either pushed forward or piled up sideways [61]. This phenomenon is usually observed for relatively ductile polymers, where ironing and plastic deformation take place readily. In addition to the surface friction between the substrate and the scratch tip, the material accumulated ahead of the tip.

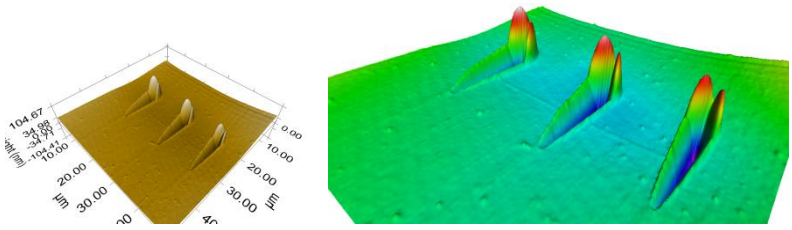

Figure 11. Representative SPM images of nanoscratch tests for END5.0.

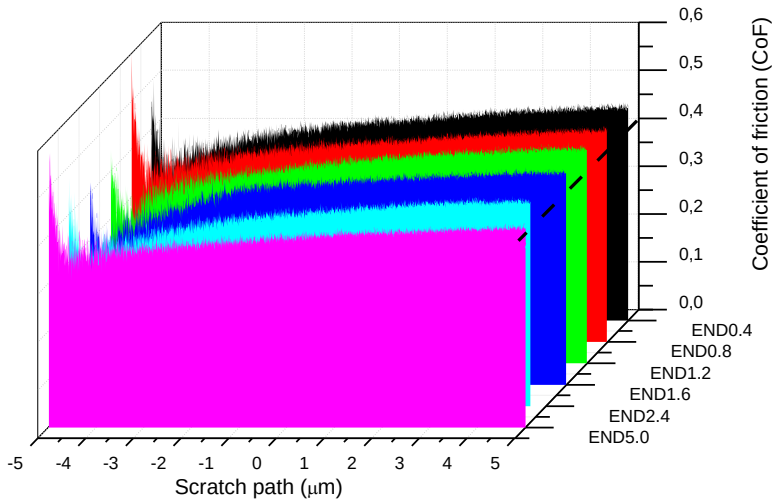

Figure 12. Coefficient of friction for END composites, obtained through nanoscratch testing.

Coefficient of friction (CoF) is defined as the ratio of the lateral force modulus to the normal force modulus, and depends on several factors including the indenter geometry, surface roughness of the sample, and the material properties of the sample. Rather than simply being a friction parameter, CoF value is also a measure of the resistance to scratch. A harder, wear-resistant material would impose more resistance to scratch and the indenter will consequently experience a larger lateral force. In Fig. 12, CoFs for all samples are presented (four identical scratches were performed at three samples of each type for statistical purposes). The average values of the steady stage are taken as the effective friction coefficient. These coefficient trends are quite similar for all samples, except for END5.0 (lower coefficient of friction, as noted).

Adhesion energy

A characteristic nanoindentation adhesion test is comprised of pressing the tip into the patterned sample, followed by unloading it at a constant rate and finally obtaining a distinctive (and often abrupt) pull-off force representing the adhering surfaces. Adhesion is observed in a load-displacement curve as a region of negative load during unloading [62-63]. The principle of this experiment is to put into contact the diamond probe tip and the flat polymer substrate and determine the maximum pull-force necessary to separate both materials. In each test the tip

(100m radius of diamond probe tip) was brought into contact with the sample surface; if interfacial forces were present, the transducer force became negative and the tip plate continued to move with the sample until the negative restoring force on the transducer became equal to the adhesive force between the tip and surface interface. The pull-off adhesion force is determined as the difference between the minimum force value and the zero offset. Three adhesion measurements on surface of samples END0.4 and END5.0 were conducted in order to study the effect of NDs addition on adhesion (Fig.13). It is evident that the introduction of NDs into the polymeric matrix increases the adhesion force (P_{adh}).

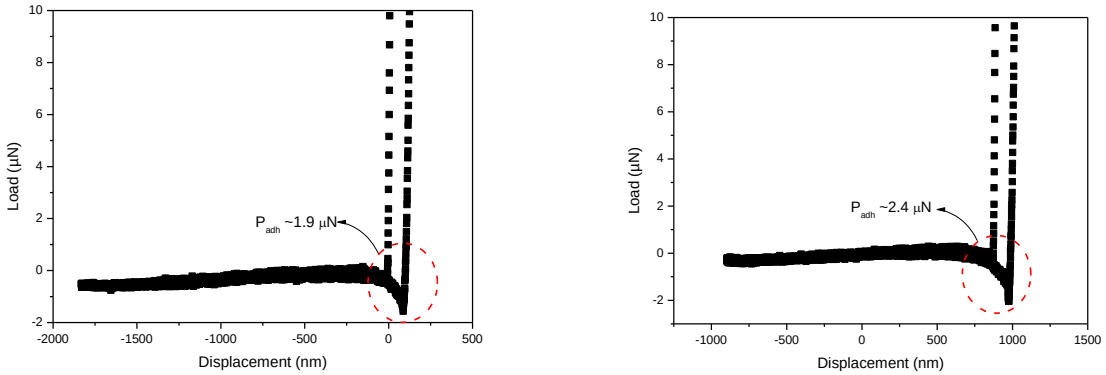

(a) (b)

Figure 13. Load versus displacement as the tip approached and retracted from (a) END0.4 and (b) END5.0.

4. Conclusion

In this work, the mechanical integrity of various polymeric matrices reinforced with different concentrations of carbon nanodiamonds is analysed and discussed. The main findings are summarized below:

END5.0 presented enhanced hardness, while elastic modulus of END0.4, END0.8 and END1.2 was higher than the rest of concentrations. A switch from hydrophobic to hydrophilic behaviour is evidenced, when passing the concentration threshold of 2% ND. The low concentration composites exhibited a switch from pile-up to sink-in deformation in the H/E value of ~0.06; such behavior is also evidenced in other polymeric materials.

Less creep deformation for the case of END5.0 was evidenced, when compared with END0.4. The change of H/E slope revealed the strengthening of nanocomposites with increasing NDs concentration (more resistant to wear) up to 2% NDs; increasing ND content results in lower resistance to wear. During the nanoscratch experiment, a buildup ahead of polymer material was created at one side (mostly) of the scratch path; as the indenter moved along the surface, the displaced material formed a pile-up which accumulated on the sides of the scratch. Coefficient trends were found quite similar for all samples, except for END5.0 (lower coefficient of friction). Adhesion measurements conducted on surface of samples END0.4 and END5.0 revealed that the introduction of NDs into the polymeric matrix increases the adhesion force (P_{adh}).

Acknowledgment

The support from the EU FP7 Project "Enhancing structural efficiency through novel dissimilar material joining techniques" (SAFEJOINT) under Grant Agreement no. 310498 is greatly acknowledged by EPK and CAC. Dr. Martin Wagner, Leunaharze,Gremany for providing us the Epilox material for this study. Dr. Guestella Salvatore for FESEM and analysis and Dr. Mauro Giorcelli for Raman analysis.

References

1. Neitzel, I.; Mochalin, V.N.; Niu , J.; Cuadrac, J.; Kontsos, A.; Palmese, G.R.; Gogotsi, Y. Maximizing Young's modulus of aminatednanodiamond-epoxy composites measured in compression, *Polymer***2012**, *53*, 5965-5971.

2. Mochalin, V.N; Shenderova O.; Ho, D.; Gogotsi , Y. The properties and applications of nanodiamonds, *Nat. Nanotechol.***2012**, *7*, 11-23.

3. Kulakova, I.; Surface Chemistry of Nanodiamonds. *Phys. Sol. Stat.*, **2004**, *46*, 636–643.

4. Osswald, S.; Yushin, G.; Mochalin, V; Kucheyev, SO; Gogotsi, Y. Control of sp2/sp3 carbon ratio and surface chemistry of nanodiamond powders by selective oxidation in air.*J. Am. Chem. Soc***2006**, *128*, 11635-11642.

5. Mochalin, V; Osswald, S.; Gogotsi , Y. Contribution of functional groups to the Raman spectrum of nanodiamond powders. *Chem. Mater.***2008**, *21*, 273-279.

6. Krueger, A.; Lang, D. .Functionality is Key: Recent Progress in the Surface Modification of Nanodiamond. *Adv. Funct. Mat.***2012**, *22*, 890-906.

7. Špitalský, Z.; Kromka, A.; Matejka, L.;Cernoch, P.; Kovárová, J.; Kotek, J; Šlouf, M. Effect OfNanodiamond Particles On Properties Of Epoxy Composites, *Adv. Compos. Lett.***2008**, *17*, 29-34.

8. Stravato, A.; Knight, R.; Mochalin, V.; S. C. Picardi. HVOF-Sprayed Nylon11 + Nanodiamond Composite Coatings: Production & Characterization. *J. Therm. Spray Technol.* **2008**, *17*, 812-817.

9. Zhang, Q.; Naito,K.; Tanaka,Y.; Kagawa,Y.; Polyimide/Diamond Nanocomposites: Microstructure and Indentation Behavior. *Macromol.Rap.Comm***2007**, *28*, 2069-2073.

10. Dolmatov VY. Detonation synthesis ultradispersed diamonds: properties and application. *UspekhiKhimii***2001**, *70*, 687-708.

11. Yanhong, H.;, Shenderova, O. A., Hu, Z.; Padgett, C. W; Brenner, D. W. Carbon nanostructures for advanced composites. *Rep. Prog. Phys.***2006**, *69*, 1847-95.

12. Shenderova, OA.;Zhirnov, VV; Brenner, DW.; Carbon nanostructures. *Crit. Rev. Solid State Mater.***2002**, *27*, 227-356.

13. Behler, KD.;Stravato, A.; Mochalin, V.; Korneva, G.; Yushi. n, G.; Gogotsi, Y. Nanodiamond-polymer composite fibers and coatings. *ACS Nano***2009**, *3*, 363-369.

14. Neitzel, I.; Mochalin, V.; Knoke, I.; Palmese, G.R.; Gogotsi, Y. Mechanical properties of epoxy composites with high contents of nanodiamond, *Compos. Sci. Technol*. **2011**, *71*, 710-716.

15. Neitzel, I.; Mochalin, V.; Bares, J.A.; Carpick, R.W.; Erdemir, A.; Gogotsi, Y. Tribological Properties of Nanodiamond-Epoxy Composites, *Tribology Letters***2012**, *47*, 195-202.

16. Dolmatov, V.Yu.; Polymer-diamond composites based on detonation nanodiamonds. Part 2, *J. Superhard Mater.***2007**, *29*, 65-75.

17. Kurkin, T.S.; Ozerin, A.N.; Kechek'yan, A.S.; Ozerina, L.A.; Obolonkova, E.S.; Beshenko, M.A.; V. Yu. Dolmatov. Structure of oriented fibers based on poly(vinyl alcohol) modified by detonation nanodiamonds, *Polym. Sci. Series A.* **2008**, *50*, 43-50.

18. Maitra, U.; Prasad, K.E.; Ramamurty, U.; Rao, C.N.R. Mechanical properties of nanodiamond-reinforced polymer-matrix composites, *Solid State Commun*. **2009**, *149*, 1693-1697.

19. Korobko, A.P.; Bessonova, N.P.; Krasheninnikov, S.V.; Konyukhova, E.V.; Drozd, S.N.; Chvalun, S.N. Nanodiamonds as modifier of ethylene-1-octene copolymer structure and properties, *Diamond Relat. Mater.*,**2007**, *16*, 2141-2144.

20. Špitalský, Z.; Kromka, A.; Matejka, L.;Cernoch, P.; Kovárová, J.; Kotek, J.; Šlouf, M. Effect of nanodiamond particles of epoxy composites. *Adv. Compos.Lett.***2008**, 17.

21. Cadek, M.; Coleman, J. N.; Barron, V.; Hedicke, K.; Blau, W. J. Morphological and mechanical properties of carbon-nanotube-reinforced semicrystalline and amorphous polymer composites. *Appl. Phys. Lett.* **2002**, *81*, 5123-5125.

22. Zhai, Y.J.; Wang, Z.C.; Huang, W.; Huang, J.J.; Wang, Y.Y.; Zhao, Y.Q. Improved mechanical properties of epoxy reinforced by low content nanodiamond powder. *Mater. Sci. Eng.* **2011**, *528*, 7295-7300.

23. Ayatollahi, M.; Alishahi, E.; Shadlou, S. Mechanical Behavior of Nanodiamond/Epoxy Nanocomposites. *Int. J. Fracture***2011**, *170*, 95-100.

24. Charitidis, C.A., Nanomechanical and nanotribological properties of carbon-based thin films: A review. *Int. J. Refract. Met. H. Mater.* **2010**, *28*, 51-70.

25. Papageorgiou, D. P.; Koumoulos, E. P.; Charitidis, C. A.; Boudouvis, A. G.; Papathanasiou, A. G. Evaluating the Robustness of Top Coatings Comprising Plasma-Deposited Fluorocarbons in Electrowetting Systems, *J. Adhes. Sci. Technol.* **2012**, *26*, 2001-2015.

26. Huang, L.; Lu, J.; Troyon, M. Nanomechanical properties of nanostructured titanium prepared by SMAT. *Surf.Coat. Tech.***2006**, *201*, 208-213.

27. Oliver, W. C.; Pharr, G. M. An improved technique for determining hardness and elastic modulus using load and displacement sensing indentation experiments, *J. Mater. Res.***2011**, *7*, 1564-1583.

28. Sneddon, I.N. Boussinesq's problem for a rigid cone. *Math. Proc. Cambridge***2008**, *44*, 492-507.

29. King, R.B. Elastic analysis of some punch problems for a layered medium. *Int. J. Solids Struct.***1987**, *23*, 657-1664.

30. Koumoulos, E.P.; Charitidis, C.A.; Daniolos, N.M.; Pantelis, D.I.; Nanomechanical properties of friction stir welded AA6082-T6 aluminum alloy. *Mater. Sci. Eng. B.***2011**, *176*, 1585-1589.

31. Bei, H.; George, E.P.; Hay, J.L.; Pharr, G.M. Influence of Indenter Tip Geometry on Elastic Deformation during Nanoindentation. *Phys Rev Lett*.**2005**, *95*, 045501–045504.

32. Koumoulos, E.P.; Giorcelli, M.; Jagadale P.; Tagliaferro A.; Charitidis, C.A.; Carbon nanotube/ polymer nanocomposites: a study on mechanical integrity through nanoindentation, *Polym. Compos.***2013**, accepted for publication.

33. Loubet, J.L.; Georges, J. M.; and Meille, G.; in Vickers Indentation Curves of Elasto-Plastic Materials. In ASTM STP 889, Microindentation Techniques in Materials Science and Engineering, P. J. Blau and B. R. Lawn, Eds.; ASTM International, *West Conshohoken,* **1986**; pp. 72-89.

34. Li, H.; Ghosh, A.; Han, Y.H.; Bradt, R.C. The frictional of the indentation size effect in low load microhardness testing. *J. Mater. Res.* **1993**, *8*, 1028–32.

35. Ma, Q.; Clarke, D.R. Size-dependent hardness of silver single-crystals. *J. Mater. Res.***1995**; *10*, 853–63.

36. Gaillard, Y.; Tromas, C.; Woirgard, J.; Quantitative analysis of dislocation pile-ups nucleated during Nanoindentation in MgO. *Acta Mater.***2006**, *54*, 1409–1417.

37. Leipner, H.S.; Lorenz, D.; Zeckzer, A.; Lei, H.; Grau, P. Nanoindentation pop-in effect in semiconductors. *Phys. B Condens.Matter.***2001**, *308–310*, 446–449.

38. Chiu, Y.L.; Ngan, A.H.W. Time-dependent characteristics of incipient plasticity in nanoindentation of a Ni3Al single crystal. *Acta Mater.***2002**, *50*, 1599–1611.

39. Gaillard,Y.; Tromas, C.; Woirgard, J. Pop-in phenomenon in MgO and LiF: observation of dislocation structures. *Philos. Mag. Lett*. **2003**, *83*, 553–561.

40. Tromas, C.; Gaillard, Y. Dislocation Organization around a Nanoindentation Imprint. Encyclopedia of materials science and technology, **2004**, pp. 1–4.

41. Meyer E. Investigations of hardness testing and hardness. *Phys. Z***1908**, *9*, 66–74.

42. Pharr, G.M.; Oliver, W.C.; Brotzen, F.R. On the generality of the relationship among contact stiffness, contact area, and elastic modulus during indentation", *J. Mater. Res.***1992**, *7*, 613–617.

43. Nix, W.D. Elastic and plastic properties of thin films on substrates: Nanoindentation techniques. *Mater.Sci. Eng. A***1997**, *234–236*, 37–44.

44. Chaudhri, M.M.; Winter, M. The load-bearing area of a hardness indentation.*J. Phys. D Appl. Phys.***1988**, *21*, 370-374.

45. Alcala, J.; Barone, A.C.; Anglada, M. The influence of plastic hardening on surface deformation modes around Vickers and spherical indents".*Acta Mater.***2000**, *48*, 3451–64.

46. Fischer-Cripps AC. A simple phenomenological approach to nanoindentation creep.*Mater.Sci. Eng.* A **2004**, *385*, 74–82.

47. Rar, A.; Sohn S.; Oliver, W.C.; Goldsby L.D.; Tullis, E.T.; Pharr, M.G. On the Measurement of Creep by Nanoindentation with Continuous Stiffness Techniques.*MRS Proc.*, **2004**, *841*, R4.2

48. Koumoulos, EP.; Charitidis, CA.;Papageorgiou, DP.; Papathanasiou, AG.; Boudouvis, AG. Nanomechanical and nanotribological properties of hydrophobic fluorocarbon dielectric coating on tetraethoxysilane for electrowetting applications.*Surf.Coat. Technol.***2012**, *206*, 3823–3831.

49. Pelletier, H.; Krier, J.; Mille, P.; Cornet, A. Limits of using bilinear stress-strain curve for finite element modeling of nanoindentation response on bulk materials. *J. Thin. Sol. Fil.* **2000**, *379*, 147-155.

50. Mandal, S.; Kose, S.; Frank, A.; Elmustafa, A.A. A numerical study on pile-up in nanoindentation creep.*Int. J. Surf. Sci. Eng.***2008**, *2*, 41-51.

51. Yang, S.; Zhang, YW.;Zeng, KY. Extracting the mechanical properties of a viscoelastic polymeric film on a hard elastic substrate.*J. Mater. Res.***2004**, *19*, 3053-3061.

52. Yang, S.; Zhang, YW.;Zeng, KY. Analysis of Nanoindentation Creep for Polymeric Materials.*J. App. Phys.***2004**, *95*, 3655-3666.

53. Hill, R.; Storakers, B.; Zdunek, A.B.; A theoretical study of the BrinellHardness. *Math. Phys. Sci.* **1989**, *423*, 301-330.

54. Nie, H.Y.; Walzak, M.J.; McIntyre, N.S. Scratch resistance anisotropy in biaxially oriented polypropylene and poly(ethylene terephthalate) films. *Appl. Surf. Sci.* **2006**, *253*, 2320-2326.

55. Jiang, H.; Browning, R.; Mouse, A.; Sue H.J. *Appl. Surf. Sci.* **2008**, *254*, 4494-4499.

56. Archard, J.F.; Contact and rubbing of flat surfaces, *J. Appl. Phys.***1953**, *241*, 891–988.

57. Lee, JW.; Duh, JG. Nanomechanical properties evaluation of chromium nitride films by nanoindentation and nanowear techniques. *Surf.Coat. Technol.***2004**, *188-189*, 655-661.

58. Cheng, YT.; Cheng, CM.; What is indentation hardness?. *Surf.Coat. Technol.***2000**, *133–134*, 417–424.

59. Leyland, A.; Matthews, A. Design criteria for wear-resistant nanostructured and glassy-metal coatings. *Surf.Coat. Technol.***2004**, *177–178*, 317–324.

60. Leyland, A.; Matthews, A.; Optimization of Nanostructured Tribological Coatings, in: Nanostructured Coatings: Nanostructured Coatings, Nanostructure Science and Technology; *Cavaleiro A., De Hosson J.T.M., Eds.; Springer,***2006**; pp 511–538.

61. Kartsonakis, I.A.; Balaskas, A.C.; Koumoulos E.P.; Charitidis, C.A.; Kordas, G. Evaluation of corrosion resistance of magnesium alloy ZK10 coated with hybrid organic–inorganic film including containers. *Corr. Sci.* **2012**, *65*, 481-493.

62. Charitidis, C.A.; Koumoulos, E.P.; Tsikourkitoudi, V.P.; Dragatogiannis, D.A.; Lolas, G.; Influence of accelerated aging on nanomechanical properties, creep behaviour and adhesive forces of PDMS. *Plast.Rubber Compos.***2012**, *41*, 94-99.

63. Chen, B.; Oppenheimer, P.G.; Shean, T.A.V.; Wirth, C.T.; Hofmann, S.; Robertson, J. Adhesive Properties of Gecko-Inspired Mimetic via Micropatterned Carbon Nanotube Forests, *J. Phys. Chem. C***2012**, *116*, 20047-20053.

Table

Element	Weight%
C (Carbon)	97.53
O (Oxygen)	2.15
Si (Silicon)	0.12
Cl (Chloride)	0.20
Total	*100.00*

Figure

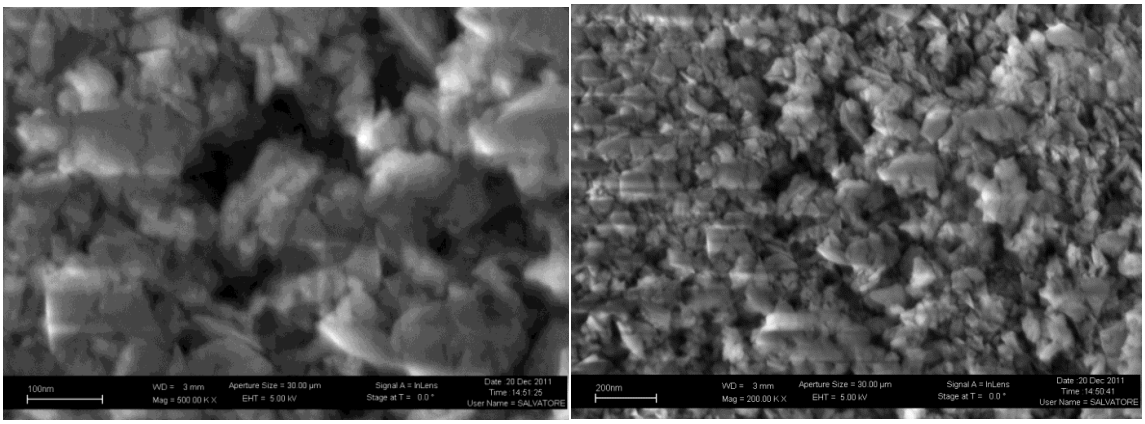

Figure 1. FESEM analysis of NDs.

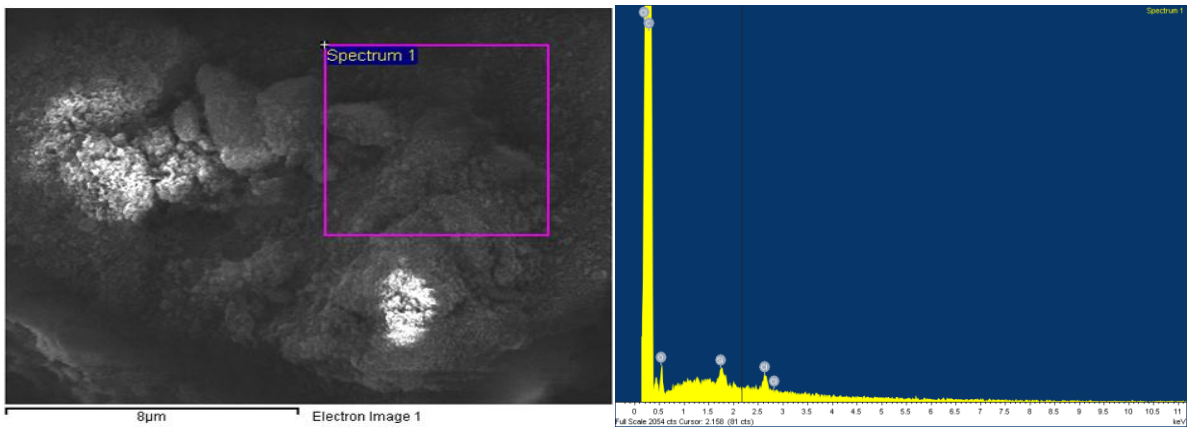

Figure 2. EDS analysis of NDs.

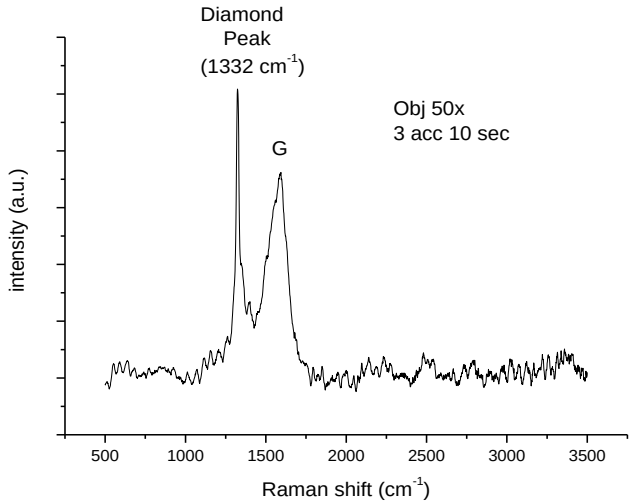

Figure 3. Micro Raman analysis of NDs.

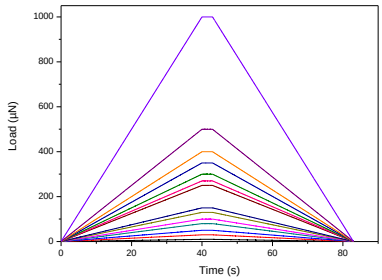

Figure 4. Load curves as a function of time

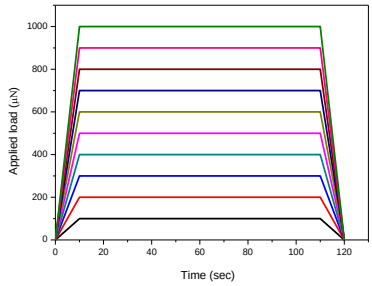

Figure 5. Applied load curves as a function of creep time

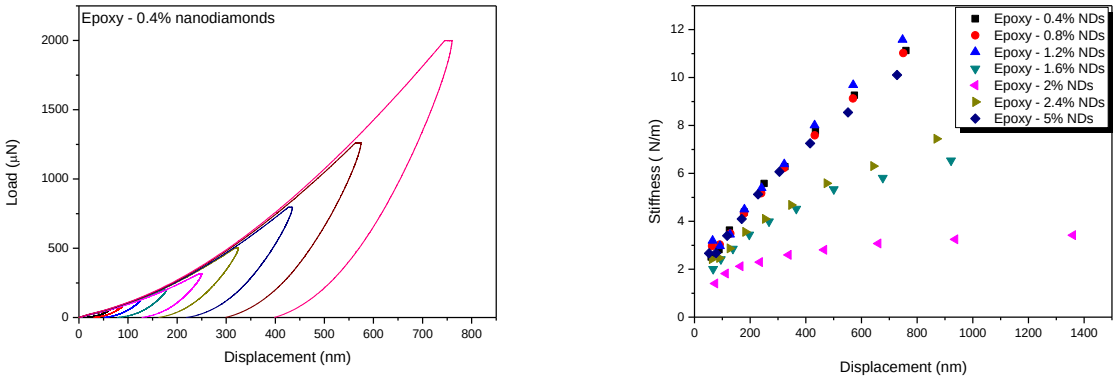

Figure 6. (a) Load – unload curves of END0.4, as a function of displacement and (b) stiffness as a function of displacement, for all samples.

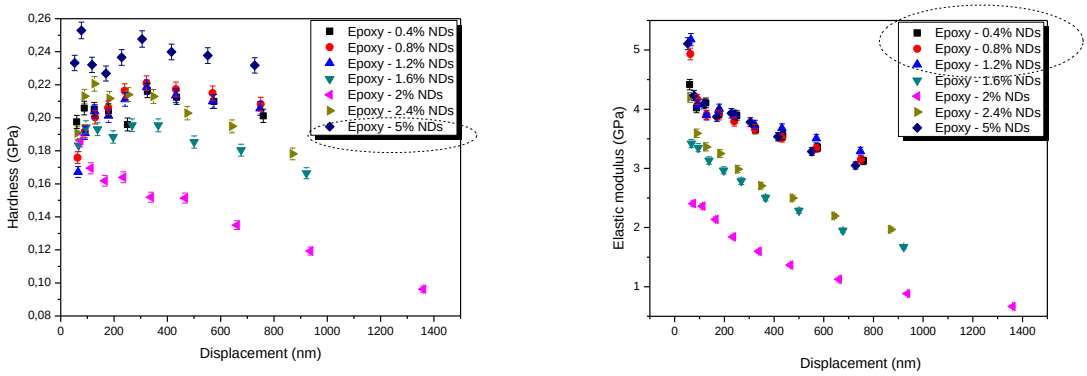

Figure 7. Hardness and the elastic modulus as a function of displacement, for all samples.

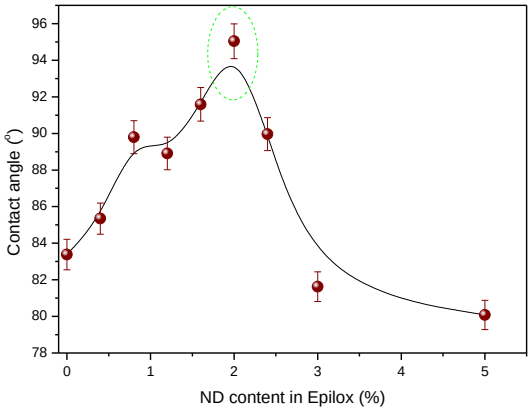

Figure 8. Contact angle as a function of ND concentration.

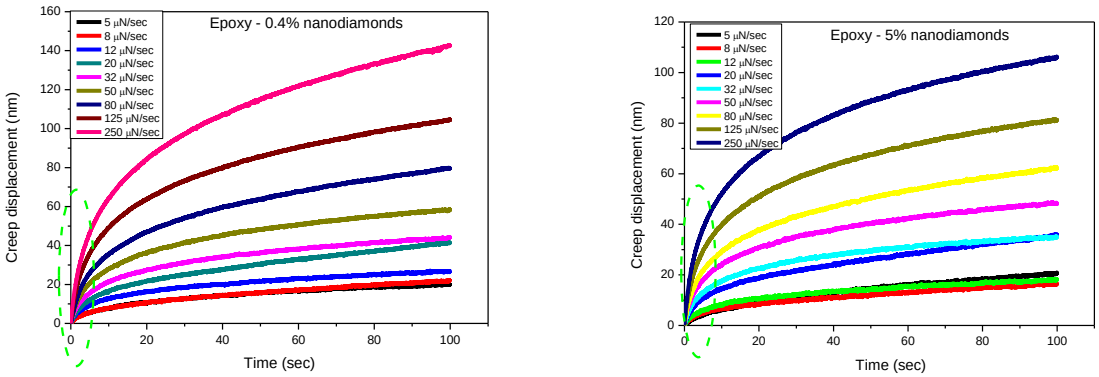

Figure 9. Creep displacement as a function of hold time for END0.4 and END5.

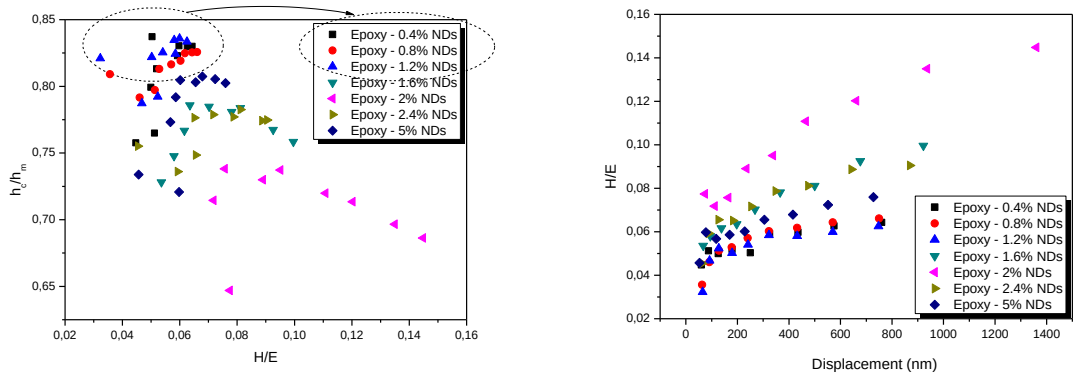

(a) (b)

Figure 10. (a) Normalised pile-up/sink-in height hc/h m plotted vs. displacement and (b) the ratio of hardness/elastic modulus vs. displacement is plotted.

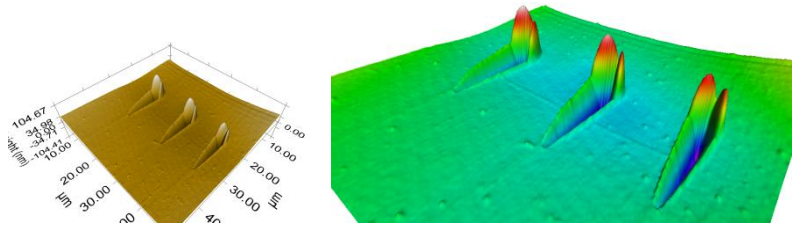

Figure 11. Representative SPM images of nanoscratch tests for END5.0.

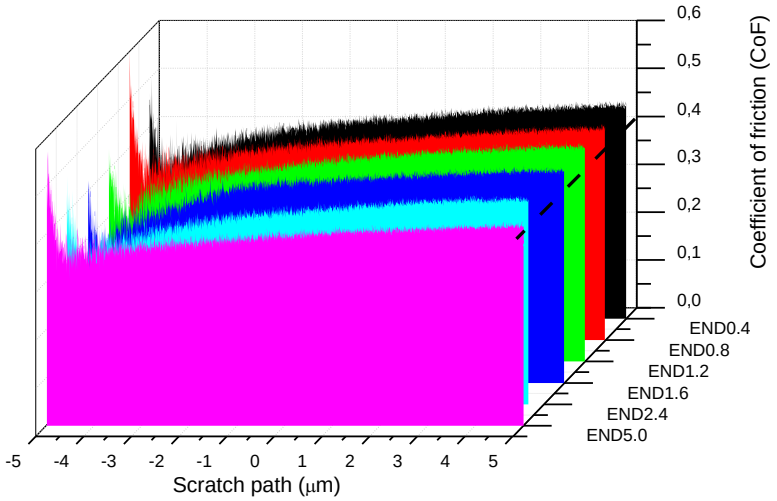

Figure 12. Coefficient of friction for END composites, obtained through nanoscratch testing.

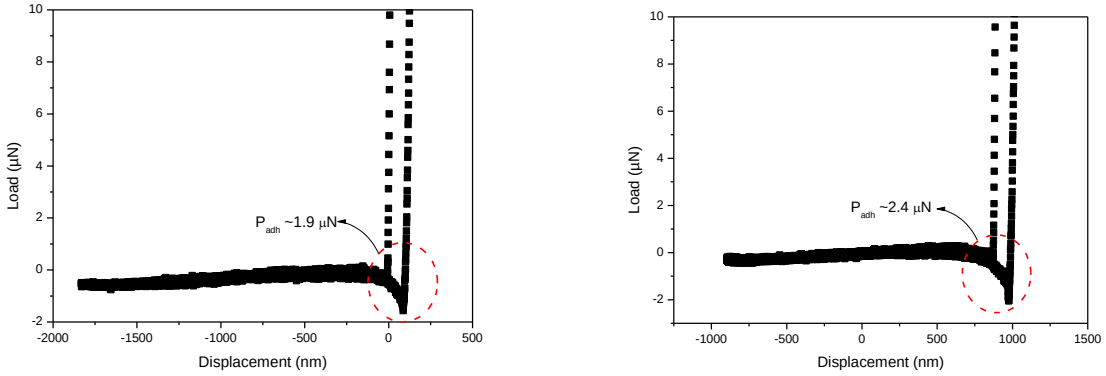

Figure 13. Load versus displacement as the tip approached and retracted from (a) END0.4 and (b) END5.0.

Carbon Nanotube/Polymer Nanocomposites: A Study on Mechanical Integrity Through Nanoindentation

Elias P. Koumoulos,[1] Pravin Jagdale,[2] Ioannis A. Kartsonakis,[1] Mauro Giorcelli,[2] Alberto Tagliaferro,[2] Constantinos A. Charitidis[1]

[1]*National Technical University of Athens, School of Chemical Engineering, 9 Heroon, Polytechniou St., Zografos, Athens, GR-157 73, Greece*

[2]*Applied Sciences and Technology Department, Politecnico di Torino, Corso Duca degli Abruzzi 24, Torino, IT-10129, Italy*

Carbon nanotubes (CNTs) are under intense investigation in materials science owing to their potential for modifying the mechanical proprieties of their composites. In this work, nanomechanical and nanotribological properties of polymer composites, reinforced with multiwall carbon nanotubes (MWCNTs) and single wall carbon nanotubes (SWCNTs), have been studied using the nanoindentation and nanoscratch technique. In particular, three different epoxy resins reinforced using several percentage of two different types of MWCNTs have been studied (range 0–7 wt%). Another resin was reinforced using MWCNTs (range 0–2.5 wt%) and SWCNTs (range 0–5 wt%) as fillers. Hardness and elastic modulus using nanoindenter instrument have been evaluated, while the coefficient of friction of the nanocomposites is obtained using nanoscratch. The results show an evident dependence with the percentage of CNTs. For all types of resins, an optimum in nanomechanical properties is found at intermediate levels of CNTs filling. POLYM. COMPOS., 00:000–000, 2014. © 2014 Society of Plastics Engineers

INTRODUCTION

Polymer composites, consisting of additives and polymer matrices, including thermoplastics, thermosets, and elastomers, are considered as an important group of relatively inexpensive materials for many engineering applications. Epoxy resin (ER) category is one of the most common thermoset polymer categories used in the formation of polymer nanotube composites; these polymers cure when mixed with a crosslinker, a catalyzing agent or hardener. ERs have been widely used in practical applications such as adhesives, construction materials, composites, laminates, and coatings due to their excellent mechanical properties, low cost, ease of processing, good adhesion to many substrates, and good chemical resistance [1]. As a new type of reinforcement, single and multi wall carbon nanotubes (SWCNTs and MWCNTs, respectively) have been widely investigated as their incorporation into appropriate matrixes (metals, ceramics, and polymers) produces composites with improved mechanical performance [2–4]. CNT/metal composites have been used in several applications, such as fillers in metal-metal joints [5, 6]; however, the main research efforts are focused on CNT/polymer composites. Charitidis et al. [7] studied the nanomechanical and nanotribological behavior of polyvinylbutyral/CNT composites with varying filler content and illustrated the dependence of CNT concentration on nanomechanical properties.

The investigation of mechanical behavior of polymeric composites filled with CNTs is a topic of ongoing research, as CNTs are highly desirable candidates for improvement of polymers' properties. Several properties have been examined, such as elasticity [8, 9], damage [10], buckling [11, 12], tribology [13, 14], and toughness [15] of CNT composites. Changes in the glass transition behavior of polymers as a result of adding CNTs are also reported [16, 17]. A previous study focused on the effect of CNT reinforcement on the tribological performance of ER composites; it was found that 1 wt% CNTs in ER yield optimal tribological performance [18].

Among thermosets, ERs have been very often studied as a potential matrix for nanocomposites with CNTs. Small quantity of CNTs, often between 0.1% and 5.0% (w/w), is added to the polymeric matrix aiming to improve mechanical and thermal properties [19]. Li et al. [20] studied the nanomechanical properties of SWCNTs

Correspondence to: Constantinos A. Charitidis; e-mail: charitidis@chemeng.ntua.gr

Contract grant sponsor: EU FP7 Project "Enhancing structural efficiency through novel dissimilar material joining techniques" (SAFEJOINT); contract grant number: 310498.

DOI 10.1002/pc.23049

Published online in Wiley Online Library (wileyonlinelibrary.com).

TABLE 1. Description of MWCNTs and SWCNTs.

Properties	MW-1	MW-2	SW-1
Outer diameter	30–50 nm	< 8 nm	1–2 nm
Inside diameter	5–10 nm	2–5 nm	0.8–1.6 nm
Ash	< 1.5 wt%	< 1.5 wt%	< 1.5 wt%
Purity	> 95 wt%	> 95 wt%	> 90 wt%
Length	10–20 μm	10–30 μm	0.5–2 μm
Specific surface area	60 m^2/g	500 m^2/g	407 m^2/g
Electrical conductivity	> 100 S/cm	> 100 S/cm	> 100 S/cm
Bulk density	0.28 g/cm^3	0.27 g/cm^3	0.14 g/cm^3
True density	~2.1 g/cm^3	~2.1 g/cm^3	~ 2.1 g/cm^3

reinforced epoxy composites with varying weight percentage (0, 1, 3, and 5 wt%) via nanoindentation and nanoscratch technique; the addition of 5 wt% SWCNTs increased the elastic modulus by 75% and hardness by 30%, when compared with the pure epoxy. An improvement by 80% in tensile modulus was obtained when thermoplastic poly(vinyl alcohol) (PVA) was mixed with only 1 wt% CNTs [21]. An increase of 28% in tensile Young's modulus was observed in the rubbery system using 1 wt% functionalized nanotubes, compared with the unreinforced rubbery epoxy [22].

In literature, the indentation size effect (ISE) is reported to occur in various materials during the nanoindentation experiment. For metals, the ISE has been widely investigated and is related to geometrically necessary dislocations [23]. Size effects have been also evidenced in polymers; yet, the current literature is quite sparse to explain the reasons of its origin. However, there are only very few rationales providing explanations for the existence of size effects in polymers [24], including higher gradient based models [25–28], change in the material properties through depth [29, 30], surface roughness [31, 32], friction, and adhesion [33]. Characterization of various forms of carbon materials and specifically is conducted to determine the vibrational modes of CNTs and their composites (structural, electronic and phonon properties of CNTs concerning their crystallite size, diameter, defects present, sp^2–sp[3] hybridization, metallic/semiconducting behavior) [34–37].

Recently, the viscoelastic and creep behavior of CNT-based composites gained momentum toward using them for damping applications. Zhou et al. [38] utilized uniaxial tensile test to measure the loss factor of nanocomposites based on SWCNTs. Alternatively, Suher et al. [39] utilized direct viscoelastic shear mode of CNT-epoxy composite thin films to characterize the complex compliance and material loss factor. The investigators reported a 1,400% increase in loss factor (damping ratio) of the baseline epoxy by adding 50% CNTs by volume. Long-term viscoelastic/viscoplastic behavior of CNT-based composites was investigated by Zhang et al. [40], using uniaxial tensile tests; it was demonstrated that SWCNTs additives in low weight fractions (0.1%–0.25%) are effective in limiting the load induced re-orientation of the epoxy chain, resulting in significant decrease of creep response.

The scope of this work is the synthesis and evaluation of mechanical integrity of CNT-based polymer composites using nanoindentation and nanoscratch techniques, to reveal the deformation mechanisms and nanomechanical properties; the variation of polymer matrix material is investigated, together with possible interphase properties (concetration, matrix) effect on the results.

MATERIALS AND METHODS

Materials

Two thermoset resins, a thermoplastic polymer and an elstomer resin were used to produce composites by addition of several varying percentages of two different types of (MWCNTs) (MW-1, MW-2, range 0–7 wt%) and one type of SWCNTs (SW-1, range 0–5 wt%) and were purchased from Cheap Tubes. Their characteristics are reported in Table 1.

Preparation of Thermoset Henkel Resin (Hysol EA-9360 Resin and Crosslinker)

Henkel (Hysol EA-9360 Part A) is off-white viscous paste, with a density of 1.18 g/cm^3 (high peel strength, excellent static stress durability, and room temperature cure). Henkel (Hysol EA-9360 Part B) is a blue paste, with a density of 1 g/cm^3. The mixing ratio of resin and crosslinker is 100:43 by weight. The chemical compositions of the Henkel resin and crosslinker are given below (Table 2).

Method of preparation of Henkel/MWCNTs: Resin, crosslinker, and MW-2 were thoroughly mixed in specific ratio with mechanical stirring (20,000 RPM for 2 min); the composite mixture was then degassed in low vacuum. Before the onset of polymerization, the polymer was set into the mold. Chemical reaction between resin and crosslinker resulted in exothermic reaction. Handling strength for these composite occurred in 24 h (when temperature > 25°C) and complete curing was achieved after 5–7 days at 25°C. For faster curing, the molds were kept in the oven at 90°C for 1 h or 70°C for 4 h. Samples were prepared with four different MW-2 concentrations: 0.8, 3, 5, and 7 wt%.

Preparation of Thermoset ER (Epilox)

Resin (T 19-36/700) is a commercially modified, colorless, low viscosity (650–750 mPa s at 25°C) (ER) with reduced crystallization tendency having density 1.14 g/cm^3. Its main components are Bisphenol A (30%–60%), Crystalline silica (quartz) (1%–10%), Glycidyl ether (1%–10%), and Inert fillers (10%–60 %). Hardener (H 10–31) is a liquid, colorless, low viscosity (400–600 mPa s) modified cycloaliphatic polyamine epoxide adduct having density 1 g/cm^3.

 DOI 10.1002/pc

TABLE 2. The chemical composition of the Henkel (resin and crosslinker).

Henkel resin hysol (EA-9360) Resin	Chemical composition (wt%)	Crosslinker	
Epoxy resin proprietary	30–60	Piperazine derivative proprietary	30–60
Polyfunctional epoxy resin proprietary	10–30	Butadiene-acrylonitrile copolymer	10–30
Synthetic rubber proprietary	10–30	Silica amorphous (fumed)	5–10
Glass spheres proprietary	5–10	Benzyl alcohol	5–10
Filler proprietary	1–5	Cycloaliphatic amine proprietary	5–10
Substituted silane proprietary	1–5	Phenol	1–5
		Diethylene glycol Di-(3-aminopropyl)ether	1–5
		Substituted piperazine proprietary	1–5

Method of preparation of Epilox/MWCNTs: Samples preparation was performed as in the previous case using MW-1 in concentrations ranging from 2 to 7 wt%.

Preparation of Poly(vinyl butyral)

Poly(vinyl butyral) (PVB) is a resin usually used for applications that require strong binding, optical clarity, adhesion to many surfaces, toughness, and flexibility. It is prepared from polyvinyl alcohol by reaction with butyraldehyde. The IUPAC name of the polymer is poly[(2-propyl-1,3-dioxane-4,6-diyl) methylene]; it is in white powder form with specific gravity 1.0830 g/cm^3.

Method of preparation of PVB/MWCNTs: In preparation of MW-2–PVB (Butvar B-98, Sigma Aldrich) polymer composites, Ethanol (Carlo Erba), and 1-Butanol (Sigma-Aldrich) solvents were used with vigorous stirring and sonication; degassing was important for eliminating the entrapped solvent gas bubbles under vacuum. The composite was placed in oven at 70°C for curing. Samples were prepared with four different MW-2 concentrations: 0.5%, 1%, 3%, and 5%.

Preparation of Polydimethylsiloxane

The resin was the commercially available Silicon Elastomer Sylgard 184 (Dow corning), a silicon based clear colorless low viscous liquid having specific gravity 1.11 g/cm^3. It is chemically stable and not forming hazardous polymerization. After polymerization and crosslinking, polydimethylsiloxane (PDMS) samples revealed an external hydrophobic surface.

Method of preparation of PDMS/M-SWCNTs: The mixing ratio of base and curing agent was 1:1 by weight and curing time for the composite was 48 h at 25°C. Composites were prepared with ten different contents of MW-2: 0.1%, 0.2%, 0.3%, 0.4%, 0.5%, 1%, 1.5%, 2%, 2.5%, and 3% and seven concentrations of SWCNTs: 0.1%, 0.2%, 0.5%, 1%, 3%, 4%, and 5%.

FE-SEM and Energy Dispersive X-Ray Spectroscopy

Sample morphology was investigated by a scanning field emission electron microscope (FE-SEM, Zeiss Supra 40), connected to an Energy Dispersive X-ray Spectroscopy (Oxford Inca Energy 450), used to determine the average elemental composition, in particular the presence of noncarbon elements.

Nanoindentation and Nanoscratch Testing

Nanoindentation testing was performed using Hysitron TriboLab® Nanomechanical Test Instrument, which allows the application of loads from 1 μN to 30 mN and records the displacement as a function of applied loads with a high load resolution (1 nN) and a high displacement resolution (0.04 nm). The TriboLab® used in this study is equipped with a Scanning Probe Microscope (SPM), in which a sharp probe tip moves in a raster scan pattern across a sample surface using a three-axis piezo positioner. In all nanoindentation tests, a total of 10 indents are averaged to determine the mean hardness $(H)$and elastic modulus(E)values for statistical purposes, with a spacing of 50 μm, in a clean area environment with 45% humidity and 23°C ambient temperature. To operate under closed loop load or displacement control, feedback control option was used. All nanoindentation measurements have been performed with the standard three-sided pyramidal Berkovich probe, with an average radius of curvature of about 100 nm [41]. Nanoscratch testing is a versatile tool for analysis of the mechanical properties of thin films and bulk materials [42]. The scratch tests performed in this work included three main segments. First, a pre-scratch scan under a very small load (1 μN) was performed. Then, the indenter scrapes the sample under a certain force and a scratch was generated. In the case of creep experiment, loading and unloading times were identical (10 s), while creep time was set to 100 s (40 and 3 s for conventional nanoindentation testing, respectively). Concerning nanoscratch, the lateral displacement was set to 10 μm.

Based on the half-space elastic deformation theory, H and E values can be extracted from the experimental data (load displacement curves) using the Oliver-Pharr (O&P) method [43, 44]. The derived expressions for calculating the elastic modulus from indentation experiments are based on Sneddon's [45] elastic contact theory:

$$E_r = \frac{S\sqrt{\pi}}{2\beta\sqrt{A_c}} \tag{1}$$

where S is the unloading stiffness (initial slope of the unloading load–displacement curve at the maximum

displacement of penetration (or peak load)), A_c is the projected contact area between the tip and the substrate and β is a constant that depends on the geometry of the indenter (β = 1.167 for Berkovich tip [43, 44]). Conventional nanoindentation hardness refers to the mean contact pressure; this hardness, which is the contact hardness (H_c)is actually dependent upon the geometry of the indenter (*Eqs. 2–4*).

$$H_c = F/A \tag{2}$$

where,

$$A(h_c) = 24,5h_c^2 + a_1 h_c + a_{1/2} h_c^{1/2} + \ldots + a_{1/16} h_c^{1/16} \tag{3}$$

and

$$h_c = h_m - \varepsilon \frac{P_m}{S_m} \tag{4}$$

where h_m is the total penetration displacement of the indenter at peak load, P_m is the peak load at the indenter displacement h_m, and ε is an indenter geometry constant, equal to 0.75 for Berkovich indenter [43–46]. Before indentation, the area function of the indenter tip was calibrated in a fused silica, a standard material for this purpose [47, 48].

RESULTS AND DISCUSSION

Structural Characterization

FE-SEM images are illustrated in Fig. 1. The impurities [49, 50] have been determined by EDX: Ni 1.87%, Fe 0.56%, 0.21 Cl, and S 0.02% in case of MW-1 and Co 1.1%, Cl 1.0%, S 0.3%, Al 0.2% in case of MW-2.

Nanomechanical Characterization

The hardness and the elastic modulus as a function of displacement and the plots of the maximum applied force versus contact depth for all samples are presented in Figs. 2–6. Hardness and elastic modulus values of Epilox MW-1 samples were found to deviate at surface region (∼0–200 nm), probably due to roundness of the tip and ISE, tending to reach a constant value of 0.2 and 4 GPa, respectively. The same observation can be drawn for Henkel MW-2, PVB MW-2, and PDMS with MWCNTs and SWCNTs samples. The reasons for the wide range in hardness and modulus values obtained from these nanoindentation measurements are currently unknown, but it is likely due to a combination of factors, e.g., graded surface structure due to CNTs concentration, adhesive forces between the tip and the sample, etc. Due to the very low contact area between the indenter and the sample, very high stresses can be developed. The high hydrostatic pressure exerted by the surrounding material allows significant deformation at room temperature when conventional mechanical testing only leads to fracture. It is revealed that some materials exhibit ISE, which shows an increase in hardness with decreasing applied load [51]. Apparently, the existence of ISE may hamper the accurate measurement of hardness value, and is attributed to experimental artifact, a consequence of inadequate measurement capability or presence of oxides (for the case of metallic materials) on the surface [52]. ISE is reported to be strongly dependent on polymeric material structure after nanoindentation experiments in different types of polymers [53, 54].

Enhanced nanomechanical properties for Henkel MW-2 (Fig. 3a and b) are revealed for the case of 3% MW-2, while samples with 7% MW-2 exhibit low *H* (for depth below 250 nm) and *E* values. No significant differences are observed between 0% and 0.8% MW-2 (same for 5% and 7% MW-2). Concerning Epilox MW-1 samples (Fig. 6a and b), enhanced nanomechanical properties are revealed for the case of 2% MW-1, while sample with 7% MW-1 exhibit low *H* (for depth below 250 nm) and *E* values. Increased nanomechanical properties (*H*, *E*) are observed in the case of 1% MW-2 addition in the PVB (Fig. 7a and b), while specimens with 5% MW-2 exhibit decreasing *H* and *E* values (for depth below 100 nm). As for PDMS with MWCNTs (Fig. 6a and b), the main enhancement of hardness is evidenced at concentrations of 0.2%–0.4% MW-2 and elastic modulus values are increased for samples with 0.2%, 0.3%, and 0.5% MW-2. The specimen filled with 0.5% SW-1 exhibited increased hardness; the lowest values of elastic modulus are observed for pure PDMS, as shown in Fig. 7a and b. The elastic modulus values for the composites with SW-1 concentrations varying from 0.1% to 5% did not reveal significant deviation. In Figs. 3–7, the intermediate levels of CNTs filling with optimum in nanomechanical properties are noted with dashed circle, where applicable. At low concentration (PVBC1.0) the good interfacial interaction leads to the stretching of the PVB molecules attached to the CNTs. A tube–tube slip in individual CNTs present in clusters also occurs. As CNT concentration increases, there is a large increase in the stiffness of the system, which results in reducing the energy dissipated during the experiment; however, there is more tube–tube slip in the system at higher concentrations, as percolation, coupled to a better dispersion leads to a higher contact surface among CNTs. The mechanical properties are reported to deteriorate with an increase in CNT content, after a threshold concentration, a fact that is tentatively attributed to extensive tube–tube slip mechanism. At concentrations higher than percolation threshold, particle contacts are not only unavoidable, due to statistical considerations, but also due to the sticky inter-particles potential, they give a rise to larger agglomerates acting as mechanical defects for the resulting composite [55–61].

In Figs. 2–6c, the maximum applied load versus contact depth for all composites is presented. The empirical equation is used for describing the ISE in the Meyer's

 DOI 10.1002/pc

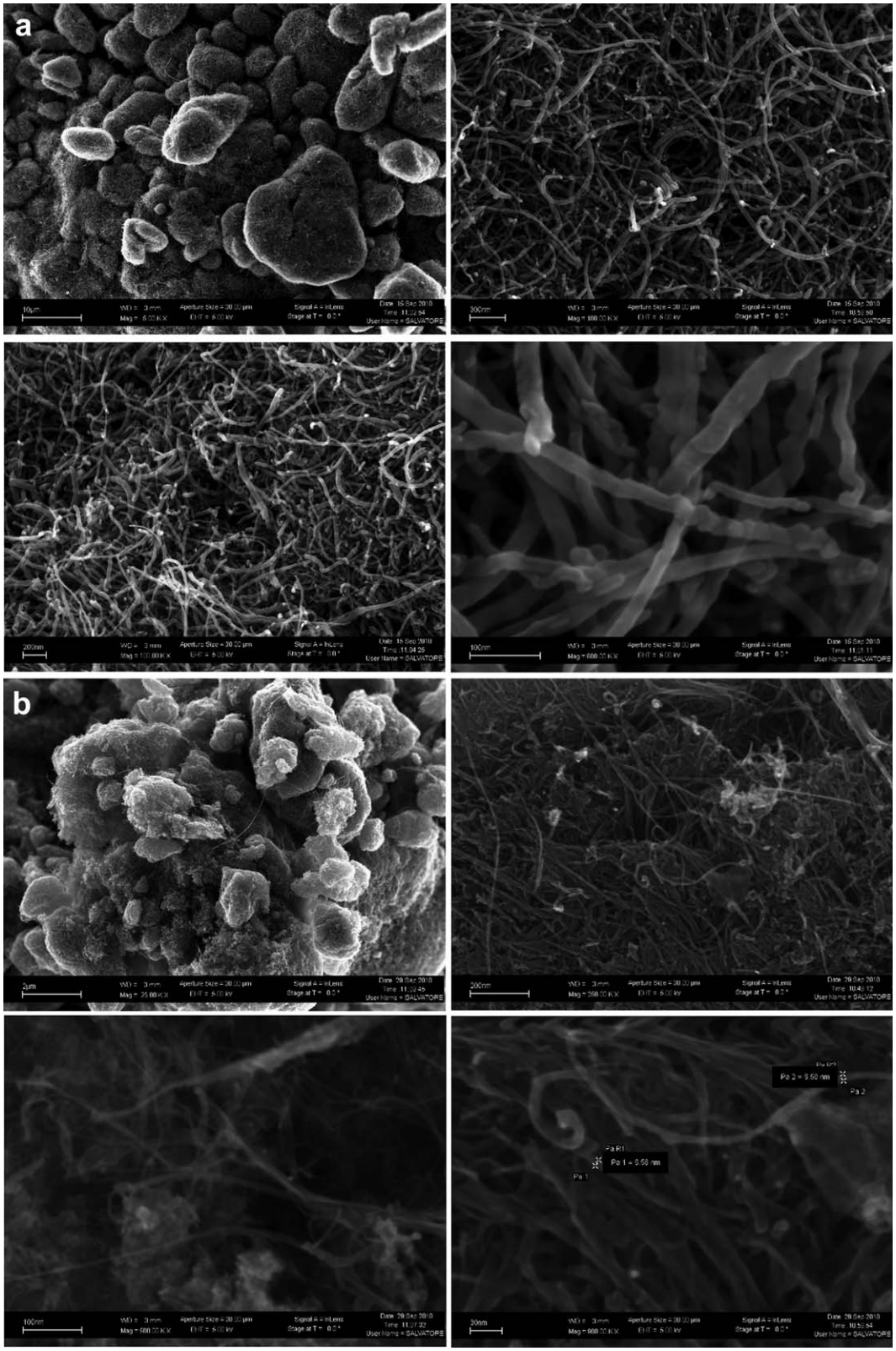

FIG. 1. Scanning electron microscopy (FE-SEM) images of (a) MW-1, (b) MW-2, (c) Epilox–7% SW-1, (d) Henkel–5% MW-2, and (e) PVB–5% MW-2.

law [62–64], which uses a correlation technique between the applied indentation test load and the resultant indentation size using a simple power law, $P_{max} = Ch_c^n$, where c and n are constants derived directly from curve fitting of the experimental data. Compared with the definition of the apparent hardness, no ISE would be

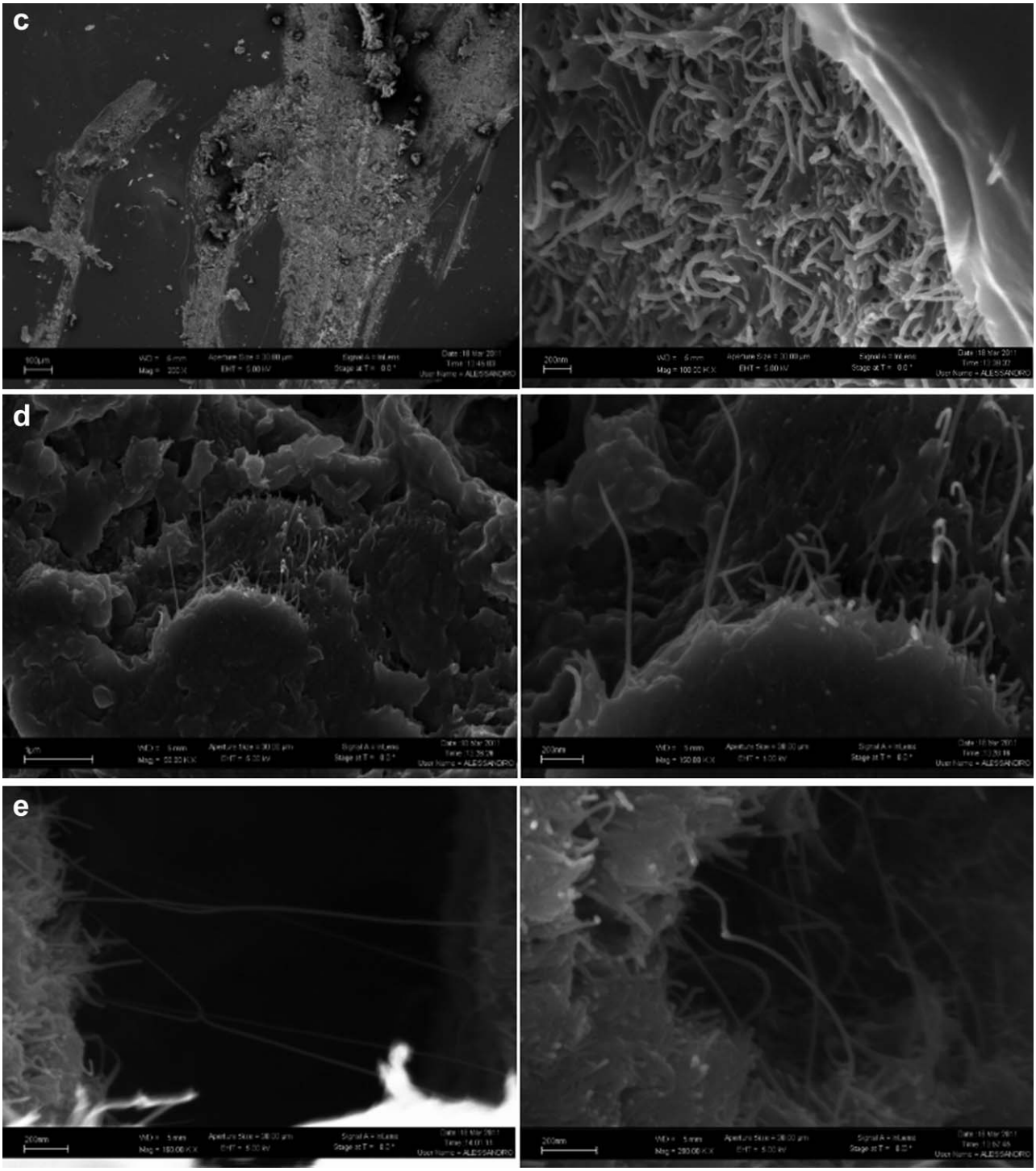

FIG. 1. (Continued)

observed for $n = 2$. The calculated constants are presented in Table 3.

Wear Analysis-Deformation Mechanism (Pile-up/Sink-in)

An important feature of indentation experiments is that the material around the contact area tends to deform upward (pile-up) or downward (sink-in) with respect to the indented surface plane. The occurrence of such pile-up and sink-in patterns is usually interpreted in terms of the strain-hardening behavior of the indented material [65–68]. According to these studies the surface around indents tends to pile up against the indenter in cases where the indented sample is heavily prestrained with only little reserves for further work-hardening or has generally a low strain-hardening potential. On the other hand

 DOI 10.1002/pc

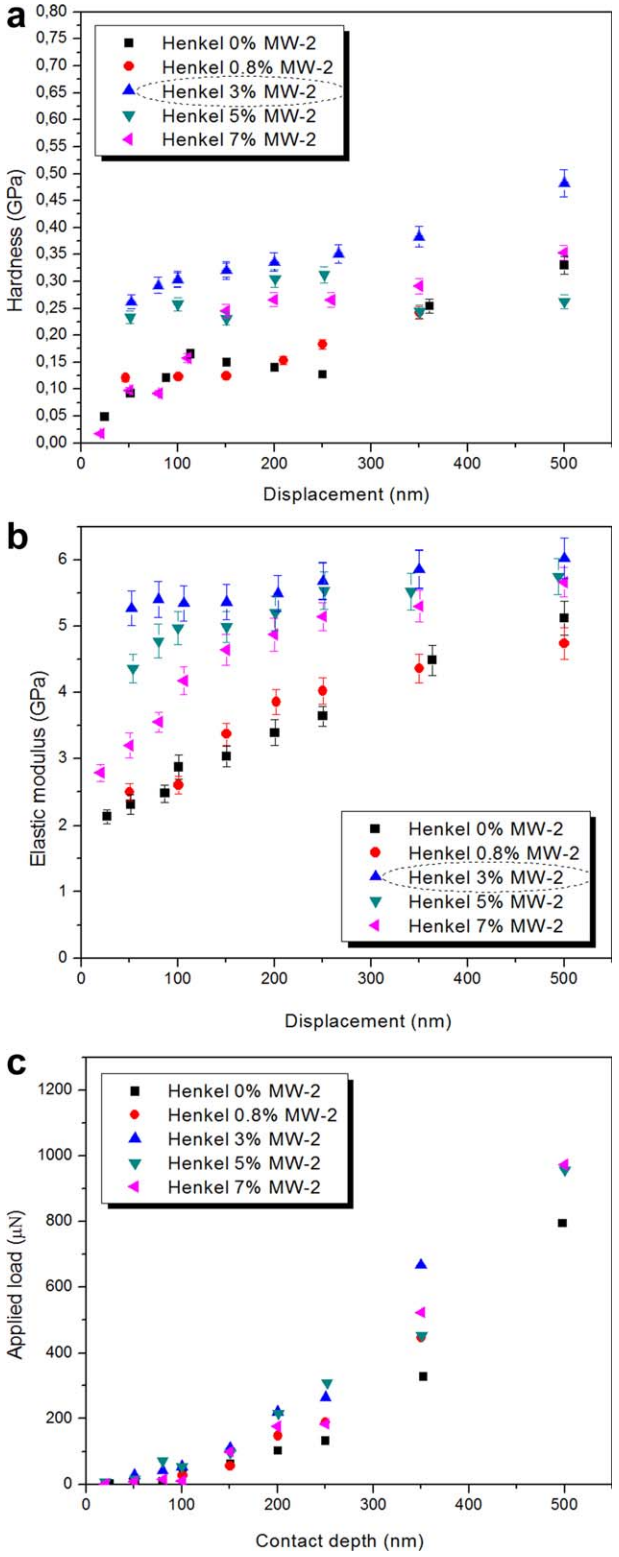

FIG. 2. (a) Hardness, (b) elastic modulus as a function of displacement, and (c) plots of P_{max} versus contact depth according to the Meyer's law for Henkel MW-2 samples. [Color figure can be viewed in the online issue, which is available at wileyonlinelibrary.com.]

when the sample has a high strain-hardening potential, the surface around indents tends to sink in. The reason for this relationship between strain hardening behavior and displacement patterns is plausible: well-annealed soft metals which exhibit a high strain-hardening rate tend to show far off field plasticity yielding a large lateral smear out of the plastic out-of-plane displacement field. Good knowledge of the deformation zone around an indent is of

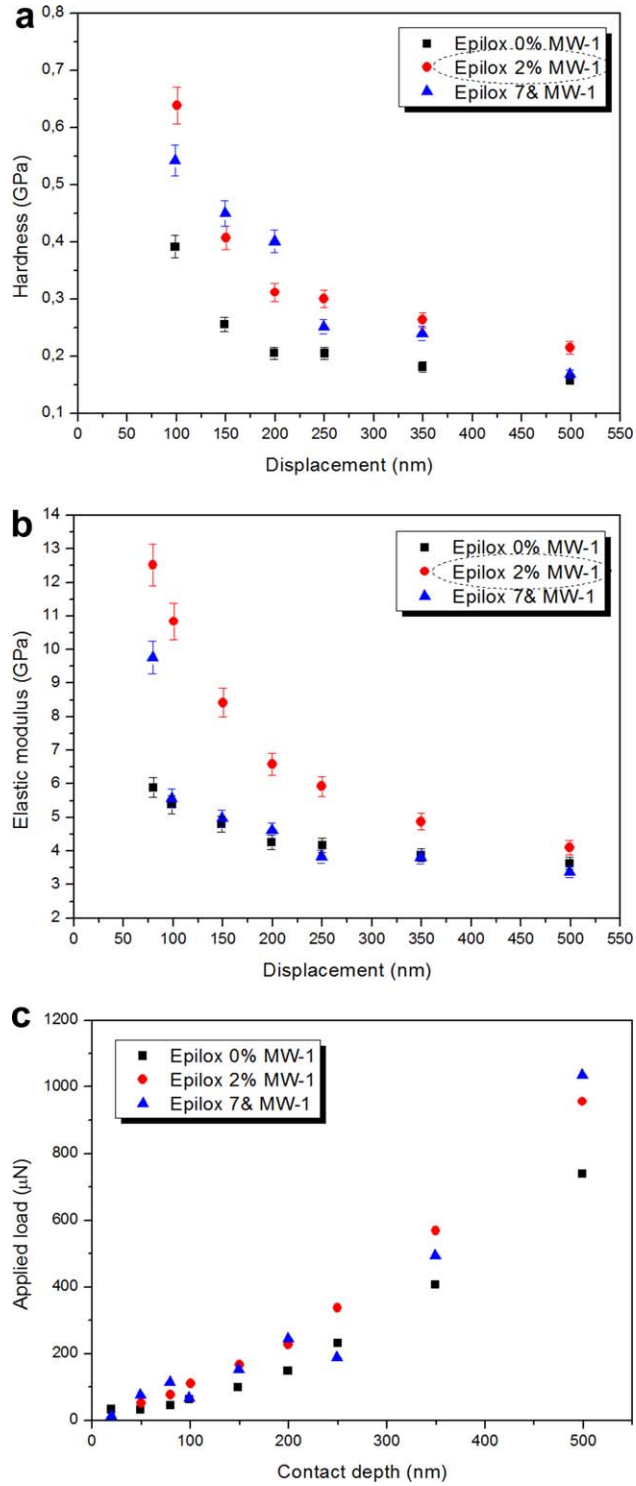

FIG. 3. (a) Hardness, (b) elastic modulus as a function of displacement, and (c) plots of P_{max} versus contact depth according to the Meyer's law for Epilox MW-1 samples. [Color figure can be viewed in the online issue, which is available at wileyonlinelibrary.com.]

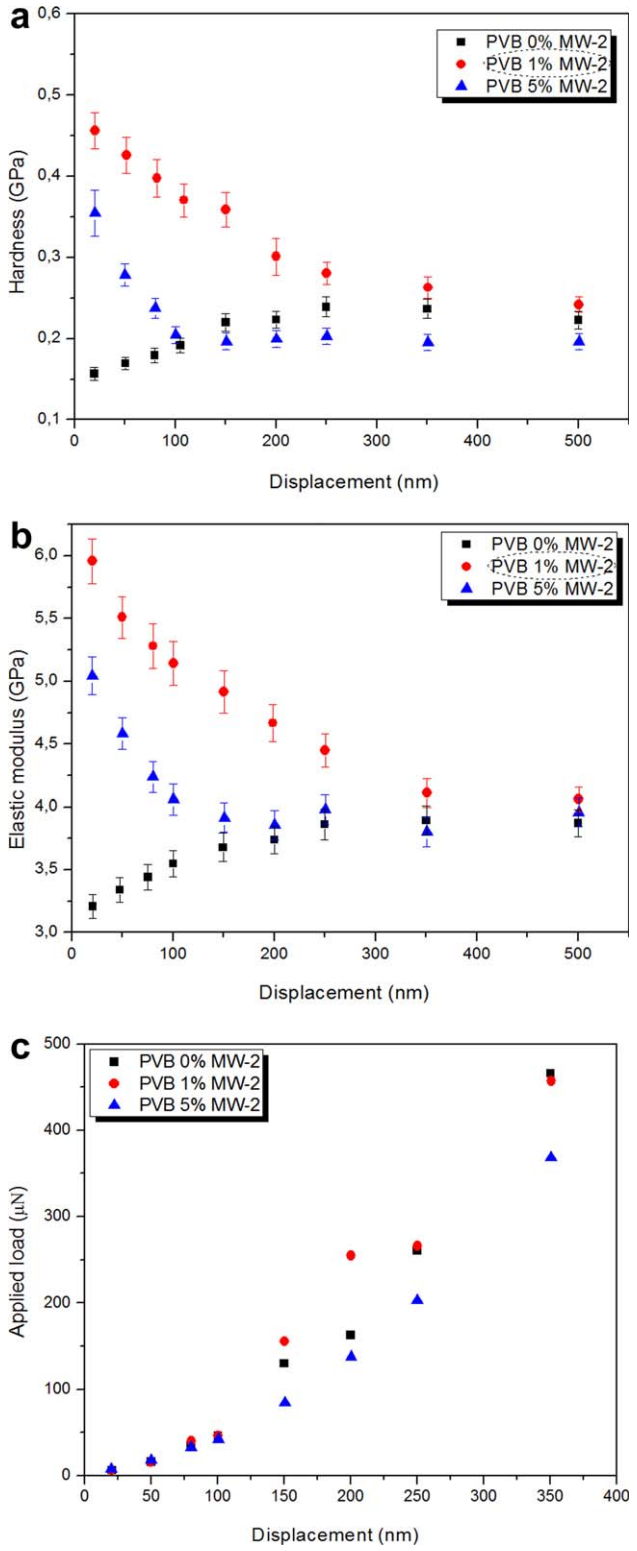

FIG. 4. (a) Hardness, (b) elastic modulus as a function of displacement, and (c) plots of P_{max} versus contact depth according to the Meyer's law for PVB MW-2 samples. [Color figure can be viewed in the online issue, which is available at wileyonlinelibrary.com.]

considerable importance for nanoindentation testing because the shape of the out-of-plane displacement zone determines the actual contact area between the indenter and the specimen. Sink-in patterns reduce and pile-up patterns increase the contact area. These differences in the surface deformation mode affect the quantitative analysis of the hardness measurements. Not taking the piling-up or sinking-in into account in micro- and nanoindentation

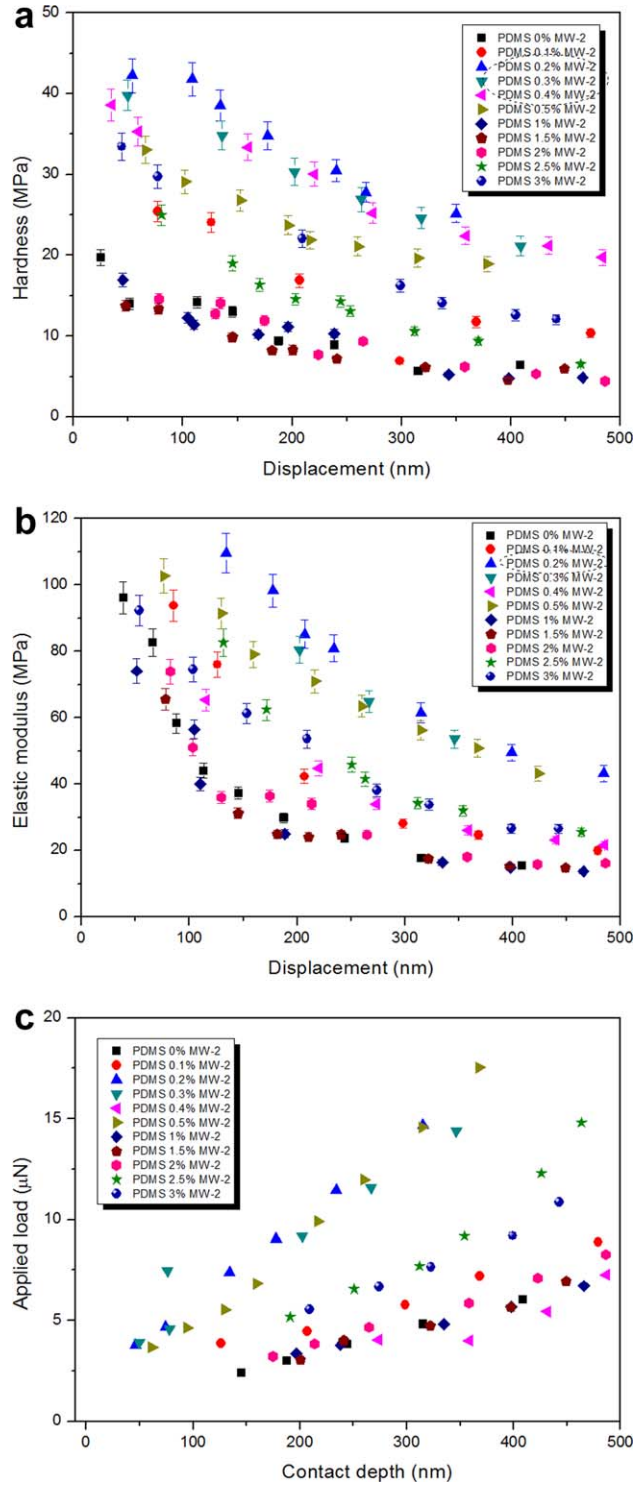

FIG. 5. (a) Hardness, (b) elastic modulus as a function of displacement, and (c) plots of P_{max} versus contact depth according to the Meyer's law for PDMS MW-2 samples. [Color figure can be viewed in the online issue, which is available at wileyonlinelibrary.com.]

DOI 10.1002/pc

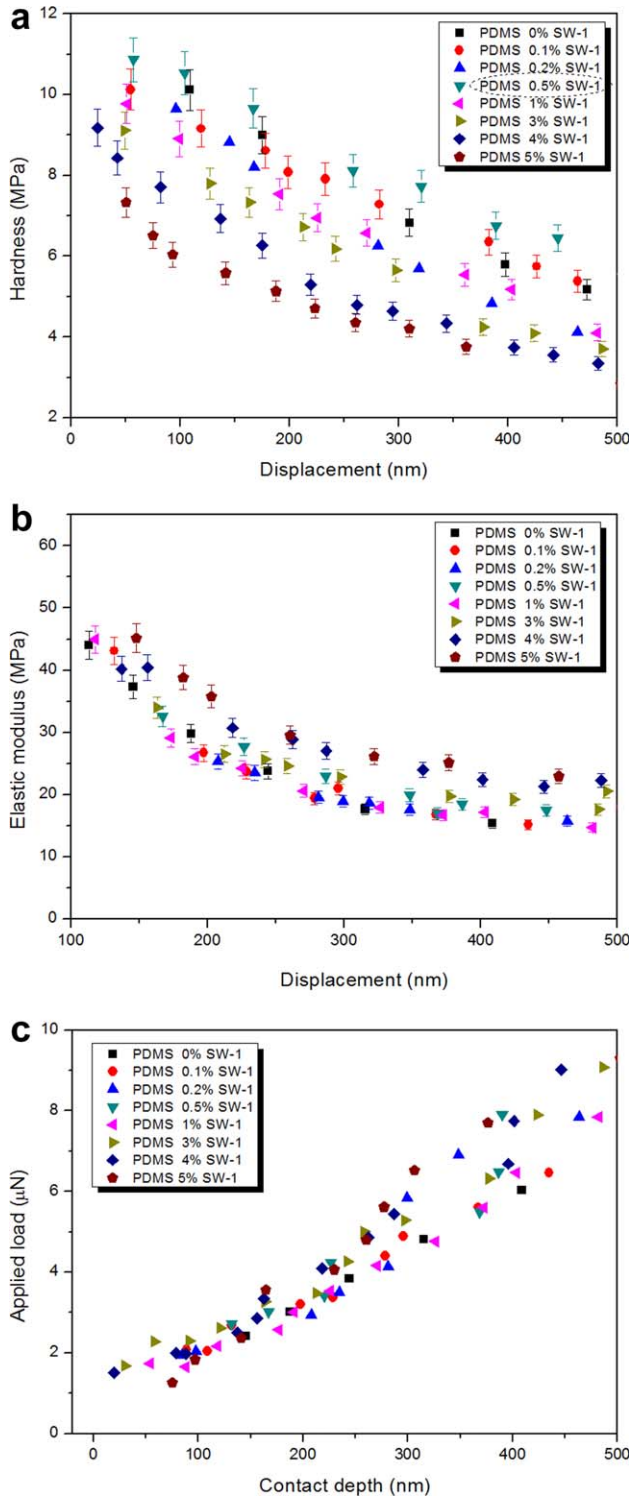

FIG. 6. (a) Hardness, (b) elastic modulus as a function of displacement, and (c) plots of P_{max} versus contact depth according to the Meyer's law for PDMS SW-1 samples. [Color figure can be viewed in the online issue, which is available at wileyonlinelibrary.com.]

hardness tests can result in significant errors when extracting hardness values from the experimental data [65, 66].

The presence of creep during nanoindentation has an effect on pile-up, which results in incorrect measurement of the material properties. Fischer-Cripps observed this behavior, in case where the measured elastic modulus was much less than expected [69]. Rar et al. [70]

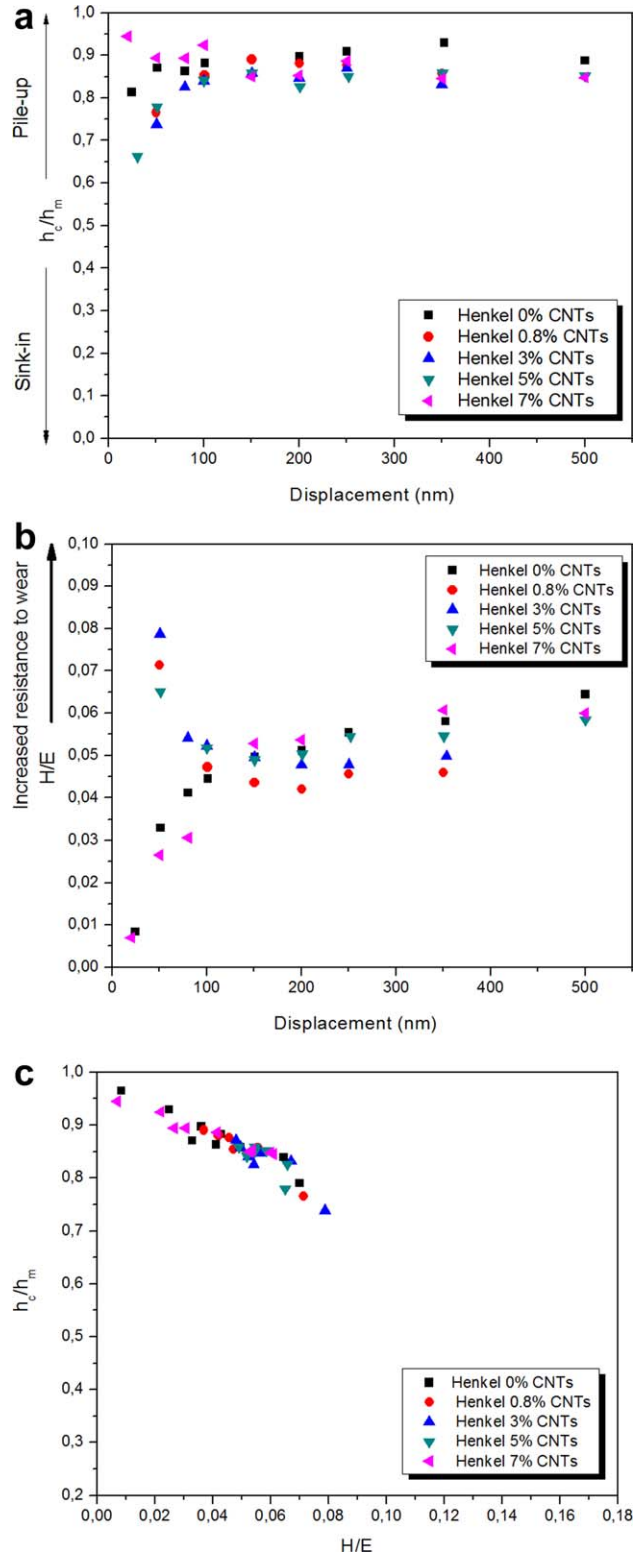

FIG. 7. (a) Normalized pile-up/sink-in height h_c/h_m versus displacement, (b) wear ratio (H/E) versus displacement, and (c) H/E ratio versus normalized pile-up/sink-in height h_c/h_m of Henkel MW-2 samples. [Color figure can be viewed in the online issue, which is available at wileyonlinelibrary.com.]

TABLE 3. Meyer's law and constant for all examined samples.

CNT content (%)	0	0.1	0.2	0.3	0.4	0.5	0.8	1	1.5	2	2.5	3	4	5	7
Epilox MW-1	2.13									1.46					1.84
Henkel MW-2	3.27						2.26					2.17		1.58	2.02
PVB MW-2	1.68							1.29						1.70	
PDMS MW-2	1.16	1.09	0.93	0.85	0.64	1.03		1.16	1.21	1.23	1.12	0.97			
PDMS SW-1	1.16	1.25	1.13			0.94		1.02			1.26		1.27		0.99

observed that the same material when allowed to creep for a long duration produced a higher value of pile-up/sink-in indicating a switch from an initial elastic sink-in to a plastic pile-up. In Figs. 7–11a and b, the normalized pile-up/sink-in height h_c/h_m and the normalized hardness H/E are plotted vs. displacement. In Figs. 7–11c, the normalized pile-up/sink-in height h_c/h_m vs. the normalized hardness is plotted, following the almost linear observed in literature [42, 71]. Higher stresses are expected in high H/E, hard materials, and high stress concentrations develop toward the indenter tip, whereas in case of low H/E, soft materials, the stresses are lower and are distributed more evenly across the cross-section of the material [70]. Rate sensitive materials experience less pile-up compared to rate insensitive materials due strain hardening. Cheng and Cheng [72] reported a 22% pile-up for a work hardening exponent. This is consistent with the fact that when h_c/h_m approaches 1 for small H/E, deformation is intimately dominated by pile-up [73, 74]. On the other hand when h_c/h_m approaches 0 for large H/E, it corresponds to purely elastic deformation and is apparently dominated by sink-in in a manner prescribed by Hertzian contact mechanics [75].

The ratio of hardness/elastic modulus (H/E) is of significant interest in tribology; this ratio is indicative of the good wear resistance in a disparate range of materials [76, 77]: ceramic, metallic and polymeric (e.g., c-BN, tool steel and nylon, respectively), which are equally effective in resisting attrition for their particular intended application. In Figs. 7–11, the change of H/E slope reveals the strengthening of nanocomposites with increasing CNTs concentration (more resistant to wear). In Fig. 9a at low displacement ranges, composites with 0% and 7% CNTs exhibit a rather sink-in deformation, which is further switched to pile-up (at ~100 nm of displacement). Henkel composite with 7% MW-2 revealed higher resistance to wear (H/E) than that of other filler concentrations; the same behavior is presented in the case of Epilox 7% MW-1. Also, it is evident that the PDMS filled with 0.4% MW-2 and 0.1% SW-1 exhibit enhanced wear resistance, as illustrated in Figs. 10 and 11b. The deformation mechanism (h_c/h_m) for almost all nanocomposites exhibit a linear trend, as presented in Figs. 7–11c. However, the deformation mechanism of PVB during nanoindentation changes significantly with the addition of MW-2, with respect to the H/E ratio. In Fig. 12, the H/E ratio versus normalized pile-up/sink-in height h_c/h_m of all examined composites is presented.

Analysis Beyond Nanomechanical Properties

Nanotribological Properties. In Fig. 13, coefficients of friction for Epilox composites are presented, as representative for all samples. In the initial stages the CoF is higher; afterward, it reaches a plateau that represents the effective value. For Epilox MW-1 nanocomposites, the addition of 2% MW-1 increases the CoF compared to plain polymer matrix, while 7% MW-1 sample exhibits lower CoF, which could imply sliding of nanotubes inside the polymer matrix. The behavior in case of Henkel MW-2 nanocomposites is almost identical; the concentration of 5% MW-2 is a threshold, beyond which the nanocomposite exhibits lower coefficient of friction. PVB MW-2 nanocomposite exhibits decreased CoF for 5% MW-2, compared with the addition of 1% MW-2 in the polymer matrix.

Creep Investigation. During nanoindentation, the applied load can be controlled at a constant value, whereas the penetration of the indenter tip into the sample surface is continuously recorded. This is often called constant-load indentation creep test, and it has been widely used to study the time-dependent properties of crystalline materials. The nanoindentation creep consists of two stages, transient (primary creep) and steady state (secondary creep) [78]. The stress exponent, n, of the steady-state creep can be derived from the constant load indentation tests [79–83]. In a nanoindentation creep experiment, the tip is pushed into the surface at a constant rate of indentation until a prefixed load or penetration displacement is plausible, then the load is held constant while the indenter continues to creep into the material. With the indenter tip held fixed at that load or displacement, the material beneath the indenter tip continues to deform in time and finally the indenter tip is retracted from the material. Creep within a specimen occurs during the hold time of the loading phase of nanoindentation testing and manifests itself as a change of indentation displacement with the load, kept constant. It is postulated that the stress fields in the material underneath the indenter develop a chemical potential gradient that lead to a thermally activated diffusional flux of atoms moving from below the indenter to the surface and along the interface between the indenter and the specimen, even under an elastic contact [7, 84, 85]. In Fig. 14, the change in depth of indenter as a function of hold time (applied loading rate

 DOI 10.1002/pc

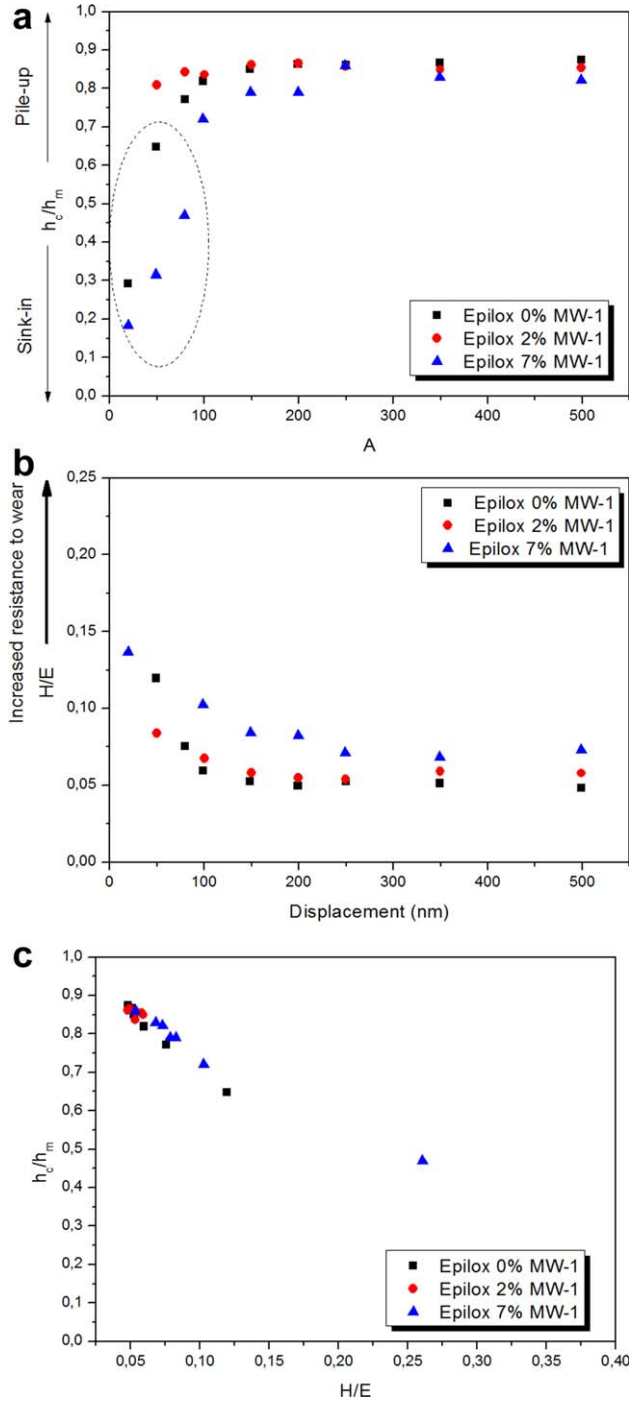

FIG. 8. (a) Normalized pile-up/sink-in height h_c/h_m versus displacement, (b) wear ratio (H/E) versus displacement, and (c) H/E ratio versus normalized pile-up/sink-in height h_c/h_m of Epilox MW-1 samples. [Color figure can be viewed in the online issue, which is available at wileyonlinelibrary.com.]

10 μN/s) for Henkel MW-2, Epilox MW-1, and PVB MW-2 composites is illustrated.

Adhesion Energy. Mechanical properties of surfaces are significant for the comprehension of behavior of adhesive and sliding contacts. Consideration of the adhesion energy at the tip/sample interface is a requisite for determining accurate elastic modulus values of PDMS samples and other soft, elastomeric materials from nanoindentation experiments, as the soft material samples are expected to have significant adhesive forces [86]. A

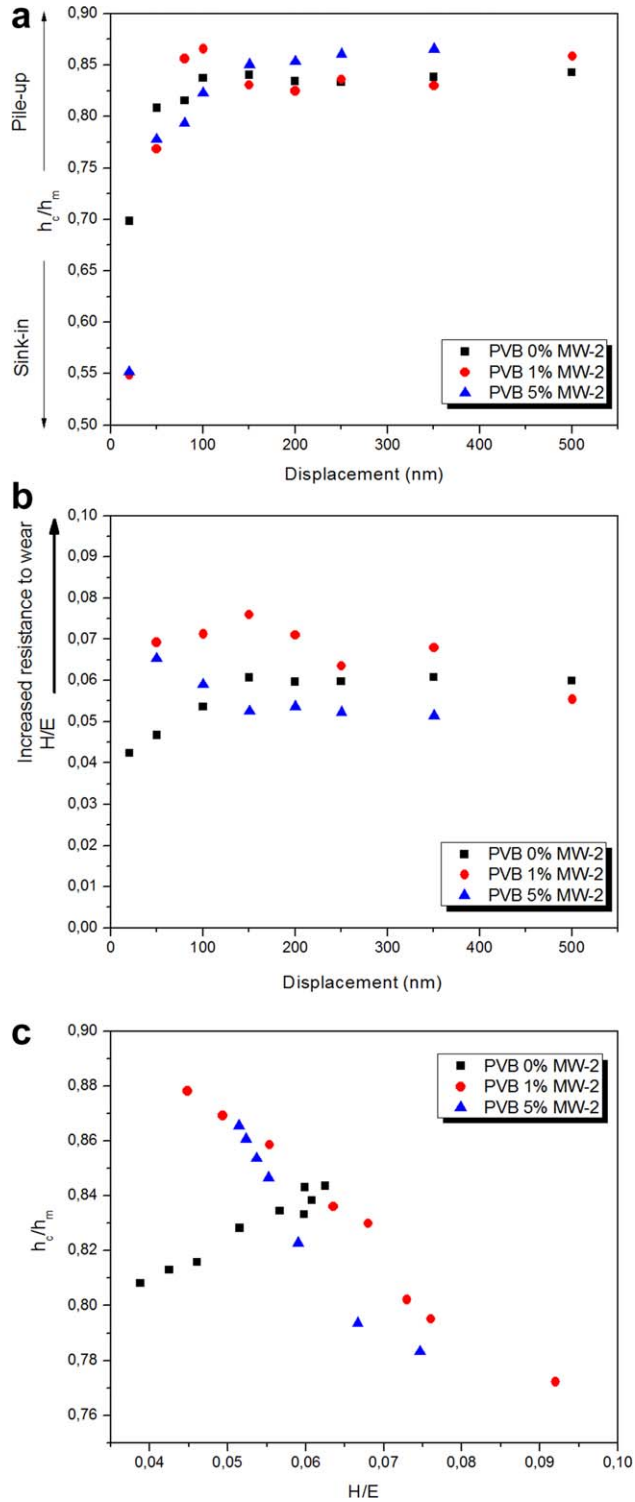

FIG. 9. (a) Normalized pile-up/sink-in height h_c/h_m versus displacement, (b) wear ratio (H/E) versus displacement, and (c) H/E ratio versus normalized pile-up/sink-in height h_c/h_m of PVB MW-2 samples. [Color figure can be viewed in the online issue, which is available at wileyonlinelibrary.com.]

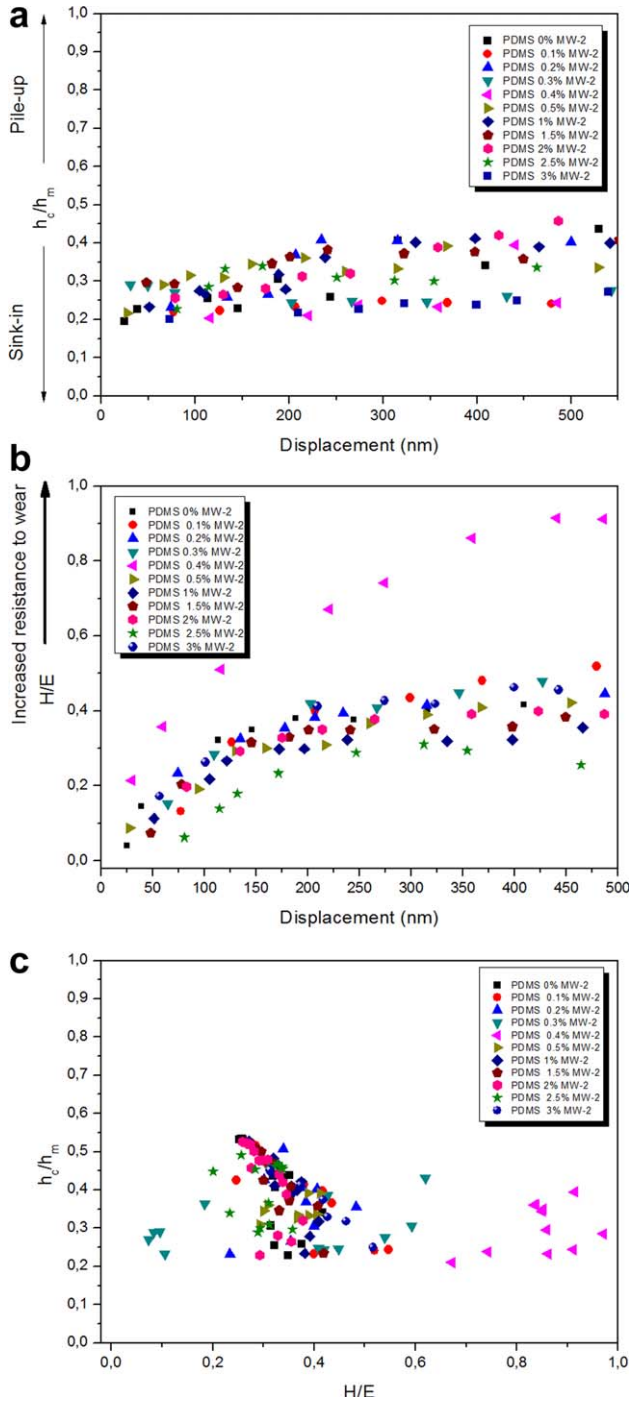

FIG. 10. (a) Normalized pile-up/sink-in height h_c/h_m versus displacement, (b) wear ratio (H/E) versus displacement, and (c) H/E ratio versus normalized pile-up/sink-in height h_c/h_m of PDMS MW-2 samples. [Color figure can be viewed in the online issue, which is available at wileyonlinelibrary.com.]

characteristic nanoindentation adhesion test is comprised of pressing the tip into the patterned sample, followed by unloading it at a constant rate and finally obtaining a distinctive (and often abrupt) pull-off force representing the adhering surfaces. Adhesion is observed in a load-displacement curve as a region of negative load during unloading [87, 88]. The principle of this experiment is to put into contact the diamond probe tip and the flat polymer substrate and determine the maximum pull-force necessary to separate both materials. In each test the tip (100 m radius of diamond probe tip) was brought into contact with the sample surface; if interfacial forces were present, the transducer force became negative and the tip plate

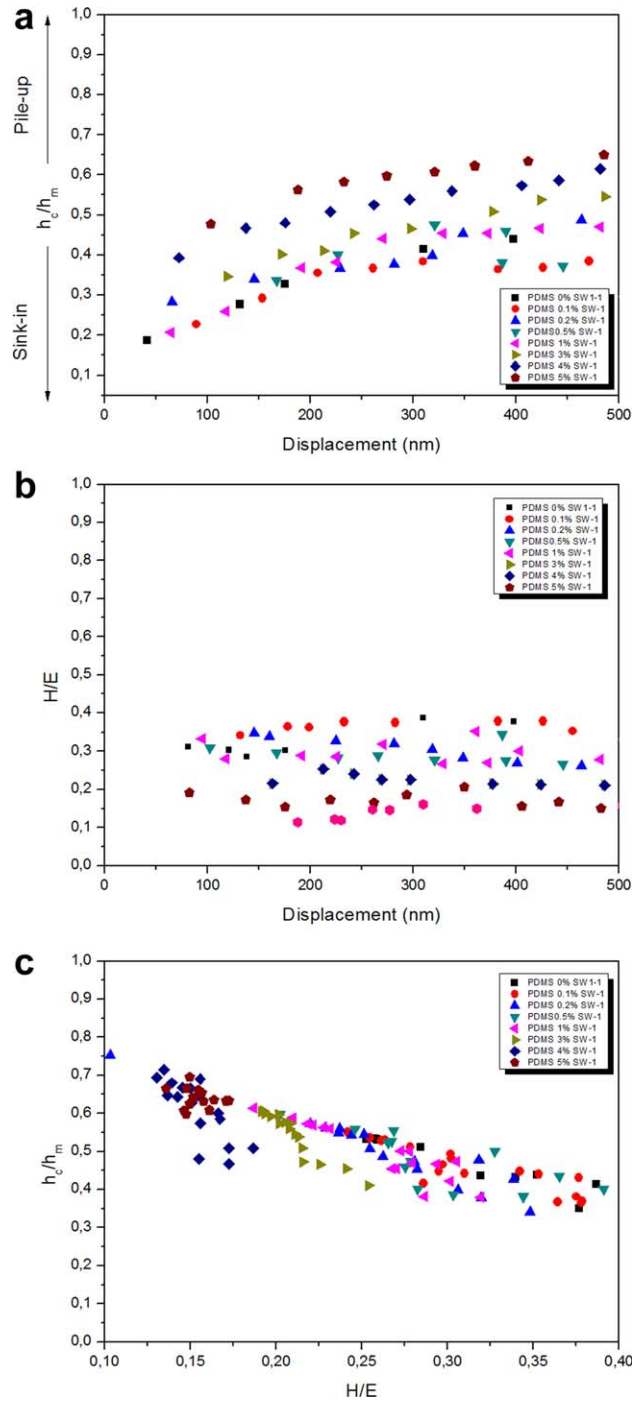

FIG. 11. (a) Normalized pile-up/sink-in height h_c/h_m versus displacement, (b) wear ratio (H/E) versus displacement, and (c) H/E ratio versus normalized pile-up/sink-in height h_c/h_m of PDMS SW-1 samples. [Color figure can be viewed in the online issue, which is available at wileyonlinelibrary.com.]

DOI 10.1002/pc

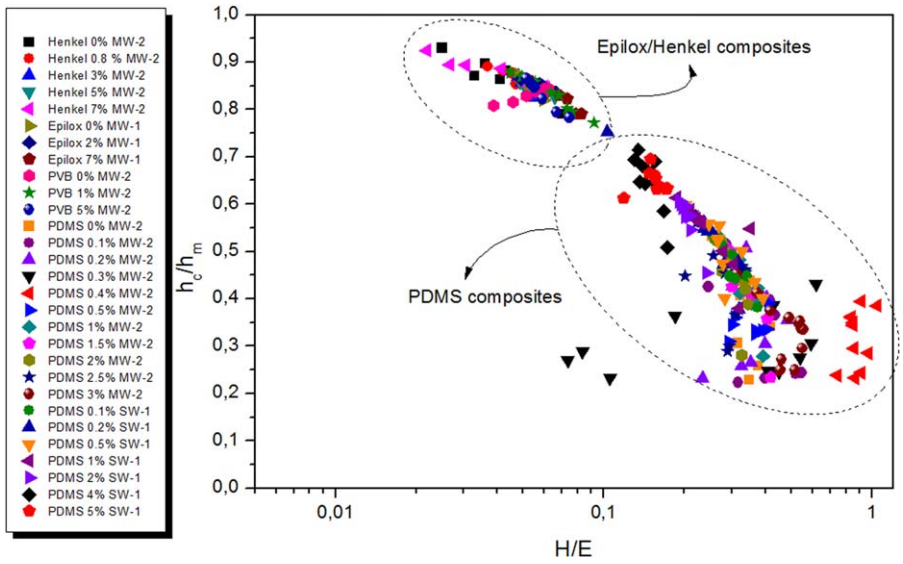

FIG. 12. H/E ratio versus normalized pile-up/sink-in height h_c/h_m of all composites. [Color figure can be viewed in the online issue, which is available at wileyonlinelibrary.com.]

continued to move with the sample until the negative restoring force on the transducer became equal to the adhesive force between the tip and PDMS surface interface. The pull-off adhesion force is determined as the difference between the minimum force value and the zero offset. Three adhesion measurements on surface of each sample were conducted for plain PDMS and PDMS with 5% SW-1concentration to study the effect of CNTs addition on adhesion. Figure 15a and b shows two load-unload curves versus displacement of pure PDMS and PDMS incorporated with 5% SW-1 obtained during the nanoindentation, as the tip approached and retracted from the samples. It is evident that the introduction of CNTs into the polymeric matrix decreases the adhesion force (P_{adh}).

CONCLUSIONS

In this work, the mechanical integrity of various polymeric matrices reinforced with different concentrations of CNTs is analyzed and discussed. The main findings are summarized below:

Instrumented nanoindentation, it is a valuable tool to evaluate both the mechanical and time-dependent properties for epoxies and their nanocomposites filled with MWCNTs and SWCNTs. The addition of CNTs resulted in the improvement of nanomechanical properties for Henkel 3% MW-2, Epilox 2% MW-1, PVB 1% MW-2, PDMS 0.2%–0.5% MW-2 composites, as PDMS 0.5% SW-1 exhibited increased hardness. Higher resistance to wear (H/E) was observed for Henkel 7% MW-2, Epilox 7% MW-1, PDMS 0.4% MW-2, and PDMS 0.1% SW-1.

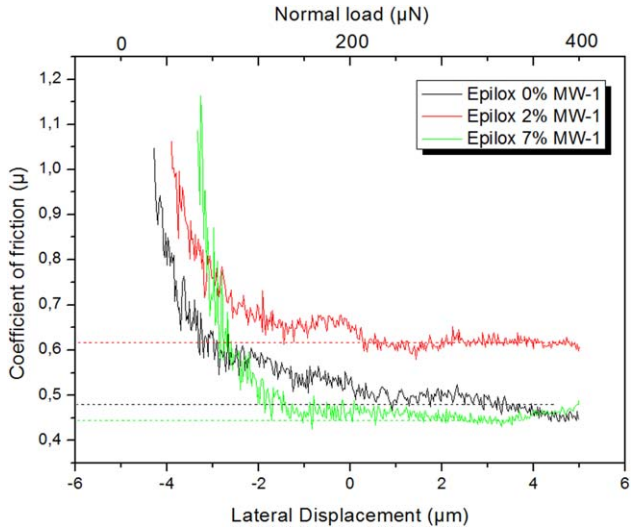

FIG. 13. Coefficients of friction for Epilox nanocomposites. [Color figure can be viewed in the online issue, which is available at wileyonlinelibrary.com.]

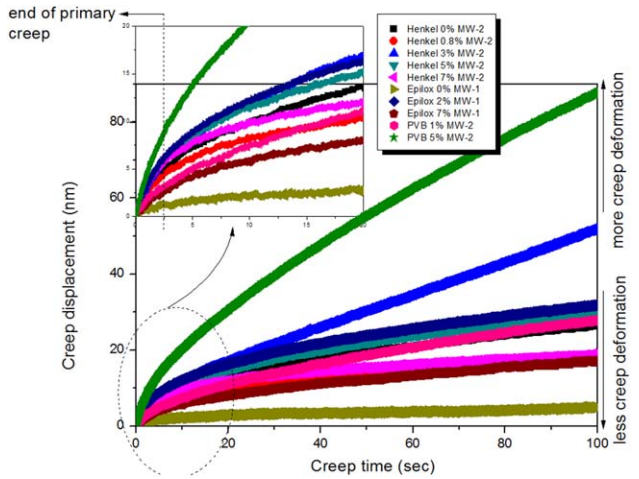

FIG. 14. Change in depth of indenter as a function of hold time (applied loading rate 10 μN/s) for Henkel MW-2, Epilox MW-1, and PVB MW-2 composites. [Color figure can be viewed in the online issue, which is available at wileyonlinelibrary.com.]

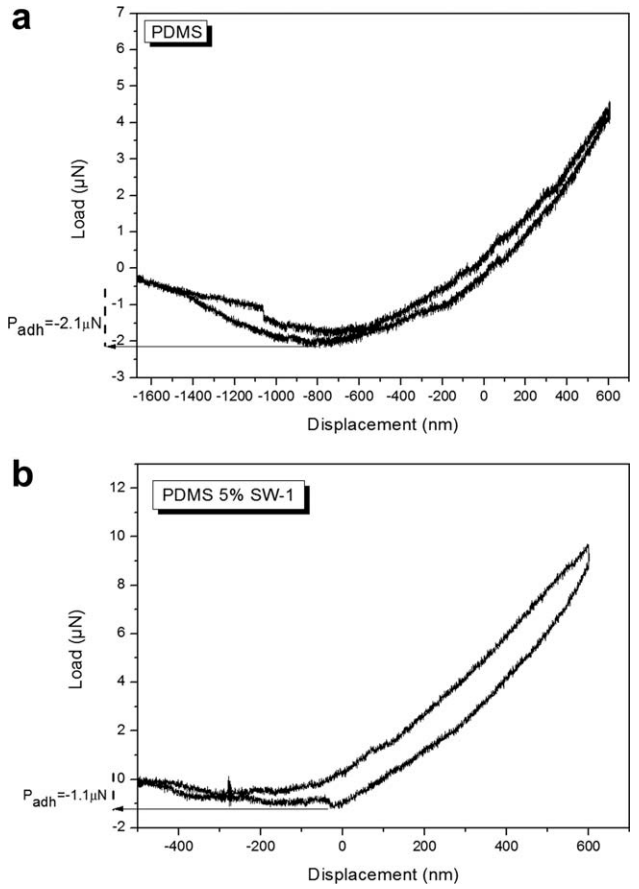

FIG. 15. Load versus displacement as the tip approached and retracted from (a) PDMS and (b) PDMS 5% SW-1.

Nanocomposite samples retained better mechanical properties compared to the neat polymer matrix; however, for each polymer-CNTs system a threshold–concentration was identified, beyond which an obvious deterioration of nanomechanical properties occurs. The introduction of 2% MW-1 into Epilox matrix increased the coefficient of friction in comparison with the pure polymer. The concentration of 5% MW-2 in Henkel and PVB is a threshold, beyond which the nanocomposites exhibited lower coefficient of friction. A decrease in adhesive energy in the case of PDMS filled with 5% SW-1 was revealed, indicating that the adhesive force plays a key role at the nanometer scale in indentation tests.

ACKNOWLEDGMENTS

P.J., M.G., and A.T. acknowledge Salvatore Guastella for his support in performing FE-SEM analysis.

REFERENCES

1. O. Jacobs, W. Xu, B. Schädel, and W. Wu, *Tribol. Lett.*, **23**, 65 (2006).
2. S.R. Bakshi, D. Lahiri, and A. Agarwal, *Int. Mater. Rev.*, **55**, 41 (2010).
3. R.Z. Ma, J. Wu, B.Q. Wei, J. Liang, and D.H. Wu, *J. Mater. Sci.*, **33**, 5243 (1998).
4. B.X. Yang, K.P. Pramoda, G.Q. Xu, and S.H. Goh, *Adv. Funct. Mater.*, **17**, 2062 (2007).
5. Z.Y. Liu, B.L. Xiao, W.G. Wang, and Z.Y. Ma, *Carbon*, **50**, 1843 (2012).
6. Z.Y. Liu, B.L. Xiao, W.G. Wang, and Z.Y. Ma, *Carbon*, **62**, 35 (2013).
7. C.A. Charitidis, E.P. Koumoulos, M. Giorcelli, S. Musso, P. Jagadale, and A. Tagliaferro, *Polym. Compos.*, **34**, 1950 (2013).
8. W.H. Li, X.H. Chen, C.S. Chen, L.S. Xu, Z. Yang, and Y.G. Wang, *Polym. Compos.*, **29**, 972 (2008).
9. A. Selmi, C. Friebel, I. Doghri, and H. Hassis, *Compos. Sci. Technol.*, **67**, 2071 (2007).
10. C.C. Kao and R.J. Young, *J. Mater. Sci.*, **45**, 1425 (2010).
11. C. Bower, R. Rosen, L. Jin, J. Han, and O. Zhou, *Appl. Phys. Lett.*, **74**, 3317 (1999).
12. C.Y. Li and T.W. Chou, *Compos. Sci. Technol.*, **66**, 2409 (2006).
13. L.F. Giraldo, B.L. López, and W. Bostow, *Polym. Eng. Sci.*, **49**, 896 (2009).
14. C. Wang, T. Xue, B. Dong, Z. Wang, and H.L. Li, *Wear*, **265**, 1923 (2008).
15. L.Y. Sun, R.F. Gibson, F. Gordaninejad, and J. Suhr, *Compos. Sci. Technol.*, **69**, 2392 (2009).
16. X. Gong, J. Liu, S. Baskaran, R.D. Voise, and J.S. Young, *Chem. Mater.*, **12**, 1049 (2000).
17. M.S.P. Shaffer and A.H. Windle, *Adv. Mater.*, **11**, 937 (1999).
18. H. Chen, O. Jacobs, W. Wu, G. Rüdiger, and B. Schädel, *Polym. Test.*, **26**, 351 (2007).
19. M.N. dos Santos, C.V. Opelt, F.H. Lafratta, C.M. Lepienski, S.H. Pezzin, and L.A.F. Coelho, *Mater. Sci. Eng. A*, **528**, 4318 (2011).
20. X. Li, H. Gao, W.A. Scrivens, D. Fei, X. Xu, M.A. Sutton, A.P. Reynolds, and M.L. Myrick, *Nanotechnology*, **15**, 1416 (2004).
21. M. Cadek, J.N. Coleman, and V. Barron, *Appl. Phys. Lett.*, **81**, 5123 (2002).
22. L. Liu and H.D. Wagner, *Compos. Sci. Technol.*, **65**, 1861 (2005).
23. W.D. Nix and H. Gao, *J. Mech. Phys. Solids*, **46**, 411 (1998).
24. F. Alisafaei, C.S. Han, and S.H.R. Sanei, *Polym. Test.*, **32**, 1220 (2013).
25. D.C.C. Lam and A.C.M. Chong, *J. Mater. Res.*, **14**, 3784 (1999).
26. A.C.M. Chong and D.C.C. Lam, *J. Mater. Res.*, **14**, 4130 (1999).
27. S. Nikolov, C.S. Han, and D. Raabe, *Int. J. Sol. Struct.*, **44**, 1582 (2007).
28. C.S. Han and S. Nikolov, *J. Mater. Res.*, **22**, 1662 (2007).
29. B.J. Briscoe, L. Fiori, and E. Pelillo, *J. Phys. D*, **31**, 2395 (1998).
30. C.A. Charitidis, *Ind. Eng. Chem. Res.*, **50**, 565 (2011).
31. T.Y. Zhang and W.H. Xu, *J. Mater. Res.*, **17**, 1715 (2002).

 DOI 10.1002/pc

32. T.Y. Zhang, W.H. Xu, and M.H. Zhao, *Acta Mater.*, **52**, 57 (2004).
33. D.C.C. Lam, F. Yang, A.C.M. Chong, J. Wang, and P. Tong, *J. Mech. Phys. Sol.*, **51**, 1477 (2003).
34. C.C. Kao and R.J. Young, *Compos. Sci. Technol.*, **64**, 2291 (2004).
35. H. Hiura, T. Ebbese, K. Tanigaki, and H. Takahashi, *Chem. Phys. Lett.*, **202**, 509 (1993).
36. M.S. Dresselhaus, G. Dresselhaus, R. Saito, and A. Jorio, *Phys. Rep.*, **409**, 47 (2005).
37. A. Bassil, P. Puech, G. Landa, W. Bacsa, S. Barrau, P. Demont, C. Lacabanne, E. Perez, R. Bacsa, E. Flahaut, A. Peigney, and C. Laurent, *J. Appl. Phys.*, **97**, 3430 (2005).
38. X. Zhou, K.W. Wang, C.E. Bakis, "The Investigation of Carbon Nanotube Based Polymers for Improved Structural Damping," in *SPIE Proceedings on Smart Structures and Materials Conference*, San Diego, CA, March 14–18 (2004). doi:10.1117/12.538624.
39. J. Suher, N. Koratkar, P. Keblinski, and P. Ajayan, *Nat. Mater.*, **4**, 134 (2005).
40. W. Zhang, A. Joshi, Z. Wang, R.S. Kane, and N. Koratkar, *Nanotechnology*, **18**, 185703 (2007).
41. C.A. Charitidis, *Int. J. Refract. Met. H.*, **28**, 51 (2010).
42. E.P. Koumoulos, C.A. Charitidis, D.P. Papageorgiou, A.G. Papathanasiou, and A.G. Boudouvis, *Surf. Coat. Technol.*, **206**, 3823 (2012).
43. M. Troyon and L. Huang, *Surf. Coat. Technol.*, **201**, 208 (2006).
44. W.C. Oliver and G.M. Pharr, *J. Mater. Res.*, **7**, 1564 (1992).
45. .I.N. Sneddon, *Math. Proc. Cambridge*, **44**, 492 (1948).
46. R.B. King, *Int. J. Solids Struct.*, **23**, 1657 (1987).
47. E.P. Koumoulos, C.A. Charitidis, N.M. Daniolos, and D.I. Pantelis, *Mater. Sci. Eng. B*, **176**, 1585 (2011).
48. H. Bei, E.P. George, J.L. Hay, *and G.M. Pharr. Phys. Rev. Lett.*, **95**, 045501 (2005).
49. H. Vašková and V. Křesálek, *Int. J. Math. Model. Meth. Appl. Sci.*, **5**, 1197 (2011).
50. G. Socrates, *Infrared and Raman Characteristic Group Frequencies: Tables and Charts*, 3rd ed.,, Wiley, London (2004).
51. P.J. Blay and B.R. Lawn, *Microindentation Techniques in Materials Science and Engineering*, ASTM STP 889, 72 (1986).
52. H. Li, A. Ghosh, Y.H. Han, and R.C. Bradt, *J. Mater. Res.*, **8**, 1028 (1993).
53. C.S. Han and S. Nikolov, *J. Mater. Res.*, **22**, 1662 (2007).
54. C.S. Han, *Mater. Sci. Eng. A*, **527**, 619 (2010).
55. Y. Li, T. Yu, T. Pui, P. Chen, L. Zheng, and K. Liao, *Comp. Sci. Technol.*, **71**, 1665 (2011).
56. K.T. Kim and W.H. Jo, *Polym. Sci. Part A: Polym. Chem.*, **48**, 4184 (2010).
57. G.S. Zhuang, G.X. Sui, Z.S. Sun, and R.Yang, *Appl. Polym. Sci.*, **102**, 3664 (2006).
58. R. Ribeiro, S. Banda, Z. Ounaies, H. Ucisik, M. Usta, and H. Liang, *Mater. Sci.*, **47**, 649 (2012).
59. M. Nadler, J. Werner, T. Mahrholz, U. Riedel, and W. Hufenbach, *Comp. A Appl. Sci. Man.*, **40**, 932 (2009).
60. B. Fiedler, F.H. Gojny, M.H.G. Wichmann, M.C.M. Nolte, and K. Schulte, *Comp. Sci. Technol.*, **66**, 3115 (2006).
61. K. Prashantha, J. Soulestin, M.F. Lacrampe, M. Claes, G. Dupin, and P. Krawczak, *Expr. Polym. Lett.*, **2**, 735 (2008).
62. E. Meyer, *Phys. Z*, **9**, 66 (1908).
63. U. Kolemen, *J. Alloy Compd.*, **425**, 429 (2006).
64. O. Şahin, O. Uzun, U. Kolemen, and N. Ucar, *J. Phys.: Condens. Matter*, **19**, 306001 (2007).
65. G.M. Pharr, W.C. Oliver, and F.R. Brotzen, *J. Mater. Res.*, **7**, 613 (1992).
66. W.D. Nix, *Mater. Sci. Eng. A*, **234**, 37 (1997).
67. M.M. Chaudhri and M. Winter, *J. Phys. D: Appl. Phys.*, **21**, 370 (1988).
68. J. Alcala, A.C. Barone, and M. Anglada, *Acta Mater.*, **48**, 3451 (2000).
69. A.C. Fischer-Cripps, *Mater. Sci. Eng. A*, **385**, 74 (2004).
70. A. Rar, S. Sohn, W.C. Oliver, D.L. Goldsby, T.E. Tullis, and G.M. Pharr, *Mater. Res. Soc.*, **119**, 841 (2004).
71. C.A. Charitidis, E.P. Koumoulos, V. Nikolakis, and D.A. Dragatogiannis, *Thin Solid Films*, **526**, 168 (2012).
72. Y.T. Cheng and C.M. Cheng, *Philos. Mag. Lett.*, **78**, 115 (1998).
73. R. Hill, B. Storakers, and A.B. Zdunek, *Math. Phys. Eng. Sci.*, **423**, 301 (1989).
74. S. Biwa and B. Storakers, *J. Mech. Phys. Solids*, **43**, 1303 (1995).
75. H. Hertz, *On the Contact of Rigid Elastic Solids and on Hardness*, Macmillan (1896).
76. A. Leyland and A. Matthews, *Surf. Coat. Technol.*, **177**, 317 (2004).
77. A. Leyland and A. Matthews, *Optimization of Nanostructured Tribological Coatings*, Springer, 511 (2006).
78. H. Chien-Chao, W. Mao-Kuo, and L. Sanboh, *Int. J. Plasticity*, **27**, 1093 (2010).
79. M.J. Mayo and W.D. Nix, *Acta Metall.*, **36**, 2183 (1988).
80. B.N. Lucas and W.C. Oliver, *Metall. Mater. Trans. A*, **30**, 601 (1999).
81. W.B. Li and R. Warren, *Acta Metall. Mater.*, **41**, 3065 (1993).
82. H. Li and A.H.W. Ngan, *J. Mater. Res.*, **19**, 513 (2004).
83. Z.Q. Cao and X. Zhang, *Scripta Mater.*, **56**, 249 (2007).
84. H. Pelletier, J. Krier, A. Cornet, and P. Mille, *J. Thin Solid Films*, **379**, 147 (2000).
85. S. Mandal, S. Kose, A. Frank, and A.A. Elmustafa, *Int. J. Surf. Sci. Eng.*, **2**, 41 (2008).
86. C.A. Charitidis, E.P. Koumoulos, V.P. Tsikourkitoudi, D.A. Dragatogiannis, and G. Lolas, *Plast. Rubber Compos.*, **41**, 94 (2012).
87. B. Chen, P.G. Oppenheimer, T.A.V. Shean, C.T. Wirth, S. Hofmann, and J. Robertson, *J. Phys. Chem. C*, **116**, 20047 (2012).

Lubricants **2013**, *1*, 22-47; doi:10.3390/lubricants1020022

OPEN ACCESS

lubricants

ISSN 2075-4442

www.mdpi.com/journal/lubricants

Review

Nanotribological Behavior of Carbon Based Thin Films: Friction and Lubricity Mechanisms at the Nanoscale

Costas A. Charitidis *, Elias P. Koumoulos and Dimitrios A. Dragatogiannis

Department of Chemical Engineering 9 Heroon, National Technical University of Athens, Polytechneiou Street, Zografos, Athens GR-15780, Greece; E-Mails: elikoum@chemeng.ntua.gr (E.P.K.); dragatogiannis@hotmail.com (D.A.D.)

* Author to whom correspondence should be addressed; E-Mail: charitidis@chemeng.ntua.gr; Tel.: +30-2107-724-046; Fax: +30-2107-722-339.

Received: 31 December 2012; in revised form: 28 January 2013 / Accepted: 1 March 2013 / Published: 2 April 2013

Abstract: The use of materials with very attractive friction and wear properties has raised much attention in research and industrial sectors. A wide range of tribological applications, including rolling and sliding bearings, machining, mechanical seals, biomedical implants and microelectromechanical systems (MEMS), require thin films with high mechanical strength, chemical inertness, broad optical transparency, high refractive index, wide bandgap excellent thermal conductivity and extremely low thermal expansion. Carbon based thin films like diamond, diamond-like carbon, carbon nitride and cubic boron nitride known as "super-hard" material have been studied thoroughly as the ideal candidate for tribological applications. In this study, the results of experimental and simulation works on the nanotribological behavior of carbon films and fundamental mechanisms of friction and lubricity at the nano-scale are reviewed. The study is focused on the nanomechanical properties and analysis of the nanoscratching processes at low loads to obtain quantitative analysis, the comparison obtain quantitative analysis, the comparison of their elastic/plastic deformation response, and nanotribological behavior of the a-C, ta-C, a-C:H, CN_x, and a-C:M films. For ta-C and a-C:M films new data are presented and discussed.

Keywords: amorphous carbon films; nanocomposites; nanoindentation; friction; nanotribology; lubricity; wear; molecular dynamics

---

1. Introduction

1.1. Definition

Carbon-based thin films possess unique and adjustable combination of properties such as high hardness, wear resistance, chemical resistance and good tribological performances. Among critical variables to tailor carbon thin film's properties for specific application are the distribution of the carbon hybridization states (sp^1, sp^2, sp^3 bonds), the atomic H content, the content in dopants such as Si, F, N, B and O. Several types of carbon and carbon-based thin films are mentioned [1]:

(i) a-C and hydrogenated amorphous carbon (a-C:H) films with a mixture of sp^2 and sp^3 bonding, highly sp^3-boned material (ta-C) and sp^2-bonded carbon
(ii) Carbon nitride (a-CN_x)
(iii) Metal/Amorphous carbon (a-C:M) composite films

Nanotribological and nanomechanics studies are essential in order to develop fundamental understanding of interfacial phenomena on a small scale in micro/nanostructures used in magnetic storage systems, micro/nanoelectromechanical systems (MEMS/NEMS), and other applications. In nanomanufacturing technology, many small-scale devices cannot be miniaturized further, because friction and wear appear to be exceedingly large in nanoscale machines. Many drawbacks seems to arise because the surface-to-volume ratio is large in small systems and thus surface forces such as friction become relatively large. The friction force at the nano-scale increases with the applied normal load and the tip size because of the increase in the contact area [2]. The friction at the nano-scale is governed mainly by its adhesive characteristics, but the friction at the micro-scale is greatly affected by the wear behavior since the asperity contacts are predominantly plastic and deformation is an important factor [2]. The lower frictional property of diamond-like carbon (DLC) at the nano-scale compared to that of Si-wafer is attributed to the smaller contact area and the lower adhesive force, which are affected by the lower interfacial energy.

The coefficient of friction (CoF) represents, in principle, the friction between the structural material and diamond indenter probe. It is, in perspective, a dynamic rather than static, friction coefficient. In the contact-area-based approach, the CoF is decomposed into two components: shear (CoFS) and plowing (CoFP) [3,4]. The shear contribution is related to surface chemistry, whereas the plowing contribution is related to plastic deformation of the sample. Many theoretical studies and, most recently, an increasing number of experiments indicate that shear forces can be tremendously small between two atomically flat surfaces. These findings spur the hope for new avenues to reduce friction in nanoscale applications [5]. The last two decades, the frictional behavior of a single-asperity contact can be studied due to the introduction of new experimental tools (Atomic Force Microscopy, Lateral Force Microscopes), which made the nanometer and atomic scales accessible to tribologists [6–10]. It is the hope that once the atomic-scale manifestations of friction at such a nanometer-sized single asperity have been clarified, macroscopic friction could be explained with the help of statistics, *i.e.*, by the summation of the interactions of a large number of small individual contacts, which form the macroscopic roughness of the contact interface [10]. A unified and clear understanding behind the

mechanism of nano-scale friction is yet to be achieved. Given the importance of this topic, driven by the development of nanotechnology, the need for continued research effort in nano-tribology remains.

1.2. Scientific Fundamentals

When two solid bodies contact each other and one body begins to slide against the other, a frictional phenomenon appears. The friction force is defined as the drag against sliding, appearing along the contacting surfaces. According to the relative motion of two bodies, the friction forces are classified into static and dynamic ones, having different physical origins. The static friction force is characterized by the maximum force necessary to begin to slide one body against the other, whereas the dynamic friction force is the force applied to continue to slide one body against the other with a finite velocity (the energy must be dissipated during sliding). Experimentally, it is known that the dynamic friction force depends less on the sliding velocity.

Carbon-based thin films possess unique and adjustable combination of properties such as high hardness (H) and elastic modulus (E), wear resistance, chemical resistance and good tribological performances. Among critical variables to tailor a-C film's properties for specific application are the distribution of the carbon hybridization states (sp^1, sp^2, sp^3 bonds), the atomic H content, and the content in dopants such as Si, F, N, B and O.

Diamond related materials (*i.e.*, carbon nitride and cubic boron nitride [c-BN]) are some of the harder materials known and provide advantageous properties (e.g., high mechanical strength, chemical inertness, and very attractive friction and wear properties). Most of these superhard materials provide optical transparency, enhanced refractive index and excellent thermal conductivity, to name a few. All the aforementioned qualities make diamond, DLC, and other related materials ideal candidate materials in the industrial field [1,11,12].

Carbon-based thin films have been developed to address a broad range of film applications, including one that demands outstanding tribological performance in a wide variety of operating environments. Carbon can adopt a large number of stable forms because of its ability to hybridize in multiple stable bonding states and to bond strongly with many other atoms. In addition to tailoring the hybridization state and the atomic H content, various dopants, such as Si, N, B, F, O, can be used to modify the surface energy, electrical, and mechanical properties. Amorphous carbon (a-C) is a disordered material with short range order, which is directly related to the optical and electric properties. The interatomic distances and interbonding angles can significantly deviate from those of the crystalline fully sp^2-(sp^3-) bonded graphite (diamond) lattice, since a-C contains mixtures of hybrid bonding states (sp^1, sp^2, sp^3). Amorphous carbon (a-C) films possess a unique and adjustable combination of properties such as high hardness, wear resistance, chemical resistance and good tribological performances. They have low CoFs and provide protection for the counterparts [11,12–16].

Hydrogenated amorphous carbon (a-C: H), also called DLC (in literature some definitions of DLC can be found, *i.e.*, a-C:H including sp^3 bonds -even very few-, a-C:H which is predominantly sp^3 bonded *etc.*), is an amorphous network composed of carbon and hydrogen. This network consists of strongly cross-linked carbon atoms with mainly sp^2 (graphitic-like) and sp^3 (diamond-like) bonds.

The properties of these films depend strongly on the hydrogen content and the sp^3/sp^2 ratio, which in turn, depend on the deposition process and its parameters. Another subclass of DLC, the tetrahedral

amorphous carbon films (ta-C), are hydrogen free and the carbon atoms are mostly (>80%) carbon sp^3 hybridized. The ta-C films are mainly produced from pure carbon targets by filtered vacuum arc or by pulsed laser deposition. Considerable research effort has been dedicated to the study of tribology, over many decades. This has been driven by the importance of mechanical devices in an array of modern era applications. A readily observable technological trend is toward miniaturization and there has been a lot of discussion about the possibility of producing mechanical devices with dimensions measured at the micro/nano-scale [17]. There has been a clear trend toward smaller electronic devices, which has driven the development of techniques for micro-fabricating Si and the production of MEMS (e.g., data recording head and accelerometer). Nevertheless, the further development of MEMS and particularly moving mechanical arrays (MMA) has been restricted due to the poor tribological properties of Si. It is essential for many MEMS components to have a low friction and low wear surface. Until recently, little work has been devoted to nanotribology and this is perhaps partially due to the lack of effective test methods that are relevant to the operational conditions of proposed MEMS devices, in which case loads of a few micro/milli-Newtons are typical at contact areas and moving distances of a few microns, contact pressures of tens to hundreds of MPa with wear depths limited to nm [18–20]. There is a limited relevance to the use of macro-scale testing for predicting nanoscale behavior [21]. Advances of microelectromechanical system technology in the past decade render the understanding of scale effects in tribology especially important, because surface to volume ratio grows with miniaturization and surface phenomena dominate. Microscale and nanoscale friction force measurements can be obtained with various instruments, such as friction force microscope, atomic force microscopy, and scratch test with apparatus able to make finely controlled low-load scratches (in the range of nN–μN) [22–26]. In Figure 1, the compositions of the various forms of amorphous C-H alloys on a ternary phase diagram with a hardness map are presented [11].

Figure 1. Different compositions of common carbon-based materials in correspondence with hardness and coefficient of friction [1,11].

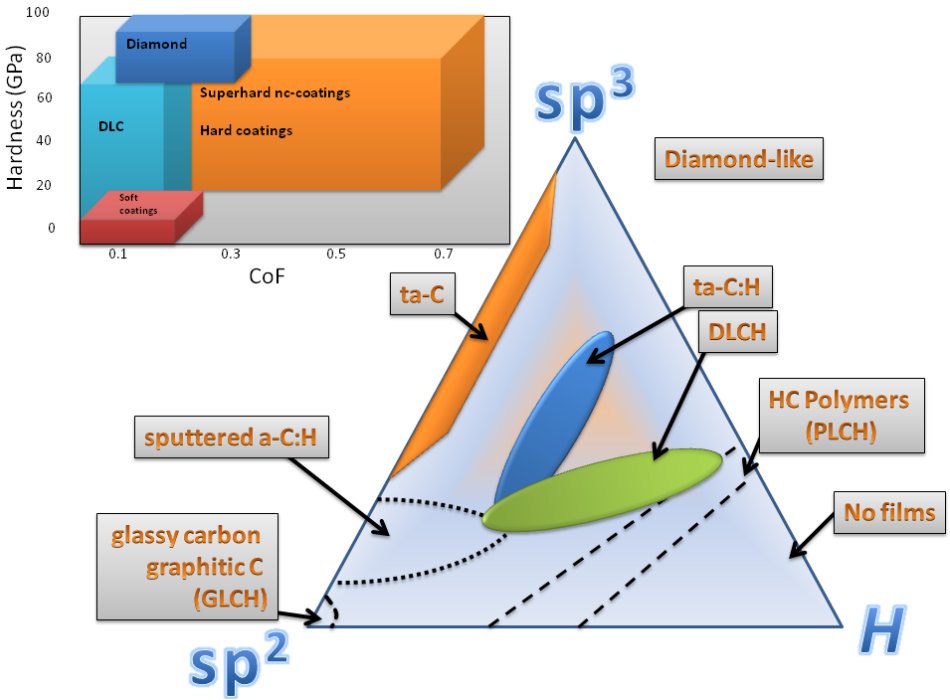

In many studies, continuum mechanics appears to provide an accurate description of the nanometer-scale contact area and other contact properties of carbon based thin films. Homogeneity, isotropy, linearity, and elasticity of the materials are important parameters to consider (several modified continuum contact mechanical models describing other cases have been applied). On the other hand, the current experimental testing systems exhibit significant difficulties in providing results in nanoscale (at a few nm). The difficulties with experimental methods at very small depths can, in general, be easily resolved by using atomistic simulations to solve a variety of problems at the nano scale and to simulate experiments. Defining contact area is one of the major challenges for understanding friction in nanoscale contacts of carbon based structures. Widely in the literature, friction laws are established in nanoscale contacts by large-scale Molecular Dynamics (MD) simulations with realistic force fields (absence—or not—of van der Waals forces). Many challenges can be overcome by MD simulations in order to identify atomistic phenomena underlying friction. By understanding friction at the atomic level, it is possible to build a useful design strategy for the development of low-friction technology. For instance, as reported by MD simulations, adhesion between the probe and the carbon film increases the calculated friction, while tribochemical reactions within the film led to a restructuring of the film and a reduction in friction [27,28]. In addition, there is actually no standard that relates adhesion and friction, which means that range of expected reduction in friction per unit reduction of adhesion, is not known.

2. Discussion

2.1. Surface Chemistry

The low macroscopic friction of diamond in air ($\mu = 0.05–0.1$) has been attributed to the passivation of the surface by –H and –OH groups and/or by the production of lubricious sp^2-bonded species. Nanotribology studies put these ideas to the test, and a significant recent success has been the clear demonstration that –H termination reduces nanoscale friction dramatically [29]. Removal of the H from the surface causes an increase in the average CoF by more than two orders of magnitude compared with the *H*-terminated surface; dangling bonds can bridge an interface and increase the contribution of adhesion to friction, and passivation of those reactive bonds can reduce those forces in a dramatic way.

Comparing many other a-C:H thin films from Plasma Enhanced Chemical Vapor Deposition (PECVD), High-Density Plasma (HDP) and other Ultra High Vacuum (UHV) processes, a threshold (not constant) in hydrogen content can be evidenced for each process between superlow friction, at high hydrogen content, and high friction, at low hydrogen content, attributed to differences in the structure of the films, especially different amounts of hydrogen unbounded to carbon and the presence of aromatic clusters. Hydrogen amount on the surface has an effect on the interactions between contacting surfaces. In the film, it will have an effect on the cross-linking of the random network of carbon atoms. Increase of hydrogen content usually leads to more “polymer-like” structures, with high fraction of C-H sp^3 bonds, but such tendency is also strongly dependent on deposition process. Adhesion results in loss of superlow friction, probably due to interactions between the π-orbitals of sp^2 carbon atoms. Essentially, in order to achieve superlow friction, one has to control the composition of

the sliding surfaces as well as the rheology of the transfer film [30]. Either the hydrogen content of the pristine a-C:H film is sufficient to avoid sp^2 carbon interactions, providing also a viscoplastic character to the film which probably helps in transfer film growth, or one has to feed the a-C:H and transfer film surface with hydrogen to avoid adhesive interactions and to modify the interfacial material, in order to allow a "healing" effect on the damaged surfaces. Oxygen might act in a selective removal process of sp^2 carbon atoms. However, at higher pressures of oxygen, the removal of the transfer film is almost complete, leading to CoF in the 0.2–0.3 range (role of the transfer film on friction reduction) [31].

The tribological behavior of carbon-based thin films is strongly affected by their chemical composition, polycrystalline structure and surface morphology [32]. In all environments, the tribological behavior of carbon thin films is controlled by an interfacial transfer layer formed during friction. The aforementioned layer is formed by a friction-induced modification of the top layer of the film into a material of low shear strength. Despite this comprehension at a macroscopic scale, very little is reported on the mechanisms that control friction at a nanoscopic level. In addition, it has been demonstrated that for graphite and hydrogenated carbon films the macro-tribological behavior is not directly comparable with the nanotribological one, due to dependence of wear, plastic deformation and delamination on the contact area [32]. For the case of a-CN_x films, higher CoF is attributed to the fact that N atoms change the polycrystalline structure of the carbon films and thus the number of phonon modes available for excitation. The improved properties of the a-CN_x films are attributed to a "fullerene-like" microstructure with curved and intersecting basal planes. The determination of this "fullerene-like" microstructure being responsible of a lower CoF at a nanoscopic scale, could be performed through molecular dynamics calculations.

2.2. Bulk Chemistry—Additives

The changes in the structure, composition and mechanical properties of the film with increasing additive content may take important positions in controlling the film friction and wear behavior. Especially, the bonding ratio of film among several factors, which might take important positions in controlling the wear behavior, would be the main reasons for its low CoF and better wear resistance [33]. It is generally believed that an increase of bonding ratio (sp^3/sp^2) might increase wear resistance, but separate study is difficult since it is difficult to grow films that vary one of these independently of the other [34]. While the amount of H and the sp^3/sp^2 bonding ratio influence nanotribology, detailed comprehensive studies necessarily involve varying these parameters independently to elucidate their individual contributions to the mechanical and tribological behavior.

In need of superhard and yet tough ceramic films, a-C-based films prove to be good candidates [35]. Bias graded deposition creates a graded bonding structure such that the sp^2 hybridization become more intense towards the substrate-film interface to provide better toughness and adhesion while sp^3 bonding gets more intense towards the surface of the film to render higher H for tribological performance. Co-sputtering of Al with graphite embeds elemental Al into a-C to form a-C(Al) film which is reported to greatly reduce growth-induced stresses acquired during deposition, at the expense of H because of the reduction in the amount of sp^3 bonding. Co-sputtering of Ti and Al with graphite produces nc-TiC to embed in a-C(Al) matrix, while formation of nc-TiC helps partially restore the hardness lost due to doping of Al. Comparing with a-C film deposited under constant substrate bias, the bias-graded

deposition leads to less friction and improves adhesion of amorphous carbon by twofolds [35]. Nanocrystalline TiC embedding in amorphous carbon results in an increase of adhesion up to four times with a slight increase in CoF. The incorporation of Al in the amorphous carbon matrix results in an increase of adhesion strength and reduces the CoF by 20% [35]. Under ambient condition, the nanocomposite films exhibit higher friction than a-C films while under oil lubrication the nanocomposite films experience less friction. For nc-TiC/a-C(Al) film, a low CoF of only 0.04 is revealed. The incorporation of F has been found to alter the hydrophobicity of DLC films, and this also influences the frictional characteristics. Using a Chemical Vapor Deposition (CVD) process, increasing the F concentration increases the water contact angle (from 72–95°, as F content is increased from 0%–35%) [36]. In literature, adhesion and friction measured by Atomic Force Microscopy (AFM) in air decreases with increasing contact angle. The reduced adhesion is attributed to the reduction of capillary interactions, but the presence of a capillary has not been observed directly. Regardless, this demonstrates the important effect that adhesion forces have on nanoscale friction. Numerous significant studies of literature have lead to new perspectives, indicating that for hard carbon systems, surface chemistry dominates the tribology in the wearless regime, while bulk chemistry matters more after the wear threshold has been reached.

In Figure 2 a schematic representation of the CoF ranges for a-C, ta-C, a-CN_x and various DLC films along with chemical structure embedded. Data presented in Figure 2 are based on Table 1, where tribological properties of carbon-based thin films deposited by various methods are presented according to literature studies.

Figure 2. Schematic representation of the CoF ranges for a-C, ta-C, a-CN_x and DLC films along with chemical structure embedded, according to Table 1.

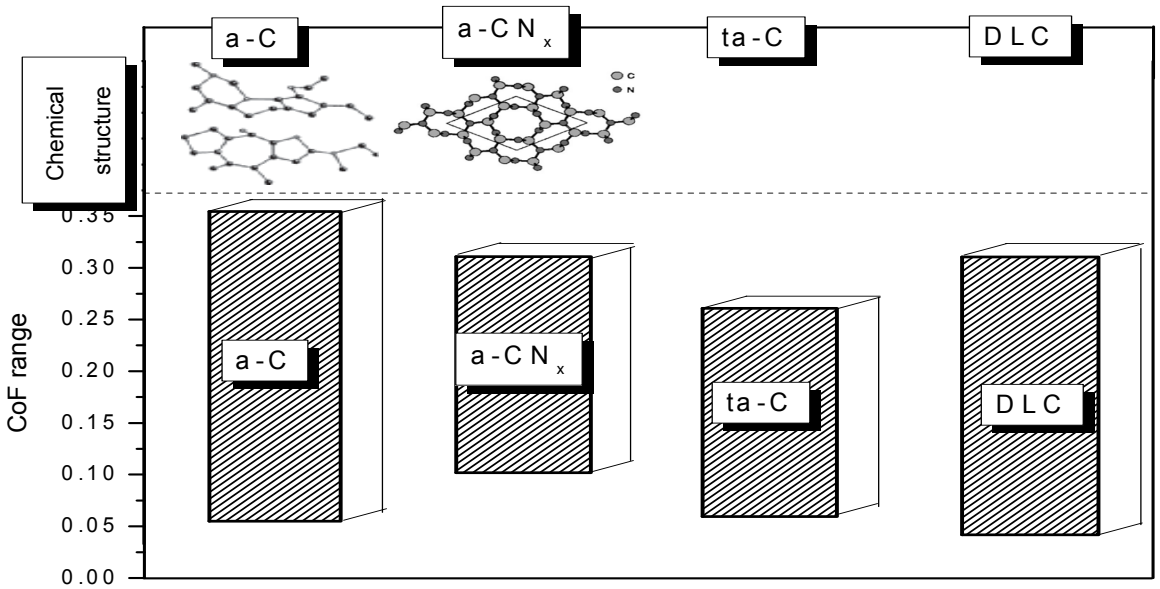

Table 1. Tribological properties of carbon-based thin films deposited by various methods.

Carbon Thin Film Type	Deposition method	Thickness (nm)	H^3/E^2 (GPa)	H/E	CoF at Load (mN)	
a-C sp^3 rich *multilayer* [37]	MS	90	0.235	0.093	0.25	
		274	0.44	0.1231	0.2	
a-C *multilayer* [38]	MS	115	0.383	0.1263		
a-C sp^3 rich [37]	MS	30	0.1704	0.0973		
a-C sp^2 rich [37]	MS	30	0.0303	0.0615	0.35	0.35
a-C sp^2 rich [37]	EB	30	0.01	0.05		
a-C [37]	UBMS		0.4087	0.1148	0.25	0.25
a-C:H [39]	PECVD	1140	0.2244	0.125		
		550	0.3347	0.1343		
ta-C [1]	S-bend		0.649	0.123	0.05	
ta-C [1]	FCVA	70	0.3704	0.111	0.1	
ta-C:H [40]	EC	70	1.389	1.167	0.01–0.12	1–20
a-CN_x [38]	MS	222	0.2142	0.109	0.1–0.3	1–20
ta-C [41]	FCVA	76	0.8935	0.1057	0.1–0.15	1–20
ta-C [42]	PLD	120			0.07	
		130			0.07	
		210			0.11	
DLC:Ti [41]	CFUMS	1000	0.2944	0.1056	0.1–0.4	1–80
DLC:Mo [43]	MS	650	0.2203	0.1192		
DLC:Silver [44]	PECVD	500			0.17–0.24	1–20
ta-C [45]	FCVA	50	0.2518	0.07	0.08–0.14	1–5
ta-C [46]	OPBD-FCVA		0.861	0.1071		
a-CN_x [45]	MS	280	0.0274	0.07		
			0.1292	0.085		
ta-C *multilayer* [46]	OPBD-FCVA		0.8137	0.144	0.12	
a-C [47]	CFUBMS	200	0.3456	0.12	0.1	
a-C:H [48]	PIII	70			0–0.6	0–14
a-C:Ti [49]	PCVD	500			0.05–0.1	1–200
ta-C:Si [46]	FCVA	5			0.23	
		20			0.12–0.24	1–18
		60			0.12–0.3	1–18
		80			0.1–0.25	1–7
a-CN_x [50]	FCVA	100	3.502	0.232		
			1.6	0.2		
a-C [51]	Sputtering	29	2.185	0.236	0.15–0.25	25–300
		46	2.687	0.251	0.22–0.28	25–200
		85	1.643	0.208	0.2–0.3	25–400

Table 1. *Cont.*

DLC:9Cr18	Vacuum Magnetic-Filtering Arc Plasma Deposition	500	0.121	0.059	0.15–20	0–180
DLC:40CrNiMo [52]		500	0.185	0.064	0.15–40	0–84
a-C	PVD		0.15–0.5	0.1		
a-C:H	PACVD		0.48–0.37	0.14–0.11		
a-CN_x [53]	PACVD		0.1–0.18	0.1		
a-CN_x	RF Sputtering PECVD	250–400	0.1–0.18	0.1		
DLC [54]			0.315	0.108		
DLC:Al_2O_3-TiC ceramic (AlTiC),	PECVD		0.099	0.062	0.06	
DLC:Si (1 0 0),	PECVD	250	0.687	0.1625	0.052	150
DLC:fused silica and	PECVD		4.88	0.4333	0.045	
DLC:SU8 photoresist [55]	PECVD		7.29	0.9	0.037	
a-C:F:H	RF-PECVD	400	0.111	0.1053	0.15	0.01–0.12
a-C:F:N:H [56]	RF-PECVD		0.047	0.079	0.13	
DLC:c-Si [57]	PECVD				0.2/0.3	
a-C (H: 28.1 GPa)	DC Magnetron Sputtering	1 to 1.6 μm			0.15	
bias-graded a-C (H: 25.1 GPa)					0.14	
nc-TiC/a-C (H: 27.4 GPa)					0.22	
nc-TiC/a-C(Al) (H: 19.6 GPa) [29]					0.18	
Si-DLC (0 at.%)	RFPACVD	1000			1.6632	2000
Si-DLC (1.0 at.%)		1000			1.0189	
Si-DLC (2.0 at.%) [33]		1000			0.5895	
Cr/a-C [58]	Unbalanced Magnetron Sputter	2000	0.1766	0.097		
		149	0.2298	0.111		
DLC/C40	PVD-CVD				0.15	
DLC/Ni 50% Cr	PVD-CVD				0.1	
DLC/Al_2O_3-13% TiO_2	PVD-CVD				0.65	1000
DLC/WC-Co [59]	PVD-CVD				0.1	
DLC [60]	Linear Ion Beam	2.2	0.0222	0.0666		0.2–12.8
nc-Ti (N,C)/a-C:H	Pulsed DC magnetron Sputtering	400				
31.1 H at.%			0.1370	0.099	0.21	
42.6 H at.%			0.0774	0.0957	0.25	
47.3 H at.% [61]			0.0359	0.0847	0.35	
Ti-DLC/alumina	ClosefieldUnbalanced MS	1000	0.2944	0.1056	0.12–0.25	5–10
Ti-DLC/steel [43]						
a-CN_x-TiN_x/G/Ti ratio	PLD	1200				
Pure Ti			0.1613	0.0872	0.34	
0.5			0.1587	0.0821	0.24	

Table 1. *Cont.*

1			0.1968	0.08651	0.19	980
2			0.2071	0.0874	0.17	
Pure graphite [62]			0.2021	0.0858	0.11	
a-C:H polymerlike	ECR-CVD	630–1150	0.007	0.05–0.08	0.4	900–2000
a-C:H fullerenelike [63]			0.012	0.06–0.12	0.1	
		aCN_x TiN				
aCN_x/TiN [64]	Pulsed laser deposition	25 28	0.2636	0.0938	0.28	
		33 21	0.1924	0.0877	0.16	
		42 12	0.1799	0.0884	0.13	
a-CN_x on Ti-TiN/CN_x gradient underlayer			0.32308	0.11042	0.123	
M1			0.30977	0.11043	0.115	
M2			0.19287	0.09471	0.109	
M3	Direct Current		0.14146	0.08698	0.108	
M4	Magnetron	180				500–8500
a-CN_x on Ti interlayer	Sputtering		0.22401	0.09956	0.223	
P1			0.15602	0.08945	0.218	
P2			0.07756	0.07097	0.205	
P3			0.04585	0.06131	0.207	
M4 [65]						
DLC:glass	RF-PECVD	100	0.1814	0.12		
DLC:silicon [66]			0.13	0.1		

2.3. Applied Load Effect

Several single asperity nanotribological studies of carbon-based materials have been performed in the literature [30]. In case of carbon-based measurements, tip selection is mandatory. However, commercial tips are typically composed of diamond, Si or Si_3N_4, with only a few other coated tips available. Several coated tips are reported in literature; the benefit of film tip with the same material as the sample is the matching of the interface that would be found in an actual device composed entirely of that material. In this case, further modeling and experimental work is required to clarify the exact role that contact area plays at the nanoscale. Despite the important insight into the tribological properties of carbon-based films derived from previous studies, relatively less attention has been paid on the friction behavior and films deformation mode dependence on the applied normal load, especially in the case of carbon-based thin films subjected to low normal loads [67]. The influence of the normal load (from 2 to 20 mN) on the friction of amorphous carbon nitride (CN_x) films grown on Si (100) substrates by reactive ion sputtering and energetic ion bombardment during deposition (IBD) is studied in [68]. In Figure 3 the nanotribological performance of carbon-based thin films (dependence of CoF on the applied load), according to Table 1, is presented.

Figure 3. Dependence of CoF on the applied load for carbon-based thin films, according to Table 1.

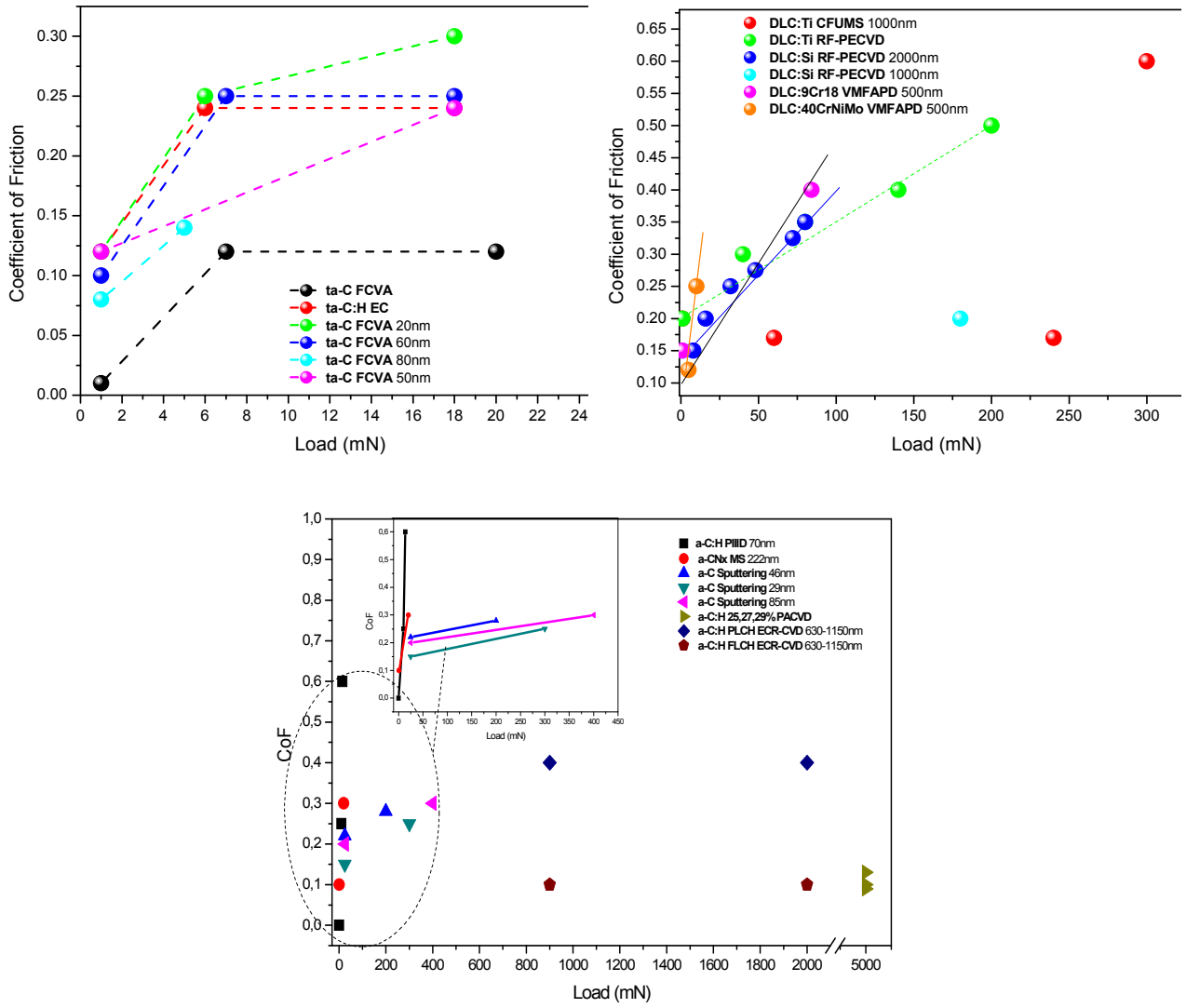

The mechanical and tribological properties of ta-C films are closer to those of bulk diamond than the a-C coatings. Hydrogenated a-C films in principle show a higher coefficient of friction than the a-C and ta-C materials due to the significant amount of hydrogen and differentiation of sp^3 bonding structures.

The tribological characteristics of interface strongly depend on orientation, topography, chemical composition, bonding structure, elastic/plastic properties, and environment. In case of physical origins of friction and energy dissipation determination, precise measurements of these factors must be considered [32].

Applications involving sliding and/or contacting surfaces require certain properties of film, such as resistance to fracture, low friction and low wear properties, which are determined through measurement of key physical properties such as *H*, *E* and surface roughness due to the relationships between these physical and the desired tribological properties. Film adhesion and fracture susceptibility of the film-substrate couple is commonly determined through scratch test for critical load investigation.

2.4. Orientation Effect in Crystalline Diamond

At the macroscopic scale, diamond single crystals show strong orientation effects (friction and wear depend on both the surface orientation and the sliding direction), whereas at the nanoscale the findings are considerably different (attributed in part to wear avoidance, but it may also be as a result of an enhanced influence of local atomic interactions). In several studies performed on single-crystal, H-terminated diamond (111) and (001) surfaces with a quite low diamond tip radius, no difference in average friction force values was observed between the two surfaces except for qualitative differences in the friction images, attributable to the different lattice spacing and orientations [69,70].

The high CoFs of rough diamond films with (111) orientation can be attributed to the abrasive cutting and plowing effects of sharp surface asperities on the softer counterface pins. If a favorable (100) growth orientation is present, such films can also afford low CoFs to sliding surfaces, despite relatively higher measured surface roughness. In general, previous studies confirmed that regardless of the grain size, diamond films with a smooth surface finish provide very low friction to sliding counterfaces. Apart from physical roughness and chemical passivation effects, phase transformation or structural changes can also play a major role in the friction and wear performance of carbon thin films. The extent of such changes can be dominated by environmental species or by ambient temperature. Phase transformation can readily occur even in natural diamond [71] when extreme contact pressures and/or high frictional heating are present at local asperity levels. Real contact occurs first between these asperities, and their tips can either fracture or undergo phase transformation because of the extreme pressures and high frictional heating. Thermodynamically, graphite is the most stable form of C, whereas diamond is metastable. It is also known that when excited thermally or by ion bombardment, diamond can transform to a graphitic form [72,73]. The graphitic debris particles can gradually accumulate at the sliding contact interface and then begin to dominate the long-term sliding friction and wear performance of these films. Most of the debris particles derived from sliding diamond surfaces exhibit a graphitic microstructure [39,40]. Raman Spectroscopy, Electron Diffraction, Electron Energy Loss Spectroscopy, and Transmission Electron Microscopy have concurrently confirmed the presence of highly disordered graphitic debris particles at sliding contact interfaces [39].

2.5. Film Thickness Effect

The wear rate reduces with increasing applied load and more significantly with reducing carbon based thin film thickness. In certain cases a clear exponential reduction of specific wear rate with reducing film thickness over the range of 2000–10 nm occurs. The initial film thickness is of importance, since wear rate of thick films is not reported to decrease exponentially as the substrate approaches [74]. While a little change in film H and E with film thickness is revealed, the main mechanism of wear operating is ascribed to three-body abrasion, although fatigue fracture is thought to significantly contribute.

2.6. Film Roughness Effect—Lubricant Use

Although RMS surface roughness does not carry any information about slopes, sizes or frequencies of asperities, it is still an important parameter for predicting and understanding the properties of

tribological systems [75]. Previous investigations with carbon films indicated that CoF increases with increase of roughness [76,77]. Extensive studies of friction dependence on the surface roughness report an increase, over a wide range of surface roughness, in the CoF with very smooth or very rough surfaces. Friction coefficient increase is attributed to real contact area excessive growing, whereas in the latter it is due to the need to lift one surface over the asperities of the other. In intermediate ranges of roughness, friction is at its minimum and does not depend on the roughness. In a ratchetting mechanism, relative motion between two surfaces is achieved by asperities riding over each other (asperities slope angle increase), leading to increase of CoF with increasing roughness [76]. In energy-loss mechanism, asperities push each other, resulting in increased CoF with roughness. In case of film surface polishing for roughness reduction, the film does not contain any such carbonaceous layer to transfer (friction coefficient does not vary with addition of lubricant). Additives are easily adsorbed on the surface of the film and able to form boundary lubrication, which is independent of the quality of the additives as the film is nanocrystalline and contains an exceptionally high amount of surface atoms. In case of higher temperature, adsorbed additives diffuse to the bulk of the film. In this case, presence of high amount of grain boundary and higher temperature augment the process of diffusion. The characteristic of the adsorbed boundary layer is altered and its functional structure and lubrication abilities are lost. When contact temperature is low, less diffusion of additives of the lubricant occurs to the bulk of the film and boundary lubrication forming with line contact is easier. If temperature rises at the contact point with ball contact, additives tend to diffuse to the bulk of the film due to high amount of grain boundary in nanocrystalline film. Thus, formation of boundary lubrication becomes difficult giving rise to increase in friction coefficient [78].

Figure 4 shows that ta-C films have ultra-low roughness (RMS roughness ~0.12 nm) and that are independent of the film's thickness, thus providing films equally smooth when 11 or 60 nm thick. These are unique properties since films usually form through a series of stages of nucleation, coalescence and possible roughening which, in general, lead to island formation for the thinnest films.

Figure 4. Correlation of roughness and thickness of ta-C films deposited with HCA and FCVA.

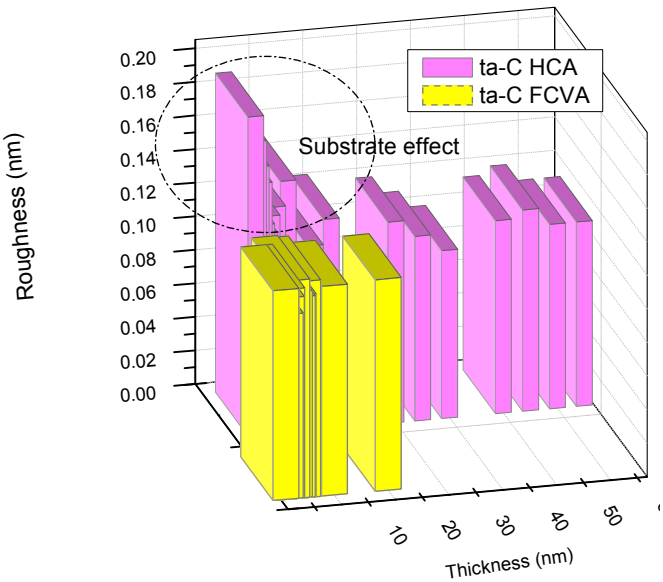

2.7. Graphite—Superlubricity Effect

When a tip is sheared over the surface of a crystal lattice, it often moves in an unstable "stick-slip" pattern that matches the lattice. This was first observed on graphite and has since been reported on many other materials including diamond [79], and it is attributed to energy storing of the compliance of the system (cantilever, tip, and contact zone) as shear is applied. When the lateral force (gradient in the sliding direction) drops below the net system stiffness, the essence of mechanical instability leads to sudden energy release. As lateral interaction force is necessarily periodic by virtue of the symmetry of the crystal surface, stick-slip behavior repeats once every lattice site, creating stunning images that match the lattice periodicity. In this case, the remaining frictional dissipation [70,80–82] is below recordable values and the phenomenon has been labeled (perhaps misleadingly) "superlubricity" (friction is dramatically lower). A key to achieve this transition to instability-free low friction is to obliterate the periodicity of the lateral potential by making the interface incommensurate. When deposited on atomically smooth or highly polished substrates (such as Si wafers or cleaved sapphire or mica surfaces), carbon films can attain the kinds of smoothness that are needed for eliminating the deleterious effects of surface roughness on friction. At thicknesses as low as 2–5 nm, they provide very uniform coverage and mimic the original surface roughness of the underlying substrates. If necessary, the sliding surfaces of carbon films can be polished after the deposition. As for achieving a high degree of chemical inertness on sliding carbon surfaces, researchers have pursued two complementary or closely-related approaches. Specifically, they have either used a hydrogen-rich gas discharge plasma during film deposition [70,79,81–88] or they have introduced hydrogen gas into the test chamber during tribological testing [88–93]. The control of surface chemistry or chemical interactions at sliding DLC interfaces is extremely important for the friction and wear behavior of carbon-based thin films. Specifically, by controlling or effectively eliminating the intrinsic and extrinsic sources of friction in carbon films, one should be able to achieve ultra- and superlow CoF under both dry and lubricated sliding conditions [94].

2.8. Effect of Environment

Tribochemical reactions do occur, but physisorption of environmental species also plays a role [30]. An understanding of humidity effect of these materials nanoscopically is only beginning to emerge. Adhesion shows no dependence on relative humidity (RH), indicating that the conventional picture of meniscus formation leading to higher friction and adhesion does not represent the mechanism at play in this system, as the adhesion should change with RH. Using hydrocarbon-coated tips, the frictional properties of diamond and amorphous carbon are found to differ between air (at 40%–60% RH) and dry Ar environments. Interfacial shear strengths are reported to be highest for a-C in air, followed by diamond in air, then a-C in dry Ar, and finally diamond in dry Ar (adhesive forces are also lower subjected dry Ar environment). Higher friction in ambient conditions is attributed to the presence of water on the surface of the samples [30]. Wear and frictional behavior of carbon-based films rubbed against brass in water are reported to be affected by the water temperature and dissolved ions. Elevated temperature with frictional heat generation prevents the formation of intact and lubricious tribo-layer leading to higher friction and wear [95]. When adsorbed gases are removed from sliding diamond

surfaces, friction increases rapidly because the dangling surface bonds are free and highly activated to form strong bonds across the sliding contact interface. Despite a large discrepancy in time and length scales, molecular dynamics simulation has provided significant insight into the extent of physical, chemical, and mechanical interactions that occur at sliding diamond interfaces on the atomic scale [1].

Sliding friction forces at nanometer scale are determined by two competitive processes. The first process is the thermally activated stick and slip behavior when friction is attributed to the adhesive forces between the two surfaces in contact. Additionally, capillary effects due to water vapor condensation must be taken into consideration, especially for tests performed in air.

2.9. Effect of Substrate Material, Thickness and Roughness

Other important factors are film thickness, substrate roughness, and substrate stiffness, as reported in literature [55,96–99]. For hard carbon films on substrates, of particular interest for hard-disk applications, numerous groups have reported that a critical film thickness (usually >5 nm) needs to be achieved for the film to exhibit the exceptional nanoscale friction and wear properties known to these materials [94]. Furthermore, the roughness and E of the substrate can affect film properties. Consequently, according to the conformal way in which carbon films coat a substrate, substrate roughness is transferred to the film. Lower E of the substrate can lead to bending under applied loads, which in turn may increase contact area and thus friction [55]. When film thickness reaches a practical lower limit, determining the intrinsic properties and likewise the functionality of the films for wear- and corrosion-resistant applications poses a challenge. The final film roughness of carbon films strongly depends on the surface roughness of the substrate. The films deposited on substrates with relatively low surface roughness showed an increase in the final film roughness values, due to the higher deposition rate at the peaks and the lower lateral growth at the valleys [100]. It has been observed that the formation of radial cracks precedes ring cracks in carbon films on the rougher steel substrates. Ring crack formation was delayed, and happened at higher loads for the rougher samples, due to the early formation of the radial cracks at the film-substrate interface, coupled with the plastic deformation of asperities on the surface of the film. The population of radial cracks at the interface of film and substrate is proportional to the relative substrate surface roughness, *i.e.*, on the distribution of interfacial asperities.

2.10. Tribological Properties: The Significance of Ratio H/E

It is known that many of the mechanisms of film failure begin with or directly involve plastic deformation. Consequently, a particular concern in the usefulness of a-C films as protective overcoat materials in hard disk and/or wear-resistant applications is that these films must be highly resistant to plastic deformation during contact events [1]. The film has to undergo a high proportion of elastic deformation occurring when indenting, resulting in high values of H (which reflect the small amounts of plastic deformation occurring), and not only high H as is generally held. One possible way to extract the elasticity can occur via Johnson analysis for solids of revolution [101,102], taking into account the Tresca criterion ($p_0 = 1.6Y$, where Y is the yield stress) and the Tabor relation ($H = 3Y$), the load (P_y) to initiate the yield (plastic deformation) is proportional to the term (H^3/E^2): $P_y = K(H^3/E^2)$. The term H^3/E^2 combines the H and E values of a material and sets the amount of elasticity exhibited by the

film [1,102]. In Figures 5 and 6 schematic representations of the H^3/E^2 (1.0 for diamond) and H/E (0.1 for diamond) correlated with CoF are presented (according to Table 1), respectively.

Figure 5. Schematic representation of the H^3/E^2 correlated with CoF for four types of carbon thin films.

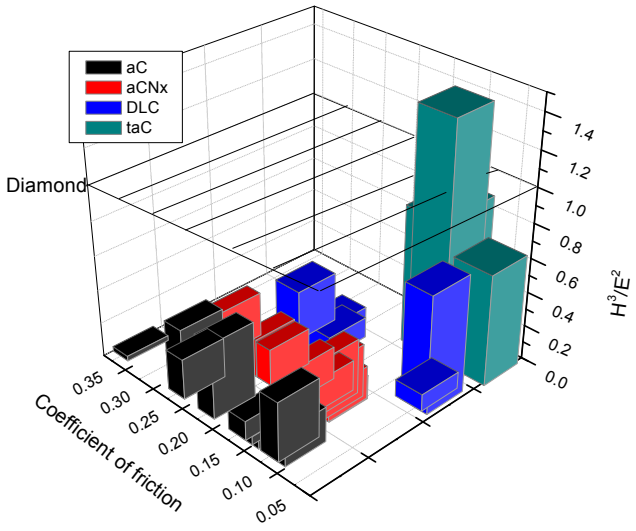

Figure 6. Schematic representation of the H/E correlated with CoF for four types of carbon thin films. Line is guide to the eye.

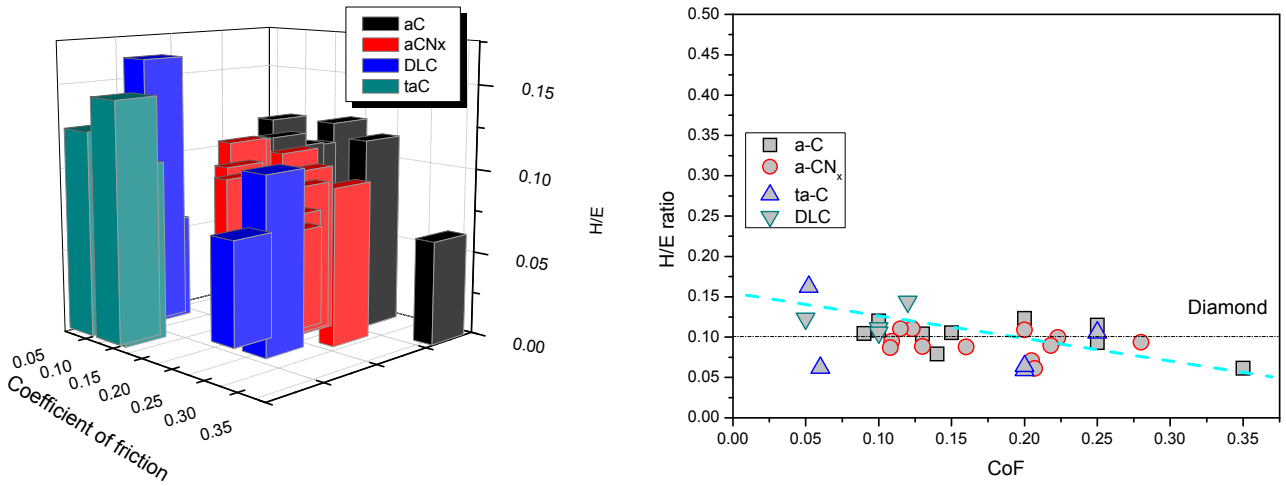

Ranking of materials according to their H/E ratio can provide extremely close agreement to their ranking in terms of wear, as reported in literature [103]. Whilst many researchers have, over the years, confirmed the importance of high H in mitigating wear, the case for a reciprocal relationship between wear resistance and E is less well-proven. Despite the lack of conclusive evidence for a need to enhance elasticity (*i.e.*, to reduce E) in order to improve wear resistance, the intuitive logic of this route has remained, returning to the H/E ratio as a ranking parameter [103]. The ratio of H to E appears in the so-called "plasticity index", which is widely quoted as a valuable measure in determining the limit of elastic behavior in a surface contact, which is clearly important for the avoidance of wear [103]. The H/E as an indicator of film durability is related to the elastic strain to failure capability (and resilience)

of a candidate material [104], regarding the need for tribological films to accommodate some degree of substrate deformation.

2.11. Nanoscale Contact Mechanisms Using Atomistic Simulations

All factors presented above (see 2.1–2.10), which determine nanotribological behavior of carbon based thin films, have been studied extensively during the last decade using atomistic simulations [105–114]. Atomistic simulations based on MD have immersed as alternative in order to explain friction and transitions between different mechanisms of carbon based films, since analytical models based on continuum mechanics fail to explain friction behavior at the nanoscale. In addition, main computational parts of multiscale tribological calculations for friction and lubricity are based on MD simulations [105].

The definition of the contact edge becomes ambiguous when the atomistic nature of the interface dominates its physical behavior [106–108].

The cohesive energies and chemical reactions of hydrocarbon systems as well as the elastic constants of solid carbon-based materials are accurately described by the Reactive Empirical Bond-Order (REBO) potential [109]. The range of the REBO potential extends as far as the chemical interactions and does not include dispersive forces. The van der Waals interactions are therefore integrated with REBO using an analytical switching function in the regime where the two potentials overlap.

Mylvaganam *et al.* [110] conducted MD simulations to study the behavior of carbon-diamond, graphite and carbon nanotube-on contact sliding against a diamond asperity vacuum. It was found that, on the nanoscale, graphite and carbon nanotubes exhibit low coefficients of friction, while carbon nanotubes act as a better solid lubricant with a friction coefficient of only about 0.03 in vacuum on the nano/micro scales. The mechanisms of the difference in frictional properties of the three forms of carbon at different dimensional scales were due to the difference in their atomic structures [110]. Gao *et al.* [27] used MD simulations in order to explore film thickness, counterface termination, and long-range interactions on tribological properties, identifying detailed tribochemical reactions and their effect on friction and wear. The thickness of the amorphous films had no influence on the calculated friction, proving that the structure of the film near the interface is what is dominating the friction. Additionally, the simulation results suggested that the structure of the film, especially the sp^3-to-sp^2 ratio, could profoundly affect the tribological properties of the film. Films that contain a larger fraction of surface sp^2-hybridized carbon will exhibit higher levels of friction than those films with more surface sp^3-hybridized carbon; this increase in friction is attributed to the increased adhesion from tribochemistry. It should also be noted that changing the sp^3-to-sp^2 ratio within a carbon film will also change its hardness and may also change the film's phonon frequencies. Adhesion, due to the bonding between a carbon on the counterface and a carbon in the film, contributes significantly to the friction. While adhesion between the probe and the film increases the calculated friction; tribochemical reactions within the film lead to a restructuring of the film and a reduction in friction [27]. In addition, there is actually no standard that relates adhesion and friction, which means that range of expected reduction in friction per unit reduction of adhesion is not known [28]. Recently, the first analytical model that can describe the interplay between adhesive forces at the interface and subsurface plastic deformation for single-asperity sliding contacts has been developed by Maneesh Mishra *et al.* [111].

As it is referred by Bhushan *et al.* [112] adhesion is the main contribution to the friction for nanoscale experiments.

MD simulation studies conducted by Zhang *et al.* [113] on hydrogenated carbon (CH_x) films showed the reduction of friction coefficient with surface hydrogenation. These results suggest that pulsed DC magnetron sputtering can produce CH_x films with friction properties similar to those obtained by plasma-enhanced CVD [113].

The hydrogen concentration is crucial for the running-in behavior and the resulting steady-state friction coefficient of a-C: H tribo-contacts [114]. Similar observations on running-in have been made previously by Gao *et al.* [27]. Two passivation mechanisms and an explanation of the observed sp^3 to sp^2 transformation, which is seen under dry as well as lubricated sliding can be extracted from MD simulations performed by Pastewka *et al.* [114]. An obvious strategy for reducing friction is to reduce the strength of interatomic interaction between the surfaces, which can be done by surface treatment with the intention of reducing the free surface energies, for example, or by deliberately choosing weakly adhering materials. This is not unlike the macroscopic strategy of lowering friction by selecting metallurgically incompatible materials [28]. MD simulation methods are useful to gain insight for nano-scale interactions and obtain quantitative results for various system models and operating conditions. However, there are still several problems that need to be tackled to obtain simulation results that are closer to the real world [6].

3. Conclusions

Due to very unique structures, attractive properties and performance characteristics of carbon based thin films, both the scientific and industrial communities are drawing significant attention to their synthesis, processing and functionalization. Dedicated scientific studies on carbon-based thin films in recent years have led to the development of more exotic versions consisting of unique nanophases and/or structures. Tetrahedral amorphous carbon films are good candidates, among other types of carbon-based films, in terms of the best combination of high *H* and *E* values, lower CoF, highly elastic deformation under static nanoindentation testing and nanoscratching up to relatively high normal loads and plastic deformation for high normal loads, however without evidence of film failure. Table 1 summarizes the results of experimental techniques on nanotribological properties of carbon based films.

Connection of the nano-, micro- and macro-scale tribological behavior in terms of experiments (better control and accurate description of the nanoidentation and atomic force microscopy tips) and computational techniques of the tribological interaction of the carbon-based materials remains a challenge. Studies on origin of friction, adhesion, wear and other tribological features at the atomic scale, since they are highly dependent on the surface interactions, using sophisticated experimental and computational tools should be continued in order to provide a deeper understanding of friction in nanoscale. MD simulation methods are useful to gain insight for nano-scale interactions and obtain quantitative results for various system models and operating conditions. However, there are still several problems that need to be tackled to obtain simulation results that are closer to the real world. Table 2 summarizes simulation conditions, used material and results from molecular dynamics techniques applied on carbon based thin film structures in order to study mechanisms of friction and lubricity.

Table 2. Summary of molecular dynamic simulations of carbon based films nanotribological systems.

Year	Simulation condition	Used materials	Results
1999 Cagin *et al.* [115]	Brenner's potential	Bare diamond hydrogenated diamond	Dangling bond of surface caused higher friction force
2002 Gao *et al.* [27]	Brenner's reactive empirical bond-order potential (REBO)	Hydrogen-terminated diamond (111) counterfaces are in sliding contact with diamond (111) surfaces coated with amorphous, hydrogen-free carbon films	Effects of film thickness, adhesion, and long-range interactions
2004 Sulin Zhang *et al.* [113]	Tersoff-Brenner form	Hydrogenated carbon films (CH_x)	Determine how surface hydrogenation affects friction coefficient
2010 Pastewka *et al.* [114]	Modified Brenner's reactive empirical bond-order potential (REBO)	Diamond-like carbon (DLC) coatings	Atomistic insights into the running-in, lubrication, and failure of hydrogenated diamond-like carbon coatings
2010 Mylvaganam *et al.*[110]	Many-body Tersoff-Brenner potential	Carbon-diamond, graphite and carbon nanotube	Nanotubes are the best solid lubricant as it has a low coefficient of friction that can be maintained across any dimensional scales from nano to macro scales due to the large aspect ratio of length to diameter
2012 Bucholz *et al.*[116]	Brenner's reactive empirical bond-order potential (REBO) coupled with a Lennard-Jones (LJ) potential	Carbon nano-onions	The ability of the nano-onions to roll is inhibited both by increased contact pressure and the presence of a diamond core within the nanoparticles that enhances the formation of interfacial bonds during friction

References

1. Charitidis, C.A. Nanomechanical and nanotribological properties of carbon-based thin films: A review. *Int. J. Refract. Metals Hard Mater.* **2010**, *28*, 51.
2. Yoon, E.S.; Singh, R.A.; Oh, H.J.; Kong, H. The effect of contact area on nano/micro-scale friction. *Wear* **2005**, *259*, 1424.
3. Lafaye, S.; Gauthier, C.; Schirrer, R. Ploughing friction of a conical tip with blunted spherical extremity: Analytic model with elastic recovery. *Tribol. Lett.* **2006**, *21*, 95.
4. Goddard, J.; Wilman, H. A theory of friction and wear during the abrasion of metals. *Wear* **1962**, *5*, 114.
5. Müser, M.H. Structural lubricity: Role of dimension and symmetry. *Europhys. Lett.* **2004**, *66*, 97.
6. Kim, H.J.; Kim, D.E. Nano-scale Friction: A Review. *Int. J. Precis. Eng. Manuf.* **2009**, *10*, 141.

7. Carpick, R.W.; Salmeron, M. Scratching the surface: Fundamental investigations of tribology with atomic force microscopy. *Chem. Rev*. **1997**, *97*, 1163.
8. Urbakh, M.; Klafter, J.; Gourdon, D.; Israelachvili, J. The nonlinear nature of friction. *Nature* **2004**, *430*, 525.
9. Bhushan, B.; Israelachvili, J.N.; Landman, U. Nanotribology: Friction, wear and lubrication at the atomic scale. *Nature* **1995**, *374*, 607.
10. Hölscher, H.; Schirmeisen, A.; Schwarz, U.D. Principles of atomic friction: from sticking atoms to superlubric sliding. *Phil. Trans. R. Soc. A* **2008**, *336*, 1383.
11. Robertson, J. Diamond-like amorphous carbon. *Mater. Sci. Eng. R*: *Rep.* **2002**, *3*, 129.
12. Ferrari, A.C. *Tribology of Diamond-Like Carbon Films*; Donnet, C., Erdemir, A., Eds.; Springer: New York, NY, USA, 2008; Chapter 2, p. 25.
13. Jacob, W.; Moller, W. On the structure of thin hydrocarbon films. *Appl. Phys.* **1993**, *63*, 1771.
14. Grill, A. Diamond-like carbon: State of the art. *Diam. Relat. Mater.* **1999**, *8*, 428.
15. Ronkainen, H.; Varjus, S.; Koskinen, J.; Holmberg, K. Differentiating the tribological performance of hydrogenated and hydrogen-free DLC coatings. *Wear* **2001**, *249*, 260.
16. Liu, Y.; Erdemir, A.; Meletis, E.I. A study of the wear mechanism of ond-like carbon, films. *Surf. Coat. Technol*. **1996**, *82*, 48.
17. Cao, G. *Nanostructures and Nanomaterials: Synthesis, Properties and Applications*; Imperial College Press: London, UK, 2004; pp. 391–392.
18. Kim, S.H.; Asay, D.B.; Dugger, M.T. Nanotribology and MEMS. *Nanotoday* **2007**, *2*, 22.
19. Bhushan, B. Micro/nanotribology and its applications to magnetic storage devices and MEMS. *Tribol. Int.* **1995**, *28*, 85.
20. Kim, D.; Cao, D.; Bryant, M.D.; Meng, W.J.; Ling, F.F. Tribological study of microbearings for MEMS applications. *Tribology* **2005**, *127*, 537.
21. Achanta, S.; Drees, D.; Celis, J.-P. Friction and nanowear of hard coatings in reciprocating sliding at milli-Newtons loads. *Wear* **2005**, *259*, 719.
22. Schonherr, H.; Vancsob, G.J. Molecular resolution imaging and friction anisotropy of highly oriented polyethylene and poly(tetrafluoroethylene) by scanning force microscopy with chemically modified probes. *Macromolecules* **1997**, *30*, 6391.
23. Wei, B.; Komvopoulos, K. Nanoscale indentation hardness and wear characterization of hydrogenated carbon thin films. *ASME J. Tribol.* **1996**, *118*, 431.
24. Bhushan, B.; Dandavate, C. Thin-film friction and adhesion studies using atomic force microscopy. *J. Appl. Phys.* **2000**, *87*, 1201.
25. Deng, H.; Scharf, T.W.; Barnard, J.A. Adhesion assessment of silicon carbide, carbon, and carbon nitride ultrathin overcoats by nanoscratch techniques. *J. Appl. Phys.* **1997**, *81*, 5396.
26. Charitidis, C.; Logothetidis, S.; Gioti, M. A comparative study of the nanoscratching behavior of amorphous carbon films grown under various deposition conditions. *Surf. Coat. Technol.* **2000**, *125*, 201.
27. Gao, G.T.; Mikulski, P.T.; Harrison, J.A. Molecular-scale tribology of amorphous carbon coatings: Effects of film thickness, adhesion, and long-range interactions. *J. Am. Chem. Soc.* **2002**, *124*, 7202–7209.
28. Wong, C.H. Friction at Nanoscale. *J. Appl. Mech. Eng.* **2012**, *1*, 1–2.

29. Gardos, M.N.; Gabelich, S.A. Atmospheric effects of friction, friction noise and wear with silicon and diamond. Part III. SEM tribometry of polycrystalline diamond in vacuum and hydrogen. *Tribol. Lett.* **1999**, *6*, 103–112.
30. Grierson, D.S.; Carpick, R.W. Nanotribology of carbon-based materials. *Nanotoday* **2007**, *2*, 12–21.
31. Fontaine, J.; Le Mogne, T.; Loubet, J.L.; Belin, M. Achieving superlow friction with hydrogenated amorphous carbon: Some key requirements. *Thin Solid Films* **2005**, *482*, 99–108.
32. Riedo, E.; Chevrier, J.; Comin, F.; Brune, H. Nanotribology of carbon-based thin films: The influence of film structure and surface morphology. *Surf. Sci.* **2001**, *477*, 25.
33. Kim, H.G.; Ahn, S.H.; Kim, J.G.; Park, S.J.; Lee, K.R. Effect of Si-incorporation on wear—Corrosion properties of diamond-like carbon films. *Thin Solid Films* **2005**, *482*, 299–304.
34. Jiang, Z.; Lu, C.J.; Bogy, D.B.; Bhatia, C.S.; Miyamoto, T. Nanotribological characterization of hydrogenated carbon films by scanning probe microscopy. *Thin Solid Films* **1995**, *258*, 75–81.
35. Xuan, S.Z.; Bui, L.; Zeng, X.T.; Li, X. Towards high adherent and tough a-C coatings. *Thin Solid Films* **2005**, *482*, 138.
36. Prioli, R.; Jacobsohn, L.G.; Maia da Costa, M.E.H.; Freire, F.L. Nanotribological properties of amorphous carbon-fluorine films. *Tribol. Lett.* **2003**, *15*, 177–180.
37. Logothetidis, S.; Charitidis, C.; Patsalas, P. Engineering properties of fully sp^3- to sp^2-bonded carbon films and their modifications after post-growth ion irradiation. *Diam. Relat. Mater.* **2002**, *11*, 1095–1099.
38. Lu, W.; Komvopoulos, K.; Patsalas, P.; Charitidis, C.; Gioti, M.; Logothetidis, S. Microstructure and nanomechanical and optical properties of single- and multi-layer carbon films synthesized by radio frequency sputtering. *Surf. Coat. Technol.* **2003**, *168*, 12–22.
39. Bruno, P.; Cicala, G.; Losacco, A.M.; Decuzzi, P. Mechanical properties of PECVD hydrogenated amorphous carbon coatings via nanoindentation and nanoscratching techniques. *Surf. Coat. Technol.* **2004**, *180–181*, 259–264.
40. Jahanmir, S.; Deckman, D.E.; Ives, L.K.; Feldman, A.; Farrabaugh, E. Tribological characteristics of synthesized diamond films on silicon carbide. *Wear* **1989**, *133*, 73–81.
41. Ferrari, A.C.; Robertson, J.; Beghi, M.G.; Bottani, C.E.; Ferulano, R.; Pastorelli, R. Elastic constants of tetrahedral amorphous carbon films by surface Brillouin scattering. *Appl. Phys. Lett.* **1999**, *75*, 1893–1895.
42. Bonelli, M.; Ferrari, A.C.; Fioravanti, A.; Li Bassi, A.; Miotello, A.; Ossi, P.M. Structure and mechanical properties of low stress tetrahedral amorphous carbon films prepared by pulsed laser deposition. *Eur. Phys. J. B—Condens. Matter Complex Syst.* **2002**, *25*, 269–280.
43. Ouyang, J.H.; Sasaki, S.; Murakami, T. Properties of titanium containing diamond like carbon coatings. *Wear* **2009**, *266*, 96–102.
44. Malaczynski, G.W.; Elmoursi, A.A.; Leung, C.H.; Hamdi, A.H.; Campbell, A.B. Improved adhesion of diamondlike coatings using shallow carbon implantation. *J. Mater. Res.* **2000**, *15*, 590–592.
45. Lemoine, P.; Zhao, J.F.; Quinn, J.P.; McLaughlin, J.A.; Maguire, P. Hardness measurements at shallow depths on ultra-thin amorphous carbon films deposited onto silicon and Al_2O_3-TiC substrates. *Thin Solid Films* **2000**, *379*, 166–172.

46. Quinn, J.P.; Lemoine, P.; Maguire, P.; Mc Laughlin, J.A. Ultra-thin tetrahedral amorphous carbon films with strong adhesion, as measured by nanoscratch testing. *Diam. Relat. Mater.* **2004**, *13*, 1385–1390.
47. Teo, E.H.T.; Chua, D.H.C.; Tay, B.K. Mechanical properties of alternating high-low sp^3 content thick non-hydrogenated diamond-like amorphous carbon films. *Diam. Relat. Mater.* **2007**, *16*, 1882–1886.
48. Xu, M.; Cai, X.; Zhao, J.; Chen, Q.; Chu, P.K. Comparative studies on influence of acetylene to argon flow rate ratios on nano-scratch behavior of a-C:H films produced on steel substrates by plasma immersion ion implantation and deposition. *Thin Solid Films* **2007**, *516*, 252–256.
49. Huang, L.Y.; Xu, K.W.; Lu, J.; Guelorget, B. Nano-scratching process and fracture mechanism of amorphous carbon films. *Wear* **2003**, *254*, 1032–1036.
50. Druza, B.; Yevtukhov, Y.; Novotny, V.; Zaritsky, I.; Kanarov, V.; Polyakov, V.; Rukavishnikov, A. Nitrogenated carbon films deposited using filtered cathodic arc. *Diam. Relat. Mater.* **2000**, *9*, 668–674.
51. Ma, X.-G.; Komvopoulos, K.; Wan, D.; Bogy, D.B.; Kim, Y.-S. Effects of film thickness and contact load on nanotribological properties of sputtered amorphous carbon thin films. *Wear* **2003**, *254*, 1010–1018.
52. Zhang, T.H.; Huan, Y. Nanoindentation and nanoscratch behaviors of DLC coatings on different steel substrates. *Compos. Sci. Technol.* **2005**, *65*, 1409–1413.
53. Bandorf, R.; Paulkowski, D.M.; Schiffmann, K.I.; Küster, R.L.A. Tribological improvement of moving microparts by application of thin films and micropatterning. *J. Phys.*: *Condens. Matter* **2008**, *20*, doi:10.1088/0953-8984/20/35/354018.
54. Bandorf, R.; Luthje, H.; Schiffmann, K.; Staedler, T.; Wortmann, A. Sub-micron coatings with low friction and wear for micro actuators. *Microsyst. Technol.* **2002**, *8*, 51–54.
55. Staedler, T.; Schiffmann, K. Correlation of nanomechanical and nanotribological behavior of thin DLC coatings on different substrates. *Surf. Sci.* **2001**, *482*, 1125–1129.
56. Maia da Costa, M.E.H.; Sanchez, C.M.T.; Jacobsohn, L.G.; Freire, F.L., Jr. Structural, mechanical, and nanoscale tribological properties of nitrogen-incorporated fluorine-carbon films. *Thin Solid Films* **2005**, *482*, 109–114.
57. Corbella, C.; Polo, M.C.; Oncins, G.; Pascual, E.; Andújar, J.L.; Bertran, E. Time-resolved electrical measurements of a pulsed-dc methane discharge used in diamond-like carbon films. *Thin Solid Films* **2005**, *482*, 172–176.
58. Wilson, G.M.; Sullivan, J.L. An investigation into the effect of film thickness on nanowear with amorphous carbon-based coatings. *Wear* **2009**, *266*, 1039–1043.
59. Bolelli, G.; Lusvarghi, L.; Mantini, F.P.; Pitacco, F.; Volz, H. Enhanced tribological properties of PECVD DLC coated thermally sprayed coatings. *Surf. Coat. Technol.* **2008**, *202*, 4382–4386.
60. Crombez, R.; Mc Minis, J.; Veerasamy, V.S.; Shen, W. Experimental study of mechanical properties and scratch resistance of ultra-thin diamond-like-carbon (DLC) coatings deposited on glass. *Tribol. Int.* **2011**, *44*, 55–62.

61. Tsotsos, C.; Polychronopoulou, K.; Demas, N.G.; Constantinides, G.; Gravani, S.; Böbel, K.; Baker, M.A.; Polycarpou, A.A.; Rebholz, C. Mechanical and high pressure tribological properties of nanocrystalline Ti(N,C) and amorphous C:H nanocomposite coatings. *Diam. Relat. Mater.* **2010**, *19*, 960–963.
62. Zheng, X.H.; Tu, J.P.; Song, R.G. Microstructure and tribological performance of CN_x-TiN_x composite films prepared by pulsed laser deposition. *Mater. Design* **2010**, *31*, 1716–1719.
63. Buijnsters, J.G.; Camero, M.; Vázquez, L.; Agulló-Rueda, F.; Gago, R.; Jiménez, I.; Gómez-Aleixandre, C.; Albella, J.M. Tribological study of hydrogenated amorphous carbon films with tailored microstructure and composition produced by bias-enhanced plasma chemical vapour deposition. *Diam. Relat. Mater.* **2010**, *19*, 1093–1102.
64. Zheng, X.H.; Tu, J.P.; Song, R.G. Fabrication, microstructure and tribological behavior of pulsed laser deposited a-CN_x/TiN multilayer films. *Surf. Coat. Technol.* **2010**, *205*, 902–908.
65. Liu, D.G.; Tu, J.P.; Hong, C.F.; Gu, C.D.; Mai, Y.J.; Chen, R. Improving mechanical properties of a-CN_x films by Ti-TiN/CN_x gradient multilayer. *App. Surf. Sci.* **2010**, *257*, 487–494.
66. Borrero-Lopez, O.J.; Hoffman, M.J.; Bendavid, A.; Martin, P.J. Substrate effects on the mechanical properties and contact damage of diamond-like carbon thin films. *Diam. Relat. Mater.* **2010**, *19*, 1273–1280.
67. Gao, G.; Cannara, R.J.; Carpick, R.W.; Harrison, J.A. Atomic-scale friction on diamond: A comparison of different sliding directions on (001) and (111) surfaces using MD and AFM. *Langmuir* **2007**, *23*, 5394–5405.
68. Charitidis, C.; Logothetidis, S. Effects of normal load on nanotribological properties of sputtered carbon nitride films. *Diam. Relat. Mater.* **2005**, *14*, 98.
69. Enomoto, Y.; Tabor, D. The frictional anisotropy of diamond. *Proc. R. Soc. Lond. A* **1981**, *373*, 405.
70. Germann, G.J.; Cohen, S.R.; Neubauer, G.; McClelland, G.M.; Seki, H. Atomic scale friction of a diamond tip on diamond (100) and (111) surfaces. *Appl. Phys.* **1993**, *73*, 163.
71. Gogotsi, Y.G.; Kailer, A.; Nickel, K.G. Pressure-induced phase transformations in diamond. *J. Appl. Phys.* **1998**, *84*, 1299–1304.
72. Lee, E.H.; Hembree, D.M., Jr.; Rao, G.R.; Mansur, L.K. Raman scattering from ion-implanted diamond, graphite, and polymers. *Phys. Rev. B* **1993**, *48*, 15540–15551.
73. Erdemir, A.; Halter, M.; Fenske, G.R.; Zuiker, C.; Csencsits, R.; Krauss, A.R.; Gruen, D.M. Friction and wear mechanisms of smooth diamond films during sliding in air and dry nitrogen, *Tribol. Trans.* **1997**, *40*, 667–673.
74. Carpinteri, A.; Paggi, M. Size-scale effects on the friction coefficient. *Int. J. Solids Struct.* **2005**, *42*, 2901–2910.
75. Tomala, A.; Roy, M.; Franek, F. Nanotribology of Mo–Se–C films. *Philos. Mag.* **2010**, *90*, 3827–3843.
76. Hayward, I.P.; Singer, I.L.; Seitzman, L.E. The effect of roughness on the friction of diamond on CVD diamond coatings. *Wear* **1991**, *157*, 215.
77. Bull, S.J.; Chalkar, P.R.; Johnston, C.; Moore, V. The effect of roughness on the friction and wear of diamond thin film. *Surf. Coat. Technol.* **1994**, *68*, 603–610.

78. Schneider, A.; Steinmueller-Nethl, D.; Roy, M.; Franek, F. Enhanced tribological performances of nanocrystalline diamond film. *Int. J. Refract. Metals Hard Mater.* **2010**, *28*, 40–50.
79. Enachescu, M.; Van Den Oetelaar, R.J.A.; Carpick, R.W.; Ogletree, D.F.; Flipse, C.F.J.; Salmeron, M. Atomic force microscopy study of an ideally hard contact: The diamond (111)/tungsten carbide interface. *Phys. Rev. Lett.* **1998**, *81*, 1877–1880.
80. Medyanik, S.N.; Liu, W.K.; Sung, I.H.; Carpick, R.W. Predictions and observations of multiple slip modes in atomic-scale friction. *Phys. Rev. Lett.* **2006**, *97*, 1361061-4.
81. Socoliuc, A.; Bennewitz, R.; Gnecco, E.; Meyer, E. Transition from stick-slip to continuous sliding in atomic friction: Entering a new regime of ultralow friction. *Phys. Rev. Lett.* **2004**, *92*, doi:10.1103/PhysRevLett.97.136106.
82. Krylov, S.Y.; Dijksman, J.A.; Van Loo, W.A.; Frenken, J.W.M. Stick-slip motion in spite of a slippery contact: Do we get what we see in atomic friction? *Phys. Rev. Lett.* **2006**, *97*, doi:10.1103/PhysRevLett.97.166103.
83. Erdemir, A.; Eryilmaz, O.L.; Fenske, G. Synthesis of diamondlike carbon films with superlow friction and wear properties. *J. Vac. Sci. Technol. A: Vac. Surf. Films* **2000**, *18*, 1987–1992.
84. Donnet, C.; Belin, M.; Auge, J.C.; Martin, J.M.; Grill, A.; Patel, V. Tribochemistry of diamond-like carbon coatings in various environments. *Surf. Coat. Technol.* **1994**, *68*, 626–631.
85. Erdemir, A. The role of hydrogen in tribological properties of diamond-like carbon films. *Surf. Coat. Technol.* **2001**, *146*, 292–297.
86. Donnet, C.; Mogne, T.L.; Ponsonnet, L.; Belin, M.; Grill, A.; Patel, V.; Jahnes, C. The respective role of oxygen and water vapor on the tribology of hydrogenated diamond-like carbon coatings. *Tribol. Lett.* **1998**, *4*, 259–265.
87. Erdemir, A. Superlubricity and wearless sliding in diamond-like carbon films. *Mater. Res. Soc. Symp. Proc.* **2002**, *697*, 391–403.
88. Erdemir, A.; Eryilmaz, O.L.; Nilufer, I.B.; Fenske, G.R. Synthesis of superlow-friction carbon films from highly hydrogenated methane plasmas. *Surf. Coat. Technol.* **2000**, *133*, 448–454.
89. Erdemir, A.; Nilufer, I.B.; Eryilmaz, O.L.; Beschliesser, M.; Fenske, G.R. Friction and wear performance of diamond-like carbon films grown in various source gas plasmas. *Surf. Coat. Technol.* **1999**, *120*, 589–593.
90. Erdemir, A.; Eryilmaz, O.L.; Nilufer, I.B.; Fenske, G.R. Effect of source gas chemistry on tribological performance of diamond-like carbon films. *Diam. Relat. Mater.* **2000**, *9*, 632–637.
91. Donnet, C.; Grill, A. Friction control of diamond-like carbon coatings. *Surf. Coat. Technol.* **1997**, *94*, 456–462.
92. Donnet, C.; Fontaine, J.; Grill, A.; Le Mogne, T. The role of hydrogen on the friction mechanism of diamond-like carbon films. *Tribol. Lett.* **2001**, *9*, 137–142.
93. Fontaine, J.; Belin, M.; Le Mogne, T.; Grill, A. How to restore superlow friction of DLC: The healing effect of hydrogen gas. *Tribol. Int.* **2004**, *37*, 869–877.
94. Erdemir, A.; Donnet, C. Tribology of diamond-like carbon films: Recent progress and future prospects. *J. Phys. D*: *Appl. Phys.* **2006**, *39*, R311.
95. Uchidate, M.; Liu, H.; Iwabuchi, A.; Yamamoto, K. Effects of water environment on tribological properties of DLC rubbed against brass. *Wear* **2009**, *267*, 1589–1594.

96. Sundararajan, S.; Bhushan, B. Micro/Nanotribology of ultra-thin hard amorphous carbon coatings using atomic force/friction force microscopy. *Wear* **1999**, *225*, 678–689.
97. Lu, W.; Komvopoulos, K. Nanomechanical and nanotribological properties of carbon, chromium, and titanium carbide ultrathin films. *J. Tribol.* **2001**, *123*, 717–724.
98. Beake, B.D.; Lau, S.P. Nanotribological and nanomechanical properties of 5–80 nm tetrahedral amorphous carbon films on silicon. *Diam. Relat. Mater.* **2005**, *14*, 1535–1542.
99. Jiang, Z.; Lu, C.J.; Bogy, D.B.; Bhatia, C.S.; Miyamoto, T. Nanotribological evaluations of hydrogenated carbon films as thin as 5 nm on magnetic rigid disks. *IEEE Trans. Magn.* **1995**, *31*, 3015–3017.
100. Singh, R.K.; Xie, Z.H.; Bendavid, A.; Martin, P.J.; Munroe, P.; Hoffman, M. Effect of substrate roughness on the contact damage of DLC coatings. *Diam. Relat. Mater.* **2008**, *17*, 975–979.
101. Johnson, K.L. *Contact Mechanics*; Cambridge University Press: Cambridge, UK, 1985; p. 155.
102. Charitidis, C.; Logothetidis, S.; Douka, P. Nanoindentation and nanoscratching studies of amorphous carbon films. *Diam. Relat. Mater.* **1999**, *8*, 558–562.
103. Leyland, A.; Matthews, A. On the significance of the *H*/*E* ratio in wear control: A nanocomposite film approach to optimised tribological behavior. *Wear* **2000**, *246*, 1.
104. Leyland, A.; Matthews, A. Design criteria for wear-resistant nanostructured and glassy-metal coatings. *Surf. Coat. Technol.* **2004**, *177*, 317–324.
105. Sham, T.-L.; Tichy, J. A scheme for hybrid molecular dynamics/finite element analysis of thin film lubrication. *Wear* **1997**, *207*, 100–106.
106. Mo, Y.; Turner, K.T.; Szlufarska, I. Friction laws at the nanoscale. *Nature* **2009**, *457*, 1116–1119.
107. Johnson, K.L. Adhesion and friction between a smooth elastic spherical asperity and a plane surface. *Proc. R. Soc. Lond. Ser. A* **1997**, *453*, 163–179.
108. Luan, B.; Robbins, M.O. Contact of single asperities with varying adhesion: Comparing continuum mechanics to atomistic simulations. *Phys. Rev. E* **2006**, *74*, doi:10.1103/PhysRevE.74.026111.
109. Brenner, D.W.; Shenderova, O.A.; Harrison, J.A.; Stuart, S.J.; Ni, B.; Sinnott, S.B. A second-generation reactive empirical bond order (REBO) potential energy expression for hydrocarbons. *J. Phys. Condens. Matter* **2002**, *14*, 783.
110. Mylvaganam, K.; Zhang, L.C. Nano-Friction of some carbon allotropes. *J. Comput. Theor. Nanosci.* **2010**, *7*, 2199–2202.
111. Mishra, M.; Egberts, P.; Bennewitz, R.; Szlufarska, I. Friction model for single-asperity elastic-plastic contacts. *Phys. Rev. B* **2012**, *86*, doi:10.1103/PhysRevB.86.045452.
112. Bhushan, B. Nanotribology, nanomechanics and nanomaterials characterization. *Philos. Trans. R. Soc. A*: *Math. Phys. Eng. Sci.* **2008**, *366*, 1351–1381.
113. Zhang, S.; Wagner, G.; Medyanik, S.N.; Liu, W.K.; Yu, Y.H.; Chung, Y.W. Experimental and molecular dynamics simulation studies of friction behavior of hydrogenated carbon films. *Surf. Coat. Technol.* **2004**, *177*, 818–823.
114. Pastewka, L.; Moser, S.; Moseler, M. Atomistic insights into the running-in, lubrication, and failure of hydrogenated diamond-like carbon coatings. *Tribol. Lett.* **2010**, *39*, 49–61.

115. Çagin, T.; Che, J.; Gardos, M.N.; Fijany, A.; Goddard, W.A., III. Simulation and experiments on friction and wear of diamond: A material for MEMS and NEMS application. *Nanotechnology* **1999**, *10*, 278.
116. Bucholz, E.W.; Phillpot, S.R.; Sinnott, S.B. Molecular dynamics investigation of the lubrication mechanism of carbon nano-onions. *Comput. Mater. Sci.* **2012**, *54*, 91–96.

Nanomechanical and Tribological Properties of Carbon Nanotube/Polyvinyl Butyral Composites

Constantinos A. Charitidis,[1] Elias P. Koumoulos,[1] Mauro Giorcelli,[2] Simone Musso,[2,3] Pravin Jagadale,[2] Alberto Tagliaferro[2]

[1]*Department of Materials Science and Engineering, National Technical University of Athens, School of Chemical Engineering, Athens GR-157 80, Greece*

[2]*Applied Science and Technology Department, Politecnico di Torino, Torino IT-10129, Italy*

[3]*Department of Civil and Environmental Engineering, Massachusetts Institute of Technology, 77 Massachusetts Avenue, Cambridge, MA, 02139, USA*

The surface and subsurface mechanical and tribological properties of multiwall carbon nanotube (MWCNTs)/polyvinyl butyral (PVB) composites have been studied. Hardness and elastic modulus were obtained from nanoindentation, whereas the coefficient of friction of the composites was obtained using a nanoscratch method. The results show a clear impact of the percentage of CNTs filling on the monitored properties. Considerable improvement in the scratch resistance is obtained by the addition of CNTs and a maximum increase in nanomechanical properties is found at intermediate levels of CNTs filling. Creep studies revealed that a higher loading rate results in a greater primary creep deformation and leads to an increase of the total creep deformation, whereas the addition of MWCNTs affects the elastic recovery of the PVB matrix. POLYM. COMPOS., 34:1950–1960, 2013.

INTRODUCTION

Composites with nanofillers are a promising new class of materials which combine the advantages of the matrix (usually a polymer) and the fillers [1]. Carbon nanotubes (CNTs), with their extraordinary mechanical and electrical properties, high aspect ratio, and low density, have been extensively studied to improve the polymer matrix characteristics [2]. A key point in using CNTs as filler in polymer matrix is their dispersion in the matrix. This aspect is crucial to uniformly transfer the filler properties to the matrix. Several techniques have been employed to disperse CNTs, and results point out that the entanglement of CNTs is a key negative issue [3]. Therefore, it is important to start from a less entangled material to obtain a better dispersion of CNTs in the matrix. Multiwall CNTs (MWCNTs), having greater diameter than the single-wall CNTs (SWCNTs), are easier to disperse in polymer matrix. Several investigations have studied the elasticity [4,5], damage [6], buckling [7,8], tribology [9,10], and toughness [11] of CNTs-based composites. Other groups have investigated the changes in the glass transition behavior of polymers as a result of adding carbon nanotubes [12,13]. Recently, the viscoelastic and creep behavior of CNTs-based composites gained momentum toward using them for damping applications. Zhou et al. [14] have utilized uniaxial tensile test to measure the loss factor of composites based on SWCNTs. Alternatively, Suher et al. [15] utilized direct viscoelastic shear mode of CNTs–epoxy composite thin films to characterize the complex compliance and material loss factor. The investigators reported a 1,400% increase in loss factor (damping ratio) of the baseline epoxy by adding 50% CNTs by volume. Long-term viscoelastic/viscoplastic behavior of CNTs-based composites was investigated by Zhang et al. [16], using uniaxial tensile tests. It was demonstrated that SWCNTs additives in low-weight fractions (0.1–0.25%) are effective in limiting the load induced reorientation of the epoxy chain; resulting in significant slowing of the creep response. Efforts for modeling the viscoelastic properties of CNTs-based composites are carried out using both macroscale and microscale models. Plaseied and Fatemi [17] implemented a three-parameter Findley-type creep law [18] for predicting the creep compliance of a composite based on vinyl ester with 0.5 wt% of carbon nanofibers. Li et al. [19] developed a micromechanics model for predicting the linear viscoelastic properties of CNTs-reinforced polymer composites. Aside

Correspondence to: Constantinos A. Charitidis;
e-mail: charitidis@chemeng.ntua.gr
DOI 10.1002/pc.22602
Published online in Wiley Online Library (wileyonlinelibrary.com).

TABLE 1. MWCNTs characteristics.

Property	Value
Outer diameter (nm)	<8
Inside diameter (nm)	2–5
Ash (wt%)	<1.5
Purity (wt%)	>95
Length (μm)	10–30
Specific surface area (m^2/g)	500
Powder density (g/cm^3)	0.27
True density (g/cm^3)	~2.1

from the previously mentioned investigations, there are not many studies that report the creep behavior of CNTs-based composites under accelerated creep environment (high loads and high temperatures). Moreover, despite the increasing use of instrumented nanoindentation, there are even fewer investigations reporting the creep behavior of these composites via nanoindentation. In this article, we extend the use of instrumented nanoindentation to MWCNTs–PVB composite at different loads and loading rates. Furthermore, we utilize these nanoindentation tests to provide the creep time-dependent deformation during indentation at constant loads. The trends of the properties versus CNTs content will be also elucidated.

EXPERIMENTAL

Sample Preparation

Polyvinyl butyral (PVB) is a resin mainly used for applications that require strong binding, optical clarity, adhesion to different surfaces, toughness, and flexibility. It is prepared from polyvinyl alcohol by reaction with butyraldehyde. The IUPAC name of the polymer is poly[(2-propyl-1,3-dioxane-4,6-diyl) methylene]. It is in white powder form with specific gravity of 1.0830 g/cm^3. The characteristics of the MWCNTs, purchased from Cheap Tubes, used in this work are summarized in Table 1. To prepare CNTs–PVB (Butvar B-98, Sigma-Aldrich) composites, PVB was dissolved in a mixture of ethanol (Carlo Erba) (two parts) and 1-butanol (Sigma-Aldrich) (three parts) solvents. The CNTs was added into the PVB solution. The uniform dispersion of CNTs in composite solution was achieved by vigorous stirring (1,200 rpm). Viscous nature of the solution entrapped the gas bubbles. Sonication (ultrasonic frequency, 37 KHz) was carried out for 10 min so as to release the entrapped bubbles in the mixture. A 20-min degassing in vacuum step was subsequently undertaken to fully get rid of the trapped solvent gas bubbles. The composite was then cured in oven at 70°C for 4 h. Samples were prepared with four different MWCNTs contents: 0.5, 1, 3, and 5 wt%, on both sides of the percolation threshold [20]. Samples are labeled PVBC*x* where *x* is the CNTs content in wt% (i.e., PVBC3.0 is 3% sample).

Sample Characterization

Sample morphology was checked by a scanning field emission electron microscope (FE-SEM, Zeiss Supra 40), connected to an energy-dispersive X-ray Spectroscopy (Oxford Inca Energy 450), used to determine the average elemental composition, in particular the presence of non-carbon elements. The quality of nanotubes (i.e., the degree of graphitization of their walls) was monitored by Raman Spectroscopy (Renishaw Ramascope MicroRaman; laser excitation, 514 nm).

Nanoindentation testing was performed with Hysitron TriboLab® Nanomechanical Test Instrument, which allows the application of loads from 1 to $3 \cdot 10^4$ μN and records the displacement as a function of applied loads with high load (1 nN) and displacement (0.04 nm) resolutions. The TriboLab® employed in this study is equipped with a scanning probe microscope (SPM), in which a sharp probe tip moves in a raster scan pattern across a sample surface using a three-axis piezo positioner. In all nanoindentation tests, a total of 10 indents are performed with a spacing of 50 μm in a clean area environment with 45% humidity and 23°C ambient temperature. Data are subsequently averaged to determine statistically significant values of hardness (H) and elastic modulus (E). To operate under closed loop load or displacement control, feedback control option was used. All nanoindentation measurements have been performed with the standard three-sided pyramidal Berkovich probe, with an average radius of curvature of ~100 nm [21,22].

For conventional nanoindentation testing, identical loading and unloading time of 40 s were used and a 3-s delay was set between the end of the loading phase and the onset of the unloading one. In the case of creep experiment, loading and unloading times were identical (10 s), whereas creep time was set to 100 s. In a nanoindentation creep experiment, the tip is pushed into the surface at a constant rate of indentation until a prefixed load or penetration displacement is reached, then the load is held constant, whereas the indenter continues to creep into the material. When the indenter tip is held fixed at that load or displacement, the material beneath the indenter tip continues to deform in time. Finally, the indenter tip is retracted from the material. Creep within a specimen occurs during the hold time of the loading phase of nanoindentation testing and manifests itself as a change of indentation displacement, whereas the load is kept constant.

Hardness (H) and elastic modulus (E) values were extracted from the experimental data (load–displacement curves) using the Oliver–Pharr method [23,24], based on the half-space elastic deformation theory [25,26]. Prior to indentation, the area function of the indenter tip was calibrated in fused silica, a standard material for this purpose [27,28]. Nanoscratch testing is a versatile tool for the analysis of the mechanical properties of thin films and bulk materials [22]. The scratch tests

performed in this study consisted of three main segments. First, a prescratch scan under a very small load (1 μN) was carried out. Then, the indenter scraped the sample under a certain force and a scratch was generated. The normal applied loads used in this study were 0–400 μN. The length of the scratches was 10 μm. In all nanoscratch tests, a total of four scratches were performed for statistical purposes.

RESULTS AND DISCUSSION

Structural Characterization

FESEM analysis of MWCNTs shows (Fig. 1) that their diameter is consistent with the producer datasheet (Table 1). The impurities have been determined by EDX: Co (catalyst residual) 1.1%, Cl 1.0%, S 0.3%, and Al 0.2%.

The Raman spectrum shown in Fig. 1 clearly indicates well-resolved *D* and *G* peaks as well as a sharp *G′* peak. Although the *D*-peak is correlated with the size of the sp^2 regions, the *G*-peak is generated by the stretch of sp^2 bonds. *G′* is the first overtone of the *D*-peak. The *I*(*D*)/*I*(*G*) ratio of *D*- to *G*-peak intensities is equal to 0.34, whereas *I*(*D*)/*I*(*G′*) turns out to be 0.92. The low value of *I*(*D*)/*I*(*G*) and the sharpness of the *G*- and *D*-peaks indicate that the CNTs have well-graphitized walls. The low background indicates that the amount of disordered (amorphous) carbon is very low (amorphous carbon gives rise to very broad and heavily overlapping *D*- and *G*-peaks, not observed in Fig. 1c) [29].

To check the internal and subsurface distribution of CNTs, samples were cryofractured and subsequently examined by FESEM. Cryofracture is performed by dipping samples in liquid nitrogen and breaking them as soon as they are taken out, so that the samples remain brittle and there is no PVB elongation or CNTs dislocation during breaking process. In Fig. 2a–c, the image for pure PVB, PVBC1.0, and PVBC5.0, respectively, is shown. It can be observed that few that are close to the surface-clustered CNTs are present in PVBC1.0. This can account (as explained below) for some spread in the surface mechanical properties of the sample. On the other hand, the dispersion of CNTs in sample PVBC5.0 appears good (Fig. 2c). In the latter case, the percolation threshold is overcome. Hence, during the stirring step, contact between CNTs occurs, leading to a more efficient unbundling.

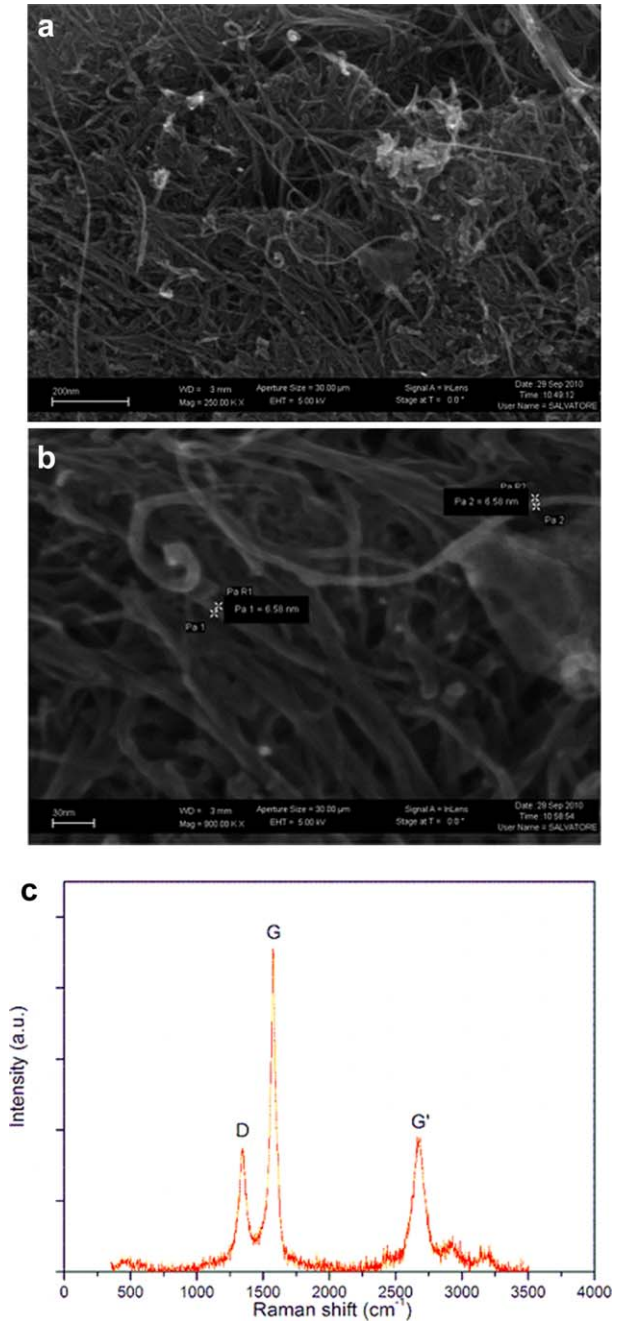

FIG. 1. (a) SEM image of MWCNTs, (b) evaluation of outer diameter (~6.6 nm) and (c) Raman spectrum of MWCNTs (*D*-peak is correlated with the size of the sp^2 regions, the *G*-peak is generated by the stretch of sp^2 bonds and *G′* is the first overtone of the *D*-peak). [Color figure can be viewed in the online issue, which is available at wileyonlinelibrary.com.]

Nanomechanical/Nanotribological Characterization—SPM Imaging

One of the challenges in studying the local mechanical properties in a small volume of material having microstructural gradients is that the traditional methods, for example tensile test and microhardness test, used to evaluate the mechanical behavior of bulk materials are not applicable, contrary to nanoindentation. Owing to the very low contact area between the indenter and the sample, very high stresses can be developed. The high hydrostatic pressure exerted by the surrounding material allows plastic deformation at room temperature when conventional mechanical testing leads only to fracture. At low loads, a very prominent phenomenon is the so-called indentation size effect (ISE) owing to imperfection in tip geometry [27]. Apparently, the existence of ISE may

DOI 10.1002/pc

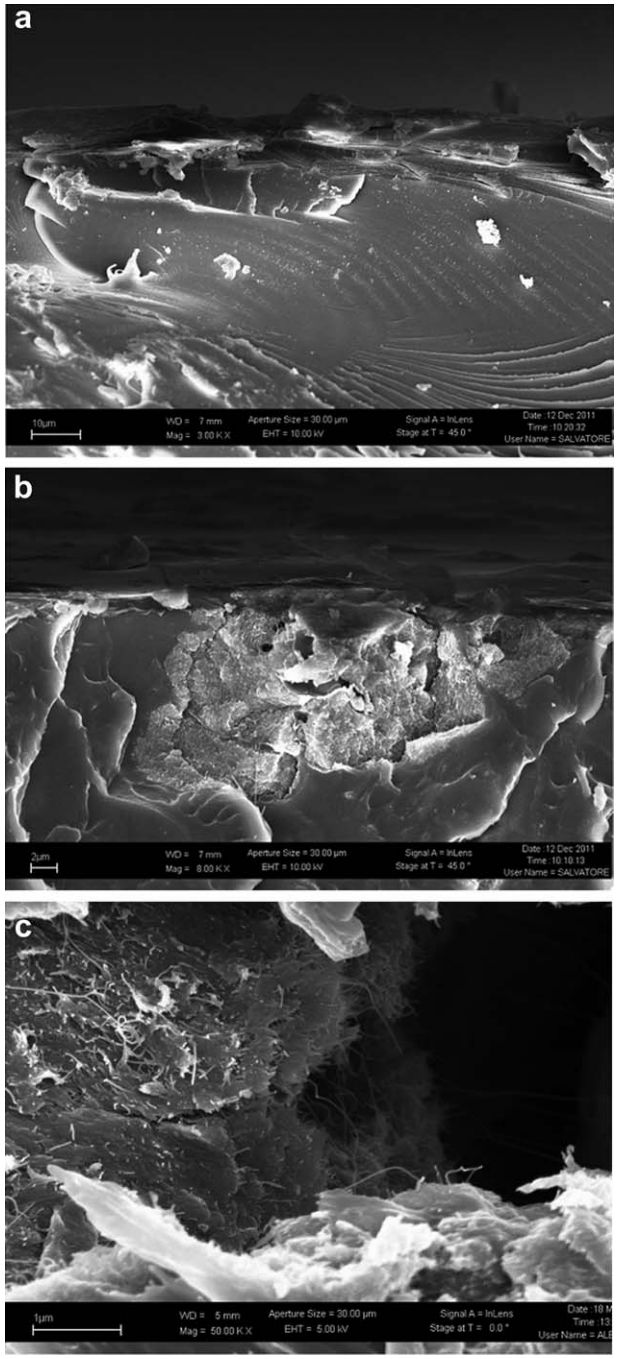

FIG. 2. SEM images of cryofractured samples PVB (a), PVBC1.0 (b), and PVBC5.0 (c).

hamper the accurate measurement of hardness value, and it is attributed to experimental artifact, a consequence of inadequate measurement capability [27].

Hardness and *E*-values were found to deviate at surface region (~0–200 nm), probably owing to roundness of the tip and ISE, tending to reach a constant value of 0.2 and 3.5 GPa, respectively. The reasons for the wide range in hardness and modulus values obtained from these nanoindentation measurements are currently unknown, but it is likely owing to a combination of factors, for example graded surface structure owing to CNTs concentration, adhesive forces between the tip and the sample and CNTs bundling. Improved nanomechanical properties are revealed for the case of PVBC1.0 addition in the polymer matrix, whereas PVBC5.0 samples exhibit decreasing H and *E*-values (for $h > 100$ nm) close to the plain PVB nanomechanical values (Fig. 3). Compared with other concentrations, the case of 1% MWCNTs is the optimal concentration threshold that strengthens the PVB matrix.

In nanoindentation testing, the volume tested is limited. Figure 3b shows that increasing displacement (i.e., tested volume) leads to a decrease in elastic modulus. Further penetrating in the material, the evaluated elastic modulus values will reach toward its bulk value. The empirical equation for describing the ISE in Meyer's law [30,31] is used, which uses a correlation technique between the applied indentation test load and the resultant indentation size using a simple power law, $P_{\max} = \mathrm{Ch}_C^n$, where C and n are constants derived directly from curve fitting of the experimental data. In particular, the exponent n, sometimes referred to as the Meyer index, and it is usually considered as a measure of ISE. Following the definition of the apparent hardness, $n = 2$ will indicate no ISE [30,31]. At low concentration (PVBC1.0), the good interfacial interaction leads to the stretching of the PVB molecules attached to the CNTs. A tube–tube slip in individual CNTs present in clusters also occurs. As CNTs concentration is increased (PVBC5.0), there is a large increase in the stiffness of the system, which results in reducing the energy dissipated during the experiment; however, there is more tube–tube slip in the system at higher (PVBC5.0) concentration, as percolation, coupled to a better dispersion (see above), leads to a higher contact surface among CNTs. The mechanical properties are reported to deteriorate with an increase in CNTs content, after a threshold concentration, a fact that is tentatively attributed to extensive tube–tube slip mechanism. At concentrations higher than percolation threshold, particle contacts are not only unavoidable, owing to statistical considerations, but, owing to the sticky interparticle potential, they give rise to larger agglomerates, acting as mechanical defects for the resulting composite [32–38].

The nanoindentation data for the material examined in this study are shown in Fig. 4a. The data show mostly nonlinear relationships (apart from PVBC3.0, where n is calculated ~1.05), implying that the traditional Meyer's law was suitable for describing the nanoindentation data. Through nonlinear regression analyses, the best-fit values of n-parameters are 1.72 for PVB and PVBC5.0, and ~1.5 for PVBC1.0 and PVBC0.5. These n-values highlight that hardness values are apparently higher at lower loads, pointing out the presence of an ISE, more relevant in the case of PVBC0.5 sample. In Fig. 4b and c, H and E ranges of PVB–CNTs composites for a displacement of 100–500 nm are shown. The range for H and E of PVBC5.0 is narrow compared to the respective range for PVBC1.0, confirming the good dispersion of CNTs in the PVB matrix and the presence of subsurface bundles in PVBC1.0 sample.

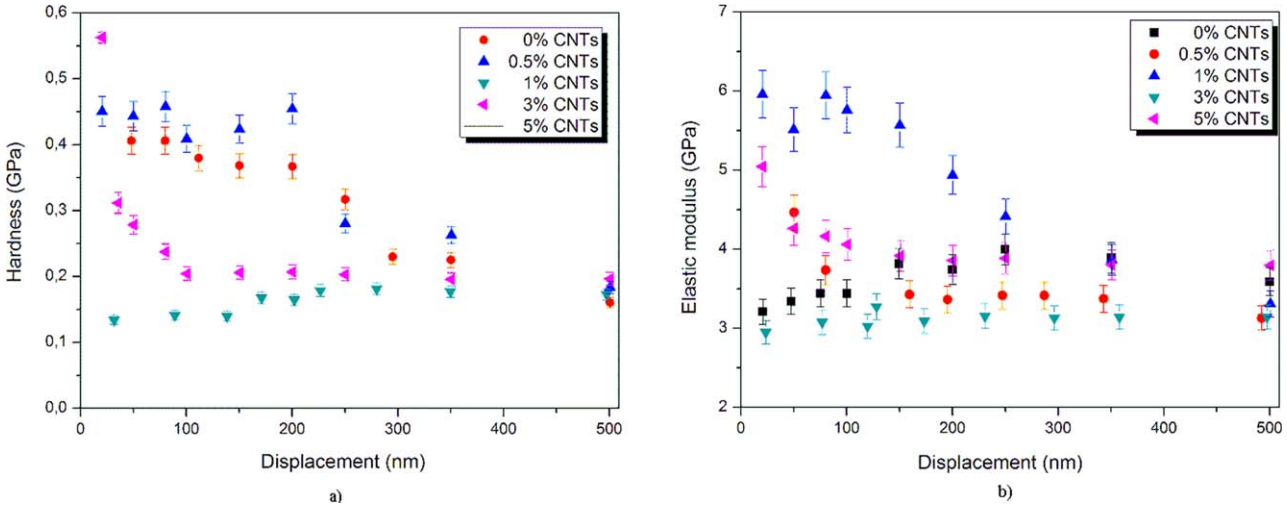

FIG. 3. (a) Hardness and (b) elastic modulus of PVB–CNTs composites as a function of displacement. Hardness and *E*-values deviate at surface region (∼0–200 nm), probably owing to roundness of the tip and ISE (addition of CNTs may decrease hardness, whereas increasing elastic modulus), tending to reach a constant value of 0.2 and 3.5 GPa. [Color figure can be viewed in the online issue, which is available at wileyonlinelibrary.com.]

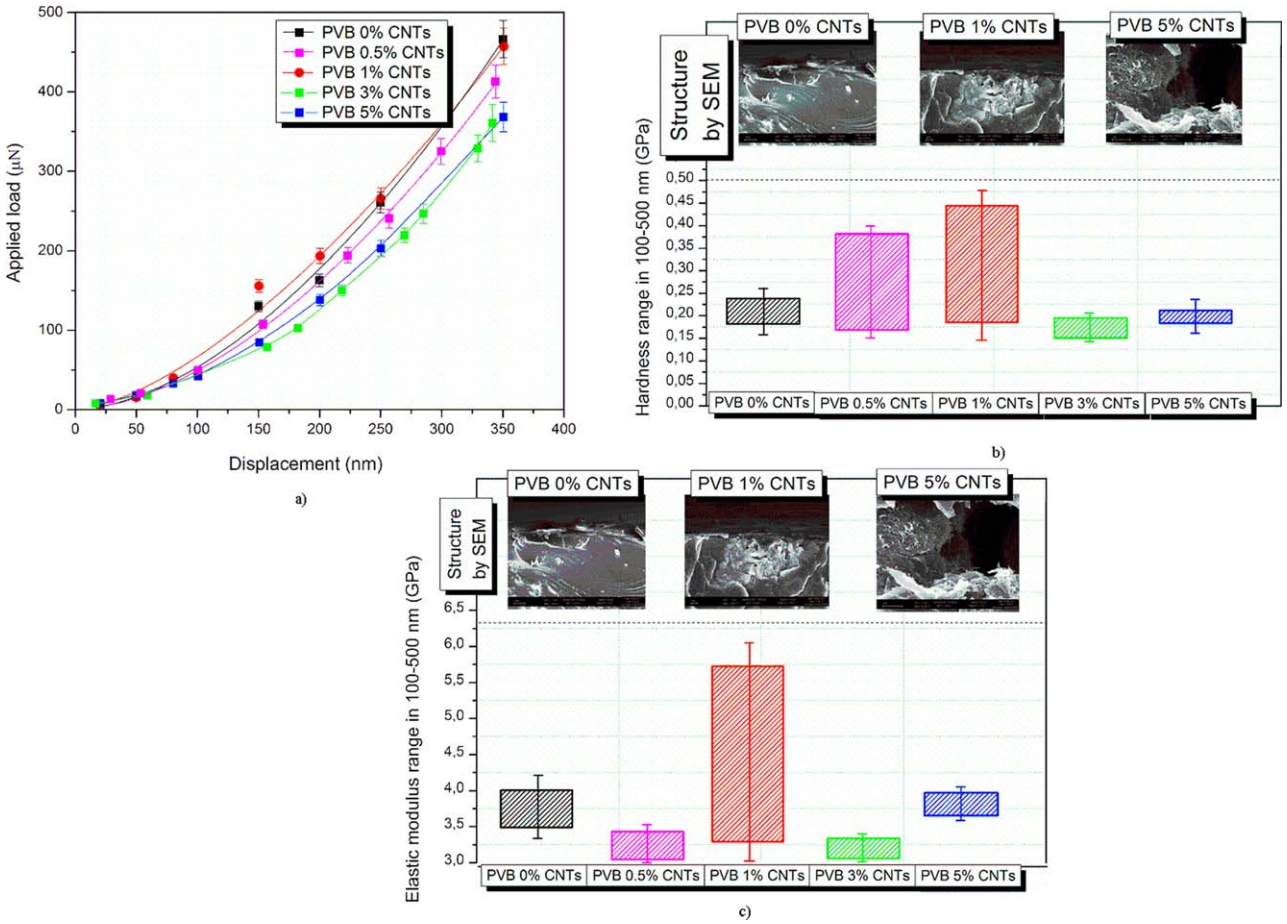

FIG. 4. (a) Plots of P_{max} versus h_c according to Meyer's law for PVB–CNTs composites, (b) hardness ranges of PVB–CNTs composites for the displacement of 100–500 nm, and (c) elastic modulus ranges of PVB–CNTs composites for the displacement of 100–500 nm. [Color figure can be viewed in the online issue, which is available at wileyonlinelibrary.com.]

 DOI 10.1002/pc

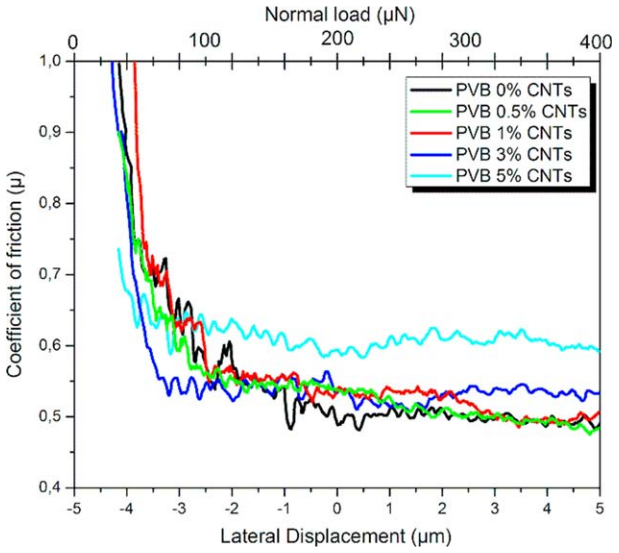

FIG. 5. CoF for PVB–CNTs composites, obtained through nanoscratch testing. PVB with 5% CNTs exhibits increased CoF, compared with plain and PVB nanocomposites; hence, nanoscratching revealed that there is considerable improvement in the scratch resistance owing to the addition of CNTs. [Color figure can be viewed in the online issue, which is available at wileyonlinelibrary.com.]

When the scratch tip ploughs through the material ahead of it, the material will be either pushed forward or piled up sideways [22]. This last phenomenon is usually observed for relatively ductile polymers, where ironing and plastic deformation take place readily. In addition to the surface friction between the substrate and the scratch tip, the material accumulated ahead of the tip.

Coefficient of friction (CoF) is defined as the ratio of the lateral force modulus to the normal force modulus, and depends on several factors including the indenter geometry, surface roughness of the sample, and the material properties of the sample. Rather than simply being a friction parameter, CoF value is also a measure of the resistance to scratch. A harder, wear-resistant material would impose more resistance to scratch and the indenter will consequently experience a larger lateral force. In Fig. 5, CoFs for all samples are shown (four identical scratches were performed at three samples of each type for statistical purposes). As the first half of the data is influenced by the surface morphology, the average was calculated using the data from the latter half of the scratch. The friction coefficient changes from 1 to 0.5 continuously at the beginning of scratching, which is corresponding to the loading stage, for PVBC1.0 and plain PVB matrix. Then, it remains unaltered at 0.5 for about 25 s during the steady scratching process. The average values of the steady state are taken as the effective friction coefficient. These coefficient trends are quite similar for both samples, implying no significant differences between them. For plain PVB matrix, the friction coefficient decreases with increasing normal load to a minimum value (∼0.5) and remains constant, implying plastic flow is the dominant deformation mode. For PVBC1.0, the friction coefficient decreases with increasing normal load to a minimum temporary value (∼0.52) corresponding to the initiation of scratching, then increases to finally decrease to ∼0.48. The main friction mechanism in the first stage was adhesion, whereas both adhesion and ploughing contribute to the friction coefficient in the last stage. PVBC5.0 exhibits increased CoF, compared with plain PVB matrix and PVBC1.0; hence, nanoscratching revealed that there is considerable improvement in the scratch resistance owing to the addition of CNTs.

Wear Analysis—Deformation Mechanism

An important feature of indentation experiments is that the material around the contact area tends to deform upward (pile-up) or downward (sink-in) with respect to the indented surface plane. The occurrence of such pile-up and sink-in patterns is usually interpreted in terms of the strain-hardening behavior of the indented material [39–42]. Good knowledge of the deformation zone around an indent is of considerable importance for nanoindentation testing because the shape of the out-of-plane displacement zone determines the actual contact area between the indenter and the specimen. Sink-in patterns reduce and pile-up patterns increase the contact area. These differences in the surface deformation mode affect the quantitative analysis of the hardness measurements. Not taking the piling-up or sinking-in into account in micro- and nanoindentation hardness tests can result in significant errors when extracting hardness values from the experimental data [39,40]. The presence of creep during nanoindentation has an effect on pile-up, which results in incorrect measurement of the material properties. Fischer-Cripps [43] observed this behavior, in case where the measured elastic modulus was much less than expected. Rar et al. [44] observed that the same material when allowed to creep for a long duration produced a higher value of pile-up/sink-in, indicating a switch from an initial elastic sink-in to a plastic pile-up.

In Fig. 6, the normalized pile-up/sink-in height h_c/h_m is plotted versus displacement (a) and the normalized hardness H/E (b). Rate-sensitive materials experience less pile-up compared to rate-insensitive materials owing to strain hardening. Cheng and Cheng [45] reported a 22% pile-up for a work hardening exponent. This is consistent with the fact that when h_c/h_m approaches 1 for small H/E, deformation is intimately dominated by pile-up [46,47]. On the other hand, when h_c/h_m approaches 0 for large H/E, it corresponds to purely elastic deformation and is apparently dominated by sink-in in a manner prescribed by Hertzian contact mechanics [48]. Higher stresses are expected in high H/E, hard materials, and high stress concentrations develop toward the indenter tip, whereas in the case of low H/E, soft materials, the stresses are lower and are distributed more evenly across the cross-section of the material [49,50]. The high ratio of hardness to

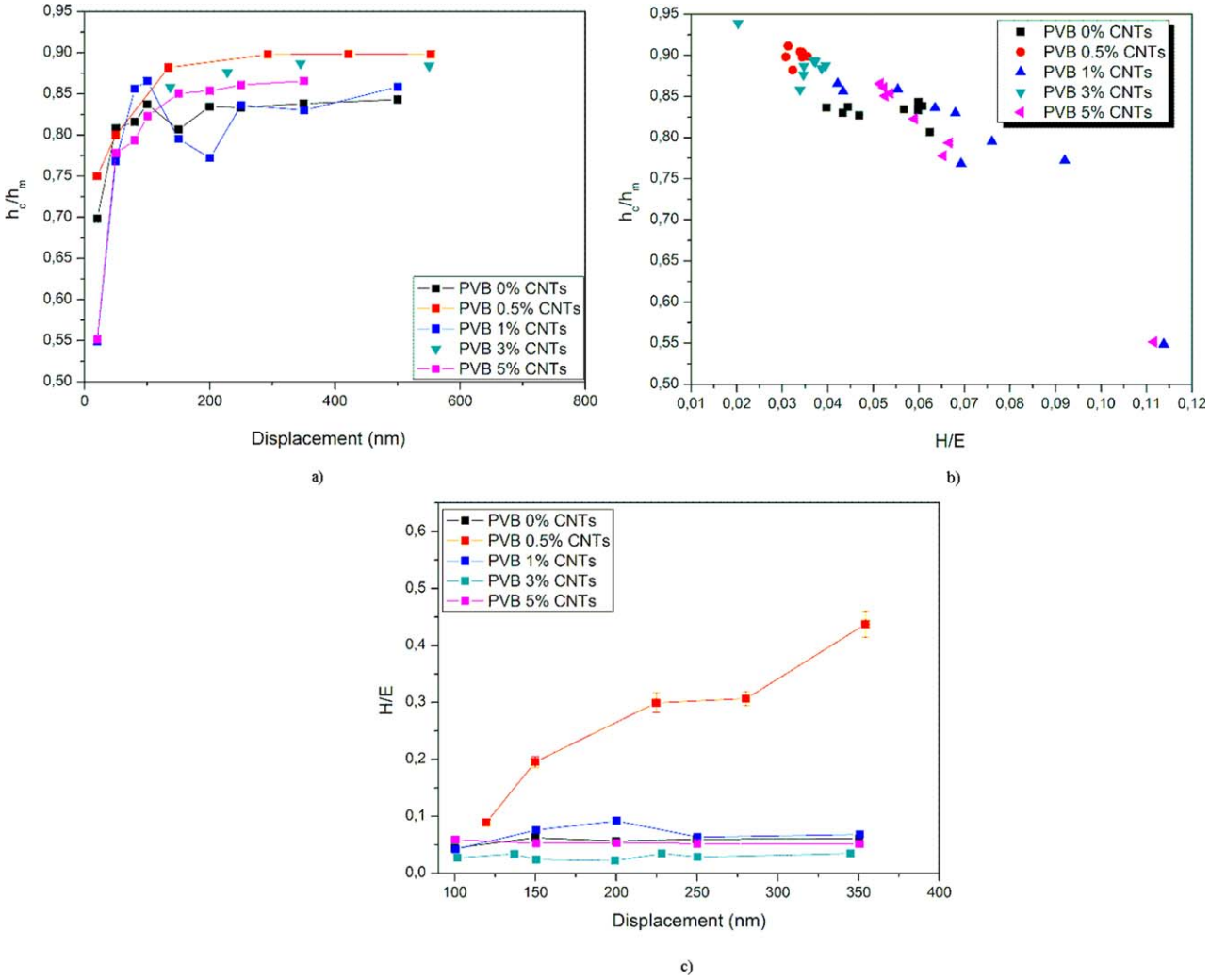

FIG. 6. (a) Normalized pile-up/sink-in height h_c/h_m plotted versus displacement and (b) normalized hardness H/E. Additionally, the ratio of hardness/elastic modulus versus displacement is plotted (c). [Color figure can be viewed in the online issue, which is available at wileyonlinelibrary.com.]

elastic modulus (H/E) is indicative of the good wear resistance in a disparate range of materials [50,51]: ceramic, metallic, and polymeric (e.g., c-BN, tool steel, and nylon, respectively), which are equally effective in resisting attrition for their particular intended application. In Fig. 6, the change of H/E slope reveals the strengthening of composites with addition of 0.5% CNTs (PVBC0.5), whereas H/E decreases with addition of 3 and 5% CNTs in the PVB matrix (PVBC3.0 and PVBC5.0); however, lower deviation of H/E values for PVBC5.0 reveals the good dispersion on the matrix, with impact in almost stable behavior at resistance to wear for the displacement range from ~100 to 350 nm. As shown in Fig. 6b, it is clear that while for the pure PVB, h_c/h_m is independent of the normalized hardness H/E, the addition of CNTs leads to a decrease of h_c/h_m for increasing H/E values; this is attributed to the switch from pile-up to sink-in deformation behavior, after the addition of CNTs.

Creep Investigation—Onset of Plasticity

The nanoindentation creep consists of two stages, transient (primary creep), and steady state (secondary creep) [52–57]. It is postulated that the stress fields in the material underneath the indenter develop a chemical potential gradient that lead to a thermally activated diffusional flux of atoms moving from below the indenter to the surface and along the interface between the indenter and the specimen, even under an elastic contact [58,59]. In Fig. 7, the penetration of the indenter tip into the sample surface (i.e., creep displacement) during the peak load holding against the holding time is shown, for each experiment. The magnitude of the total creep displacement during the peak load holding is strongly load dependent, that is, larger peak load causes larger penetration. The creep displacement increases but at a decreasing rate, and it becomes almost linear with regard to the holding time (an initial sharp rise in creep displacement in the early part of

 DOI 10.1002/pc

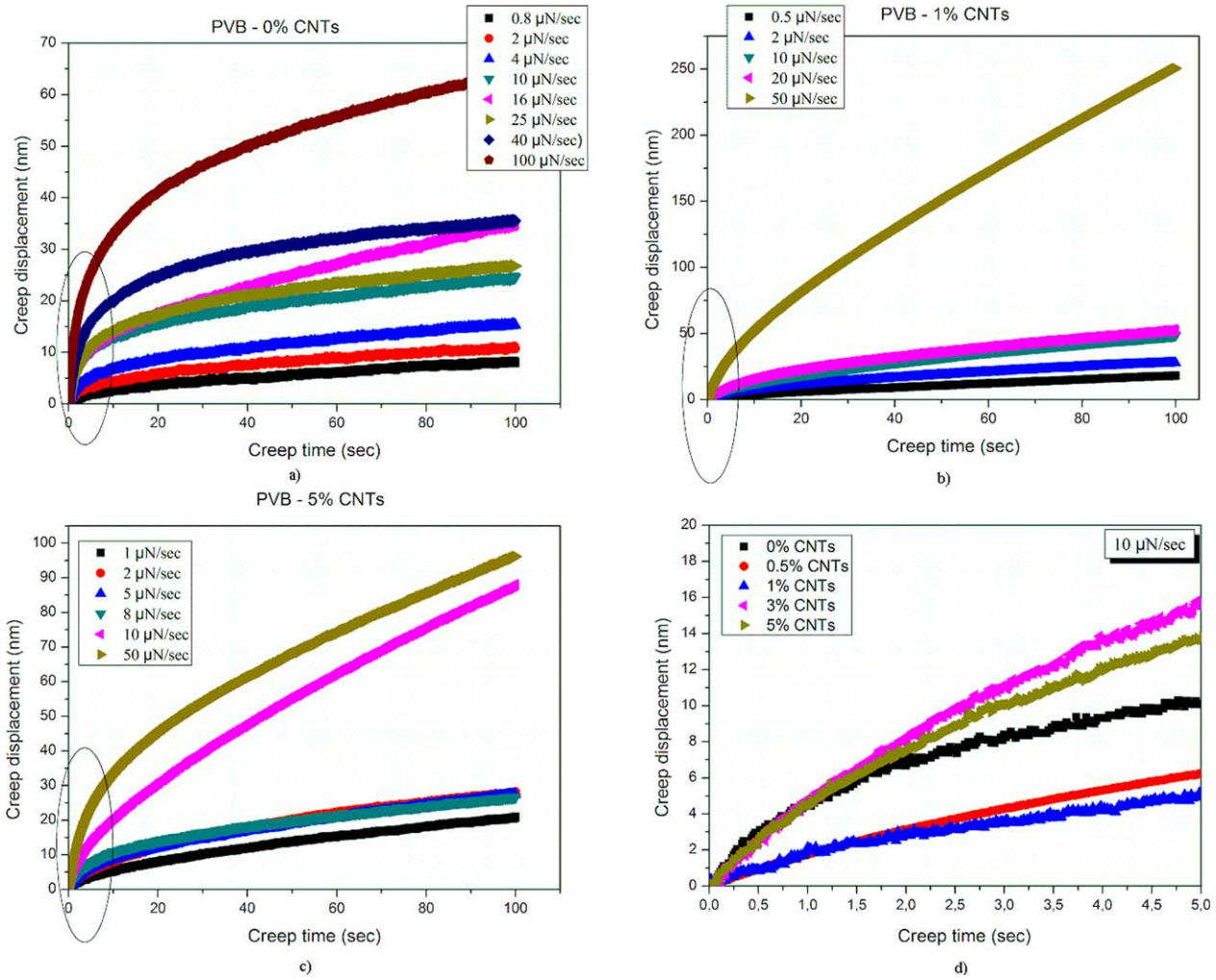

FIG. 7. Comparison of the creep curves under different loading rates (a–d). The displacement axis was reset to show only the creep displacement, and time was reset to zero at the beginning of the hold period to facilitate comparison. The primary creep stage is noted in circle (a–c). [Color figure can be viewed in the online issue, which is available at wileyonlinelibrary.com.]

the creep segment, followed by a region showing a smaller rate of increase in creep displacement). The general profile of these curves is similar to the strain versus time plot obtained for the uniaxial tensile creep testing of bulk materials that exhibit power-law creep behavior [58,59]. The initial stage of the curves (noted in circle) in Fig. 7 corresponds to transient creep, and after this initial displacement, the descent of the indenter continues but the rate of descent decreases to attain a steady-state value. The transient creep deformation showed a dependence upon the loading rate. As shown in Fig. 7, a higher loading rate causes a greater primary creep deformation and leads to an increase of the total creep deformation. This behavior may be attributed to the fact that at the lowest loading rate (that obviously leads to a longer time needed to reach the final load value), a relevant creep deformation may also occur during the loading process [60]. As a consequence, the creep during the holding time will decrease. Moreover, the substructure formed beneath the indenter owing to the indentation stress may be different at different loading strain rates, and this substructure will affect the subsequent creep behavior [61].

In Fig. 7d, the direct creep comparison of plain PVB and PVB with CNTs is shown; the insertion of 1% CNTs strengthens the material, whereas the addition of 3 and 5% CNTs reveals a rather creep behavior, which is in line with the nanotube–nanotube slipping assumption, probably attributed to the fact that at 3 and 5 wt% the percolation threshold [62] is overcome and a CNTs network is present. Nanoindentation tends to produce relatively high local stresses and it is fairly common experience for these to generate obvious time-dependent effects, such as progressive indenter penetration when a constant load is maintained. Consequently, it will be quite often necessary to take into account the possibility of creep affecting the results when experimental nanoindentation data are to be used to obtain constitutive relations. Figure 8 shows the loading–unloading curves for PVB

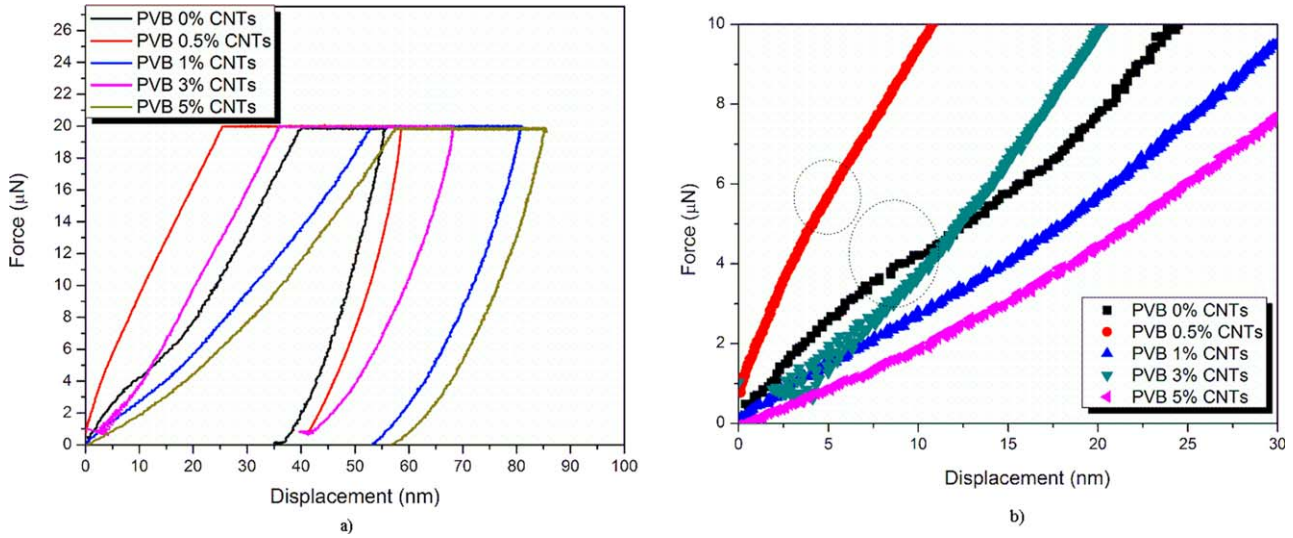

FIG. 8. Loading–unloading curves of PVB–CTN composites for applied load of 20 μN. The loading–unloading curves exhibit interesting local discontinuities measured in the load-controlled test of this study; these are characteristic of energy-absorbing or energy-releasing events occurring beneath the indenter tip. The transition from purely elastic to elastic/plastic deformation, that is gradual slope change (yield-type "pop-in") is observed only for the case of plain PVB at ~8 nm. [Color figure can be viewed in the online issue, which is available at wileyonlinelibrary.com.]

composites, which exhibit interesting local discontinuities measured in the load-controlled test of this study; these are characteristic of energy-absorbing or energy-releasing events occurring beneath the indenter tip. However, the transition from purely elastic to elastic/plastic deformation, that is gradual slope change (yield-type "pop-in"), is observed only for the case of plain PVB at ~8 nm. As nanoindentation is a localized process, an increase in local crystallinity can also lead to an increase in value of the hardness and modulus. A measure of the plasticity of a material is given by the "plasticity index" which, in the case of nanoindentation, can be taken as the ratio of the area enclosed between the loading–unloading curves to the area under the loading part of the curve.

For a perfectly plastic material, this value is 1, whereas for a viscoelastic material it is between 0 and 1. It is seen that the addition of CNTs has significant effect on the plasticity index; all PVB composites exhibit similar behavior, more plastic than plain PVB (note that the creep undergone by the material during the holding at maximum load should not be taken into account in the calculation). This shows that the addition of MWCNTs affects the elastic recovery of PVB matrix.

CONCLUSIONS

The improvements in the properties of polymer–MWCNTs were not as high as anticipated through the use of mixture rule, indicating either that an insufficient dispersion or that the hypothesis of the model are not fully fulfilled by this composite. Nevertheless, composite samples showed better mechanical properties compared to the neat polymer matrix. For larger nanoindentation creep load, the creep resistance induced by the addition of MWCNTs is reduced. This behavior might indicate a failure of the polymer–MWCNTs interface at high load levels. PVBC1.0 exhibited improved nanomechanical properties, whereas PVBC5.0 revealed decreasing H- and E-values (for $h > 100$ nm) almost reaching the plain PVB nanomechanical values. However, the dispersion of CNTs has a great impact in nanomechanical properties and should be taken into consideration; good dispersion is also confirmed by the constant values of H and E for PVBC5.0 (for $h > 100$nm), whereas, for example for PVBC1.0, H and E are lower than PVBC5.0 for 500 nm of displacement. The ranges of H and E for PBVC5.0 are narrow compared to the respective range for PVBC1.0, confirming the good dispersion of CNTs in the PVB matrix, revealing that there is considerable improvement in the scratch resistance owing to the addition of carbon nanotubes. Lower deviation of H/E values for PVBC5.0 reveals the good dispersion on the matrix, with impact in almost stable behavior at resistance to wear. Higher loading rate results in a greater primary creep deformation and leads to an increase of the total creep deformation. The insertion of 1% CNTs strengthens the material, whereas the addition of 5% CNTs leads to a rather creep behavior, which is in line with the nanotube–nanotube slipping assumption. The addition of MWCNTs affects the elastic recovery of PVB matrix, as revealed by load–displacement curves for all samples. Furthermore, scatter in the values of nanomechanical properties can be used as a tool to investigate nonuniform subsurface dispersion of CNTs.

ACKNOWLEDGEMENTS

C.A. Charitidis and E.P. Koumoulos greatefully acknowledge the EU FP7 Project "Enhancing structural

efficiency through novel dissimilar material joining techniques" (SAFEJOINT) under Grant Agreement no. 310498 for partial support of this work. Also, Salvatore Guastella is kindly acknowledged for providing the FESEM results.

REFERENCES

1. S.C. Tjong, *Mater. Sci. Eng. R Rep.*, **53**, 73 (2006).
2. E.T. Thostenson and T.W. Chou, *Carbon*, **44**, 3022 (2006).
3. S. Pegel, P. Potschke, T. Villmow, D. Stoyan, and G. Heinrich, *Polymer*, **5**, 2123 (2009).
4. W.H. Li, X.H. Chen, C.S. Chen, L.S. Xu, Z. Yang, and Y.G. Wang, *Polym. Compos.*, **29**, 972 (2008).
5. A. Selmi, C. Friebel, I. Doghri, and H. Hassis, *Compos. Sci. Techol.*, **67**, 2071 (2007).
6. C.C. Kao and R.J. Young, *J. Mater. Sci.*, **45**, 1425 (2010).
7. C. Bower, R. Rosen, J. Han, and O. Zhou, *Appl. Phys. Lett.*, **74**, 3317 (1999).
8. C.Y. Li and T.W. Wei, *Compos. Sci. Techo.*, **66**, 2409 (2006).
9. L.F. Giraldo, B.L. Lopez, and W. Bostow, *Polym. Eng. Sci.*, **49**, 896 (2009).
10. C. Wang, T. Xue, B. Dong, Z. Wang, and H.L. Li, *Wear*, **265**, 1923 (2008).
11. L.Y. Sun, R.F. Gibson, F. Gordaninejad, and J. Suher, *Compos. Sci. Technol.*, **69**, 2392 (2009).
12. X. Gong, J. Liu, S. Baskaran, R. Voise, and J.S. Young, *Chem. Mater.* **12**, 1049 (2000).
13. M.S. Shaffer and A.H. Windle, *Adv Mater.*, **11**, 937 (1999).
14. X. Zhou, K.W. Wang, and C.E. Bakis, *J. Compos. Mater.*, **44**, 2301 (2010).
15. J. Suher, N. Koratkar, P. Keblinski, and P. Ajayan, *Nat. Mater.*, **4**, 134 (2005).
16. W. Zhang, A. Joshi, Z. Wang, R.S. Kane, and N. Koratkar, *Nanotechnology*, **18**, 185703 (2007).
17. A. Plaseied and A. Fatemi, *J. Reinf. Plast. Compos.*, **28**, 1775 (2009).
18. W.N. Findley, J.S. Lai, and K. Onaran, Creep and Relaxation of Nonlinear Viscoelastic Materials: With an Introduction to Linear Viscoelasticity, Dover Publication, New York, 344 (1989).
19. K. Li, X.L. Gao, and A.K. Roy, *Mech. Adv. Mater. Struct.*, **13**, 317 (2006).
20. I.-Y. Jeon, D.W. Chang, N. Ashok Kumar, and J.-B. Baek. "Functionalization of carbon nanotubes," in Carbon Nanotubes - Polymer Nanocomposites, S. Yellampalli, Ed., InTech, DOI: 10.5772/18396 (2011).
21. C.A. Charitidis, *Int. J. Refract. Met. Hard Mater.*, **28**, 51 (2010).
22. E.P. Koumoulos, C.A. Charitidis, D.P. Papageorgiou, A.G. Papathanasiou, and A.G. Boudouvis, *Surf. Coat. Technol.*, **206**, 3823 (2012).
23. M. Troyon and L. Huang, *Surf. Coat. Technol.* **201**, 1613 (2006).
24. W.C. Oliver and G.M. Pharr, *Mater. Res.*, **7**, 1564 (1992).
25. I.N. Sneddon, *Math. Proc. Camb. Philos. Soc.*, **44**, 492 (1948).
26. R.B. King, *Int. J. Solid Struct.*, **23**, 1657 (1987).
27. E.P. Koumoulos, C.A. Charitidis, N.M. Daniolos, and D.I. Pantelis, *Mater. Sci. Eng. B*, **176**, 1585 (2011).
28. H. Bei, E.P. George, J.L. Hay, and G.M. Pharr, *Phys. Rev. Lett.* **95**, 045501 (2005).
29. M.S. Dresselhaus, G. Dresselhaus, R. Saito, and A. Jorio, *Phys. Rep.*, **409**, 47 (2005).
30. U. Kolemen, *J. Alloys Comp.* **425**, 429 (2006).
31. O. Sahin, O. Uzun, U. Kolemen, and N. Ucar, *Mater. Charact.*, **58**, 197 (2007).
32. Y. Li, T. Yu, T. Pui, P. Chen, L. Zheng, and K. Liao, *Compos. Sci. Technol.*, **71**, 1665 (2011).
33. K.T. Kim and W.H. Jo, *J. Polym. Sci.: Part A Polym. Chem.*, **48**, 4184 (2010).
34. G.S. Zhuang, G.X. Sui, Z.S. Sun, and R. Yang, Pseudoreinforcement effect of multiwalled carbon nanotubes in epoxy matrix composites. *J. Appl. Polym. Sci.*, **102**, 3664 (2006).
35. R. Ribeiro, S. Banda, Z. Ounaies, H. Ucisik, M. Usta, and H. Liang, *J. Mater. Sci.*, **47**, 649 (2012).
36. M. Nadler, J. Werner, T. Mahrholz, U. Riedel, and W. Hufenbach, *Compos. Part A: Appl. Sci. Manuf.*, **40**, 932 (2009).
37. B. Fiedler, F.H. Gojny, M.H.G. Wichmann, M.C.M. Nolte, and K. Schulte, *Compos. Sci. Technol.* **66**, 3115 (2006).
38. K. Prashantha, J. Soulestin, M.F. Lacrampe, M. Claes, G. Dupin, P. Krawczak, *eXP Polym. Lett.* **2**, 735 (2008).
39. G.M. Pharr, W.C. Oliver, and F.R. Brotzen, *J. Mater. Res.*, **7**, 613 (1992).
40. W.D. Nix, *Mater. Sci. Eng. A*, 234–236, **37** (1997).
41. M.M. Chaudhri and M. Winter, *J. Phys. D Appl. Phys.* **21**, 370 (1988).
42. J. Alcala, A.C. Barone, and M. Anglada, *Acta Mater.*, **48**, 3451 (2000).
43. A.C. Fischer-Cripps, *Mater. Sci. Eng. A*, **385**, 74 (2004).
44. A. Rar, S. Sohn, W.C. Oliver, D.L. Goldsby, T.E. Tullis, and G.M. Pharr, On the Measurement of Creep by Nanoindentation with Continuous Stiffness Techniques, Materials Research Society, Boston, MA, USA, 119 (2005).
45. Y.T. Cheng and C.M. Cheng, *Philos. Mag. Lett.*, **78**, 115 (1998).
46. R. Hill, B. Storakers, and A.B. Zdunek, *Math. Phys. Sci.*, **423**, 301 (1989).
47. S. Biwa and B. Storakers, *J. Mech. Phys. Solid*, **43**, 1303 (1995).
48. H. Hertz, Miscellaneous Papers, Macmillan, New York (1896).
49. Y.T. Cheng and C.M. Cheng, *Surf. Coat. Technol.*, 133–134, **417** (2000).
50. A. Leyland and A. Matthews, *Surf. Coat. Technol.*, 177–178, **317** (2004).
51. A. Leyland and A. Matthews, Optimization of Nanostructured Tribological Coatings, Springer, New York, 511 (2007).
52. C.C. Huang, M.K. Wei, and S. Lee, *Int. J. Plast.*, **27**, 1093 (2011).
53. M.J. Mayo and W.D. Nix, *Acta Metall.*, **36**, 2183 (1988).

54. B.N. Lucas and W.C. Oliver, *Metall. Mater. Trans. A*, **30**, 601 (1999).
55. W.B. Li and R. Warren, *Acta Metall.*, **41**, 3065 (1993).
56. H. Li and A.H.W. Ngan, *J. Mater. Res.*, **19**, 513 (2004).
57. Z.Q. Cao and X. Zhang, *Scr. Mater.*, **56**, 249 (2007).
58. H. Pelletier, J. Krier, P. Mille, and A. Cornet, *Thin Solid Film*, **379**, 147 (2000).
59. S. Mandal, S. Kose, A. Frank, and A.A. Elmustafa, *Int. J. Surf. Sci. Eng.*, **2**, 41 (2008).
60. S. Yang, Y.W. Zhang, and K.Y. Zeng, *J. Mater. Res.* **19**, 3053 (2004).
61. S. Yang, Y.W. Zhang, and K.Y. Zeng, *J. Appl. Phys.*, **95**, 3655 (2004).
62. A. Chiolerio, M. Castellino, P. Jagdale, M. Giorcelli, S. Bianco, and A. Tagliaferro, "Electrical properties of CNT-based polymeric matrix nanocomposites," in Yellampalli Siva. Carbon Nanotubes—Polymer Nanocomposites, ISBN/ISSN: 9789533074986, INTECH Open Access Publisher, Rijeka, Croatia, 215 (2011).

 DOI 10.1002/pc

Polymer Degradation and Stability 96 (2011) 470–476

Contents lists available at ScienceDirect

Polymer Degradation and Stability

journal homepage: www.elsevier.com/locate/polydegstab

Mechanical behaviour of a poydimethylsiloxane elastomer after outdoor weathering in two different weathering locations

Panagiota N. Eleni [a,*], Magdalini K. Krokida [a], Gregory L. Polyzois [b], Constantinos A. Charitidis [a], Elias P. Koumoulos [a], Vasiliki P. Tsikourkitoudi [a], Ioannis Ziomas [a]

[a] School of Chemical Engineering, National Technical University of Athens, Zografou Campus, 15780 Athens, Greece
[b] Department of Prosthodontics, Division of Removable Prosthodontics, Dental School, University of Athens, 2 Thivon Str Goudi, 115 27 Athens, Greece

ARTICLE INFO

Article history:
Received 20 July 2010
Received in revised form
5 January 2011
Accepted 13 January 2011
Available online 26 January 2011

Keywords:
Compression
Nanoindentation analysis
Natural weathering
Polydimethylsiloxane
Tensile testing

ABSTRACT

The degradation of maxillofacial prosthetic elastomers that occur during physical weathering is usually responsible for the replacement of the prosthesis. In this study the mechanical behaviour of a polydimethylsiloxane (PDMS) elastomer was investigated, after 1 year outdoor weathering in two different weathering locations in Greece (Thessaloniki, Athens). The hypothesis investigated was that irradiation time did not affect the measured properties. Specimens (Elastomer 42) were prepared according to manufacturer's instructions and exposed to solar radiation for 1 year. Compression, tensile and nanoindentation tests were performed before and after the exposure. Compression and tensile data were also subjected to analysis of variance (ANOVA) and Tukey Post hoc tests at a level of $\alpha = .05$. These properties were selected due to their clinical significance for fabrication and maintenance of a facial prosthesis. According to statistical analysis all the measured properties changed significantly after outdoor weathering. More specifically, most of the properties presented significant changes after six months of weathering. The observed changes also depended on the weathering locations. The hypothesis investigated was rejected. Material A became harder and the observed differences in the mechanical behaviour resulted from photo-degradation and hydrolysis that might occur due to weathering. The study also provides new information about maxillofacial prosthetics serviceability obtained from nanoindentation tests.

1. Introduction

External maxillofacial prostheses are used to rehabilitate anatomy, function or cosmetics of facial regions that are missing or changed due to disease, accident or congenital malformation, and cannot be surgically restored [1,2]. Different types of materials are used to fabricate maxillofacial prostheses including poly(methyl methacrylate), poly(vinyl chloride), chlorinated polyethylene, polyurethanes, and silicones [2–5]. Polymeric materials are highly versatile, with low thermal stability and little resistance to solar radiation and therefore their performance is still far from ideal [6]. Polydimethylsiloxanes are the most widely used materials in maxillofacial prosthesis mainly due to their easy manipulation. In addition, comparing to other polymer prosthetics, they present excellent overall radiation resistance [7–11].

Natural or outdoor weathering of polymers can induce significant changes in their chemical, physical, and mechanical properties. The main climate characteristics that cause degradation are sunlight, temperature, moisture, wind, dust and pollutants. More precisely, deterioration is a photo-oxidative attack; that is the combined action of oxygen and sunlight on their chemical structure. Thus, it is preferable to have factual information on the actual long term performance of a material outdoors instead of an artificial weathering. The destructive effect of the weather on polymeric materials has strong dependence on geographic location, season, time of day, cloud cover and exposure orientation, since the critical weather factors vary with these conditions. Different climate conditions can also be observed during different seasons and years, so it is preferable to run outdoor tests during different seasons and over a period of at least one year [12]. Artificial weathering can also approximate the outdoor performance of polymers and in many cases is used to predict the lifetime of polymers under service conditions [13–15]. However, accelerated weathering might influence the degradation mechanism and could lead to totally wrong estimates of the lifetime of polymers [13,16,17]. In previous studies

* Corresponding author. Tel.: +30 2107723149; fax: +30 2107723155.
E-mail address: peleni@central.ntua.gr (P.N. Eleni).

0141-3910/$ – see front matter © 2011 Elsevier Ltd. All rights reserved.
doi:10.1016/j.polymdegradstab.2011.01.017

mathematical modelling has been presented as an essential process in order to predict the measured properties with solar or accelerated irradiation time [18–21].

The aim of this study was to investigate the effect of irradiation time and weathering location after aging for 1 year on some mechanical properties i.e. tensile and compress strength, modulus of elasticity, elongation at break, and nano-hardness, of a maxillofacial PDMS elastomer. Our null hypothesis stated that the examined mechanical properties of maxillofacial silicone elastomer are not affected by irradiation time and weathering location.

2. Materials and methods

2.1. Materials

The commercial material used and the curing conditions employed in this study are shown in Table 1. Forty two rectangular specimens ($15 \times 20 \times 35$ mm) for nanomechanical analysis, and forty two dumbbell-shaped type II for tensile tests were fabricated. Six specimens from each shape were considered as control.

2.2. Outdoor weathering

Outdoor weathering experiments were performed in two different weathering locations in Greece, in Athens and Thessaloniki. Specimens were placed on the roof of the laboratory of atmospheric physics of Aristotle University of Thessaloniki from May 2007 through May 2008 and on the roof of the school of Chemical Engineering of National Technical University of Athens from July 2007 through July 2008. The monthly average radiation and climatic data in Thessaloniki and Athens during outdoor weathering are presented in Tables 2 and 3, respectively. During the weathering, specimens were left uncovered and exposed to the environmental conditions. The exposure rack was adjusted to an angle of 5° from the horizontal to avoid standing water and maximize the amount of sunlight on the specimens. Every two months 3 rectangular and 3 dumbbell-shaped specimens from each location were analyzed. Before specimens were measured, they were cleaned for 10 min in distilled water in an ultrasonic cleaner, dried to a constant weight in a desiccator to an accuracy of 0.001 g (Kern EW balance, Kern & Sohn GmbH, Ziegelei, 72336 Balingenand) and tested. First compression was conducted and at the sixth and twelfth month after compression nanoindentation analysis was also performed. The dumbbell-shaped specimens were placed in tension in order to perform tensile tests.

2.3. Compression test

Compression tests were conducted using a Universal Testing Machine Zwick model Z2.5/TN1S (Germany). The uniaxial compression tests were performed at room temperature (25 °C). Constant deformation rate was set at 5 mm/min for all examined materials. Force and deformation were recorded electronically and the resulting stress–strain compression curves were constructed.

Table 2
Monthly average radiation and climatic data during outdoor weathering.

Date	Radiation and climatic data		
	T (°C)	Rain (mm)	TSR (kW/m^2)
May 2007	20.65	56.80	0.22
June 2007	26.10	42.60	0.22
July 2007	28.20	0.00	0.33
August 2007	27.00	53.20	0.27
September 2007	21.20	34.80	0.18
October 2007	17.10	64.40	0.13
November 2007	11.10	49.00	0.08
December 2007	6.70	15.00	0.06
January 2008	6.70	25.80	0.08
February 2008	8.40	20.8	0.12
March 2008	12.90	14.00	0.14
April 2008	15.00	73.10	0.20
May 2008	19.60	25.70	0.29

T = Temperature, Rain = Monthly summative rain height, TSR = total solar radiation, Data source: Laboratory of Atmospheric Physics of Aristotle University of Thessaloniki, personal communication, 2007–2008.

2.4. Tensile test

The dumbbell-shaped specimens were placed in tension in a Universal Testing Machine Zwick model Z2.5/TN1S (Germany) that was supplied with automatic extensometer. The extensometer grips were set to a standard length of 20 mm, and the crosshead speed was set at 5 mm/min for all examined materials. The uniaxial tensile tests were performed at room temperature (25 °C). Force and elongation measurements were recorded electronically and the resulting stress–strain tensile curves were constructed.

2.5. Nanoindentation analysis

The nanoindentation analysis was performed using a Hysitron TriboLab® (Brazil) Nanomechanical. Test instrument allowing the application of loads from 1 to 10.000 μN and the recording of penetration depths as a function of applied loads with a high load resolution (1 nN) and a high displacement resolution (0.04 nm). The TriboLab® employed in this study was equipped with a Scanning Probe Microscope (SPM), in which a sharp probe tip moved in a raster scan pattern across a sample surface using a three-axis piezo positioner. In all depth-sensing tests a total of 10 indents were averaged to determine the mean values of nano-Hardness (H) and modulus of Elasticity (E) for statistical purposes, with a spacing of 50 μm (~45% relative humidity, 23 °C).

2.6. Mathematical modelling

Several mathematical models were used in order to predict the dependence of stress, strain, elasticity and viscoelasticity parameter on irradiation time for both compression and tensile tests.

Mathematical models were fitted to the experimental data and then to statistical analysis of variance (ANOVA). Mathematical models which, according to statistical analysis, present the lower standard deviation value from the experimental data were selected. Thus the selected mathematical models that were the most suitable

Table 1
Materials of the study.

Coding	Material	Type	Manufacturer	Mixing ratio	Curing method
A	Elastomer 42	Addition (platinum) type-RTV (room temperature vulcanizing)	Technovent Ltd, Principality House, Newport, South Wales, UK	(10:1)	Curing at 100 °C for 2 h

Table 3
Monthly average radiation and climatic data during outdoor weathering.

Date	Radiation and climatic data		
	T (°C)	Rain (mm)	TSR (kW/m^2)
July 2007	29.02	0.0	0.33
August 2007	27.90	16.2	0.29
September 2007	22.56	0.0	0.24
October 2007	18.13	79.2	0.16
November 2007	12.99	34.6	0.09
December 2007	8.41	54.2	0.08
January 2008	7.42	27.0	0.09
February 2008	7.76	31.6	0.14
March 2008	11.17	55.0	0.20
April 2008	15.64	62.0	0.23
May 2008	19.73	2.2	0.30
June 2008	25.76	1.2	0.34
July 2008	27.78	0.0	0.33

T = Temperature, RH = Relative humidity, TSR = Total solar radiation, Data source: METEONET (http://meteonet.chi.civil.ntua.gr/gr/divs.html), Laboratory of Hydrology and Resources Management, NTUA, 2007–2008.

and simple, referring to compression and tensile data, are summarized in Tables 4 and 5, respectively [22,23].

The stress–strain equation (Table 4) that describes the viscoelastic behaviour (Fig. 1a) involves four parameters: the maximum stress (σ_{max}), the corresponding strain (ε_{max}), the modulus of elasticity (E), and the viscoelasticity parameter (p). Maximum stress and strain represent the maximum point to which the samples can be compressed. The modulus of elasticity represents the linear elastic behaviour part of the stress–strain curve and shows the elastic nature of the material. The viscoelasticity parameter represents the exponential part of the curve.

Tensile data were fitted in the described equations in Table 5. The examined silicone elastomer (PDMS-material A) is brittle and does not indicate yield point on its tensile behaviour (Fig. 1b). The stress–strain equation (Table 5) that describes the viscoelastic behaviour involves four parameters: σ_{max}, ε_{max}, E, and p.

2.7. Statistical analysis

Compression and tensile data were subjected to statistical analysis. All data were first evaluated for homogeneity of variances by Levene's test and Kolmogorov–Smirnov for normality. Two-way analysis of variance was used to evaluate any differences between specimens subjected to weathering in Athens and Thessaloniki, in order to detect significant differences among the two weathering locations, the time intervals and possible interaction effects between these two factors. In addition, an overall one way ANOVA and Tukey post hoc tests were applied to detect differences among all the groups for the properties that two-way analysis presented significant interaction effects between two factors. All analyses were computed with the SPSS for Windows software (SPSS 16.0, SPSS Inc, Chicago, Ill.) at a significance level of $\alpha = .05$.

Table 4
Mathematical model for compression tests.

Compression test
Viscoelastic behaviour (stress–strain equation)
$\sigma_c = E_c{*}\varepsilon_c + (\sigma_{max,c} - E_c{*}\varepsilon_{max,c}){*}(\varepsilon_c/\varepsilon_{max,c})^{p_c}$
Parameters
$\sigma_{max,c}$ – maximum stress (MPa)
$\varepsilon_{max,c}$ – maximum strain (mm/mm)
E_c – elasticity parameter (MPa)
p_c – viscoelasticity parameter (–)
Parameter equations
$\sigma_{max,c} = \sigma_{0,c} + \sigma_{1,c}{*}(t_{ir}/t_0)^{k_{1,c}}$
$\varepsilon_{max,c} = \varepsilon_{0,c} + \varepsilon_{1,c}{*}(t_{ir}/t_0)^{k_{2,c}}$
$E_c = E_{0,c} + E_{1,c}{*}(t_{ir}/t_0)^{k_{3,c}}$
$p_c = p_{0,c} + p_{1,c}{*}(t_{ir}/t_0)^{k_{4,c}}$
where
t_{ir} – irradiation time (h)
t_0 – reference time (h)

Table 5
Mathematical model for tensile tests.

Tensile test
Viscoelastic behaviour (stress–strain equation)
$\sigma_t = E_t{*}\varepsilon_t + (\sigma_{max,t} - E_t{*}\varepsilon_{max,t}){*}(\varepsilon_t/\varepsilon_{max,t})^{p_t}$
Parameters
$\sigma_{max,t}$ – maximum stress (MPa)
$\varepsilon_{max,t}$ – maximum strain (mm/mm)
E_t – elasticity parameter (MPa)
p_t – viscoelasticity parameter (–)
Parameter equations
$\sigma_{max,t} = \sigma_{0,t} + \sigma_{1,t}{*}(t_{ir}/t_0)^{k_5}$
$\varepsilon_{max,t} = \varepsilon_{0,t} + \varepsilon_{1,t}{*}(t_{ir}/t_0)^{k_6}$
$E_t = E_{0,t} + E_{1,t}{*}(t_{ir}/t_0)^{k_7}$
$p_t = p_{0,t} + p_{1,t}{*}(t_{ir}/t_0)^{k_8}$
where
t_{ir} – irradiation time (h)
t_0 – reference time (h)

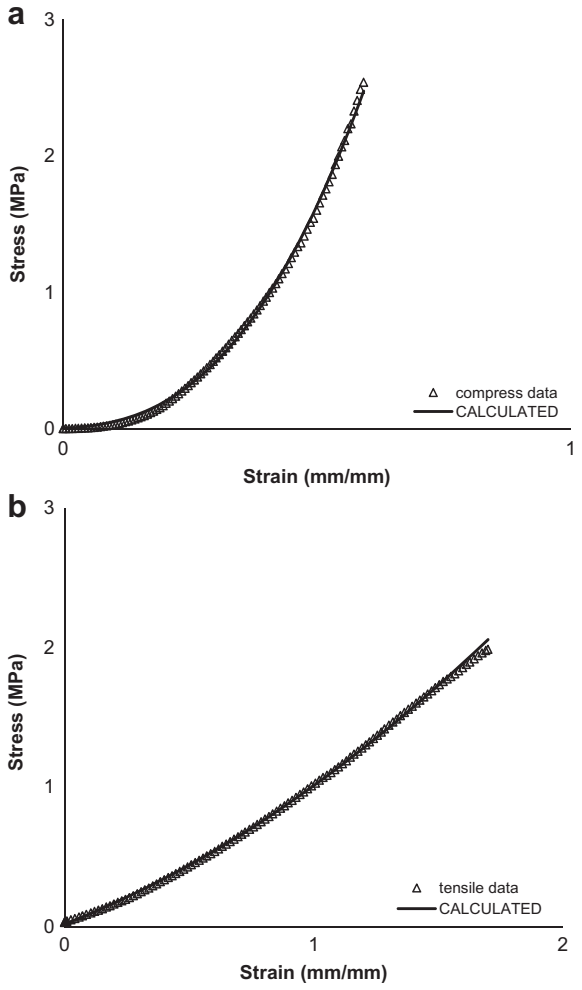

Fig. 1. Typical curves for (a) compression and (b) tensile analysis.

3. Results

The typical curves obtained from compress and tensile tests are presented in Fig. 1a and b, respectively. The mathematical models were fitted to the experimental data. The correlation of σ_{max}, ε_{max}, E and p of compression and tensile analysis with irradiation time is presented in Fig. 2. Figures clearly illustrate that material A presents a decrement in σ_{max} and ε_{max} for both weathering locations. In addition, elasticity and viscoelasticity parameters were increased as irradiation time increased.

The values of the parameters involved in mathematical models, for compression and tensile tests, were calculated using equations in Tables 4 and 5, respectively. The mathematical models' parameters estimation results are summarized in Tables 6 and 7 for compression and tensile analysis, respectively.

A typical nanoindentation test provides load–displacement data, which are the deformation responses of a material. In general, traditional mechanical property parameters, such as nano-Hardness (H) and modulus of Elasticity (E), can be determined. Attention had been paid on analyzing the unloading curve (first 30% of the unloading data) to obtain contact area for the determination of H and E. Most analyses are based on the Oliver–Pharr (O&P) method [24], which determines the contact area in the use of the unloading tangent (green line, Fig. 3) together with the known area function. In Fig. 3, typical load–unload curves on samples i) control and ii) after 1 year weathering in Athens are presented. As can be seen in Fig. 3, for the same displacement (1700 nm), a control sample revealed higher H, E values in comparison to those of 1 year Athens sample. PDMS control sample showed greater resistance (enhanced nanomechanical properties), whereas the degradation (surface-bulk degradation) of 1 year physically aged PDMS (1 year Athens) is confirmed. (For interpretation of the references to colour in Fig. 3, the reader is referred to the web version of this article.)

Adhesion between the tip and the sample can interfere with measurements of modulus using the compliance method in polymeric and soft tissue samples [25–28]. Adhesion is observed in a load–displacement curve as a region of negative load during unloading. Recent studies of soft polymers (silicones) have demonstrated that the compliance method overestimates the sample modulus when there is significant tip-sample adhesion [25,28]

The surface degradation of PDMS (cross-linking density, molecular weight, polar/non-polar molecules) caused by hydrolysis, irradiation and oxidation had mainly affected the hydrophobicity of the surface resulting lower adhesion with the tip [29,30].

Statistical analysis indicates significant changes due to irradiation time and weathering location. In addition, an interaction of time intervals and weathering locations were also detected for E_c, $\varepsilon_{max,t}$, E_t and p_t. The results are summarized in Table 8. All the measured properties changed significantly while irradiation time was increased. More specifically for samples irradiated in Athens, $\sigma_{max,c}$ and p_c changed significantly after eight months, $\varepsilon_{max,c}$ and E_c after two months and p_c, $\sigma_{max,t}$, $\varepsilon_{max,t}$, E_t and p_t after four months. Moreover, for samples which were irradiated in Thessaloniki, $\sigma_{max,c}$, $\varepsilon_{max,c}$, σ_t, and $\varepsilon_{max,t}$, changed significantly after two months, E_c after six months and p_c, E_t and p_t after eight months. For all the properties except p_t significant differences were detected between the two weathering locations. Moreover, $\varepsilon_{max,c}$, E_c, E_t, $\sigma_{max,t}$ and p_t were significantly different concerning the weathering location. Greater changes were detected in samples in Athens except the σ_t which presented greater changes in samples in Thessaloniki. Post hoc analyses presented similar behaviour for E_c, E_t and p_t in Thessaloniki and Athens at the first two and the fifth time interval (second, fourth and tenth month).

4. Discussion

The null hypothesis was rejected, since according to statistical analysis significant changes in mechanical properties were observed.

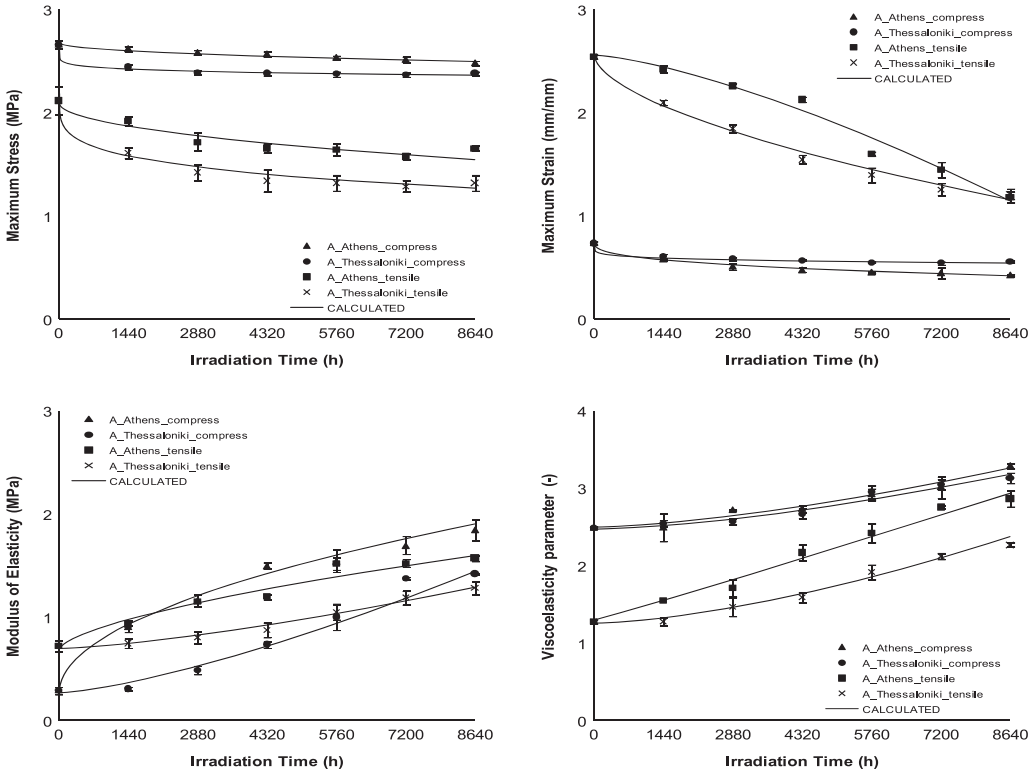

Fig. 2. Maximum stress, maximum strain, elasticity parameter and viscoelasticity parameter of compression and tensile analysis correlated with irradiation time.

Table 6
Parameter estimation for compression model.

Weathering location	$\sigma_{0,c}$ (MPa)	$\sigma_{1,c}$ (MPa)	$\varepsilon_{0,c}$ (mm/mm)	$\varepsilon_{1,c}$ (mm/mm)	$E_{0,c}$ (MPa)	$E_{1,c}$ (MPa)	$p_{0,c}$ (−)	$p_{1,c}$ (−)	k_1 (−)	k_2 (−)	k_3 (−)	k_4 (−)
Athens	2.10	−0.39	2.56	−0.53	0.69	0.59	1.30	0.80	0.49	1.40	0.63	1.04
Thessaloniki	2.22	−0.81	2.56	−0.94	0.70	0.23	1.26	0.38	0.22	0.58	1.39	1.55

Table 7
Parameter estimation for tensile model.

Weathering location	$\sigma_{0,t}$ (MPa)	$\sigma_{1,t}$ (MPa)	$\varepsilon_{0,t}$ (mm/mm)	$\varepsilon_{1,t}$ (mm/mm)	$E_{0,t}$ (MPa)	$E_{1,t}$ (MPa)	$p_{0,t}$ (−)	$p_{1,t}$ (−)	k_5 (−)	k_6 (−)	k_7 (−)	k_8 (−)
Athens	2.69	−0.13	0.75	−0.26	0.27	1.15	2.50	0.27	0.46	0.35	0.50	1.50
Thessaloniki	2.65	−0.26	0.73	−0.16	0.27	0.45	2.47	0.25	0.13	0.17	1.38	1.52

Maxillofacial materials' hardness is a measure of flexibility. Tensile strength is important to express overall strength characteristics. The resulting strain (elongation) is a measure of flexibility and an indicator of the overall flexibility of a prosthetic material with facial movement. It also defines the resistance of a facial prosthetic elastomer to rupture during use and maintenance. This property also defines the material's ability to accommodate facial movement [31]. Relationships between physical structure and mechanical properties allow the understanding of mechanical behaviour around working temperature as well as the physical aging [8].

The weathering of polymers leads to changes in physical and chemical characteristics that cause a significant deterioration in important mechanical properties. When a photo-oxidative degradation occurs the following steps can be considered:

1. Initiation Step: Free radicals, such as HO^*_2, P^* (free polymer radical) and $^*OH$ are formed due to the presence of air (oxygen) under UV/VIS irradiation.
2. Propagation Step: The reaction of free polymer radicals with oxygen, leads to a production of polymer oxy and peroxy-radicals and secondary polymer radicals, which result in chain scission. The propagation step is very much dependent on the efficiency of the decomposition, photolysis and/or thermolysis of polymer hydroperoxides (POOH), during which new free radicals, such as polymer oxy radical (PO^*) and hydroxyl radical (HO^*), are formed.
3. Termination Step: The termination of the polymer radicals occurs mainly by bimolecular recombination, but also between low molecular radicals, such as hydroxyl (OH^*) and hydroperoxy (HO^*_2) and other available radicals (R^*). There are several factors that influence the recombination reactions, such as concentration of radicals formed and structural parameters of the polymeric matrix (free volumes). Moreover, oxygen pressure controls which of the reactions overrules. For example when the oxygen pressure is high (atmospheric pressure), the termination reaction almost exclusively occurs by bimolecular reaction of PO^*. The reaction of different free radicals with each other resulting in cross-linking [32].

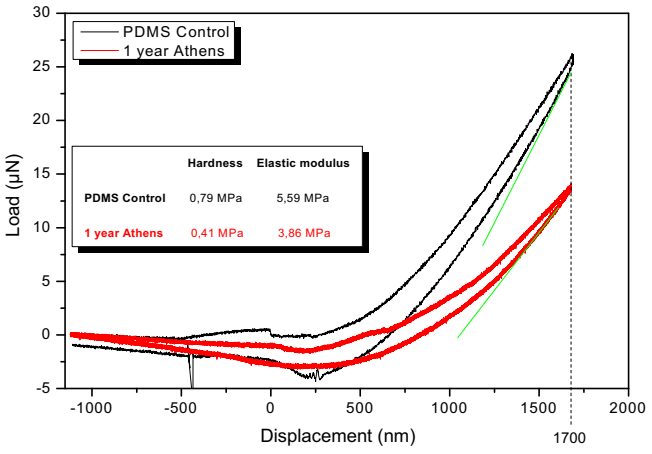

Fig. 3. Typical load–unload curves obtained from nanoindentation testing for pristine (material A Control) and 1 year physically aged (material A after weathering 1 year in Athens).

The main structural modifications in irradiated polymers are changes in molecular weight distribution – due to main chain scission, cross-linking and end linking – and the production of volatile degradation products [33–35]. The main volatile products of irradiated polydimethylsiloxanes are hydrogen, methane and ethane gases [36]. All these phenomena tend to modify the materials' physical properties.

The changes of physical properties affect the polymer's structural network in different ways. The structural networks density increases during cross-linking, due to the formation of bonds between the existing chain segments or between the chains. Therefore, cross-linking leads to harder materials. On the other hand, when chain scission is the dominant mechanism, the fracturing bonds within the main chain or between two different chains, incur a decrement in density of the structural network and the materials become softer. In irradiated polymers, both the above mechanisms take place.

Over the past 50 years a solid understanding of the relationship between polymer structure and the relative yields of cross-linking and chain scission has been acquired. Thus, NMR and IR experiments show that polydimethylsiloxanes, undergo mostly primarily cross-linking reactions [36].

Elasticity and strength are highly dependent on the molecular weight and the degree of cross-linking of a polymer. Flory mathematical model correlates polymers' network density with E (Equation (1)) [37].

$$E = \frac{RT\rho}{\overline{M_c}}\left(\varepsilon + \frac{2}{\varepsilon^2}\right) \quad (1)$$

where M_c is the molecular weight between cross-links and ρ symbolizes the network density.

The correlation between Elastic modulus and molecular weight (M_c), which was determined from swelling measurements, is illustrated in Fig. 4.

The comparison of modulus (E) values measured using nanoindentation to handbook or manufacturer values can often be

Table 8
Statistical analysis and significant changes.

	$\sigma_{max,c}$	$\varepsilon_{max,c}$	E_c	p_c	$\sigma_{max,t}$	$\varepsilon_{max,t}$	E_t	p_t
Weathering location	$p < 0.05$	$p < 0.05$	$p < 0.05$	$p < 0.05$	$p < 0.05$	$p < 0.05$	$p < 0.05$	$p > 0.05$
Irradiation time	$p < 0.05$	$p < 0.05$	$p < 0.05$	$p < 0.05$	$p < 0.05$	$p < 0.05$	$p < 0.05$	$p < 0.05$
Interaction (weathering location * Irradiation time)	$p > 0.05$	$p > 0.05$	$p < 0.05$	$p > 0.05$	$p > 0.05$	$p < 0.05$	$p < 0.05$	$p < 0.05$

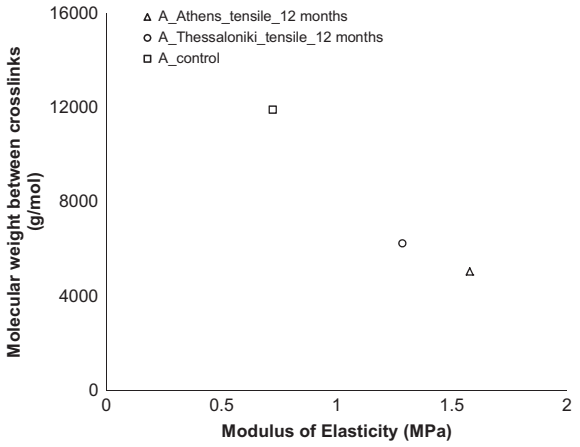

Fig. 4. Elastic modulus correlated with molecular weight between cross-links.

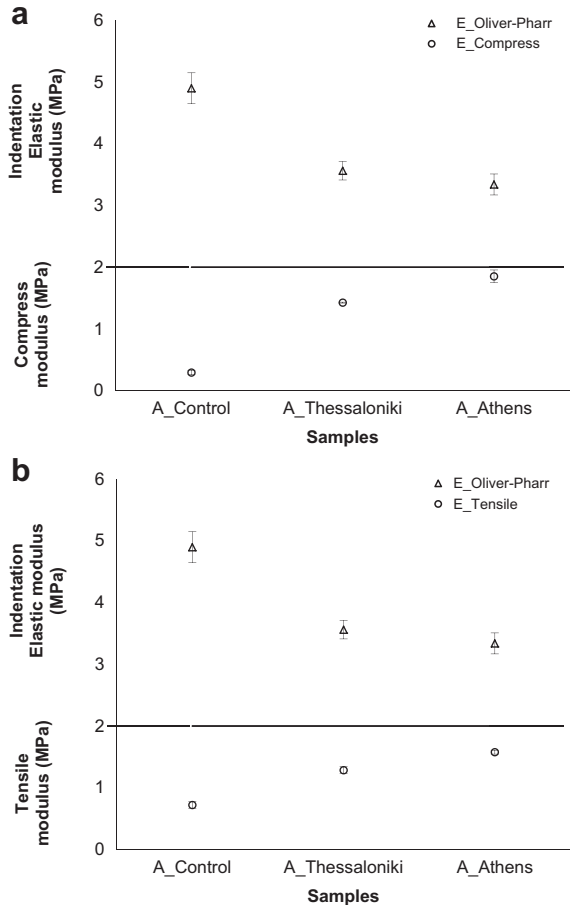

Fig. 5. Comparison of elastic moduli obtained from nanoindentation (using the Oliver–Pharr model), (a) compressive and (b) tensile testing.

misleading, because quoted values of E for many polymer systems can cover a large range due to potential variations in microstructure, semicrystalline morphology, anisotropy, molecular weight, cross-link density, etc. The comparison of elastic moduli obtained from nanoindentation (using the Oliver–Pharr model), tensile and compressive testing is illustrated in Fig. 5a and b, respectively.

It is important to note that nanoindentation and tensile tests do not measure the same properties. Generally nanoindentation modulus (Elastic modulus) values, using the standard O&P method, are higher than results from standard tensile tests. Several reasons have been invoked to explain this: Surface effects (the initial part of the load–displacement curve is affected by surface roughness, surface oxidation [38] and other surface phenomena), the type of loading is compressive in nanoindentation (not tensile), the test frequencies are quite different (70 Hz for nanoindentation, compared to a much lower frequency in the tensile test) and hydrostatic pressure generated below the Berkovich indenter [39].

Nanoindentation has not been widely used to examine maxillofacial polymers, although elastic modulus which is obtained from nanoindentation is a measure of surface hardness and elasticity as well as nano-Hardness. These properties also provide significant information for maxillofacial materials and for the deterioration due to aging, cleaning solutions and skin secretions that first reflected in the surface and then affect the bulk of the material. Thus, nanoindentation tests are highly important as far as the serviceability of maxillofacial prosthetics is concerned.

The serviceability of prosthesis is one of the major concerns in maxillofacial surgery. It is very important for patients to be given the adequate information concerning the expected average longevity of their prostheses, along with information on factors affecting the longevity (i.e., environmental staining, cosmetics and cleaning regimes) [40]. Thus, the results from this study could be very helpful in order for someone to draw conclusions about the mechanical behaviour of prosthesis after outdoor weathering. In this study, mechanical behaviour of maxillofacial prosthetics, including polydimethylsiloxanes, was affected by irradiation and other climate conditions, after outdoor weathering, as also reported in other studies [21,41–45]. The alterations which occur in the examined properties before and after weathering, are in accordance with previous studies concerning materials' structure [21,36,46]. The weathering in different location, if possible is suggested due to the variety of weathering characteristics among different locations [12]. The results show that the examined properties present a similar trend in both locations, although the effect was more severe for the samples which were placed in Athens.

5. Conclusions

The hypothesis investigated was rejected, since according to statistical analysis significant changes in mechanical properties were observed. In order to correlate the irradiation time with the measured properties, mathematical models were fitted to the experimental data. The differences in mathematical models' parameters indicated changes in the measured properties while irradiation time was increased. Moreover, significant differences were observed almost in all the measured properties between the samples in the two weathering locations.

The observed differences in the mechanical behaviour, between the control (unirradiated samples) and irradiated samples and between the two weathering locations, resulted from photodegradation and hydrolysis that might occur due to weathering. Material A became harder and according to theoretical approaches, which were analyzed above, its network density increased. Since cross-linking made samples lose their elasticity and become harder with an increment in their network density it is possible that this is the dominant mechanism in material A during irradiation.

The study also provides new information about maxillofacial prosthetics serviceability obtained from nanoindentation tests.

Acknowledgements

The authors wish to thank Dr. Anastasia Poupkou and the laboratory of Atmospheric Physics of Aristotle University of Thessaloniki for the technical support in these experiments.

References

[1] Khan Z, Gettleman L, Jacobsen C. Conference report: materials research in maxillofacial prosthetics. Journal of Dental Research 1992;71:1541–2.
[2] Bellamy KE, Waters MGJ. Designing a prosthesis to simulate the elastic properties of skin. Bio-Medical Materials & Engineering 2005;15(1):21–7.
[3] Li X, Zhao Y, Li S, Liu X, Wu G, Zhen L, et al. Comparison of mechanical properties of Cosmesil M511and A-2186 maxillofacial silicone elastomers. Journal of US–China Medical Science 2007;4:34–7.
[4] Kiat-amnuay S, Waters PJ, Roberts D, Gettleman L. Adhesive retention of silicone and chlorinated polyethylene for maxillofacial prostheses. Journal of Prosthetic Dentistry 2008;99(6):483–8.
[5] Lemon JC, Kiatamnuay S, Gettleman L, Martin JW, Chambers MS. Facial prosthetic rehabilitation: preprosthetic surgical techniques and biomaterials. Current Opinion in Otolaryngology & Head and Neck Surgery 2005;13(4):255–62.
[6] Rosa DS, Angelini JMG, Agnelli JAM, Mei LHI. The use of optical microscopy to follow the degradation of isotactic polypropylene (iPP) subjected to natural and accelerated ageing. Polymer Testing 2005;24(8):1022–6.
[7] Polyzois G, Stafford GD, Winter R. A study of some mechanical properties of an RTV polydimethylsiloxane for extraoral maxillofacial prostheses. Clinical Materials 1992;9(1):21–9.
[8] Lacoste-Ferré M, Demont P, Dandurand J, Dantras E, Blandin M, Lacabanne C. Thermo-mechanical analysis of dental silicone polymers. Journal of Materials Science 2006;41(22):7611–6.
[9] Dollase T, Spiess HW, Gottlieb M, Yerushalmi-Rozen R. Crystallization of PDMS: the effect of physical and chemical crosslinks. Europhysics Letters 2002;60(3):390–6.
[10] Abbasi F, Mirzadeh H, Katbab A. Modification of polysiloxane polymers for biomedical applications: a review. Polymer International 2001;50 (12):1279–87.
[11] Virlogeux F, Bianchini D, Delor JF, Baba M, Lacoste J. Evaluation of crosslinking after accelerated photo-ageing of silicone rubber. Polymer International 2004;53(2):163–8.
[12] Tran NH, Scarbecz M, Gary JJ. In vitro evaluation of color change in maxillofacial elastomer through the use of an ultraviolet light absorber and a hindered amine light stabilizer. Journal of Prosthetic Dentistry 2004;91 (5):483–90.
[13] Gijsman P, Hennekens J, Janssen K. Comparison of UV degradation chemistry in accelerated (xenon) aging tests and outdoor tests (II). Polymer Degradation and Stability 1994;46:63–74.
[14] Dootz ER, Koran A, Craig RG. Physical properties of three maxillofacial materials as a function of accelerated aging. Journal of Prosthetic Dentistry 1994;71(4):379–83.
[15] Gulmine JV, Janissek PR, Heise HM, Akcelrud L. Degradation profile of polyethylene after artificial accelerated weathering. Polymer Degradation and Stability 2003;79(3):385–97.
[16] Sampers J. Importance of weathering factors other than UV radiation and temperature in outdoor exposure. Polymer Degradation and Stability 2002;76 (3):455–65.
[17] Pospisil J, Pilar J, Billingham NC, Marek A, Horak Z, Nespurek S. Factors affecting accelerated testing of polymer photostability. Polymer Degradation and Stability 2006;91:417–22.
[18] Eleni PN, Katsavou I, Krokida MK, Polyzois GL. Color stability of facial silicone prosthetic elastomers after artificial weathering. Dental Research Journal 2008;5(2):71–9.
[19] Eleni PN, Krokida MK, Frangou MJ, Polyzois GL, Maroulis ZB, Marinos-Kouris D. Structural damages of maxillofacial biopolymers under solar aging. Journal of Materials Science: Materials in Medicine 2007;18(9):1675–81.
[20] Eleni PN, Krokida MK, Polyzois GL. The effect of artificial accelerated weathering on the mechanical properties of maxillofacial polymers PDMS and CPE. Biomedical Materials 2009;4(3):035001.
[21] Eleni PN, Katsavou I, Krokida MK, Polyzois GL, Gettleman L. Mechanical behaviour of facial prosthetic elastomers after outdoor weathering. Dental Materials 2009;25(12):1493–502.
[22] Krokida MK, Karathanos VT, Maroulis ZB. Compression analysis of dehydrated agricultural products. Drying Technology 2000;18:395–408.
[23] Krokida MK, Kiranoudis CT, Maroulis ZB. Viscoelastic behaviour of dehydrated products during rehydration. Journal of Food Engineering 1999;40 (4):269–77.
[24] Oliver WC, Pharr GM. Improved technique for determining hardness and elastic modulus using load and displacement sensing indentation experiments. Journal of Materials Research 1992;7(6):1564–80.
[25] Carrillo F, Gupta S, Balooch M, Marshall SJ, Marshall GW, Pruitt L, et al. Nanoindentation of polydimethylsiloxane elastomers: effect of crosslinking, work of adhesion, and fluid environment on elastic modulus. Journal of Materials Research 2006;21(2):535–7.
[26] Klapperich C, Komvopoulos K, Pruitt L. Nanomechanical properties of polymers determined from nanoindentation experiments. Journal of Tribology 2001;123(3):624–31.
[27] Grunlan JC, Xia X, Rowenhorst D, Gerberich WW. Preparation and evaluation of tungsten tips relative to diamond for nanoindentation of soft materials. Review of Scientific Instruments 2001;72(6):2804–10.
[28] Carrillo F, Gupta S, Balooch M, Marshall SJ, Marshall GW, Pruitt L, et al. Nanoindentation of polydimethylsiloxane elastomers: effect of crosslinking, work of adhesion, and fluid environment on elastic modulus. Journal of Materials Research 2005;20(10):2820–30.
[29] Meincken M, Berhane TA, Mallon PE. Tracking the hydrophobicity recovery of PDMS compounds using the adhesive force determined by AFM force distance measurements. Polymer 2005;46(1):203–8.
[30] Brogly M, Noel O, Awada H, Castelein G, Schultz J. A nanoscale study of the adhesive contact. Comptes Rendus Chimie 2006;9(1):99–110.
[31] Waters M, Jagger R, Polyzois G, Williams K. Dynamic mechanical thermal analysis of maxillofacial elastomers. Journal of Prosthetic Dentistry 1997;78 (5):501–5.
[32] Rabek JF. Polymer photodegradation: mechanisms and experimental. N. York: Chapman and Hall; 1995. p. 24–5.
[33] Dootz ER, Koran A, Craig RG. Physical property comparison of 11 soft denture lining materials as a function of accelerated aging. Journal of Prosthetic Dentistry 1993;69(1):114–9.
[34] Guo J-H. Aging processes in pharmaceutical polymers. Pharmaceutical Science & Technology Today 1999;2(12):478–83.
[35] Maxwell RS, Cohenour R, Sung W, Solyom D, Patel M. The effects of [gamma]-radiation on the thermal, mechanical, and segmental dynamics of a silica filled, room temperature vulcanized polysiloxane rubber. Polymer Degradation and Stability 2003;80:443–50.
[36] Kroschwitz JI, Mark HF. Radiation chemistry of polymers. N.Y.: John Wiley & Sons; 2005.
[37] Flory PJ. Principles of polymer chemistry. Ithaca, NY: Cornell University Press; 1953.
[38] Briscoe BJ, Savio Sebastian K. The elastoplastic response of poly(methyl methacrylate) to indentation. Proceedings of the Royal Society A: Mathematical, Physical and Engineering Sciences 1996;452(1946):439–57.
[39] Hu Y, Shen L, Yang H, Wang M, Liu T, Liang T, et al. Nanoindentation studies on Nylon 11/clay nanocomposites. Polymer Testing 2006;25(4):492–7.
[40] Hooper SM, Westcott TP, Evans LL, Bocca AP, Jagger DC. Implant-supported facial prostheses provided by a maxillofacial unit in a U.K. regional hospital: longevity and patient opinions. Journal of Prosthodontics 2005;14(1):32–8.
[41] Feldman D. Polymer weathering: photo-oxidation. Journal of Polymers and the Environment 2002;10(4):163–73.
[42] White JR, Turnbull A. Weathering of polymers: mechanisms of degradation and stabilization, testing strategies and modelling. Journal of Materials Science 1994;29(3):584–613.
[43] Haug SP, Moore BK, Andres CJ. Color stability and colorant effect on maxillofacial elastomers. Part II: weathering effect on physical properties. Journal of Prosthetic Dentistry 1999;81(4):423–30.
[44] Vallıs E, Sarmoria C, Villar M, Lazzari M, Chiantore O. Model polydimethylsiloxanes subjected to thermal weathering: effect on molecular weight distributions. Polymer Degradation and Stability 2000;69(1):67–71.
[45] Bellamy K, Limbert G, Waters MG, Middleton J. An elastomeric material for facial prostheses: synthesis, experimental and numerical testing aspects. Biomaterials 2003;24:5061–6.
[46] Shah H, Munisamy S, Vaidyanathan TK. Artificial aging of chlorinated polyethylene and maxillofacial silicone elastomer. In: IADR 86th general session & exhibition, Toronto; 2008.

JOURNAL OF NANOSTRUCTURED POLYMERS AND NANOCOMPOSITES 7/1 32-42

ADHESIVE FORCES AND TIME DEPENDENT BEHAVIOUR (CREEP AND LOADING RATE EFFECTS) ON NANOMECHANICAL PROPERTIES OF POLYDIMETHYLSILOXANE (PDMS) AND PDMS NANOCOMPOSITE

C.A. Charitidis*, E.P. Koumoulos, V.P. Tsikourkitoudi, S.P. Vasilakos, P.A. Tarantili

School of Chemical Engineering, National Technical University of Athens, 9 Heroon Polytechniou St., Zographos, Athens, Greece GR- 157 80

Received 12 November 2010; accepted 12 January 2011

Abstract

In the present study, nanoindentation technique was used to investigate the nanomechanical and time dependent behaviour of silicone elastomers, namely polydimethylsiloxane (PDMS) and PDMS nanocomposite, through Oliver & Pharr model. Considerable uncertainties arise when applying the nanoindentation technique to very soft materials with elastic modulus (E) below 5 MPa or adhesive PDMS samples. Detailed observations for the initial and adhesive contact of PDMS indentations with Berkovich indenter were also investigated. Significant initial penetration displacements were created during the finding surface process. Moreover, the plastic deformation where no load had yet been applied to PDMS was investigated and compared with similar studies using Atomic Force Microscopy. It was found that when the indenter tip was pulled away from the sample, the adhesive attraction deformed the soft polymer along the direction of the tip motion and caused a negative indentation (zero- load plastic deformation). Furthermore, an analysis of nanoindentation creep behaviour of PDMS was performed. The results showed that the nanomechanical properties of PDMS, namely hardness (H) and E, depend on the hold time incorporated in the experiment. A hold time of 300 s should be used in order to avoid a deviation in the calculation of H and E due to a change in the unloading curve that results in the inaccurate determination of stiffness. The effect of loading rate values of PDMS on H and E was also studied. With the increase of loading rate, H and E were found to decrease until they reached constant values. Therefore, a loading rate of 3 μN/s is recommended in order to avoid a deviation in the calculation of H and E values.

Keywords: Adhesive forces, Time- dependent properties, Creep, Loading rate, Nanoindentation, Polysiloxane nanocomposites

1. Introduction

1.1 Polydimethylsiloxane (PDMS) nanocomposites: Material properties and uses

Polydimethylsiloxane (PDMS) is a silicone elastomer. Due to its properties it can be used not only as a component for the development of Micro- Electro- Mechanical Systems (MEMS), but also as a microfluidic component for biomedical applications. Additionally, based on its biocompatibility and ease of processing it can be used as a substrate in biological tissues and drug delivery applications [1-4]. It is chemically inert, thermally stable, permeable to gases and simple to handle and manipulate. Furthermore, exhibits isotropic and homogeneous properties, and can conform to submicron features to develop microstructures.

Soft elastic substrates such as PDMS are often used in biological experiments to study cell locomotion, mechanical/traction forces and the organization of focal adhesions of cells, among many other topics [5-7]. In this regard, further investigation of the structural and surface properties of PDMS in nanoscale is needed in order to accelerate its wider adoption for the development of BioMEMS devices and applications [8]. It can also be easily processed to have a range of elastic modulus (E) values that are physiologically relevant [9]. Finally, PDMS is a medical- grade, Food and Drug Administration approved polymer that is well characterized as a cell culture substrate for micro- contact printing (μCP) of extra- cellular matrix (ECM) proteins [10].

On the other hand, a recognized drawback of PDMS is its inherent mechanical weakness which could be overcome by reinforcing it with particulate fillers such as silica and titania [11]. Due to the high cost and easy agglomeration of aerosilica, researchers have focused on the development of other reinforcing fillers, such as montmorillonite (MMT), as a substitute.

*Corresponding author e-mail: charitidis@chemeng.ntua.gr

Nanocomposites of PDMS containing organically modified montmorillonite (OMMT) can be prepared by various techniques, including simple mechanical mixing or melt intercalation and are said to exhibit increased solvent resistance with mechanical properties and thermal stability very close to those of aerosilica- filled silicone rubber [12-13]. In addition, a two step process was reported for the preparation of exfoliated/intercalated polymer/MMT nanocomposites, which included preparation of MMT solution via in situ polymerization of dimethyldichlorosilane inside the galleries of layered silicate hosts and then, after separation of most PDMS, the treated–MMT solution was blended with several polymers [14].

Regarding the modification of clay nanofiller, various chemicals were studied, such as soft siloxane surfactant or *N,N*-di(2-hydroxyethyl)-N-dodecyl-N-methylammonium chloride as intercalation agent [15-16].

It should be noted that in order to overcome difficulties during preparation of high temperature vulcanized silicone rubber (HTV- SR) nanocomposites, a master batch of MMT was prepared by solution intercalation by Wang and Chen. The deriving nanocomposites showed enhanced tensile and thermal properties in comparison with HTV- SR/OMMT-20% [17]. Finally, an alternative technique was proposed by Horsch et al., who used supercritical carbon dioxide ($scCO_2$) to delaminate dry clays and found that the extent of dispersion is dependent on the CO_2-philicity of the nanoclay, whereas the natural clay was partially dispersed with $scCO_2$, using a CO_2-philic PDMS matrix [18].

1.2 Polymers' viscoelastic behaviour

1.2.1 Nanoindentation on Polymers

The mechanical behaviour of polymers is usually described by viscoelastic and/or viscoplastic characteristics, depending on time (or frequency) as well as temperature, which makes the mechanical response of the polymer systems complicated. For the measurement of the mechanical properties of bulk polymers the indentation method is preferred mainly because both the specimen preparation and the experimental procedure are straightforward and make possible the study of size effects on mechanical properties at micro- and nano- scales [19]. The related literature reveals that significant initial penetration displacements can be created during the finding surface process [20]. For soft nanocomposite surfaces, the initial contact load can create an initial penetration displacement in the order of nanometer, so that the contact area tends to be underestimated, which leads to an overestimation of hardness (H) and E values.

1.2.2 Adhesion

Gupta et al. [21] investigated the effects of adhesion on the E determined from nanoindentation results for soft PDMS elastomers with different nanoclays concentrations (load range 0-16μN). They conclude that including adhesive forces in the analysis of the nanoindentation data elucidates the apparent linearity of the load-displacement curves (almost full elastic behaviour).

In the present work, the load- displacement curves for all PDMS concentrations revealed a highly elastic behaviour for a large range of applied load (0-60μN) and this linear characteristic may be attributed to the distinct contact conditions caused by the strong adhesion between the tip and the sample [22]. Recent studies in this field have shown that consideration of the adhesion energy at the tip- PDMS interface is a significantly important parameter and needs to be taken into account for consistent E determination of soft materials by nanoindentation [20].

1.2.3 Creep

One of the commonly used methods in order to take into account the viscoelastic properties of polymeric materials during nanoindentation is to hold the indenter at the maximum load for a period of time [23,24]. This, however, leads to creep effects during indentation, in which the measured H and E are dependent on holding time, maximum load and loading/unloading rates [25]. The term creep is often used to describe a delayed response to an applied stress or strain that may be a result of visco- elastic or visco- plastic deformation [26]. Nevertheless, creep influences the maximum displacement and the unloading curve in a way that non negligible deviations of H and E calculations may occur [27].

1.2.4 Loading Rate

Soft materials exhibit viscoelastic behaviour and their mechanical response is strongly dependent on loading rate and time, e.g. E increases as the loading rate decreases [22].

Within the scope of this work was the investigation of interactions between the Berkovich tip and the PDMS nanocomposites surface containing 8 parts per hundred (phr) of montmorillonite nanoclays before, during and after contact. Furthermore, creep behaviour of PDMS was investigated at a constant maximum load. Different holding times were incorporated into each test at the maximum load in the range from 5 to 2000 s. The nanoindentation technique was used

to characterize nanomechanical properties, namely H and E, of PDMS specimens and PDMS nanocomposites at different loading rates. The influence of polymer's viscosity and the effect of loading rate on H and E values of PDMS were also studied.

2. Experimental Details

2.1 Materials and sample preparation

Silanol terminated PDMS (Gelest Inc.) was vulcanized using 10 phr tetrapropoxysilane (TPOS, Aldrich) as crosslinker and 0.1 phr dibutyl tin dilaurate (Aldrich) as catalyst. Commercial organic modified montmorillonite (OMMT) clay under the trade name Cloisite® 30B supplied by Southern Clay Products Inc., was used as reinforcing nanofiller at a concentration of 8 phr.

Pristine PDMS and PDMS with nanoclays were prepared. Efficient dispersion of nanoparticles was achieved by sonicating the PDMS and the appropriate amount of clay for 8 min with an ultrasound probe (room temperature). The cross- linking system was then added and dispersed into the mixture and the samples were cast into molds and cured at room temperature for 12 hours, to produce rectangular sheets of 3 mm thickness.

2.2 Instrumentation and methods

X- ray diffractometer (XRD)

XRD spectra of clay and nanocomposites were obtained in order to detect the evolution of the clay d001 reflection. A Siemens 5000 apparatus (35kV, 25mA) employed, using CuKα X- ray radiation with a wavelength of λ=0.154 nm. The diffractograms were obtained by scanning in the 2θ range from 2-10°, at a rate of 2°/min.

Nanoindentation analysis

The nanoindentation tests in this work were performed using a Hysitron TriboLab® Nanomechanical Test Instrument, equipped with a Berkovich tip (100 nm tip radius) which allows the application of loads from 1 to 10^4 μN. The instrument is capable of recording penetration displacements as a function of applied loads with a high load resolution (1 nN) and a high displacement resolution (0.04 nm). In order to operate under closed loop load or displacement control, feedback control option was used (typical option when indenting viscoelastic materials with time dependent behaviour, such as biomaterials and polymers, where creep and stress relaxation tests are performed). The pre-load (when the indenter touches the surface) was set to 0.1 μN, in order to avoid surface deformation and pre-indent (typical low pre-load setting for soft, adhesive or pressure sensitive materials). The above TriboLab® instrument is equipped with a Scanning Probe Microscope (SPM), in which the sharp probe tip moves in a raster scan pattern across a sample surface using a three- axis piezo positioner. In all depth- sensing tests a total of 10 indents were averaged to determine the mean H and E values for statistical purposes, with a spacing of 50 μm (~45% relative humidity, 23°C).

3 Results and Discussion

3.1 X- ray diffractometer (XRD)

XRD analysis was conducted for the assessment of the status of clay dispersion within the polymer matrix. It is well known that using Bragg's rule ($2 d \sin\theta = n \lambda$), the basal spacing for the clay layers can be calculated.

The XRD patterns for Cloisite 30B and sample of PDMS with 8 phr Cloisite 30B are shown in Fig. 1.

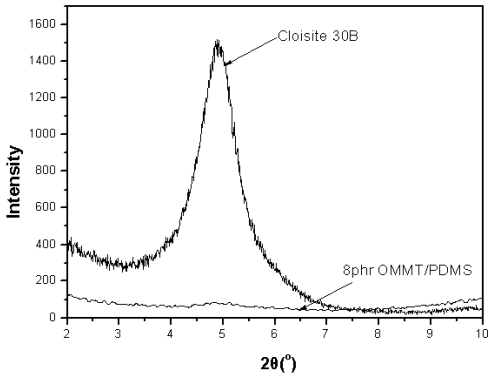

Fig. 1: XRD patterns of Cloisite 30B and 8 phr OMMT/PDMS nanocomposites.

Cloisite 30B is characterized by relatively high content of organic modifier (30%) and high inter- gallery spacing (18.5 Å), which facilitates its intercalation in the PDMS matrix. In addition, it is possible that the hydroxyl- groups incorporated in the organic modification of Cloisite 30B enhances compatibility of the nanofiller with the silicone rubber system. The featureless patterns for 8 phr OMMT loading, suggest that exfoliation or delamination hybrid was formed.

However, it is reported that in real nanocomposites complete exfoliation cannot be achieved, but most materials show a combination of various dispersion states, either as a result of inhomogeneous mixing or, simply, due to the fact that the transition from intercalated structure to an exfoliated cannot be clearly defined and numerous intermediate states may exist [28].

3.2 Nanomechanical Properties

Fig. 2 presents typical load-displacement curves where the applied load is plotted in accordance with the displacement of the indenter. Additionally, the H and E of the PDMS and PDMS nanocomposite (with an average surface roughness of ~100nm) with surface topography through SPM (0 and 8 phr of nanoclays amount) are also presented. The addition of nanoclay amount in the PDMS matrix creates surface incongruity (SPM images), while strengthens the PDMS elastomer.

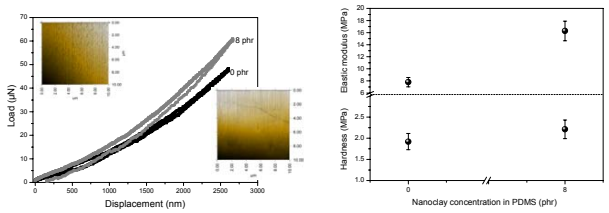

Fig. 2: Load-displacement curves for PDMS (0 and 8%) through nanoindentation (SPM images of both samples are also embedded), and nanomechanical properties (at ~2600 nm of displacement).

The ratio of hardness to elastic modulus is of significant interest in tribology. Higher stresses are expected in high H/E, hard materials, and high stress concentrations develop towards the indenter tip, whereas in the case of low H/E, soft materials, the stresses are lower and are distributed more evenly across the cross-section of the material [29, 30]. The high ratio of hardness to elastic modulus (H/E) is indicative of good wear resistance in a disparate range of materials [30]: ceramic, metallic and polymeric (for example: c-BN, tool steel, nylon, respectively), which are equally effective in resisting attrition for their particular intended application. In Fig. 3, the change of H/E slope reveals that the addition of nanoclay amount strengthens the PDMS-montmorillonite nanocomposite.

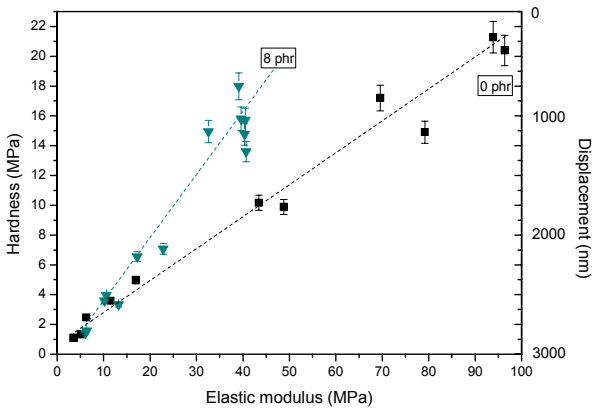

Fig. 3: Relationship between H and E for 0, 5 and 8 phr of nanoclays in the PDMS matrix

3.3 Adhesive Forces – Zero- Load Plastic Deformation (ZLPD)

The load vs. displacement plot (Fig. 4) into the PDMS (8 phr) surface illustrates the insensitivity of this signal to surface contact on soft materials. Nearly 850 nm of displacement were required before 12 μN of load were registered (rate 0.1 μN/s). The dynamic load signal (dynamic contact stiffness) can be used to provide much greater sensitivity to surface contact and surface stiffness in comparison with a change in a quasi- static load or stiffness measurement. The dynamic load signal as the tip approaches the surface, snaps into contact because of surface forces, and measures the increase in the surface stiffness with displacement [31].

To obtain the indentation of the Berkovich tip into the sample from a load plot, the point where the tip starts to contact the sample surface needs to be determined on the approaching load curve. The point where the interaction becomes attractive is assigned to be the point where the tip contacts the surface, as shown in Figs. 4 and 5. From Fig. 4, we can see that when the tip is pulled away from the sample the adhesive attraction deforms the soft polymer along the direction of the tip motion and causes a negative indentation (i.e., polymer extension under a tensile stress). At point "1", where the tip is drawn into the sample surface because of the adhesive interaction, the stored elastic energy and the surface energy are balanced. The indentation between the point where the tip starts to contact the sample surface and point "1" is defined as the adhesion- induced indentation. Point "2" corresponds to the attractive adherence force.

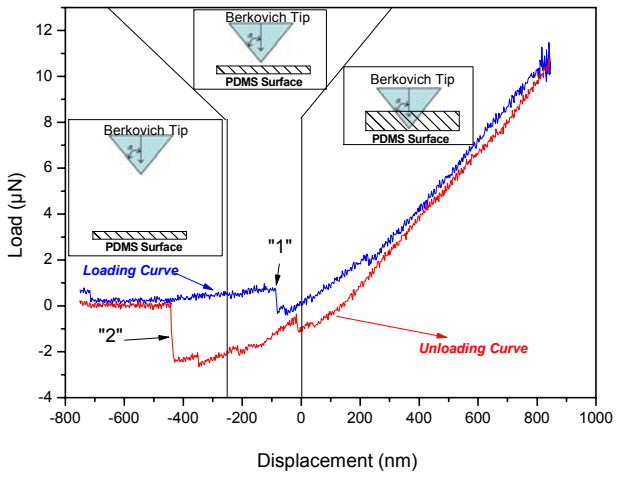

Fig. 4: Load (dynamic contact stiffness) vs Displacement as the tip approaches the surface, snaps into contact because of surface forces in the surface of 8 phr OMMT/PDMS.

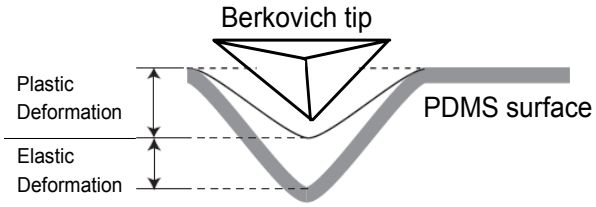

Fig. 5: The schematic drawing to show the ZLPD during nanoindentation.

The adhesion hysteresis is widely believed to be due to energy dissipation in the bulk material and at the crack tip. Considerable work has been done to investigate the different mechanisms for the adhesion hysteresis qualitatively or quantitatively. Silberzan et al. [32], Choi et al. [33-35], Kim et al. [36], Mason et al. [37], and Perutz et al. [38-39] studied the adhesion hysteresis of PDMS- PDMS self adhesion systems and PDMS self- assembled monolayer systems using the macroscopic Johnson– Kendall– Roberts (JKR) [40] method. In those experiments, the polymer cross- link density, sol fraction, surface functionality, loading and unloading rates, and dwell time of contact were varied. The contributions to the adhesion hysteresis from the viscoelasticity of the bulk material were ignored, because the loading and unloading processes were controlled to follow a quasi equilibrium process. Instead, hydrogen bonds, cross linking, and physical chain entanglements were found to dominate the adhesion hysteresis. Pickering and Vancso [41], Vakarelski et al. [42], Noel et al. [43] and Gillies et al. [44] used Atomic Force Microscopy (AFM) to study the adhesion hysteresis of polymer systems concluding that the viscoelasticity was the dominant factor.

The energy which has to be overcome is the energy required to bend the cantilever until it reaches F_{adh}. The Derjaguin- Muller- Toporov (DMT) [45] and the JKR theories establish a relationship between the adhesion force (F_{adh}), the Berkovich- PDMS interaction constant (k) and the thermodynamic work of adhesion (W_{adh}), given by Equation 1:

$$W_{adh} = -k * F_{adh} \quad (1)$$

where k depends on the tip- sample system interactions and the tip radius.

The dependence of F_{adh} on the W_{adh} is presented in Fig. 6. This dependence of F_{adh} on the W_{adh} is in good agreement with findings of other researchers [40, 46-49]. Song et al. [48] performed indentations to untreated and UV- treated PDMS and compared the obtained F_{adh} values (43.1 and 1.7 nN, respectively). Similar studies revealed dependence on the hydrophobicity of the PDMS surface (F_{adh} ~ 60nN [47,49]) and the crosslinking density (F_{adh} from 93.1 to 43.6 μN with decreasing crosslinker concentration [46]).

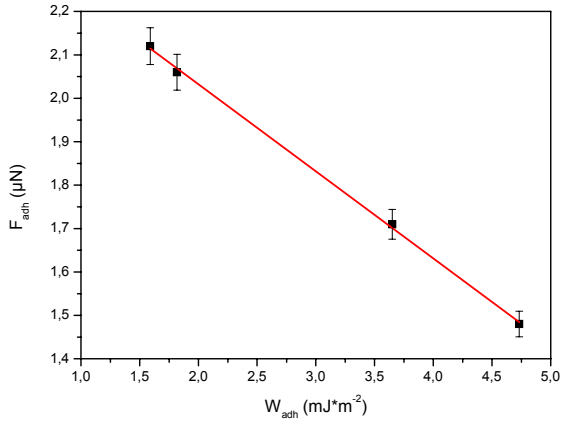

Fig. 6: Work of adhesion calculated through Eq.1 for various F_{adh}, with a slope of - 5.

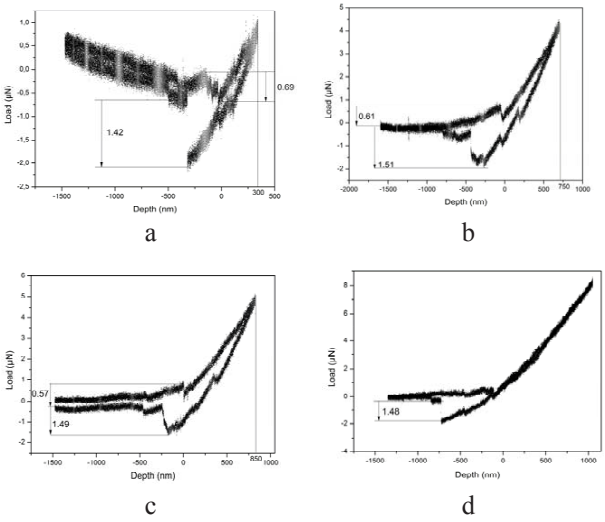

Fig. 7: Load- Unload plots at different applied loads on PDMS 0phr (this work).

Approaching and retracting parts of load curves are often not identical (Fig. 7). This is due to various reasons. For instance in liquids hydrodynamic drag is one of the reasons [50], since it causes a difference in the zero- load line. In order to prevent a jump- in contact the use of stiffer tips is proposed in relative studies (however sensitivity is lost). Due to this fact, alternative techniques have been performed to access the unstable regime such as the application of a load feedback (electric or magnetic) to balance the surface force [51-57], kinetic force experiments [58-59] and using a microsphere rather than a microfabricated tip (the hydrodynamic drag can be used to compensate for the attraction) [47]. Another instability occurs

when tip or sample surface are not perfectly rigid but are deformed by the tip. In this case of elastic deformation, Pethica and Sutton showed that at sufficiently small separations, typically 1–2 Å, the tip and the sample will jump together, irrespective of apparatus construction [60]. A similar jump occurs for non- elastic deformations. In this case, however, the jump depends on the rate of the plastic deformation [61]. When retracting the tip adhesion often keeps it in contact with the surface until the tip load overcomes the pull- off force (also called adhesion force) F_{adh}. This even happens in purely elastic, non- dissipative situations.

Carillo et al. [46] performed adhesion experiments in aqueous solution in order to study the influence of experimental environment on the adhesion work. Their results indicated a significant decrease in the adhesive force when testing was performed in distilled water. Since the contribution of electrostatic attraction to the total adhesive force is relatively large for PDMS (in addition to the dispersive interactions due to the non-polar behavior of PDMS), the decrease found in the measured F_{adh} is probably the result of the weakening of the electrostatic charge under wet conditions. Moreover, the F_{adh} values do not seem to be converging to zero (repellant interaction of PDMS (an inherent hydrophobic material mainly due to the presence of –CH3 groups) with water, and constant presence of the dispersive van der Waals forces). Thus, the current calculation methods, though seemingly adequate for adhesive polymeric materials, need proper modification of the current experimental protocol in order to capture both the dynamic response of materials for which viscous or rubbery flow conditions exist (i.e., where energy loss is a more significant factor) and the adhesion tip-sample interactions [22].

The Hertzian model was used to obtain the optimal fit (in the least- square sense) of the later part of the experimental load curve, and the difference between the experimental and the fitting curves at the beginning part of the curve represents the so called zero-load plastic deformation (ZLPD) (i.e., the residual plastic deformation, see Fig. 8) [62, 63]. The fitting deviate from the curve at ~1500 nN, revealing a ZLPD of 150 nm, for 0.8 μN/s loading rate. For lower applied loads (~7 nN), PDMS revealed a ZLPD of 22 nm for 1.7 μm/s loading rate using AFM [64].

The problem of the analytical techniques comes from the influence of interfacial adhesive forces, which can affect the indentation contact area and has not been validated for very soft materials, with E below 5 MPa. Some authors have demonstrated the validity of the nanoindentation in measuring the E of pure PDMS with different degrees of cross- linking [46].

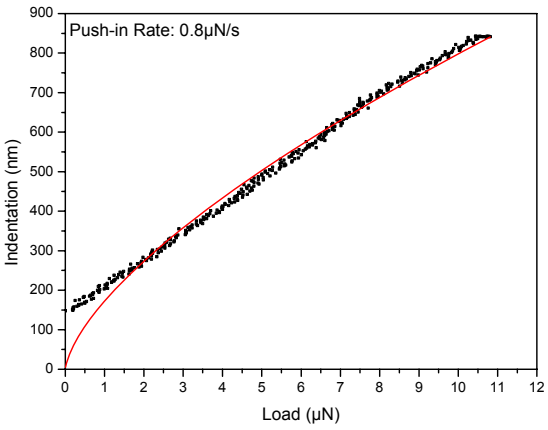

Fig. 8: Indentation vs Load along with comparison to the curve- fitting (red- line) obtained by using the Hertzian model, where the difference between the experimental and the fitted curves at the beginning portion represents the zero- load plastic deformation.

3.4 Investigation of creep effect

The nanoindentation creep tests were performed on pristine PDMS samples. Hold times in the range from 5 to 2000 s were selected. Loading and unloading time were chosen from similar measurements presented in the literature [19] and were 4 s and 15 s, respectively. Fig. 8 shows the dependence of H and E on the hold time. The H and E values were estimated by the Oliver- Pharr (O&P) model [65] (fitting on the first 30% of unloading data, where the slope indicates stiffness (S)). The deviations in H and E values due to creep effect are presented in Table 1. A zero hold time results in relative high H and E values (1.92 MPa and 7.79 MPa, respectively). The properties of materials with marked creep behaviour, such as PDMS, make it difficult to find measurement conditions that allow a comparison of H and E results that are independent of the hold time at maximum applied load. The current investigation shows that it is possible to find a hold period where the influence of the creep rate on the H and E results can be negligible. The recommended hold times are independent of load but can depend on the plastic displacement to film thickness ratio in the case of coatings. If the recommended hold time is used, the creep no longer has an influence on the results. These results reveal that only after around 300 s (Fig. 9), the deviation in H and E, due to creep effect, can be negligible. Chudoba et al. [66] investigated the effect of creep of a 3.4 μm aluminum layer

on BK7 glass and a change in H and E values of 18% and more than 50%, respectively, was found. Aluminum is another material with marked creep behavior. Chudoba et al. recommended a hold time of 187 s for aluminum. Fig. 10 presents the load- displacement curves of PDMS for hold times of 0, 500 and 2000 s. The curve without hold time at maximum applied load shows a bowing ("nose") in the upper part of the unloading curve, which leads to the high E deviation described previously. The reason is the inaccurate determination of S at maximum load, as E is directly proportional to S. As the hold time increases, the indenter continues to penetrate in the sample.

Table 1. H and E deviations as the hold time increases. H_o is the hardness value (1.92 MPa) and E_o is the elastic modulus value (7.79 MPa) for zero holding time and Ht, Et values measured for various hold times.

Hold Time - (s)	H_t/H_0	E_t/E_0
0	**1**	**1**
3	0.81	0.65
5	0.51	0.30
10	0.56	0.32
25	0.45	0.29
50	0.40	0.30
75	0.39	0.28
100	0.32	0.27
150	0.32	0.26
250	0.23	0.23
500	0.09	0.21
1200	0.09	0.19
2000	0.11	0.18

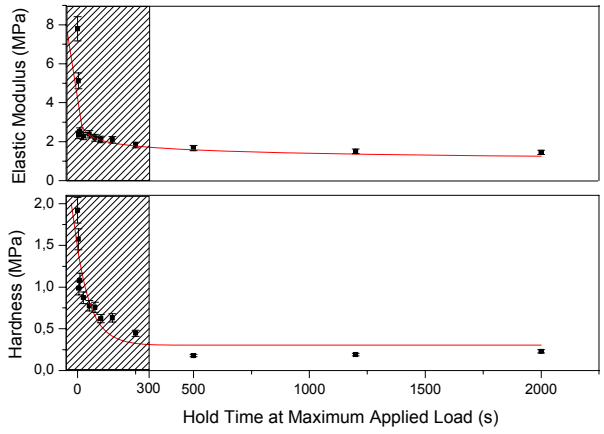

Fig. 9. H and E as a function of hold time (lines are guide to the eye). The hold time should be at least 300 s to avoid high deviations in H and E values.

3.5 Investigation of the loading rate effect

Taking into account the concern regarding the influence of polymer's viscosity [67-68], the effect of loading rate on H and E of PDMS was investigated.

The effect of loading rate on H and E values was studied for loading rates 0.1, 0.8, 1.2, 1.5, 8, 20 and 40 μN/s in PDMS (8phr) with a maximum load of 80 μN through a three- segment process (hold time 3 s between load and unload segments). It was found that H and E values are relatively high (3.33 and 9.77 MPa, respectively) for a loading rate of 0.1 μN/s. H and E values decrease with the increase of loading rate and reaching constant values (~2 and 5.8 MPa, respectively) (Fig. 10), which is in good agreement with similar studies on polymers [21]. The unloading rate was the same with that of loading in each case. The H and E values estimated by the O&P model and the deviation in H and E values are presented in Tables 2 and 3, respectively. In order to avoid the loading rate effect on H and E values, the loading time should be at least 3 μN/s (Fig. 11).

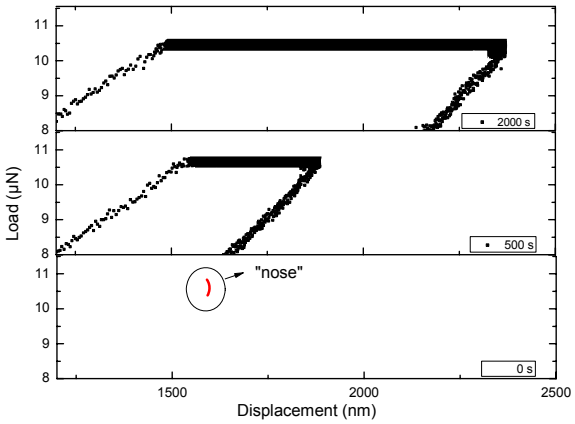

Fig. 10. Load- displacement curves for PDMS. The curve without hold time at maximum applied load shows a "nose" in the upper part of the unloading curve. As the hold time increases, the indenter continues to penetrate to the sample. Low hold times caused a deviation that cannot be neglected in the measurement of the nanomechanical properties, as the curve is steeper.

Since the same load profile was applied during a longer time interval at low loading- unloading rates than that of high loading- unloading rates, a larger amount of kinetic energy was applied to the PDMS at low loading rate than that at high loading rate, resulting in differences in nanomechanical properties because of the time- dependent viscoelastic behaviour of PDMS. This is because in case of PDMS, a viscoelastic material whose glass transition temperature is far below room temperature, when the push- in rate is low, the PDMS molecules are able to move (i.e., deform, and subsequently recover to their equilibrium conformation) in response to the applied deformation. The results obtained with time-dependent testing (through creep and loading rate study) imply that the process is dominated by viscoelasticity.

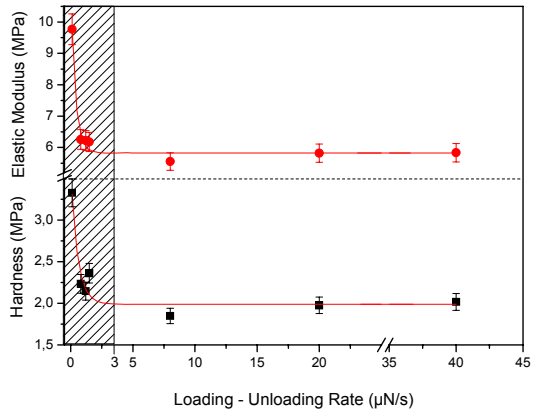

Fig. 11: H and E values for different loading rates (lines are guide to the eye). The loading rate should be, at least, 3 μN/s in order to avoid high deviations in H and E values.

Table 2: H and E values estimated by O&P model [65].

Loading – Unloading Rate (μN/s)	Hardness (MPa)	Elastic modulus (MPa)
0.1	3.33 ± 0.17	9.77 ± 0.49
0.8	2.23 ± 0.11	6.26 ± 0.31
1.2	2.15 ± 0.11	6.23 ± 0.31
1.5	2.36 ± 0.12	6.18 ± 0.31
8.0	1.85 ± 0.09	5.55 ± 0.28
20.0	1.97 ± 0.10	5.82 ± 0.29
40.0	2.02 ± 0.11	5.84 ± 0.29

Table 3: H and E deviations as the loading rate increases. H_o is the hardness value (3.33 MPa) and E_o is the elastic modulus value (9.77 MPa) for 0.1 μN/s loading rate and H_t, E_t values measured for various loading rates.

Loading Rate (μN/s)	H_t/H_0	E_t/E_0
0.1	**1**	**1**
0.8	0.66	0.64
1.2	0.64	0.63
1.5	0.70	0.63
8	0.55	0.56
20	0.59	0.59
40	0.60	0.59

4. Conclusions

The nanomechanical properties (namely hardness and elastic modulus) and the ratio H/E revealed that the addition of nanoclay amount strengthens the PDMS-montmorillonite nanocomposite. Consideration of the adhesion energy at the tip- sample interface is requisite for determining accurate elastic moduli of PDMS samples and other soft, elastomeric materials from nanoindentation experiments, since soft material samples are expected to have significant adhesive forces. The analysis of ZLPD of PDMS revealed that after the tip of the indenter was pulled away from the sample, the adhesive attraction deformed the soft polymer along the direction of the tip motion and caused a negative indentation (for applied load ~4.5 μN). The findings of the present study suggest that the adhesion energy at the tip- PDMS surface interface as well as the hold time and the loading/unloading rate are significantly important parameters and need to be taken into account for consistent elastic E determination of soft materials by nanoindentation. This implies that the process is dominated by viscoelasticity.

Creep and loading rate analysis revealed the time dependent behaviour and its effect on the nanomechanical properties of PDMS. With low hold- time appliance, a non- negligible deviation of E was caused, as the unloading curve became steeper and the S couldn't be accurately determined. A hold time of at least 300 s should be used in order to avoid the creep effect in H and E values. Moreover, the effect of loading rate revealed that with the increase of loading rate, H and E decreased until they reached constant values. As PDMS is a viscoelastic material and its glass transition temperature is far below room temperature, when the push- in rate is low, the PDMS molecules are able to move (i.e., deform, and subsequently recover to their equilibrium conformation) in response to the applied deformation. Thus, a larger amount of kinetic energy was applied to the PDMS at low loading rate than that at high loading rate, resulting in differences in nanomechanical properties. The loading rate of at least 3 μN/s is proposed in order to avoid the loading rate effect in H and E values.

For quantitatively accurate and reproducible results, nanoindentation of soft and adhesive materials requires further validation and suitable modification. These challenges present numerous opportunities for the continued development of indentation instrumentation and techniques and a redesign of the experimental protocol is needed.

References:

1. **Silva, M.N, Desai, R., Odde, D.J.** Micro- patterning of animal cells on PDMS substrates in the presence of serum without use of adhesion inhibitors, *J. Biomed Microdev.* **6** (2004) 219–222.
2. **Roure, O., Saez, A., Buguin, A., Austin, R.H., Chavrier, P., Siberzan, P., Ladoux, B.,** Force mapping in epithelial cell migration, *Proc. Natl. Acad. Sci.* **102** (2005) 2390–2395.
3. **Ostuni, E., Kane, R., Chen, S.C., Ingber, D.E., Whitesides, G.M.,** Patterning mammalian cells using elastomeric membranes, *Langm.* **16** (2000) 7811- 7819.
4. **Peterson, S.L., McDonald, A., Gourley, P.L., Sasaki, D.Y.,** Poly(dimethylsiloxane) thin films as biocompatible coatings for microfluidic devices: Cell culture and flow studies with glial cells, *J. Biomed. Mater. Res.* Part A.**72** (2005) 10-18.
5. **Balaban, N.Q., Schwarz, U.S., Riveline, D., Goichberg, P., Tzur, G., Sabanay, I., Mahalu, D., Safran,**

S., Bershadsky, A., Addadi, L., Geiger, B., Force and focal adhesion assembly: a close relationship studied using elastic micropatterned substrates, *J. Nat. Cell Biol.* **3** (2001) 466–472.

6. **Burton, K., Taylor, D.L.,** Traction forces of cytokinesis measured with optically modified elastic substrata, *J. Nat.* **385** (1997) 450–454.
7. **Harris, A.K., Wild, P., Stopak, D.,** Silicone rubber substrata: a new wrinkle in the study of cell locomotion, *J. Scien.* **208** (1980) 177–179.
8. **Mata, A., Fleischman, A.J., Roy, S.,** Characterization of polydimethylsiloxane (PDMS) properties for biomedical micro/nanosystems, *J. Bio. Micro.* **7** (2005) 281–293.
9. **Brown, X.Q., Ookawa, K., Wong, J.Y.,** Evaluation of polydimethylsiloxane scaffolds with physiologically- relevant elastic moduli: interplay of substrate mechanics and surface chemistry effects on vascular smooth muscle cell response, *J. Biomater.* **26** (2005) 3123–3129.
10. **Tan, J.L., Liu, W., Nelson, C.M., Raghavan, S., Chen, C.S.,** Simple approach to micropattern cells on common culture substrates by tuning substrate wettability, *J. Tis. Eng.* **10** (2004) 865-872.
11. **Clarson, S.J., Semlyen, J.A.,** Siloxane Polymers. PTR Prentice Hall, New Jersey, 1993, pp. 193-215.
12. **Wang, S., Long, C., Wang, X., Li, Q., Qi, Z.,** Synthesis and properties of silicone rubber/organomontmorillonite hybrid nanocomposites, *J. Appl. Polym. Sci.* **69** (1998) 1557-1561.
13. **Burnside, S.D., Giannelis, E.P.,** Synthesis and properties of new poly(dimethylsiloxane) nanocomposites, *J. Chem. Mater.* **7** (1995) 1597-1600.
14. **Ma, J., Xu, J., Ren, J.H., Yu, Z.Z., Mai, Y.W.,** A new approach to polymer/montmorillonite nanocomposites. *J. Polym.* **44** (2003) 4619-4624.
15. **Ma, J., Yu, Z.Z., Kuan, H.C., Dasari, A., Mai, Y.W.,** A New Strategy to Exfoliate Silicone Rubber/Clay Nanocomposites, *J. Macromol. Rapid. Commun.* **26** (2005) 830-833.
16. **Wang, J., Chen, Y., Jin, Q.,** Organic Montmorillonite as a Substitute for Aerosilica in Addition- Type Liquid Silicone Rubber Systems, *J. Macromol. Chem. Phys.* **206** (2005) 2512-2520.
17. **Wang, J., Chen, Y.,** Preparation of an organomontmorillonite master batch and its application to high- temperature- vulcanized silicone- rubber systems, *J. Appl. Polym. Sci.* **107** (2008) 2059-2066.
18. **Horsch, S., Serhatkulu, G., Gulari, E., Kannan, R.M.,** Supercritical CO_2 dispersion of nano- clays and clay/polymer nanocomposites, *J. Polym.* **47** (2006) 7485-7496.
19. **Choi, S.T., Jung, S.J., Earmme, Y.Y.,** Modified-creep experiment of an elastomer film on a rigid substrate using nanoindentation with a flat- ended cylindrical tip, *J. Scrip. Mater.* **58** (2008) 199-202.
20. **Kaufman, J.D., Klapperich, C.M.,** Surface detection errors cause overestimation of the modulus in nanoindentation on soft materials, *J. Mech. Behav. Biomed. Mat.* **2**(2009) 312-317.
21. **Gupta, S., Carrillo, F., Li, C., Pruitt, L., Puttlitz, A.,** Adhesive Forces Significantly Affect Elastic Modulus Determination of Soft Polymeric Materials in Nanoindentation, *Mater. Lett.* **1** (2007) 448-451.
22. **Koumoulos, E.P., Charitidis, C.A., Vasilakos, S., Tarantili, P.A.,** Nanoindentation Of Nanocomposites Polydimethylsiloxane Elastomers. 7th Conference Of Chemical Engineering, Patra 2009.; Lu, H., Wang, B., Ma, J., Huang, G., Viswanathan, H., Measurement of Creep Compliance of Solid Polymers by Nanoindentation, *J. Mech. Time- Dep. Mater.* **7** (2003) 189–207.
23. **Briscoe, B.J., Sebastian, K.S., Adams, M.J.** The effect of indenter geometry on the elastic response to indentation, *J. Phys. D Appl. Phys.* **27** (1994) 1156-1162.
24. **Briscoe, B.J., Fiori, L., Pelillo, E.,** Nano- indentation of polymeric surfaces, *J. Phys. D Appl. Phys.* **31** (1998) 2395-2405.
25. **Yang, S., Zhang, Y.W., Zeng, K.,** Analysis of nanoindentation creep for polymeric materials, *J. App. Phys.* **95** (2004) 3655-3666.
26. **Fischer-Cripps, A.C.,** A simple phenomenological approach to nanoindentation creep, *J. Mater. Sci. Eng. A* **385** (2004) 74-82.
27. CSM Instruments Applications Bulletin No. 22 April 2006.
28. **Schmidt, D.F., Clément, F., Giannelis, E.P.,** On the origins of silicate dispersion in polysiloxane/layered-Silicate nanocomposites, *J. Adv. Funct. Mater.* **16** (2006) 417-425.
29. **Cheng, Y.T., Cheng, C.M.** What is indentation hardness?, *J. Surf. Coat. Tech.* **133-134** (2000) 417-424.
30. **Leyland, A., Matthews, A.,** Design criteria for wear-resistant nanostructured and glassy-metal coatings, *J. Surf. Coat. Tech.* **177-178** (2004) 317-324.
31. **White, C.C., Vanlandingham, M.R., Drzal, P.L., Chang, N.K., Chang, S.H.,** Viscoelastic characterization of polymers using instrumented indentation. II. Dynamic testing. *J. Pol. Sci.* **43** (2005) 1812–1824.

32 **Silberzan, P., Perutz, S., Kramer, E.J., Chaudhury, M.K.,** Study of the Self- Adhesion Hysteresis of a Siloxane Elastomer Using the JKR Method, *Lang.* **10** (1994) 2466-2470.

33. **Choi, G.Y., Kang, J.F., Ulman, A., Zurawsky, W.,** Acid−Base Interaction in the Adhesion between Two Solid Surfaces, *Lang.* **15** (1999) 8783-8786.
34. **Choi, G.Y., Kim, S., Ulman, A.,** Adhesion hysteresis studies of extracted poly(dimethylsiloxane) using contact mechanics, *Lang.* **13** (1997) 6333-6338.

35. **Choi, G.Y., Zurawsky, W., Ulman, A.,** Molecular Weight Effects in Adhesion, Lang. **15** (1999) 8447-8450.
36. **Kim, S., Choi, G.Y., Ulman, A., Fleischer, C.,** Effect of Chemical Functionality on Adhesion Hysteresis, Lang. **13** (1997) 6850-6856.
37. **Mason, R., Emerson, J., Koberstein, J.T.,** Self-Adhesion Hysteresis In Polydimethylsiloxane Elastomers, *J. Adhes.* **25** (2004) 119-143.
38. **Perutz, S., Kramer, E.J., Baney, J., Hui, C.Y., Cohen, C.,** Investigation of adhesion hysteresis in poly(dimethylsiloxane) networks using the JKR technique. *J. Polym. Sci.* **36** (1998) 2129-2139.
39. **Perutz, S., Kramer, E.J., Baney, J., Hui, C.Y.,** Adhesion between Hydrolyzed Surfaces of Poly(dimethylsiloxane) Networks, *J. Macrom.* **30** (1997) 7964-7969.
40. **Takano, H., Kenseth, J.R., Wong, S.S., O'Brien, J.S., Porter, M.D.,** Chemical and Biochemical Analysis Using Scanning Force Microscopy, *J. Chem. Rev.* **99** (1999) 2845-2890.
41. **Pickering, J.P., Vancso, G.J.,** Influence of tip indentation depth on the adhesive behavior of viscoelastic polydimethylsiloxane networks studied by atomic force microscopy, *Macrom. Symp.* **167** (2001) 189-199.
42. **Vakarelski, I.U., Toritani, A., Nakayama, M., Hisashitani, K.,** Deformation and adhesion of elastomer microparticles evaluated by AFM, *Lang.* **17** (2001) 4739-4745.
43. **Noel, O., Brogly, M., Castelein, G., Schultz, J.,** In situ estimation of the chemical and mechanical contributions in local adhesion force measurement with AFM: the specific case of polymers, *J. Eur. Polym.* **40** (2004) 965-974.
44. **Gillies, G., Prestidge, C.A., Attard, P.,** An AFM Study of the Deformation and Nanorheology of Cross- Linked PDMS Droplets, *Lang.* **18** (2002) 1674-1679.
45. **Derjaguin, B.V., Muller, V.M., Toporov, Y.P.,** Effect of contact deformations on the adhesion of particles, *J. Colloid. Inter. Sci.* **53** (1975) 314-326.
46. **Carrillo, F., Gupta, S., Balooch, M., Marshall, S.J., Marshall, G.W., Pruitt, L., Puttlitz, C.M.,** Nanoindentation of polydimethylsiloxane elastomers: effect of crosslinking, work of adhesion, and fluid environment on elastic modulus, *J. Mater. Res.* **20** (2005) 2820-2830.
47. **Meincken, M., Berhane, T.A., Mallon, P.E.,** Tracking the hydrophobicity recovery of PDMS compounds using the adhesive force determined by AFM force distance measurements, *J. Polym.* **46** (2005) 203-205.
48. **Song, J., Tranchida, D., Vansco, G.J.,** Contact Mechanics of UV/Ozone- Treated by AFM and JKR Testing: Mechanical Performance from Nano- to Micrometer Length Scales, *J. Macromol.* **41** (2008) 6757-6762.
49. **Brogly, M., Noel, O., Awada, H., Castelein, G., Schultz, J.,** A nanoscale study of the adhesive contact, C.R. *Chimie* **9** (2006) 99-110.
50. **Vinogradova, O.I., Butt, H.J., Yakubov, G.E., Feuillebois, F.,** Dynamic effects on force measurements. 1. Viscous drag on the atomic force microscope cantilever, *J. Rev. Sci. Instrum.* **72** (2001) 2330-2339.
51. **Miller, G.L., Griffith, J.E., Wagner, E.R.,** A rocking beam electrostatic balance for the measurement of small forces, *J. Rev. Sci. Instrum.* **62** (1991) 705-709.
52. **Bryant, J., Kim, H.S., Deeken, R.H., Cheng, Y.C.,** Surface force measurements on picometer and piconewton scales, *J. Vac. Sci. Technol. A* **8** (1990) 3502-3505.
53. **Grigg, D.A., Russel, P.E., Griffith, J.E.,** Rocking- beam force- balance approach to atomic force microscopy, *J. Ultramic.* **42-44** (1992) 1504-1508.
54. **Mertz, J., Marti, O., Mlynek, J.,** Regulation of a microcantilever response by force feedback, *Appl. Phys. Lett.* **62** (1993) 2344-2346.
55. **Jarvis, S.P., Oral, A., Weihs, T.P., Pethica, J.B.**, A novel force microscope and point contact probe, *J. Rev. Sci. Instrum.* **64** (1993) 3515-3520.
56. **Jarvis, S.P., Yamada, H., Yamamoto, S.I., Tokumoto, H., Pethica, J.B.,** Direct mechanical measurement of interatomic potentials, *J. Nat.* **84** (1996) 247-249.
57. **Jarvis, S.P., Tokumoto, H.,** Measurement and interpretation of forces in the atomic force microscope, *J. Prob. Microsc.* **1** (1997) 65-79.
58. **Butt, H.J.,** A Technique for Measuring the Force between a Colloidal Particle in Water and a Bubble, *J. Colloid. Interf. Sci.* **166** (1994) 109-117.
59. **Vinogradova, O.I., Horn, R.G.,** Attractive Forces between Surfaces: What Can and Cannot Be Learned from a Jump- In Study with the Surface Forces Apparatus?, *Lang.* **17** (2001) 1604- 1607.
60. **Pethica, J.B., Sutton, A.P.**,On the stability of a tip and flat at very small separations, *J. Vac. Sci. Technol. A* **6** (1988) 2490-2494.
61. **Butt, H.J., Döppenschmidt, A., Hüttl, G., Müller, E., Vinogradova, O.I.,** Analysis of plastic deformation in atomic force microscopy: Application to ice, *J. Chem. Phys.* **113** (2000) 1194-1203.
62. **Butt, H.J., Capella, B., Kappl, M.,** Force measurements with the atomic force microscope: Technique, interpretation and applications, *J. Surf. Sci. Rep.* **59** (2005) 1-152.
63. **Charitidis, C.A.,** Nanoscale deformation and nanomechanical properties of Polydimethylsiloxane (PDMS), *Ind. Eng. Chem. Res.* **50** (2010) 565–570.
64. **Kim, K.S., Lin, Z., Shrotriya, P., Sundararajan, S., Zou, Q.,** Iterative control approach to high- speed force- distance curve measurement using AFM:Time-

dependent response of PDMS example, *J. Ultramic.* **108** (2008) 911-920.
65. **Oliver, W.C., Pharr, G.M.,** An Improved Technique for Determining Hardness and Elastic Modulus Using Load and Displacement Sensing Indentation Experiments, *J. Mater. Res.* **7** (1992) 1564-1583.
66. **Chudoba, T., Richter, F.,** Investigation of creep behaviour under load during indentation experiments and its influence on hardness and modulus results, *J. Surf. Coat. Tech.* **148** (2001) 191-198.
67. **Sakai, M., Nakano, Y.,** Elastoplastic load- depth hysteresis in pyramidal indentation, *J. Mater. Res.* **17** (2002) 2161–2173.
68. **Oyen, M.L., Cook, R.F.,** Load- displacement behavior during sharp indentation of viscous- elastic- plastic materials, *J. Mater. Res.* **18** (2003) 139–150.

Nanomechanical properties of Physically-aged Polydimethylsiloxane

E.P. Koumoulos, V.P. Tsikourkitoudi, C.A. Charitidis*, P.N. Eleni, M.K. Krokida, I.C. Ziomas,

National Technical University of Athens, Department of Chemical Engineering 9 Heroon, Polytechniou st., Zografos, Athens, GR-157 80, Greece

* charitidis@chemeng.ntua.gr

ABSTRACT

Polymers exposed outdoors can be degraded through the action of several agents, including: solar ultraviolet (UV) radiation, water, pollutants (in gaseous form or, more potently, as acid-rain), elevated temperature and temperature changes. In most of the cases, the main cause of property deterioration is photooxidation. As with thermal degradation, a sequence of oxidative reactions follows in which both chain scission and crosslinking may occur. When chain scission is the dominant mechanism, the fracturing bonds within the main chain or between two different chains, incur a decrease in density of the structural network and the materials become softer. In the present study, nanoindentation is used in order to investigate the natural weathering effects on the nanomechanical properties of polydimethylsiloxane (PDMS) elastomer.

INTRODUCTION

PDMS is an elastomer with a wide range of biomedical applications as a consequence of its physiological inertness, good blood compatibility, low toxicity, good thermal and oxidative stability, low modulus and antiadhesive properties [1]. Nanoindentation is a technique which has been widely used to characterize the mechanical properties of materials at surface or subsurface (e.g. hardness (H) and elastic modulus (E)) [2].

EXPERIMENTAL

The nanoindentation analysis in this work has been performed using a Hysitron TriboLab® Nanomechanical Test Instrument (equipped with a Scanning Probe Microscope (SPM) and a Berkovich probe). In all depth-sensing tests a total of 10 indents are averaged to determine the mean H & E values for statistical purposes, with a spacing of 50 μm (~45% RH, 23°C). Outdoor weathering experiments were performed in Athens and Thessaloniki and lasted 1 year, in order to avoid the correlation of the results with seasonal weathering conditions (specimens were left uncovered and exposed to environment conditions).

RESULTS & DISCUSSION

In Fig. 1a & 1b,c the nanoindentation schematic and H & E vs. Displacement are presented. Higher H and E values reveal the existence of a surface area (~750nm) with enhanced nanomechanical properties.

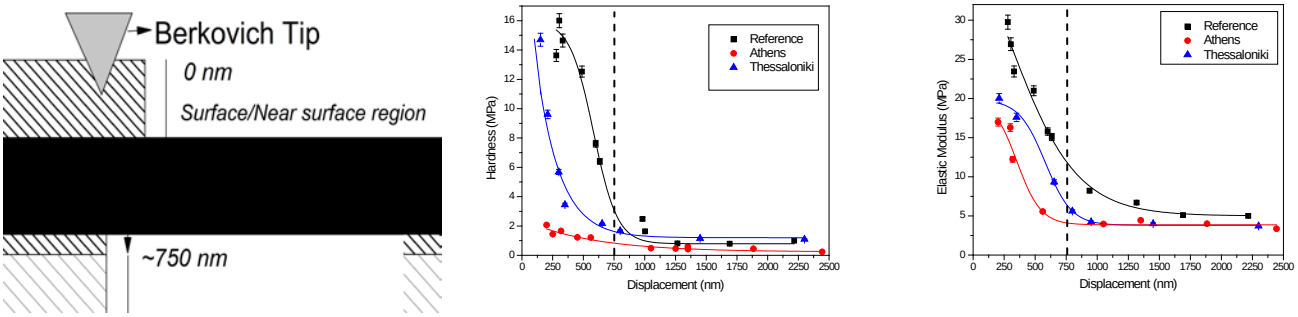

Fig. 1. Nanohardness and Elastic modulus of PDMS vs. Displacement (Reference sample, Athens and Thessaloniki for 12 months weathering ageing, respectively)

The weathering-treated PDMS samples of 6 and 12 months showed no significant differences, implying that degradation mechanisms had been almost completed by the 6th month of ageing (Fig. 2).

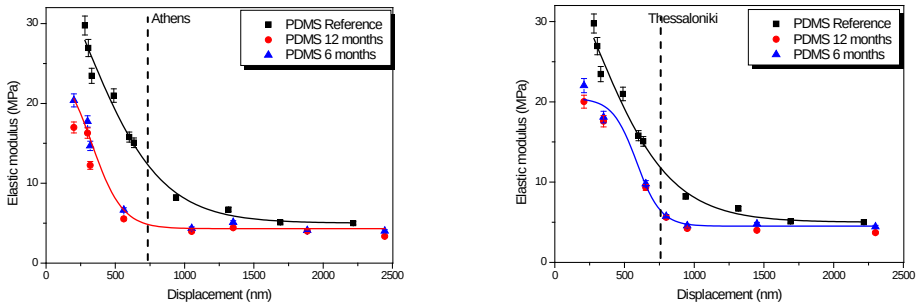

Fig. 2. Elastic modulus of PDMS (Reference sample, Athens and Thessaloniki for 6 and 12 months weathering ageing, respectively)

It is critical to investigate which of the mechanisms of degradation due to weathering is supreme, in order to explain the structural analysis [3, 4]. In case of PDMS the main mechanism of degradation due to weathering is hydrolysis through the surface cracks created by radiation (Fig.3). Those cracks reach a critical depth (high hydrolysis degradation); thus, the bulk region of the polymer is mainly affected-degraded by UV irradiation, whereas the surface region (containing cracks, thickness ~750nm) is mainly affected by hydrolysis and oxidation.

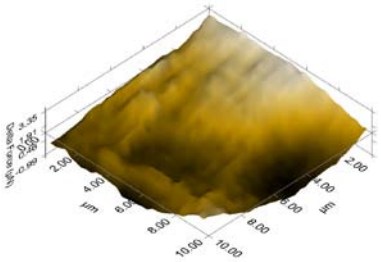

Fig.3. Surface cracks (holes) after 6 months of physical ageing (weathering) (SPM image)

The changes of physical properties affect the polymer structural network in different ways [5]: 1.The density of the structural network increases during cross-linking, due to the formation of bonds between the existing monomers or between the chains. Therefore, cross-linking leads to harder materials, 2. when chain scission is the dominant mechanism, the fracturing bonds within the main chain or between two different chains, incur a decrease in density of the structural network and the materials become softer. In case of PDMS the main mechanism of degradation due to weathering is hydrolysis through the surface cracks created by radiation.

CONCLUSIONS

In this study the exact surface region (with higher values of hardness and elastic modulus) was clearly defined (~750nm). In case of PDMS the main mechanism of degradation due to weathering is hydrolysis through the surface cracks created by radiation. Those cracks reach a critical depth (high hydrolysis degradation); thus, the bulk region of the polymer is mainly affected-degraded by UV irradiation, whereas the surface region (containing cracks, depth <750nm) is mainly affected by hydrolysis and oxidation. The weathering-treated PDMS samples of 6 and 12 months showed no significant differences, implying that degradation mechanisms had been almost completed by the 6th month of ageing.

REFERENCES

[1] Abbasi F, Mirzadeh H, Katbab A. *Pol Inter*. 2001; 50(12): 1279 – 1287.

[2] Charitidis CA. *Int J Refract Met*. 2010; 28: 51–70; Charitidis CA. Nanoscale deformation and nanomechanical properties of Polydimethylsiloxane (PDMS), *Indus & Eng Chem Res*, (in publication 2010).

[3] White J, *Comptes Rendus Chimie*. 2006; 9(11-12): 1396-1408.

[4] Eleni PN, Katsavou I, Krokida MK, Polyzois GL, Gettleman L. *Den Mater*. 2009; 25(12): 1493-1502.

[5] Eleni PN, Krokida MK, Polyzois GL. Biomed. Mater. 2009; 4(3): 035001.

J Nanopart Res (2013) 15:1871
DOI 10.1007/s11051-013-1871-3

RESEARCH PAPER

Hybrid organic–inorganic coatings including nanocontainers for corrosion protection of magnesium alloy ZK30

I. A. Kartsonakis · E. P. Koumoulos · C. A. Charitidis · G. Kordas

Received: 30 November 2012 / Accepted: 15 July 2013 / Published online: 30 July 2013

Abstract This study is focused on the fabrication, characterization, and application of corrosion protective coatings to magnesium alloy ZK30. Hybrid organic–inorganic coatings were synthesized using organic-modified silicates together with resins based on bisphenol A diglycidyl ether. Cerium molybdate nanocontainers (ncs) with diameter 100 ± 20 nm were loaded with corrosion inhibitor 2-mercaptobenzothiazole and incorporated into the coatings in order to improve their anticorrosion properties. The coatings were investigated for their anticorrosion and nanomechanical properties. The morphology of the coatings was examined by scanning electron microscopy. The composition was estimated by energy-dispersive X-ray analysis. The mechanical integrity of the coatings was studied through nanoindentation and nanoscratch techniques. Scanning probe microscope imaging of the coatings revealed that the addition of ncs creates surface incongruity; however, the hardness to modulus ratio revealed significant strengthening of the coating with increase of ncs. Studies on their corrosion behavior in 0.5 M sodium chloride solutions at room temperature were made using electrochemical impedance spectroscopy. Artificial defects were formatted on the surface of the films in order for possible self-healing effects to be evaluated. The results showed that the coated magnesium alloys exhibited only capacitive response after exposure to corrosive environment for 16 months. This behavior denotes that the coatings have enhanced barrier properties and act as an insulator. Finally, the scratched coatings revealed a partial recovery due to the increase of charge–transfer resistance as the immersion time elapsed.

Keywords Nanocontainers · Impedance · Magnesium · Corrosion · Nanoindentation

Special Issue Editors: Juan Manuel Rojo, Vasileios Koutsos

This article is part of the topical collection on Nanostructured Materials 2012

I. A. Kartsonakis (✉) · G. Kordas
Sol-Gel Laboratory, IAMPPNM, NCSR 'DEMOKRITOS', 15310 Agia Paraskevi, Greece
e-mail: ikartsonakis@ims.demokritos.gr

I. A. Kartsonakis · E. P. Koumoulos · C. A. Charitidis (✉)
School of Chemical Engineering NTUA, 9 Heroon Polytechniou St., 15780 Zographos, Greece
e-mail: charitidis@chemeng.ntua.gr

Introduction

Magnesium alloys are widely used in the aircraft and guided weapons industries and in automotive construction because of their light weight and high strength/weight ratio. Their unique properties such as high stiffness/weight ratio, ease of machinability, high damping capacity, and casting qualities are required in a wide range of applications. Magnesium

is used as a canning material for uranium in gas-cooled reactors. Moreover, magnesium and its alloys can be used as sacrificial anodes for cathodic protection. Finally, magnesium is itself used for alloying with other metals for different applications (Loose 1976). On the contrary, magnesium and its alloys are poor to corrosion resistance because of their high chemical activity and low electrode potential (Froes et al. 1998). Several coating applications have been developed in order to improve the corrosion resistance of magnesium and its alloys, such as electrolytic plasma oxidation (Makar and Kruger 1993), inorganic pretreatments (Hoche et al. 2003), ion beam-assisted deposition (Ma et al. 2007), anodizing process (Liang et al. 2009), vapor-phase method for self-assembled monolayer (Choi et al. 2007), etc.

Lots of studies have been focused on the development of corrosion protective coatings on magnesium alloys substrates that would be able to recover an appeared damage or defect. The concept was the introduction of corrosion inhibitors into the coatings in order to inhibit at a first stage and to recover at a second stage possible damage of the coatings due to corrosion process. The corrosion protective coatings were inorganic, organic, or hybrid organic–inorganic including corrosion inhibitors based on inorganic or organic compounds (Lamaka et al. 2009; Scharnagl et al. 2009). Moreover, various nanoparticles were encapsulated into sol–gel coatings for enhancement of their anticorrosion properties (Wang et al. 2010). On the other hand, the incorporation of corrosion inhibitors into the coating matrix depressed its coherence which resulted in reduced corrosion protection. In order to overcome the aforementioned disadvantage, the corrosion inhibitors were encapsulated into various types of containers. An improvement on the corrosion protection of magnesium alloys was accomplished via the incorporation of nanocontainers (ncs) that had been previously loaded with corrosion inhibitors, into hybrid organic–inorganic coatings (Kartsonakis et al. 2012).

However, a protective coating should be examined not only for his enhanced corrosion protective and self-healing properties but also for its mechanical properties, as well. Nanoindentation and nanoscratch testing have been widely applied for the measurement of mechanical properties of thin films (Schuh 2006; Li and Bhushan 2002). Nanoindentation can provide information about the mechanical behavior of the material when deformed at the sub-micron scale. The method proposed by Oliver and Pharr (1992) allows determining the hardness and the elastic modulus from the nanoindentation load–displacement data. Nanoscratch is a versatile tool for analysis of thin films and bulk materials, where a single scratch with a ramped normal load is useful for critical load, film adhesion, and mar studies. Nanoscratch provides the capability of investigating modes of deformation and fracture beyond standard indentation techniques, and is accomplished by applying a normal load in a controlled mode while measuring the force required for moving the tip laterally across the sample. The trough path is typically observed using optical or scanning probe microscopy (SPM) imaging (in situ SPM imaging of the sample with nanometer resolution for immediate feedback of the test results). The critical load corresponding to the failure can provide qualitative nature of the scratch resistance or adhesion strength of the film, depending not only on adhesion strength but also on several intrinsic (testing conditions such as loading rate, scratching speed, and indenter shape) and extrinsic (connected to film–substrate system like material properties, friction coefficient, and physical dimensions) factors (Koumoulos et al. 2012).

The aim of this study is the synthesis and application of corrosion protective coatings on magnesium alloy ZK30 as well as the production of ceramic ncs. The coatings consist of epoxy-based resins together with organic-modified silicates. Moreover, the ceramic ncs are loaded with corrosion inhibitor 2-mercaprobenzothiazole (MBT). The influence of the ceramic ncs' incorporation on the improvement of the corrosion protection properties of the coatings is investigated. Moreover, the ability of the coatings for partial recovery and self-healing properties is examined, too. Experiments on the evaluation of the contribution of each factor (coating, inhibitor, and nc) to the corrosion protection of the metal alloy are conducted. Finally, studies on the nanomechanical properties of the coatings are carried out. The novelty of this study is the application of coatings on magnesium alloy ZK30 that would have enhanced barrier properties and act as an insulator after their exposure to corrosive environment for more than a year. Furthermore, these coatings would reveal partial self-healing properties due to the incorporation of ceramic ncs loaded with corrosion inhibitor. It should be mentioned that magnesium alloy ZK30 is very susceptible to corrosion. According to

the literature already published, no coatings with the aforementioned enhanced barrier effect properties (acting as an insulator) after exposure to corrosive environment for more than a year (16 months) have been synthesized and applied to magnesium alloy ZK30, yet (Lamaka et al. 2009).

Experimental

Materials

Magnesium alloy ZK30 was obtained from Alubin, Israel. All chemicals were of analytical reagent grade. MBT (Sigma-Aldrich, St. Louis, USA), cerium(III) acetylacetonate ($Ce(acac)_3$, Sigma-Aldrich, St. Louis, USA), sodium molybdate (Na_2MoO_4, Sigma-Aldrich, St. Louis, USA), potassium persulfate (KPS, Sigma-Aldrich, St. Louis, USA), acetone (Sigma-Aldrich, St. Louis, USA), USA), *N*-(2-aminoethyl)-3-(trimethoxysilyl)propylamine (Z 6020, Sigma-Aldrich, St. Louis, USA), epoxy resin based on phenol 4,4′-(1-methylethylidene) bis-("Araldite GY 257", GY 257, Ciba-Geigy), 2,2′-diaminodiethylamine (HY 943, Sigma-Aldrich, St. Louis, USA) were used without further purification. Methylmethacrylate (MMA, Sigma-Aldrich, St. Louis, USA) and methacrylic acid (MAA, Sigma-Aldrich, St. Louis, USA) were double-distilled under reduced pressure prior to use.

Synthesis of cerium molybdate nanocontainers (ncs)

Cerium molybdate (CeMo) ncs were produced using a three-step process. At first, anionic-charged organic nanospheres were synthesized using polymerization in suspension. In a three-neck flask, distilled water used as a solvent, monomers MMA and MAA, and KPS used as an initiator, were mixed with vigorous stirring (Table 1). The mixture was left to react at 80 °C for 12 h. The polymerization process was accomplished in inert atmosphere via the insertion of nitrogen gas into the reaction mixture. The produced polymer was centrifuged and washed with distilled water three times. Then, the fabricated poly(MMA-*co*-MAA) nanospheres were used as templates and coated with $Ce(acac)_3$ and Na_2MoO_4 via the sol–gel process. Distilled water, $Ce(acac)_3$, and Na_2MoO_4 were added in a flask with vigorous stirring (Table 2). The pH of the mixture was adjusted to 10 using sodium hydroxide; the flask was sealed and placed for curing at 95 °C for 3 days. After that, the produced CeMo nanocomposites were centrifuged and washed with water. Finally, the CeMo ncs were synthesised after heat treatment in air of the nanocomposites at 500 °C for 3 h with a heating rate of 10 °C min^{-1}.

Table 1 The conditions used in the preparation of poly(-MMA-*co*-MAA) nanospheres at 80 °C

Materials	Quantity (g)
MMA	20
MAA	0.4
KPS	0.4
Water	400

Table 2 Conditions of preparation of coated spheres

Materials	Quantity (g)
Poly(MMA-*co*-MAA)	20.0
Cerium(III) acetylacetonate	10.0
Sodium molybdate	1.0
Water	1000

The loading of the ncs with MBT was similar to our previous work (Kartsonakis et al. 2008). The CeMo ncs were placed in sealed flask under vacuum conditions. Saturated solution of MBT in acetone was added into the sealed flask. The mixture was left with vigorous stirring for 24 h. Then the ncs were centrifuged and washed with ethanol.

Preparation of coating

The synthesis of the coating includes the hydrolysis of Z 6020 in absolute ethanol for 1 h (solution A). Simultaneously, the epoxy resin GY 257 is dissolved in absolute ethanol (solution B). After that, solutions A and B are intermixed formatting solution C. Then, HY 943 is dissolved in 25 ml acetone (solution D). Finally, solutions C and D are intermixed and stirred

Table 3 Conditions used for the preparation of coating solution

Reagents	Z 6020	GY 257	HY 943	Ethanol	Acetone
% w/w	2.0	20.0	2.0	56.0	20.0

for 8 h (Table 3). The loaded ncs (10 wt%) are added to the above solution, with vigorous stirring, 1 h prior the dip-coating process.

Dip-coating process

Optimum protection for the ZK30 is achieved by a coating formed with a constant withdrawing speed of 5.33 mm s^{-1} and curing at 70 °C for 4 days. Each panel is dipped three times. The specimens are withdrawn in a direction parallel to their lengths. All the panels are cleaned from impurities prior the dip-coating process. The procedure includes the immersion of the panels into 96 % v/v ethanol for 20 min at room temperature, under sonication. After that, the panels are rinsed with distilled water and inserted into a degreaser solution (mixture of sodium hydroxide and sodium carbonate in water) for 10 min at 70 °C. Then, the panels are immersed in distilled water for a few minutes at 40 °C. The next step includes the insertion of the panels in hydrofluoronic acid 10 % w/w for 20 min at room temperature. Finally, the panels are rinsed with distilled water and left to dry in air. Four different types of coatings were prepared. At first, coatings free of additives (inhibitor or ncs) were synthesized (ZK30-Coat). Then, coatings that had only inhibitor (ZK30-Coat-MBT) or empty ncs (ZK30-Coat-nc) were prepared. Finally, coatings that had ncs loaded with inhibitor (ZK30-Coat-ncMBT) were fabricated.

Morphology, composition, and thermal characterization

The morphology of the produced ncs was estimated by transmission electron microscopy (TEM) CM 20 Philips Eindhoven, operated at 200 kV accelerating voltage. The morphology of the coatings was determined by scanning electron microscopy (SEM) using a Philips Quanta Inspect (FEI Company) microscope with W (tungsten) filament 25 kV equipped with EDAX GENESIS (AMETEX PROCESS and ANALYTICAL INSTRUMENTS). Furthermore, the estimation of the % w/w loading of the ncs with the corrosion inhibitor MBT was accomplished via thermogravimetric analysis (TGA) using a Perkin Elmer (Pyris Diamand S II) analyzer at the heating rate of 10 °C min^{-1} in air. The crystal nature of the magnesium alloy was estimated via X-ray diffraction (XRD) analysis using a powder diffractometer (SIEMENS D-500 equipped with a CuK_a lamp with wavelength 1.5418 Å).

Electrochemical measurements

The corrosion resistance of these coatings was studied by electrochemical impedance spectroscopy (EIS) using a SI 1287 Solartron electrochemical interface connected with a SI 1260 Impedance/gain-phase analyzer. Corrosion test process includes the exposure of the coated panels to 0.5 M NaCl solution for 16 months. The experiments were performed at room temperature, in a Faraday cage, at the open-circuit potential, using a three-electrode electrochemical cell, consisting of working electrode (≈ 2.0 cm^2 of exposed area), saturated calomel electrode as reference, and platinum as counter electrode. The measuring frequency ranged from 50 kHz down to 5 mHz. The rms voltage was 10 mV. Spectra were treated with the "Z-view Software" using the adequate equivalent electric circuits.

Nanomechanical measurements

Scratch tests were performed using a Rockwell indenter equipped with diamond (radius 200 μm). Finally, microhardness measurements were taken using a Shimadzu microhardness tester HMV-2. The indenter was a diamond in a pyramid shape with 136° angle between the opposite sides. Hardness (H) and elastic modulus (E) values were extracted from the experimental data (load–displacement curves) using the Oliver–Pharr (O&P) method (Troyon and Huang 2006; Oliver and Pharr 1992), based on the half-space elastic deformation theory. The equations used to calculate the elastic modulus from indentation experiments are based on Sneddon's (1948) elastic contact theory:

$$E_r = \frac{S\sqrt{\pi}}{2\beta\sqrt{A_c}}, \quad (1)$$

where S is the unloading stiffness (initial slope of the unloading load–displacement curve at the maximum displacement of penetration [or peak load]), A_c is the projected contact area between the tip and the substrate, and β is a constant that depends on the geometry of the indenter ($\beta = 1.167$ for Berkovich tip) (Troyon and Huang 2006; Oliver and Pharr 1992).

Conventional nanoindentation hardness refers to the mean contact pressure; this hardness, which is the contact hardness H_c is actually dependent upon the geometry of the indenter:

$$H_c = \frac{F}{A(h_c)}, \tag{2}$$

where,

$$A(h_c) = 24.5h_c^2 + a_1 h_c + a_{1/2}h_c^{1/2} + \cdots + a_{1/16}h_c^{1/16}, \tag{3}$$

$$h_c = h_m - \varepsilon\frac{P_m}{S_m}, \tag{4}$$

and h_c is the total penetration displacement of the indenter at peak load, P_m is the peak load at the indenter displacement h_c, and ε is a constant, equal to 0.75 for Berkovich indenter (Troyon and Huang 2006; Oliver and Pharr 1992; Sneddon 1948; King 1987; Koumoulos et al. 2011). The leading term ($24.5h_c^2$) of (Eq. 3) describes a perfect Berkovich indenter, whereas the others describe deviations from the Berkovich geometry due to blunting at the tip (Oliver and Pharr 1992). The total plastic work was calculated through integration of load–unload curves. Prior to indentation, the area function of the indenter tip was calibrated in fused silica, a standard material for this purpose (Bei et al. 2005).

The scratch tests performed in this work included three main segments, namely pre-scan, scratch, and post-scan (Koumoulos et al. 2012). First, a pre-scan under a very small load (1 μN) was carried out. Then, the indenter scraped the sample under a certain force and scratch would be generated. The maximum normal applied load used in this work was 500 μN. The length of the scratches was 10 μm.

Results and discussion

Magnesium ZK30

The composition of the magnesium alloy ZK30 is 3 wt% Zn, 0.6 wt% Zr, and the rest is Mg (Stippich et al. 1998). Its crystal nature was estimated via XRD and is demonstrated in Fig. 1. The position of the peaks denotes that the alloy consists of magnesium 96-901-2002 and magnesium 96-901-3059 (database COD REV 64680 2012.08.23). The SEM backscattered images of the alloy are illustrated in Fig. 2. It can be seen that no discrete separate metal phases exist. The energy-dispersive X-ray (EDX) analysis revealed that the surface of the metal panel consists of magnesium, oxygen, and tin. The silicon element is ascribed to the polishing treatment of the alloy with colloidal silicon that is described below. The magnesium ZK30 alloy panel was treated under specific conditions prior the XRD analysis and backscattered SEM images. At first, it was polished with emery paper (380, 800, 1200, and 4000 grids) and pore neoprene cloth together with 0.04-μm colloidal silica, and then it was immersed into acetone solution under sonication for 30 min. Finally, it was left to dry under inert gas.

CeMo ncs

The calcining of CeMo nanocomposites at 500 °C leads to the fabrication of hollow nanospheres. Figure 3 illustrates the TEM images of the produced CeMo ncs. It can be seen that the ncs are hollow, spheres, uniform in size, and their diameter is 100 ± 20 nm. The polydispersity index (U) for the CeMo ncs was estimated measuring the size of 100 ncs, according to the following equation:

$$U = \frac{D_w}{D_n},$$

where $D_w = \sum_{i1}^{k} n_i D_i^4 \Big/ \sum_{i1}^{k} n_i D_i^3$ is the weight-average diameter,

$$D_n = \sum_{i1}^{k} n_i D_i \Big/ \sum_{i1}^{k} n_i,$$

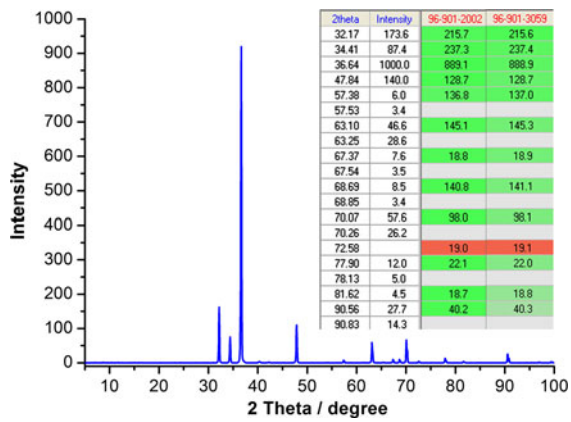

Fig. 1 XRD analysis of magnesium alloy ZK30

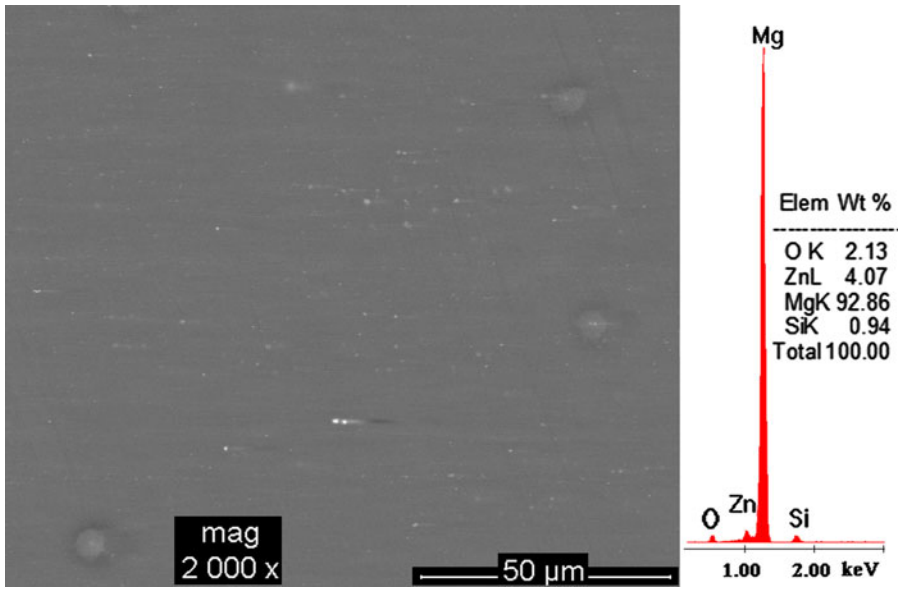

Fig. 2 SEM backscattered images of magnesium alloy ZK30

is the number-average diameter and D_i is the determined nc diameter (Yang et al. 2009). The calculated polydispersity index of CeMo ncs is $U = 1.229$ (Table 4). Both MMA and MAA monomers were selected for the synthesis of organic templates because the copolymerization of MMA/MAA in a molar ratio of 10/1 produced anionic-charged organic spheres in water. Furthermore, the anionic charge of the synthesized nanospheres was enhanced by the use of KPS as initiator that gives anionic-charged radicals above 70 °C.

The % w/w loading of the ncs with MBT was estimated via TGA analysis (Fig. 4). These diagrams present the heat treatment behavior of pure MBT as well as of CeMo ncs loaded with MBT. The pure corrosion inhibitor is completely burned off above 350 °C. On the contrary, temperature retardation in the MBT burn off is observed in the presence of CeMo ncs. A slight weight loss in the range of 50–150 °C can be attributed to the desorption of acetone as well as to the desorption of free and physically adsorbed water on CeMo ncs (Patel et al. 2013; Sonawane et al. 2012). Moreover, two weight losses are depicted in the diagram of CeMo ncs loaded with MBT versus temperature; a first one in the range of 200–330 °C that is ascribed to the presence of the inhibitor on the shell or into the pores of the shell of the ncs and a second one between 330 and 500 °C that is attributed to the encapsulation of the inhibitor into the interior part of the ncs. The temperature retardation of the MBT burn off (approximately 150 °C higher than pure MBT) clearly denotes that the inhibitor has been encapsulated into the ncs.

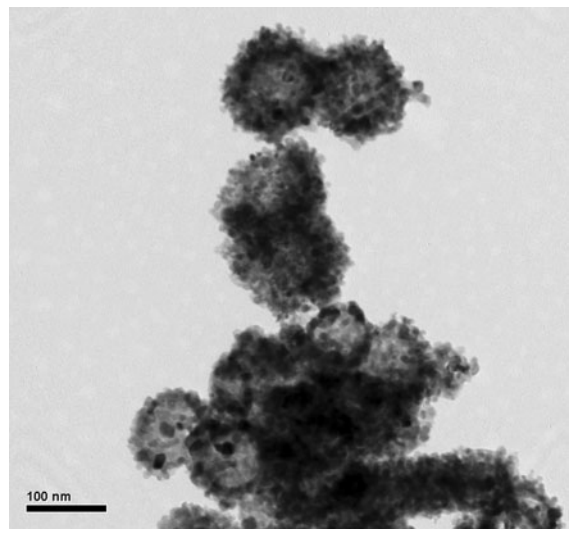

Fig. 3 TEM images of the produced CeMo nanocontainers

Table 4 Size and size distribution of CeMo nanocontainers

D_n (nm)	D_w (nm)	U
93.835	115.383	1.229

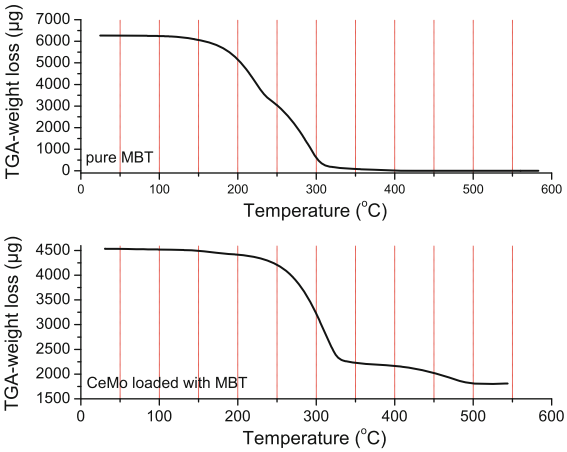

Fig. 4 TGA analysis of the pure MBT and of the CeMo nanocontainers loaded with MBT

Surface characterization

The ZK30-Coat-ncMBT, ZK30-Coat-MBT, and ZK30-Coat samples were exposed to 0.05 M NaCl prepared with ultrapure water for 1 year and 4 months (16 months), at room temperature. The uncoated magnesium ZK30 and the coating including empty CeMo ncs were exposed for 2 and 4 months, respectively, because of their overwhelming destruction. The visual photographs of the samples after their exposure to corrosive environment are depicted in Fig. 5. The surface of the uncoated magnesium ZK30 has been completely destroyed after 2 months of exposure revealing scratches and dents (Fig. 5d). Similarly, the coating including empty CeMo ncs (ZK30-Coat-nc) demonstrates cracks and scratches after 4 months of immersion to corrosive environment (Fig. 5e). On the other hand, the surfaces of the other three coatings do not present cracks or scratches after their exposure into NaCl solution for 16 months [ZK30-Coat (Fig. 5a), ZK30-Coat-MBT (Fig. 5b), and ZK30-Coat-ncMBT (Fig. 5c)]. The coating without ncs or inhibitor (ZK30-Coat) is crack free but presents few stains. The coating including inhibitor (ZK30-Coat-MBT) depicts lots of pits. Finally, the coating including ncs loaded with MBT (ZK30-Coat-ncMBT) is crack free and no pits of scratches are observed. Optically, the incorporation of loaded ncs into the coating presents the best anticorrosive behavior.

The surface morphologies and EDX analysis of the coatings ZK30-Coat, ZK30-Coat-MBT, and ZK30-Coat-ncMBT are demonstrated in Fig. 6. All the

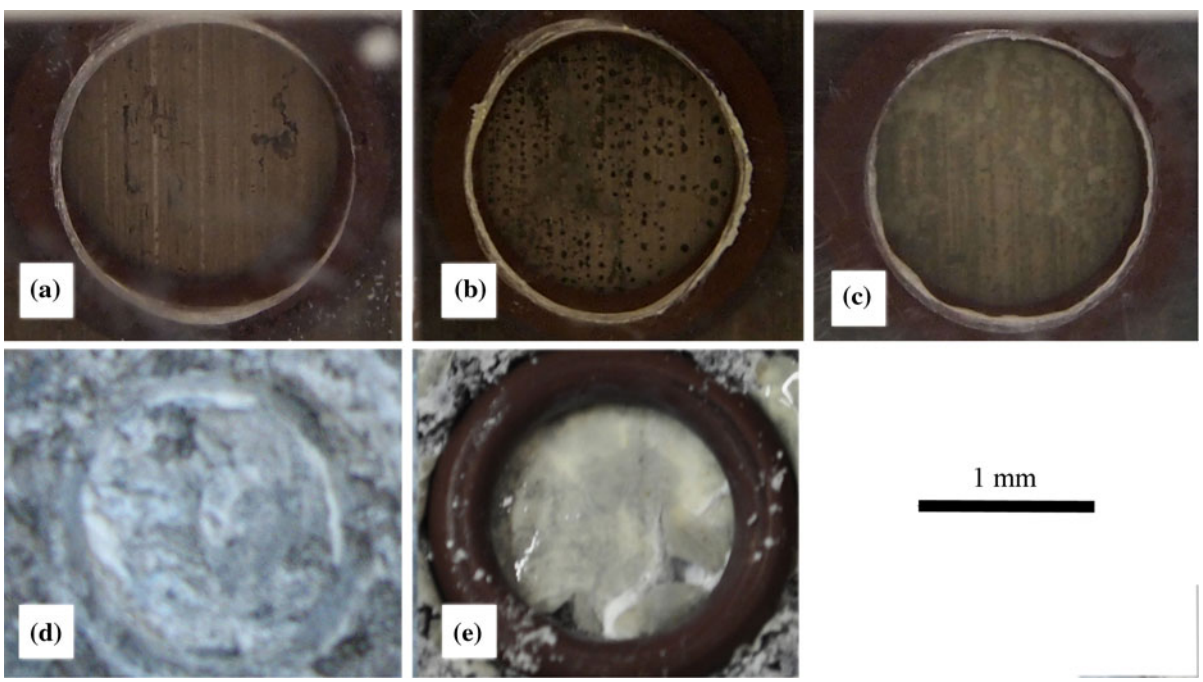

Fig. 5 Visual coating photographs of **a** ZK30-Coat after 16 months, **b** ZK30-Coat-MBT after 16 months, **c** ZK30-Coat-ncMBT after 16 months, **d** bare MgZK10 after 2 months, and **e** ZK30-Coat-nc after 4 months exposure to 0.5 M NaCl solution at room temperature

coatings are crack free without macroscopic defects such as pinholes and no uncoated areas are observed. Few white-colored aggregations are appeared for the ZK30-Coat, ZK30-Coat-MBT coatings (Fig. 6a, b). The ZK30-Coat-ncMBT coating surface is coarse due to the incorporation of ncs (Fig. 6c). The EDX analysis of the aforementioned coatings revealed carbon, silicon, and oxygen elements due to film formation on the substrates. Moreover, the EDX analysis of the coating including CeMo ncs loaded with MBT presented cerium and molybdenum elements that ascribed to the incorporation of the ncs. The EDX analysis of the white-colored aggregations depicted that they consist of carbon and oxygen. The dispersion of the ncs into the coating was estimated via cerium elemental mapping analysis (Fig. 7). This figure illustrates the cerium elemental mapping analysis on the right and the corresponding SEM micrograph on the left. It can be seen that the ncs have been well distributed into the coating without agglomerations.

The coating thickness is a crucial parameter for estimation of corrosion protection properties. Cross section SEM images of ZK30-Coat, ZK30-Coat-MBT, ZK30-Coat-nc, and ZK30-Coat-ncMBT are demonstrated in Fig. 8. The thicker coating (35–38 μm) is the one including loaded ncs (ZK30-Coat-ncMBT, Fig. 8d). On the contrary, the thinner coating (13–17 μm) is the one including empty ncs (ZK30-Coat-nc, Fig. 8c). The thicknesses of ZK30-Coat (Fig. 8a) and ZK30-Coat-MBT (Fig. 8b) are 20 ± 2 and 24 ± 1 μm, respectively. Comparing the four thickness values and the corresponding visual photographs of the coatings (Fig. 5), it can be assumed that the thicker coating (ZK30-Coat-ncMBT) demonstrated the best visual performance after exposure to corrosive environment. This can be attributed to the difficulty of the corrosive agents and electrolytes to reach the substrate due to the enhanced thickness.

The surface morphologies of the ZK30-Coat, ZK30-Coat-MBT, and ZK30-Coat-ncMBT coatings after their exposure for 16 months to 0.5 M NaCl prepared in ultrapure water are demonstrated in Fig. 9. The coating without ncs or inhibitor (ZK30-Coat, Fig. 9a) is uniform without stains, pits, or craters. It presents few white aggregations that consist of the same elements as the whole coating that are carbon, oxygen, and silicon, as the EDX analysis proved. The

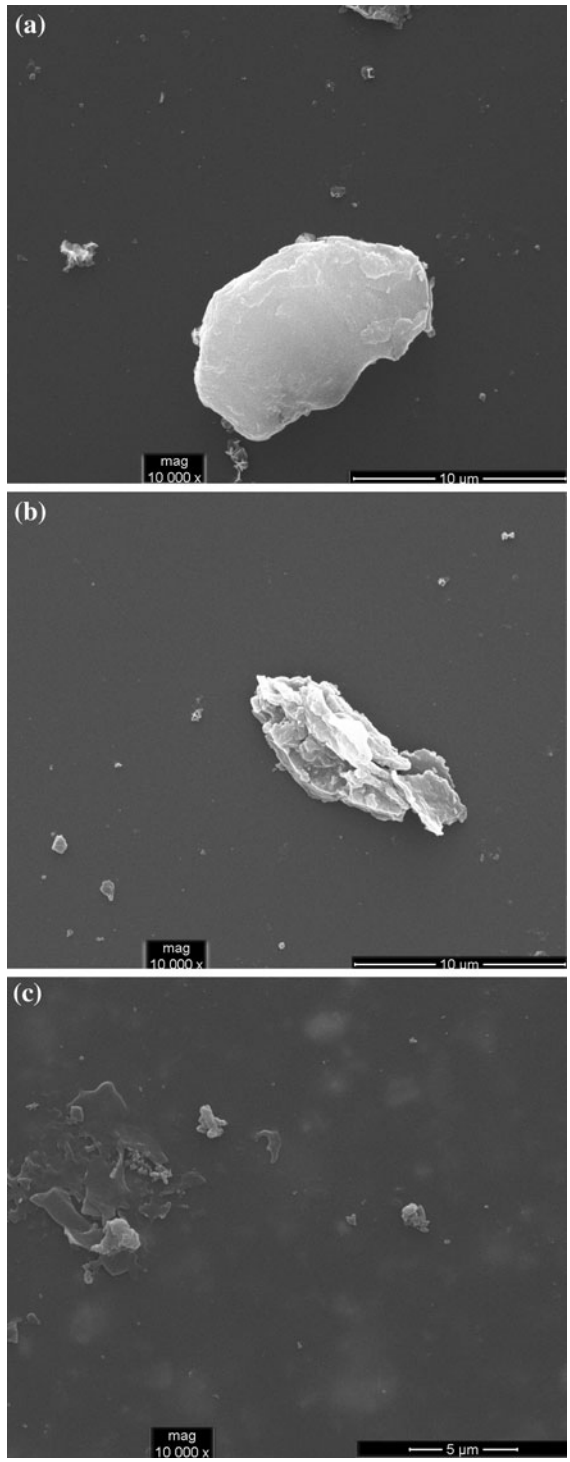

Fig. 6 SEM images of **a** ZK30-Coat, **b** ZK30-Coat-MBT, and **c** ZK30-Coat-ncMBT

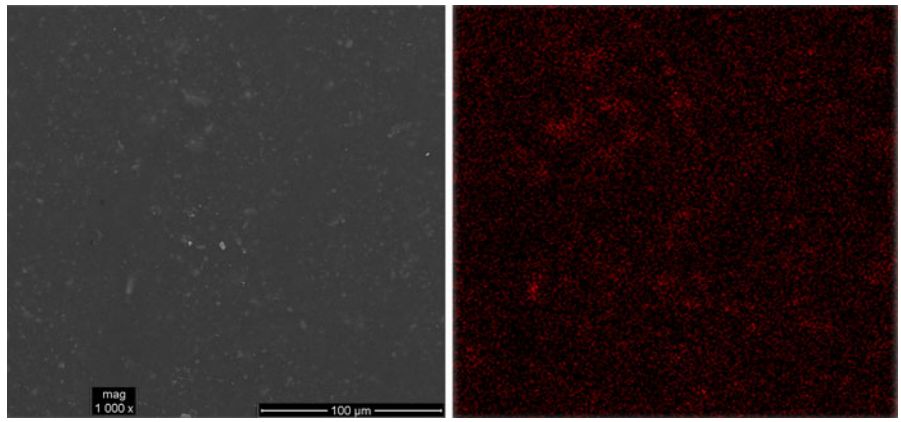

Fig. 7 Mapping micrograph (*right*) and corresponding SEM image (*left*) of ZK30-Coat-ncMBT coating

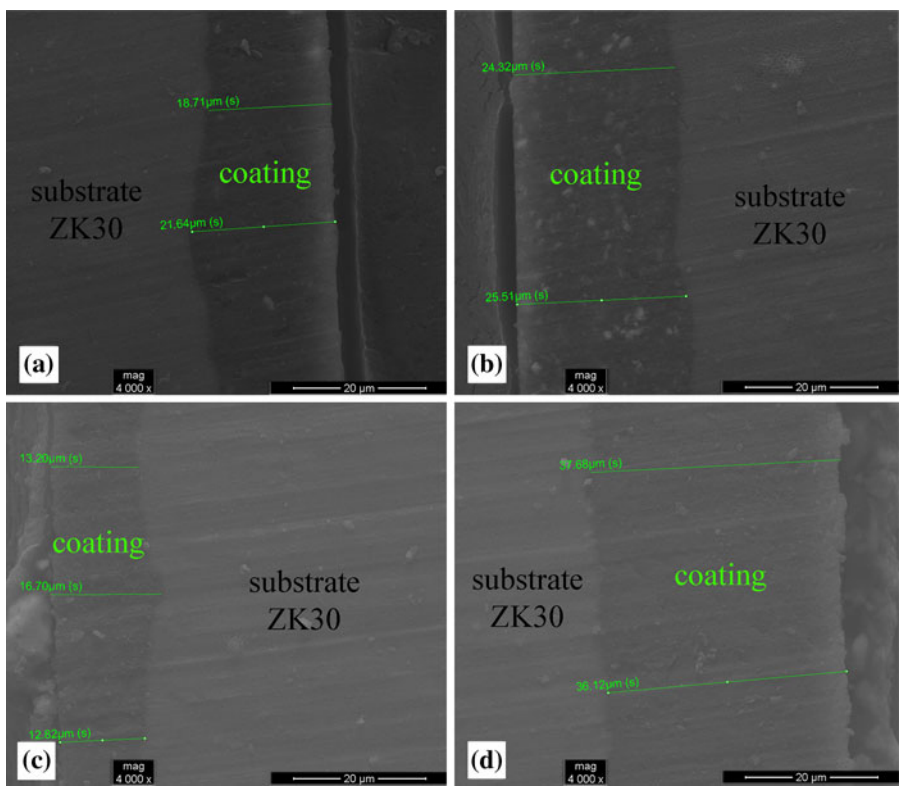

Fig. 8 Cross section SEM images of **a** ZK30-Coat, **b** ZK30-Coat-MBT, **c** ZK30-Coat-nc, and **d** ZK30-Coat-ncMBT

coating including corrosion inhibitor (ZK30-Coat-MBT, Fig. 9b) presents pits and craters. It has been partially damaged and it also demonstrates aggregations that consist of carbon, oxygen, and silicon, as the EDX analysis proved. Finally, the coating including CeMo ncs loaded with corrosion inhibitor (ZK30-Coat-ncMBT, Fig. 9c) does not have pits, holes, or scratches but it has a few aggregations that part of them consist of cerium and molybdenum elements due to the presence of the ncs and the rest consist of carbon, oxygen, and silicon, as the EDX analysis proved, as well.

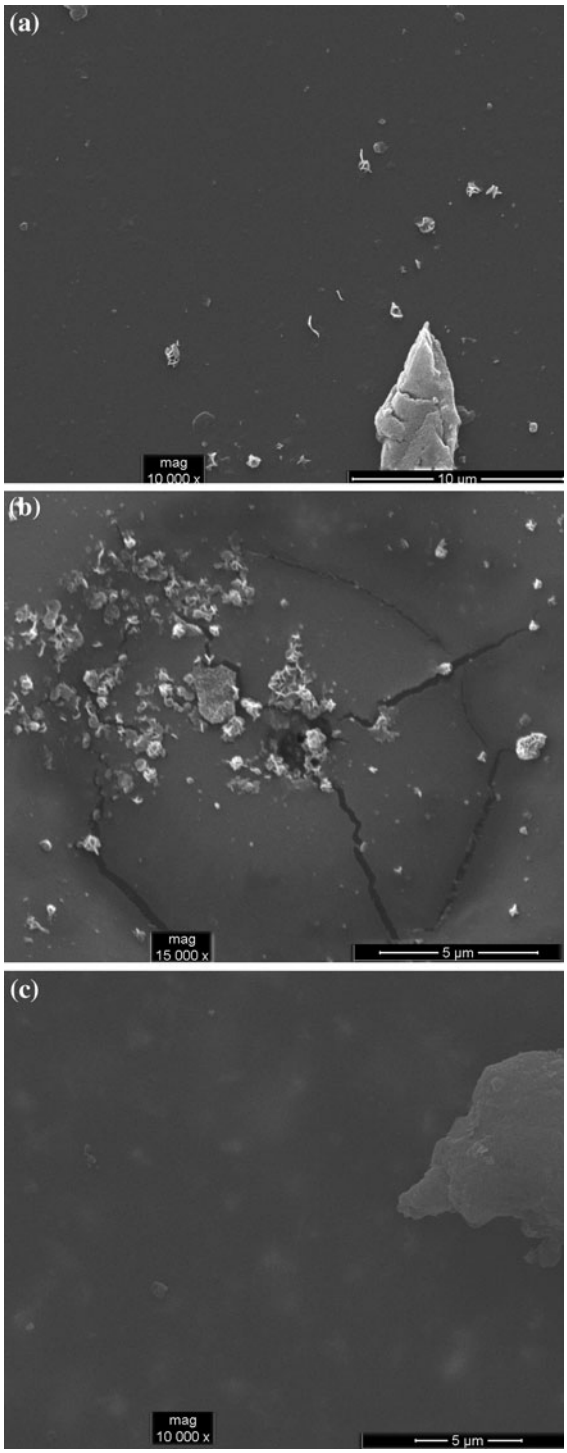

Fig. 9 The surface morphologies of the **a** ZK30-Coat, **b** ZK30-Coat-MBT, and **c** ZK30-Coat-ncMBT coatings after their exposure for 16 months to 0.5 M NaCl

Electrochemical measurements

The corrosion protection properties of the coatings were estimated via EIS in 0.5 M NaCl solution prepared with ultrapure water. Figure 10 depicts the impedance spectra obtained during 16-month immersion period for the ZK30-Coat, ZK30-Coat-MBT, and ZK30-Coat-ncMBT coatings. The Bode spectra for the three coatings are characterized by the presence of a capacitive response during the whole period of exposure. The phase angle is between −90° and −80° in the measured frequency range revealing that the coatings behave as a capacitor. This behavior denotes that the coatings have enhanced barrier properties and act as an insulator (Trabelsi et al. 2006).

In order for the corrosive behavior of the three aforementioned coatings to be better studied and possible self-healing ability to be evaluated, artificial defects of 1 mm were created into the coatings. Then the coated substrates were exposed to 5 mM NaCl solution prepared with ultrapure water. Figure 11 presents the EIS Bode spectra of the artificial defected coating including CeMo ncs loaded with corrosion inhibitor (ZK30-Coat-ncMBT) acquired after 22 h of immersion. A consecutive increase of the absolute total impedance values is observed as the time elapses. The coating reveals three time constants; one in the

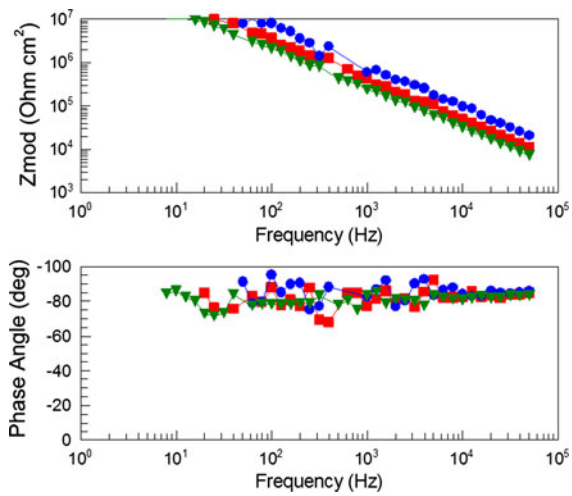

Fig. 10 EIS Bode plots of coatings after exposure to 0.5 M NaCl solution at room temperature for 16 months (*filled square*) ZK30-Coat, (*filled circle*) ZK30-Coat-MBT for 4 months, (*filled triangle*) ZK30-Coat-ncMBT

high frequency range due to the film, a second small one in the middle frequency range that can be ascribed to the response of processes occurring at the coating/substrate interface, and a third time constant in the low frequency range which is attributed to corrosion process. The EIS results of the aforementioned artificial defected coating were fitted using the equivalent circuit of Fig. 12. This circuit consists of seven components and corresponds to a spectrum that reveals three time constants. It is an equivalent circuit that has the resistance and the capacitance of the coating (R_{coat}–CPE_{coat}), an interface capacitance and the corresponding interface resistance (R_{int}–CPE_{int}) and a charge–transfer resistance and a double-layer capacitance (R_{ct}–CPE_{dl}). In this equivalent circuit, constant-phase elements were used instead of pure capacitors. This modification is obligatory in the case the phase shift of a capacitor is different from −90° (Hsu and Mansfeld 2001). The impedance of a R-CPE parallel association is given by: $Z_{R-CPE} = \frac{R}{1+RY_0(j\omega)^n}$, where Y_0 is the admittance of the CPE and n is the CPE exponent. Constant-phase elements correspond to a capacitor when the CPE exponent (n) is one. Using the Cole–Cole approach together with CPE, the capacitance can be calculated from the fittings by: $C = \sqrt[n]{\frac{RY_0}{R^n}}$ (Barsoukov and Macdonald 2005; Cole and Cole 1942). Figure 13 presents the evolution of R_{coat}, R_{int}, and R_{ct} as a function of time in 5 mM NaCl solution prepared with ultrapure water for the ZK30-Coat-ncMBT coating. The fitting results demonstrate that there is a consecutive increase of R_{int} denoting that a layer is created on the substrate attributed to a complex between the metal–inhibitor complex and the metal-hydroxyls [$Mg(OH)_2$]. The R_{ct} is increased one order of magnitude the first 3 h. However, a slight decrease is observed as the immersion time elapses until the 22nd hour. Finally, the small values of R_{coat} are attributed to the artificial defect that has been created on the coating (Table 5).

It should be mentioned that in order for partial recovery of the coating to exist the values of charge–transfer resistance (R_{ct}) should be increased as the immersion time elapses. These results denote that the ZK30-Coat-ncMBT coating is being recovered after the formation of the artificial defect and suggest that it probably has self-healing properties. Self-healing can be defined as the partial recovery of the protective properties of the coated system when marred

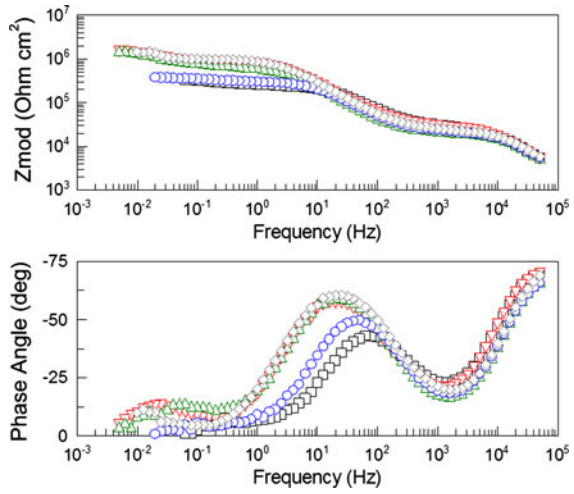

Fig. 11 EIS Bode spectra of the artificial defected ZK30-Coat-ncMBT coating after 22 h of exposure to 5 mM NaCl solution at room temperature

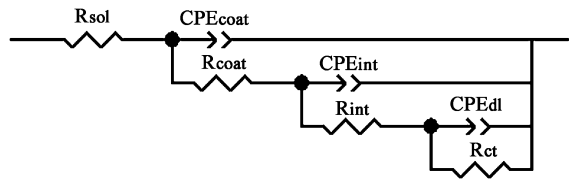

Fig. 12 Equivalent circuit used for numerical simulation of the EIS data of the coatings

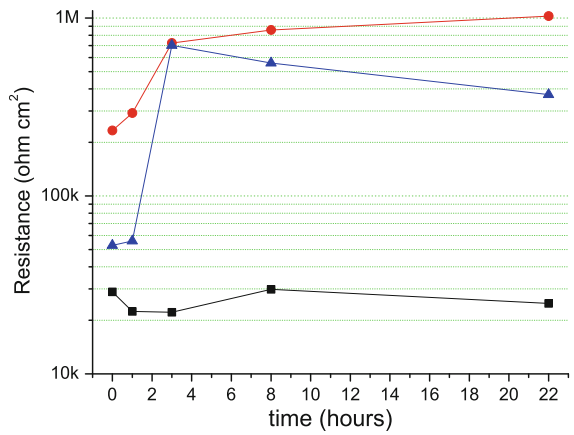

Fig. 13 The evolution of (*filled square*) R_{coat}, (*filled circle*) R_{int}, and (*filled triangle*) R_{ct} as a function of time in 5 mM NaCl solution for the ZK30-Coat-ncMBT coating

Table 5 Fitting parameters CPE_{coat}-T, CPE_{coat}-P, R_{coat}, C_{coat}, CPE_{int}-T, CPE_{int}-P, R_{int}, C_{int}, CPE_{dl}-T, CPE_{dl}-P, R_{ct}, and C_{dl} for the ZK30-Coat-ncMBT coating

Time (h)	CPE_{coat}-T (F cm^{-2} s^{-n})	CPE_{coat}-P	R_{coat} (Ohm cm^2)	C_{coat} (F cm^{-2})
0	1.78×10^{-9}	0.91178	2.89×10^{4}	6.84×10^{-10}
1	1.68×10^{-9}	0.91144	2.24×10^{4}	6.26×10^{-10}
3	1.64×10^{-9}	0.91387	2.22×10^{4}	6.26×10^{-10}
8	1.96×10^{-9}	0.90609	2.98×10^{4}	7.15×10^{-10}
22	1.73×10^{-9}	0.90186	2.49×10^{4}	5.78×10^{-10}
Time (h)	CPE_{int}-T (F cm^{-2} s^{-n})	CPE_{int}-P	R_{int} (Ohm cm^2)	C_{int} (F cm^{-2})
0	8.14×10^{-8}	0.82693	2.33×10^{5}	3.55×10^{-8}
1	9.90×10^{-8}	0.8526	2.92×10^{5}	5.36×10^{-8}
3	1.12×10^{-7}	0.85862	7.22×10^{5}	7.37×10^{-8}
8	9.79×10^{-8}	0.84162	8.56×10^{5}	6.14×10^{-8}
22	9.39×10^{-8}	0.84378	1.02×10^{6}	6.09×10^{-8}
Time (h)	CPE_{dl}-T (F cm^{-2} s^{-n})	CPE_{dl}-P	R_{ct} (Ohm cm^2)	C_{dl} (F cm^{-2})
0	1.05×10^{-5}	0.99916	5.27×10^{4}	1.08×10^{-5}
1	2.19×10^{-5}	0.94245	5.59×10^{4}	2.22×10^{-5}
3	7.32×10^{-6}	0.87434	7.01×10^{5}	9.27×10^{-6}
8	1.61×10^{-5}	0.98895	5.58×10^{5}	1.49×10^{-5}
22	3.14×10^{-5}	0.99824	3.71×10^{5}	2.28×10^{-5}

(Montemor et al. 2009). As the R_{ct} values of the other three artificial defected coatings (ZK30-Coat, ZK30-Coat-MBT, and ZK30-Coat-nc) were not increased at the immersion time to corrosive environment elapsed, it can be concluded that the partial recovery of the ZK30-Coat-ncMBT coating is ascribed to the presence of the encapsulated inhibitor into the ncs that is released after the corrosion onset via the formation of a metal–MBT complex. In aqueous solutions, magnesium is dissociated by the electrochemical reaction with water and a crystalline film of magnesium hydroxide, $Mg(OH)_2$, as well as hydrogen gas are produced. The overall corrosion reaction for magnesium in aqueous solutions is

$$Mg(s) + 2H_2O(l) \rightarrow Mg(OH)_2(s) + H_2(g).$$

This overall reaction can be described in terms of anodic and cathodic reactions as follows:

$$Mg \rightarrow Mg^{2+} + 2e^{-},$$

and/or

$$Mg(s) + 2(OH)^{-} \rightarrow Mg(OH)_2(s) + 2e^{-} \text{ (anodic reaction, dissolution of Mg)},$$

and

$$2H^{+} + 2e^{-} \rightarrow H_2(g) \text{ (cathodic reaction evolution of hydrogen gas)}.$$

A subsequent reaction, giving OH^{-}, can occur,

$$2H_2O + 2e^{-} \rightarrow H_2(g) + 2(OH)^{-}.$$

The produced hydroxide film, brucite, has a hexagonal crystalline structure that is layered, alternating between Mg and hydroxide ions facilitating easy basal cleavage (Winston Revie 2000). It is believed that the inhibitor is released from the containers through diffusion unless the containers are broken by a scratch on the coating. MBT contains S and N atoms in the organic ring and is attached to the magnesium through the S or N atoms that may change the electron density in the metal at the point of attachment. This fact results in the retardation of cathodic or anodic reaction of corrosion of magnesium (as described above) since electrons are consumed at the cathode and furnished at the anode (Sanyal 1981).

EDX analysis was conducted on the artificial defected area of the ZK30-Coat-ncMBT coating after its exposure to 5 mM NaCl solution for 22 h in order

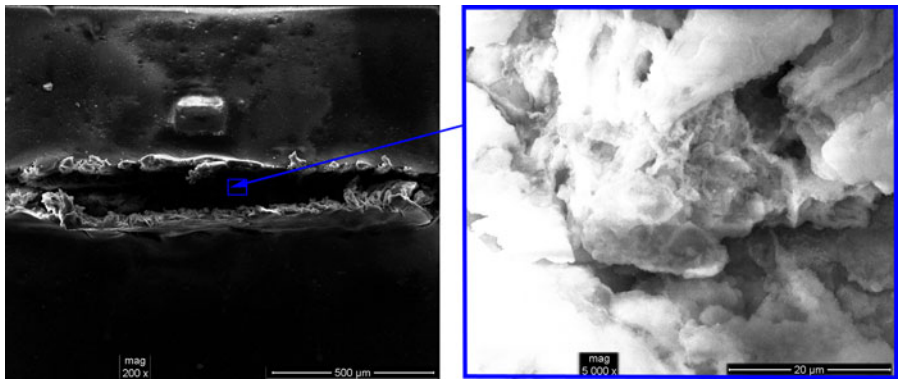

Fig. 14 SEM image of ZK30-Coat-ncMBT coating having an artificial defect after exposure to 5 mM NaCl solution at room temperature for 22 h

Table 6 The % w/w element concentration of artificial defected ZK30-Coat-ncMBT coating after exposure at 5 mM NaCl solution for 22 h

Elements	Mg	Zn	O	Ce	C	Cl
Wt%	35.56	11.01	41.17	0.98	10.10	1.17

for partial recovery of the film to be evaluated by the presence of cerium and carbon elements (Fig. 14). Table 6 illustrates the presence of cerium and carbon elements confirming the partial recovery of the coating.

Nanomechanical measurements

The nanomechanical properties (namely H and E) of coatings are presented in Fig. 13. The incorporation of ncs (with or without inhibitor) affects the mechanical integrity of the coatings, revealing a clear mechanical degradation of epoxy coating; while H is slightly decreased, samples exhibit deviation in E values. In Fig. 15a, at surface region (0–400 nm), H decrease implies deterioration of the coating (further penetration into the coating does not significantly reveal H deviation, where all coatings exhibit a hardness of $\sim$0.3 GPa); clear decrease of E also occurs.

The ratio of hardness to elastic modulus is of significant interest in tribology. Higher stresses are expected in high H/E, hard materials, and high stress concentrations develop toward the indenter tip, whereas in the case of low H/E, soft materials, the stresses are lower and are distributed more evenly across the cross section of the material (Cheng and

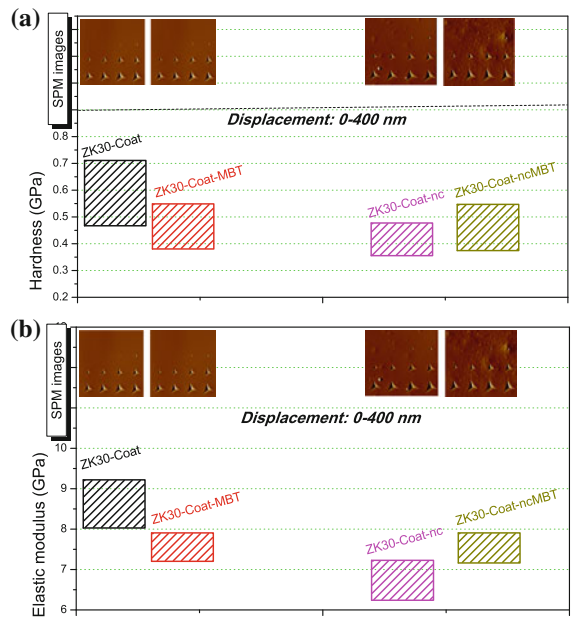

Fig. 15 Nanomechanical properties, **a** namely hardness and **b** elastic modulus of the coatings: ZK30-Coat, ZK30-Coat-MBT, ZK30-Coat-nc, and ZK30-Coat-ncMBT

Cheng 2000; Leyland and Matthews 2004). The high ratio of hardness to elastic modulus (H/E) is indicative of good wear resistance in a disparate range of materials (Leyland and Matthews 2004): ceramic, metallic, and polymeric (for example: c-BN, tool steel, and nylon, respectively), which are equally effective in resisting attrition for their particular intended application. In Fig. 16, the change of H/E slope reveals that the addition of nc and inhibitor amount strengthens (increase of wear resistance) the epoxy coating after $\sim$800 nm of displacement (Fig. 16b),

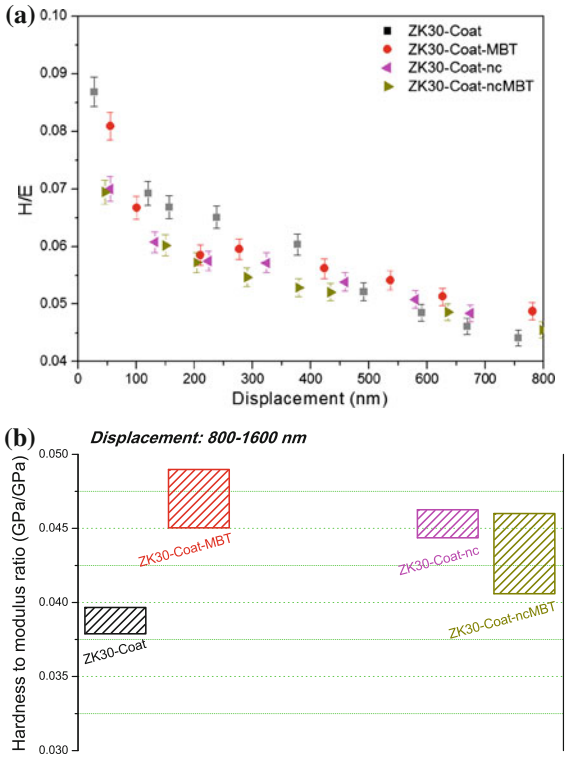

Fig. 16 Correlation of *H*/*E* ratio to displacement, for all coatings: ZK30-Coat, ZK30-Coat-MBT, ZK30-Coat-nc, and ZK30-Coat-ncMBT

having no significant impact on surface region (0–800 nm), where all coatings exhibited similar (increased) *H*/*E* ratio (Fig. 16a).

% Plasticity

% Plasticity values of the materials at different displacements were calculated by integrated areas under the loading curve and the unloading curve. At low displacements, the samples revealed elastoplastic behavior, while for higher displacements the samples exhibited the typical plastic behavior (~86 %). Taking into account the % Plasticity, it was found that the change from elastic to plastic deformation, noted in circle, is observed at almost identical displacement (~100 nm) for all coatings (Fig. 17).

Nanoscratch measurements

The nanoscratch technique provides materials characteristics such as wear resistance and frictional properties

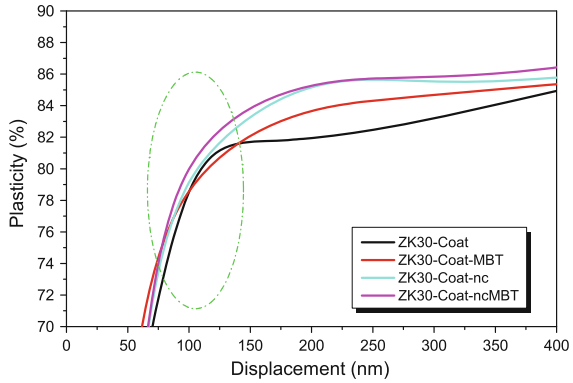

Fig. 17 % Plasticity versus displacement for all coatings: ZK30-Coat, ZK30-Coat-MBT, ZK30-Coat-nc, and ZK30-Coat-ncMBT

of polymers (Han et al. 1999; Kim and Hodzic 2003; Overney 1995; Wong et al. 2004) and polymer–matrix composites at micro- and nano-scale (Hodzic et al. 2000; Kim et al. 2001; Dasari et al. 2007; Ni et al. 2005). The application of this method so as to acquire surface characteristics is mainly dependent on mechanical integrity of the coating and its formulation, especially at nanoscale (Dasari et al. 2009); ductility, modulus, crystallinity, chain orientation, filler dispersion, and uniformity could have a major impact in data obtained with nanoscratch. Nanoscratch gives the opportunity to study the mechanisms of deformation and fracture, which cannot be observed by conventional penetration techniques. Several experiments can be performed using nanoscratch; however, establishment of appropriate load functions is required as proper setup. Nanoscratch data combined with SPM imaging provide information on the deformation mechanisms of the material, monitoring simultaneous vertical and lateral stresses. A diamond is drawn into the material and moves horizontally at constant rate with linearly increasing load, recording displacement and load at both axes. The coefficient of friction (μ) is then calculated. Post-scratch reveals the elastic recovery of the material, while SPM imaging is used for determination of plastic deformation ahead and aside of the indenter tip (Koumoulos et al. 2012).

Since all scratch tests were performed at the same environmental conditions, it is indicative that the observed increase in the μ values of the samples attributed to incorporation of nanoparticles (loaded–unloaded ncs). The sources of the adhesive forces between the tip and the samples surface can be divided in van der Waals attraction and meniscus formation

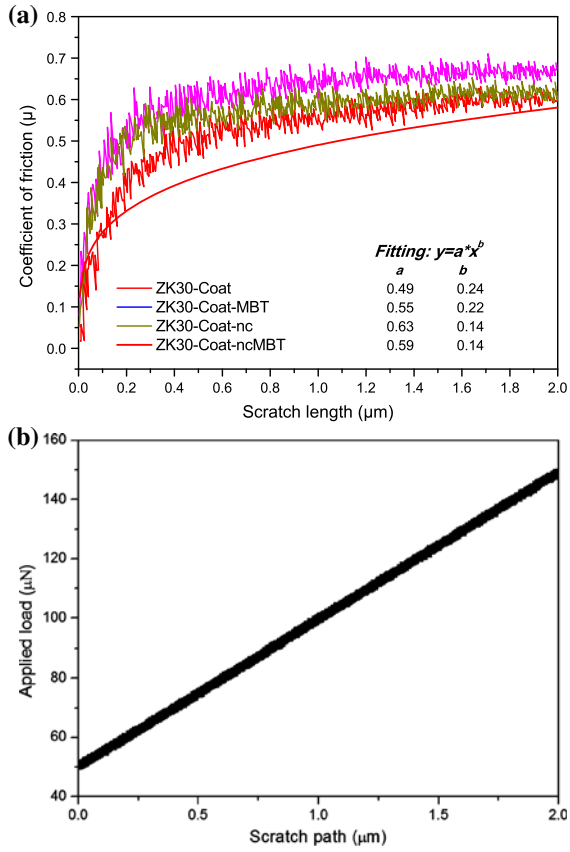

Fig. 18 **a** Coefficient of friction for all samples, **b** with regard to scratch path (linear correlation of normal applied load with scratch path)

(Bhushan 1999, 2002). The lower decrease of the μ values measured for neat epoxy is attributed to cohesive strength of the coating.

Figure 18 presents the effect of normal load on μ of all tested samples, with regard to scratch path (linear correlation of normal applied load with scratch path) for the first 2 μm of scratch path (all samples after 2 μm of scratch path exhibit similar behavior). When the μ values between two sliding surfaces reduce, it indicates that the amount of energy is transformed into heat or noise instead of motion, which resulted in a smoother and efficient motion. The measured μ values are the ratio of the lateral forces to the normal forces and can be expressed as the sum of plowing and adhesive friction coefficient. If the plowing term of friction component is considered negligible, then μ would be independent of the normal load (Bull 1999). In Fig. 18 the increasing trend of μ follows the empirical equation $\mu \propto a \times F_N^b$(representative red fitting line for neat epoxy), implying that plowing component is an important deformation mode which increases with normal load (Charitidis and Logothetidis 2005). Increasing coefficient of friction implies enhanced resistance to plastic deformation (neat epoxy reveals low resistance).

As seen in the images in Fig. 19, there is a build-up of polymer material mostly ahead of the scratch (Nie et al. 2006). As the indenter moves along the surface, the displaced material forms a pile-up which accumulates on the sides of the scratch. A groove is formed which is roughly of the shape of a triangular prism. For the Berkovich tip, it should be noted that the orientation of the tip with respect to the scratch direction is very important. As the indenter scratches, total volume swiped by the indenter will depend on the projected area of the indenter along the scratch axis. These

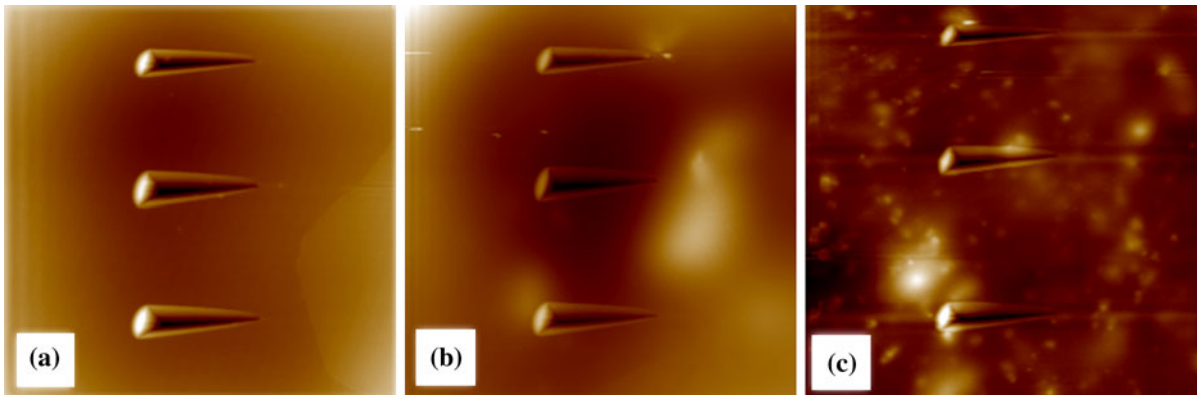

Fig. 19 Representative SPM images of nanoscratch tests for **a** ZK30-Coat, **b** ZK30-Coat-nc, and **c** ZK30-Coat-ncMBT coatings (50×50 μm^2)

build-ups lead us to believe that the films were plastically deformed (build-up is most likely an accumulation of compressed materials).

Conclusions

Hybrid organic–inorganic coatings were synthesized and applied on magnesium alloy ZK30. The coatings demonstrated improved corrosion protective properties. EIS measurements depicted that the coatings have enhanced barrier properties and act as an insulator after exposure for 16 months in 0.5 M NaCl solution. Furthermore, CeMo ncs were fabricated and loaded with corrosion inhibitor MBT. The incorporation of the loaded ncs into the hybrid organic–inorganic coatings presented partial recovery of the films suggesting possible self-healing effect.

The incorporation of ncs (with or without inhibitor) affects the mechanical integrity of the coatings, revealing a clear mechanical degradation of epoxy coating; while H is slightly decreased, samples exhibit deviation in E values. The change of H/E slope reveals that the addition of nc and inhibitor amount strengthens (increase of wear resistance) the epoxy coating after $\sim$800 nm of displacement. At low displacements, the samples revealed elastoplastic behavior, while for higher displacements the samples exhibited the typical plastic behavior ($\sim$86 %). The increasing trend of μ follows the typical power-law equation implying that plowing component is an important deformation mode which increases with normal load. Increased coefficient of friction was found for all nanocomposites, implying enhanced resistance to plastic deformation.

Acknowledgments The authors want to thank Alubin, Israel for providing the samples of Mg ZK30.

References

Barsoukov E, Macdonald JR (2005) Impedance spectroscopy theory, experiment, and applications. Wiley, Hoboken, pp 13–20

Bei H, George EP, Hay JL, Pharr GM (2005) Influence of indenter tip geometry on elastic deformation during nanoindentation. Phys Rev Lett 95:045501–045504

Bhushan B (1999) Principles and applications of tribology. Wiley, New York

Bhushan B (2002) Introduction to tribology. Wiley, New York

Bull SJ (1999) Can scratch testing be used as a model for the abrasive wear of hard coatings? Wear 233–235:412–423

Charitidis CA, Logothetidis S (2005) Effects of normal load on nanotribological properties of sputtered carbon nitride films. Diam Relat Mater 14:98–108

Cheng YT, Cheng CM (2000) What is indentation hardness? Surf Coat Technol 133–134:417–424

Choi J, Nakao S, Kim J, Ikeyama M, Kato T (2007) Corrosion protection of DLC coatings on magnesium alloy. Diam Relat Mater 16:1361–1364

Cole KS, Cole RH (1942) Dispersion and absorption in dielectrics. II. Direct current characteristics. J Chem Phys 10: 98–105

Dasari A, Yu Z-Z, Mai Y-W (2007) Nanoscratching of nylon 66-based ternary nanocomposites. Acta Mater 55:635–646

Dasari A, Yu Z-Z, Mai Y-W (2009) Fundamental aspects and recent progress on wear/scratch damage in polymer nanocomposites. Mater Sci Eng R 63:31–80

Froes FH, Elieser D, Aghion E (1998) The science, technology and application of magnesium. J Miner Met Mater Soc 5:30–34

Han YC, Schmitt S, Friedrich K (1999) Nanoscale indentation and scratch of short carbon fiber reinforced PEEK/PTFE composite blend by atomic force microscope lithography. Appl Compos Mater 6:1–18

Hoche H, Scheerer H, Probst D, Broszeit E, Berger C (2003) Plasma anodisation as an environmental harmless method for the corrosion protection of magnesium alloys. Surf Coat Technol 174:1002–1007

Hodzic A, Stachurski ZH, Kim JK (2000) Nano-indentation of polymer–glass interfaces. Part I. Experimental and mechanical analysis. Polymer 41:6895–6905

Hsu CH, Mansfeld F (2001) Technical Note: concerning the conversion of the constant phase element parameter Y0 into a capacitance. Corrosion 57:747–748

Kartsonakis IA, Ioannis Daniilidis I, Kordas G (2008) Encapsulation of the corrosion inhibitor 8-hydroxyquinoline into Ceria Nanocontainers. J Sol-Gel Sci Technol 48:24–31

Kartsonakis IA, Balaskas AC, Koumoulos EP, Charitidis CA, Kordas G (2012) Evaluation of corrosion resistance of magnesium alloy ZK10 coated with hybrid organic–inorganic film including containers. Corros Sci 65:481–493

Kim JK, Hodzic A (2003) Nanoscale characterisation of thickness and properties of interphase in polymer matrix composites. J Adhesion 79:383–414

Kim JK, Sham ML, Wu JS (2001) Nanoscale characterisation of interphase in silane treated glass fibre composites. Composites A 32:607–618

King RB (1987) Elastic analysis of some punch problems for a layered medium. Int J Solids Struct 23:1657–1664

Koumoulos EP, Charitidis CA, Daniolos NM, Pantelis DI (2011) Nanomechanical properties of friction stir welded AA6082-T6 aluminum alloy. Mater Sci Eng B 176: 1585–1589

Koumoulos EP, Charitidis CA, Papageorgiou DP, Papathanasiou AG, Boudouvis AG (2012) Nanomechanical and nanotribological properties of hydrophobic fluorocarbon dielectric coating on tetraethoxysilane for electrowetting applications. Surf Coat Technol 206:3823–3831

Lamaka SV, Knornschild G, Snihirova DV, Taryba MG, Zheludkevich ML, Ferreira MGS (2009) Complex

anticorrosion coating for ZK30 magnesium alloy. Electrochim Acta 55:131–141

Leyland A, Matthews A (2004) Design criteria for wear-resistant nanostructured and glassy-metal coatings. Surf Coat Technol 177–178:317–324

Li X, Bhushan B (2002) A review of nanoindentation continuous stiffness measurement technique its applications. J Mater Charact 48:11–36

Liang J, Srinivasan PB, Blawert C, Dietzel W (2009) Comparison of electrochemical corrosion behavior of MgO and ZrO_2 coatings on AM50 magnesium alloy formed by plasma electrolytic oxidation. Corros Sci 51:2483–2492

Loose WS (1976) Magnesium and magnesium alloys. In: Uhlig HH (ed) Corrosion handbook, 1st edn. The Electrochemical Society, Wiley, New York, pp 218–251

Ma Y, Hu H, Northwood D, Nie X (2007) Optimization of the electrolytic plasma oxidation processes for corrosion protection of magnesium alloy AM50 using the Taguchi method. J Mater Process Technol 182:58–64

Makar GL, Kruger J (1993) Corrosion of magnesium. Int Mater Rev 38:138–153

Montemor MF, Pinto R, Ferreira MGS (2009) Chemical composition and corrosion protection of silane films modified with CeO_2 nanoparticles. Electrochim Acta 54:5179–5189

Ni H, Li XD, Gao HS, Nguyen TP (2005) Nanoscale structural and. mechanical characterization of bamboo-like polymer/silicon nanocomposite films. Nanotechnology 16:1746–1753

Nie HY, Walzak MJ, McIntyre NS (2006) Scratch resistance anisotropy in biaxially oriented polypropylene and poly(ethylene terephthalate) films. Appl Surf Sci 253:2320–2326

Oliver WC, Pharr GM (1992) An improved technique for determining hardness and elastic-modulus using load and displacement sensing indentation experiments. J Mater Res 7:1564–1583

Overney RM (1995) Nanotribological studies on polymers. Trends Polym Sci 3:359–364

Patel MA, Bhanvase BA, Sonawane SH (2013) Production of cerium zinc molybdate nano pigment by innovative ultrasound assisted approach. Ultrason Sonochem 20:906–913

Sanyal B (1981) Organic compounds as corrosion inhibitors in different environments—a review. Prog Org Coat 9:165–236

Scharnagl N, Blawert C, Dietzel W (2009) Corrosion protection of magnesium alloy AZ31 by coating with poly(ether imides) (PEI). Surf Coat Technol 203:1423–1428

Schuh CA (2006) Nanoindentation studies of materials. J Mater Today 9:32–40

Sneddon IN (1948) Boussinesq's problem for a rigid cone. Math Proc Camb Philos Soc 44:492–507

Sonawane SH, Bhanvase BA, Jamali AA, Dubey SK, Kale SS, Pinjari DV, Kulkarni RD, Gogate PR, Pandit AB (2012) Improved active anticorrosion coatings using layer-by-layer assembled ZnO nanocontainers with benzotriazole. Chem Eng J 189–190:464–472

Stippich F, Vera E, Wolf GK, Berg G, Friedrich Chr (1998) Enhanced corrosion protection of magnesium oxide coatings on magnesium deposited by ion beam-assisted evaporation. Surf Coat Technol 103–104:29–35

Trabelsi W, Triki E, Dhouibi L, Ferreira MGS, Zheludkevich ML, Montemor MF (2006) The use of pre-treatment based on doped silane solutions for improved corrosion resistance of galvanised steel substrates. Surf Coat Technol 200: 4240–4250

Troyon M, Huang L (2006) Comparison of different analysis methods in nanoindentation and influence on the correction factor for contact area. Surf Coat Technol 201:1613–1619

Wang H, Akid R, Gobara M (2010) Scratch-resistant anticorrosion sol–gel coating for the protection of AZ31 magnesium alloy via a low temperature sol–gel route. Corros Sci 52:2565–2570

Winston Revie R (2000) Uhlig's corrosion handbook, 2nd edn. Wiley, New York, pp 799–800

Wong JSS, Sue HJ, Zeng KY, Li RKY, Mai Y-W (2004) Scratch damage of polymers in nanoscale. Acta Mater 52:431–443

Yang X, Chen L, Huang B, Bai F, Yang X (2009) Synthesis of pH-sensitive hollow polymer microspheres and their applications drug carriers. Polymer 50:3556–3563

Corrosion Science 57 (2012) 56–66

Contents lists available at SciVerse ScienceDirect

Corrosion Science

journal homepage: www.elsevier.com/locate/corsci

Hybrid organic–inorganic multilayer coatings including nanocontainers for corrosion protection of metal alloys

I.A. Kartsonakis [a,b,*], E.P. Koumoulos [b], A.C. Balaskas [a], G.S. Pappas [a], C.A. Charitidis [b], G.C. Kordas [a]

[a] Sol-Gel Laboratory, IMS, NCSR 'DEMOKRITOS', 15310 Agia Paraskevi, Greece
[b] School of Chemical Engineering, NTUA, 9 Heroon Polytechniou St., 15780 Zographos, Greece

ARTICLE INFO

Article history:
Received 27 September 2011
Accepted 27 December 2011
Available online 3 January 2012

Keywords:
A. Aluminium
B. EIS
C. Electrodeposited films
C. Pitting corrosion

ABSTRACT

The development of new technology that prevents corrosion of aluminium alloys (AA) 2024-T3 was made. AA 2024-T3 panels were coated with two layers the first one consists of conductive polymers (CP) and the second one, on the top, is made of sol–gel coatings. Ceramic nanocontainers loaded with corrosion inhibitors were incorporated into the CP coatings. Studies on the corrosion resistance of these coatings demonstrated that the presence of loaded nanocontainers into the CP coatings improved the corrosion protective properties of the films by increasing the total impedance values, and decreasing both anodic and cathodic currents relatively to coatings without nanocontainers.

1. Introduction

Corrosion of aluminium alloys (AA) has an enormous economic impact. Chromate surface treatments and chromate-containing epoxy primers are often used for corrosion control of AA. However, lots of efforts have been made in order new techniques to be found for the replacement of hexavalent chromium. Alternative protection of AA is urgent since hexavalent chromium provokes human disease [1]. The new techniques are based on sol–gel coatings, hybrid organic–inorganic coatings and on coatings with conductive copolymers. The coatings are made by electro-polymerisation, dip coating and spray techniques.

Cabral et al. studied the corrosion behaviour of AA2024-T3 pre-treated with bis-[triethoxysilylpropyl]tetrasulphide. Simultaneously, the work investigated the influence of the Cu-rich intermetallic particles on the formation of the silane film [2]. Yang and his collaborators synthesized and used a sol–gel conversion coating for aluminium corrosion protection. The sol–gel coating consisted of SiO_2 and ZrO_2. They concluded that their coating inhibited local dissolution on the aluminium surface in Harrison's solution [3]. Pathak and his co-workers prepared a 3-glycidoxypropyltrimethoxysilane, methyltrimethoxysilane and hexamethoxymethylmelamine sol–gel solution. Aluminium substrates were dip coated in those solution and the results revealed that the coatings act as barrier to corrosive electrolytes [4]. Raps et al. produced hybrid films by the controllable sol–gel route. Corrosion inhibitors were incorporated to the coatings in order to provide active protective effect. He studied the barrier properties and the active corrosion protection of the films on AA2024-T3 [5].

CP have received considerable attention in particular aromatic polymers like polyaniline (PAni), polypyrrole (PPy) and polythiophene [6]. CP consist of conjugated chains containing π-electrons delocalized along the polymer backbone. In their neutral form, CP are semi conductive materials that can be doped and converted into electrically conductive forms. The doping can be either oxidative or reductive, though oxidative doping is more common. There are three states of CP: non-conducting (uncharged), oxidised (p-doped) where electrons are removed from the backbone, and reduced (n-doped) (least common), where electrons are added to the backbone. The doping processes are usually reversible, and typical conductivities can be switched between those of insulators ($<10^{-10}$ S/cm) and those of metals (10^5 S/cm) [7]. CP (their conducting forms) are usually classified as the cation salts of highly conjugated polymers. The cation salts are obtained by electrochemical oxidation and electrochemical polymerisation or chemical oxidation (removal of an electron). It is also possible to obtain the anion salts of the same highly conjugated polymers by either electrochemical reduction or by treatment with reagents such as solutions of sodium naphthalide [8].

Corrosion protection using CP was first suggested by MacDiarmid [9]. PAni has been used a lot for corrosion protection of AA. Homogeneous and adherent PAni–montmorillonite (MMT) nanocomposite coatings were electro-synthesized on AA 3004 using galvanostatic polarisation method by Shabani-Nooshabadi et al. The enhanced corrosion protection effect of the PAni–MMT nanocomposite relative to pure PAni in the form of coating on metallic

* Corresponding author at: Sol-Gel Laboratory, IMS, NCSR 'DEMOKRITOS', 15310 Agia Paraskevi, Greece. Tel.: +30 2106503304; fax: +30 2106547690.
E-mail address: ikartsonakis@ims.demokritos.gr (I.A. Kartsonakis).

0010-938X/$ - see front matter © 2011 Elsevier Ltd. All rights reserved.
doi:10.1016/j.corsci.2011.12.034

surface was attributed to the combination of the redox catalytic property of PAni and the barrier effect of the MMT nanoclay platelets dispersing in the composite [10]. AA5182 cold rolled samples were coated by thin films of emeraldine base (EB) obtained from a 5% solution in *N*-methylpyrrolidinone by Cecchetto et al. Accelerated corrosion tests proved this coating very effective for corrosion protection of AA in neutral environment [11]. Epstein and his coworkers studied corrosion protection capabilities of PAni in the EB form and self-doped sulphonated PAni form for AA 3003 and AA 2024-T3. The PAni solutions were drop cast on the AA and demonstrated less corrosion than the uncoated AA coupons after immersing them in 0.1 M NaCl solution for 10–66 h [12]. Huerta-Vilca et al. electro-synthesized PAni on AA 2024-T3. Their PAni-coated AA 2024-T3 did not suffer marked corrosion when immersed in 0.1 M NaCl solution for 2.5 months [13]. Conroy et al. electro-deposited PAni films at pure aluminium potentiostatically. They concluded that little evidence of any corrosion protection occurred after exposure of their samples in aggressive chloride-containing solutions [14].

PPy has also been studied for its corrosion protection on AA. He et al. synthesized poly(3-octylpyrrole) and solvent-cast it on AA 2024-T3. A significant delay of over 20 h in dilute Harrison solution before any current flow was detected [15]. Gelling and her companions electro-deposited poly(3-octyl pyrrole) or poly(3-octadecyl pyrrole) on AA 2024-T3. Furthermore, they put and a polyurethane topcoat. They concluded that their coatings had the ability to inhibit corrosion in dilute Harrison solution [16].

Apart from the above experiments, few studies have been made on the electro-deposition of copolymers of PAni–PPy on AA. Iroh et al. successfully synthesized different kinds of conducting polymers, including PPy–PAni composites on AA 2024-T3. They concluded that the process ability and corrosion performance of PPy–PAni composite coatings are significantly better than those for either PPy or PAni coatings [17]. Akundy and his co-workers have achieved to electro-deposited PAni–PPy composite coatings on aluminium by using cyclic voltammetry [18]. Tsirimpis et al. investigated the protection offered by the combination of PPy and PAni, when applied onto pre-treated AA 2024-T3 substrates by cyclic voltammetry. The produced coatings adhered strongly to the substrate, and presented high uniformity as well as improved corrosion resistance when compared with the bare substrate [19].

In the present work we developed a system that prevents corrosion of AA 2024-T3. The metal alloys were coated with two layers the first one consists of CP coating including with CeO_2 loaded with 2-mercaptobenzothiazole (MBT) and the second one on the top was made of sol–gel coating. The CP coating consists of copolymer polyaniline–polypyrrole (PAni–PPy) copolymers. MBT was selected due to its corrosion inhibitor properties [20]. The coatings were tested for their corrosion protection properties using electrochemical impedance spectroscopy (EIS) and potentiodynamic polarisation (PP) methods.

2. Experimental

2.1. Materials

All chemicals were of analytical reagent grade. Oxalic acid (Sigma–Aldrich), cerium (III) acetylacetonate ($Ce(acac)_3$, Sigma–Aldrich), polyvinylpyrrolidone (PVP, average molecular weight = 55,000, Sigma–Aldrich), potassium persulphate (KPS, Sigma–Aldrich), sodium dodecyl sulphate (SDS, Sigma–Aldrich), *N*-(2-aminoethyl)-3-(trimethoxysilyl)propylamine (Sigma–Aldrich), epoxy resin "Araldite GY 257" (Ciba-Geigy), 2,2′-diaminodiethylamine (Sigma–Aldrich) and 2-mercaptobenzothiazole (MBT, Sigma–Aldrich) were used without further purification. Pyrrole (Sigma–Aldrich), aniline (Sigma–Aldrich) and styrene (Sigma–Aldrich), were double distilled under reduced pressure prior to use.

2.2. Synthesis of CeO_2 nanocontainers loaded with MBT

Ceria nanocontainers were prepared and 15% w/w loaded with corrosion inhibitor MBT according to our previous work [21]. They were synthesized through a two-step process. At first, the method of emulsion polymerisation was used to produce anionic polystyrene latex, used as core particles. For this purpose, the reaction was carried out in a 500-cm^3 container under the conditions listed in Table 1. To eliminate the effect of oxygen, the solution was purged with nitrogen before the process was initiated. The polymerisation process lasted for 20 h. The resulting dispersions were centrifuged at 14,000 rpm for 30 min, the supernatant solutions were discarded, and then the particles were resuspended in doubly distilled water using a sonicator.

The polystyrene lattices were coated via the sol–gel method to form a ceria oxide layer. The sol–gel coatings were prepared by controlled hydrolysis of $Ce(acac)_3$ aqueous solution in the presence of polystyrene latex and PVP. These dispersions were aged for 3 days in an oven preheated to 100 °C (Table 2). The resulting dispersions were centrifuged at 14,000 rpm for 30 min, the supernatant solutions were discarded, and then the particles were resuspended in doubly distilled water with a sonicator. This process was repeated three times, and the purified powders were dried in a desiccator. To produce hollow cerium dioxide nanospheres, the polystyrene cores were removed by calcination. Initially, the coated nanospheres were placed on a glass slide and dried, first at room temperature and then for 1 h at 60 °C. Then, the composite was calcinated for 4 h in air in a furnace at 600 °C with a heating rate 10 °C min^{-1}. In order the surface ratio, pore diameter and pore volume of the ceramic nanocontainers to be estimated, porosity measurements were conducted. The samples of the empty nanocontainers were degassed at 300 °C for 18 h prior the measurements.

Furthermore, the obtained ceria nanocontainers were loaded with the corrosion inhibitor. For this purpose, MBT was dissolved in acetone in order a saturated solution to be prepared. Ceria nanocontainers were placed in a sealed container. The air of the inner side of the nanocontainers was eliminated with a vacuum system. Then, the saturated solution of MBT in acetone was inserted in the sealed container and the whole mixture was stirred at room temperature for 24 h. Finally the ceria nanocontainers loaded with MBT were collected through centrifugation and drying under vacuum at 100 °C overnight.

2.3. Preparation of CP coatings

The CP layer including nanocontainers loaded with MBT was carried out via electro-deposition using cyclic voltammetry in a typical three-electrode cell connected to a Solartron 1470 PGstat electrochemical interface instrument. For this purpose, a 100 ml aqueous solution was prepared that was 0.07% w/v to loaded nanocontainers, 0.1 M pyrrole, 0.1 M aniline and 0.4 M oxalic acid. An AA 2024-T3 panel was used as the working electrode, a platinum

Table 1
The conditions used in the preparation of polystyrene latex at 80 °C.

Material	Quantity (g)
Styrene	4.53
KPS	1.00
SDS	0.21
Water	460

Table 2
Conditions of preparation of coated nanospheres.

Material	Quantity (g)
Polystyrene	1.13
PVP	1.60
$Ce(acac)_3$	2.40
Water	160

sheet as the counter while a saturated calomel electrode (SCE) served as reference. Under these conditions, electro-polymerisation preferably occurs on the working electrode forming a conducting polymer layer containing ceria nanocontainers. The potential was scanned between −1 and 3 V versus SCE at a rate of 15 mV s^{-1}. After the polymerisation process, the coated panels were washed thoroughly with distilled water in order to eliminated solution residues (monomers, oxalic acid) and left in air to dry. The AA 2024-T3 panel had been previously cleaned, under specific conditions. These conditions include the insertion of the panel into 2% w/w NaOH for 3 min at 40 °C. After that, the panel is rinsed with distilled water and is inserted into 4.33 M HNO_3 for 30 s at room temperature. Finally, the panel is rinsed with distilled water.

2.4. Dip coating process

The dip coating procedure included the dip of the panel into an ORMOSIL solution for six times with a rate of 32 cm/min. Every time, the panel stayed in the solution for 1 min. Then, the panel was irradiated with Infra-Red lamps for 24 h at 80 °C. The ORMOSIL solution was prepared under the condition listed in Table 3. Acetone and ethanol were used as solvents. The process for the preparation of the ORMOSIL solution included five steps. At first *N*-(2-aminoethyl)-3-(trimethoxysilyl)propylamine was hydrolyzed in absolute ethanol for 1 h (solution A). Then, epoxy resin "Araldite GY 257" was dissolved in absolute ethanol (solution B). Solutions A and B were intermixed formatting solution C. After that, 2,2′-diaminodiethylaminewas dissolved in 25 ml acetone (solution D). Finally, solutions C and D were intermixed and stirred for 12 h at ambient temperature.

All the synthesized coatings are listed in Table 4. Coat-Combo-CeO_2-MBT refers to AA2024-T3 that was coated with a copolymer PAni–PPy coating including CeO_2 nanocontainers loaded with MBT via electro-deposition and with a sol–gel coating via the dip coating process, Coat-Combo refers to AA2024-T3 that was coated with a copolymer PAni–PPy coating via electro-deposition and with a sol–gel coating via the dip coating process, Coat refers to AA2024-T3 that was coated with a sol–gel coating via the dip coating process, and Combo refers to AA2024-T3 that was coated with a copolymer PAni–PPy coating via electro-deposition.

2.5. Characterization

The electro-deposition of the CP coatings on AA 2024-T3 panels was carried out with a Solartron 1470 PGstat electrochemical interface instrument. The morphology of the CP coatings and ORMOSILs layers were determined by SEM using a PHILIPS Quanta Inspect (FEI Company) microscope with W (tungsted) filament 25 kV equipped with EDAX GENESIS (Ametex Process and Analytical Instruments). Furthermore, PAni–PPy copolymer and ORMOSILs coatings were characterized by Reflectance Infrared Spectroscopy using a Perkin–Elmer spectrometer. The zeta potential of the nanocontainers was estimated by (DLS) using a Zetasizer DTS 1060 (Malvern Instruments). Nitrogen adsorption experiments and pore size measurements were performed using a volumetric static sorption apparatus (Autosorb-1 MP, Quantachrome Instruments).

Table 3
Conditions for preparation of ORMOSIL solution.

Material	Quantity (g)
N-(2-Aminoethyl)-3-(trimethoxysilyl)propylamine	3.00
Epoxy resin "Araldite GY 257"	34.74
2,2′-Diaminodiethylamine	3.70
Ethanol	100.00
Acetone	75.00

Table 4
Tabulated description of the synthesized coatings.

Coating	Description
Combo	AA2024-T3 that was coated with a copolymer PAni–PPy coating via electro-deposition
Coat	AA2024-T3 that was coated with a sol–gel coating via the dip coating process
Coat-Combo	AA2024-T3 that was coated with a copolymer PAni–PPy coating via electro-deposition and with a sol–gel coating via the dip coating process
Combo-CeO_2-MBT	AA2024-T3 that was coated with a copolymer PAni–PPy coating including CeO_2 nanocontainers loaded with MBT via electro-deposition
Coat-Combo-CeO_2-MBT	AA2024-T3 that was coated with a copolymer PAni–PPy coating including CeO_2 nanocontainers loaded with MBT via electro-deposition and with a sol–gel coating via the dip coating process

Studies on the corrosion resistance of these coatings by PP were made using a Solartron 1470 PGstat electrochemical interface instrument. The exposed geometric area was 1 cm^2 for all the PP measurements. Using Cyclic Potentiodynamic Polarisation, the polarisation resistance (R_p), corrosion current (i_o) and the corrosion potential (E_o) were estimated. The potential was scanned between −0.4 V versus open circuit potential (OCP) and 0 V versus SCE. Anodic and cathodic branches of polarisation curves were recorded with the potential change rate of 1 mV s^{-1}. All the samples were in vertical position; the experiments were carried out at room temperature. For every result a minimum of three repetition measurements were taken. The R_p and i_o are derived by extrapolating the linear portions of the polarisation curves found at potentials ±20 mV away from the open circuit potential. The extrapolation leads to an intersection, which corresponds to i_o. Following, R_p is derived by the equation $i_o = \frac{1}{2.3R_p}\left(\frac{b_a b_c}{b_a + b_c}\right)$, where b_a, b_c are the anodic and cathodic Tafel coefficients, respectively [22]. Moreover, the corrosion inhibition efficiency, *IE*, was evaluated by using the equation $\%IE = \frac{i_{o(bareMetal)} - i_{o(coating)}}{i_{o(bareMetal)}} \times 100$, where $i_{o(bareMetal)}$ and $i_{o(coating)}$ are the corrosion currents of bare metal and of the coating, respectively [23–25].

EIS measurements were made using a SI 1287 Solartron Electrochemical interface connected with a SI 1260 impedance/gain-phase analyser. The experiments were performed at room temperature, in a Faraday cage, at the open circuit potential, using a three-electrode electrochemical cell, consisting of working electrode (≈3.15 cm^2 of exposed area), saturated calomel electrode (SCE) as reference and platinum as counter electrode. The measuring frequency ranged from 100 kHz down to 5 mHz. The rms voltage was 10 mV (SCE). Spectra were treated using the Z-view Software using the adequate equivalent electric circuits. The number of frequency points was 10 points per decade.

Nanoindentation testing was performed with a nanomechanical test instrument, which allows the application of loads from 1 to 30.000 μN and records the displacement as a function of applied loads with a high load resolution (1 nN) and a high displacement

resolution. The nanomechanical test instrument employed in this study is equipped with a Scanning Probe Microscope (SPM), in which a sharp probe tip moves in a raster scan pattern across a sample surface using a three-axis piezo positioner. In all depth-sensing tests a total of 10 indents are averaged to determine the mean hardness (H) and elastic modulus (E) values for statistical purposes, with a spacing of 50 μm, in a clean area environment with 45% humidity and 23 °C ambient temperature. In order to operate under closed loop load or displacement control, feedback control option was used. All nanoindentation measurements have been performed with the standard three-sided pyramidal Berkovich probe, with an average radius of curvature of about 100 nm [26], with 40 s loading and unloading segment time separately and 3 s of holding time, to avoid residual viscoelasticity [27,28]. Prior to indentation, the area function of the indenter tip was measured in a fused silica, a standard material for this purpose [29].

3. Results

3.1. CeO_2 nanocontainers

The produced nanocontainers from the aforementioned experimental process are demonstrated in Fig. 1. It can be seen that their diameter is 85 ± 5 nm. The specific area of the empty nanocontainers was calculated with the B.E.T. method in the range of relative pressure 0.05–0.35 P/P_0 and was found to be 84.52 $m^2\ g^{-1}$. The pore size distribution was calculated through the B.J.H. method at desorption isotherm and the mean pore radius found to be 4.475 nm with a pore volume 0.285 cc g^{-1}. The hysteresis through desorption is characteristic for curves of type IV (IUPAC). This fact indicates the presence of mesopores in the sample (Figs. 2 and 3). The zeta potential of the loaded nanocontainers was negative 22.1 mV (Fig. 4).

3.2. Cyclic voltammetry

The cyclic voltammetry patterns of the electro-polymerisation (electro-deposition) of copolymer PAni–PPy including CeO_2 nanocontainers (Combo-CeO_2-MBT) for the first, second, fifth and all the cycles are depicted on Fig. 5. For the 1st scan (cycle 1) from −1 to 3 V (SCE), two anodic peaks of 5.59 and 24.4 mA/cm^2 occur

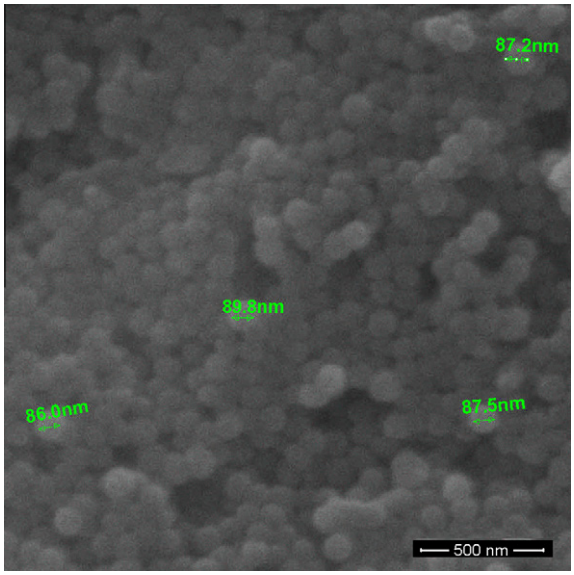

Fig. 1. Scanning electron micrograph of ceria nanocontainers loaded with MBT.

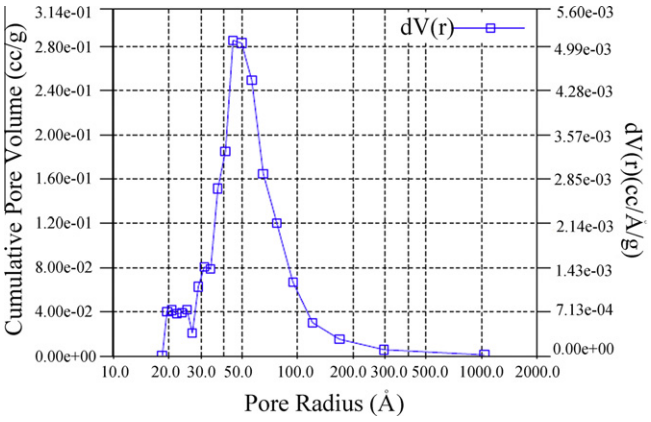

Fig. 2. BJH pore distribution of cerium oxide nanocontainers.

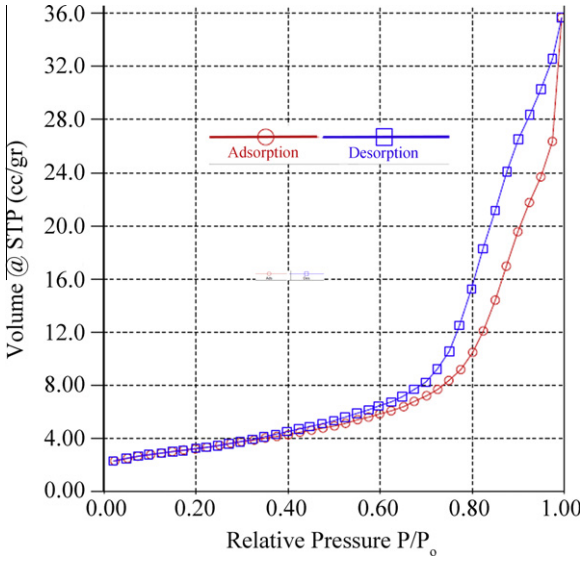

Fig. 3. Isotherms of cerium oxide nanocontainers.

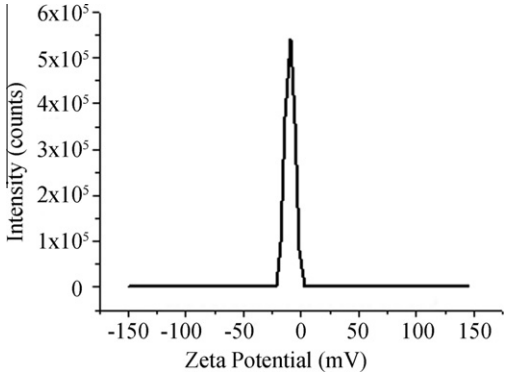

Fig. 4. Zeta potential of CeO_2 nanocontainers loaded with MBT after suspension in water.

at 0.14 and 1.88 V versus SCE, respectively. The first peak is attributed to the oxidation and absorption of hydrogen [30] and the second peak corresponds to the oxidation of the monomers aniline, pyrrole and the synthesized oligomers or copolymer of PAni–PPy [18]. On the other hand, for the 1st scan (cycle 1) from 3 to −1 V

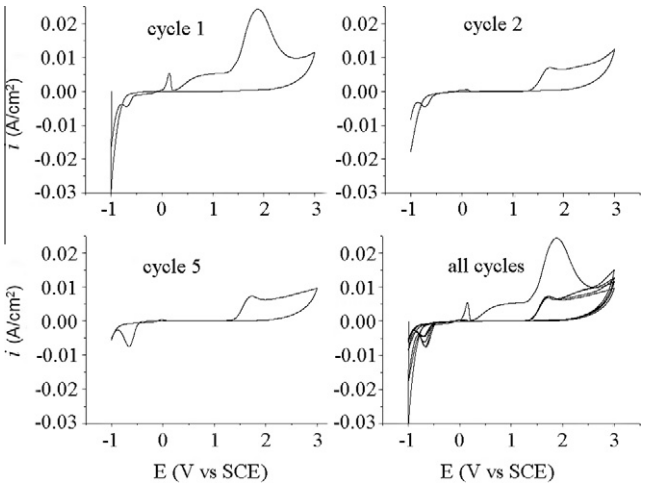

Fig. 5. Cyclic voltammograms of the electropolymerisation of PAni–PPy including loaded CeO_2 nanocontainers.

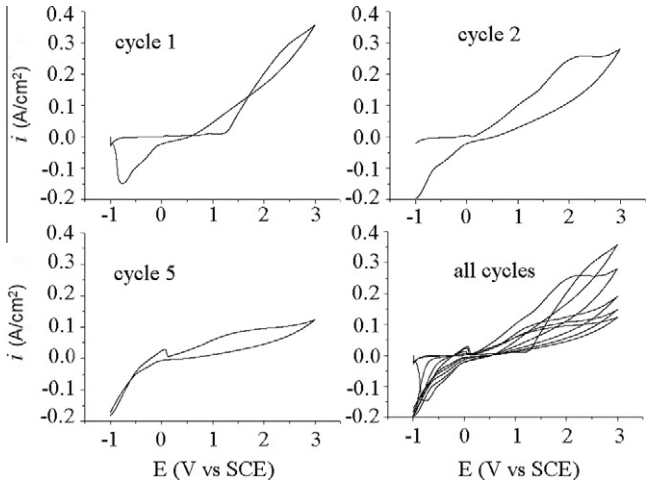

Fig. 7. Cyclic voltammograms of PPy electropolymerisation.

there is a cathodic peak of -0.40 mA/cm^2 occurs at -0.68 V (SCE) which is due to the reduction of the oxidised monomers aniline, pyrrole and the synthesized oligomers or copolymer of PAni–PPy. All the peaks reduce in intensity with the increase in number of cycles. The process ends at -1 V (SCE) so the copolymer coating finally is almost in reduced state apart from that which has been oxidised due to the influence of oxygen that is dissolved in the solution. The zeta potential of the nanocontainers was negative (Fig. 4) so it can be assumed that they were incorporated to the coating during the anodic process.

Fig. 6 depicts the cyclic voltammetry patterns of the electropolymerisation of polymer PAni for the first, second, fifth and all the cycles. During the 1st scan, an anodic peak of 3.07 mA/cm^2 that occurs at 0.12 V versus SCE is demonstrated and is attributed to the adsorption and oxidation of hydrogen [31]. The intensity of this peak is reduced as the number of cycles increases. Furthermore, the increase in number of cycles reveals an additional peak of 45.33 mA/cm^2 that occurs at 0.002 V versus SCE. This peak is due to the coating of PAni to the substrate [31] and it has and a corresponding cathodic peak of -0.29 mA/cm^2 at -0.5 V versus SCE.

The cyclic voltammetry patterns of the electro-polymerisation of polymer PPy for the first, second, fifth and all the cycles are presented on Fig. 7. Two anodic peaks occur, one at 0.08 V versus SCE which is due to the adsorption and oxidation of hydrogen and a second between 1.25 and 2.54 V versus SCE which is due to the oxidation of the monomer [32]. This peak is shifted to lower potentials as the number of cycles increases. There is also a corresponding cathodic peak at -0.76 V versus SCE which is attributed to the reduction of the monomer [32].

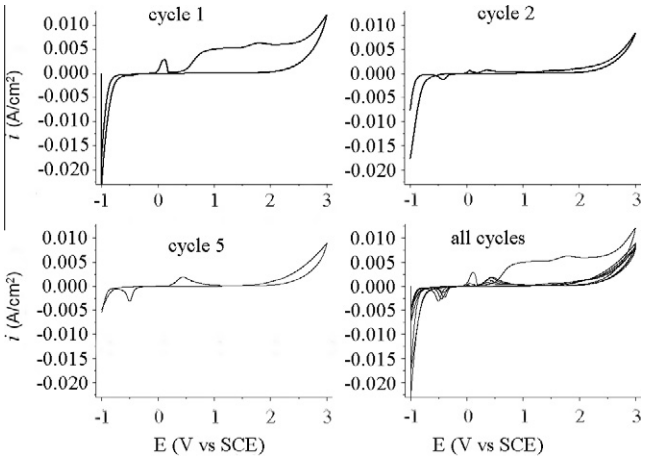

Fig. 6. Cyclic voltammograms of PAni electropolymerisation.

3.3. Scanning electron microscopy analysis

The morphology as well as the elemental Cemaping of the coating of PAni–PPy composite including CeO_2 loaded nanocontainers coating formed on AA 2024-T3 (Combo-CeO_2-MBT) are both illustrated in Fig. 8. The EDX analysis confirms that the Combo-CeO_2-MBT coating contains CeO_2 loaded nanocontainers. Aluminium and copper are from the substrate (AA 2024-T3) and gold appears due to the gold coating that was applied to the spheres (Fig. 9). The surface morphology of the sample Coat-Combo-CeO_2-MBT before and after exposure to corrosive environment 0.05 M NaCl for 72 h is illustrated in Fig. 10a and b, respectively. It can be seen that both surfaces are crack free and no signs of corrosion pits are revealed. On the other hand, both surfaces are not smooth and present aggregated particles. EDX analysis of both surfaces demonstrates the presence of carbon and silicon due to the coating and cerium due to the nanocontainers (Table 5). The values of oxygen remain the same before and after the exposure of the sample to corrosive environment and this fact clearly denotes that no formation of aluminium oxide occurs that can be ascribed to corrosion onset. Furthermore, chloride is revealed for the sample that was exposed to corrosive environment. The thickness of the sample Coat-Combo-CeO_2-MBT is illustrated in Fig. 11A coating consists of two layers can be clearly observed. It can be seen that the thickness of the first layer that consists of PAni–PPy composite including CeO_2 loaded nanocontainers is 3.00 ± 1.00 μm. The thickness of the second layer that consists of sol–gel, on the top, is 18.00 ± 3.00 μm.

3.4. FT-infrared spectroscopy analysis

The FT-IR spectrum for the AA 2024-T3 coated with the two layers (Coat-Combo-CeO_2-MBT) is presented in Fig. 12. Considering the spectrum it can be seen that the peaks at 897–934 cm^{-1} are due to N–H out of plane vibration and the peaks at 3172–3282 cm^{-1} are attributed to –NH_2 vibration of 2,2′-diaminodiethylamine. The peak at 966 cm^{-1} is due to epoxy ring of epoxy resin "Araldite GY 257". The peaks between 2917 and 2952 cm^{-1} and those at 2813 and 2885 cm^{-1} are attributed to R-CH_3 asymmetric stretching vibration of epoxy resin "Araldite GY 257" and the peaks at 1900 and

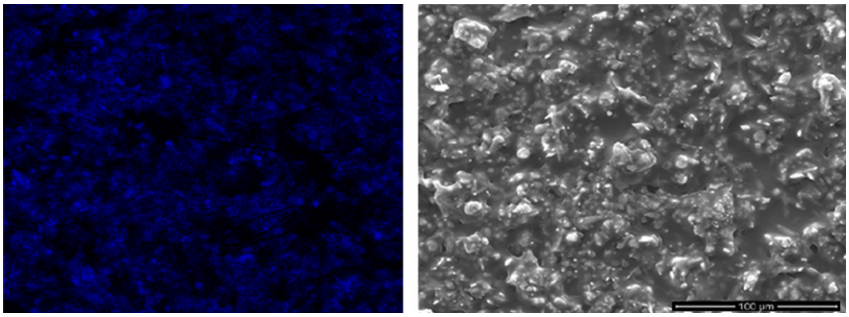

Fig. 8. Scanning electron micrograph and corresponding cerium elemental mapping of AA 2024-T3 that was coated with a copolymer PAni–PPy coating including CeO_2 nanocontainers loaded with MBT via electro-deposition (Combo-CeO_2-MBT coating).

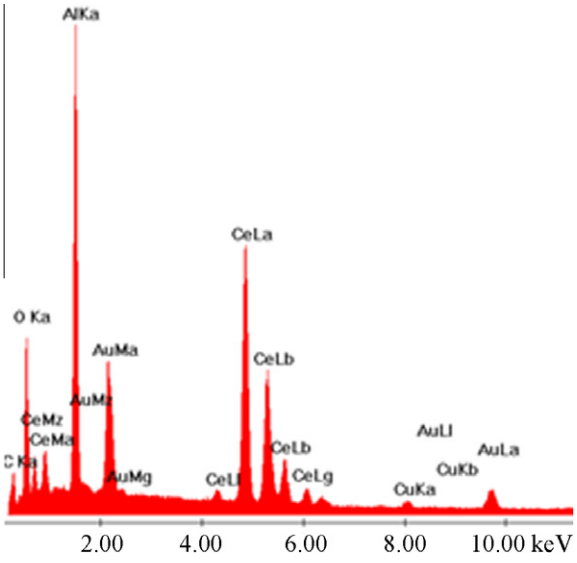

Fig. 9. EDAX analysis of AA 2024-T3 that was coated with a copolymer PAni–PPy coating including CeO_2 nanocontainers loaded with MBT via electro-deposition and with a sol–gel coating via the dip coating process (Coat-Combo-CeO_2-MBT coating).

3045 cm^{-1} are due to phenyl vibration of epoxy resin "Araldite GY 257", as well. The peaks between 550 and 600 cm^{-1} are ascribed to C–H out of plane deformation of aromatic ring of epoxy resin "Araldite GY 257". The chemical compound *N*-(2-aminoethyl)-3-(trimethoxysilyl)propylamine presents peak at 2847 cm^{-1} which is attributed to $-NH_2$ and Si–O–CH_3 asymmetric vibration of CH_3, peaks between 3378 and 3410 cm^{-1} which are due to –NH symmetric and asymmetric stretching vibrations. Furthermore, *N*-(2-aminoethyl)-3-(trimethoxysilyl)propylamine presents peaks at

Table 5
% w/w Element concentration of the coating Coat-Combo-CeO_2-MBT.

Coatings	C	Al	O	Si	Cl	Ce
Coat-Combo-CeO_2-MBT	82.73	1.19	10.26	1.47	–	4.34
Coat-Combo-CeO_2-MBT[a]	78.97	0.30	11.59	1.83	2.86	4.44

[a] After exposure at 0.05 M NaCl solution at room temperature for 72 h.

800–850 and 1170–1210 cm^{-1} due to Si-O-CH_3 symmetric vibration. *N*-(2-Aminoethyl)-3-(trimethoxysilyl)propylamine and 2,2′-diaminodiethylamine have peaks at 755 cm^{-1} due to $-NH_2$and C–H_2, 1363–1367 due to C–H symmetric vibration, 1037 cm^{-1} due to C–C and NH_2, between 1100 and 1122 cm^{-1} due to vibrations of firstly and secondary amines, 1285–1304 cm^{-1} due to C–H_2 and C–NH_2 vibrations, at 1450–1460 and 1600–1620 cm^{-1} which are attributed to firstly amine vibration, at 1330–1360 and 1500–1520 cm^{-1} due to secondary amine vibrations. The peaks in the range of 2050–2140, at 2280 and at 3380 correspond to $-NH_3^+$ and they are asymmetric N–H stretching vibrations [33–37]. CeO_2 have peaks at 425–523 cm^{-1} but cannot be seen at this spectrum. Aluminium oxide exhibits broad peaks between 500 and 1000 cm^{-1}. Furthermore, due to the thickness of the sol–gel top coating (18.00 ± 3.00 μm, Fig. 10) the peaks of CP coating also cannot be seen at this spectrum. Fig. 13 depicts the chemical structures of *N*-(2-aminoethyl)-3-(trimethoxysilyl)propylamine, 2,2′-diaminodiethylamineand epoxy resin "Araldite GY 257".

3.5. Corrosion test

Corrosion test process includes the exposure of the panels to 0.05 M NaCl solution for 72 h. Fig. 14 presents the polarisation curves for the samples Coat-Combo-CeO_2-MBT (the AA2024-T3 was coated with the CP coating including loaded nanocontainers

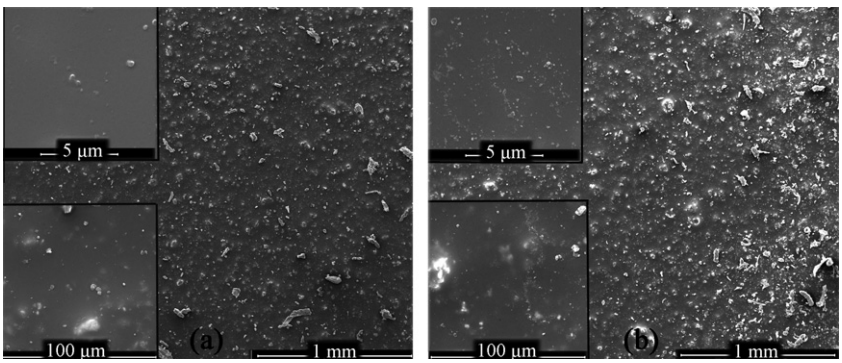

Fig. 10. Scanning electron micrograph of AA 2024-T3 that was coated with a copolymer PAni–PPy coating including CeO_2 nanocontainers loaded with MBT via electro-deposition and with a sol–gel coating via the dip coating process (Coat-Combo-CeO_2-MBT coating) (a) before and (b) after exposure to 0.05 M NaCl solution at room temperature for 72 h.

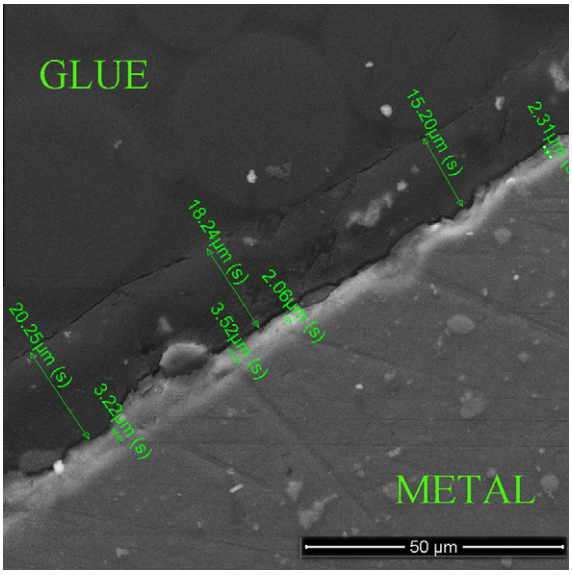

Fig. 11. Cross-section image of AA 2024-T3 that was coated with a copolymer PAni–PPy coating including CeO_2 nanocontainers loaded with MBT via electro-deposition and with a sol–gel coating via the dip coating process (Coat-Combo-CeO_2-MBT coating).

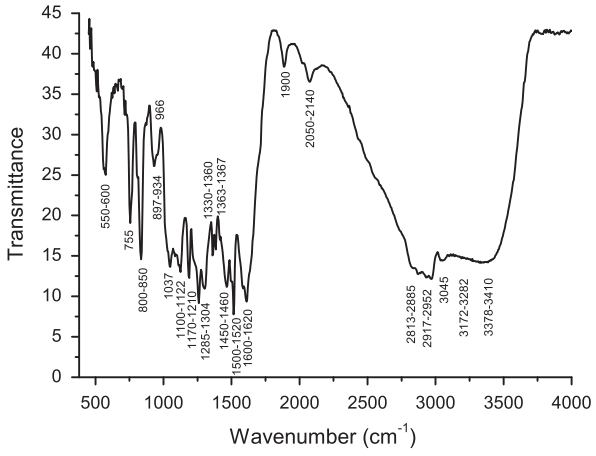

Fig. 12. Infrared spectra of AA 2024-T3 that was coated with a copolymer PAni–PPy coating including CeO_2 nanocontainers loaded with MBT via electro-deposition and with a sol–gel coating via the dip coating process (Coat-Combo-CeO_2-MBT coating).

and the sol–gel coating), Coat-Combo (the AA2024-T3 was coated with the CP coating without nanocontainers and the sol–gel coating), Coat (the AA2024-T3 was coated only with the sol–gel coating), Combo (the AA2024-T3 was coated only with CP coating) and Bare AA2024-T3. Bare AA 2024-T3 is included at the diagram for comparison reasons. It can be seen that there is a remarkable decrease of both anodic and cathodic currents of the sample Coat-Combo-CeO_2-MBT relatively to the other coated samples and the bare aluminium. The decrease in the rate of the anodic and cathodic currents may be explained by a decrease in the active area of the electrodes, which is function of the coating. Table 6 presents the tabulated values of i_o, R_p and *IE* after 72 h of exposure to 0.05 M NaCl. The results of Table 6 indicate that all the coatings demonstrate a decrease of their corrosion current compare to bare AA2024-T3. Furthermore, all the coatings present an increase of their polarisation resistance. The highest depression of i_o as well as the highest increase of R_p are observed for the Coat-Combo-CeO_2-MBT that are one and a half order of magnitude, respectively. Additionally, Coat-Combo-CeO_2-MBT depicts the highest values of *IE*. This inhibition of corrosion action clearly denotes that the combination of conductive polymer layer including loaded nanocontainers together with the layer of ORMOSIL presents increased corrosion protective properties. It should be mentioned that the i_o, R_p and *IE* values for the Coat-Combo coating cannot be taken into account due to the shape of the corresponding polarisation curve that does not allow accurate estimation of i_o, R_p and *IE*.

Considering the literature, PP method has been used in lots of studies for estimating the corrosion performance of various protecting coatings on AA 2024-T3. Metroke et al. synthesized ORMOSIL coatings of tetramethoxysilane and 3-glycidoxypropyltrimethoxysilane with various acids that their values for i_o and R_p were in the range of 1.51×10^{-4}–3.16×10^{-2} mA/cm^2 and 1–157 kΩ/cm^2, respectively. The coatings were exposed to 1 M NaCl for 30 min [38]. Wu et al. prepared ORMOSIL coatings of 3-glycidoxypropyltrimethoxysilane, tetraethoxysilane and tetraethylenepentamine that their values for i_o and R_p were in the range of 17.1–27.8 nA/cm^2 and 899–1461 kΩ/m^2, respectively. The coatings were exposed to 0.1 wt.% NaCl for 30 min [39,40]. Shah et al. deposited PAni coating using oxalic acid as electrolyte. The i_o value of the coating was5.43×10^{-1} μA/cm^2, after exposure to 3.5 wt.% NaCl [31]. Huerta-Vilca et al. electro-synthesized PAni for corrosion protection of AA 2024-T3. The i_o values of the coating were in the range of 1.36×10^{-2}–1.45×10^{-1} mA/cm^2, after exposure to 0.1 M NaCl [13]. Finally, in our previous work, electro-depositions of copolymers PAni–PPy on AA 2024-T3 presented values for i_o and R_p in the range of 7.29×10^{-6}–9.56×10^{-1} μA/cm^2 and 32.7–97.9 kΩ/cm^2, respectively, after exposure to 3.5 wt.% NaCl for 72 h [19]. It can be seen that the concentration of the corrosive solutions as well as the exposure time differ from the concentration (0.05 M NaCl) and exposure time (72 h) that were used in our studies for the corrosion tests. So, the values for i_o and R_p cannot be comparable.

The corrosion protection properties of the coated samples were additionally estimated using EIS. Corrosion test process includes also the exposure of the coated panels to 0.05 M NaCl solution. The Bode plots of the EIS spectra obtained for all the coated samples after 72 h are depicted in Fig. 15. Bare AA2024-T3 is presented as reference. The total impedance values can be used for the estimation of the coating with the best corrosion protection properties. It is clearly denoted form the impedance value at low frequency range that the samples Coat-Combo-CeO_2-MBT and Coat demonstrate the best corrosion protective behaviour after 72 h of exposure in corrosive environment as their value are the highest compare to all the other coatings (3×10^5 Ω cm^2). On the other hand, it can be seen that the coating Coat-Combo-CeO_2-MBT presents an increased time constant in the range of the high frequencies that is ascribed to its enhanced barrier properties. The absence of time constants in the high frequency range for the other coatings clearly denotes low barrier properties. These properties can be attributed to possible cracks that were formed on the coatings after their exposure to corrosive environment. The cracks permit the penetration of water molecules and chloride ions into the coating. These results confirm that the encapsulation of loaded containers into the coating (Coat-Combo-CeO_2-MBT) provides enhanced corrosion protection.

The interpretation of the EIS results for the sample Coat-Combo-CeO_2-MBT obtained during immersion in the NaCl solutions was performed by numerical fitting, using the equivalent circuit illustrated in Fig. 16. In this equivalent circuit, constant phase elements were used instead of pure capacitors. This modification is obligatory in the case the phase shift of a capacitor is different from −90° [41]. The impedance of a R-CPE parallel association is given by: $Z_{\text{R-CPE}} = \frac{R}{1+RY_0(j\omega)^n}$, where Y_0 is the admittance of the CPE and n is the CPE exponent. Constant phase elements correspond to a

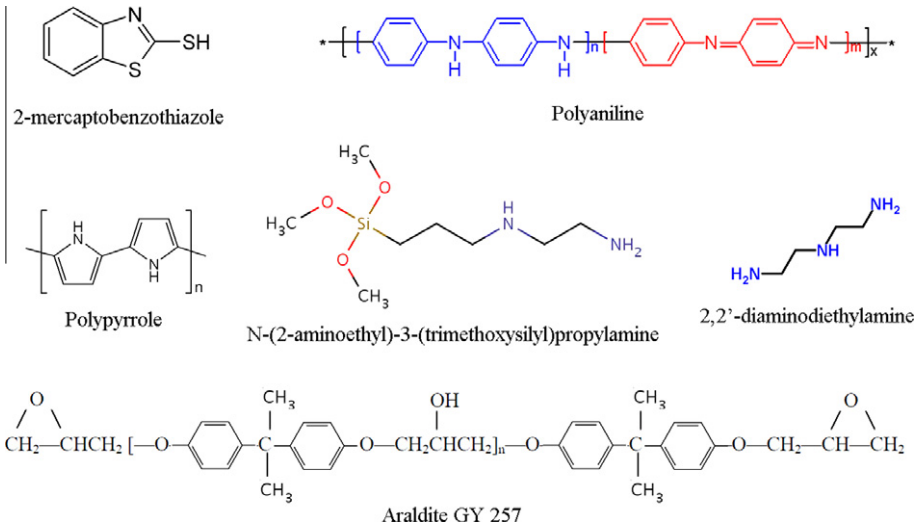

Fig. 13. Chemical structures of 2-mercaptobenzothiazole, polyaniline, polypyrrole, *N*-(2-aminoethyl)-3-(trimethoxysilyl)propylamine, 2,2′-diaminodiethylamine and epoxy resin "Araldite GY 257".

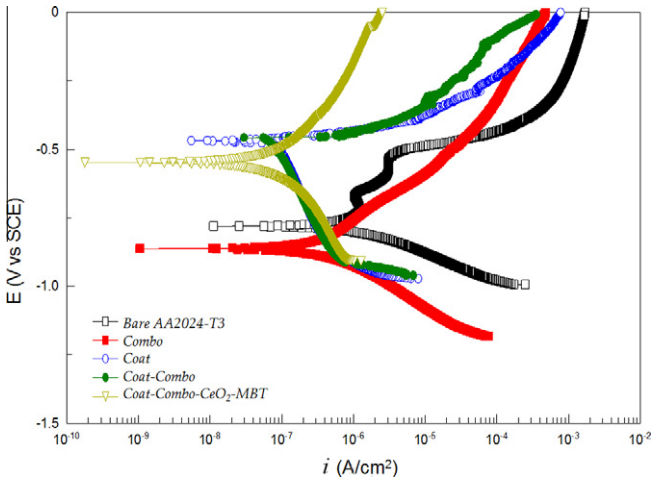

Fig. 14. Polarisation curves for AA 2024-T3 that was coated with (▽) a copolymer PAni–PPy coating including CeO_2 nanocontainers loaded with MBT via electro-deposition and with a sol–gel coating via the dip coating process (Coat-Combo-CeO_2-MBT), (●) a copolymer PAni–PPy coating via electro-deposition and with a sol–gel coating via the dip coating process (Coat-Combo), (○) a sol–gel coating via the dip coating process (Coat), (■) a copolymer PAni–PPy coating via electro-deposition (Combo) and (□) uncoated AA2024-T3 after exposure to 0.05 M NaCl solution at room temperature for 72 h.

Table 6
Tabulated values for coatings acquired after 72 h of exposure to 0.05 M NaCl.

	R_p (Ω/cm^2)	i_o (A/cm^2)	E_o (mV versus SCE)	%IE
AA2024-T3	2.53×10^4	1.03×10^{-6}	-7.79×10^2	–
Combo	8.78×10^4	2.97×10^{-7}	-8.62×10^2	71.16
Coat	1.24×10^5	2.11×10^{-7}	-4.71×10^2	79.51
Coat-Combo	2.87×10^4	9.09×10^{-7}	-4.66×10^2	11.74
Coat-Combo-CeO_2-MBT	5.98×10^5	4.36×10^{-8}	-5.48×10^2	95.77

capacitor when the CPE exponent (n) is one. Using the Cole–Cole approach together with CPE, the capacitance can be calculated from the fittings by: $C = \sqrt[n]{\frac{RY_0}{R^n}}$ [42,43]. The equivalent circuit for the coatings Coat includes the resistance and the capacitance of the coating (R_{coat}–CPE_{coat}) and a second relaxation process including a charge transfer resistance and a double layer capacitance (R_{ct}–CPE_{dl}) that simulates the behaviour of the spectra at lower frequencies. The resistance of the solution is illustrated as R_{sol}. The fitting parameters are depicted in Fig. 17 that shows the evolution of coating capacitance and resistance (C_{coat}, R_{coat}) during the immersion time in corrosive environment. The results show that the capacitive behaviour is slightly increased at the immersion time elapses from 24 to 72 h in 0.05 M NaCl solution and this fact comes in accordance with the slightly decrease of the resistance of the coating, R_{coat} (Table 7).

Considering the literature, EIS method has been used in lots of studies for the estimation of anticorrosive properties of coatings applied on AA 2024-T3. Huerta-Vilca et al. who electro-synthesized PAni on AA 2024-T3, measured the impedance value at low frequencies to be 10^4 Ω cm^2, after exposure to 0.1 M NaCl for 72 h [13]. Wang et al. applied epoxy-silica–alumina sol–gel films containing cerium nitrate corrosion inhibitor to AA 2024-T3. They measured the impedance value at low frequencies to be 1.9×10^2 kΩ cm^2, after exposure to 3.5 wt.% NaCl for 72 h [44]. Schem et al. examined coatings applied on AA 2024-T3 consist of hybrid organic–inorganic sol–gel-matrices, with up to 20 wt.% incorporated ceria nanoparticles. They found the impedance value at low frequencies to be 6 MΩ cm^2, after exposure to 3.5 wt.% NaCl for 120 h (5 days) [45]. In our previous work AA 2024-T3 panels were coated with epoxy coatings incorporated with cerium molybdate containers loaded with 2-mercaptobenzothiazole (MBT). The total impedance value was found to be 2×10^2 kΩ cm^2, after exposure to 0.05 M NaCl for 68 h [46]. Finally, the corrosion protection properties of PPy electrodeposited onto AA 2024-T3 substrates were investigated as a function of the doping agent in another previous work. We used camphor sulphonic acid, *p*-toluene sulphonic acid, phenylphosphonic acid, oxalic acid and cerium nitrate salt as doping agents. The total impedance value was found to be 3×10 kΩ cm^2, after exposure to 0.5 M NaCl for 72 h [47]. It can be concluded from all the aforementioned results that the corrosion protection properties of the proposed system have to be further improved to reach other similar hybrid systems including particles and containers that already exist, and finally to replace chromium based coatings.

3.6. Nanomechanical and nanotribological properties of the coatings

Based on the half-space elastic deformation theory, H and E values can be extracted from the experimental data (load displace-

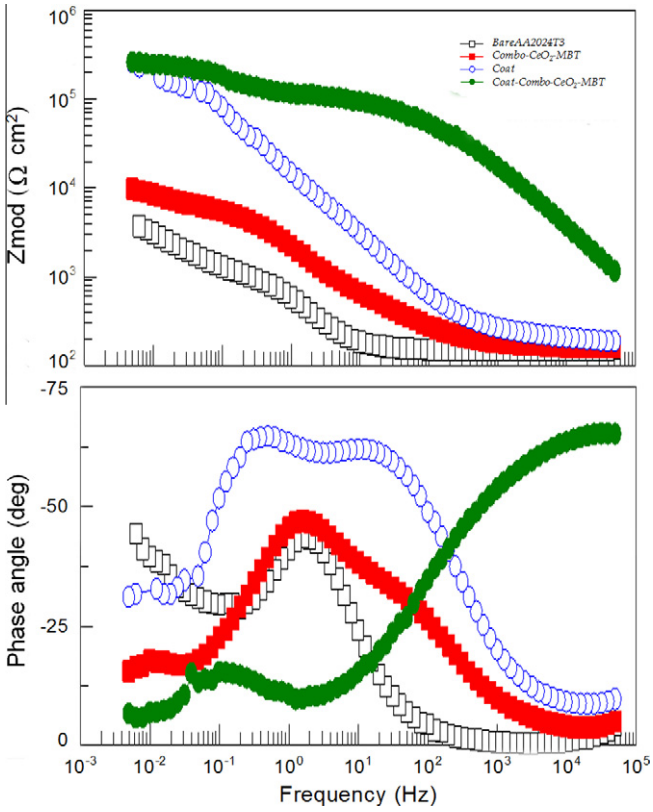

Fig. 15. EIS bode plots of AA 2024-T3 that was coated with (●) a copolymer PAni–PPy coating including CeO_2 nanocontainers loaded with MBT via electro-deposition and with a sol–gel coating via the dip coating process (Coat-Combo-CeO_2-MBT), (■) a copolymer PAni–PPy coating including CeO_2 nanocontainers loaded with MBT via electro-deposition (Combo-CeO_2-MBT), (○) a sol–gel coating via the dip coating process(Coat) and (□) uncoated AA2024-T3, after exposure to 0.05 M NaCl solution at room temperature for 72 h.

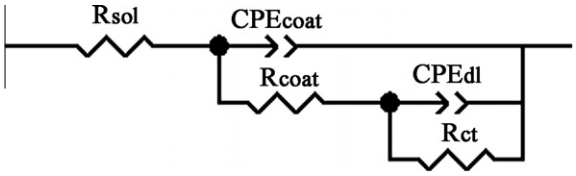

Fig. 16. Equivalent circuit used for numerical simulation of the EIS data.

ment curves) using the Oliver–Pharr (O&P) method [48]. The derived expressions for calculating the elastic modulus from indentation experiments are based on Sneddon's [49–51] elastic contact theory:

$$E_r = \frac{S\sqrt{\pi}}{2\beta\sqrt{A_c}}$$

where S is the unloading stiffness (initial slope of the unloading load–displacement curve at the maximum displacement of penetration (or peak load)), A_c is the projected contact area between the tip and the substrate and β is a constant that depends on the geometry of the indenter (β = 1.167 for Berkovich tip [48]). Conventional nanoindentation hardness refers to the mean contact pressure; this hardness, which is the contact hardness (H_c) is actually dependent upon the geometry of the indenter $H_c = F/A$ where, $A(h_c) = 24.5h_c^2 + \alpha_1 h_c + \alpha_{1/2}h_c^{1/2} + \ldots + \alpha_{1/16}h_c^{1/16}$ and

$$h_c = h_m - \varepsilon\frac{P_m}{S_m}$$

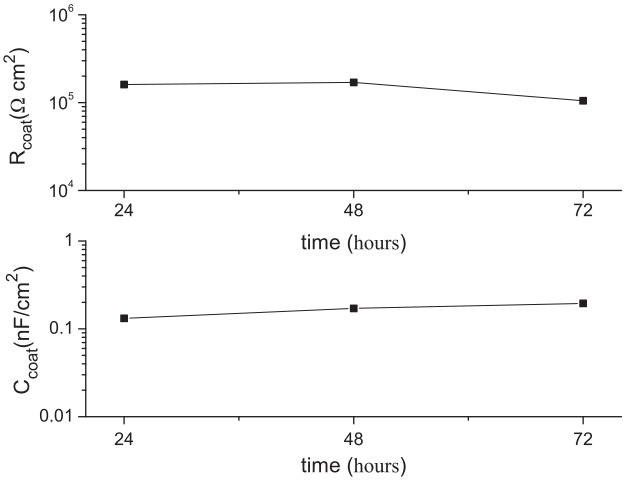

Fig. 17. R_{coat} and C_{coat} evolution of AA 2024-T3 that was coated with a copolymer PAni–PPy coating including CeO_2 nanocontainers loaded with MBT via electro-deposition and with a sol–gel coating via the dip coating process (Coat-Combo-CeO_2-MBT), as a function of time of exposure to 0.05 M NaCl solution at room temperature.

Table 7
Fitting parameters CPE_{coat}-T, CPE_{coat}-P, R_{coat}, C_{coat}, for the sample Coat-Combo-CeO_2-MBT.

Time (h)	CPE_{coat}-T (F cm^{-2} s^{-n})	CPE_{coat}-P	R_{coat} (Ω cm^2)	C_{coat} (F cm^{-2})
24	6.63×10^{-8}	0.73758	1.61×10^5	1.32×10^{-8}
48	9.51×10^{-8}	0.70645	1.70×10^5	1.71×10^{-8}
72	1.41×10^{-7}	0.68026	1.05×10^5	1.95×10^{-8}

where h_m is the total penetration displacement of the indenter at peak load, P_m is the peak load at the indenter displacement h_m, and ε is an indenter geometry constant, equal to 0.75 for Berkovich indenter [29,48].

Fig. 18 presents representative load–displacement curves for Coat-Combo-CeO_2-MBT coating. In Fig. 19, hardness and elastic modulus of Coat-Combo-CeO_2-MBT coating are demonstrated; the behaviour varies with indentation depth, according to similar work reported in the literature [52]. The ratio of hardness/elastic modulus is of significant interest in tribology. Higher stresses are expected in high H/E, hard materials, and high stress concentrations develop towards the indenter tip, whereas in the case of low H/E, soft materials, the stresses are lower and are distributed more evenly across the cross-section of the material [53,54]. The high ratio of hardness to elastic modulus (H/E) is indicative of the good wear resistance in a disparate range of materials [54]: ceramic, metallic and polymeric (e.g. c-BN, tool steel and nylon, respectively), which are equally effective in resisting attrition for their particular intended application. In Fig. 20a, the change of H/E slope reveals the strengthening of composite coating with increasing displacement.

The contact area is influenced by the formation of pile-ups and sink-ins during the indentation process. To accurately measure the indentation contact area, pile-ups/sinks-ins should be appropriately accounted for. The presence of creep during nanoindentation has an effect on pile-up, which results in incorrect measurement of the material properties. Fischer-Cripps observed this behaviour, in case where the measured elastic modulus was much less than expected [55]. Rar et al. observed that the same material when allowed to creep for a long duration produced a higher value of pile-up/sink-in indicating a switch from an initial elastic sink-into a plastic pile-up [56].

In Fig. 20b, the normalized pile-up/sink-in height h_c/h_m is plotted versus displacement. Higher stresses are expected in hard

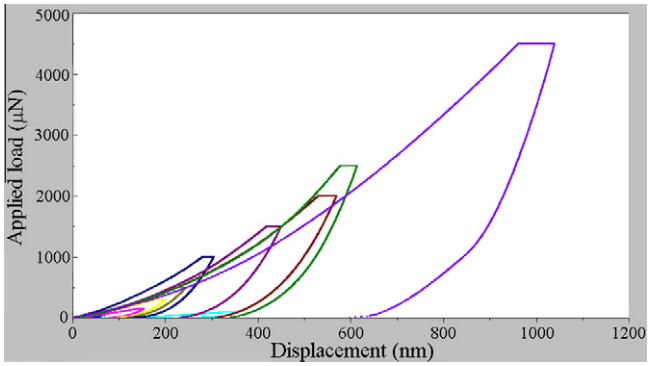

Fig. 18. Representative load–displacement curves for AA 2024-T3 that was coated with a copolymer PAni–PPy coating including CeO_2 nanocontainers loaded with MBT via electro-deposition and with a sol–gel coating via the dip coating process (Coat-Combo-CeO_2-MBT coating).

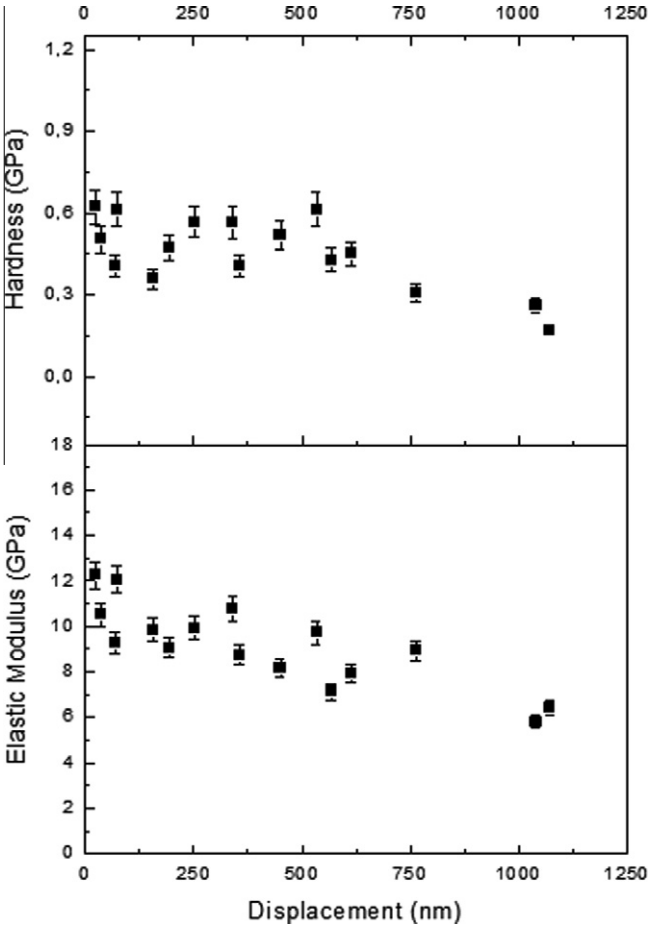

Fig. 19. Hardness and elastic modulus of AA 2024-T3 that was coated with a copolymer PAni–PPy coating including CeO_2 nanocontainers loaded with MBT via electro-deposition and with a sol–gel coating via the dip coating process (Coat-Combo-CeO_2-MBT coating).

materials and high stress concentrations develop towards the indenter tip, whereas in case of soft materials the stresses are lower and are distributed more evenly across the cross-section of the material [55]. Rate sensitive materials experience less pile-up compared to rate insensitive materials due strain hardening. When h_c/h_m approaches 1, deformation is intimately dominated by pile-up [57,58]. On the other hand, when h_c/h_m approaches 0, it corresponds to purely elastic deformation and is apparently dominated by sink-in in a manner prescribed by Hertzian contact mechanics [59].

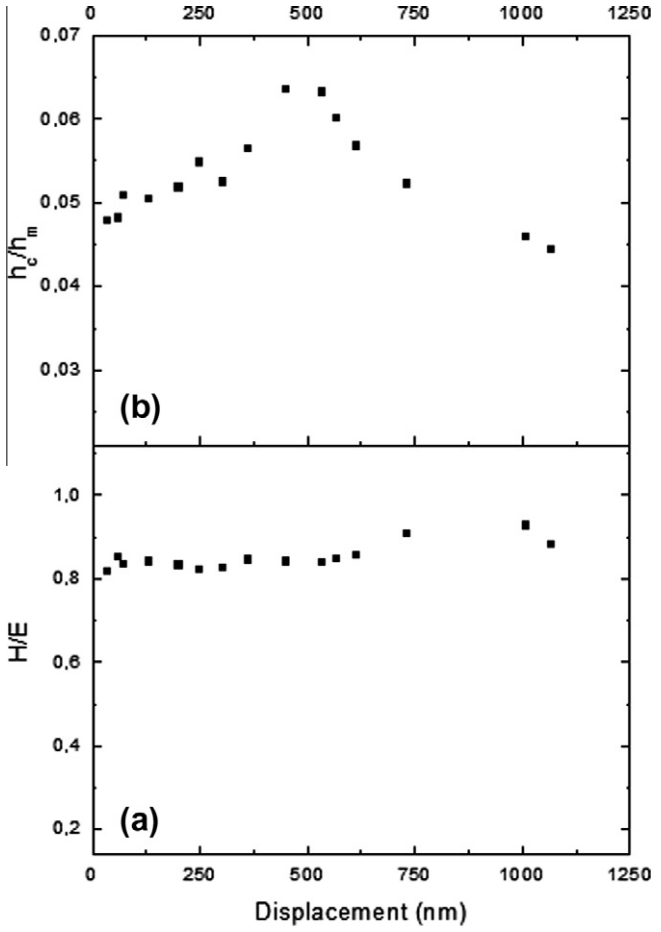

Fig. 20. (a) Wear ratio (H/E) and (b) pile up/sink in deformation of AA 2024-T3 that was coated with a copolymer PAni–PPy coating including CeO_2 nanocontainers loaded with MBT via electro-deposition and with a sol–gel coating via the dip coating process (Coat-Combo-CeO_2-MBT coating).

4. Conclusion

A novel system has been developed for the corrosion protection of AA 2024-T3. This system includes layers of CP and sol–gel. Furthermore, CeO_2 nanocontainers loaded with MBT were incorporated into CP layer. The above coatings were characterized with SEM and FT-IR. Their corrosion resistance in 0.05 M NaCl solution was estimated via EIS and PP. The results demonstrated that the incorporation of ceria nanocontainers loaded with MBT into the CP layer improved the corrosion protective properties of the coatings by increasing the total impedance value, presenting enhanced barrier properties and decreasing the anodic and cathodic currents compare to the coatings without nanocontainers. Nanomechanical and nanotribological properties of the coating consist of AA 2024-T3 that was coated with a copolymer PAni–PPy coating including CeO_2 nanocontainers loaded with MBT via electro-deposition and with a sol–gel coating via the dip coating process revealed the strengthening of composite coating with increasing displacement. To sum up, it should be mentioned that more studies have to be done in order the coatings to acquire corrosion protection properties similar to the existing chromium based coatings.

Acknowledgements

This project was supported by European Integrated Project "MULTIPROTECT" The abbreviation "MULTIPROTECT" stands for "Advanced environmentally friendly multifunctional corrosion

protection by nanotechnology" (Contract No. NMP3-CT-2005-011783).

References

[1] R.M. Park, J.F. Bena, L.T. Stayner, R.J. Smith, H.J. Gibb, P.S.J. Lees, Hexavalent chromium and lung cancer in the chromate industry: a quantitative risk assessment, Risk Anal. 24 (2004) 1099–1108.

[2] A. Cabral, R.G. Duarte, M.F. Montemor, M.L. Zheludkevich, M.G.S. Ferreira, Analytical characterisation and corrosion behaviour of bis-[triethoxysilylpropyl]tetrasulphide pre-treated AA2024-T3, Corros. Sci. 47 (2005) 869–881.

[3] N.C. Rosero-Navarro, S.A. Pellice, A. Duran, M. Aparicio, Effects of Ce-containing sol–gel coatings reinforced with SiO_2 nanoparticles on the protection of AA2024, Corros. Sci. 50 (2008) 1283–1291.

[4] S.S. Pathak, A.S. Khanna, T.J.M. Sinha, HMMM cured corrosion resistance waterborne ORMOSIL coating for aluminium alloy, Prog. Org. Coat. 60 (2007) 211–218.

[5] D. Raps, T. Hack, J. Wehr, M.L. Zheludkevich, A.C. Bastos, M.G.S. Ferreira, O. Nuyken, Electrochemical study of inhibitor-containing organic–inorganic hybrid coatings on AA2024, Corros. Sci. 51 (2009) 1012–1021.

[6] M. Aldissi, Proceedings of the international conference of science and technology of synthetic metals, Synth. Met. 27 (1988) AR13–AR14.

[7] A.J. Epstein, Electrically conducting polymers: science and technology, MRS Bull. 22 (1997) 16–23.

[8] J.H. Simpson, D.M. Rice, F.C. Rossito, P. Lahti, F.E. Karasz, A multitechnique investigation of sodium-doped poly(*p*-phenylenevinylene), Polymer 34 (1993) 4595–4601.

[9] A.G. MacDiarmid, Short Course on Conductive Polymers, SUNY, New Platz, NY, 1985.

[10] M. Shabani-Nooshabadi, S.M. Ghoreishi, M. Behpour, Direct electrosynthesis of polyaniline–montmorillonite nanocomposite coatings on aluminum alloy 3004 and their corrosion protection performance, Corros. Sci. 53 (2011) 3035–3042.

[11] L. Cecchetto, R. Ambat, A.J. Davenport, D. Delabouglise, J.-P. Petit, O. Neel, Emeraldine base as corrosion protective layer on aluminium alloy AA5182, effect of the surface microstructure, Corros. Sci. 49 (2007) 818–829.

[12] A.J. Epsteinax, J.A. Smallfield, H. Guana, M. Fahlmanb, Corrosion protection of aluminium and aluminium alloys by polyanilines: a potentiodynamic and photoelectron spectroscopy study, Synth. Met. 102 (1999) 1374–1376.

[13] D. Huerta-Vilca, S.R. Moraes, A.J. Motheo, Electrosynthesized polyaniline for the corrosion protection of aluminium alloy 2024-T3, J. Braz. Chem. Soc. 14 (2003) 52–58.

[14] K.G. Conroy, C.B. Breslin, The electrochemical deposition of polyaniline at pure aluminium: electrochemical activity and corrosion protection properties, Electrochim. Acta 48 (2003) 721–732.

[15] J. He, V. Johnston-Gelling, D.E. Tallman, G.P. Bierwagen, G.G. Wallace, Conducting polymers and corrosion III. A scanning vibrating electrode study of poly(3-octyl pyrrole) on steel and aluminium, J. Electrochem. Soc. 147 (2000) 3667–3672.

[16] V.J. Gelling, M.M. Wiest, D.E. Tallman, G.P. Bierwagen, G.G. Wallace, Electroactive-conducting polymers for corrosion control. Studies of poly(3-octyl pyrrole) and poly(3-octadecyl pyrrole) on aluminium 2024-T3 alloy, Prog. Org. Coat. 43 (2001) 149–157.

[17] J.O. Iroh, Y. Zhu, K. Shah, K. Levine, R. Rajagopalan, T. Uyar, M. Donley, R. Mantz, J. Johnson, N.N. Voevodin, V.N. Balbyshev, A.N. Khramov, Electrochemical synthesis: a novel technique for processing multi-functional coatings, Prog. Org. Coat. 47 (2003) 365–375.

[18] G.S. Akundy, R. Rajagopalan, J.O. Iroh, Electrochemical deposition of polyaniline–polypyrrole composite coatings on aluminium, J. Appl. Polym. Sci. 83 (2002) 1970–1977.

[19] A. Tsirimpis, I. Kartsonakis, I. Danilidis, P. Liatsi, G. Kordas, Synthesis of conductive polymeric composite coatings for corrosion protection applications, Prog. Org. Coat. 67 (2010) 389–397.

[20] B. Sanyal, Organic compounds as corrosion inhibitors in different environments – a review, Prog. Org. Coat. 9 (1981) 165–236.

[21] I.A. Kartsonakis, I. Daniilidis, G. Kordas, Encapsulation of the corrosion inhibitor 8-hydroxyquinoline into ceria nanocontainers, J. Sol–Gel Sci. Technol. 48 (2008) 24–31.

[22] R.G. Kelly, J.R. Scully, D.W. Shoesmith, R.G. Buchheit, Electrochemical Techniques in Corrosion Science and Engineering, Marcel Dekker Inc., 2003. pp. 60–66.

[23] G.Y. Elewady, I.A. El-Said, A.S. Fouda, Anion Surfactants as Corrosion Inhibitors for Aluminum Dissolution in HCl Solutions, Int. J. Electrochem. Sci. 3 (2008) 177–190.

[24] M. Abdallah, A.S. Fouda, S.A. Shama, E.A. Afifi, Azodyes as corrosion inhibitors for dissolution of C-steel in hydrochloric acid solution, Afr. J. Pure Appl. Chem. 2 (2008) 83–91.

[25] K.F. Khaled, New synthesized guanidine derivative as a green corrosion inhibitor for mild steel in acidic solutions, Int. J. Electrochem. Sci. 3 (2008) 462–475.

[26] C.A. Charitidis, Nanomechanical and nanotribological properties of carbon-based thin films: a review, Refract. Met. Har. Mater. 28 (2010) 51–70.

[27] G. Feng, A.H.W. Ngan, Effects of creep and thermal drift on modulus measurement using depth-sensing indentation, Mater. Res. 17 (2002) 660–668.

[28] H. Bei, E.P. George, J.L. Hay, G.M. Pharr, Influence of indenter tip geometry on elastic deformation during nanoindentation, Phys. Rev. Lett. 95 (2005) 045501-1–045501-4.

[29] M. Troyon, L. Huang, Comparison of different analysis methods in nanoindentation and influence on the correction factor for contact area, Surf. Coat. Technol. 201 (2006) 1613–1619.

[30] M.J. Croissant, T. Napporn, J.M. Léger, C. Lamy, Electrocatalytic oxidation of hydrogen at platinum-modified polyaniline electrodes, Electrochim. Acta 43 (1998) 2447–2457.

[31] K.G. Shah, G.S. Akundy, J.O. Iroh, Polyaniline coated on aluminium (Al-2024-T3): characterization and elecrtochemical studies, J. Appl. Polym. Sci. 85 (2002) 1669–1675.

[32] G.S. Akundy, J.O. Iroh, Polypyrrole coatings on aluminium-synthesis and characterization, Polymer 42 (2001) 9665–9669.

[33] M. Fahlman, S. Jasty, A.J. Epstein, Corrosion protection of iron/steel by emeraldine base polyaniline: an X-ray photoelectron spectroscopy study, Synth. Met. 85 (1997) 1323–1326.

[34] O. Hummel, A. Solti, Atlas of Polymer and Plastics Analysis, vol. 2, VCH Publications, 1988.

[35] L.J. Bellamis, The Infra-red Spectra of Complex Molecules, Chapman and Hall, 1975.

[36] R.M. Silverstein, G.C. Bassler, T.C. Morrill, Spectroscopic Identification of Organic Compounds, John Wiley & Sons, 1981.

[37] J. Mijovic, A. Fishbain, J. Wijaya, Mechanistic modeling of epoxy-amine kinetics. 2. Comparison of kinetics in thermal and microwave fields, Macromolecules 25 (1992) 986–989.

[38] T.L. Metroke, O. Kachurina, E.T. Knobbe, Spectroscopic and corrosion resistance characterization of amine and super acid-cured hybrid organic-inorganic thin films on 2024-T3 aluminum alloy, Prog. Org. Coat. 44 (2002) 185–199.

[39] K.H. Wu, M.C. Li, C.C. Yang, G.P. Wang, Domain size and thermal stability of amine-cured hybrid films as corrosion resistance treatments for aluminium alloy, J. Non-Cryst. Solids 352 (2006) 2897–2904.

[40] K.H. Wu, T.C. Chang, C.C. Yang, G.P. Wang, Dynamics and corrosion resistance of amine-cured organically modified silicate coatings on aluminium alloys, Thin Solid Films 513 (2006) 84–89.

[41] C.H. Hsu, F. Mansfeld, Technical note: concerning the conversion of the constant phase element parameter Y0 into a capacitance, Corrosion 57 (2001) 747–748.

[42] E. Barsoukov, J.R. Macdonald, Impedance Spectroscopy Theory, Experiment, and Applications, A John Wiley & Sons, Inc., Publication, USA, 2005. pp. 13–20.

[43] K.S. Cole, R.H. Cole, Dispersion and absorption in dielectrics. II. Direct current characteristics, J. Chem. Phys. 10 (1942) 98–105.

[44] H. Wang, R. Akid, A room temperature cured sol–gel anticorrosion pre-treatment for Al 2024-T3 alloys, Corros. Sci. 49 (2007) 4491–4503.

[45] M. Schem, T. Schmidt, J. Gerwann, M. Wittmar, M. Veith, G.E. Thompson, I.S. Molchan, T. Hashimoto, P. Skeldon, A.R. Phani, S. Santucci, M.L. Zheludkevich, CeO_2-filled sol–gel coatings for corrosion protection of AA2024-T3 aluminium alloy, Corros. Sci. 51 (2009) 2304–2315.

[46] I.A. Kartsonakis, A.C. Balaskas, G.C. Kordas, Influence of cerium molybdate containers on the corrosion performance of epoxy coated aluminium alloys 2024-T3, Corros. Sci. 53 (2011) 3771–3779.

[47] A.C. Balaskas, I.A. Kartsonakis, G.C. Kordas, A.M. Cabral, P.J. Morais, Influence of the doping agent on the corrosion protection properties of polypyrrole grown on aluminium alloy 2024-T3, Prog. Org. Coat. 71 (2011) 181–187.

[48] W.C. Oliver, G.M. Pharr, An improved technique for determining hardness and elastic modulus using load and displacement sensing indentation experiments, Mater. Res. 7 (1992) 1564–1583.

[49] I.N. Sneddon, Boussinesq's problem for a rigid cone, Proc. Camb. Philos. Soc. 44 (1948) 492–507.

[50] R.B. King, Elastic analysis of some punch problems for layered medium, Int. J. Sol. Struct. 23 (1987) 1657–1664.

[51] R. Rodriguez, I. Gutierrez, Correlation between nanoindentation and tensile properties influence of the indentation size effect, Mater. Sci. Eng. A 361 (2003) 377–384.

[52] G. Palmisano, Eric Le Bourhis, R. Ciriminna, D. Tranchida, M. Pagliaro, ORMOSIL thin films: tuning mechanical properties via a nanochemistry approach, Langmuir 22 (2006) 11158–11162.

[53] Y.T. Cheng, C.M. Cheng, What is indentation hardness?, Surf Coat. Technol. 133 (2000) 417–424.

[54] A. Leyland, A. Matthews, Design criteria for wear-resistant nanostructured and glassy-metal coatings, Surf. Coat. Technol. 177 (2004) 317–324.

[55] A.C. Fischer-Cripps, A simple phenomenological approach to nanoindentation creep, Mater. Sci. Eng. A 385 (2004) 74–82.

[56] A. Rar, S. Sohn, W.C. Oliver, D.L. Goldsby, T.E. Tullis, G.M. Pharr, On the measurement of creep by nanoindentation with continuous stiffness techniques, Mater. Res. Soc. (2005) (Boston, MA, USA).

[57] R. Hill, B. Storakers, A.B. Zdunek, A theoretical study of the Brinell hardness test, Math. Phys. Sci. 423 (1989) 301–330.

[58] S. Biwa, B. Storakers, An analysis of fully plastic Brinell indentation, Mech. Phys. Sol. 43 (1995) 1303–1334.

[59] H. Hertz, Experiments to Determine an Upper Limit for the Kinetic Energy of an Electric Current, Miscellaneous Papers by H. Hertz, Macmillan, 1896.

Progress in Organic Coatings 76 (2013) 459–470

Contents lists available at SciVerse ScienceDirect

Progress in Organic Coatings

journal homepage: www.elsevier.com/locate/porgcoat

ORMOSIL-epoxy coatings with ceramic containers for corrosion protection of magnesium alloys ZK10

I.A. Kartsonakis[a,b,*], A.C. Balaskas[a], E.P. Koumoulos[b], C.A. Charitidis[b], G. Kordas[a]

[a] Sol–Gel Laboratory, Institute of Advanced Materials, Physicochemical Processes, Nanotechnology and Microsystems, NCSR "DEMOKRITOS", 15310 Agia Paraskevi, Greece
[b] School of Chemical Engineering, NTUA, 9 Heroon Polytechniou St., 15780 Zographos, Greece

ARTICLE INFO

Article history:
Received 27 October 2010
Received in revised form 21 October 2012
Accepted 23 October 2012
Available online 1 December 2012

Keywords:
Nanocontainers
Corrosion
Impedance
Epoxy
ORMOSIL
Magnesium

ABSTRACT

This study is focused on corrosion protection of magnesium alloy ZK10. The aim of the research was the production of a hybrid organic–inorganic coating that would be a combination of epoxy resin, organically modified silicates as well as conductive polymer. Furthermore, ceramic containers loaded with corrosion inhibitor were incorporated into the coating for the improvement of its corrosion protection properties. The composition and structure of the coatings were investigated by Fourier transform infrared spectroscopy, energy dispersive X-ray analysis and scanning electron microscopy. Extent of the anti-corrosion protection of the formed coatings was examined electrochemically using electrochemical impedance spectroscopy. The results showed that the incorporation of the containers loaded with inhibitor into the coatings improved their corrosion protection properties. Furthermore, artificial defects of 1 mm were made to the coatings with the best anticorrosive performance in order to study the electrochemical processes taking place in the scratched area and to estimate the effect of the corrosion inhibitor in the corrosion of the substrate.

1. Introduction

Magnesium and its alloys present one of the most promising materials for the transportation industry due to its low density (it is only 65% that of aluminium and 25% that of iron), high strength/weight ratio, recycle ability, good machining and good electromagnetic shielding enabling its use in a wide range of applications [1,2]. On the other hand, engineering applications of magnesium have been limited mainly due to the poor corrosion properties of magnesium [3].

Several coating applications have been developed to improve the corrosion resistance of magnesium and its alloys, such as oxygen plasma anodization [4], electrolytic plasma oxidation [5], inorganic pre-treatments [6,7], ion beam-assisted deposition [8], anodizing process [9], TiO_2 layer as a protective coating [10], polyoxadiazole-based coating [11], etc. The corrosion protection of the aforementioned coatings is based on the synergistic effect of phase composition stability and microstructural integrity [4,5], the high stability of the compounds that constitute the surface oxide layer, the excellent paint adhesion [6–9], the structural evolvement [10] and the hydrophobic groups attached on the coating chains [11].

Hybrid organic–inorganic sol–gel coatings are a very promising way of corrosion protection of magnesium and its alloys. Studies have been made using composite coatings which consist of a molybdate conversion film and three layers of silicon sol–gel coatings [12], with sol–gel coating consists of ethanol, celloidin, cerium nitrate and magnesium nitrate [13] as well as with multilayer sol–gel coatings based on 3-methacryloxypropyl trimethoxysilane, 3-meraptopropyl trimethoxysilane and ethanol [14]. All these composite coatings act as an effective barrier for the penetration of corrosive agents and water.

The improvement of the corrosion protection Mg alloys was achieved by the incorporation of corrosion inhibitors into hybrid organic–inorganic sol–gel coatings [15,16] or organic coatings [17]. The corrosion protection mechanism can be ascribed to the combined function, i.e. strong adsorption on the alloy and compatibility with the matrix. Moreover, various nanoparticles were encapsulated into sol–gel coatings for enhancement of their anti-corrosion properties [18,19]. Furthermore, layered double hydroxide films have been used as coating for corrosion protection of Mg alloys [20].

Apart from the above corrosion protective systems, lots of studies have been focused on protective systems that are based on conductive polymers (CP) such as polyaniline [21] and polypyrrole (PPy) [22–24] together with acrylic based coatings. The reasons are

* Corresponding author at: Sol–Gel Laboratory, Institute of Advanced Materials, Physicochemical Processes, Nanotechnology and Microsystems, NCSR "DEMOKRITOS", 15310 Agia Paraskevi, Greece. Tel.: +30 2106503304; fax: +30 2106547690.
E-mail address: ikartsonakis@ims.demokritos.gr (I.A. Kartsonakis).

0300-9440/$ – see front matter © 2012 Elsevier B.V. All rights reserved.
http://dx.doi.org/10.1016/j.porgcoat.2012.10.028

Table 1
The % w/w nominal composition of MgZK10.

Element	Magnesium	Zinc	Manganese	Zirconium	Rhenium
wt%	97.45–97.95	1.35–1.45	≤0.25	0.5–0.6	0.2–0.25

that CP can act as a barrier coating, as a reservoir of inhibiting ions, as a stabilizer of a passive layer and as a sacrificial anode [22].

In the present work, we report the corrosion protection of ZK10 magnesium alloy using a hybrid organic–inorganic coating. In order the corrosion properties of the coating to be improved, PPy and TiO_2 containers loaded with corrosion inhibitor 2-mercaptobenzothiazole (2-MB) [17,25,26] were incorporated into the coating. The study encompasses the investigation of each parameter (conductive polymer, containers, inhibitor) contribution to the corrosion protection of the substrate as well as a demonstration of coatings' mechanical properties.

2. Experimental procedure

2.1. Materials and reagents

Magnesium alloy ZK10 with the nominal mass composition of Table 1 was obtained from Alubin-Israel [27]. All chemicals were of analytical reagent grade. 2-Mercaptobenzothiazole (2-MB, Sigma–Aldrich, St. Louis, USA), titanium tetraisopropoxide (TTIP, Sigma–Aldrich, St. Louis, USA), polyvinylpyrrolidone (PVP, average molecular weight: 55,000, Sigma–Aldrich, St. Louis, USA), sodium chloride (NaCl, Sigma–Aldrich, St. Louis, USA), 2,2′-Azobis (2-methylpropionamidine) dihydrochloride (AMPA, Sigma–Aldrich, St. Louis, USA), absolute ethanol (Sigma–Aldrich, St. Louis, USA), cerium(IV) sulfate [$Ce(SO_4)_2$, Sigma–Aldrich, St. Louis, USA], lignosulfonic acid (Sigma–Aldrich, St. Louis, USA), N-(2-Aminoethyl)-3-(trimethoxysilyl)propylamine (Z 6020, Sigma–Aldrich, St. Louis, USA), epoxy resin "Araldite GY 257" (GY 257, Ciba-Geigy), 2,2′-Diaminodiethylamine (HY 943, Sigma–Aldrich, St. Louis, USA) were used without further purification. Pyrrole (Sigma–Aldrich, St. Louis, USA) and styrene (Sigma–Aldrich, St. Louis, USA) were double distilled under reduced pressure prior to use.

2.2. Synthesis of TiO_2 containers loaded with 2-MB

Titania containers were prepared and loaded with corrosion inhibitor 2-MB, according to our previous work [38]. They were synthesized through a two-step process. First, cationic charged polystyrene (PS) nanospheres were prepared using polymerization in suspension. Second, these PS lattices were coated via the sol–gel method to form a titanium oxide layer. The composite was heat treated in air at 600 °C, to burn off the PS latex. Furthermore, the obtained titania containers were loaded with the corrosion inhibitor 2-MB, using saturated solutions of 2-MB in acetone into a sealed vessel under vacuum conditions.

2.3. Preparation of organically modified silicates (ORMOSIL) coating

2.3.1. Synthesis of PPy

Polymerization of pyrrole was carried out in a 250-cm^3 reactor under the condition listed in Table 2. $Ce(SO_4)_2$ was used as the oxidant and lingo as the doping agent. The polymerization process lasted for 12 h. The resulting dispersions were centrifuged at 7000 rpm for 20 min, the supernatant solutions were discarded, and then the particles were resuspended in ethanol using a sonicator. This process was repeated three times. Fig. 1 depicts the SEM of the synthesized material.

Table 2
The conditions used in the preparation of polypyrrole at 5 °C.

Material	Quantity (g)
Pyrrole	0.67
$Ce(SO_4)_2$	1.49
Lignosulfonic acid	1.25
Water	60

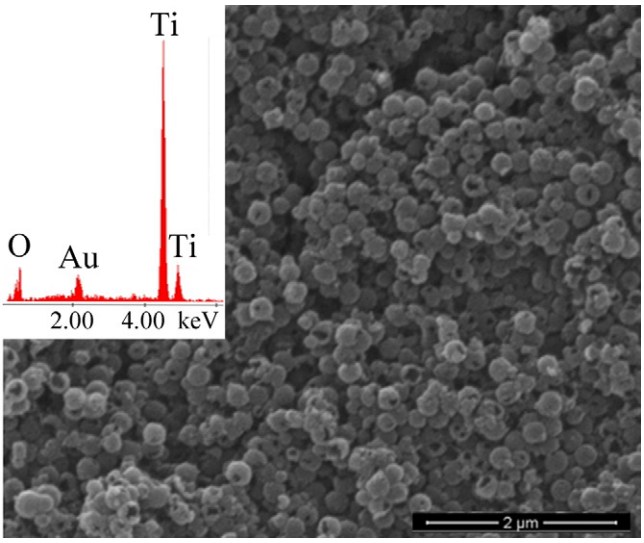

Fig. 1. SEM and EDAX analysis of TiO_2 containers.

2.3.2. Synthesis of coating

The process for the preparation of the ORMOSIL-epoxy coating incorporating PPy and TiO_2 containers loaded with 2-MB, includes 6 steps (Table 3). First of all, N-(2-aminoethyl)-3-(trimethoxysilyl)propylamine is hydrolyzed in absolute ethanol for 1 h (solution A). Then, resin Araldite GY 257 is dissolved in absolute ethanol (solution B). A solution of PPy in acetone is intermixed with solution B (solution C). Solutions A and C are intermixed formatting solution D. After that, 2.2′-diaminodiethylamine is dissolved in 25 ml acetone (solution E). Finally, solutions D and E are intermixed and stirred for 8 h. The loaded containers of TiO_2 (1%, w/v) are added to the above solution, under vigorous stirring, 1 h before the beginning of the dip coating process.

2.4. Application of the coating

The panels were dip coated into the ORMOSIL-CP-container solution for six times with a withdraw rate of 32 cm/min. The panels remained in the solution for 1 min. Then, the coated panels were heat treated at 80 °C for 15 min. The ZK10 magnesium alloys panels were previously thoroughly cleaned, under specific conditions. These conditions include the insertion of the panels into 96% (v/v) ethanol for 20 min at room temperature, under sonication. After that, the panels were rinsed with distilled water and inserted into

Table 3
The conditions used in the preparation of ORMOSIL coating.

Material	Quantity (g)
N-(2-aminoethyl)-3-(trimethoxysilyl)propylamine	3.6
Araldite GY 257	41.68
Polypyrrole	0.7
2,2′-Diaminodiethylamine	4.44
Absolute ethanol	120
Acetone	90

a degreaser solution (mixture of sodium hydroxide and sodium carbonate in water) for 10 min at 70 °C. Then, the panels were inserted in distilled water for a few minutes at 40 °C. The next step includes the insertion of the panels in hydrofluoric acid 10% (w/w) for 20 min at room temperature. Finally, the panels were rinsed with distilled water and left to dry in air.

2.5. Characterization

The morphology of the coatings and the average container size were determined by Scanning Electron Microscopy (SEM) using a PHILIPS Quanta Inspect (FEI Company) microscope with W (tungsten) filament 25 kV equipped with energy dispersive X-ray analyser (EDAX GENESIS, AMETEX PROCESS & ANALYTICAL INSTRUMENTS). Furthermore, the coatings were characterized by Reflectance Infrared Spectroscopy using a Perkin Elmer universal ATR sampling accessory spectrum 100 FT-IR spectrometer. Moreover, the corrosion resistance of these coatings was studied via electrochemical impedance spectroscopy (EIS) using a SI 1287 Solartron Electrochemical Interface connected with a SI 1260 Impedance/gain-phase analyser. Open circuit potential (OCP) studies were made using a Solartron 1470 PGstat electrochemical interface instrument. Scratch tests were performed using a Rockwell indenter equipped with diamond (radius: 200 μm). Finally, micro hardness measurements were taken using a Shimadzu microhardness tester HMV-2. The indenter was a diamond in a pyramid shape with 136° angle between the opposite sides. The loading of the inhibitor into the containers was estimated by thermogravimetric analysis (TGA) using a Perkin Elmer (Pyris Diamand S II) analyzer at the heating rate of 10 °C min^{-1} in air.

3. Results and discussion

3.1. TiO_2 containers

Fig. 1 depicts the produced TiO_2 containers. Their shape is spherical and their size is 250 ± 20 nm. The EDX analysis confirmed that the basic constituents of the containers were titanium and oxygen. Gold appears due to the coating applied to the spheres in order to be conductive for the SEM measurement.

Fig. 2 presents the TGA diagrams of empty titania containers, pure 2-MB and titania containers loaded with 2-MB. The absence of any weight loss in the spectrum of empty titania containers denotes that they do not contain organic residuals from their synthetic route. Both spectra of pure 2-MB and titania containers loaded with 2-MB demonstrate weight losses after 200 °C, corresponding to oxidative degradation of the inhibitor. Furthermore, the TGA diagram of TiO_2 containers loaded with 2-MB depicts a sharp weight loss between 200 °C and 330 °C which is due to the burn off of the inhibitor that is on the shell and into the pores of the shell of the containers. The other two weight losses between 330 °C and 430 °C as well as between 430 °C and 550 °C correspond to the degradation of the inhibitor that is inside the shell. Finally, the TiO_2 containers are 73.99% (w/w) loaded with the inhibitor 2-MB because the total weight loss between 200 °C and 550 °C is 4.462 mg that corresponds to 73.99% mass loss percentage.

3.2. Corrosion test

All coated panels were exposed to 5 mM NaCl solution for 3–288 h (12 days). The exposed area was 2 cm^2. EIS was used in order the protective abilities and the corrosion protection mechanism of the coated samples to be evaluated [30]. Fig. 3 depicts EIS bode plots of coating including PPy and TiO_2 containers loaded with inhibitor (ORMOSIL-epoxy-PPy-TiO_2-2MB), coating including TiO_2 containers loaded with inhibitor (ORMOSIL-epoxy-TiO_2-2MB), coating including PPy and empty TiO_2 containers (ORMOSIL-epoxy-PPy-TiO_2), coating including PPy and inhibitor (ORMOSIL-epoxy-PPy-2MB), coating including PPy (ORMOSIL-epoxy-PPy), coating with neither inhibitor, nor containers, nor PPy (ORMOSIL-epoxy) and Bare MgZK10, after exposure at 5 mM NaCl solution at room temperature for 24 h. The impedance at low frequencies corresponds to the polarization resistance of the coatings

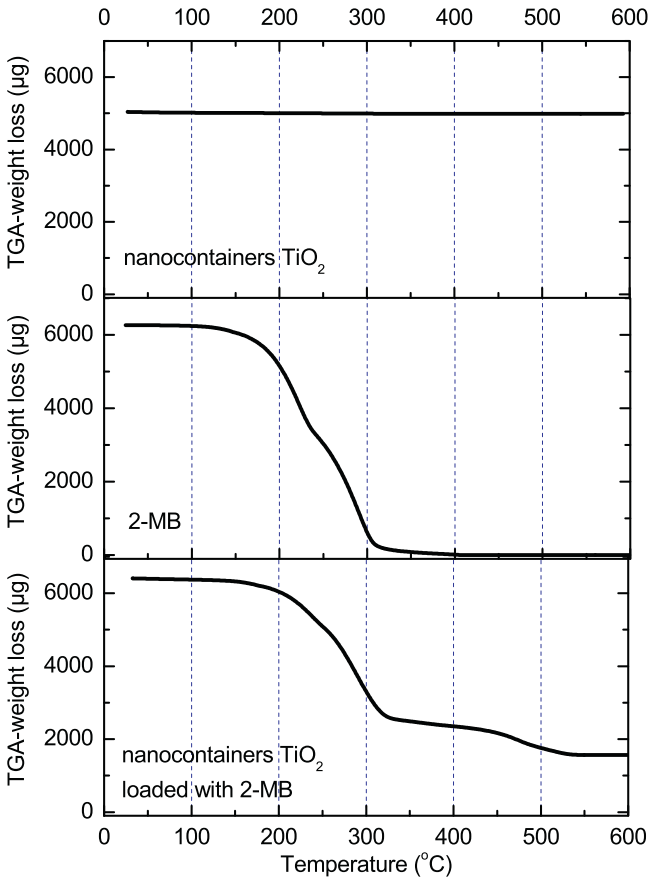

Fig. 2. TGA curve of empty TiO_2 containers, pure 2-MB and TiO_2 containers loaded with 2-MB.

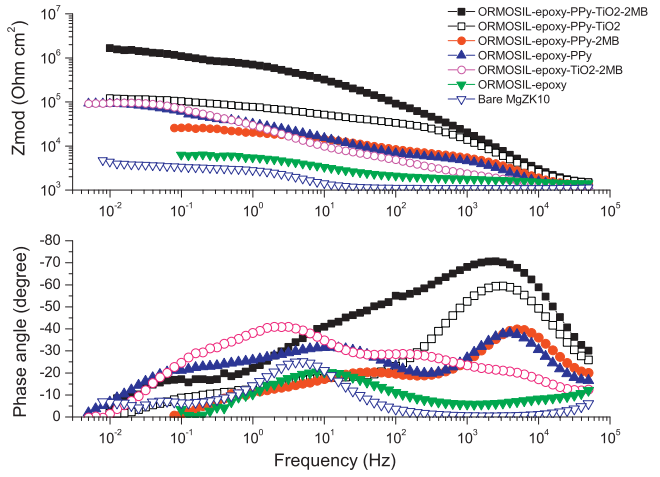

Fig. 3. EIS bode plots of samples: (■) ORMOSIL-epoxy-PPy-TiO_2-2MB, (□) ORMOSIL-epoxy-PPy-TiO_2, (●) ORMOSIL-epoxy-PPy-2MB, (▲) ORMOSIL-epoxy-PPy, (○) ORMOSIL-epoxy-TiO_2-2MB, (▼) ORMOSIL-epoxy, (▽) Bare MgZK10 after exposure at 5 mM NaCl solution at room temperature for 24 h.

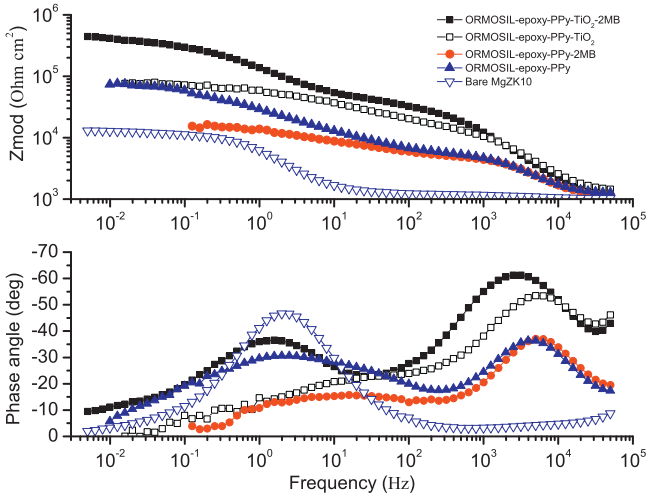

Fig. 4. EIS bode plots of samples: (■) ORMOSIL-epoxy-PPy-TiO_2-2MB, (□) ORMOSIL-epoxy-PPy-TiO_2, (●) ORMOSIL-epoxy-PPy-2MB, (▲) ORMOSIL-epoxy-PPy, (▽) Bare MgZK10 after exposure at 5 mM NaCl solution at room temperature for 12 days.

and therefore can be used to estimate the corrosion protection. The impedance values at low frequencies denote that the coating including PPy and TiO_2 containers loaded with inhibitor (ORMOSIL-epoxy-PPy-TiO_2-2MB) presented the best corrosion protection as it had the highest absolute total impedance value.

The less corrosion protection was carried out by the coating that consists of ORMOSIL and epoxy resin (ORMOSIL-epoxy). The addition of PPy to the coating (ORMOSIL-epoxy-PPy) increased the absolute total impedance value more than one order of magnitude compare to ORMOSIL-epoxy coating and proved that PPy was an important factor for the improvement of the corrosion protection of the coating. Furthermore, the coating including both PPy and empty containers (ORMOSIL-epoxy-PPy-TiO_2) increased its barrier properties and improved its anticorrosive properties, as it can be seen from the time constant in the high frequency range. Finally, the coating including TiO_2 containers loaded with 2-MB without PPy (ORMOSIL-epoxy-TiO_2-2MB), also demonstrated an improved corrosion protection but this protection was less effective compare to the corresponding one of the coating including both PPy and TiO_2 containers loaded with 2-MB (ORMOSIL-epoxy-PPy-TiO_2-2MB). It can be seen from Fig. 3 that the absolute total impedance value of ORMOSIL-epoxy-PPy-TiO_2-2MB is one order of magnitude higher than the corresponding one of ORMOSIL-epoxy-TiO_2-2MB. It should be mentioned that the coatings ORMOSIL-epoxy-PPy-TiO_2-2MB, ORMOSIL-epoxy-PPy-TiO_2 and ORMOSIL-epoxy-PPy-2MB are thicker than the coating ORMOSIL-epoxy-PPy (Fig. 14). The thickness of a coating is one of the factors that contribute to its enhanced barrier properties.

Fig. 4 illustrates the impedance spectra of ORMOSIL-epoxy-PPy-TiO_2-2MB, ORMOSIL-epoxy-PPy-TiO_2, ORMOSIL-epoxy-PPy-2MB, ORMOSIL-epoxy-PPy and Bare MgZK10, after 12 days. Considering the low frequency region of the spectra, it is clearly denoted that the sample ORMOSIL-epoxy-PPy-TiO_2-2MB offered a protection to the magnesium alloy for more than 288 h (12 days). On the other hand, lower anticorrosive properties were demonstrated by the sample ORMOSIL-epoxy-PPy-TiO_2. The absolute total impedance value was half an order of magnitude lower than the one of ORMOSIL-epoxy-PPy-TiO_2-2MB. This result confirms that the coating including empty containers is less protective than the coating including containers loaded with inhibitor 2MB. So, the loading of containers offers more effective corrosion protective coatings. Furthermore, the sample ORMOSIL-epoxy-PPy demonstrated diminished anticorrosive properties.

The sample ORMOSIL-epoxy-PPy-2MB does not include containers. It has only free inhibitor 2-MB incorporated into the coating. This sample was studied in order the role of the corrosion inhibitor alone into the coating to be estimated. In spite of the fact that there were no data at the low frequency range ($\leq$0.1 Hz) for the sample ORMOSIL-epoxy-PPy-2MB, its very low absolute total impedance values revealed inadequate corrosion protection of the magnesium alloy. In addition, the free incorporation of the inhibitor into the coating including PPy (ORMOSIL-epoxy-PPy-2MB) presented less protection to the metal alloy than the coating including PPy without inhibitor (ORMOSIL-epoxy-PPy).

Considering the results from Figs. 3 and 4, it is clearly denoted that only the coating including both PPy and TiO_2 containers loaded with inhibitor presents the most effective corrosion protection to magnesium alloy ZK10. As the protective system is complicated the contribution of each factor to the improvement of the anticorrosive properties of the coating has to be clarified. At first, the coherence of the coating is not affected by the presence of the inhibitor because the inhibitor is stored into containers and not free dispersed into the coating. Another reason is that the addition of PPy into the coating improves its coherence due to the reaction of the secondary amines of PPy with the epoxy groups of the resin [31]. Furthermore, PPy acts as a corrosion inhibitor. In aqueous solutions, magnesium is dissociated by the electrochemical reaction with water and a crystalline film of magnesium hydroxide, $Mg(OH)_2$, as well as hydrogen gas are produced. The overall corrosion reaction for magnesium in aqueous solutions is

$$Mg(s) + 2H_2O(l) \rightarrow Mg(OH)_2(s) + H_2(g).$$

This overall reaction can be described in terms of anodic and cathodic reactions as follows:

$$Mg \rightarrow Mg^{+2} + 2e^-$$

and/or

$$Mg(s) + 2(OH)^- \rightarrow Mg(OH)_2(s) + 2e^- \text{ (anodic reaction, dissolution of Mg)}$$

and

$$2H^+ + 2e^- \rightarrow H_2(g) \text{ (cathodic reaction evolution of hydrogen gas).}$$

A subsequent reaction, giving OH^-, can occur,

$$2H_2O + 2e^- \rightarrow H_2(g) + 2(OH)^-.$$

The produced hydroxide film, brucite, has a hexagonal crystalline structure that is layered, alternating between Mg and hydroxide ions facilitating easy basal cleavage [32]. It is known that CPs can interact with ions such as Cl^- and OH^- through ion exchange with the dopant. This would reduce the concentration of Cl^- and OH^- in the defect and thus slow down the corrosion reactions [33]. Moreover, PPy has the advantage of tolerance to microdefects and minor scratches as it is electronically conducting. So, PPy can repassivate any exposed areas of metal where there are defects in the passive film [34].

It is believed that the inhibitor is released from the containers though diffusion unless the containers are broken by a scratch on the coating. 2-mercaptobenzothiazole contains S and N atoms in the organic ring. It is believed that 2-MB is attached to the magnesium through the S or N atoms that may change the electron density in the metal at the point of attachment. This results in the retardation of cathodic or anodic reaction of corrosion of magnesium (as described above) since electrons are consumed at the cathode and furnished at the anode [25].

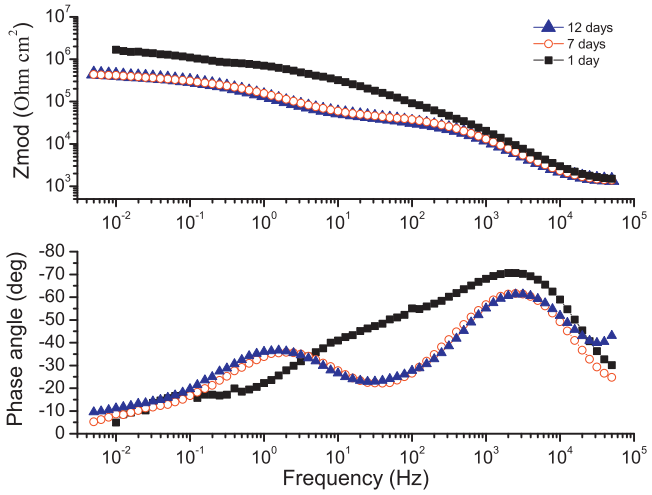

Fig. 5. EIS bode plots of the sample ORMOSIL-epoxy-PPy-TiO_2-2MB after exposure at 5 mM NaCl solution at room temperature for: (■) 1 day, (○) 7 days, (▲) 12 days.

Fig. 5 depicts the Bode plots of the EIS spectra obtained for the sample ORMOSIL-epoxy-PPy-TiO_2-2MB, after 1, 7 and 12 days. The impedance spectra present three time constants. At high frequencies are the resistance and the capacitance of the sol–gel coating (R_{coat} and C_{coat} respectively), at the midterm frequency range between 1 and 10 Hz are the resistance and the capacitance of the oxide layer (R_{oxide} and C_{oxide} respectively) that correspond to MgO, and the third constant around 0.1–0.01 Hz is ascribed to the initiation of the corrosion attack and is attributed to the existence of the double layer capacitance at the metal–electrolyte interface, C_{dl} and the corresponding polarization resistance R_{pol}. The time constant at high frequency range can be still clearly seen after 12 days of immersion to corrosive environment denoting that the coating retains its good barrier properties.

The experimental impedance spectra were fitted using equivalent circuits in order to provide adequate modelling of the physicochemical processes on the coated substrate during corrosion tests. Fig. 6 shows the equivalent circuit used to simulate the impedance spectroscopy measurements of the coatings. This type equivalent circuit consists of seven components. R_{sol} is the resistance of the NaCl solution and is placed in series with all other elements of the equivalent circuit. Constant phase elements instead of capacitances were used for fitting of all the bare and coated samples. This modification is obligatory in the case the phase shift of a capacitor is different from −90° [35]. The impedance of the CPE depends on frequency according to the following equation: $1/Z = Q(j\omega)^n$ where Z is the impedance, Q a parameter numerically equal to admittance $(1/|Z|)$ at $\omega = 1\ rad^{-1}$, ω the frequency, and n a power coefficient calculated as ratio of phase angle at maximum of corresponding time constant to −90° [36]. The capacitance values for coating, oxide and double layer elements can be calculated using the equation: $C = (Q\omega_{max})^{n-1}$, where ω_{max} is the frequency at which the imaginary impedance reaches a maximum for the respective time constant [35].

Fig. 7 shows the resulting fitting parameters as a function of the time of the exposure in 5 mM NaCl solution at room temperature. Table 4 summarizes the results of the fitted parameters obtained by fitting the measurements for different times of immersion. The results presented that R_{coat} of ORMOSIL-epoxy-PPy-TiO_2-2MB has higher values compare to R_{coat} of ORMOSIL-epoxy-PPy. Furthermore, C_{coat} exhibits higher values for ORMOSIL-epoxy-PPy compare to ORMOSIL-epoxy-PPy-TiO_2-2MB. R_{coat} of ORMOSIL-epoxy-PPy-TiO_2-2MB is reduced during the first days of immersion. This observation is due to the penetration of water molecules and

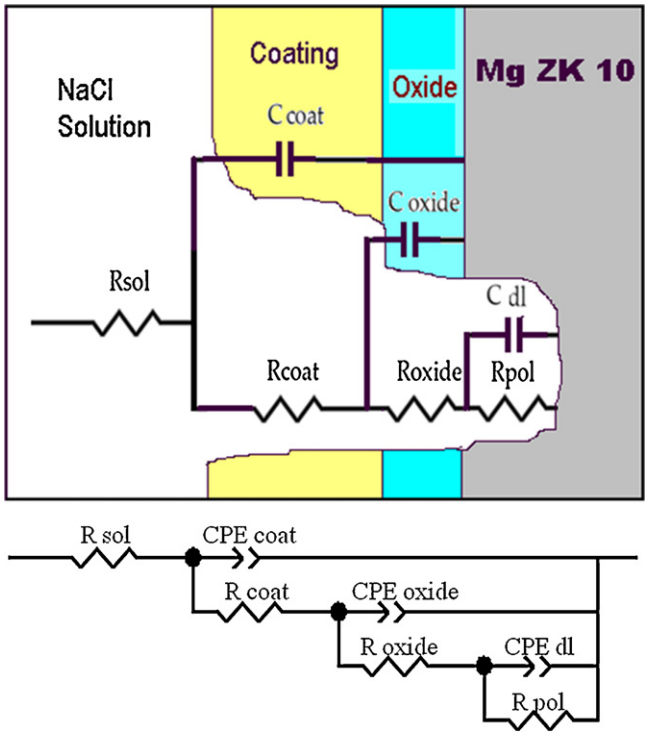

Fig. 6. Schematic representation of the physical meaning and corresponding equivalent circuit used for fitting experimental EIS spectra of MgZK10 coated samples.

chloride ions into the coating from the pores of the coatings [16,37]. Furthermore, R_{oxide} is the resistance of the intermediate oxide layer between the coating and the substrate. In the case of the coating ORMOSIL-epoxy-PPy-TiO_2-2MB R_{oxide} is also decreased during the first days of immersion due to the degradation of MgO layer. On the other hand, an increase of R_{oxide} is observed after two days of immersion due to the formation of a new layer of $Mg(OH)_2$. This layer is formed by the reaction

$$Mg^{2+} + 2OH^- \rightarrow Mg(OH)_2\ [37].$$

Fig. 7d shows R_{pol} of the two coatings as a function of exposure in 5 mM NaCl solution indicating the rate of corrosion process. One can perceive from this figure that the two coatings exhibit different behaviour. The ORMOSIL-epoxy-PPy shows a declining behaviour with the time of exposure in 5 mM NaCl solution. The ORMOSIL-epoxy-PPy-TiO_2-2MB sample shows a reduction of R_{pol} up to 72 h reaching the R_{pol} of ORMOSIL-epoxy-PPy and then R_{pol} is improved with the time still until 288 h of immersion in the 5 mM NaCl solution. This may be attributed to the continuing release of 2MB from the ceramic containers providing extended protection of the magnesium substrate. The containers function as a storage of inhibitors releasing it to the substrate when corrosion is induced by an external cause.

Artificial defects of 1 mm were made to the coatings ORMOSIL-epoxy-PPy-TiO_2-2MB, ORMOSIL-epoxy-PPy and ORMOSIL-epoxy in order to study the electrochemical processes taking place in the scratched area and to estimate the effect of the corrosion inhibitor in the corrosion of the substrate. Fig. 8 shows the variations of the open circuit potential (OCP) of the aforementioned coatings with time in 5 mM NaCl solution at room temperature for 24 h, respectively. The exposed area of all the samples for the OCP corrosion tests was 2 cm^2. All the three curves present OCP fluctuations with time, indicating pitting corrosion initiation and re-passivation. Under the experimental condition, it can be distinguished from the obtained curves that the OCP for ORMOSIL-epoxy-PPy-TiO_2-2MB,

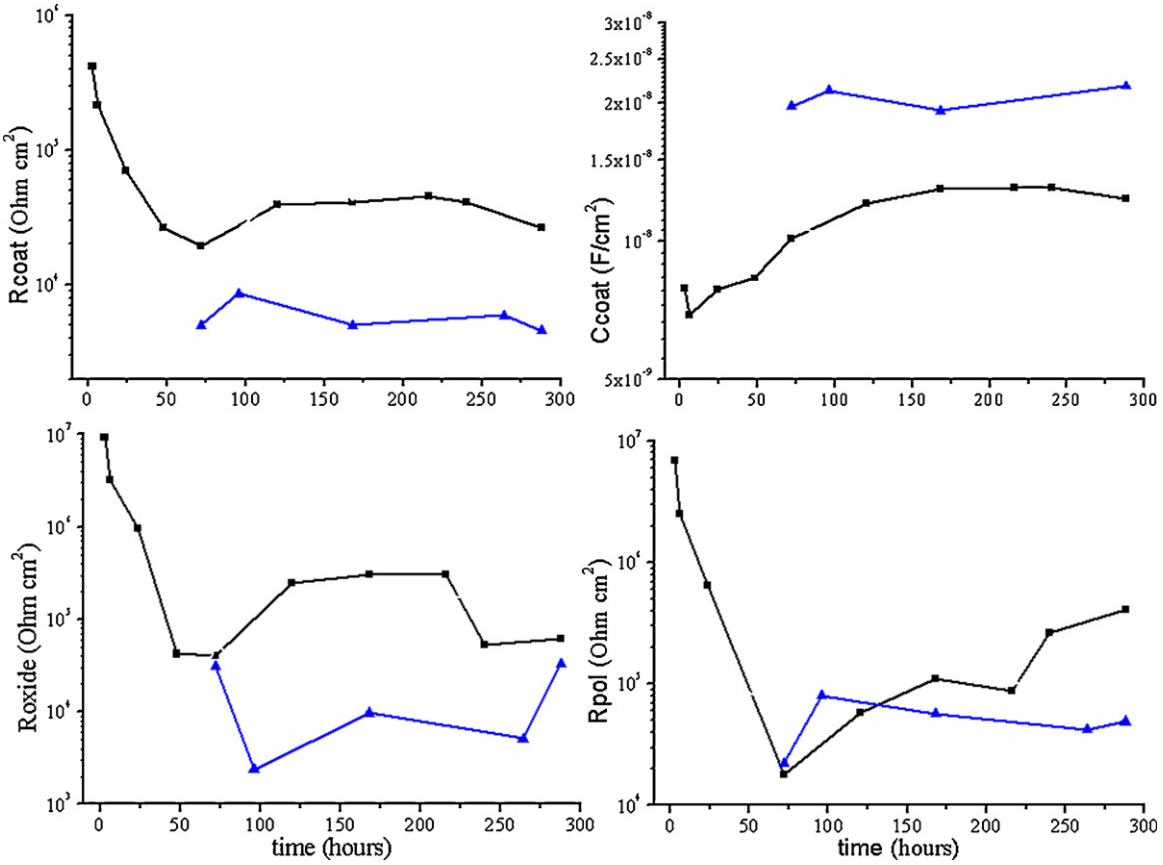

Fig. 7. Evolution of: (a) R_{coat}, (b) C_{coat}, (c) R_{oxide} and (d) R_{pol}, of samples: (■) ORMOSIL-epoxy-PPy-TiO_2-2MB, (▲) ORMOSIL-epoxy-PPy after exposure at 5 mM NaCl solution at room temperature for 12 days.

Table 4
Calculated values for EIS data obtained at different immersion times.

	Time (h)	R_{coat} (Ω cm^2)	C_{coat} (F cm^{-2})	R_{oxide} (Ω cm^2)	R_{pol} (Ω cm^2)
ORMOSIL-epoxy-PPy-TiO_2-2MB	72	1.95E+4	1.01E−8	4.03E+4	1.80E+4
	168	4.10E+4	1.30E−8	3.06E+5	1.10E+5
	288	3.97E+4	1.44E−8	3.25E+5	1.92E+5
ORMOSIL-epoxy-PPy	72	4.98E+3	1.97E−8	3.11E+4	2.24E+4
	168	4.98E+3	1.98E−8	9.69E+3	5.64E+4
	288	5.05E+3	2.28E−8	3.84E+3	7.99E+4

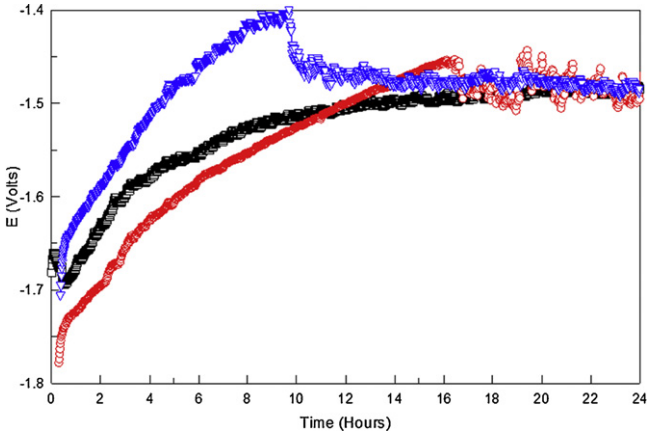

Fig. 8. OCP of coatings with artificial defects: (▽) ORMOSIL-epoxy-PPy-TiO_2-2MB, (○) ORMOSIL-epoxy-PPy and (□) ORMOSIL-epoxy.

shifts in the anodic direction and reaches −1.40 V after 10 h. Then it fluctuates between −1.45 V and −1.50 V. Also, the OCP for ORMOSIL-epoxy-PPy shifts in the anodic direction but it reaches −1.45 V after 16 h and then it fluctuates between −1.45 V and −1.52 V. The OCP of ORMOSIL-epoxy shifts in the anodic direction and reaches −1.5 V after 24 h. In spite of the fact that the OCP values do not provide any direct information on the corrosion kinetics, the initial high increase of OCP for the ORMOSIL-epoxy-PPy-TiO_2-2MB coating suggests reduction of susceptibility of the coating to corrosion process due to the presence of the inhibitor.

3.3. Morphology and chemical composition

Fig. 9 shows visual photographs of the coatings. All the samples have been exposed at 5 mM NaCl solution at room temperature. Fig. 9a presents the surface of bare MgZK10 after its exposure for 14 days (inside the circle). It can be seen from this photograph that the colour of the substrate has been totally changed and big black stains have been formed. The exposed surface seems to have been completely destroyed compare to the non-exposed

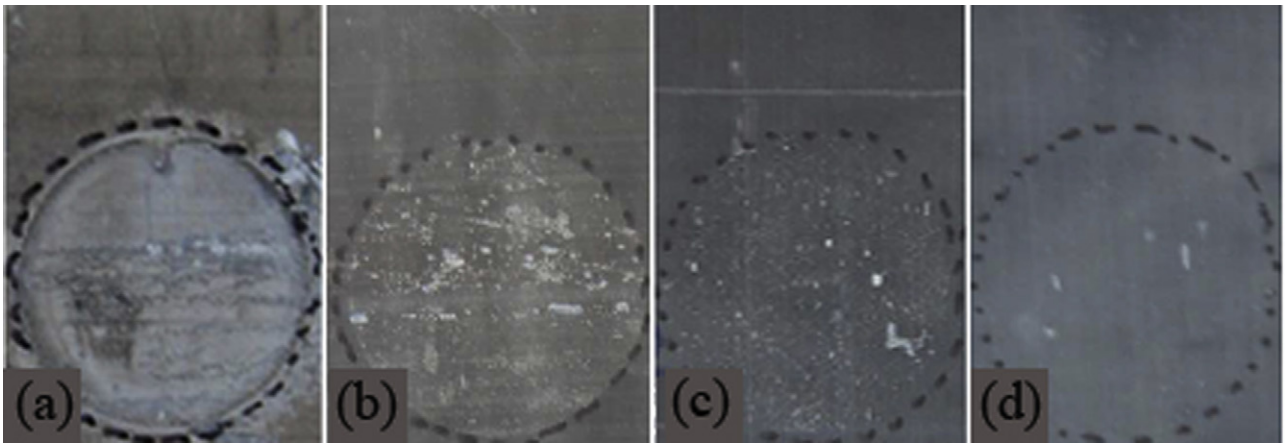

Fig. 9. Visual photographs of samples after exposure at 5 mM NaCl solution at room temperature: (a) Bare MgZK10 for 14 days, (b) ORMOSIL-epoxy-PPy for 14 days, (c) ORMOSIL-epoxy-PPy-TiO_2 for 14 days, (d) ORMOSIL-epoxy-PPy-TiO_2-2MB for 18 days.

surface (outside the circle). Fig. 9b and c presents the sample ORMOSIL-epoxy-PPy and ORMOSIL-epoxy-PPy-TiO_2 (Table 5), respectively, after their exposure at corrosive environment for 14 days. The exposed area of these samples contains lots of stains. On the other hand, their surfaces have been less destroyed compare to the bare MgZK10 sample. In Fig. 9d, the surface of sample ORMOSIL-epoxy-PPy-TiO_2-2MB is presented after its exposure at corrosive environment for 18 days. Despite the fact that this sample has been exposed 4 more days than the other three samples, its surface has fewer pits.

The SEM and EDX analysis images of the surface of bare MgZK10, ORMOSIL-epoxy-PPy and ORMOSIL-epoxy-PPy-TiO_2

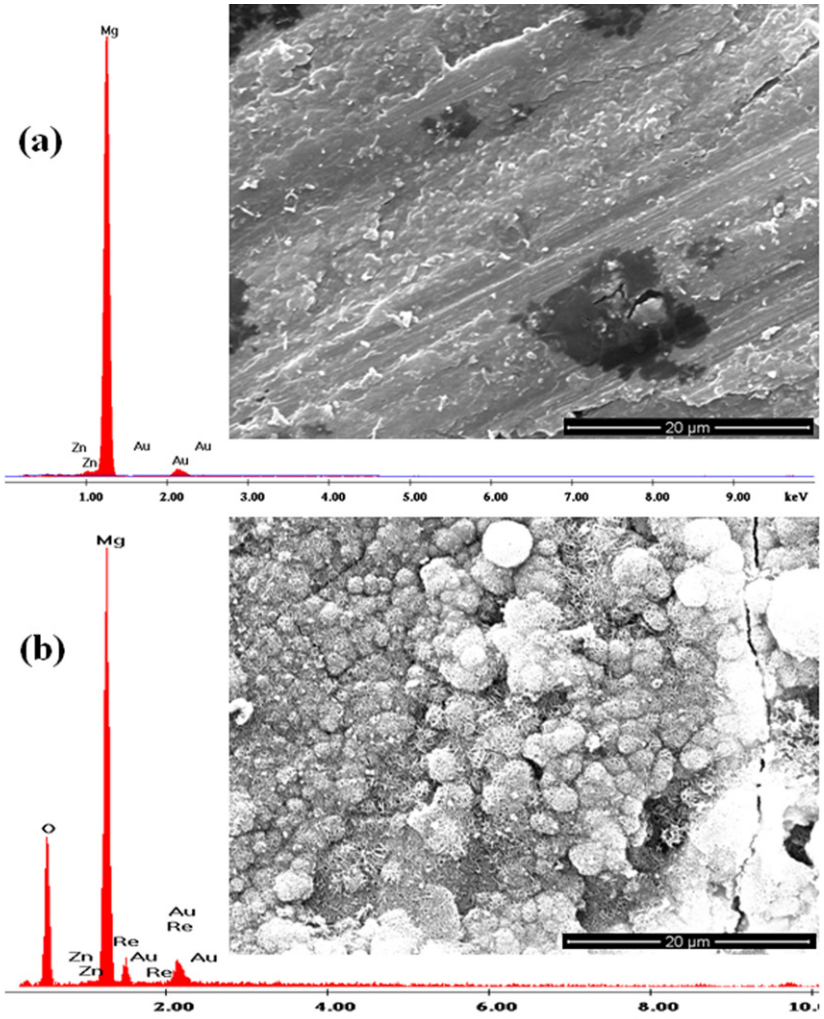

Fig. 10. SEM and EDX analysis of: (a) Bare MgZK10, (b) Bare MgZK10 after exposure at 5 mM NaCl solution at room temperature for 14 days.

Table 5
The parameters of the coatings that were applied to the magnesium substrates.

Sample	Parameters
ORMOSIL-epoxy	Coating
ORMOSIL-epoxy-PPy	Integrated coating
ORMOSIL-epoxy-PPy-2MB	Integrated coating including free inhibitor
ORMOSIL-epoxy-PPy-TiO_2	Integrated coating including empty nanocontainers
ORMOSIL-epoxy-PPy-TiO_2-2MB	Integrated coating including nanocontainers loaded with inhibitor
ORMOSIL-epoxy-TiO_2-2MB	Coating including nanocontainers loaded with inhibitor

-2MB, before and after their exposure at 5 mM NaCl solution at room temperature, are presented in Figs. 10–12. Samples bare MgZK10 and ORMOSIL-epoxy-PPy have been exposed for 14 days and sample ORMOSIL-epoxy-PPy-TiO_2-2MB has been exposed for 18 days. Symbols (a) and (b) refer to images of the samples before and after their exposure to corrosive environment. The surface of bare MgZK10 is illustrated in Fig. 10. This sample has been undergone only thermal treatment in order to be comparable to the coated samples. It can be seen from EDX diagrams that the main element is magnesium. Rhenium and zinc are also present but in much less concentration (Table 6). These results are in correspondence with the theoretical % w/w concentration of magnesium

Table 6
The % w/w element concentration of Bare MgZK10.

Element	Magnesium	Zinc	Rhenium	Oxygen	Gold
wt%	87.77	2.04	0.80	–	9.40
wt%[a]	50.43	1.01	0.72	39.13	8.72

[a] After being exposed to corrosive environment.

alloy ZK10 (Table 1). Moreover, the concentration of oxygen has been increased after corrosion process (Table 6) due to formation of magnesium oxide and magnesium hydroxide. The surface morphology of bare MgZK10 changed after the exposure of the sample to corrosive environment and became rougher (Fig. 10a and b).

The morphology of ORMOSIL-epoxy-PPy surface is presented in Fig. 11a. Small white stains of silicon oxide are observed. The surface is smoother compare to Bare MgZK10. Small cracks were formed after the corrosion process (Fig. 11b), but the surface was not completely destroyed. EDX analysis confirmed the application of the coating on the substrate due to the appearance of carbon, oxygen and silicon. Furthermore, the concentration of oxygen was slightly increased after the corrosion process indicating that new magnesium oxide or magnesium hydroxide was formed on the surface (Table 7).

Fig. 12 illustrates the surface morphology of sample ORMOSIL-epoxy-PPy-TiO_2-2MB. The surface contains pits and white stains of silicon oxides and titanium oxides can be observed. Cracks were

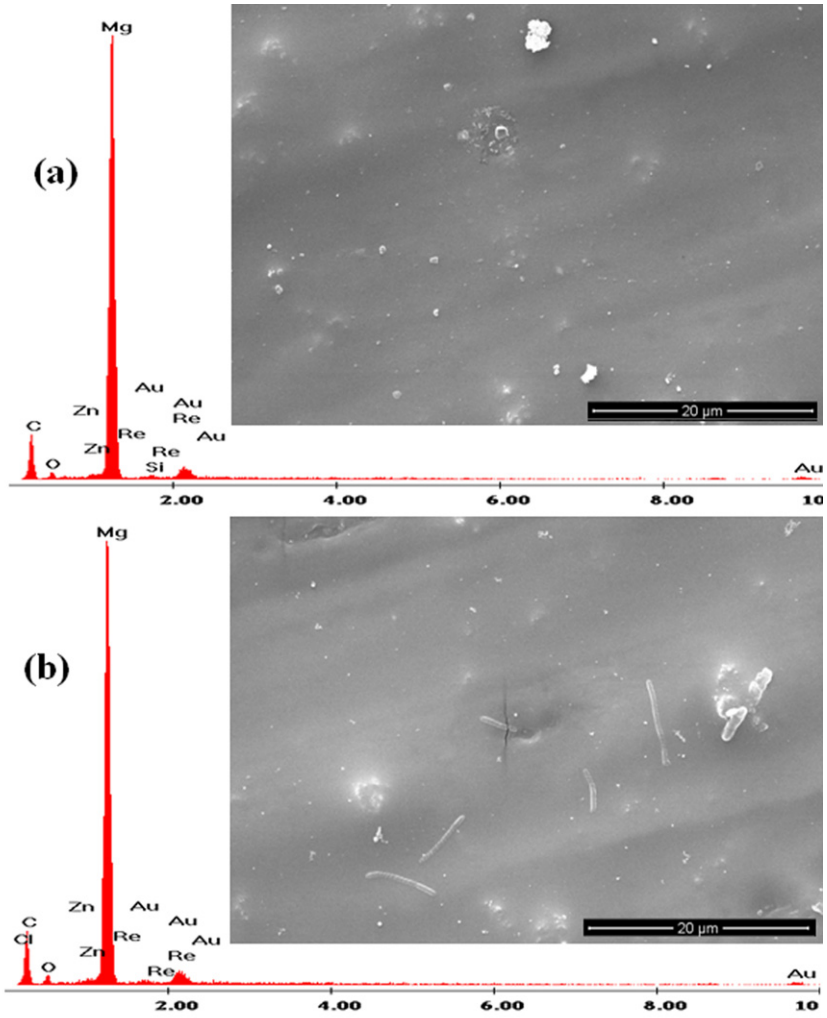

Fig. 11. SEM and EDX analysis of: (a) ORMOSIL-epoxy-PPy, (b) ORMOSIL-epoxy-PPy after exposure at 5 mM NaCl solution at room temperature for 14 days.

Table 7
The % w/w element concentration of ORMOSIL-epoxy-PPy.

Element	Mg	Zn	Re	O	Mn	C	Si	Au
wt%	41.27	0.85	0.24	3.14	0.00	48.60	0.32	5.58
wt%[a]	38.90	0.87	0.12	4.23	0.00	50.70	0.00	5.18

[a] After being exposed to corrosive environment.

Table 8
The % w/w element concentration of ORMOSIL-epoxy-PPy-TiO_2-2MB.

Element	Mg	Zn	Re	O	Mn	C	Si	S	Ti	Au
wt%	27.43	0.40	0.00	5.67	2.91	52.14	0.56	0.54	4.49	9.40
wt%[a]	30.08	0.53	0.28	6.43	3.33	48.63	0.57	0.51	4.17	5.49

[a] After being exposed to corrosive environment.

formed after the exposure of the sample to corrosive environment, but the surface was not completely destroyed. EDX diagram revealed that the coating contained containers of titanium oxide due to the remarkable concentration of titanium (Table 8). Moreover, sulfur was appeared due to the presence of inhibitor 2-MB that has been encapsulated into the containers. No significant increase of oxygen concentration was observed after the corrosion test.

The mapping of element titanium (white colour) of the sample ORMOSIL-epoxy-PPy-TiO_2-2MB is demonstrated in Fig. 13. The element titanium refers to TiO_2 containers. It can be seen that

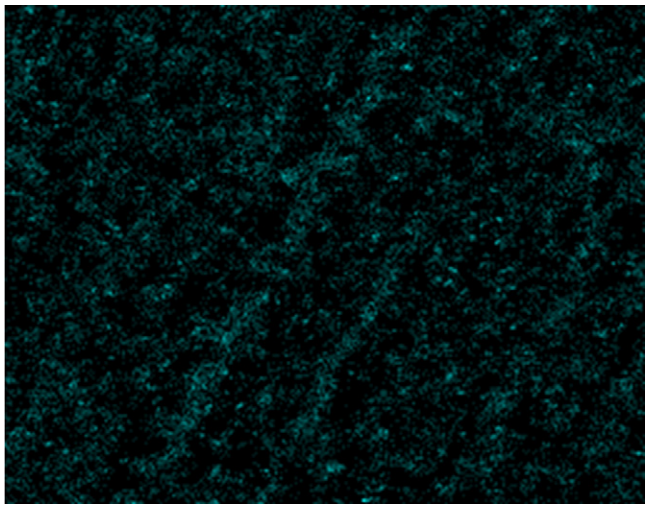

Fig. 13. Mapping SEM of MgZK10 alloy coated with ORMOSIL-epoxy-PPy-TiO_2-2MB.

the dispersion of the titania containers into the coating is very good. Apart from all the above estimations, the thickness of all the coatings was measured, additionally. Fig. 14 depicts that the thickness of (a) ORMOSIL-epoxy-PPy is $4 \pm 0.5\,\mu m$, (b) ORMOSIL

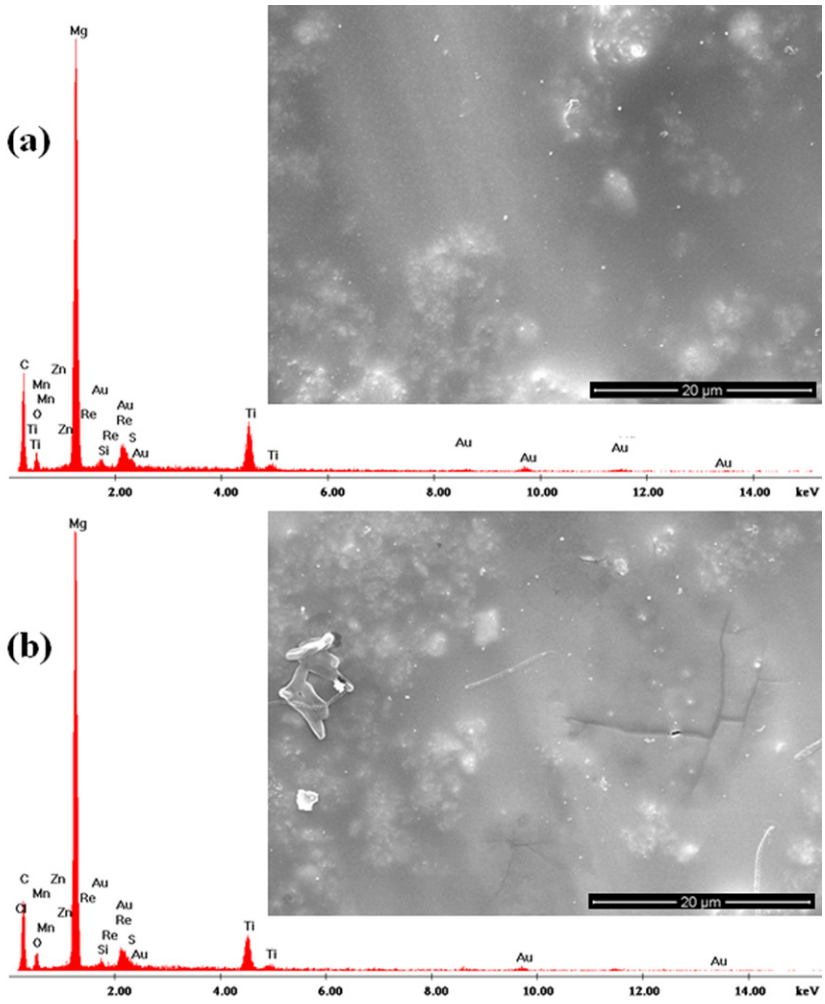

Fig. 12. SEM and EDX analysis of: (a) ORMOSIL-epoxy-PPy-TiO_2-2MB, (b) ORMOSIL-epoxy-PPy-TiO_2-2MB after exposure at 5 mM NaCl solution at room temperature for 14 days.

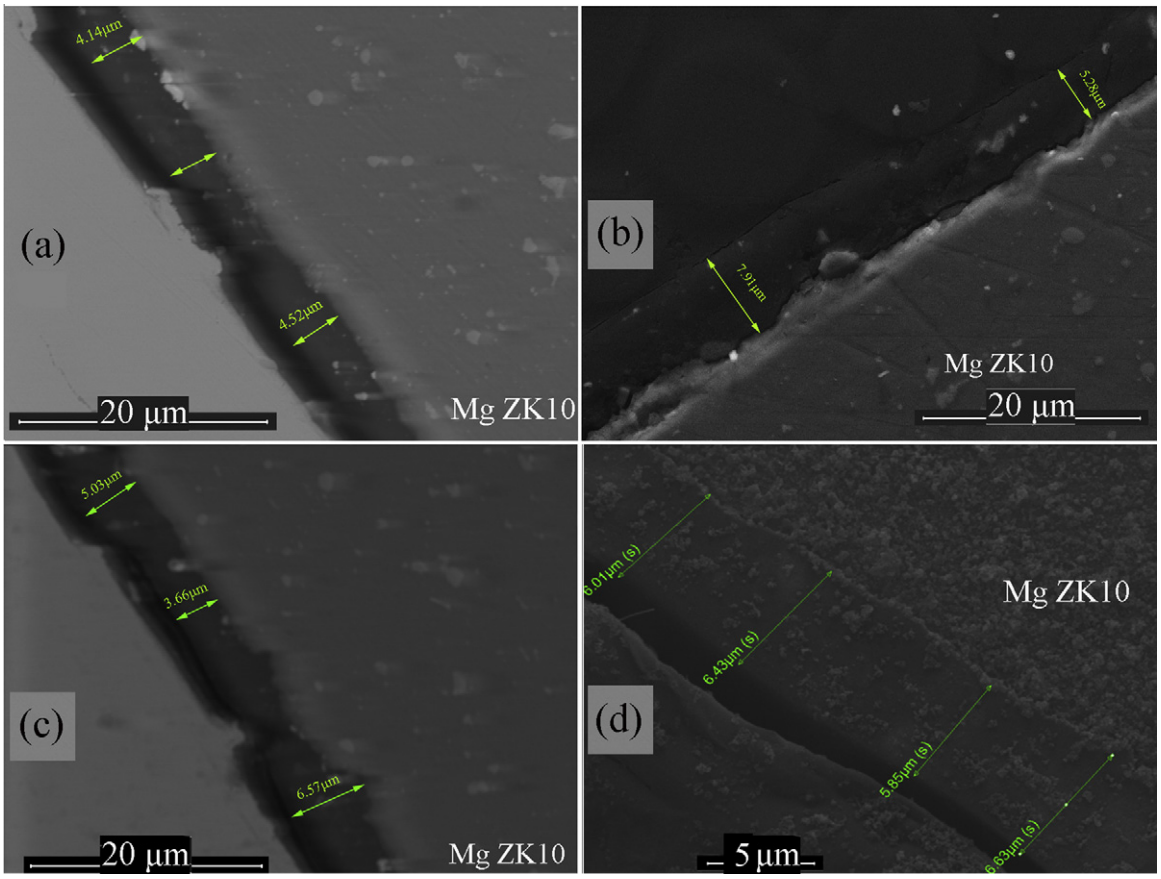

Fig. 14. Cross-section SEM of MgZK10 alloy coated with (a) ORMOSIL-epoxy-PPy, (b) ORMOSIL-epoxy-PPy-TiO_2, (c) ORMOSIL-epoxy-PPy-2MB, (d) ORMOSIL-epoxy-PPy-TiO_2-2MB.

-epoxy-PPy-TiO_2 is 6.4 ± 1.5 μm, (c) ORMOSIL-epoxy-PPy-2MB is 5 ± 1.4 μm, and (d) ORMOSIL-epoxy-PPy-TiO_2-2MB which is 6 ± 0.5 μm. It can be seen that apart from the coating ORMOSIL-epoxy-PPy (it is thinner than the other coatings) all the other coatings have roughly the same thickness.

3.4. FT-infrared spectroscopy analysis

Fig. 15 shows the FT-IR spectra for both ORMOSIL-epoxy-PPy and ORMOSIL-epoxy-PPy-TiO_2-2MB. The FT-IR spectrum of the sample ORMOSIL-epoxy-PPy-TiO_2-2MB shows absorption peaks at 510–690 cm^{-1} and reveals that containers of TiO_2 have been encapsulated to the coating [38]. Furthermore, both spectra clearly denote the presence of PPy into the coating due to the appearance of its characteristic peaks and the peaks of its doping agent, lignosulfonic acid. The peak at 1030 corresponds to sulfur oxygen stretch of lignosulfonic acid. The broad bands between 1470 and 1525 cm^{-1} are =C—H and ring C=C vibrations and correspond to aromatic C—C=C—C of lignosulfonic acid [39,40]. The peak at 1413 cm^{-1} corresponds to N—H deformation of pyrrole. The peak at 1068 cm^{-1} is also due to N—H and C—H deformation of pyrrole. The bands due to the pyrrole ring vibration are seen at 1452 cm^{-1} [42]. The characteristic peaks of HY 943, GY 257 and Z 6020 are presented in Table 9 [28,29,41,42].

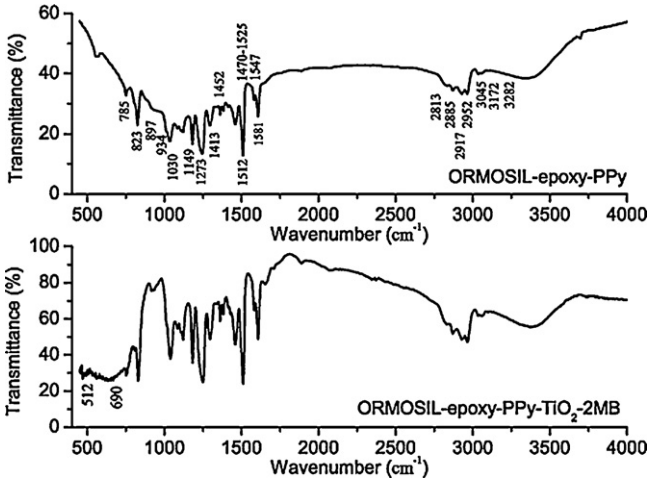

Fig. 15. FT-IR spectra of: ORMOSIL-epoxy-PPy, ORMOSIL-epoxy-PPy-TiO_2-2MB.

3.5. Mechanical properties

The mechanical adhesion between coating and substrate of the samples was examined through the scratch test with the ROCKWELL indentation test. Figs. 16 and 17 depict the scratch tests of ORMOSIL-epoxy-PPy and ORMOSIL-epoxy-PPy-TiO_2-2MB, respectively. For the tests, the probe was moved for 10 mm with a loading rate of 10 mN/s and with a speed 10 mm/min. Each figure presents the SEM image and the curve of acoustic emission versus displacement from scratch test on each sample. The slope of the curve changes when the indenter touches the interface between films and substrate, because of different friction of different materials. The SEM image confirms the film failure position, where the complete film is removed. The coatings of the sample ORMOSIL-epoxy-PPy and ORMOSIL-epoxy-PPy-TiO_2-2MB are completely removed

Table 9
FT-IR characteristic peaks of GY 257, Z 6020 and HY 943.

Compound	Ranges (cm^{-})	Comment
GY 257	966	Epoxy ring
GY 257	2917, 2952, 2813, 2885	R—CH_3 asymmetric stretching vibration
GY 257	3045	Phenyl vibration
HY 943	897–934	N—H out of plane vibration
HY 943	3172–3282	—NH_2 vibration
Z 6020	2847	—NH_2 and Si—O—CH_3 asymmetric vibration CH_3
Z 6020	3378–3410	—NH symmetric and asymmetric stretching vibrations
Z 6020	800–850, 1170–1210	Si—O—CH_3 symmetric vibration
Z 6020, HY 943	755	—NH_2 and C—H_2
Z 6020, HY 943	1037	C—C and NH_2
Z 6020, HY 943	1100–1122	Vibrations of firstly and secondary amines
Z 6020, HY 943	1285–1304	To C—H_2 and C—NH_2 vibrations
Z 6020, HY 943	1450–1465	Firstly amine vibration
Z 6020, HY 943	1500–1520	Secondary amine vibrations

after 1.44 ± 0.10 μm and 0.98 ± 0.10 μm, respectively. These results denote that the coating of the sample ORMOSIL-epoxy-PPy has better adhesion than the one of ORMOSIL-epoxy-PPy-TiO_2-2MB. This fact can be attributed to the presence of containers into the coating of sample ORMOSIL-epoxy-PPy-TiO_2-2MB that prevent the reaction of siloxane groups of the coating with the hydroxyl groups of the metal alloy.

3.6. Microhardness

Studies on the microhardness of the sample ORMOSIL-epoxy-PPy-TiO_2-2MB was also done. Eight different microhardness measurements were carried out without pretreatment. The load that was applied was 98.07 mN for 40 s. The Vickers microhardness is given by the equation $HV = 0.1891\ F/d^2$, where HV is the microhardness Vickers, F is the applied load (N) and d is the average value of the two diagonals d_1 and d_2 of the stamp that was created. The

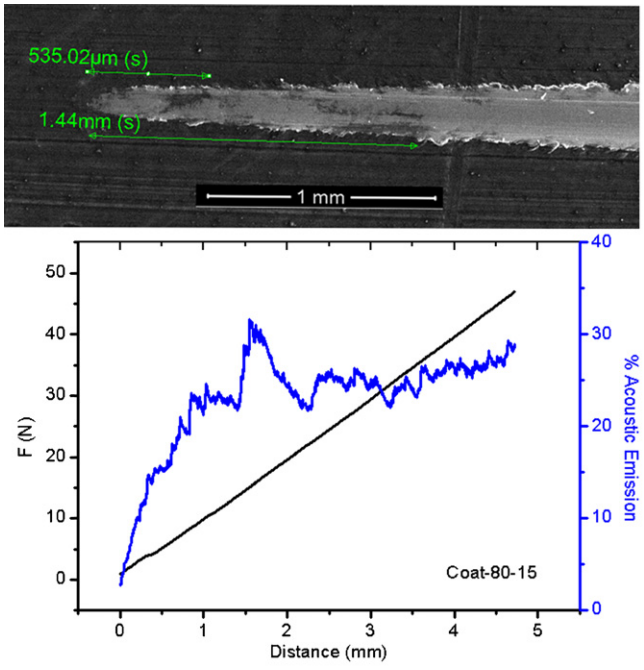

Fig. 16. SEM image and % acoustic emission–displacement curve from scratch test on sample ORMOSIL-epoxy-PPy.

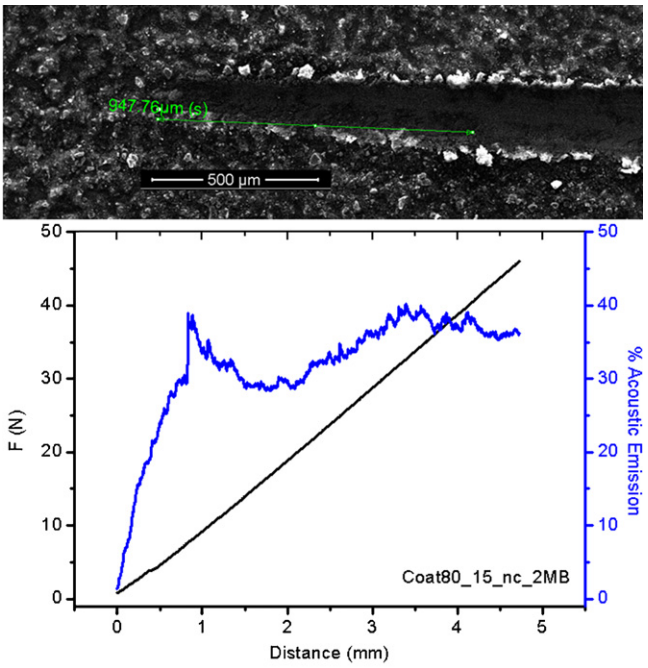

Fig. 17. SEM image and % acoustic emission–displacement curve from scratch test on sample ORMOSIL-epoxy-PPy-TiO_2-2MB.

Table 10
Vickers microhardness (HV) values of sample ORMOSIL-epoxy-PPy-TiO_2-2MB.

Vickers microhardness (HV)	Diameter d_1	Diameter d_2
25.1	24.41	29.91
27.5	22.06	29.79
33.4	21.47	25.64
32.1	23.44	24.60
34.0	26.26	20.41
33.6	24.38	22.56
32.9	23.44	23.99
39.1	21.59	21.93

values of the Vickers microhardness are presented in Table 10. It can be estimated that the sample ORMOSIL-epoxy-PPy-TiO_2-2MB has 32.2 HV Vickers microhardness.

4. Conclusion

A novel system has been developed for the corrosion protection of magnesium alloy ZK10. This system includes coatings that combine epoxy resins, ORMOSIL and CP. Furthermore, TiO_2 containers were loaded with 2-MB and then incorporated into the layers. The above coatings were characterized with SEM and FT-IR. Their corrosion resistance was examined using EIS. Experiments with empty containers incorporated into the coatings were also done. The results showed improved corrosion protection of coatings with loaded containers after 288 h immersion in 5 mM NaCl solution. Although the coating with loaded containers performs significantly better than the one without containers with respect to corrosion protection, they reduce the adhesion of the coating to the substrate. Considering these important results, this new technology can be a potential candidate for corrosion protection of magnesium alloy ZK10 that can be further improved in future work. This paper demonstrates an attempt to show the use of the ceramic containers loaded with organic inhibitors present a new system with the potential to further improve their performance. These improvements can include optimization of the porosity of the containers,

development of new ceramic container systems, identification of more efficient organic inhibitors, etc.

Acknowledgements

This project was supported by European Integrated Project "MULTIPROTECT". The abbreviation "MULTIPROTECT" stands for "Advanced environmentally friendly multifunctional corrosion protection by nanotechnology" (Contract No. NMP3-CT-2005-011783). Lots of thank to Alubin-Israel for providing the samples of MgZK10.

References

[1] J.E. Gray, B. Luan, J. Alloys Compd. 336 (2002) 88–113.
[2] B.L. Mordike, T. Ebert, Mater. Sci. Eng. A 302 (2001) 37–45.
[3] G.L. Makar, J. Kruger, Int. Mater. Rev. 38 (1993) 138–153.
[4] H. Hoche, H. Scheerer, D. Probst, E. Broszeit, C. Berger, Surf. Coat. Technol. 174 (2003) 1002–1007.
[5] J. Liang, P.B. Srinivasan, C. Blawert, W. Dietzel, Corros. Sci. 51 (2009) 2483–2492.
[6] H. Ardelean, I. Frateur, P. Marcus, Corros. Sci. 50 (2008) 1907–1918.
[7] A.S. Hamdy, Surf. Coat. Technol. 203 (2008) 240–249.
[8] F. Stippich, E. Vera, G.K. Wolf, G. Berg, Chr. Friedrich, Surf. Coat. Technol. 103–104 (1998) 29–35.
[9] H. Ardelean, I. Frateur, S. Zanna, A. Atrens, P. Marcus, Corros. Sci. 51 (2009) 3030–3038.
[10] J. Hu, G. Shaokang, C. Zhang, C. Ren, C. Wen, Z. Zeng, L. Peng, Surf. Coat. Technol. 203 (2009) 2017–2020.
[11] M.B. Kannan, D. Gomes, W. Dietzel, V. Abetz, Surf. Coat. Technol. 202 (2008) 4598–4601.
[12] J. Hu, Q. Li, X. Zhong, L. Zhang, B. Chen, Prog. Org. Coat. 66 (2009) 199–205.
[13] S. Zhang, Q. Li, J. Fan, W. Kang, W. Hu, X. Yang, Prog. Org. Coat. 66 (2009) 328–335.
[14] A.L.K. Tan, A.M. Soutar, I.F. Annergren, Y.N. Liu, Surf. Coat. Technol. 198 (2005) 478–482.
[15] H. Shi, F. Liu, E. Han, Prog. Org. Coat. 66 (2009) 183–191.
[16] S.V. Lamaka, G. Knornschild, D.V. Snihirova, M.G. Taryba, M.L. Zheludkevich, M.G.S. Ferreira, Electrochim. Acta 55 (2009) 131–141.
[17] N. Scharnagl, C. Blawert, W. Dietzel, Surf. Coat. Technol. 203 (2009) 1423–1428.
[18] H. Wang, R. Akid, M. Gobara, Corrosion 52 (2010) 2565–2570.
[19] F. Feil, W. Furbeth, M. Schutze, Electrochim. Acta 54 (2009) 2478–2486.
[20] F. Zhang, M. Sun, S. Xu, L. Zhao, B. Zhang, Chem. Eng. J. 141 (2008) 362–367.
[21] S. Sathiyanarayanan, S.S. Azim, G. Venkatachari, Prog. Org. Coat. 59 (2007) 291–296.
[22] V.T. Truong, P.K. Lai, B.T. Moore, R.F. Muscat, M.S. Russo, Synth. Met. 110 (2000) 7–15.
[23] A. Yfantis, I. Paloumpa, D. Schmeiber, D. Yfantis, Surf. Coat. Technol. 151-152 (2002) 400–404.
[24] Y.F. Jiang, X.W. Guo, Y.H. Wei, C.Q. Zhai, W.J. Ding, Synth. Met. 139 (2003) 335–339.
[25] B. Sanyal, Prog. Org. Coat. 9 (1981) 165–236.
[26] M.L. Zheludkevich, K.A. Yasakau, S.K. Poznyak, M.G.S. Ferreira, Corros. Sci. 47 (2005) 3368–3383.
[27] M. Kettner, U. Noster, H. Kilian, R. Gradinger, W. Kuhlin, A. Drevenstednt, F. Stadler, E. Ladstaetter, A. Lutz, Wrought Mg alloy for civil aircraft applications – a process chain approach, in: K.U. Kainer (Ed.), Magnesium Proceedings of the 7th International Conference on Magnesium Alloys and their Applications, Wiley-VCH Verlag GmbH Co. KGaA, Weinheim, 2007, p. 311.
[28] A.P. Valavanides, Basic Principles of Molecular Spectroscopy and Applications to Molecular Chemistry, Recent Themes, 1990.
[29] O. Hummel, A. Solti, Atlas of Polymer and Plastics Analysis, VCH Publications 2, New York, USA, 1988.
[30] S.V. Lamaka, M.L. Zheludkevich, K.A. Yasakau, R. Serra, S.K. Poznyak, M.G.S. Ferreira, Prog. Org. Coat. 58 (2007) 127–135.
[31] R. Fernandez, M. Blanco, M.J. Galante, P.A. Oyanguren, I. Mondragon, J. Appl. Polym. Sci. 112 (2009) 2999–3006.
[32] R. Winston Revie, Uhlig's Corrosion Handbook, 2nd ed., John Wiley and Sons, New York, USA, 2000, pp. 799–800.
[33] V.-T. Truong, P.K. Lai, B.T. Moore, R.F. Muscat, M.S. Russo, Synth. Met. 110 (2000) 7–15.
[34] R. Winston Revie, Uhlig's Corrosion Handbook, 2nd ed., John Wiley and Sons, New York, USA, 2000, p. 1099.
[35] C.H. Hsu, F. Mansfeld, Corrosion 57 (2001) 747–748.
[36] M.L. Zheludkevich, R. Serra, M.F. Montemor, K.A. Yasakau, I.M. Miranda Salvado, M.G.S. Ferreira, Electrochim. Acta 51 (2005) 208–217.
[37] S.V. Lamaka, M.F. Montemor, A.F. Galio, M.L. Zheludkevich, C. Trindade, L.F. Dick, M.G.S. Ferreira, Electrochim. Acta 53 (2008) 4773–4783.
[38] I.A. Kartsonakis, P. Liatsi, I. Daniilidis, D. Bouzarelou, G. Kordas, J. Phys. Chem. Solids 69 (2008) 214–221.
[39] K.K. Taylor, C.V. Cole, R. Soora, J.C. Dilday, A.M. Hill, B. Berry, T. Viswanathan, J. Appl. Polym. Sci. 108 (2008) 1496–1500.
[40] T.K. Vishnuvardhan, V.R. Kulkarni, C. Basavaraja, S.C. Raghavendra, Bull. Mater. Sci. 29 (2006) 77–83.
[41] L.J. Bellamis, The Infra-red Spectra of Complex Molecules, Chapman and Hall, London, UK, 1975.
[42] R.M. Silverstein, G.C. Bassler, T.C. Morrill, Spectroscopic Identification of Organic Compounds, John Wiley & Sons, New York, USA, 1981.

Corrosion Science 65 (2012) 481–493

Contents lists available at SciVerse ScienceDirect

Corrosion Science

journal homepage: www.elsevier.com/locate/corsci

Evaluation of corrosion resistance of magnesium alloy ZK10 coated with hybrid organic–inorganic film including containers

I.A. Kartsonakis [a,b,*], A.C. Balaskas [a], E.P. Koumoulos [b], C.A. Charitidis [b], G. Kordas [a]

[a] Sol–gel Laboratory, Institute of Advanced Materials, Physicochemical Processes, Nanotechnology and Microsystems, NCSR 'DEMOKRITOS', 15310 Agia Paraskevi, Greece
[b] School of Chemical Engineering, NTUA, 9 Heroon Polytechniou St., 15780 Zographos, Greece

ARTICLE INFO

Article history:
Received 14 February 2012
Accepted 20 August 2012
Available online 30 August 2012

Keywords:
A. Magnesium
B. EIS
B. SEM
C. Pitting corrosion
C. Polymer coatings

ABSTRACT

This study is focused on the corrosion protection of magnesium alloy ZK 10. Coatings consist of cross-linked polymers based on bisphenol A diglycidyl ether as well as organic modified silicates including cerium molybdate containers were synthesized and applied to the metal alloys. The films were investigated for their morphology and nanomechanical properties. Corrosion studies were made using open circuit potential, cyclic potentiodynamic polarization and electrochemical impedance spectroscopy after immersion in 0.5 M sodium chloride solution. The evaluation of possible self-healing effect was made via formation of artificial defect on the surface of the coatings and consequently exposure to corrosive environment.

1. Introduction

Magnesium and its alloys is used in a wide range of applications due to its low density (it is only 65% that of aluminum and 25% that of iron) as well as its high strength/weight ratio [1,2]. On the contrary, engineering applications of magnesium have been limited mainly due to the poor corrosion properties of magnesium alloys [3]. Several coating applications have been developed in order to improve the corrosion resistance of magnesium and its alloys, such as electrolytic plasma oxidation [4,5], inorganic pre-treatments [6,7], spin and dip coating methods [8–10], ion beam-assisted deposition [11], anodizing process [12], vapor phase method for self-assembled monolayer [13], etc.

A very promising application for corrosion protection of magnesium and its alloys is hybrid organic–inorganic sol–gel coatings. Ishizaki et al. applied superhydrophobic surfaces on Mg alloy AZ31 with nanostructured cerium oxide film and fluoroalkylsilane molecules [14]. Studies on the protection of Mg alloy AZ91D have been made by Hu et al. who used composite coatings which consisted of a molybdate conversion coating and three layers of silicon sol–gel coatings [15]. Shi et al. prepared sol–gel coatings for the same alloy using 3-glysicoxypropylthrimethoxysilane and tetraethoxysilane as precursors, diethylentriamine as curing agent and 2-methyl piperidine as inhibitor [16]. Furthermore, Tan et al. synthesized multilayer sol–gel coatings for corrosion protection of AZ91D based on 3-methacryloxypropyl trimethoxysilane, 3-meraptopropyl trimethoxysilane and ethanol. The multilayer approach was found to significantly improve the corrosion resistance of Mg by reducing levels of porosity [17]. Ferreira et al. developed a complex anticorrosion protection system for ZK30 magnesium alloy that based on an anodic oxide layer loaded with corrosion inhibitors in its pores which was then sealed with a sol–gel hybrid polymer. The developed complex anticorrosion coating beneficially combines increased corrosion resistance of the magnesium substrate due to the additional protective oxide layer and the greater adhesion of thin sol–gel coating to the porous anodized surface, while also conferring active protection properties owing to the corrosion inhibitor securely impregnated in the porous reservoirs [18]. Improved corrosion protective properties have also obtained via the application of epoxy based coatings on magnesium alloys [19,20].

Nanoindentation and nanoscratch tests have been widely applied for the measurement of mechanical properties of coatings and thin films [21–24]. The nanoindentation test can provide information about the mechanical behavior of the material when it is being deformed at the sub-micron scale. The method developed by Oliver and Pharr allows determining the hardness and the elastic modulus from the nanoindentation load–displacement data [25].

In this paper, we report the corrosion resistance and nanomechanical performance of hybrid organic–inorganic coatings including containers applied to magnesium alloy ZK10. The containers consist of cerium molybdate and were loaded with 2-mercaprobenzothiazole (MBT). Not only the hybrid coatings were evaluated for their corrosion protective behavior, but the contribution of

* Corresponding author at: Sol–Gel Laboratory, IMS, NCSR 'DEMOKRITOS', 15310 Agia Paraskevi, Greece. Tel.: +30 2106503302.
E-mail address: ikartsonakis@ims.demokritos.gr (I.A. Kartsonakis).

0010-938X/$ - see front matter © 2012 Elsevier Ltd. All rights reserved.
http://dx.doi.org/10.1016/j.corsci.2012.08.052

each parameter such as containers, corrosion inhibitor was estimated as well. Furthermore, their nanomechanical properties, mechanical integrity in terms of plasticity and wear resistance were examined, too.

2. Materials and experimental details

2.1. Materials and reagents

Magnesium alloy ZK10 (composition: 1.35–1.45 wt% Zn, 0.5–0.6 wt% Zr, ⩽0.25 wt% Mn, 0.2–0.25 wt% Rh and the rest is Mg) was obtained from Alubin – Israel [26]. All chemicals were of analytical reagent grade. MBT (Sigma–Aldrich, St. Louis, USA), cerium (III) acetylacetonate ($Ce(acac)_3$, Sigma–Aldrich, St. Louis, USA), polyvinylpyrrolidone (PVP, average molecular weight: 55000, Sigma–Aldrich, St. Louis, USA), potassium persulfate (KPS, Sigma–Aldrich, St. Louis, USA), sodium dodecyl sulfate (SDS, Sigma–Aldrich, St. Louis, USA), aceton (Sigma–Aldrich, St. Louis, USA), USA), *N*-(2-aminoethyl)-3-(trimethoxysilyl)propylamine (Z 6020, Sigma–Aldrich, St. Louis, USA), epoxy resin based on Phenol 4,4′-(1-methylethylidene) bis-(“Araldite GY 257”, GY 257, Ciba-Geigy), 2,2′-diaminodiethylamine (HY 943, Sigma–Aldrich, St. Louis, USA) were used without further purification. Styrene (Sigma–Aldrich, St. Louis, USA) was double distilled under reduced pressure prior to use.

2.2. Synthesis of containers

The production of cerium molybdate containers was based on a two-step process. The method of emulsion polymerization was used to produce anionic polystyrene latex, used as core particles. For this purpose, the reaction was carried out in a 500-cm^3 container under the condition listed in Table 1. To eliminate the effects of oxygen, the solution was purged with nitrogen before the process was initiated. The polymerization process lasted for 12 h. The resulting dispersions were centrifuged at 14000 rpm for 30 min, the supernatant solutions were discarded, and then the particles were resuspended in doubly distilled water using a sonicator. This process was repeated three times. The polystyrene lattices were coated via the sol–gel method to form a cerium molybdate layer. The sol–gel coatings were prepared by controlled hydrolysis of $Ce(acac)_3$ and sodium molybdate aqueous solution in the presence of polystyrene latex and PVP. These dispersions were aged for 3 days at 96 °C (Table 2). The resulting dispersions were centrifuged at 14000 rpm for 30 min, the supernatant solutions were discarded, and then the particles were resuspended in doubly distilled water with a sonicator. This process was repeated three times, and the purified powders were dried in a desiccator. The production of cerium molybdate containers included the removal of polystyrene cores by calcination. Initially, the coated spheres were placed on a glass slide and dried, first at room temperature and then for 1 h at 60 °C. Then, the composite was calcinated for 4 h in air in a furnace at 550 °C. The heating rate was 10 °C min^{-1}. The containers exhibited an average diameter of 230 ± 20 nm [27].

Table 1
The conditions used in the preparation of polystyrene latex at 80 °C.

Material	Quantity (g)
Styrene	40.0
Potassium persulfate	5.2
Sodium dodecyl sulfate	0.85
Water	1850
Spheres' size (nm)	200 ± 10[a]

[a] Determined by Scanning Electron Microscopy analysis.

Table 2
Conditions of preparation of coated spheres.

Material	Quantity (g)
Polystyrene	40.0
Polyvinylpyrrolidone	40.0
Cerium (III) acetylacetonate	24.0
Sodium molybdate	2.0
Water	3000
Spheres' size (nm)	240 ± 20[a]

[a] Determined by Scanning Electron Microscopy analysis.

The obtained cerium molybdate containers were loaded with the corrosion inhibitor MBT. The process for the loading was the following. Firstly, a saturated solution of MBT in acetone was prepared. An amount of cerium molybdate containers was placed in a sealed container. The air of the inner side of the containers was eliminated with a vacuum system. Then, the saturated solution of MBT in acetone was inserted in the sealed container and the whole mixture was stirred at room temperature for 2 h. Finally the cerium molybdate containers loaded with MBT were collected through centrifugation and drying under vacuum at 60 °C overnight. The containers were 58.08% w/w loaded with MBT [28].

The containers consist of cerium molybdate because cerium cation and molybdate anion are corrosion inhibitors [29] and were loaded with 2-mercaprobenzothiazole (MBT) which is also a corrosion inhibitor [30].

2.3. Coating preparation

The synthesis of the coating includes the hydrolysis of the organic modified silicate, Z 6020, in absolute ethanol for 1 h (solution A). Simultaneously, the epoxy resin GY 257 was dissolved in absolute ethanol (solution B). After that, solutions A and B were intermixed formatting solution C. Then, HY 943 was dissolved in 25 ml acetone (solution D). Finally, solutions C and D were intermixed and stirred for 8 h (solution E). The preparation of the hybrid coating including inhibitor without containers (HybridCoat-MBT) includes the addition of 1.5 wt% MBT in the solution E under vigorous stirring 1 h before the dip coating process. The preparation of the hybrid coatings incorporating containers empty (HybridCoat-nc) or loaded (HybridCoat-ncMBT), includes the addition of 10 wt% containers in the solution E under vigorous stirring 1 h before the dip coating process.

2.4. Dip coating process

Four different types of coatings were prepared. At first, coatings free of inhibitor or containers were synthesized (HybridCoat). Then, coatings were prepared that had incorporated only inhibitor in a free form (not encapsulated) (HybridCoat-MBT) or empty containers (HybridCoat-nc). Finally, coatings were fabricated that had containers loaded with inhibitor (HybridCoat-ncMBT). The panels were dip coated into the container solution for six times with a withdraw rate of 32 cm/min. The panels remained in the solution for 1 min. Then, the coated panels were heat treated at 70 °C for 4 days. The ZK10 magnesium alloys panels had been previously cleaned, under the following conditions. First of all, the panels were inserted into 96 v/v% ethanol for 20 min at room temperature, under sonication. After that, the panels were rinsed with distilled water and inserted into a degreaser solution (40 g/L NaOH, 20 g/L Na_2CO_3, 0.1 wt% sodium lauryl sulfate, water) for 10 min at 70 °C. Then, the panels were inserted in distilled water for a few minutes at 40 °C. The next step included the insertion of the panels in hydrofluoric acid 10 wt% for 20 min at room temperature. Finally, the panels were rinsed with distilled water and left to dry in air.

2.5. Characterization

The morphology of the coatings was determined by SEM using a PHILIPS Quanta Inspect (FEI Company) microscope with W (tungsten) filament 25 kV equipped with EDAX GENESIS (AMETEX PROCESS & ANALYTICAL INSTRUMENTS). The encapsulation of 8-HQ into the containers was evaluated via thermogravimetric analysis (TGA) using a Perkin Elmer (Pyris Diamand S II) analyzer at the heating rate of 10 °C min^{-1} in air.

The corrosion resistance of these coatings was studied by electrochemical impedance spectroscopy, in 0.5 M NaCl, using a SI 1287 Solartron Electrochemical interface connected with a SI 1260 Impedance/gain-phase analyser. The experiments were performed at room temperature, in a Faraday cage, at the open circuit potential, using a three-electrode electrochemical cell, consisting of working electrode (≈2.0 cm^2 of exposed area), saturated calomel electrode (SCE) as reference and platinum as counter electrode. The measuring frequency ranged from 100 kHz down to 5 mHz. The rms voltage was 10 mV. Spectra were treated using the Z-view Software using the adequate equivalent electric circuits. The interpretation of the results was performed by numerical fitting, using equivalent circuit. In this equivalent circuit, constant phase elements were used instead of pure capacitors. This modification is obligatory in the case the phase shift of a capacitor is different from −90° [31]. The impedance of a R-CPE parallel association is given by: $Z_{R-CPE} = \frac{R}{1+RY_0(j\omega)^n}$, where Y_0 is the admittance of the CPE and n is the CPE exponent. Constant phase elements correspond to a capacitor when the CPE exponent (n) is one. Using the Cole–Cole approach together with CPE, the capacitance can be calculated from the fittings by: $C = \sqrt[n]{\frac{RY_0}{R^n}}$ [32,33].

A Soltartron 1470 BATTERY TEST UNIT was used for cyclic potentiodynamic polarization (CPP) and open circuit potential (OCP) measurements. The exposed geometric area was 1 cm^2 for all the CPP measurements. The potential was scanned between −0.4 V versus OCP and 0 V versus SCE. The polarization curves were recorded with the potential change rate of 1 mV s^{-1}. All the samples were in vertical position; the experiments were carried out at room temperature. For every result a minimum of three repeated measurements were taken.

2.6. Nanomechanical measurements

Hardness (H) and elastic modulus (E) values were extracted from the experimental data (load displacement curves) using the Oliver–Pharr (O&P) method [19,34], based on the half-space elastic deformation theory. The equations used to calculate the elastic modulus from indentation experiments are based on Sneddon's [35] elastic contact theory: $E_r = \frac{S\sqrt{\pi}}{2\beta\sqrt{A_c}}$, where S is the unloading stiffness (initial slope of the unloading load–displacement curve at the maximum displacement of penetration (or peak load)), A_C is the projected contact area between the tip and the substrate and β is a constant that depends on the geometry of the indenter (β = 1.167 for Berkovich tip [25,34]. Conventional nanoindentation hardness refers to the mean contact pressure; this hardness, which is the contact hardness H_C is actually dependent upon the geometry of the indenter: $H_c = \frac{F}{A(h_c)}$, where $A(hc) = 24.5h_c^2 + \alpha_1 h_c + \alpha_{1/2}h_c^{1/2} + \ldots + \alpha_{1/16}h_c^{1/16}$ and $h_c = h_m - \varepsilon\frac{P_m}{S_m}$; h_c is the total penetration displacement of the indenter at peak load, P_m is the peak load at the indenter displacement h_c, and ε is a constant, equal to 0.75 for Berkovich indenter [34–36]. The leading term ($24.5h_c^2$) of (Eq. 3) describes a perfect Berkovich indenter, whereas the others describe deviations from the Berkovich geometry due to blunting at the tip [19]. The total plastic work was calculated through integration of load–unload curves. Prior to indentation, the area function of the indenter tip was calibrated in fused silica, a standard material for this purpose [37,38].

3. Results and discussion

3.1. Surface characterization

The visual photographs of all the coatings after exposure to corrosive environment are presented in Fig. 1. It can be seen from these photographs that all the coatings HybridCoat, HybridCoat-MBT and HybridCoat-ncMBT do not illustrate corrosion signals such as pits or stains after 4 months of exposure to 0.5 M NaCl solution at room temperature. On the other hand, the coating incorporating empty containers (HybridCoat-nc) demonstrates signals of corrosion attack after 2.5 months of exposure to the same corrosive environment. The visual picture of uncoated magnesium alloy ZK10 (bare MgZK10) after 2 months of exposure to 0.5 M NaCl solution at room temperature depicts that that its surface has been completely destroyed.

The SEM images of the surface of the above samples, before and after their exposure at 0.5 M NaCl solution at room temperature, are presented in Figs. 2–5. The surfaces of both HybridCoat and HybridCoat-MBT coatings are smooth without aggregated particles. They are crack free and no holes or craters are observed (Figs. 2i and 3i, respectively). The surface of the sample HybridCoat-nc also depicts no cracks but it is less smooth than those of the aforementioned samples (Fig. 4i). The surface of HybridCoat-ncMBT coating seems to be crack free without defects. It presents few aggregations that are ascribed to the incorporation of containers into the coating (Fig. 5i). However, the surfaces of all the coatings are affected after their exposure to corrosive environment. Both HybridCoat and HybridCoat-MBT coatings demonstrate small particles (Figs. 2ii and 3ii, respectively). The surface of HybridCoat-nc sample presents holes denoting that the coating has been undergone corrosion attack (Fig. 4ii). Finally, few small particles have been formed on the surface of HybridCoat-ncMBT coating (Fig. 5ii). The EDX analysis of all the samples reveals carbon due to the presence of the coating and cerium in the case of the samples HybridCoat-nc and HybridCoat-ncMBT because of the existence of containers. The values of oxygen for all the samples are kept almost the same before and after the exposure of the samples to corrosion environment apart from the sample HybridCoat-nc where holes are formed and oxygen values are increased. These results denote that no additional oxides are formed onto the metal due to corrosion attack after the exposure of the coatings to NaCl solution except for the sample HybridCoat-nc. SEM surface mapping was taken for the coating including loaded containers in order the well dispersion of the containers into the film to be estimated. The elemental cerium mapping micrograph and corresponding SEM image of coating HybridCoat-ncMBT is demonstrated in Fig. 6. Spots of cerium element can be clearly seen in the pictures. Although some aggregates are observed, the containers are quite well dispersed into the coatings. It should be mentioned that the distribution of the containers through the thickness of the coatings is an important parameter, too. The containers should not be agglomerated on the top or on the interface between the coating and the substrate. Fig. 7 illustrates the mapping EDX analysis of cerium elements on the cross-section of the sample HybridCoat-ncMBT and the corresponding SEM image. It is clearly denoted that the cerium element that corresponds to containers is well distributed through the thickness of the coating.

Studies on the thickness of all the samples revealed that both coatings HybridCoat and HybridCoat-nc have almost the same thickness (18.4 ± 0.6 μm, Fig. 8a and c). The coating of sample HybridCoat-MBT is thicker than the aforementioned samples (26.5 ± 0.3 μm, Fig. 8b). Finally, the sample HybridCoat-ncMBT

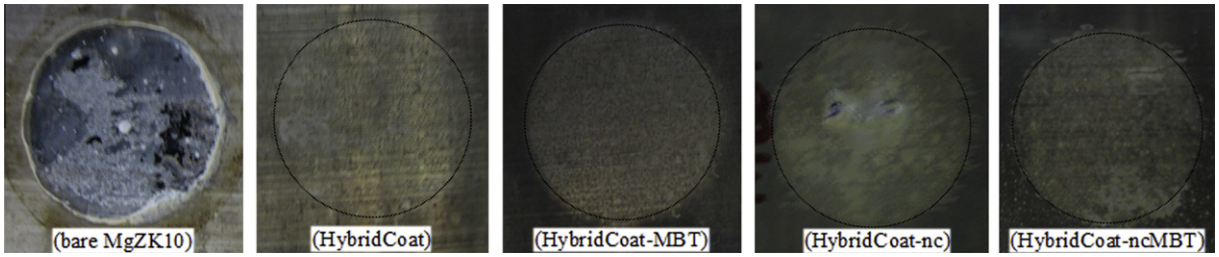

Fig. 1. Visual coating photographs of bare MgZK10 after 2 months, HybridCoat after 4 months, HybridCoat-MBT after 4 months, HybridCoat-nc after 2.5 months and HybridCoat-ncMBT after 4 months, exposure to 0.5 M NaCl solution at room temperature.

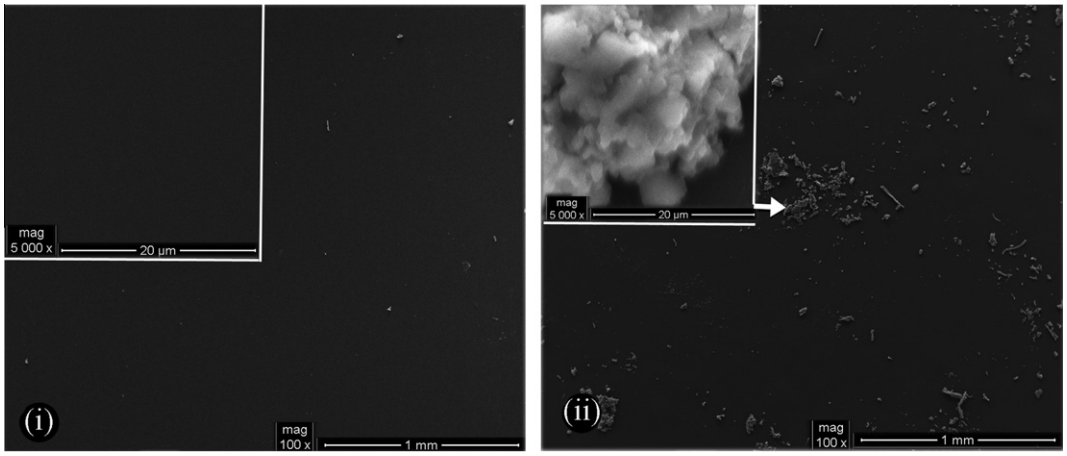

Fig. 2. SEM image of HybridCoat coating (i) before, (ii) after 4 months exposure to 0.5 M NaCl solution at room temperature.

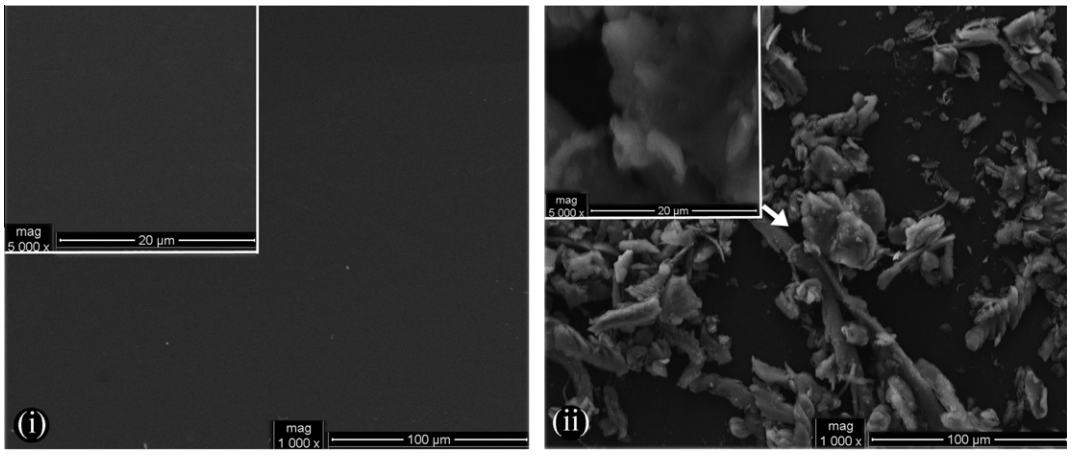

Fig. 3. SEM image of HybridCoat-MBT coating (i) before, (ii) after 4 months exposure to 0.5 M NaCl solution at room temperature.

has a thickness of (16.0 ± 0.3 μm Fig. 8d). It can be seen that the coating HybridCoat-ncMBT is roughly 10 μm thinner than the coating HybridCoat-MBT.

3.2. Electrochemical measurements

The electrochemical measurements include studies on the corrosion performance of the coatings via EIS, CPP and OCP. EIS was used in order the protective abilities and the corrosion protection mechanism of the coated samples to be estimated.

The impedance spectra obtained during immersion period for the coatings HybridCoat, HybridCoat-MBT, HybridCoat-nc and HybridCoat-ncMBT are presented in Fig. 9. The Bode spectra obtained for the three coatings HybridCoat, HybridCoat-MBT and HybridCoat-ncMBT after 4 months of exposure to corrosive environment are characterized by a capacitive response. The phase angle is between -90° to -80° in the measured frequency range revealing that the coatings behave nearly as a capacitor. This behavior denotes that the coatings have enhanced barrier properties and act as an insulator [39] as well as they have good adhesion to the substrates. The Bode spectrum for the coating including empty containers (HybridCoat-nc) presents a capacitive response during the first 2 months of exposure. As the immersion time elapses (after 2.5 months) the Bode spectrum depicts one time

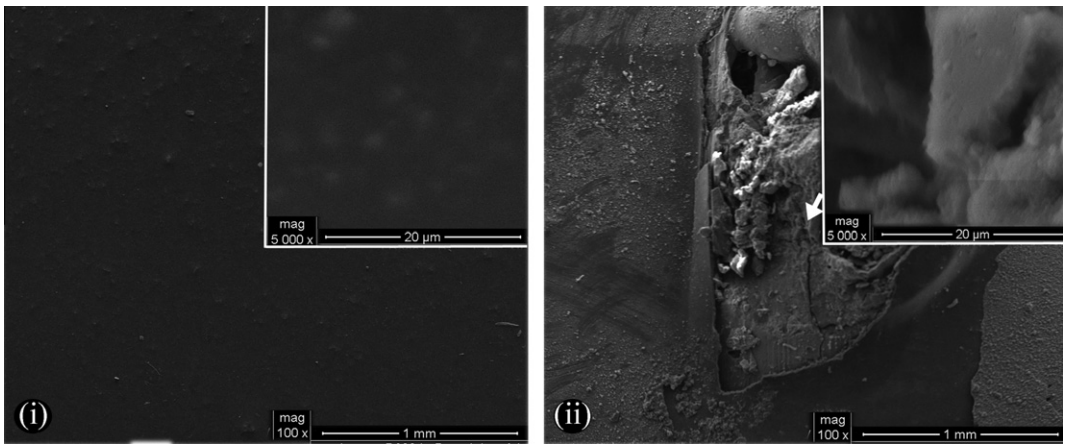

Fig. 4. SEM image of HybridCoat-nc coating (i) before, (ii) after 2.5 months exposure to 0.5 M NaCl solution at room temperature.

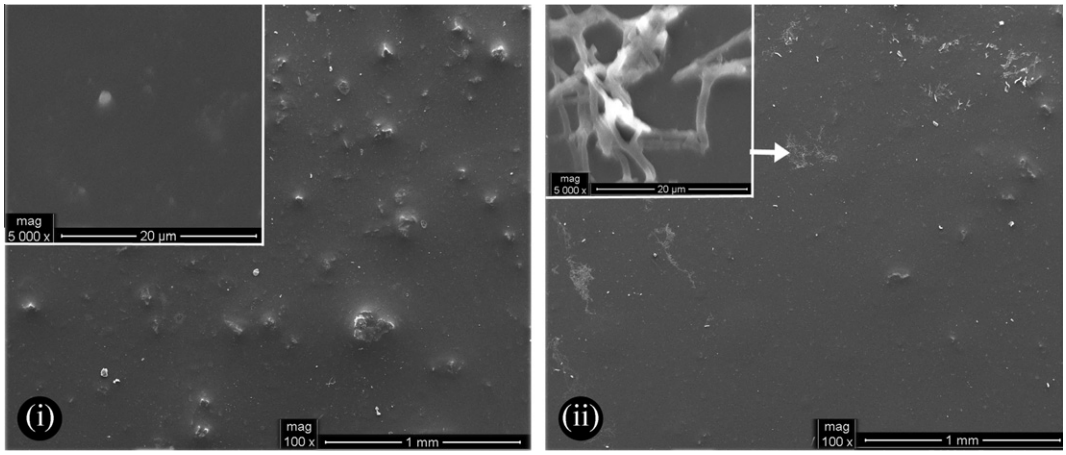

Fig. 5. SEM image of HybridCoat-ncMBT coating (i) before, (ii) after 4 months exposure to 0.5 M NaCl solution at room temperature.

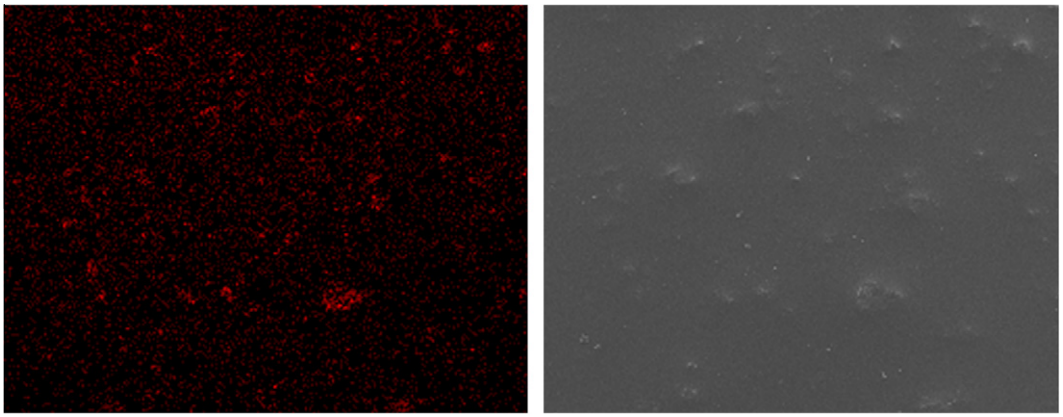

Fig. 6. Maping micrograph (left) and corresponding SEM image (right) of HybridCoat-ncMBT coating.

constant in the middle frequency range that is ascribed to magnesium oxide layer. It can be clearly seen that the barrier protection properties of the coating no longer exist due to the absence of time constant in the high frequency range. Considering the aforementioned results, it can be conducted that the hybrid organic–inorganic coating itself has enhanced anticorrosive properties that last at least 4 months of esposure to 0.5 M NaCl solution. This mean that the coating has good coherence and good adhesion to the substrate without pores or pathways. The corrosive agents become unable to penetrate into the coating and no corrosion attack is happened. Furthermore, the incorporation of corrosion inhibitor into the coating in a free form (not encapsulated into containers) does not change the anticorrosive behavior of the coating, although it diminishes the coherence of the coating. On the other hand, the

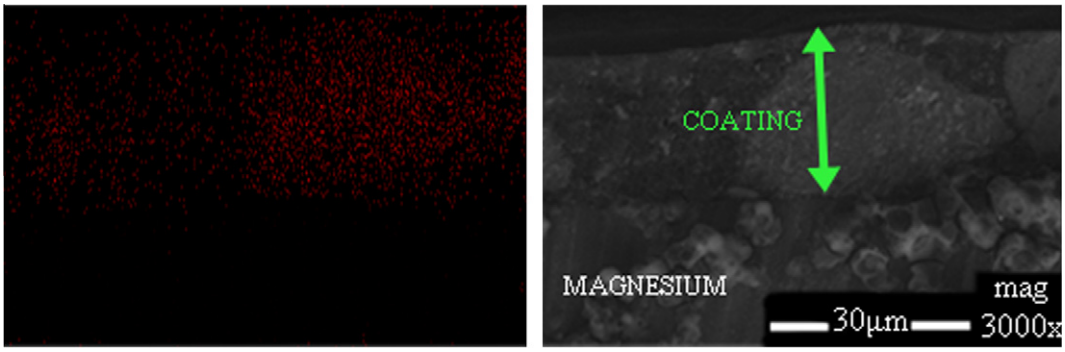

Fig. 7. Maping micrograph (left) and corresponding SEM image (right) of the cross-section of HybridCoat-ncMBT coating.

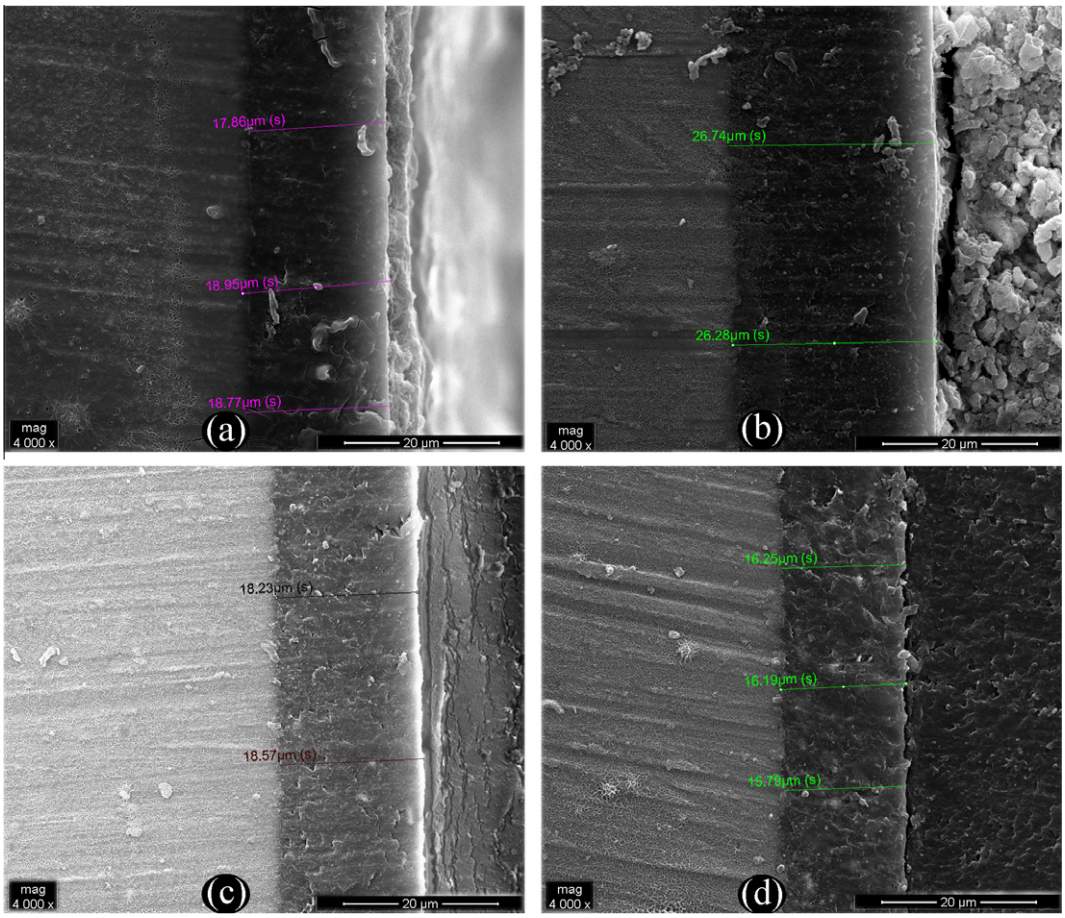

Fig. 8. Cross-section SEM of coatings: (a) HybridCoat, (b) HybridCoat-MBT, (c) HybridCoat-nc and (d) HybridCoat-ncMBT.

incorporation of containers into the coating reduces its corrosion protection efficiency. This result can be attributed to the downgrade of coating coherence after the insertion of containers. However, the incorporation of containers loaded with corrosion inhibitor MBT into the coating does not affect its corrosion protective properties due to the presence of the inhibitor. It should be clarified whether the corrosion inhibitor MBT encapsulated into containers or existing in a free form into the coating improves the anticorrosion efficiency of the coating.

In order the corrosive behavior of the coatings to be better studied and the possible self-healing ability to be evaluated, artificial defects of ~1 mm were created into the coatings. Then the coated substrates were exposed to 1 mM NaCl solution. Fig. 10 presents the EIS Bode spectra of coating without containers or inhibitor (HybridCoat) acquired after 73 h of immersion. There is a consecutive increase of the total impedance value after the fourth day. Similar behavior is revealed for the coating including loaded containers, HybridCoat-ncMBT (Fig. 11). As the immersion time elapses, the impedance values in the low frequency range are also continuously increased. Both HybridCoat and HybridCoat-ncMBT coatings reveal three time constants; one in the high frequency range due to the film, a second small one in the middle frequency range that can be ascribed to the response of processes occurring at the coating/substrate interface and a third time constant in the low frequency range which is attributed to corrosion process.

The interpretation of the results of HybridCoat and HybridCoat-ncMBT coatings after the formation of defect obtained during

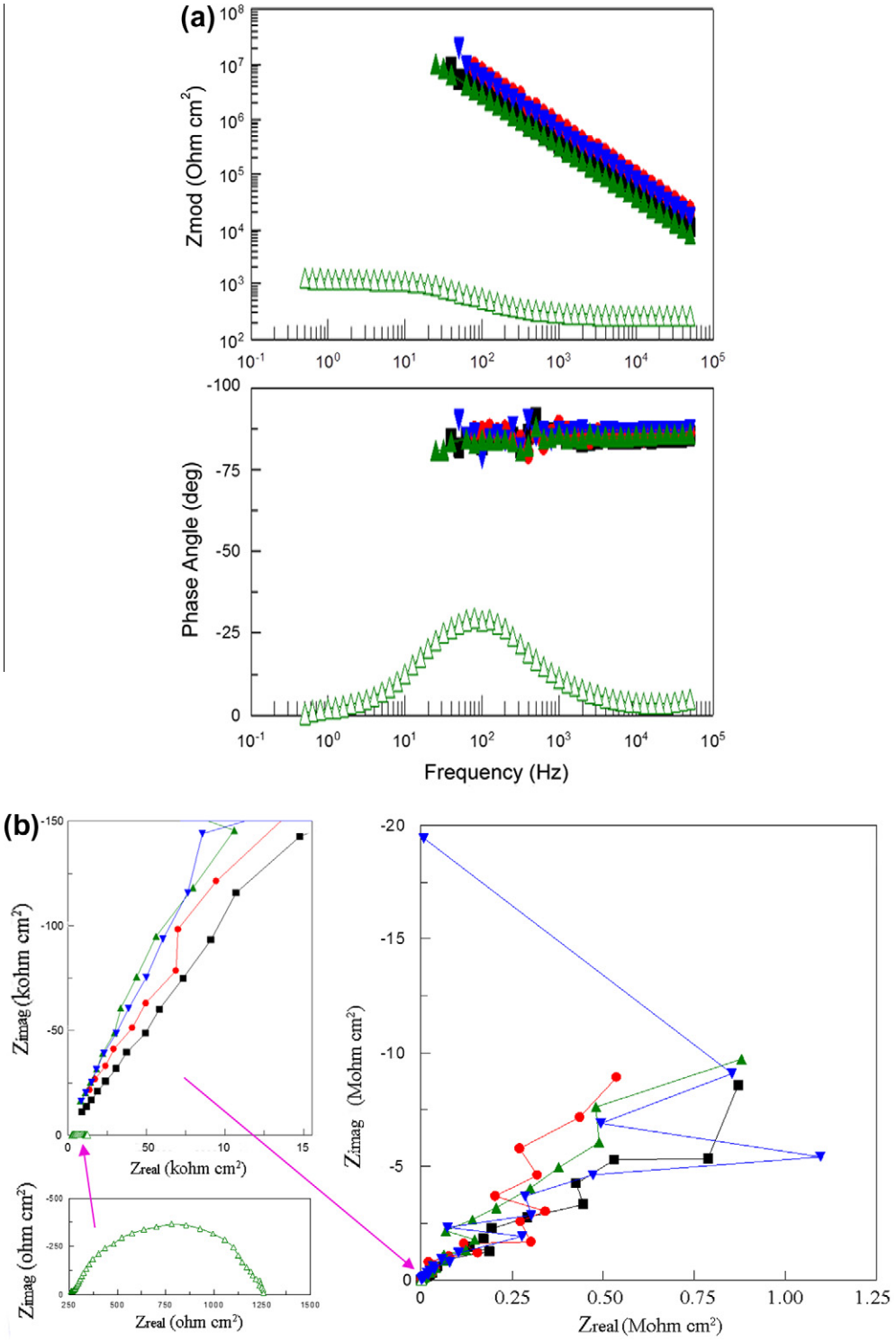

Fig. 9. (a) EIS Bode plots and (b) Nyquist plots of coating after exposure to 0.5 M NaCl solution at room temperature (■) HybridCoat for 4 months, (●) HybridCoat-MBT for 4 months, (▲) HybridCoat-nc for 2 months, (△) HybridCoat-nc for 2.5 months, (▼) HybridCoat-ncMBT for 4 months.

immersion in the NaCl solutions was performed by numerical fitting, using the equivalent circuit illustrated in Fig. 12. This circuit consists of seven components and corresponds to a spectrum that reveals three time constants. It is an equivalent circuit that has the resistance and the capacitance of the coating (R_{coat}–CPE_{coat}), an interface capacitance and the corresponding interface resistance (R_{int}–CPE_{int}) and a charge transfer resistance and a double layer capacitance (R_{ct}–CPE_{dl}).

The evolution of coating capacitance and resistance (C_{coat}, R_{coat}) and double layer capacitance and charge transfer resistance (C_{dl}, R_{ct}) as a function of time in 1 mM NaCl solution for the HybridCoat coating is demonstrated in Fig. 13. The fitting results demonstrate that at the beginning of immersion there is an increase of R_{coat} the first 3 h possibly attributed to the water uptake of the coating, after the third hour a decrease is observed due to the insertion of the electrolyte and finally the values of R_{coat} are stabilized until 73 h.

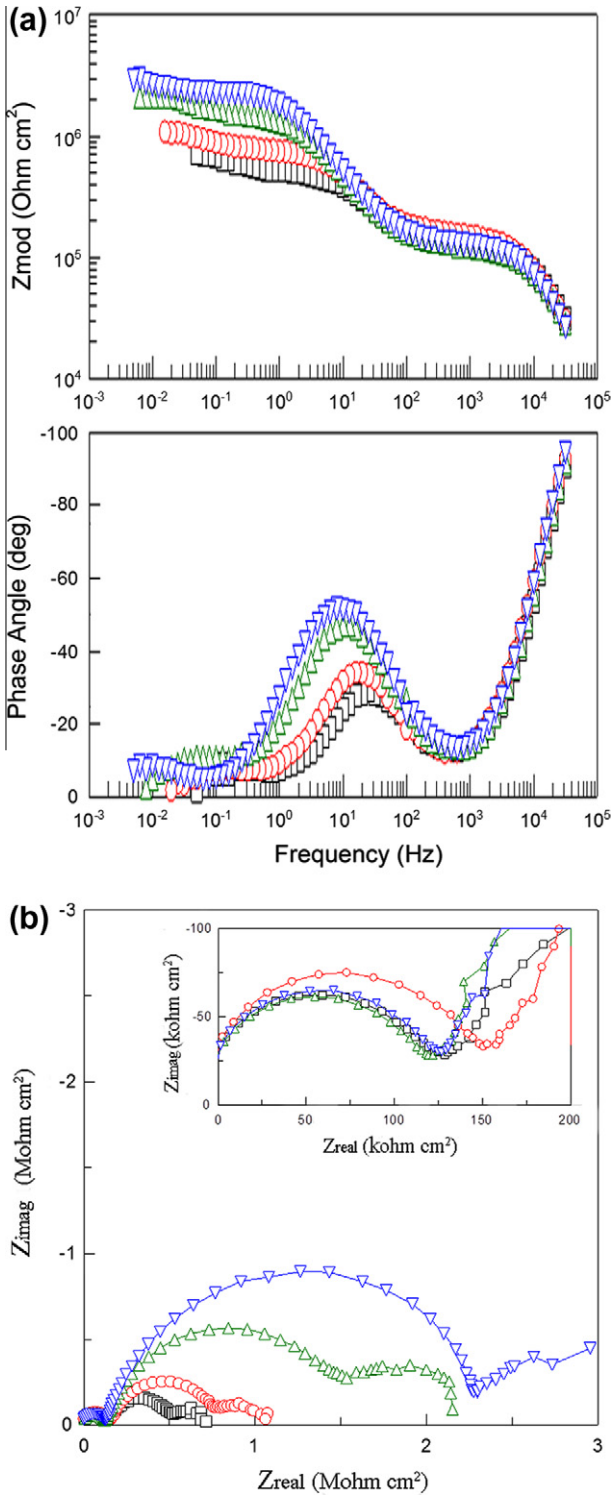

Fig. 10. (a) EIS Bode plots and (b) Nyquist plots of HybridCoat coating after artificial defect formation during immersion in 1 mM NaCl solution for (□) 0 h, (○) 1 h, (△) 10 h, (▽) 73 h.

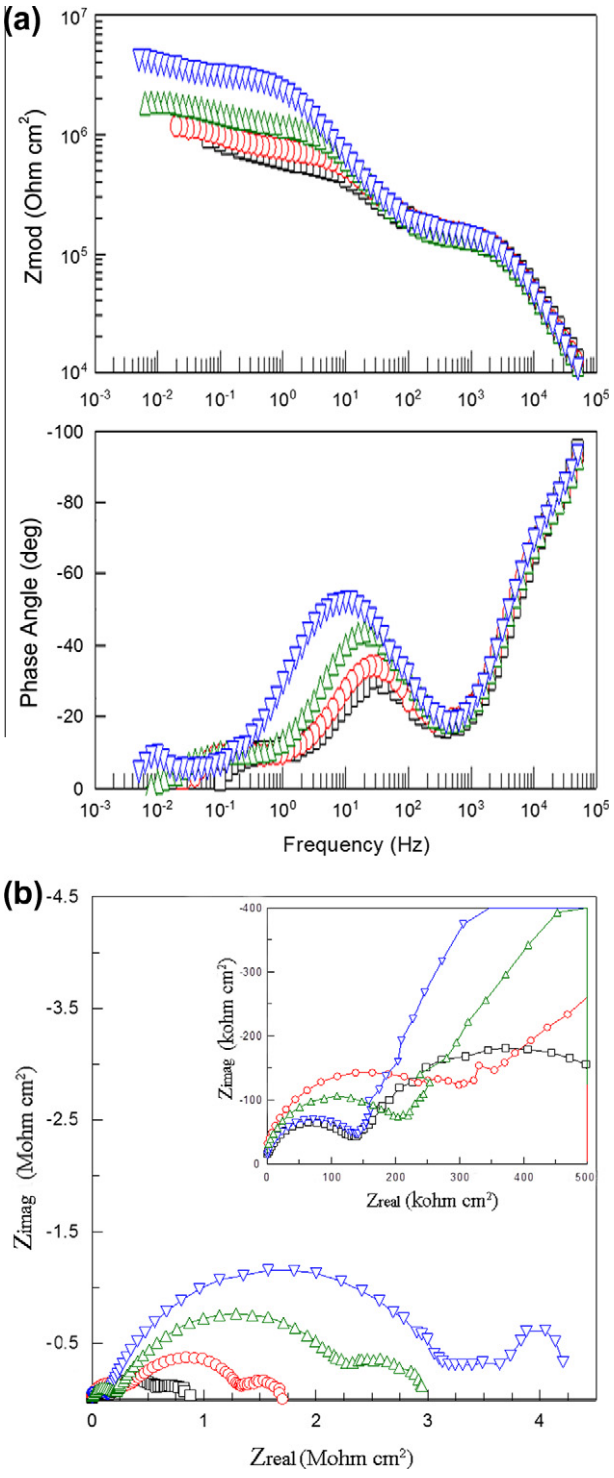

Fig. 11. (a) EIS Bode plots and (b) Nyquist plots of HybridCoat-ncMBT coating after artificial defect formation during immersion in 1 mM NaCl solution for (□) 0 h, (○) 1 h, (△) 10 h, (▽) 73 h.

The values of R_{ct} increased from the beginning of immersion until the 23 h and then a decrease of R_{ct} is demonstrated until the end of exposure to corrosive solution (73 h). The values of R_{ct} increased one order of magnitude between the first and the 23 h. Moreover, the values of the double layer capacitance are increased from the beginning until the end of the experiment (73 h) (Table 3).

Fig. 14 presents the evolution of coating capacitance and resistance (C_{coat}, R_{coat}) and double layer capacitance and charge transfer resistance (C_{dl}, R_{ct}) as a function of time in 1 mM NaCl solution for the HybridCoat-ncMBT coating. There is an increase of coating and charge transfer resistance values until the end of experiment (73 h). The R_{ct} increased 8×10^5 ohm cm^2 between 0 and 73 h. Furthermore, the values of the double layer capacitance are increased from the beginning until the third hour, then a decrease is observed and again an increase is happened from the 10 h until the end of the experiment (Table 4). It should be mentioned that in

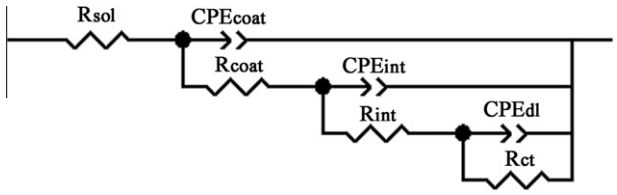

Fig. 12. Equivalent circuit used for numerical simulation of the EIS data of the coatings.

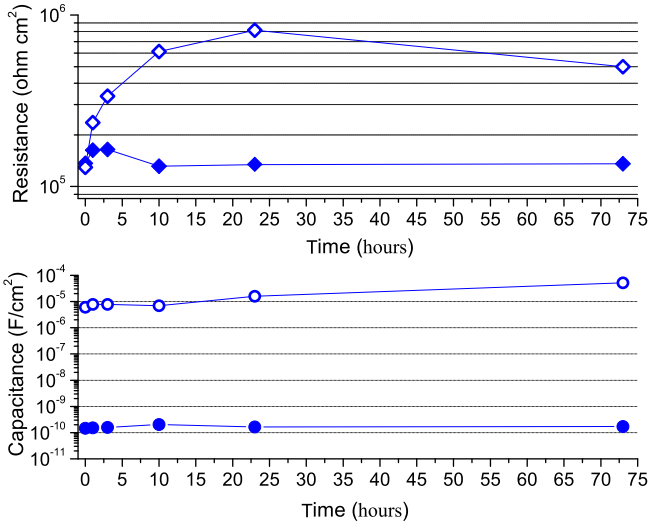

Fig. 13. Evolution of the EIS fitting parameters (●) C_{coat}, (○) C_{dl}, (◆) R_{coat}, (◊) R_{ct} as a function of time in 1 mM NaCl solution for the HybridCoat coating after the formation of defect.

Table 3
Fitting parameters CPE_{coat}–T, CPE_{coat}–P, R_{coat}, C_{coat}, CPE_{dl}–T, CPE_{dl}–P, R_{ct}, and C_{dl} for the HybridCoat coating.

Time (h)	CPE_{coat}–T F cm^{-2} s^{-n}	CPE_{coat}–P	R_{coat} ohm cm^2	C_{coat} F cm^{-2}
0	2.37×10^{-10}	0.95586	1.36×10^5	1.47×10^{-10}
1	2.40×10^{-10}	0.95822	1.63×10^5	1.54×10^{-10}
3	2.38×10^{-10}	0.96195	1.64×10^5	1.59×10^{-10}
10	2.88×10^{-10}	0.96704	1.31×10^5	2.04×10^{-10}
23	2.27×10^{-10}	0.97034	1.34×10^5	1.65×10^{-10}
73	2.05×10^{-10}	0.98353	1.36×10^5	1.72×10^{-10}
	CPE_{dl}–T F cm^{-2} s^{-n}	CPE_{dl}–P	R_{ct} ohm cm^2	C_{dl} F cm^{-2}
0	6.05×10^{-6}	0.99834	1.29×10^5	6.05×10^{-6}
1	7.77×10^{-6}	0.97299	2.36×10^5	7.77×10^{-6}
3	7.81×10^{-6}	0.99561	3.36×10^5	7.84×10^{-6}
10	6.73×10^{-6}	0.9811	6.12×10^5	6.91×10^{-6}
23	1.58×10^{-5}	0.95789	8.15×10^5	1.58×10^{-5}
73	5.16×10^{-5}	0.99972	4.99×10^5	5.17×10^{-5}

order partial recovery of the coating to exist the values of charge transfer resistance (R_{ct}) should be increased as the immersion time elapses. Considering the aforementioned results it is clearly denoted that both HybridCoat and HybridCoat-ncMBT coatings are being recovered after the formation of the artificial defects and suggest that both coatings probably have self-healing properties. Furthermore, considering the values of R_{ct} after 73 h between the two scratched coatings it results that the presence of loaded containers encapsulated into the film improves the partial recovery of the film (Tables 3 and 4). Self-healing can be defined as the partial recovery of the protective properties of the coated system when damaged [40]. The partial recovery of both coatings can be ascribed to the presence of amine groups from HY 943 that have

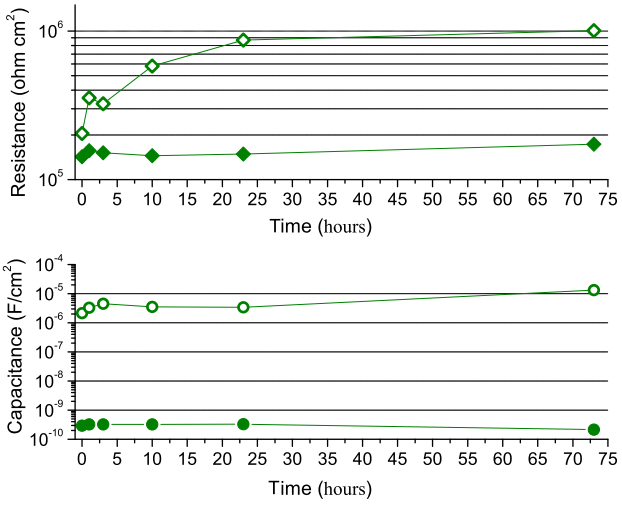

Fig. 14. Evolution of the EIS fitting parameters (●) C_{coat}, (○) C_{dl}, (◆) R_{coat}, (◊) R_{ct} as a function of time in 1 mM NaCl solution for the HybridCoat-ncMBT coating after the formation of defect.

Table 4
Fitting parameters CPE_{coat}–T, CPE_{coat}–P, R_{coat}, C_{coat}, CPE_{dl}–T, CPE_{dl}–P, R_{ct}, and C_{dl} for the HybridCoat-ncMBT coating.

Time (h)	CPE_{coat}–T F cm^{-2} s^{-n}	CPE_{coat}–P	R_{coat} ohm cm^2	C_{coat} F cm^{-2}
0	6.12×10^{-10}	0.9276	1.42×10^5	2.95×10^{-10}
1	7.70×10^{-10}	0.91247	1.56×10^5	3.24×10^{-10}
3	6.83×10^{-10}	0.92471	1.51×10^5	3.24×10^{-10}
10	6.74×10^{-10}	0.92684	1.45×10^5	3.25×10^{-10}
23	6.15×10^{-10}	0.93776	1.49×10^5	3.32×10^{-10}
73	2.26×10^{-10}	0.99551	1.73×10^5	2.16×10^{-10}
	CPE_{dl}–T F cm^{-2} s^{-n}	CPE_{dl}–P	R_{ct} ohm cm^2	C_{dl} F cm^{-2}
0	2.13×10^{-6}	0.99892	2.04×10^5	2.13×10^{-6}
1	3.24×10^{-6}	0.91348	3.55×10^5	3.28×10^{-6}
3	4.43×10^{-6}	0.9499	3.24×10^5	4.52×10^{-6}
10	3.21×10^{-6}	0.87939	5.81×10^5	3.50×10^{-6}
23	2.99×10^{-6}	0.87337	8.68×10^5	3.43×10^{-6}
73	1.20×10^{-5}	0.96354	1.00×10^6	1.32×10^{-5}

not reacted with epoxy groups from GY 257 during the curing process of the coating. However, the presence of MBT encapsulated into the containers also contribute to the partial recovery via the formation of a metal-MBT complex. In aqueous solutions, magnesium is dissociated by the electrochemical reaction with water and a crystalline film of magnesium hydroxide, $Mg(OH)_2$, as well as hydrogen gas are produced. The overall corrosion reaction for magnesium in aqueous solutions is

$$Mg(s) + 2H_2O(l) \rightarrow Mg(OH)_2(s) + H_2(g).$$

This overall reaction can be described in terms of anodic and cathodic reactions as follows:

$$Mg \rightarrow Mg^{+2} + 2e^-$$

and/or $Mg(s) + 2(OH)^- \rightarrow Mg(OH)_2(s) + 2e^-$ (anodic reaction, dissolution of Mg)

and $2H^+ + 2e^- \rightarrow H_2(g)$ (cathodic reaction evolution of hydrogen gas).

A subsequent reaction, giving OH^-, can occur,

$$2H_2O + 2e^- \rightarrow H_2(g) + 2(OH)^-.$$

The produced hydroxide film, brucite, has a hexagonal crystalline structure that is layered, alternating between Mg and hydroxide ions facilitating easy basal cleavage [41]. It is believed that the

inhibitor is released from the containers though diffusion unless the containers are broken by a scratch on the coating. MBT contains S and N atoms in the organic ring and is attached to the magnesium through the S or N atoms that may change the electron density in the metal at the point of attachment. This fact results in the retardation of cathodic or anodic reaction of corrosion of magnesium (as described above) since electrons are consumed at the cathode and furnished at the anode [30].

Fig. 15 illustrates the artificial defected HybridCoat-ncMBT coating after exposure at 1 mM NaCl solution for 73 h. The EDX analysis into the defected area revealed the presence of cerium and carbon elements confirming the partial recovery of the coating (Table 5).

Artificial defects were also created on HybridCoat-MBT and HybridCoat-nc coatings. However, both coatings did not demonstrate partial recovery effect, revealing that the incorporation of the corrosion inhibitor MBT into the coating in a free form is not effective.

The potentiodynamic polarization curves obtained on the scratched samples after 1 h and 6 h of immersion in 1 mM NaCl are demonstrated in Figs. 16 and 17, respectively. The potentiodynamic curves acquired after the exposure of the coatings for 1 h to corrosive environment disclose that the film including loaded containers or the film including inhibitor without containers demonstrate higher breakdown potential than the coatings HybridCoat and HybridCoat-nc. That is to say that incorporation of inhibitor free or encapsulated into containers shift the breakdown potential to nobler potentials (Fig. 16). The immersion of the coatings with artificial defects for 6 h into sodium chloride solution clearly denotes that the film including inhibitor encapsulated into containers reveals the best corrosion protection. It can be seen that the HybridCoat-ncMBT coating has the highest breakdown potential and then it follows the HybridCoat-MBT coating, the HybridCoat-nc coating and the HybridCoat coating (Fig. 17). So the incorporation of loaded containers into the coating improves the corrosion protection properties of the film. Furthermore, the polarization curves disclose that the anodic currents of the coatings including corrosion inhibitor encapsulated or free are lower than the coatings without corrosion inhibitor.

The variations of the open circuit potential (OCP) of the scratched coatings with time in 1 mM NaCl solution at room temperature for 6 h (360 min) are demonstrated in Fig. 18. The exposed area of all the samples for the OCP corrosion tests was 1 cm^2. All the four diagrams disclose OCP fluctuations with time, indicative pitting corrosion initiation and re-passivation [42]. Under the experimental condition, it can be distinguished from the obtained curves that the OCP for all the four coatings, shift in the anodic direction until the end of the experiment. Despite the fact that the OCP values do not provide any direct information on the corrosion kinetics, the consecutive increase of OCP for all the coatings suggests reduction of susceptibility of the films to corrosion process.

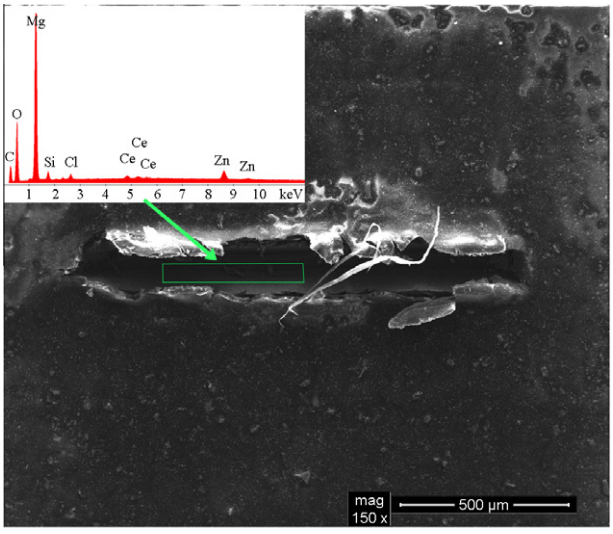

Fig. 15. SEM image of HybridCoat-ncMBT coating having an artificial defect after exposure to 1 mM NaCl solution at room temperature for 73 h.

Table 5
The % w/w element concentration of artificial defected HybridCoat-ncMBT coating after exposure at 1 mM NaCl solution for 73 h.

Element	Mg	Zn	O	Ce	C	Si	Cl
Wt%	32.82	6.49	28.25	1.67	28.49	1.53	0.75

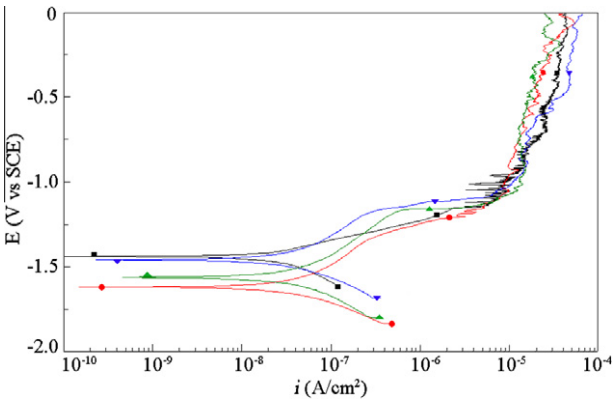

Fig. 16. Polarisation curves of coatings with artificial defects obtained after 1 h of immersion in 1 mM NaCl solution: (□) HybridCoat, (○) HybridCoat-MBT, (▽) HybridCoat-nc, (△) HybridCoat-ncMBT.

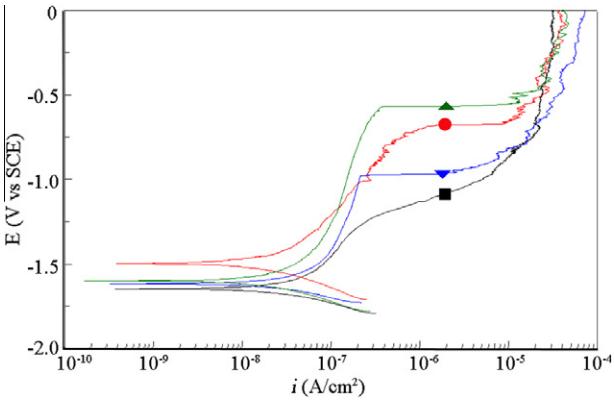

Fig. 17. Polarisation curves obtained after 6 h of immersion in 1 mM NaCl solution: (□) HybridCoat, (○) HybridCoat-MBT, (▽) HybridCoat-nc, (△) HybridCoat-ncMBT.

3.3. Nanomechanical measurements

The nanomechanical properties (namely *H* and *E*) of coatings are presented in Fig 19. The incorporation of containers (with or without inhibitor) affects the mechanical integrity of the coatings, revealing a clear mechanical degradation of epoxy coating; while *H* is slightly decreased, samples exhibit greater deviation in *E* values. In Fig. 19i, a surface region (0 ~ 600 nm) is revealed, where *H* decrease implies deterioration of the coating (further penetration

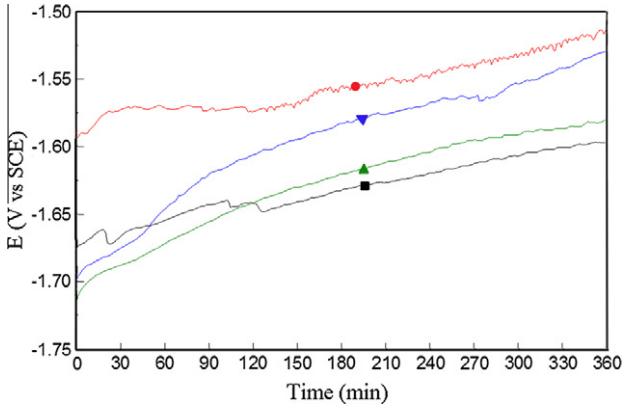

Fig. 18. OCP of coatings with artificial defects obtained after 6 h of immersion in 1 mM NaCl solution: (□) HybridCoat, (○) HybridCoat-MBT, (▽) HybridCoat-nc, (△) HybridCoat-ncMBT.

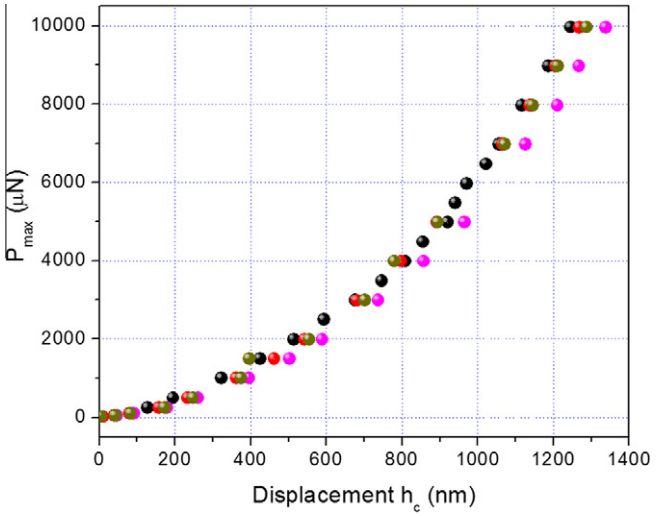

Fig. 20. Plots of P_{max} versus h_c according to the Meyer's law for all coatings: (●) HybridCoat, (●) HybridCoat-MBT, (●) HybridCoat-nc, (●) HybridCoat-ncMBT.

into the coating does not significantly reveal H deviation, where all coatings exhibit a hardness of ~0.3 Gpa). In Fig. 7ii, a clear decrease of E occurs.

The scatter of H and E values was further investigated; deviation of nanomechanical properties is reported to deviate at surface region, probably attributed to roundness of the tip and Indentation Size Effect (ISE), tending to reach a constant values at greater displacements. The reasons for the wide range in H and E values obtained from these nanoindentation measurements are currently unknown, but it is likely due to a combination of factors, e.g. graded surface structure due to containers concentration, adhesive forces between the tip and the sample or containers bundling. The empirical equation for describing the ISE in the Meyer's law [43] is used, which uses a correlation technique between the applied indentation test load and the resultant indentation size using a simple power law, $P_{max} = Ch_c^n$, where C and n are constants derived directly from curve fitting of the experimental data. In particular, the exponent n, sometimes referred to as the Meyer index, is usually considered as a measure of ISE. Compared to the definition of the apparent hardness, no ISE would be observed for $n = 2$ [43]. In our case, n ranges from 1.96 to 1.99 implying no existence of ISE (Fig. 20).

The ratio of hardness to elastic modulus is of significant interest in tribology. Higher stresses are expected in high H/E, hard materials, and high stress concentrations develop towards the indenter tip, whereas in the case of low H/E, soft materials, the stresses are lower and are distributed more evenly across the cross-section of the material [44,45]. The high ratio of hardness to elastic modulus (H/E) is indicative of good wear resistance in a disparate range of materials [45]: ceramic, metallic and polymeric (for example: c-BN, tool steel, nylon, respectively), which are equally effective in resisting attrition for their particular intended application. In Fig. 21, the change of H/E slope reveals that the addition of container and inhibitor amount strengthens (increase of wear resistance) the epoxy coating after ~600 nm of displacement (Fig. 21ii), having no significant impact on surface region (0–600 nm), where all coatings exhibited similar (increased) H/E ratio (Fig. 21i).

The % plasticity values of the materials at different displacements were calculated by integrated areas under the loading curve and the unloading curve. At low displacements, the samples revealed elastoplastic behavior, while for higher displacements the samples exhibited the typical plastic behavior (~90%). Taking into account the %plasticity, it was found that the change from elastic to

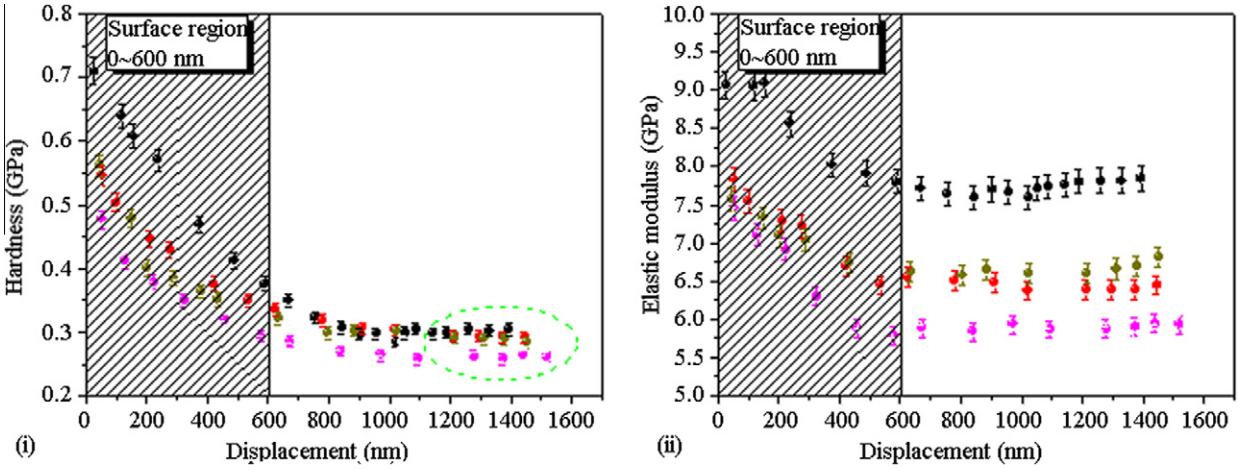

Fig. 19. Nanomechanical properties, namely hardness (i) and elastic modulus (i) of the coatings: (●) HybridCoat, (●) HybridCoat-MBT, (●) HybridCoat-nc, (●) HybridCoat-ncMBT.

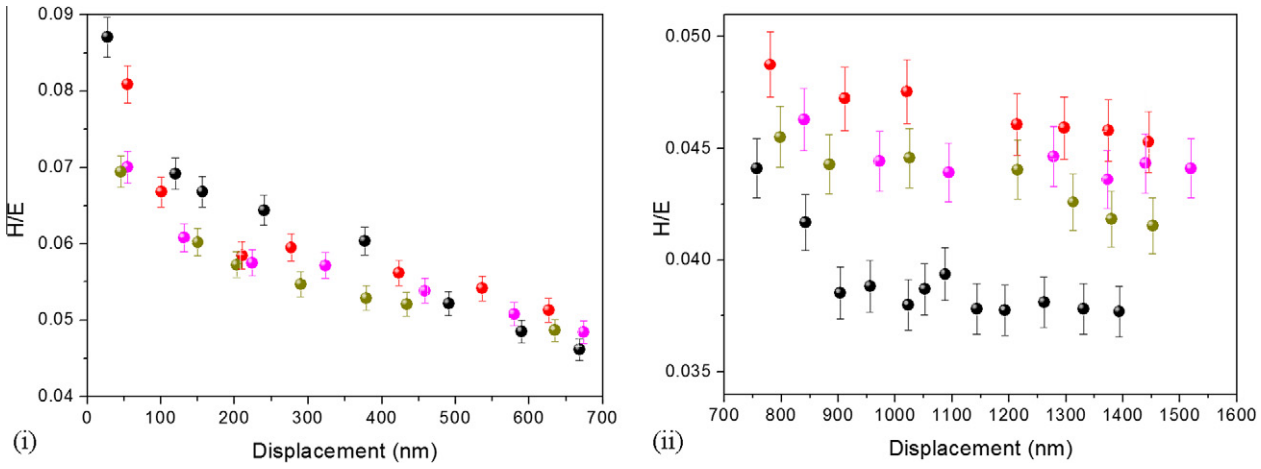

Fig. 21. Correlation of H/E ratio to displacement, for all coatings: (●) HybridCoat, (●) HybridCoat-MBT, (●) HybridCoat-nc, (●) HybridCoat-ncMBT.

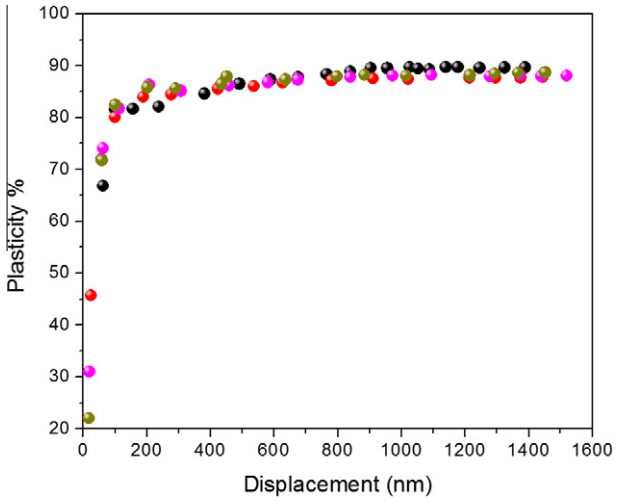

Fig. 22. %Plasticity vs. displacement for all coatings: (●) HybridCoat, (●) HybridCoat-MBT, (●) HybridCoat-nc, (●) HybridCoat-ncMBT.

plastic deformation is observed at almost identical displacement (~100 nm) for all coatings (Fig. 22).

4. Conclusions

This study demonstrates the synthesis and application on magnesium alloys ZK10 of hybrid organic–inorganic coatings. These coatings performed improved corrosion protection properties after exposure to 0.5 M NaCl solution for 4 months. Studies on artificial defected coatings immersed in 1 mM NaCl solution for 73 h presented partial self-recovery of the films. The incorporation into the films of containers loaded with corrosion inhibitor MBT enhanced the self-healing effect due to the increase of the charge transfer resistance. SPM imaging of the coatings revealed that the addition of containers creates surface incongruity; however, the hardness to modulus ratio revealed significant strengthening of the coating with increase of containers. Through nanoindentation analysis, the incorporation of containers lead to a decrease in nanomechanical properties (*H*, *E*) of the coatings (also no ISE was observed). The change of *H/E* slope depicted that the addition of containers and inhibitor amount strengthens (increase of wear resistance) the epoxy coating after 600 nm of displacement, having no significant impact on surface region (0–600 nm), where all coatings exhibited similar (increased) *H/E* ratio. Additionally, all coatings demonstrated no significant differences in the critical parameter of plasticity index.

Acknowledgement

The authors want to thank Alubin – Israel for providing the samples of Mg ZK10.

References

[1] B.L. Mordike, T. Ebert, Magnesium properties – applications – potential, Mater. Sci. Eng. A 302 (2001) 37–45.
[2] X. Cao, M. Jahazi, J.P. Immarigeon, W. Wallace, A review of laser welding techniques for magnesium alloys, J. Mater. Process. Technol. 171 (2006) 188–204.
[3] G.L. Makar, J. Kruger, Corrosion of magnesium, Int. Mater. Rev. 38 (1993) 138–153.
[4] J. Liang, P.B. Srinivasan, C. Blawert, W. Dietzel, Comparison of electrochemical corrosion behavior of MgO and ZrO_2 coatings on AM50 magnesium alloy formed by plasma electrolytic oxidation, Corros. Sci. 51 (2009) 2483–2492.
[5] F. Liu, D. Shan, Y. Song, E.-H. Han, W. Ke, Corrosion behavior of the composite ceramic coating containing zirconium oxides on AM30 magnesium alloy by plasma electrolytic oxidation, Corros. Sci. 53 (2011) 3845–3852.
[6] H. Ardelean, I. Frateur, P. Marcus, Corrosion protection of magnesium alloys by cerium, zirconium and niobium-based conversion coatings, Corros. Sci. 50 (2008) 1907–1918.
[7] H. Meifeng, L. Lei, W. Yating, Z. Cheng, H. Wenbin, Influence of microstructure on corrosion properties of multilayer Mg–Al intermetallic compound coating, Corros. Sci. 53 (2011) 1312–1321.
[8] Thiago F. Conceicao, N. Scharnagl, C. Blawert, W. Dietzel, K.U. Kainer, Corrosion protection of magnesium alloy AZ31 sheets by spin coating process with poly(ether imide) [PEI], Corros. Sci. 52 (2010) 2066–2079.
[9] Thiago F. Conceicao, N. Scharnagl, W. Dietzel, K.U. Kainer, Corrosion protection of magnesium AZ31 alloy using poly(ether imide) [PEI] coatings prepared by the dip coating method: influence of solvent and substrate pre-treatment, Corros. Sci. 53 (2011) 338–346.
[10] A. Yabuki, M. Sakai, Self-healing coatings of inorganic particles using a pH-sensitive organic agent, Corros. Sci. 53 (2011) 829–833.
[11] F. Stippich, E. Vera, G.K. Wolf, G. Berg, Chr. Friedrich, Enhanced corrosion protection of magnesium oxide coatings on magnesium deposited by ion beam-assisted evaporation, Surf. Coat. Technol. 103–104 (1998) 29–35.
[12] H. Ardelean, I. Frateur, S. Zanna, A. Atrens, P. Marcus, Corrosion protection of AZ91 magnesium alloy by anodizing in niobium and zirconium-containing electrolytes, Corros. Sci. 51 (2009) 3030–3038.
[13] T. Ishizaki, M. Okido, Y. Masuda, N. Saito, M. Sakamoto, Corrosion resistant performances of alkanoic and phosphonic acids derived self-assembled monolayers on magnesium alloy AZ31 by vapor-phase method, Langmuir 27 (2011) 6009–6017.
[14] T. Ishizaki, Y. Masuda, M. Sakamoto, Corrosion resistance and durability of superhydrophobic surface formed on magnesium alloy coated with nanostructured cerium oxide film and fluoroalkylsilane molecules in corrosive NaCl aqueous solution, Langmuir 27 (2011) 4780–4788.
[15] J. Hu, Q. Li, X. Zhong, L. Zhang, B. Chen, Composite anticorrosion coatings for AZ91D magnesium alloy with molybdate conversion coating and silicon sol–gel coatings, Prog. Org. Coat. 66 (2009) 199–205.

[16] H. Shi, F. Liu, E. Han, Corrosion protection of AZ91D magnesium alloy with sol–gel coating containing 2-methyl piperidine, Prog. Org. Coat. 66 (2009) 183–191.
[17] A.L.K. Tan, A.M. Soutar, I.F. Annergren, Y.N. Liu, Multilayer sol–gel coatings for corrosion protection of magnesium, Surf. Coat. Technol. 198 (2005) 478–482.
[18] S.V. Lamaka, G. Knornschild, D.V. Snihirova, M.G. Taryba, M.L. Zheludkevich, M.G.S. Ferreira, Complex anticorrosion coating for ZK30 magnesium alloy, Electrochim. Acta 55 (2009) 131–141.
[19] X. Lu, Y. Zuo, X. Zhao, Y. Tang, X. Feng, The study of a Mg-rich epoxy primer for protection of AZ91D magnesium alloy, Corros. Sci. 53 (2011) 153–160.
[20] Y. Zhang, Y. Shao, T. Zhang, G. Meng, F. Wang, The effect of epoxy coating containing emeraldine base and hydrofluoric acid doped polyaniline on the corrosion protection of AZ91D magnesium alloy, Corros. Sci. 53 (2011) 3747–3755.
[21] C.A. Schuh, Nanoindentation studies of materials, Mater. Today 9 (2006) 32.
[22] R. Schwaiger, B. Moser, M. Dao, N. Chollacoop, S. Suresh, Some critical experiments on the strain-rate sensitivity of nanocrystalline nickel, Acta Mater. 51 (2003) 5159.
[23] Li Xiaodong, B. Bhushan, A review of nanoindentation continuous stiffness measurement technique and its applications, Mater. Charact. 48 (1) (2002) 11–36.
[24] C.A. Charitidis, Nanomechanical and nanotribological properties of carbon-based thin films: A review, Int. J. Refract. Met. Hard Mater. 28 (2010) 51.
[25] W.C. Oliver, G.M. Pharr, An improved technique for determining hardness and elastic-modulus using load and displacement sensing indentation experiments, J. Mater. Res. 7 (1992) 1564.
[26] H.E. Friedrich, B.L. Modrike, Magnesium Technology Metallurgy, Design Data, Applications, Springer-Verlag Berlin Heidelberg, Germany, 2006. pp. 211.
[27] I.A. Kartsonakis, G. Kordas, Synthesis and characterization of cerium molybdate nanocontainers and their inhibitor complexes, J. Am. Ceram. Soc. 93 (2010) 65–73.
[28] I.A. Kartsonakis, A.C. Balaskas, G.C. Kordas, Influence of cerium molybdate containers on the corrosion performance of epoxy coated aluminium alloys 2024-T3, Corros. Sci. 53 (2011) 3771–3779.
[29] L.L. Sheir, G.T. Burstein, Corrosion, Corrosion Control, Corrosion Inhibition: Principles and Practice, vol. 2, Butterworth-Heinmann, Great Britain, pp. 17–32.
[30] B. Sanyal, Organic compounds as corrosion inhibitors in different environments – a review, Prog. Org. Coat. 9 (1981) 165–236.
[31] C.H. Hsu, F. Mansfeld, Technical note: concerning the conversion of the constant phase element parameter Y0 into a capacitance, Corrosion 57 (2001) 747–748.
[32] E. Barsoukov, J.R. Macdonald, Impedance Spectroscopy Theory, Experiment, and Applications, A John Wiley & Sons, Inc., Publication, USA, 2005. pp. 13–20.
[33] K.S. Cole, R.H. Cole, Dispersion and absorption in dielectrics. II. Direct current characteristics, J. Chem. Phys. 10 (1942) 98–105.
[34] M. Troyon, L. Huang, Comparison of different analysis methods in nanoindentation and influence on the correction factor for contact area, Surf. Coat. Technol. 201 (2006) 1613–1619.
[35] I.N. Sneddon, Boussinesq's problem for a rigid cone, Math. Proc. Cambridge Philos. Soc. 44 (1948) 492.
[36] R.B. King, Elastic analysis of some punch problems for a layered medium, Inter. J. Solids Struct. 23 (1987) 1657–1664.
[37] E.P. Koumoulos, C.A. Charitidis, N.M. Daniolos, D.I. Pantelis, Nanomechanical properties of friction stir welded AA6082-T6 aluminum alloy, Mater. Sci. Eng. B 176 (2011) 1585–1589.
[38] H. Bei, E.P. George, J.L. Hay, G.M. Pharr, Influence of indenter tip geometry on elastic deformation during nanoindentation, Phys. Rev. Lett. 95 (2005) 045501.
[39] W. Trabelsi, E. Triki, L. Dhouibi, M.G.S. Ferreira, M.L. Zheludkevich, M.F. Montemor, The use of pre-treatment based on doped silane solutions for improved corrosion resistance of galvanised steel substrates, Surf. Coat. Technol. 200 (2006) 4240–4250.
[40] M.F. Montemor, R. Pinto, M.G.S. Ferreira, Chemical composition and corrosion protection of silane films modified with CeO_2 nanoparticles, Electrochim. Acta 54 (2009) 5179–5189.
[41] R. Winston Revie, Uhlig's Corrosion Handbook, second ed., John Wiley and Sons, 2000. pp. 799-800.
[42] M. Schem, T. Schmidt, J. Gerwann, M. Wittmar, M. Veith, G.E. Thompson, I.S. Molchan, T. Hashimoto, P. Skeldon, A.R. Phani, S. Santucci, M.L. Zheludkevich, CeO_2-filled sol–gel coatings for corrosion protection of AA2024-T3 aluminium alloy, Corros. Sci. 51 (2009) 2304–2315.
[43] O. Sahin, O. Uzun, U. Kolemen, N. Ucar, Vickers microindentation hardness studies of β-Sn single crystals, Mater. Charact. 58 (2007) 197–204.
[44] Y.T. Cheng, C.M. Cheng, What is indentation hardness, Surf. Coat. Technol. 133–134 (2000) 417–424.
[45] A. Leyland, A. Matthews, Design criteria for wear-resistant nanostructured and glassy-metal coatings, Surf. Coat. Technol. 177–178 (2004) 317–324.

Corrosion Science 57 (2012) 30–41

Contents lists available at SciVerse ScienceDirect

Corrosion Science

journal homepage: www.elsevier.com/locate/corsci

Incorporation of ceramic nanocontainers into epoxy coatings for the corrosion protection of hot dip galvanized steel

I.A. Kartsonakis [a,b,*], A.C. Balaskas [a], E.P. Koumoulos [b], C.A. Charitidis [b], G.C. Kordas [a]

[a] Sol–Gel Laboratory, IMS, NCSR 'DEMOKRITOS', 15310 Agia Paraskevi, Greece
[b] School of Chemical Engineering, NTUA, 9 Heroon Polytechniou St., 15780 Zographos, Greece

ARTICLE INFO

Article history:
Received 31 August 2011
Accepted 27 December 2011
Available online 3 January 2012

Keywords:
A. Ceramic
A. Steel
B. EIS
B. SEM
C. Pitting corrosion
C. Polymer coatings

ABSTRACT

This study demonstrates the influence of ceramic nanocontainers loaded with corrosion inhibitor 2-mercaptobenzothiazole into hybrid organic–inorganic coatings on the corrosion protection of hot dip galvanized steel. The corrosion resistance of these coatings was evaluated using electrochemical impedance spectroscopy and the results disclosed that the coating including 4% w/w of loaded nanocontainers presented the highest total impedance values until the end of immersion time. On the other hand, the coating without nanocontainers and the coating including 10% w/w of loaded nanocontainers revealed self-healing properties. The mechanical integrity of the coatings is also addressed through nanoindentation and nanoscratch techniques.

1. Introduction

Hot dip galvanized steel (HDG) is steel that has been dipped in molten zinc in order to produce a rust-resistant coating. The term galvanizing usually refers to the hot dip method; it is also sometimes called zinc hot dipping. HDG steel is used in applications where steel may be exposed to weather, but where stainless steel is too expensive. The corrosion resistance of HDG steel can be improved by applications of coatings.

One of the approaches to corrosion protection of HDG steel is based on sol–gel coatings [1–5]. The most important advantages of sol–gel processing over conventional coating methods are easier fabrication of crack-free films or coatings of complex oxides and easier control of composition and microstructure of the deposited films or coatings. The final product of the sol–gel process is the formation of an inorganic oxide. Thin oxide films can be deposited on a substrate at much lower temperature than traditional ceramic methods. Such oxides can provide protection against corrosion by creating an inert barrier between the metal surface and its environment. These coatings exhibit good barrier properties; yet, their use is limited since they usually need high temperature treatments for their formation and their inherent brittleness at film thickness greater than 1 μm. Moreover, sol–gel coatings can provide only passive corrosion protection. Defects or pores presented in the sol–gel coatings allow the corrosion species to penetrate toward the metal surface and initiate the corrosion processes.

Hybrid organic inorganic coatings are another type of protective coatings for HDG steel [6,7]. These systems provide good adhesion of the organic system to the metal, good barrier properties for corrosion protection and low treatment temperatures (below 120 °C). The use of this approach allows combination of advantages of both inorganic and organic components. The organic constituent provides flexibility, reduces defectiveness and improves compatibility with polymer coatings while the inorganic part is responsible for the superior adhesion to the metal surface and the high ductility. The anticorrosive properties of hybrid organic inorganic coatings can be improved by the incorporation of nanoparticles (or nanocontainers loaded with corrosion inhibitors) in the coating [8–10].

Nanoindentation and nanoscratch tests have been widely applied for the measurement of mechanical properties of thin films [11–14]. The nanoindentation test can provide information about the mechanical behavior of the material when it is being deformed at the sub-micron scale. The method developed by Oliver and Pharr allows determining the hardness and the elastic modulus from the nanoindentation load–displacement data [15]. Nanoscratch testing is a versatile tool for analysis of both thin films and bulk materials. Nanoscratch provides the capability to investigate modes of deformation and fracture that are not possible using standard indentation techniques. Nanoscratching is accomplished by applying a normal load in a controlled mode while measuring the force required moving the tip laterally across the sample. The damage incurred from the test is then typically observed using optical or

* Corresponding author at: Sol–Gel Laboratory, IMS, NCSR 'DEMOKRITOS', 15310 Agia Paraskevi, Greece. Tel.: +30 2106503302.
E-mail address: ikartsonakis@ims.demokritos.gr (I.A. Kartsonakis).

0010-938X/$ - see front matter © 2011 Elsevier Ltd. All rights reserved.
doi:10.1016/j.corsci.2011.12.037

Scanning Probe Microscopy (SPM) imaging (in situ SPM imaging of the sample with nanometer resolution for immediate feedback of the test results). Nanoscratch can be used for such a plethora of tests, where a single scratch with a ramped normal load is useful for critical load, film adhesion and mar studies. In the scratch test, a diamond stylus is drawn over the film surface under progressively increasing normal load until the film is detached from the substrate The critical load corresponding to the failure can provide qualitative nature of the scratch resistance or adhesion strength of the film, but it is difficult to extract adhesion strength quantitatively since the critical load depends not only on adhesion strength but also on several intrinsic (testing conditions such as loading rate, scratching speed, and indenter shape) and extrinsic (connected to film–substrate system like material properties, friction coefficient, and physical dimensions) factors [16,17].

In the present work HDG steel were coated via a dip-coating process with a hybrid organic–inorganic coating that contains cerium molybdate nanocontainers loaded with corrosion inhibitor 2-mercaptobenzothiazole (MBT). This compound was selected to be loaded to nanocontainers due to its corrosion inhibitor properties [18]. Moreover, studies on the corrosion resistance of these coatings were performed using electrochemical impedance spectroscopy (EIS), while mechanical integrity was examined through nanoindentation and nanoscratch tests.

2. Materials and experimental details

2.1. Materials and reagents

All chemicals were of analytical reagent grade. 2-Mercaptobenzothiazole (MBT, Sigma–Aldrich, St. Louis, USA), cerium(III) acetylacetonate ($Ce(acac)_3$, Sigma–Aldrich, St. Louis, USA), polyvinylpyrrolidone (PVP, average molecular weight: 55,000, Sigma–Aldrich, St. Louis, USA), potassium persulfate (KPS, Sigma–Aldrich, St. Louis, USA), sodium dodecyl sulfate (SDS, Sigma–Aldrich, St. Louis, USA), aceton (Sigma–Aldrich, St. Louis, USA), USA), *N*-(2-Aminoethyl)-3-(trimethoxysilyl)propylamine (Z 6020, Sigma–Aldrich, St. Louis, USA), epoxy resin based on phenol 4,4′-(1-methylethylidene) bis-(“Araldite GY 257”, GY 257, Ciba-Geigy), 2,2′-diaminodiethylamine (HY 943, Sigma–Aldrich, St. Louis, USA) were used without further purification. Styrene (Sigma–Aldrich, St. Louis, USA) was double distilled under reduced pressure prior to use.

2.2. Synthesis of cerium molybdate nanocontainers loaded with MBT

Cerium molybdate nanocontainers were synthesized through a two-step process and then loaded with the anodic corrosion inhibitor MBT. The synthesis, characterization and the loading process of these nanocontainers are reported in our previous work [19]. Briefly, templates of polystyrene were synthesized via polymerization in emulsion. Then, the templates were coated with cerium molybdate via the sol–gel process. The nanocontainers were obtained after calcination of the coated composites and loaded using saturated solutions of MBT in acetone. The morphology of the produced nanocontainers as well as thermogravimetric analysis (TGA) diagrams including the loading results are depicted in our previous work [20]. The nanocontainers exhibited an average diameter of 230 ± 20 nm, and they were 58.08% w/w loaded with MBT.

2.3. Preparation of coating

The % w/w material concentration of the epoxy solution is presented in Table 1. The synthetic process was followed according to our previous work [20]. Initially, Z 6020 was hydrolyzed in absolute ethanol for 1 h (solution A). Then, resin GY 257 was dissolved in absolute ethanol (solution B). Solutions A and B were intermixed formatting solution C. After that, HY 943 was dissolved in acetone and was added to solution C. The appropriate amount of cerium molybdate loaded nanocontainers was added to the above solution, under vigorous stirring, 1 h before the beginning of the dip coating process.

Table 1
Conditions used for the preparation of epoxy solution.

Reagent	Z 6020	GY 257	HY 943	Ethanol	Acetone
% w/w	1.76	20.0	1.76	47.06	29.42

The panels were dip coated into the epoxy solution for six times with a withdraw rate of 32 cm/min. Each time, the panels remained into the solution for 1 min. Then, the coated panels were heat treated at temperature 70 °C for 4 days. The HDG steel panels had been cleaned, prior the dip-coating process. The metallic coupons were degreased in acetone and then immersed in a NaOH solution of pH 11 for 5 min at 50 °C for cleaning and degreasing. After this the coupons were washed with distilled water and dried in air.

Two different coatings were prepared, one including 4% w/w nanocontainers loaded with MBT (Coat-4%nc-MBT) and another one including 10% w/w nanocontainers loaded with MBT (Coat-10%nc-MBT). Moreover, the corresponding coatings including empty nanocontainers (Coat-4%nc, Coat-10%nc) were prepared. Furthermore, coatings including inhibitor without nanocontainers (Coat-MBT) as well as coatings without nanocontainers or inhibitor (Coat) were also synthesized. The coatings Coat-4%nc, Coat-10%nc, Coat-MBT and Coat were synthesized in order to be compared with the coatings including loaded nanocontainers (Coat-4%nc-MBT, Coat-10%nc-MBT).

2.4. Characterization

The morphology, the average nanocontainer size and the composition of the coatings were determined by Scanning Electron Microscopy (SEM) and Energy Dispersive X-ray Analysis (EDX) using a PHILIPS Quanta Inspect (FEI Company) microscope with W (tungsten) filament 25 kV equipped with EDAX GENESIS (AMETEX PROCESS & ANALYTICAL INSTRUMENTS). Moreover, the loading of the inhibitor into the containers was estimated by TGA using a Perkin Elmer (Pyris Diamand S II) analyzer at the heating rate of 10 °C min^{-1} in air.

EIS measurements were made using a SI 1287 Solartron Electrochemical interface connected with a SI 1260 Impedance/gain-phase analyzer. The experiments were performed at room temperature, in a Faraday cage, at the open circuit potential, using a three-electrode electrochemical cell, consisting of working electrode (≈2.00 cm^2 of exposed area), saturated calomel electrode (SCE) as reference and platinum as counter electrode. The measuring frequency ranged from 100 kHz down to 5 mHz. The RMS voltage was 10 mV. Spectra were treated using the Z-view software using the adequate equivalent electric circuits. The number of frequency points was 10 points per decade.

Nanoindentation testing was performed with a nanomechanical test instrument, which allows the application of loads from 1 to 30 mN and records the displacement as a function of applied loads with a high load resolution (1 nN) and a high displacement resolution (0.04 nm). The nanomechanical test instrument employed in this study was equipped with a Scanning Probe Microscope (SPM), in which a sharp probe tip moves in a raster scan pattern across a sample surface using a three-axis piezo positioner. In all depth-sensing tests a total of 10 indents were averaged to

determine the mean hardness (H) and elastic modulus (E) values for statistical purposes, in a clean area environment with 45% humidity and 23 °C ambient temperature. In order to operate under closed loop load control, feedback control option was used. All nanoindentation measurements have been performed with the standard three-sided pyramidal Berkovich probe, with an average radius of curvature of about 100 nm [14], with 40 s loading and unloading segment time separately and 3 s of holding time, to avoid residual viscoelasticity. Prior to indentation, the area function of the indenter tip was measured in a fused silica, a standard material for this purpose [21].

The scratch tests performed in this work included three main segments. Firstly, a pre-scan under a very small load (1 μN) was carried out; then, the indenter scraped the sample under a certain force and scratch would be generated. The normal applied loads were 300 μN, while length of the scratches was 8 μm.

3. Results and discussion

3.1. Corrosion test

Corrosion test process includes the exposure of the coated panels to 0.5 M NaCl solution at room temperature for 744 h (31 days). EIS was used in order protective abilities and the corrosion mechanism of the coated samples to be estimated. EIS is a technique with signal that has small perturbation and the surface damage of the sample is very little.

Figs. 1–6 depict the impedance spectra obtained during 31-day immersion period for the coatings Coat, Coat-MBT, Coat-4%nc, Coat-10%nc, Coat-4%nc-MBT and Coat-10%nc-MBT, respectively. The coating without nanocontainers or inhibitor (Coat) presents one time constant. It can be seen the capacitive response in the high frequency range and the corresponding resistive response in the low frequency range due to the coating protection [22]. The total impedance values measured in the low frequency range can be used to assess the corrosion resistance of the system. The low frequency impedance values for the Coat coating begin from 20 MΩ cm^2 (6 h) and finally reach to 1.7 MΩ cm^2 (31 days) (Fig. 1). The corrosion behavior of the coating including inhibitor (Coat-MBT) is illustrated in Fig. 2. At the first 7 days of immersion the Bode spectra reveal a time constant in the high frequency range which is attributed to the presence of the coating and its barrier properties and a second time constant in the middle frequency

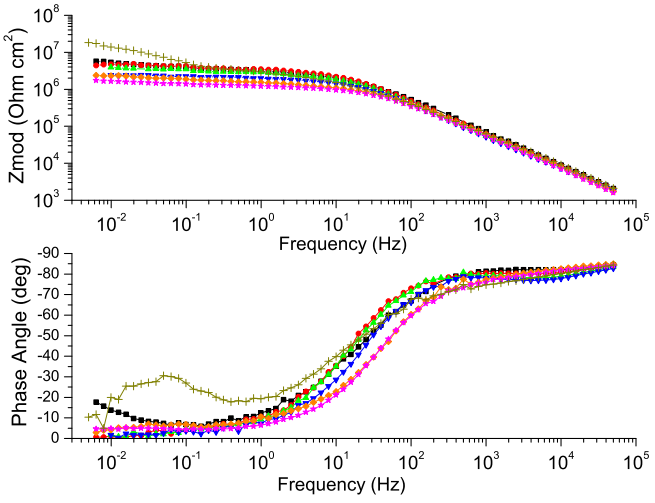

Fig. 1. EIS Bode plots of Coat coating after exposure to 0.5 M NaCl solution for (+) 6 h, (■) 24 h, (●) 96 h (4 days), (▲) 216 h (9 days), (▼) 360 h (15 days), (◆) 528 h (22 days), (★) 744 h (31 days).

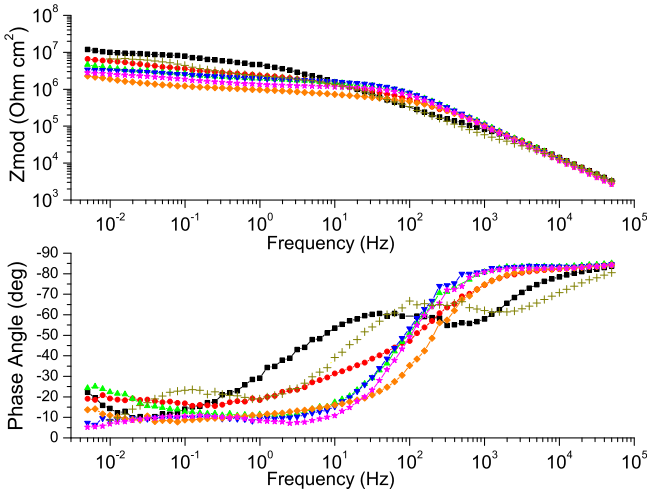

Fig. 2. EIS Bode plots of Coat-MBT coating after exposure to 0.05 M NaCl solution for (+) 6 h, (■) 24 h, (●) 96 h (4 days), (▲) 216 h (9 days), (▼) 360 h (15 days), (◆) 528 h (22 days), (★) 744 h (31 days).

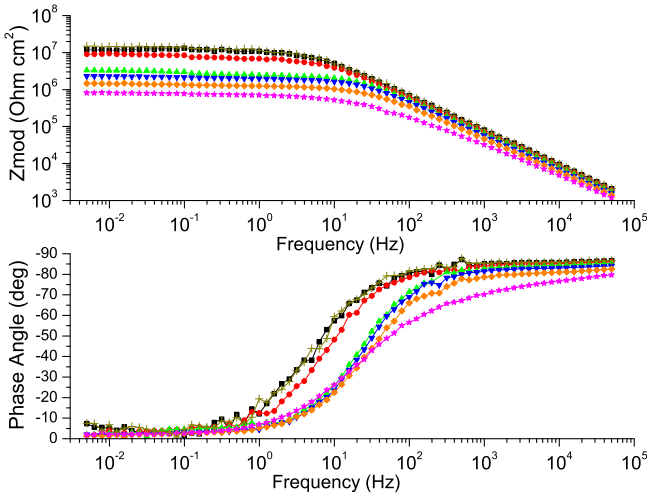

Fig. 3. EIS Bode plots of Coat-4%nc coating after exposure to 0.05 M NaCl solution for (+) 6 h, (■) 24 h, (●) 96 h (4 days), (▲) 216 h (9 days), (▼) 360 h (15 days), (◆) 528 h (22 days), (★) 744 h (31 days).

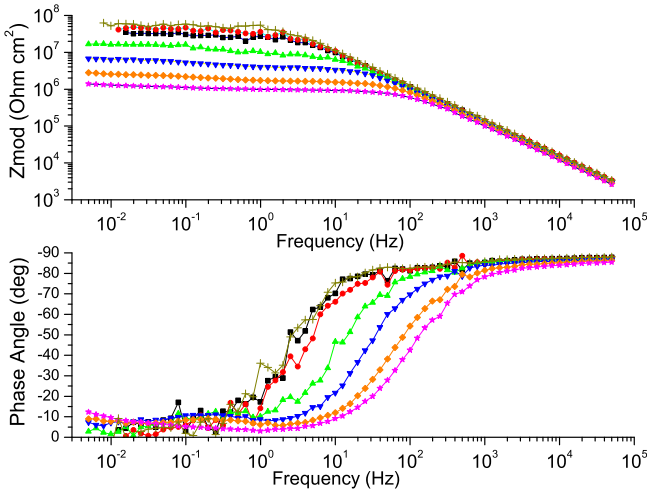

Fig. 4. EIS Bode plots of Coat-10%nc coating after exposure to 0.05 M NaCl solution for (+) 6 h, (■) 24 h, (●) 72 h (3 days), (▲) 216 h (9 days), (▼) 360 h (15 days), (◆) 528 h (22 days), (★) 744 h (31 days).

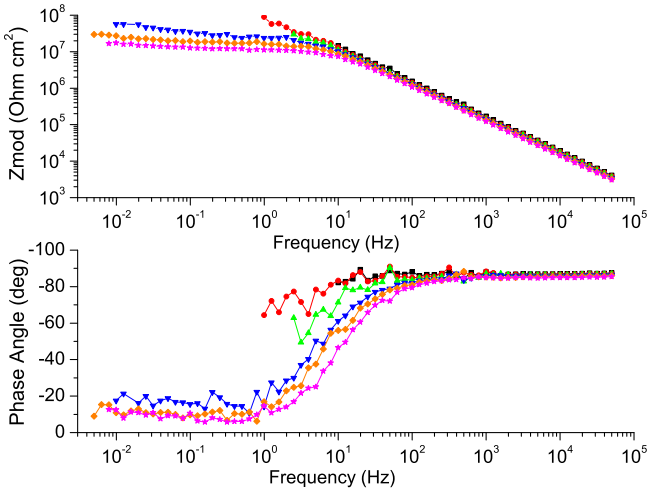

Fig. 5. EIS Bode plots of Coat-4%nc-MBT coating after exposure to 0.05 M NaCl solution for (■) 24 h, (●) 96 h (4 days), (▲) 216 h (9 days), (▼) 360 h (15 days), (◆) 528 h (22 days), (★) 744 h (31 days).

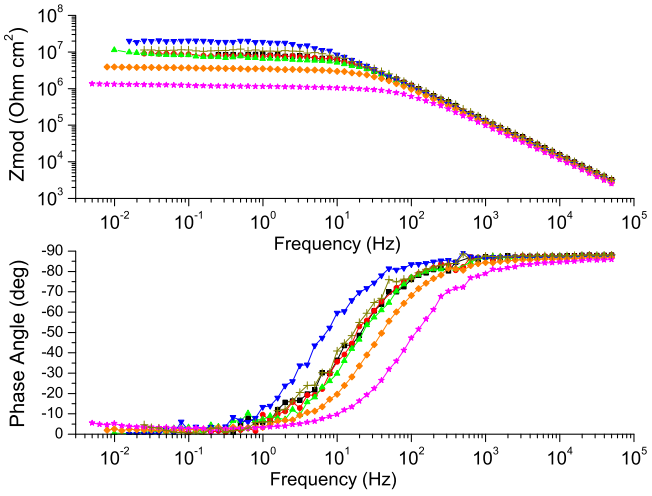

Fig. 6. EIS Bode plots of Coat-10%nc-MBT coating after exposure to 0.05 M NaCl solution for (+) 6 h, (■) 24 h, (●) 72 h (3 days), (▲) 216 h (9 days), (▼) 360 h (15 days), (◆) 528 h (22 days), (★) 744 h (31 days).

range that can be ascribed to the response of processes occurring at the coating/substrate interface [3]. As the immersion time elapses (after 7 days) the Bode spectra depict one time constant. The capacitive response in the high frequency range as well as the corresponding resistive response in the low frequency range due to the coating protection is clearly seen. The initial low frequency impedance values for the Coat-MBT coating are above 10 MΩ cm^2 whereas later on, they start to decrease attaining values to 2 MΩ cm^2 after 31 days of immersion.

EIS Bode plots of Coat-4%nc coating are demonstrated in Fig. 3. The Bode spectra depict one time constant due to the coating protection. The low frequency impedance values for the Coat-4%nc coating are 19 MΩ cm^2 (6 h) and as the time elapses reach to 0.89 MΩ cm^2 (31 days). Fig. 4 illustrates the EIS spectra of Coat-10%nc coating. The spectra present one time constant due to the coating protection. The low frequency impedance values for the Coat-10%nc coating are 71 MΩ cm^2 at the early hours of immersion (6 h) and finally go slightly above 1 MΩ cm^2 after 31 days of immersion.

The Bode spectra obtained for the coating including 4% loaded nanocontainers (Coat-4%nc-MBT) are characterized by the presence of a capacitive response during the first 9 days of immersion (Fig. 5). The phase angle is between -90° to -80° in the measured frequency range revealing that the coating behaves as a capacitor. This behavior denotes that the coating has enhanced barrier properties and acts as an insulator [22]. As the immersion time elapses, one time constant is appeared due to the coating protection. During the first 4 days of immersion the low frequency impedance values for the Coat-4%nc-MBT coating are above 100 MΩ cm^2 while later on, they start to decrease attaining values 20 MΩ cm^2 after 31 days of immersion. The coating including 10% loaded nanocontainers (Coat-10%nc-MBT) presents one time constant due to the coating protection. The low frequency impedance values for the Coat coating at the early time of immersion are 25 MΩ cm^2 (6 h) but as the time elapses the values are slightly above 1 MΩ cm^2 (31 days) (Fig. 6).

The Bode plots of the EIS spectra obtained for all the coated samples after 31 days are depicted in Fig. 7. Bare HDG steel is presented as reference. It is clearly denoted from the impedance values at low frequency range that the Coat-4%nc-MBT coating demonstrates the best corrosion protective behavior after 744 h (31 days) of exposure in corrosive environment as its value is increased compared to all the other coatings. Thus, the encapsulation of corrosion inhibitor into cerium molybdate containers and the incorporation of the loaded nanocontainers to the epoxy coating improve the corrosion protection properties of the coating for longer time compared to (i) coating with inhibitor MBT, (ii) coatings that incorporate empty nanocontainers and (iii) coating without nanocontainers. It should be mentioned the Coat-4%nc-MBT coating demonstrates better corrosion protection than the Coat-10%nc-MBT coating. This behavior reveals that the 10% w/w concentration of loaded nanocontainers does not improve the anticorrosive properties of the coating compare to a 4% w/w concentration of loaded nanocontainers. The reason is that the 10% w/w concentration may have formed agglomerates into the coating that produce conductive pathways where the electrolyte penetrates, reaching the substrate [9].

The interpretation of the EIS results obtained during immersion in the NaCl solutions was performed by numerical fitting, using the equivalent circuit illustrated in Fig. 8. In this equivalent circuit, constant phase elements were used instead of pure capacitors. This modification is obligatory in the case the phase shift of a capacitor

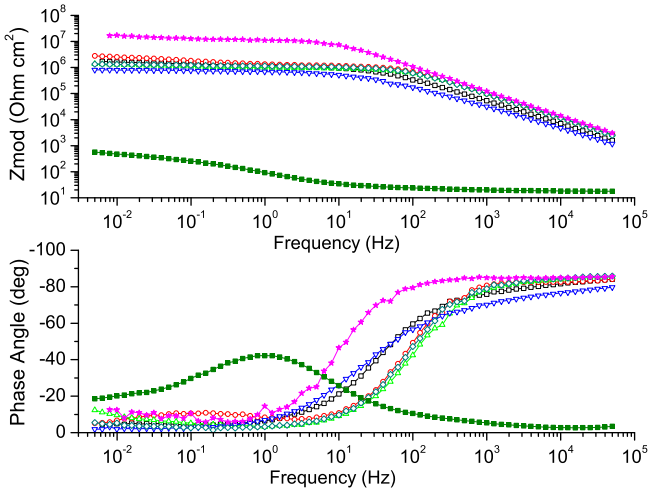

Fig. 7. EIS Bode plots of (□) Coat, (○) Coat-MBT, (△) Coat-10%nc, (▽) Coat-4%nc, (◊) Coat-10%nc-MBT, (★) Coat-4%nc-MBT, (■) Bare HDG steel after exposure to 0.5 M NaCl solution at room temperature for 744 h (31 days).

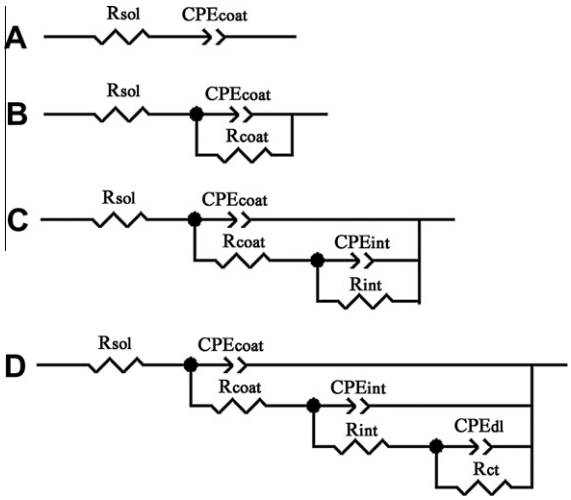

Fig. 8. Equivalent circuit used for numerical simulation of the EIS data of the coatings.

is different from −90° [23]. The impedance of a R-CPE parallel association is given by:

$$Z_{R-CPE} = \frac{R}{1 + RY_0(J\omega)^n} \quad (1)$$

where Y_0 is the admittance of the CPE and n is the CPE exponent. Constant phase elements correspond to a capacitor when the CPE exponent (n) is one. Using the Cole–Cole approach together with CPE, the capacitance can be calculated from the fittings by [24,25]:

$$C = \sqrt[n]{\frac{RY_0}{R^n}} \quad (2)$$

The equivalent circuit for the coatings Coat includes the resistance and the capacitance of the coating (R_{coat}–CPE_{coat}) (Fig. 8B). The resistance of the solution is illustrated as R_{sol}. The coating Coat-MBT for the first 7 days is simulated by an equivalent circuit that has the resistance and the capacitance of the coating (R_{coat}–CPE_{coat}) and a second relaxation process including an interface capacitance and the corresponding interface resistance (R_{int}–CPE_{int}) (Fig. 8C). The circuit of the coating Coat-4%nc is represented by Fig. 8B and includes the resistance and the capacitance of the coating (R_{coat}–CPE_{coat}).

The coating Coat-4%nc-MBT illustrates a capacitive response during the first 9 days of immersion which corresponds to capacitance of the coating (CPE_{coat}) (Fig. 8A) [22]. As the immersion time elapses, one time constant appeared and the appropriate equivalent circuit for the fitting is the one of Fig. 8B. The equivalent circuit for the coating Coat-10%nc-MBT includes a capacitive response and a resistive contribution. (Fig. 8B).

The fitting parameters that demonstrate the evolution of coating capacitance and resistance (C_{coat}, R_{coat}) during the immersion time in corrosive environment are depicted in Fig. 9. The results reveal that the coatings Coat and Coat-4%nc present the less capacitive behavior. The coatings Coat-MBT, Coat-10%nc, Coat-4%nc-MBT and Coat-10%nc-MBT illustrate the same capacitive behavior although the coating Coat-4%nc-MBT has the less capacitive values after 15 days. The corresponding coating resistance results come in accordance with the aforementioned capacitance results. It is clearly denoted that the coatings with lower capacitive values also exhibit higher resistive values. Furthermore, it is noticed that after 15 days of immersion to corrosive environment, the coating Coat-4%nc-MBT exhibits the highest resistive values. Thus, the incorporation of loaded nanocontainers into the coating improved the corrosion resistance of the coating, whereas all the coatings have increased R_{coat} values that mean that they have enhanced barrier properties. Finally, it should be mentioned that the coating Coat-4%nc-MBT does not have coating resistance values the first 9 days because it depicts only a capacitive response.

In order the corrosive behavior of the coatings to be better studied and possible self-healing ability to be evaluated, artificial defects of 1 mm were created into the coatings. Then the coated substrates were exposed to 5 mM NaCl solution. Fig. 10 presents the EIS Bode spectra of coating without nanocontainers or inhibitor (Coat) acquired after 7 days of immersion. Although a decrease of the impedance values in the low frequency range is observed during the first 3 days of immersion, there is a consecutive increase of the total impedance after the fourth day. Similar behavior is revealed for the coating including 10% loaded nanocontainers (Fig. 11). There is a decrease of the total impedance during the

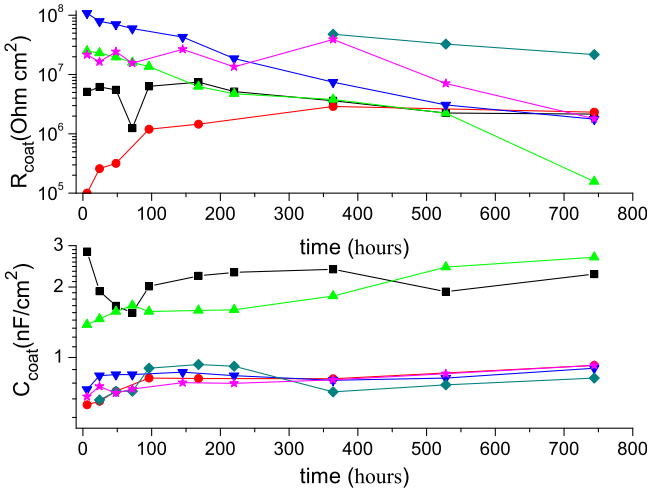

Fig. 9. R_{coat} and C_{coat} evolution of coatings: (■) Coat, (●) Coat-MBT, (▲) Coat-4%nc, (▼) Coat-10%nc, (◆) Coat-4%nc-MBT and (★) Coat-10%nc-MBT, as a function of time of exposure to 0.5 M NaCl solution at room temperature.

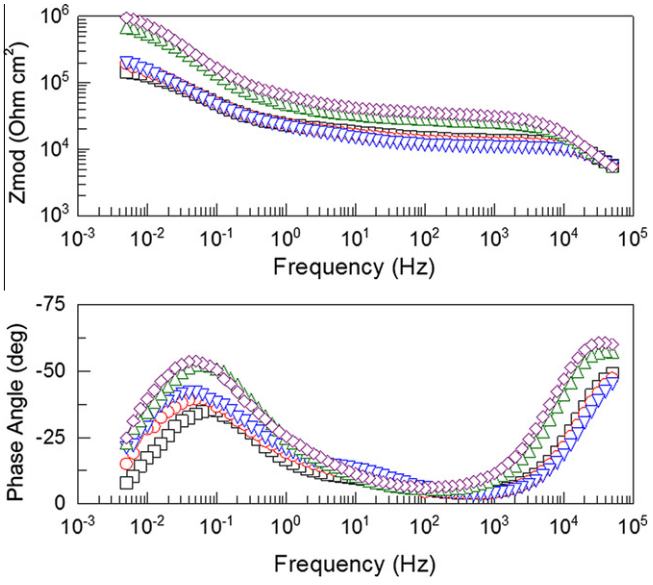

Fig. 10. EIS Bode plots of Coat coating after artificial defect formation during immersion in 5 mM NaCl solution for (□) 72 h (3 days), (○) 96 h (4 days), (▽) 120 h (5 days), (△) 144 h (6 days), (◊) 168 h (7 days).

early days of immersion, but after the sixth day the impedance values in the low frequency range are increased. Both Coat and Coat-10%nc-MBT coatings reveal three time constants; one in the high frequency range due to the film, a second small one in the middle frequency range that can be ascribed to the response of processes occurring at the coating/substrate interface and a third time constant in the low frequency range which is attributed to corrosion process.

The EIS results of Coat and Coat-10%nc-MBT coatings after the formation of defect were fitted using the equivalent circuit of Fig. 8D. This circuit consists of seven components and corresponds to a spectrum that reveals three time constants. It is an equivalent circuit that has the resistance and the capacitance of the coating (R_{coat}–CPE_{coat}), an interface capacitance and the corresponding interface resistance (R_{int}–CPE_{int}) and a charge transfer resistance and a double layer capacitance (R_{ct}–CPE_{dl}). Fig. 12 presents the evolution of C_{coat}, C_{dl}, R_{coat}, R_{ct} as a function of time in 5 mM NaCl

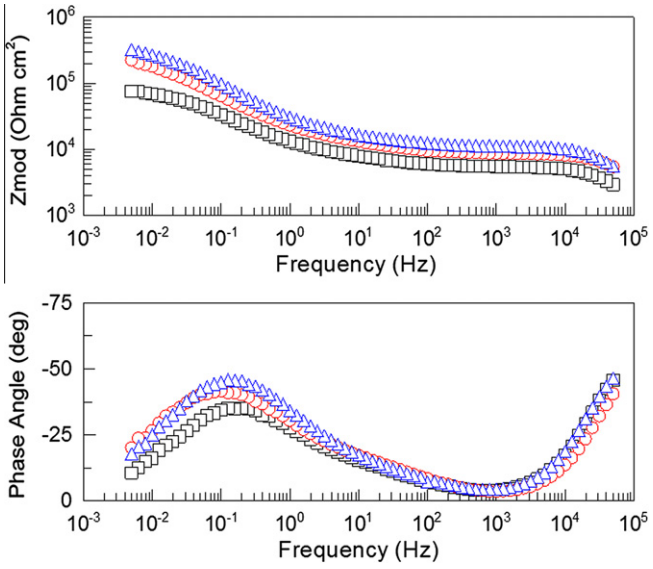

Fig. 11. EIS Bode plots of Coat-10%nc-MBT coating after artificial defect formation during immersion in 5 mM NaCl solution for (□)144 h (6 days), (○)168 h (7 days), (▽) 240 h (10 days).

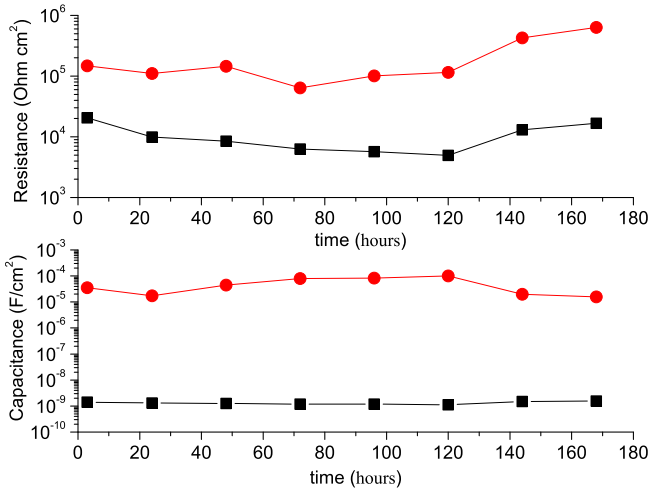

Fig. 12. Evolution of the EIS fitting parameters (■) C_{coat}, (●) C_{dl}, (■) R_{coat}, (●) R_{ct} as a function of time in 5 mM NaCl solution for the Coat coating after the formation of defect.

Table 2
Fitting parameters CPE_{coat}-T, CPE_{coat}-P, R_{coat}, C_{coat}, CPE_{dl}-T, CPE_{dl}-P, R_{ct}, and C_{dl} for the Coat coating.

Time (h)	CPE_{coat}–T F cm^{-2} s^{-n}	CPE_{coat}–P	R_{coat} Ω cm^2	C_{coat} F cm^{-2}
3	3.54×10^{-9}	0.91214	2.06×10^{4}	1.41×10^{-9}
24	2.84×10^{-9}	0.93093	9.91×10^{3}	1.30×10^{-9}
48	3.66×10^{-9}	0.9068	8.45×10^{3}	1.26×10^{-9}
72	3.34×10^{-9}	0.91264	6.30×10^{3}	1.19×10^{-9}
96	3.28×10^{-9}	0.91449	5.71×10^{3}	1.19×10^{-9}
120	3.17×10^{-9}	0.91446	4.96×10^{3}	1.13×10^{-9}
144	5.87×10^{-9}	0.87331	1.32×10^{4}	1.49×10^{-9}
168	6.63×10^{-9}	0.86295	1.67×10^{4}	1.56×10^{-9}
	CPE_{dl}–T F cm^{-2} s^{-n}	CPE_{dl}–P	R_{ct} Ω cm^2	C_{dl} F cm^{-2}
3	2.09×10^{-5}	0.68128	1.47×10^{5}	3.54×10^{-5}
24	1.42×10^{-5}	0.70204	1.11×10^{5}	1.73×10^{-5}
48	3.14×10^{-5}	0.80962	1.46×10^{5}	4.48×10^{-5}
72	5.98×10^{-5}	0.82323	6.39×10^{4}	7.97×10^{-5}
96	5.38×10^{-5}	0.79865	1.00×10^{5}	8.23×10^{-5}
120	6.01×10^{-5}	0.78735	1.15×10^{5}	1.01×10^{-5}
144	1.47×10^{-5}	0.86352	4.25×10^{5}	1.96×10^{-5}
168	1.23×10^{-5}	0.89544	6.36×10^{5}	1.56×10^{-5}

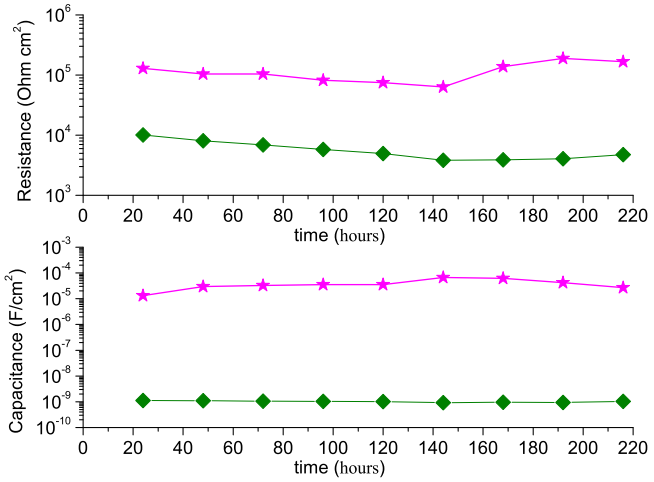

Fig. 13. Evolution of the EIS fitting parameters (◆) C_{coat}, (★) C_{dl}, (◆) R_{coat}, (★) R_{ct} as a function of time in 5 mM NaCl solution for the Coat-10%nc-MBT coating after the formation of defect.

Table 3
Fitting parameters CPE_{coat}-T, CPE_{coat}–P, R_{coat}, C_{coat}, CPE_{dl}–T, CPE_{dl}–P, R_{ct}, and C_{dl} for the Coat-10%nc-MBT coating.

Time (h)	CPE_{coat}–T F cm^{-2} s^{-n}	CPE_{coat}–P	R_{coat} Ω cm^2	C_{coat} F cm^{-2}
24	2.69×10^{-9}	0.92248	1.01×10^{3}	1.11×10^{-9}
48	2.65×10^{-9}	0.92379	8.05×10^{3}	1.09×10^{-9}
72	2.82×10^{-9}	0.91748	6.88×10^{3}	1.06×10^{-9}
96	2.32×10^{-9}	0.93275	5.78×10^{3}	1.03×10^{-9}
120	2.29×10^{-9}	0.93355	4.94×10^{3}	1.02×10^{-9}
144	1.39×10^{-9}	0.9674	3.89×10^{3}	9.26×10^{-10}
168	2.02×10^{-9}	0.94058	3.93×10^{3}	9.63×10^{-10}
192	2.53×10^{-9}	0.92055	4.04×10^{3}	9.37×10^{-10}
216	2.54×10^{-9}	0.92668	4.76×10^{3}	1.04×10^{-9}
	CPE_{dl}–T F cm^{-2} s^{-n}	CPE_{dl}–P	R_{ct} Ω cm^2	C_{dl} F cm^{-2}
24	1.13×10^{-5}	0.72822	1.30×10^{5}	1.31×10^{-5}
48	2.13×10^{-5}	0.704	1.04×10^{5}	2.97×10^{-5}
72	2.37×10^{-5}	0.73585	1.04×10^{5}	3.28×10^{-5}
96	2.57×10^{-5}	0.70364	8.22×10^{4}	3.52×10^{-5}
120	2.64×10^{-5}	0.6959	7.48×10^{4}	3.55×10^{-5}
144	4.15×10^{-5}	0.66536	6.32×10^{4}	6.73×10^{-5}
168	3.06×10^{-5}	0.6722	1.38×10^{5}	6.18×10^{-5}
192	2.37×10^{-5}	0.72197	1.89×10^{5}	4.23×10^{-5}
216	1.80×10^{-5}	0.73376	1.68×10^{5}	2.68×10^{-5}

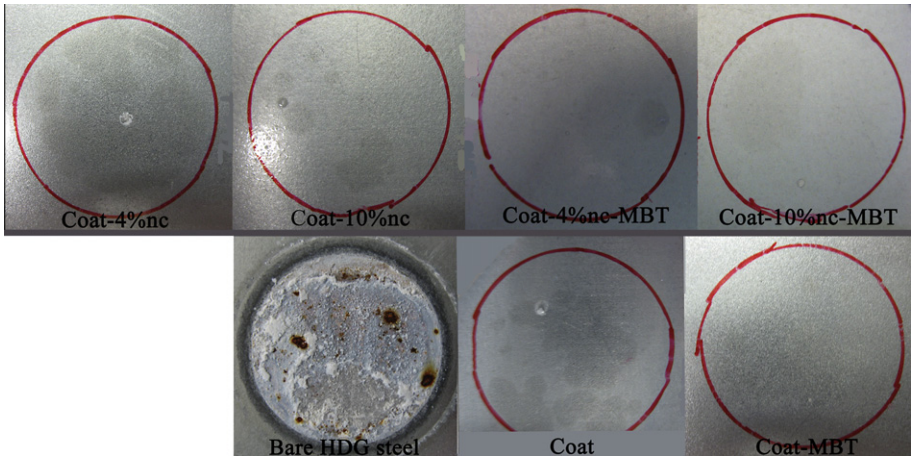

Fig. 14. Visual coating photographs after exposure to 0.5 M NaCl solution for 744 h (31 days) at room temperature.

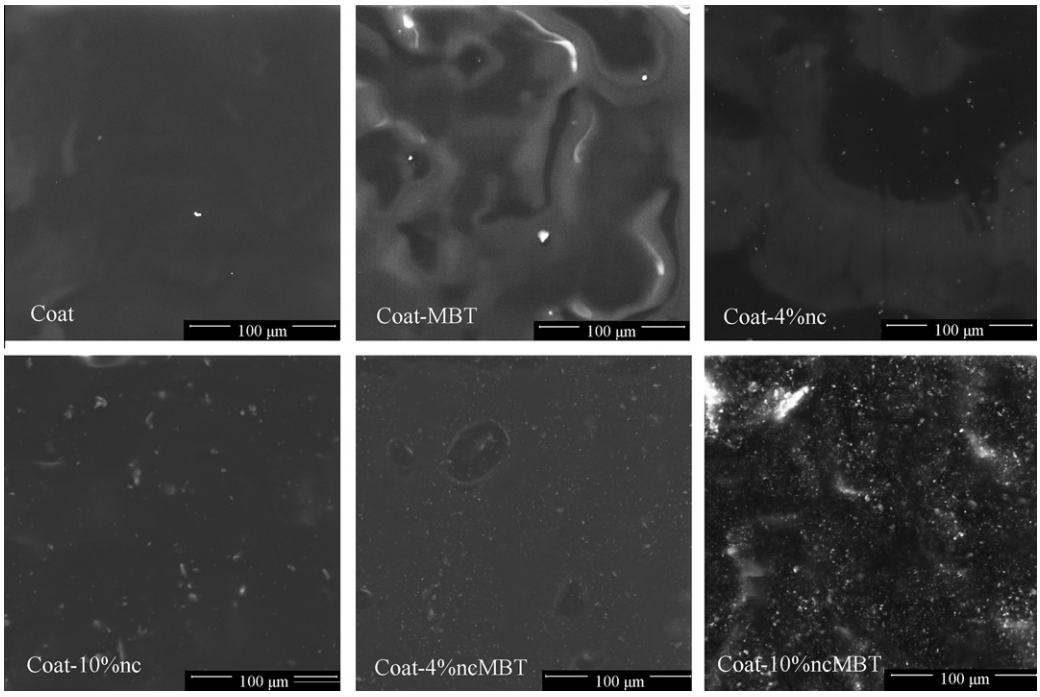

Fig. 15. Surface morphology of coatings.

solution for the Coat coating. The fitting results demonstrate that at the beginning of immersion there is a decrease of R_{coat} and R_{ct} but after the fifth day the values of R_{coat} and R_{ct} are increased. The R_{ct} increased one order of magnitude between the third and the seventh day. Moreover, the values of the double layer capacitance are increased for the first five days but after the fifth day a decrease of them is noticed until the end of the experiment (7 day) (Table 2). The same trend is observed for Coat-10%nc-MBT coating after the formation of defect (Fig. 13). There is a decrease of coating and charge transfer resistance values until the sixth day of immersion and then an increase of the values is noticed until the end of the experiment (10 days). The R_{ct} increased about six times between the sixth and the ninth day. Furthermore, there is a drop of the double layer capacitance values after the sixth day (Table 3). It should be mentioned that in order partial recovery of the coating to exist the values of charge transfer resistance (R_{ct}) should be increased as the immersion time elapses. These results denote that both Coat and Coat-10%nc-MBT coatings are being recovered after the formation of the artificial defects and suggest that both coatings probably have self-healing properties. Self-healing can be defined as the partial recovery of the protective properties of the coated system when marred [26]. The partial recovery of both coatings can be ascribed to the presence of amine groups from HY 943 that have not reacted with epoxy groups from GY 257 during the curing process of the coating.

In the presence of sodium chloride solution to the artificial defected HDG steel area, chloride ions (Cl^-) migrate to anodic sites where simonkolleite is formed. The reaction of simonkolle-

Table 4
% w/w element concentration of HDG steel coatings.

Coatings	C	N	O	S	Si	Fe	Zn	Ce
Coat-4%nc-MBT	74.13	8.25	10.43	0.55	0.93	0.11	2.74	2.87
Coat-10%nc-MBT	73.74	5.96	8.97	1.26	0.90	0.07	2.40	6.69

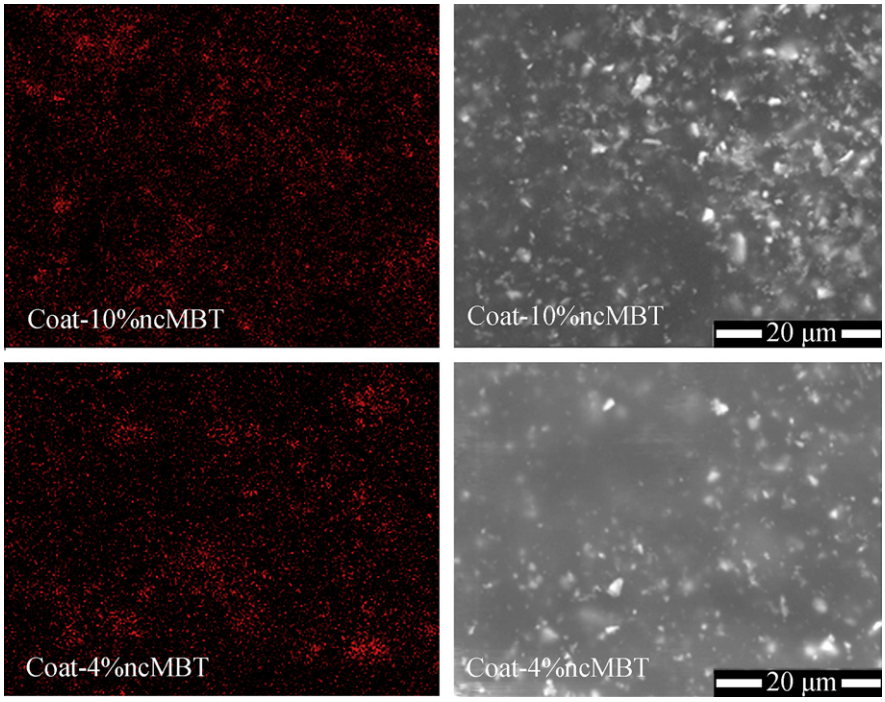

Fig. 16. Maping micrograph (left) and corresponding SEM image (right) of coatings Coat-10%nc-MBT and Coat-4%nc-MBT.

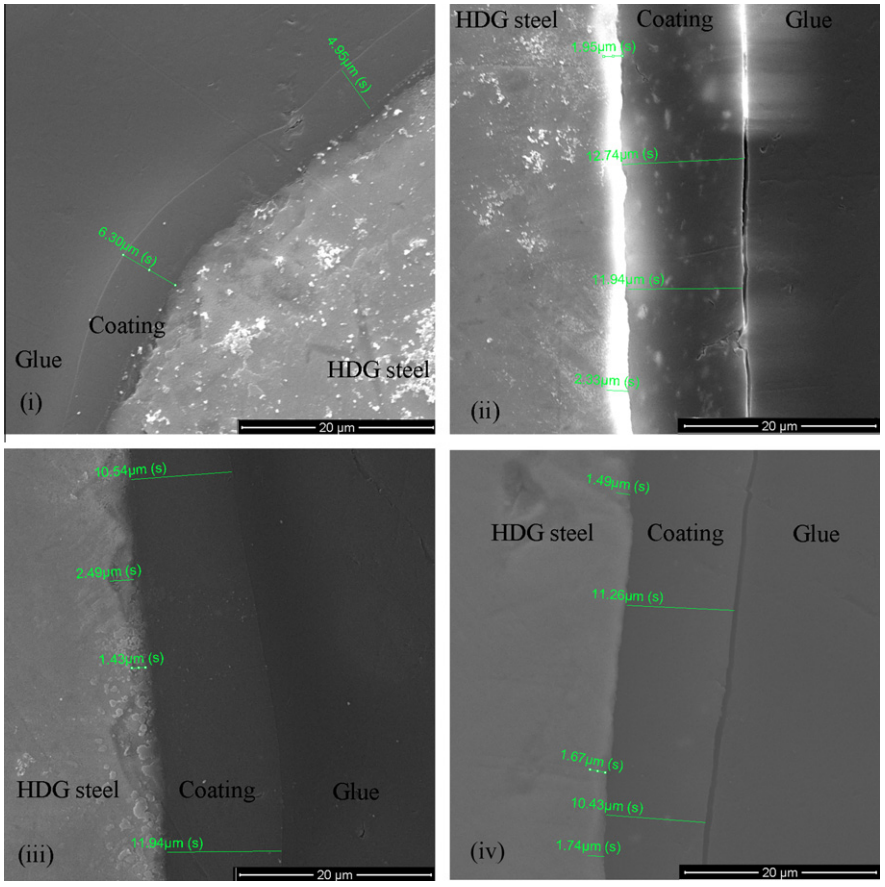

Fig. 17. Cross-section SEM of coatings: (i) Coat, (ii) Coat-MBT, (iii) Coat-10%nc-MBT, (iv) Coat-4%nc-MBT.

ite formation releases hydroxide ions increasing the local area pH [27]. The reaction between amine and epoxy groups is catalyzed by increased pH producing a new protective film [28]. Moreover, the presence of MBT inhibitor due to the loaded nanocontainers into the Coat-10%nc-MBT coating hinders the corrosion process.

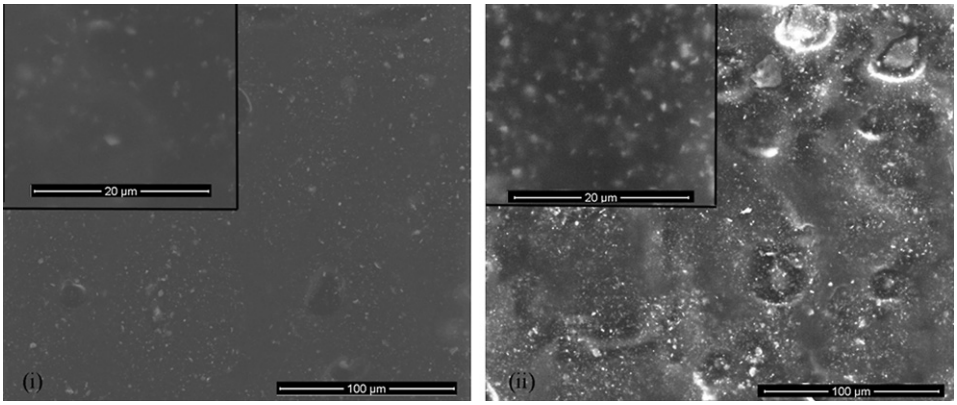

Fig. 18. SEM of coating Coat-4%nc-MBT: (i) before (ii) after exposure at 0.5 M NaCl solution at room temperature for 744 h (31 days).

On the other hand, the coatings including inhibitor or empty nanocontainers (Coat-MBT, Coat-4%nc, Coat-10%nc) do not present any recovery properties after the formation of artificial defects and exposure to corrosive environment. This result can be attributed to the blocking of the reaction between epoxy and amine groups due to the presence of inhibitor and empty nanocontainers into the coating that degrade the coherence of the matrix. Special attention should be focused on the behavior of the coating that includes 4% w/w loaded nanocontainers (Coat-4%nc-MBT). This coating does not reveal recovery action although it contains loaded nanocontainers. A possible explanation is that the presence of nanocontainers blocks possible reaction between epoxy and amine groups after the formation of artificial defects due to the degradation of the coherence of the matrix. If the concentration of loaded nanocontainers into the film is not the appropriate in order adequate amount of inhibitor MBT to exist, the inhibition of the corrosion process cannot be achieved.

3.2. Morphology of the coatings

The visual photographs of the coatings including bare HDG steel after exposure to 0.5 M NaCl solution for 744 h (31 days) are demonstrated in Fig. 14. The surfaces of the all coatings are free of pits and look intact without any sign of corrosion process. On the other hand, the bare HDG steel has been completely destroyed. Signs of corrosion attack are present such as lots of pits and stains.

The morphology and chemical composition of the coatings were achieved via SEM and EDX analysis (Fig. 15). The surfaces of all the coatings are crack free and no macroscopic defects such as pinholes or uncoated areas are depicted. Small white particles were identified via EDX analysis and it was found that they consist of the same elements with the rest coating. The darker zones seem to correspond to the presence of thicker coated zones, formed on depressions present in the alloy surface. These depressions generally develop after surface finishing and are related with dissolution of intermetallic inclusions. Furthermore, the coatings including nanocontainers present some aggregations on their surface. These particles were identified with EDX and the analysis depicted that they consist of cerium and oxygen elements. This result denotes that a part of the cerium molybdate nanocontainers is aggregated on the surface of the coating during the dip-coating process. The EDX analysis for the coated samples demonstrates carbon, nitrogen, oxygen and silicon from the coating, zinc and iron from the substrate (Table 4). Moreover, for the coatings including nanocon-

Table 5
% w/w element concentration of the coating Coat-4%nc-MBT.

Coatings	C	N	O	Si	S	Cl	Ce	Zn
Coat-4%nc-MBT	73.81	5.96	8.97	0.90	0.26	–	6.69	2.40
Coat-4%nc-MBT[a]	79.41	–	10.75	1.04	1.35	0.44	5.30	1.71

[a] After exposure at 0.5 M NaCl solution at room temperature for 744 h (31 days).

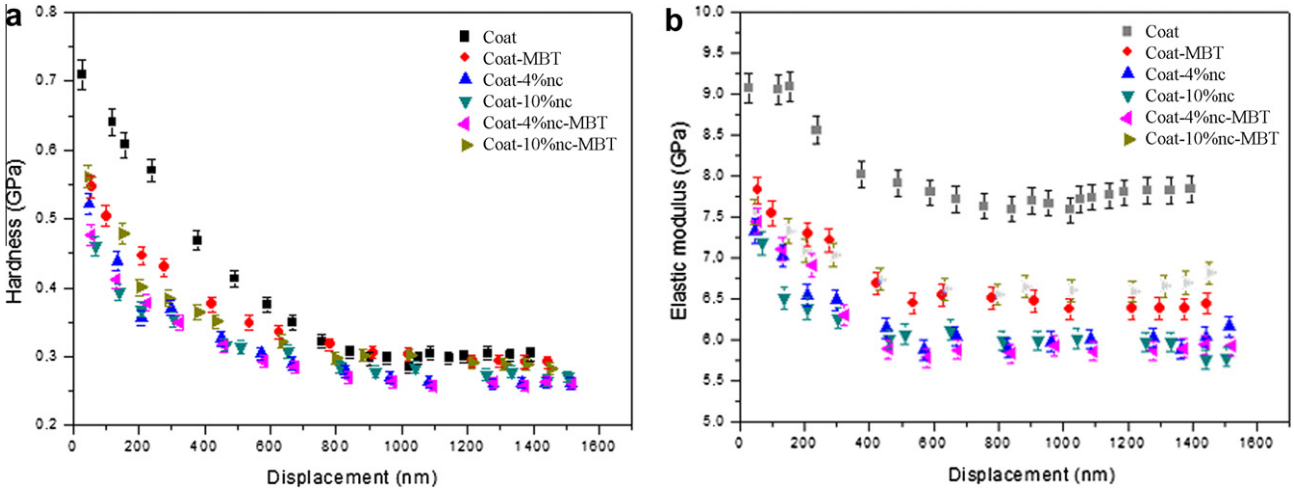

Fig. 19. Nanomechanical properties (H, E) of coatings.

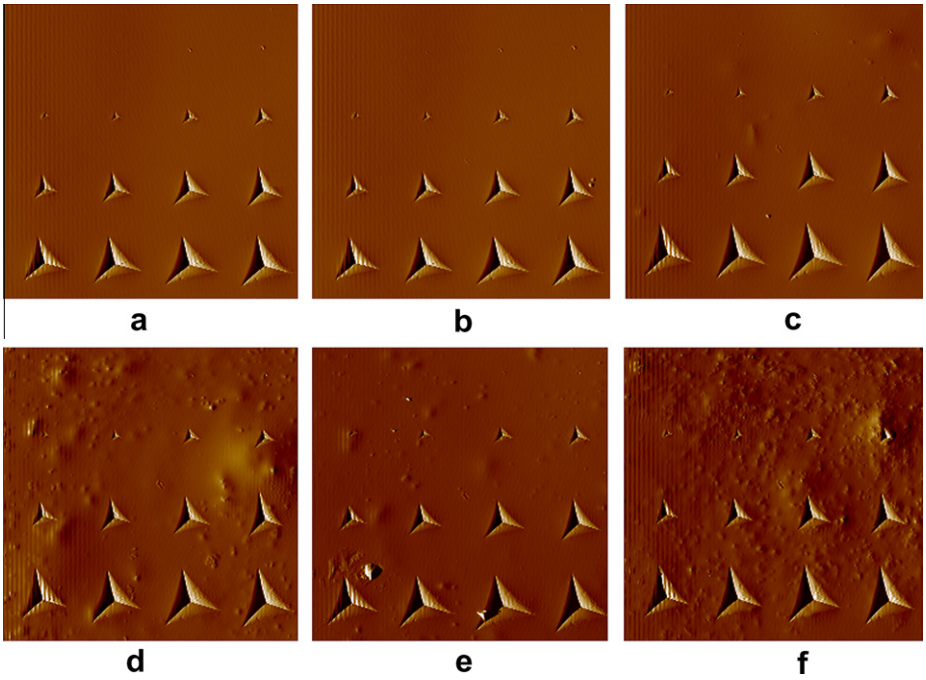

Fig. 20. SPM images of indenting imprints on epoxy coatings: (a) Coat, (b) Coat-MBT, (c) Coat-4%nc, (d) Coat-4%nc-MBT, (e) Coat-10%nc and (f) Coat-10%nc-MBT.

tainers, cerium and sulfur elements are also presented. SEM surface mapping was taken for all the samples including nanocontainers in order the well dispersion of the nanocontainers into the coatings to be estimated. The elemental cerium mapping micrograph and corresponding SEM image of coatings Coat-10%nc-MBT and Coat-4%nc-MBT are demonstrated in Fig. 16. Spots of cerium element can be clearly seen in the pictures. Although some aggregates are observed, the nanocontainers are quite well dispersed into the coatings.

The thicknesses of Coat, Coat-MBT, Coat-10%nc-MBT and Coat-4%nc-MBT coatings are presented in Fig. 17. It can be seen in all the pictures the thin coating of zinc that is due to the treatment of HDG steel. The presence of inhibitor or nanocontainers increases the thickness of the coatings. The Coat-MBT, Coat-10%nc-MBT and Coat-4%nc-MBT coatings are thicker than the coating free of inhibitor or nanocontainers (Coat). The thicknesses of Coat-MBT, Coat-10%nc-MBT and Coat-4%nc-MBT are between 10 μm and 12 μm, while the thickness of Coat is in the range of 5–7 μm.

The Coat-4%nc-MBT coating presented the highest total impedance value after immersion in 0.5 M NaCl for 744 h (31 days), (Fig. 7). The morphology and chemical composition before and after exposure to corrosive environment of the Coat-4%nc-MBT coating are illustrated in Fig. 18. The surfaces of both coatings present the same characteristics. They are coarse but no cracks are detected. It can be seen that the immersion into the corrosive environment did not affect the coating. EDX analysis confirmed the application of the coating on the substrate due to the appearance of carbon, oxygen and silicon. Furthermore, the concentration of oxygen remains almost the same after the corrosion process (Table 5). This result clearly denotes that no new oxide/hydroxide film has been formed.

3.3. Nanomechanical and nanotribological properties of the coatings

The nanomechanical properties hardness and Young modulus (namely H and E, respectively) of coatings are presented in Fig. 19. The incorporation of nanocontainers (with or without inhibitor) affects the mechanical integrity of the coatings, revealing a clear mechanical degradation of epoxy coating; while H is slightly decreased, samples exhibit greater deviation in E values. The addition (and further increase) of nanocontainers in the epoxy matrix creates surface incongruity (Fig. 20).

The ratio of hardness to elastic modulus is of significant interest in tribology. Higher stresses are expected in high H/E, hard materials, and high stress concentrations develop towards the indenter tip, whereas in the case of low H/E, soft materials, the stresses are lower and are distributed more evenly across the cross-section of the material [29,30]. The high ratio of hardness to elastic modulus (H/E) is indicative of good wear resistance in a disparate range of materials [30,31]: ceramic, metallic and polymeric (for example: c-BN, tool steel, nylon, respectively), which are equally effective in resisting attrition for their particular intended application. In Fig. 21, the change of H/E slope reveals that the addition of nanocontainer and inhibitor amount strengthens (increase of wear resistance) the epoxy coating after ~800 nm of displacement, hav-

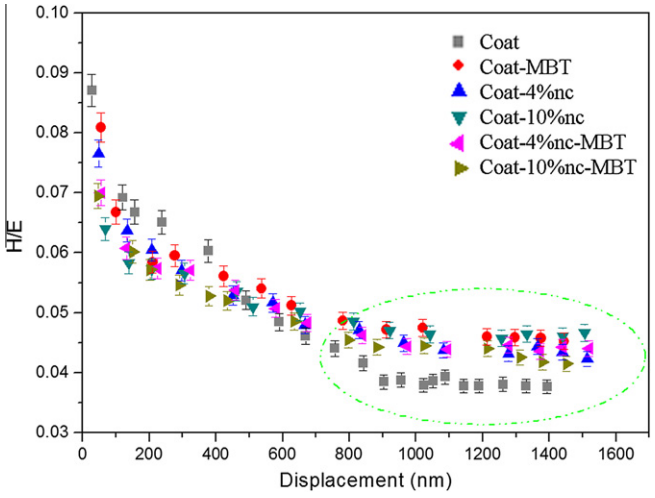

Fig. 21. Correlation of H/E ratio to displacement, for all the coatings.

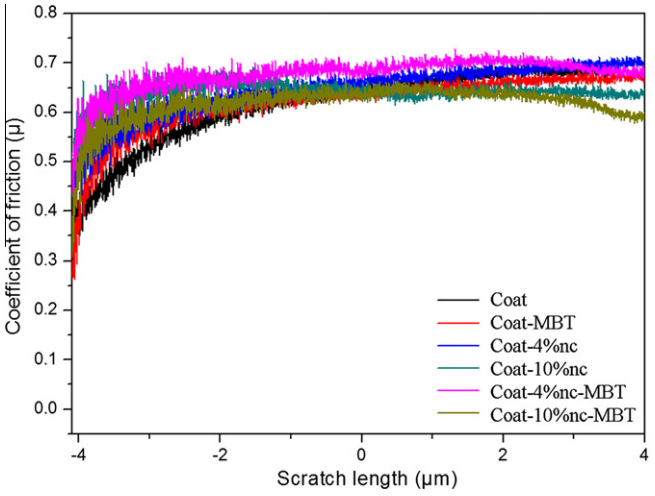

Fig. 22. Coefficient of friction for all coatings through nanoscratch testing.

ing no significant impact on surface region (0–800 nm), where all coatings exhibited similar (increased) H/E ratio.

Fig. 22 illustrates the coefficients of friction for all coatings. Incorporation of nanocontainers increases the coefficients of friction, for the whole scratch path; however, when the tip further penetrates the sample, the behavior is almost identical for all samples. In case of coating Coat-10%nc-MBT, an abrupt change in coefficient of friction almost at the end of scratch path implies possible failure of the coating.

4. Conclusion

A new system has been developed for the corrosion protection of HDG steel. This system includes hybrid organic–inorganic coatings together with cerium molybdate nanocontainers loaded with corrosion inhibitor MBT. The corrosion resistance of the coatings was examined using EIS. The results revealed improved corrosion protection after immersion in 0.5 M NaCl solution for 744 h (31 days). The addition of nanocontainers loaded with corrosion inhibitor improved the anticorrosive properties of the coatings compare to the coatings that have empty nanocontainers or the coatings that have only the inhibitor.

The concentration of the loaded nanocontainers into the coating is an important factor for further improvement of the anticorrosive properties of the coating. The coating including 4% w/w of loaded nanocontainers demonstrates the highest total impedance values until the end of the immersion time. In order possible self-healing properties of the coatings to be estimated, artificial defects formatted on the coatings. Only the coating without inhibitor or nanocontainers and the coating including 10% w/w loaded nanocontainers presented partial recovery action of the defected area after immersion in 5 mM NaCl solution. These results disclose self-healing properties of the coatings.

SPM imaging of the coatings revealed that the addition (and further increase) of nanocontainers in the epoxy matrix creates surface incongruity; however the change of H/E slope depicts that the addition of nanocontainer and inhibitor amount strengthens (increase of wear resistance) the epoxy coating after ~800 nm of displacement, having no significant impact on surface region (0–800 nm), where all coatings exhibited similar (increased) H/E ratio. Additionally, the coefficient of friction increases with addition of nanocontainers for low displacements, while greater displacements the behavior is almost identical for all samples.

The next step is the improvement of the system by reducing the curing time of the coatings and by the addition of different types of nanocontainers loaded with anodic or cathodic corrosion inhibitors.

Acknowledgements

Dr. I.A. Kartsonakis would like to thank Dr. M.F. Montemor for the fruitful discussion on the obtained results. Furthermore, the authors want to thank "Chemetall GmbH"-Frankfurt, for providing the samples of HDG steel.

References

[1] F. Deflorian, S. Rossi, M. Fedel, C. Motte, Electrochemical investigation of high-performance silane sol–gel films containing clay nanoparticles, Prog. Org. Coat. 69 (2010) 158–166.
[2] C.Y. Tsai, J.S. Liu, P.L. Chen, C.S. Lin, Effect of Mg^{+2} on the microstructure and corrosion resistance of the phosphate conversion coating on hot-dip galvanized sheet steel, Corros. Sci. 52 (2010) 3907–3916.
[3] M.F. Montemor, M.G.S. Ferreira, Cerium salt activated nanoparticles as fillers for silane films: evaluation of the corrosion inhibition performance on galvanised steel substrates, Electrochim. Acta 52 (2007) 6976–6987.
[4] K. Gang, L. Liu, L. Jintang, C. Chunshan, Z. Zheng, Corrosion behaviour of lanthanum-based conversion coating modified with citric acid on hot dip galvanized steel in aerated 1M NaCl solution, Corros. Sci. 53 (2011) 1621–1626.
[5] A.M. Cabral, W. Trabelsi, R. Serra, M.F. Montemor, M.L. Zheludkevich, M.G.S. Ferreira, The corrosion resistance of hot-dip galvanized steel pre-treated with bis-[triethoxysilylpropyl] tetrasulfide solutions doped with $Ce(NO)_3$, Corros. Sci. 48 (2006) 3740–3758.
[6] A.M.P. Simoes, R.O. Carbonari, A.R. Di Sarli, B. Del Amo, R. Romagnoli, An environmentally acceptable primer for galvanized steel: Formulation and evaluation by SVET, Corros. Sci. 53 (2011) 464–472.
[7] J.B. Bajat, V.B. Miskovic-Stankovic, J.P. Popic, D.M. Drazic, Adhesion characteristics and corrosion stability of epoxy coatings electrodeposited on phosphate hot-dip galvanized steel, Prog. Org. Coat. 63 (2008) 201–208.
[8] M. Taryba, S.V. Lamaka, D. Snihirova, M.G.S. Ferreira, M.F. Montemor, W.K. Wijting, S. Towes, G. Grundmeier, The combined use of scanning vibrating electrode technique, micro-petentiometry to assess the self-repair processes in defects on "Smart" Coatings applied to galvanized steel, Electrochim. Acta 56 (2011) 4475–4488.
[9] B. Ramezanzadeh, M.M. Attar, Studying the effects of micro and nano sized ZnO particles on the corrosion resistance and deterioration behavior of an epoxy-polyamide coating on hot-dip galvanized steel, Prog. Org. Coat., doi: 10.1016/j.porgcoat.2011.03.026.
[10] B. Ramezanzadeh, M.M. Attar, An evaluation of the corrosion resistance and adhesion properties of an epoxy-nanocomposite on a hot-dip galvanized steel (HDG) treated by different kinds of conversion coatings, Surf. Coat. Techn., doi:10.1016/j.surfcoat.2011.04.001.
[11] C.A. Schuh, Nanoindentation studies of materials, Mater. Today 9 (2006) 32.
[12] R. Schwaiger, B. Moser, M. Dao, N. Chollacoop, S. Suresh, Some critical experiments on the strain-rate sensitivity of nanocrystalline nickel, Acta Mater 51 (2003) 5159.
[13] Li Xiaodong, B. Bhushan, A review of nanoindentation continuous stiffness measurement technique its applications, Mater. Charact. 48 (1) (2002) 11–36.
[14] C.A. Charitidis, Nanomechanical and nanotribological properties of carbon-based thin films: a review, Refract. Met. Har. Mater. 28 (2010) 51.
[15] W.C. Oliver, G.M. Pharr, An improved technique for determining hardness and elastic-modulus using load and displacement sensing indentation experiments, J. Mater. Res. 7 (1992) 1564.
[16] B.R. Kim, M.J. Ko, The assessment of the fracture behavior in spin-on organosilicates by nanoindentation and nanoscratch tests, Thin Solid Films 517 (2009) 3216.
[17] D.P. Papageorgiou, E.P. Koumoulos, C.A. Charitidis, A.G. Boudouvis, A.G. Papathanasiou, Evaluating the robustness of top coatings comprising plasma-deposited fluorocarbons in electrowetting systems, J. Adhes. Sci. Technol. arXiv:1110.4238v1.
[18] B. Sanyal, Organic Compounds as Corrosion Inhibitors in Different Environments-A Review, Prog. Org. Coat. 9 (1981) 165–236.
[19] I.A. Kartsonakis, G. Kordas, Synthesis and characterization of cerium molybdate nanocontainers and their inhibitor complexes, J. Am. Ceram. Soc. 93 (2010) 65–73.
[20] I.A. Kartsonakis, A.C. Balaskas, G.C. Kordas, Influence of cerium molybdate containers on the corrosion performance of epoxy coated aluminium alloys 2024–T3, Corros. Sci. 53 (2011) 3771–3779.
[21] H. Bei, E.P. George, J.L. Hay, G.M. Pharr, Influence of indenter tip geometry on elastic deformation during nanoindentation, Phys. Rev. Lett. 95 (2005) 045501.
[22] W. Trabelsi, E. Triki, L. Dhouibi, M.G.S. Ferreira, M.L. Zheludkevich, M.F. Montemor, The use of pre-treatment based on doped silane solutions for improved corrosion resistance of galvanised steel substrates, Surf. Coat. Techn. 200 (2006) 4240–4250.
[23] C.H. Hsu, F. Mansfeld, Technical note: concerning the conversion of the constant phase element parameter Y0 into a capacitance, Corrosion 57 (2001) 747–748.

[24] E. Barsoukov, J.R. Macdonald, Impedance Spectroscopy Theory, Experiment and Applications, A John Wiley & Sons, Inc., Publication, USA, 2005 . pp. 13–20.
[25] K.S. Cole, R.H. Cole, Dispersion and absorption in dielectrics. II. Direct current characteristics, J. Chem. Phys. 10 (1942) 98–105.
[26] M.F. Montemor, R. Pinto, M.G.S. Ferreira, Chemical composition and corrosion protection of silane films modified with CeO_2 nanoparticles, Electrochim. Acta 54 (2009) 5179–5189.
[27] N.C. Hosking, M.A. Ström, P.H. Shipway, C.D. Rudd, Corrosion resistance of zinc–magnesium coated steel, Corros. Sci. 49 (2007) 3669–3695.
[28] J. McMerry, Organic Chemistry, Thompson Learning, seventh edition, p. 665, p. 920.
[29] Y.T. Cheng, C.M. Cheng, What is indentation hardness, J. Surf. Coat. Tech. 133–134 (2000) 417–424.
[30] A. Leyland, A. Matthews, Design criteria for wear-resistant nanostructured and glassy-metal coatings, J. Surf. Coat. Tech. 177–178 (2004) 317–324.
[31] C.A. Charitidis, E.P. Koumoulos, V.P. Tsikourkitoudi, S.P. Vasilakos, P.A. Tarantili, Adhesive forces and time dependent behaviour (creep and loading rate effects) on nanomechanical properties of polydimethylsiloxane (PDMS), J. Nanostructured Polymers Nanocomposites 7 (2011) 32–42.

International Journal of Structural Integrity

Synthesis, structural and nanomechanical properties of cobalt based thin films

Elias P. Koumoulos Vasiliki P. Tsikourkitoudi Ioannis A. Kartsonakis Vassileios E. Markakis Nikolaos Papadopoulos Evangelos Hristoforou Costas A. Charitidis

Synthesis, structural and nanomechanical properties of cobalt based thin films

Elias P. Koumoulos, Vasiliki P. Tsikourkitoudi, Ioannis A. Kartsonakis and Vassileios E. Markakis
School of Chemical Engineering, National Technical University of Athens, Athens, Greece
Nikolaos Papadopoulos and Evangelos Hristoforou
School of Mining Engineering and Metallurgy, National Technical University of Athens, Athens, Greece, and
Costas A. Charitidis
School of Chemical Engineering, National Technical University of Athens, Athens, Greece

Received 15 October 2013
Revised 23 December 2013
Accepted 22 January 2014

Abstract

Purpose – The purpose of this paper is to produce cobalt (Co)-based thin films by metalorganic chemical vapor deposition (CVD) technique and then to evaluate structural and mechanical integrity.
Design/methodology/approach – Co-based thin films were produced by metalorganic CVD technique. Boronizing, carburization and nitridation of the produced Co thin films were accomplished through a post-treatment stage of thermal diffusion into as-deposited Co thin films, in order to produce cobalt boride (Co_2B), cobalt carbide and cobalt nitride thin films in the surface layer of Co. The surface topography and the crystal structure of the produced thin films were evaluated through scanning electron microscopy and X-ray diffraction, respectively. The mechanical integrity of the produced thin films was evaluated through nanoindentation technique.
Findings – The obtained results indicate that Co_2B thin film exhibits the highest nanomechanical properties (i.e. *H* and *E*), while Co thin film has enhanced plasticity. The cobalt oxide thin film exhibits higher resistance to wear in comparison to the cobalt thin film, a fact that is confirmed by the nanoscratch analysis showing lower coefficient of friction for the oxide.
Originality/value – This work is original.

Keywords Boron-doped cobalt thin film, Carbon-doped cobalt thin film, Chemical vapour deposition, Hardness and elastic modulus, Nanoindentation, Nitrogen-doped cobalt thin film
Paper type Research paper

1. Introduction

A key problem for typical sensors is lack of sensitivity. Even with systems with good detection limits, a lack of sensitivity in the detector means that they can only provide a binary (good/bad) assessment of sensing quality, with no indication of variability at levels still deemed to be acceptable. Furthermore, most commercially available sensors do not give adequate (or indeed any) information on calibration, drift or accuracy and hence the reliability of these sensors is unknown. Residual stresses are also developed during the microfabrication process of sensor devices, e.g. MEMS gas sensors, which

The authors wish to acknowledge NTUA funded project for basic research PEVE-NTUA-2010/65187900 and Alexandros S. Onassis Public Benefit Foundation for the support of this work. The authors are indebted to Professor P. Patsalas for his support and contribution in XRD analysis.

International Journal of Structural Integrity
Vol. 6 No. 2, 2015
pp. 225-242

1757-9864
DOI 10.1108/IJSI-10-2013-0031

can seriously affect their operating performance and reliability, as they can cause rupture and/or delamination of the thin film (Sadek and Moussa, 2007).

Microelectromechanical components such as microcantilevers, microbridges or micromembranes are usually used in microtransduction for actuation and sensing. One layer achieves the structural and elastic recovery function and the other layer acts as the active part by deforming under actuations (Pustan *et al.*, 2013). Determination of the failure mechanisms of micro/nanocomponents is the key to the design of reliable products. Issues on micro/nanosystems reliability are seeking to discover methods qand new technologies to increase their lifetime. The slow movement of atoms under mechanical stress is expected to be one of the major problems especially when flexible parts deflect (Pustan, 2011). It is possible to define the system reliability (i.e. related to the lifetime properties of the whole device or system), the component reliability (i.e. referred to the failure modes of the sub-components and provides to the designer the information to predict them) and the material reliability (i.e. focussed on the material collapse under certain conditions of stress and building processes). Main structural reliability issues as loads, working conditions, environmental variations, process parameters, geometrical characteristics, etc. can be addressed to one of these areas of investigation (De Pasquale *et al.*, 2009).

The mechanical and tribological behavior of magnetic and storage devices is of critical importance in determining long-term stability and reliability of such devices. The good maintenance of the mechanical and tribological properties of the aforementioned devices can significantly impact their commercialization. Nanoindentation technique can be a useful tool for the control of stresses for the successful and reliable operation of such devices. The variation of nanomechanical/nanotribological response of sensors should be kept within a narrow range (defined percentage of range). Nanoscratch testing is a versatile tool for analysis of the mechanical attributes of thin films and bulk materials and can be used for a plethora of tests, where a single scratch with a ramped load is useful for critical load, film adhesion and mar studies (Koumoulos *et al.*, 2012). Nanoscratch data, coupled with *in situ* images, provide detailed information concerning a material's behavior under simultaneous normal and lateral stresses.

In the present study, nanoindentation and nanoscratch techniques are utilized in order to investigate the nanomechanical (i.e. hardness, H and elastic modulus, E) and nanotribological properties of chemical vapor deposited (CVD) cobalt (Co)-based thin films (borides, carbides and nitrides); additionally, Co and cobalt oxide (Co_3O_4) thin films comparison has been conducted in terms of nanomechanical and nanotribological properties. All these cobalt-based thin films can be used in innovative sensing and data storage applications due to their useful properties (Mane *et al.*, 2001). Co thin films appear as a promising perspective regarding sensors and magnetic devices, since cobalt exhibits the highest magnetic anisotropy among transition metals (Papadopoulos *et al.*, 2008). Co_3O_4 thin films have also been considered for uses as magnetic detectors, counter electrodes, humidity or oxygen optical sensors (Ando *et al.*, 1997), solar-selective absorbers and protective layers (Mane *et al.*, 2001). CVD is a widely used technique for the production of highly dense films with good adhesion to the substrate (Papadopoulos *et al.*, 2011).

Transition metal borides are newly recognized as hard materials with a high-elastic modulus. Their mechanical properties make them attractive for deployment in innovative applications. Cobalt boride (Co_2B) materials are usually known for their functional properties (hydrogen catalysis, magnetism, corrosion, biomedics). Co_2B have been actively researched as catalysts for hydrogen storage and fuel cell applications, because of the fine electrochemical properties (e.g. electrochemical reversibility, high

charge-discharge capacity) inherited from Co and leveraged by the antitoxicant effect of boron (B). The oxidation resistance makes Co_2B an interesting option for corrosion- and wear-resistant surface coatings. Other applications seek to exploit these materials for their marked magnetic and (anisotropic) magnetostrictive properties or for biomedics and drug delivery.

Cobalt nitride (Co_2N) are receiving special attention in the research field of storage devices. With respect to their thermal, mechanical and magnetic properties, they are catalogued as new materials for high-performance magnets because of their strong uniaxial anisotropy and high saturation magnetization. The electrical, magnetic and catalytic properties of Cobalt carbide (Co_3C) make their application as thin films technologically important. It is difficult to assess the mechanical properties of thin films using traditional indentation tests, due to their small size. For this reason, nanoindentation has proven to be a powerful technique as it can probe the mechanical properties of the samples at shallow contact depths, reducing the scale of the contact. Thus, the mechanical properties of the thin films can be assessed without major contribution from the substrate. Recently, nanoindentation has proven to be a powerful technique in providing information on mechanical properties (hardness, H and elastic modulus, E) of thin films, based on analysis of load-displacement curves (Koumoulos *et al.*, 2012). Nanoindentation has attracted increasing interest, since allows a reliable characterization contrary to traditional methods, i.e. microhardness and tensile test. The shapes of the load-displacement curves differ from one material to another and these differences usually indicate different mechanical properties.

In the present study, Co thin films were produced through CVD. Boronizing, carburization and nitridation of the produced Co thin films were accomplished through a post-treatment stage of thermal diffusion into them, in order to produce Co_2B, Co_3C and Co_2N thin films. The surface topography and the crystal structure of the produced thin films were evaluated through scanning electron microscopy (SEM) and X-ray diffraction (XRD), respectively. The mechanical integrity of the thin films was evaluated through nanoindentation technique.

2. Experimental details

2.1 Growth of Co, and B, C, N-doped Co thin films

Co thin films were grown in a vertical, cylindrical MOCVD stainless-steel reactor, specifically developed for the deposition of magnetic films, either singled or multilayered. The reactor had computer controlled switching of gases for abrupt transients during deposition of multilayered structures. It also employed two independent precursor lines and four separate gas delivery lines for maintaining inert (He or Ar), reductive (H_2) or oxidizing (O_2) atmosphere. Prior to reactor's entrance heat-traced lines were used.

The substrates were positioned onto a stainless-steel block, with three four-inch recessed pockets. The three zone resistance heating was controlled by Ch-Al thermocouples embedded at the block's bottom surface with PID controllers. Two rotary vane pumps in-line connected were used for reactor's evacuation down to a base pressure of 10^{-4} mbar and process pumping accurately controlled by a manual throttle valve.

Silicon (Si) and blanket silicon dioxide were used as substrates. These were *ex situ* cleaned by a 30-sec Piranha etch solution, and then by a subsequent acetone and methanol rinse. Finally, they were washed with double-distilled water followed by drying in a high purity Ar atmosphere. In the case of the Si substrates an additional first step was employed. These were dipped for 1 min in a 10 percent solution of HF acid and were immediately rinsed by double-distilled water.

The Co films were deposited from a Co carbonyl precursor. The latter was introduced to the reactor as an aerosol mixture, formed by the dissolution of Co carbonyl into dichloromethane, 0.1 M concentrated. In a typical experiment a liquid (solution) flow of 7 g/h was mixed with a hydrogen gas flow of 0.05 l/min at 27°C. The mixture (aerosol) was then introduced to the reactor, the temperature of which had been adjusted to 140°C. The thickness of the produced film is about 100 nm.

Boronizing, carburization and nitridation were accomplished through a post-treatment stage of thermal diffusion into as-deposited Co films.

Boronizing. In boronizing, a suitable powdery mixture of a boronizing agent and an activator (pack boronizing) was heated to high temperatures to allow for the diffusion of B ions to the film's bulk. More specifically, the initial step of boronizing was preparation of the B powder mixture for heat treatment. The B powder mixture comprised of the following compounds:

- 9 g boron carbide (B_4C)-boronizing agent;
- 0.8 g aluminum oxide (Al_2O_3)-diluent/diluter = did not participate in the reaction but prevented the caking of the boronizing agent; and
- 0.2 g Na_2CO_3-activator = activated the B atoms at high temperatures thus allowing them to diffuse in to the metal.

Initially, Al_2O_3 and Na_2CO_3 were mixed together in order to have a fine mixture and also to eliminate any clusters present in the mixture. Then, gradually, B_4C was added to this mixture and ground well in order to have a homogeneous mixture of the three compounds. Finally, the mixture was mixed in the blender. The crucible containing the Co film embedded in the B powder mixture was covered by a lid and was placed in the furnace at 950°C. An inert atmosphere was maintained in the furnace by pumping argon (Ar) gas. After about four hours, the furnace was left to cool to room temperature. The crucible lid was removed and the sample was extracted from the powder mixture. The sample was then cleaned in an ultrasonic bath.

Carburization. As far as the carbide of the Co film is concerned, its formation was based on the principle that adsorbed carbon (C) atoms can be sub-surface buried at higher temperatures. The Co_3C was initially formed by injecting 10 ml of gaseous acetylene over a period of 10 min and at 50°C inside the column of an inverse gas chromatography apparatus, where the Co sample had been placed. In this way, acetylene was directly adsorbed at the surface of the film. Then, the sample was placed in a tubular quartz furnace and was heat treated for 1 hour at 400°C in the presence of a constant Ar flow (30 ml/min). At this temperature, acetylene was completely de-hydrogenated, thus favoring the formation of carbides, which were subsequently diffused in the Co matrix leading to Co_3C formation.

Nitridation. In the case of the Co_2N film, thermal diffusion was accomplished with the aid of a constant hydrazine (N_2H_4) flow. Instead of explosive N_2H_4, nitridation is also viable through evaporation of liquid ammonia. However, in this case much higher temperatures (1,200°C) for vapor decomposition are needed.

More specifically, N_2H_4 (bp of 114°C) was placed in a quartz bubbler inside a heating mantle, the latter used for keeping a constant temperature of 40°C. At this temperature, N_2H_4 was highly volatile and therefore its vapors could be transferred easily to the reaction zone without the need of a carrier gas. Nevertheless, a constant Ar flow of 20 ml/min was maintained inside the bubbler to dilute the liquid precursor and thus

minimizing the risk of explosion. The vapors were transferred to the same tubular quartz reactor used for Co_3C formation inside of which the as-deposited Co film had been placed over a slightly inclined quartz susceptor. The furnace temperature was maintained at 400°C with the thermal diffusion process lasting 1 hour. At this temperature, N_2H_4 was endothermically decomposed into hydrogen and nitrogen (N). Nitride formation was due to consumption of the first atomic layers of the Co film's surface by molecular N.

The produced films were characterized by SEM, XRD and Nanoindentation technique for the study of their nanomechanical properties.

2.2 SEM

The surface topography of the produced thin films was investigated by SEM using a PHILIPS Quanta Inspect (FEI Company, Eindhoven, the Netherlands) microscope with tungsten filament 25 kV equipped with Edax Genesis (Ametex Process & Analytical Instruments, Newark, DE).

2.3 XRD

The XRD patterns were obtained using a powder diffractometer (Siemens D-500, Siemens AG, Munich, Germany) and the CuKa line (wavelength 0.15418 nm) in the 10-100° angular range. A Fast Fourier Transform using 5,096 points and a cut off filter of 6.5 Hz has been employed in order to minimize the high-frequency electronic noise of the XRD data.

2.4 Nanoindentation-nanoscratch

The nanoindentation tests in this work were performed using a nanomechanical test instrument, equipped with a Berkovich tip (120 nm tip radius) which allows the application of loads from 1 to 130,000 μN. The instrument is capable of recording penetration displacements as a function of applied loads with a high load resolution (1 nN) and a high displacement resolution (0.04 nm). The above instrument is equipped with a scanning probe microscope (SPM), in which the sharp probe tip moves in a raster scan pattern across a sample surface using a three-axis piezo positioner. In all depth-sensing tests, a total of ten indents were averaged to determine the mean H and E values for statistical purposes, with a spacing of 50 μm (~45 percent relative humidity, 23°C). Prior to indentation, the area function of the indenter tip was calibrated in a fused silica, a standard material for this purpose.

The scratch tests performed in this work included three main segments. First, a pre-scratch scan under a very low load (0.2 μN) was carried out. Then, the indenter scraped the sample under a ramp loading from an initial load of 0.2 μN to a maximum value of 500 μN at the end of the scratch. The scratch path was 10 μm and the tip velocity 0.2 μm/s. Finally, a post-scratch was carried under a low load (2 μN). The applied load during the initial scratch and post-scratch was very low in order to avoid any damage or permanent deformation of the films. In all scratch tests, a total of five scratches were averaged for statistical purposes, with a spacing of 10 μm (~45 percent relative humidity, 23°C).

3. Results and discussion

3.1 XRD

The crystal structure of the produced Co-based thin films was investigated through XRD analysis. The spectra of the produced samples are presented in Figure 1. The main crystalline phase for each sample (obtained by the XRD analysis) is presented in the Table I.

Figure 1 indicates diffraction of $Co_3(BO_3)_2$ compound; additionally, appearance of a diffraction peak corresponding to (211) plane occurs, revealing the existence of crystalline Co_2B (Sabarou and Ataie, 2012). Additionally, the presence of carbides is evidenced (Zhang *et al.*, 2011); this XRD result indicates that the product is a mixture of two phases of Co_2C and Co_3C. Focussing on the 43.8° 2θ peak, some Co_2Ne appears to exist as a separate phase (Co_2N) (Cong *et al.*, 2012); the diffraction peaks appearing at 2θ value of 44.1 can be ascribed to Co_4N (Cheng *et al.*, 2009).

Intermediate phases of Co silicides were detected, probably due to the relatively high deposition temperature, which allowed diffusion of Si out from the substrate. Discrete peaks corresponding to typical Si angles of diffraction were detected (Figure 1), but this was, to some extent, attributed to the film's low thickness, which has been proven by AFM and MFM measurements (presented elsewhere; Papadopoulos *et al.*, 2011). The presence of peaks corresponding to Si angles can be attributed to the free from deposition wafer area that is left for many reasons, one of which is to directly measure the thickness of the thin film.

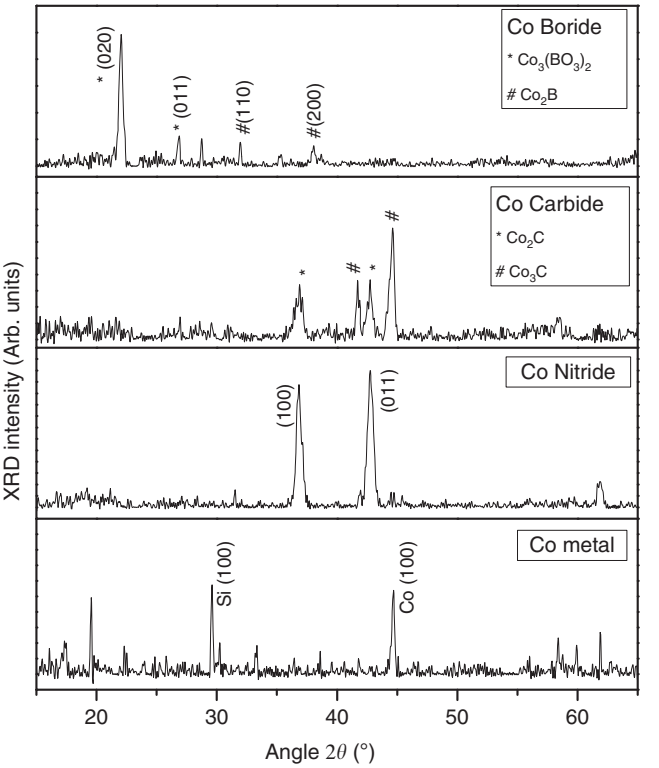

Figure 1.
XRD spectra of the produced samples

Table I.
Main crystalline phase for each sample (obtained by the XRD analysis)

Cobalt carbide	Co_3C
Cobalt boride	Co_2B
Cobalt nitride	Co_2N

3.2 SEM

SEM and EDX were performed to study the morphologies of the samples and the elemental distribution on the external surface. Figure 2 presents SEM images, where the morphology of the thin films can be observed. The spectra obtained through EDX analysis are presented in Figures 3-6 for each sample. The Tables II-V presents the percent *w/v* content of the elements that constitute each thin film. The presence of C in Co and Co_2N thin films can be explained due to the fact that electrically conductive double-stick C tape was used to stick the samples on the specimen's holders of the SEM. It was found that no significant change in morphologies was observed upon Co_3C and nitride employed (SEM revealed a three-dimensional nucleus growth, also observed in pure Co); Co_2B granules appeared in irregular shapes.

3.3 Nanoindentation

3.3.1 Co-based thin films comparison. In Figure 7 typical load unload of the produced thin films are presented. Co_2B thin film exhibits higher resistance to applied load, i.e. higher applied load values are needed in order to reach the same displacement (higher

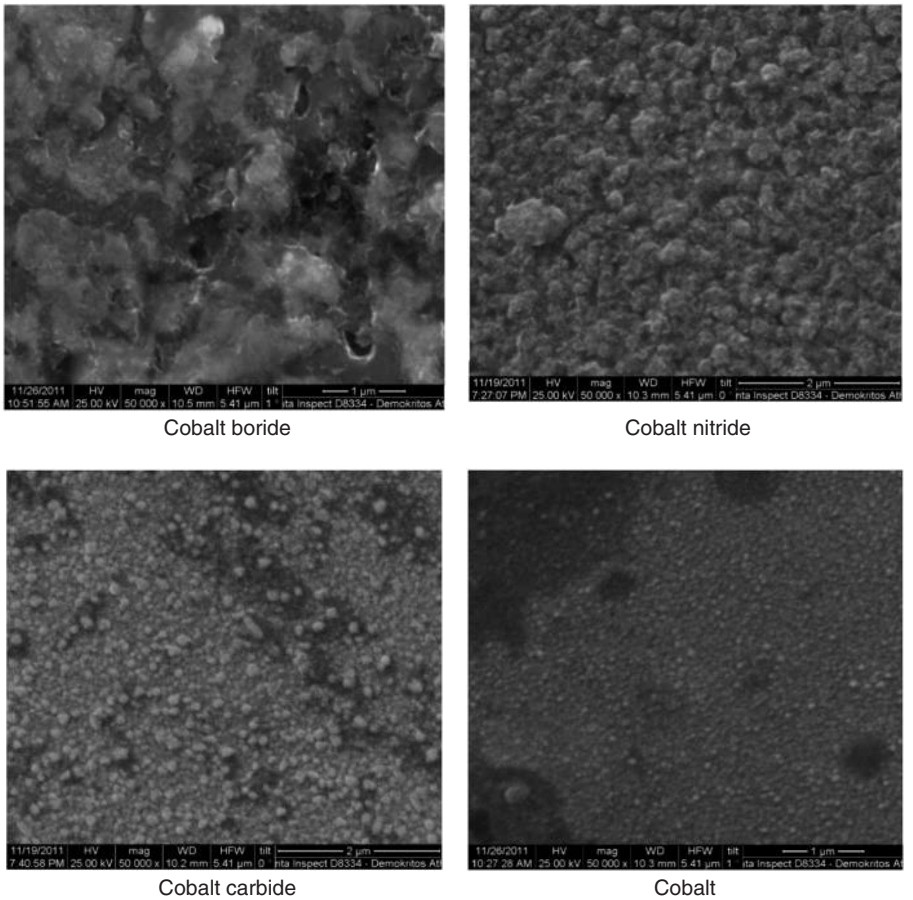

Figure 2.
SEM images, where the morphology of the thin films can be observed

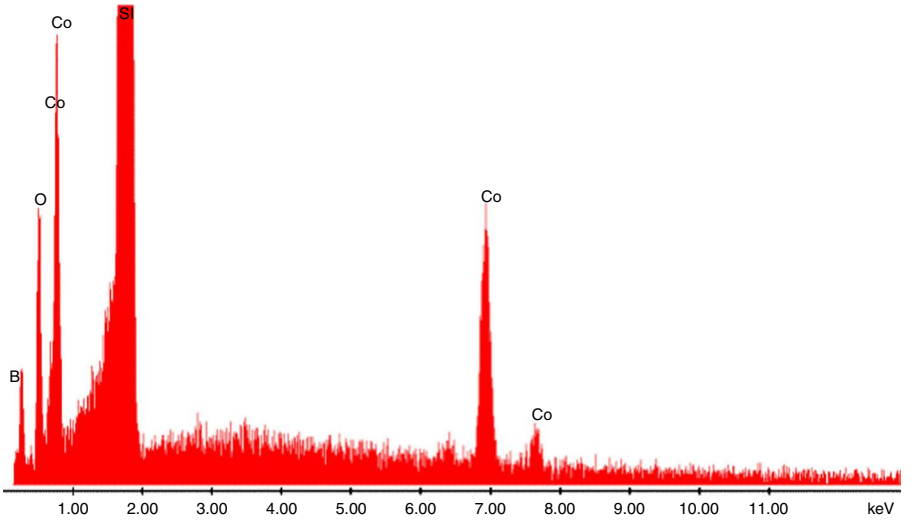

Figure 3.
EDX analysis of Co_2B thin film

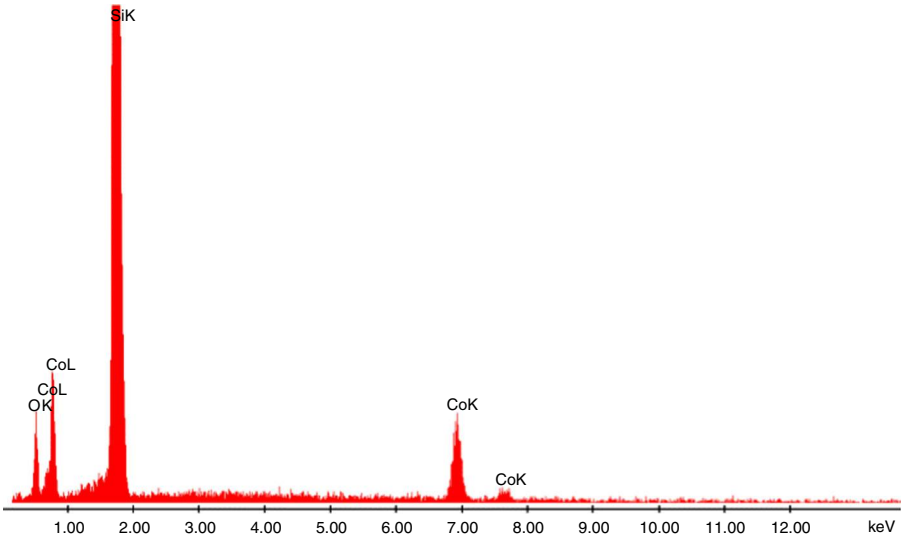

Figure 4.
EDX analysis of Co_3C thin film

values of hardness) followed by the Co_3C and Co_2N thin films. The presence of B is associated with the introduction of covalent bonds and with a progressive amorphization of the solid structure of pure crystalline Co, which are both potentially strengthening factors. In the case of Co thin film, greater plasticity is revealed, i.e. energy stored at the material after the indentation is over (total integration of curve area).

In higher displacements, the load-unload curves of the thin films have a similar behavior with the pure Co thin film. The nanomechanical properties of the thin films are calculated using the Oliver and Pharr model (O&P), which calculates the contact area between the indenter tip and the sample using the tangent of the upper part (30 percent)

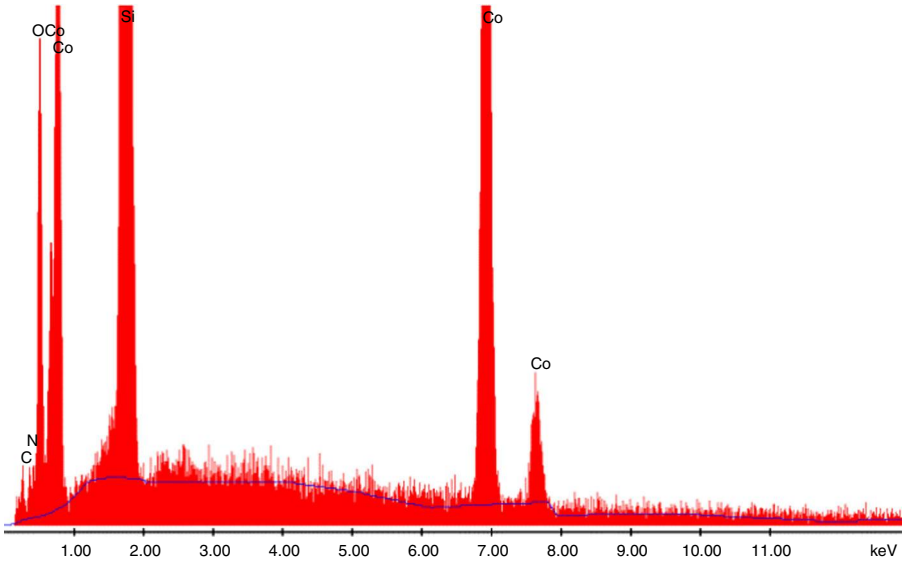

Figure 5.
EDX analysis of Co_2N thin film

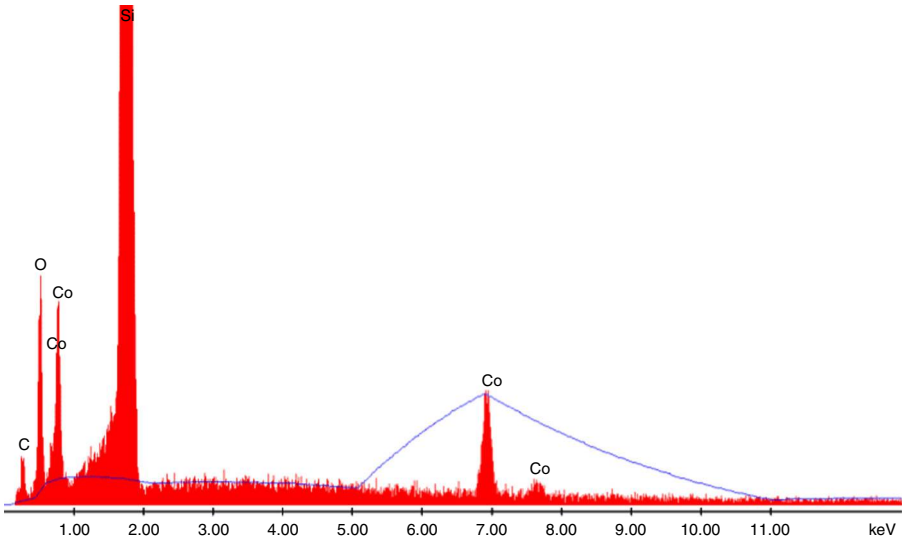

Figure 6.
EDX analysis of Co thin film

	Wt%	At%
B	40.28	63.20
O	4.34	4.60
Si	51.47	31.08
Co	3.91	1.13

Table II.
Percent *w/v* content of the elements of CB thin film

of the unloading curve, which is considered to be linear, along with the known area function. In O&P model, the derived expressions for calculating the elastic modulus from indentation experiments are based on Sneddon's elastic contact theory (Equation (1)):

$$E_r = \frac{S\sqrt{\pi}}{2\beta\sqrt{A_c}} \tag{1}$$

where S is the unloading stiffness (initial slope of the unloading load-displacement curve at the maximum displacement), A_c is the projected contact area between the tip and the substrate and β is a constant that depends on the geometry of the indenter ($\beta = 1.167$ for Berkovich tip). Conventional nanoindentation hardness refers to the mean contact pressure, which depends on the geometry of the indenter (Equation (2)):

$$H_c = \frac{F}{A} \tag{2}$$

The graph in Figure 8 shows the values of H and E for each sample. Figure 8(a) presents the nanomechanical properties of each thin films in the first atomic layers (~20 nm) where the incorporation of B, N and C atoms was is no effect from the substrate. It is obvious from Figure 8(b) which presents the nanomechanical properties of the thin films is that the nanomechanical properties approximate the nanomechanical properties of pure Co.

The obtained H and E values are in good agreement with similar measurements presented in the literature.

Table III. Percent *w/v* content of the elements of CC thin film

	Wt%	At%
C	7.48	15.59
O	9.38	14.68
Si	73.76	65.74
Co	9.38	3.99

Table IV. Percent *w/v* content of the elements of CN thin film

	Wt%	At%
C	6.07	13.02
N	3.59	6.60
O	11.09	17.85
Si	58.13	53.30
Co	21.11	9.22

Table V. Percent *w/v* content of the elements of Co thin film

	Wt%	At%
C	12.61	24.28
O	8.97	12.97
Si	74.11	61.05
Co	4.31	1.69

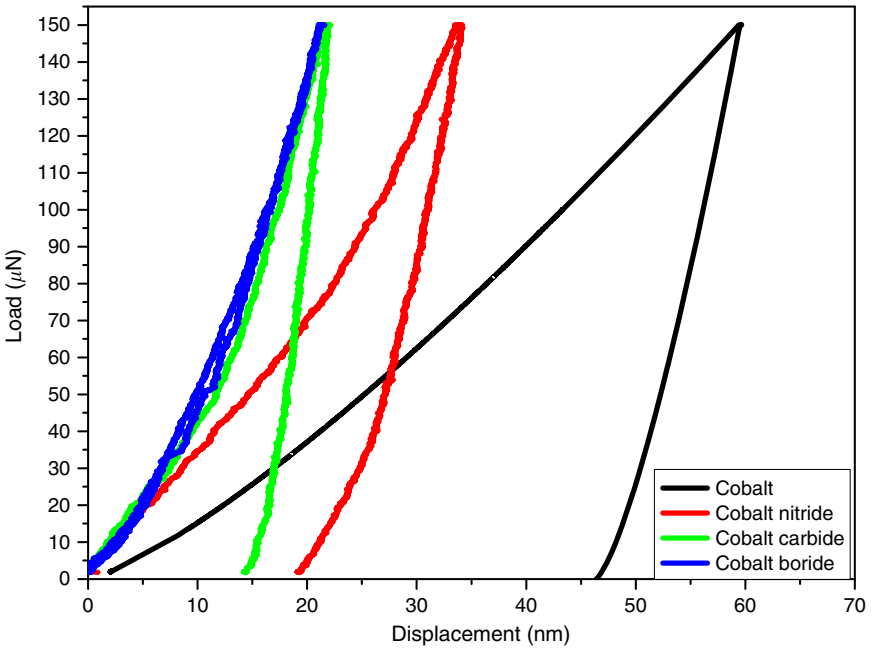

Figure 7.
Typical load unload of the produced Co-based thin films

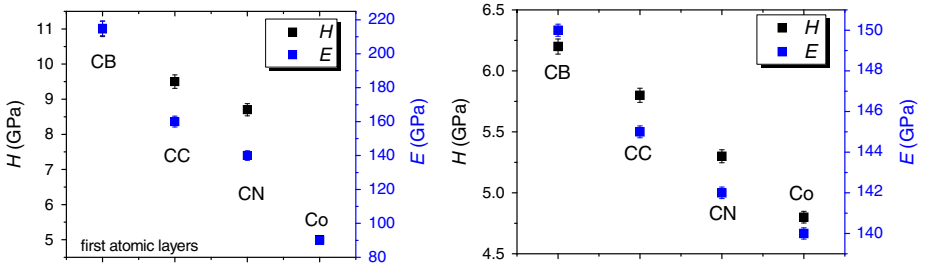

Figure 8.
(a) Nanomechanical properties of each thin films in the first atomic layers (~20 nm); and (b) nanomechanical properties of the thin films

3.3.2 Co-Co_3O_4 comparison. The load-unload curves of the probed materials are presented in Figure 9 (comparison for applied loads of 500 and 1,000 μN). Co_3O_4 thin film exhibits higher resistance to applied load (i.e. higher applied load values are needed in order to reach the same displacement). In the case of Co, greater plasticity is revealed, i.e. energy stored at the material after the indentation is over (total integration of curve area). The nanomechanical properties of the thin films, i.e. H and E, are presented elsewhere (Tsikourkitoudi *et al.*, 2011) and are in good agreement with similar measurements of the literature (Graça *et al.*, 2007).

In Figure 10, SPM images of Co and Co_3O_4 thin films are presented for applied loads of 2,500 and 5,000 μN; the indents are noted in black circle.

The H/E ratio is of significant interest in tribology, as it can be used as a ranking parameter for materials in terms of wear. This ratio multiplied by a geometric factor is the "plasticity index," which is a valuable measure for the determination of the limit of elastic behavior in a surface contact (describes the deformation properties of rough

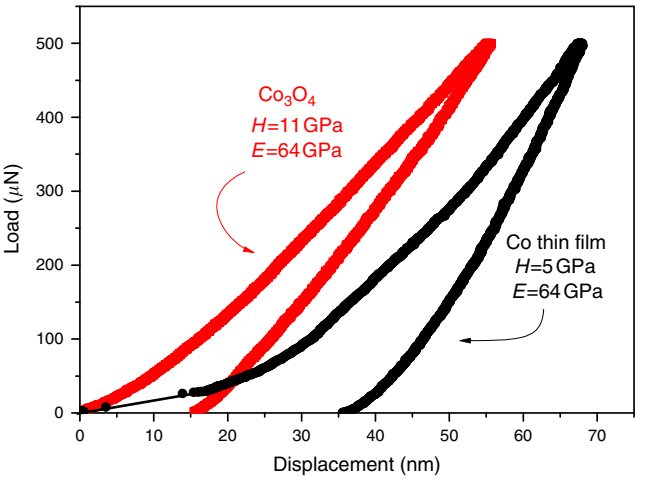

Figure 9.
Load-unload curves of Co (black) and Co_3O_4 (red) thin films (applied load of 500 μN)

surfaces) (Leyland and Matthews, 2000). Figure 11 shows the H/E ratio as a function of the displacement of the indenter. The Co_3O_4 thin film exhibits higher resistance to wear in comparison to the Co thin film.

In Figure 12, the coefficient of friction of the two thin films is presented in accordance to the scratch path. The coefficient of friction is the ratio of the lateral forces to the normal forces and can be expressed as the sum of adhesive and ploughing friction coefficient. The Co_3O_4 thin film exhibits lower coefficient of friction compared to the Co thin film.

In Figure 13, nanoscratch depth profiles are presented for maximum normal load of 500 μN. The scratch scan curve corresponds to tip penetration profile during testing and the post-scratch curve corresponds to the final profile of the surface after scratching (i.e. plastic deformation of the probed film). The difference between scratch and post-scratch curve determines the elastic recovery of the films. The statistical error for the scratch depths is < 10 nm, while the displacement resolution of the nanoindenter used in this work is better than 0.04 nm, making it possible to compare the scratch depths of different films. As it can be observed in Figure 12, the deformation of the films is mainly plastic all over the scratch path. As far as the Co thin film is concerned, fluctuations during scratch can be observed indicating possible failure of the film. The increase in displacement during post-scratch can be attributed to a late recovery of deformation of the thin film in comparison to the substrate, a fact that induces shear stresses along the interface causing spallation of the film (Bull, 1997). No sharp deviation is observed in the scratch curve of the Co_3O_4 thin film. Thus, the film has not been peeled off during load scratch process. However, a low increase in the deformation displacement can be observed, indicating a critical load ($L_{cL} = 150$ μN) for the delamination of the film, caused by high compressive stresses. The load values, corresponding to the point where the Co_3O_4 thin film fails during post-scratch, are almost equal to 150 and 290 μN. The absence of fluctuations in the post-scan curve for a scratch depth larger than 20 nm implies that the film does not delaminate after unloading, showing good adhesion to the substrate despite the relative high stress values and there is no cracks generation, material removal and debris. These events

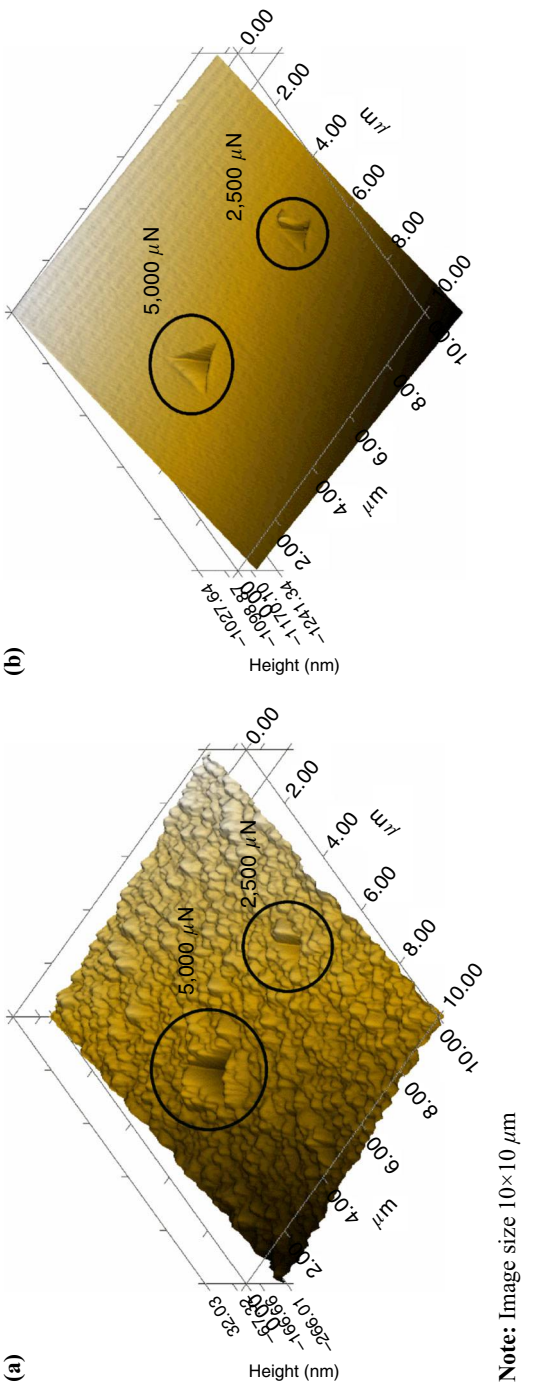

Note: Image size 10×10 μm

Figure 10.
3D SPM image of indents (2500 and 5000 μN) on (a) Co; and (b) Co_3O_4 thin film

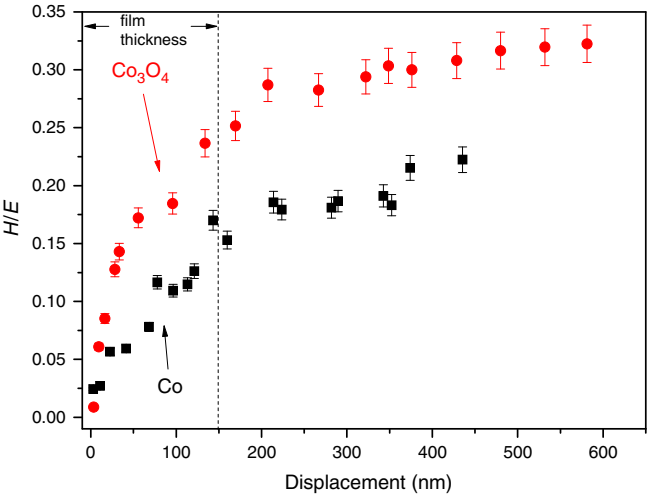

Figure 11.
Hardness to modulus ratio (resistance to wear) as a function of the displacement of the indenter for both thin films

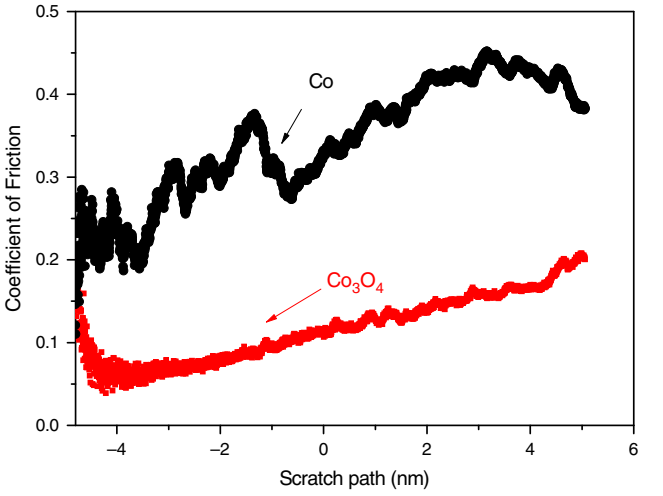

Figure 12.
Coefficient of friction for both thin films

show that during scratching, plastic deformation successively occurs with increasing normal load due to the high-elastic deformation, and film does not delaminate up to the normal load of 290 mN. In Figure 14, SPM images of the scratches for both thin films are presented (AFM images are presented elsewhere; Tsikourkitoudi *et al.*, 2012).

4. Conclusions

In the present study, Co thin films were produced through metalorganic CVD technique. Boronizing, carburization and nitridation of the produced Co thin films were accomplished through a post-treatment stage of thermal diffusion into them, in order to produce Co_2B, Co_3C and Co_2N thin films. The surface topography and the crystal structure of the produced thin films were evaluated through SEM and XRD,

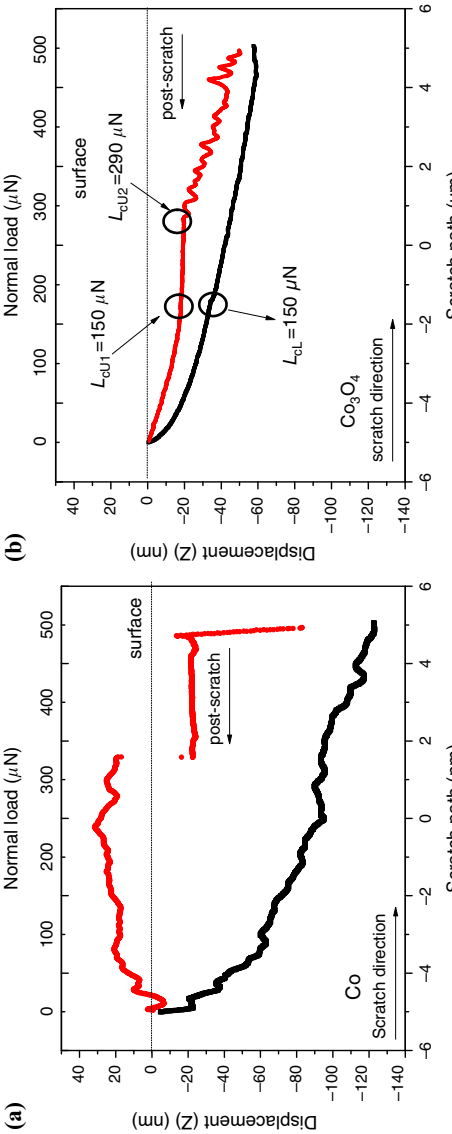

Notes: (a) Co; (b) Co_3O_4 thin film, tested with ramping normal load 0.2-500 μN

Figure 13.
Nanoscratch depth profile

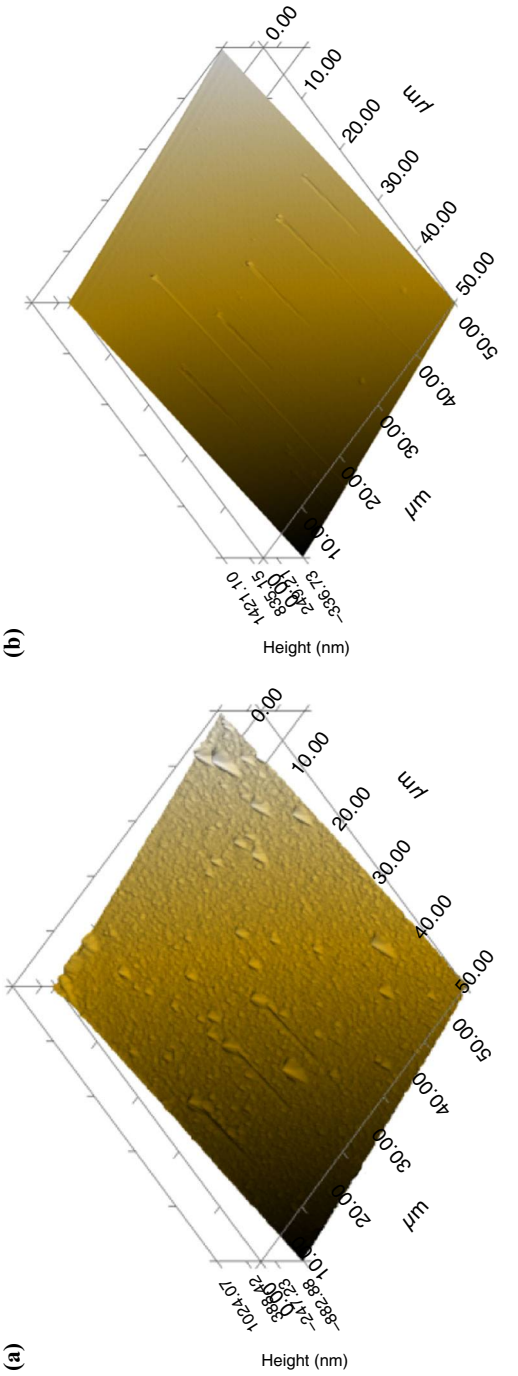

Figure 14.
SPM images of the scratches for both thin films

respectively. XRD analysis indicated that the main crystalline phase for cobalt carbide is Co_3C, for cobalt boride is Co_2B and for cobalt nitride is Co_2N. The mechanical integrity of the thin films was evaluated through nanoindentation technique. The obtained results indicate that Co_2B thin film exhibits the highest nanomechanical properties (i.e. H and E), while Co thin film has enhanced plasticity. The obtained H and E values were in good agreement with literature. The Co_3O_4 thin film exhibits higher resistance to wear in comparison to the Co thin film, a fact that is confirmed by the nanoscratch analysis showing lower coefficient of friction for the Co_3O_4 thin film compared to the Co thin film. Furthermore, nanoscratch depth profiles have been performed for maximum normal load of 500 μN. The deformation of the films is mainly plastic all over the scratch path. For the Co thin film, an increase in displacement during post-scratch is observed which can be attributed to shear stresses that induce a late recovery of deformation of the thin film in comparison to the substrate. A critical load of 150 μN can cause a limited delamination of the Co_3O_4 thin film. The load values, corresponding to the point where the Co_3O_4 thin film fails during post-scratch, are around 150 and 290 μN. Among the future scopes of the present work is the examination of the obtained thin films as potential H_2 sensors.

References

Ando, M., Kobayashi, T., Iijima, S. and Haruta, M.J. (1997), "Optical recognition of CO and H_2 by use of gas-sensitive Au-Co_3O_4 composite films", *Materials Chemistry*, Vol. 7 No. 9, pp. 1779-1783.

Bull, S.J. (1997), "Failure mode maps in the thin film scratch adhesion test", *Tribology International*, Vol. 30 No. 7, pp. 491-498.

Cheng, H., Huang, H., Wang, A., Wang, X. and Zhang, T. (2009), "Preparation of cobalt nitride from Co-Al hydrotalcite and its application in hydrazine decomposition", *Topics in Catalysis*, Vol. 52 No. 11, pp. 1535-1540.

Cong, Y., Park, H.S., Dang, H.X., Fan, F.R.F., Bard, A.J. and Mullins, C.B. (2012), "Tantalum cobalt nitride photocatalysts for water oxidation under visible light", *Chemistry of Materials*, Vol. 24 No. 3, pp. 579-586.

De Pasquale, G., Soma, A. and Ballestra, A. (2009), "Mechanical fatigue analysis of gold microbeams for RF-MEMS applications by pull-in voltage monitoring", *Analog Integrated Circuits and Signal Processing*, Vol. 61 No. 3, pp. 215-222.

Graça, S., Colaço, R. and Vilar, R. (2007), "Indentation size effect in nickel and cobalt laser clad coatings", *Surface and Coatings Technology*, Vol. 202, pp. 538-548.

Koumoulos, E.P., Charitidis, C.A., Papageorgiou, D.P., Papathanasiou, A.G. and Boudouvis, A.G. (2012), "Nanomechanical and nanotribological properties of hydrophobic fluorocarbon dielectric coating on tetraethoxysilane for electrowetting applications", *Surface and Coatings Technology*, Vol. 206 Nos 19-20, pp. 3823-3831.

Leyland, A. and Matthews, A. (2000), "On the significance of H/E ratio in wear control: a nanocomposite coating approach to oprimised tribological behavior", *Wear*, Vol. 246 Nos 1/2, pp. 1-11.

Mane, A.U., Shalini, K. and Shivashankar, S.A. (2001), "Cobalt oxide thin films prepared by metalorganic chemical vapor deposition from cobalt acetylacetonate", *Physique*, Vol. 4 No. 11, pp. 3-63.

Papadopoulos, N., Karayianni, C.-S., Tsakiridis, P., Sarantopoulou, E. and Hristoforou, E. (2011), "Effects of MOCVD thin cobalt films' structure and surface characteristics on their magnetic behavior", *Chemical Vapor Deposition*, Vol. 17 Nos 7/9, pp. 211-220.

Papadopoulos, N.D., Illekova, E., Karayanni, H.S. and Hristoforou, E. (2008), "Synthesis and characterization of cobalt precursors for the growth of magnetic thin films by the MOCVD method", *Optoelectronics and Advanced Materials*, Vol. 10 No. 5, pp. 1098-1102.

Pustan, M. (2011), "Nanomaterial behaviour of a gold microcantilever subjected to plastic deformations", *Digest Journal of Nanomaterials and Biostructures*, Vol. 6 No. 1, pp. 285-290.

Pustan, M., Dudescu, C., Birleanu, C. and Rymuza, Z. (2013), "Nanomechanical studies and materials characterization of metal/polymer bilayer MEMS cantilevers", *International Journal of Materials Research*, Vol. 4 No. 4, pp. 408-414.

Sabarou, H. and Ataie, A. (2012), "Chemico- thermal synthesis of nano-structured cobalt with distinct magnetic property", *Journal of Nanostructures*, Vol. 2 No. 1, pp. 9-17.

Sadek, K. and Moussa, W. (2007), "Studying the effect of deposition conditions on the performance and reliability of MEMS gas sensors", *Sensors*, Vol. 7 No. 3, pp. 319-340.

Tsikourkitoudi, V.P., Koumoulos, E.P., Papadopoulos, N. and Charitidis, C.A. (2011), "Growth, structural and mechanical characterization and reliability of chemical vapor deposited Co and Co_3O_4 thin films as candidate materials for sensing applications", *Key Engineering Materials*, Vol. 495, pp. 108-111.

Tsikourkitoudi, V.P., Koumoulos, E.P., Papadopoulos, N., Hristoforou, E. and Charitidis C.A. (2012), "Growth, structural and mechanical characterization and reliability of chemical vapor deposited Co and Co_3O_4 thin films as candidate materials for sensing applications", *Journal Of Optoelectronics and Advanced Materials*, Vol. 14 No. 1, pp. 169-175.

Zhang, Y., Chaubey, G.S., Rong, C., Ding, Y., Poudyal, N., Tsai, P., Zhang, Q. and Liu, J.P. (2011), "Controlled synthesis and magnetic properties of hard magnetic Co_xC ($x = 2$, 3), nanocrystals", *Journal of Magnetism and Magnetic Materials*, Vol. 323 No. 11, pp. 1495-1500.

Further reading

Charitidis, C., Logothetidis, S. and Gioti, M. (2000), "A comparative study of the nanoscratching behavior of amorphous carbon films grown under various deposition conditions", *Surface and Coatings Technology*, Vol. 125 Nos 1/3, pp. 201-206.

Chen, Y.-T. and Jian, S.R. (2009), "The structural, magnetic and nanomechanical properties of hexagonal Co thin films", *Alloys and Compounds*, Vol. 481 Nos 1/2, pp. 365-368.

Corresponding author

Professor Costas A. Charitidis can be contacted at: charitidis@chemeng.ntua.gr

Tribology International 82 (2015) 89–94

Contents lists available at ScienceDirect

Tribology International

journal homepage: www.elsevier.com/locate/triboint

Tribological characterization of chemical vapor deposited Co and Co_3O_4 thin films for sensing reliability in engineering applications

Elias P. Koumoulos [a], Vassileios Markakis [a], Vasiliki P. Tsikourkitoudi [a], Costas A. Charitidis [a,*], Nikolaos Papadopoulos [b], Evangelos Hristoforou [b]

[a] School of Chemical Engineering, National Technical University of Athens, 9 Heroon Polytechniou Street, Zographos, Athens 15780, Greece
[b] School of Mining Engineering and Metallurgy, National Technical University of Athens, 9 Heroon Polytechniou Street, Zographos, Athens GR-157 80, Greece

ARTICLE INFO

Article history:
Received 7 March 2014
Received in revised form
23 July 2014
Accepted 16 September 2014
Available online 17 October 2014

Keywords:
Cobalt oxide
Thin films
Nanoindentation
Coefficient of friction

ABSTRACT

In the present study, nanoindentation and nanoscratch techniques are applied in order to obtain the nanomechanical properties (hardness, *H*, and elastic modulus, *E*) of chemical vapor deposited Co and Co_3O_4 thin films (promising candidates for magnetic sensing and data storage applications) and evaluate the functionality of the thin film–substrate system. A wear analysis is also performed based on the *H*/*E* ratio.

1. Introduction

The mechanical and tribological behavior of magnetic and storage devices is of critical importance in determining long-term stability and reliability of such devices. The good maintenance of the mechanical and tribological properties of the aforementioned devices can significantly impact their commercialization. Nanoindentation technique can be a useful tool for the measurement of stresses for the successful and reliable operation of such devices. The variation of nanomechanical/nanotribological response of sensors should be kept within a narrow range (defined percentage of range). Nanoscratch testing is a versatile tool for analysis of the mechanical attributes of thin films and bulk materials and can be used for a plethora of tests, where a single scratch with a ramped load is useful for critical load, film adhesion and mar studies [1]. Nanoscratch data, coupled with scanning probe microscope (SPM) images, provide detailed information concerning a material's behavior under simultaneous normal and lateral stresses.

In the present study, nanoindentation and nanoscratch techniques are utilized in order to investigate the nanomechanical (i.e. hardness, *H*, and elastic modulus, *E*) and nanotribological properties of chemical vapor deposited (CVD) Co and Co_3O_4 thin films, which can be used in innovative sensing and data storage applications due to their useful properties [2]. Cobalt thin films appear as a promising perspective regarding sensors and magnetic devices, since cobalt exhibits the highest magnetic anisotropy among transition metals [3]. Co_3O_4 thin films have also been considered for uses as magnetic detectors, counter electrodes, humidity or oxygen optical sensors [4], solar-selective absorbers and protective layers [2]. CVD is a widely used technique for the production of highly dense films with good adhesion to the substrate [5].

2. Experimental section

The films were grown in a vertical, cylindrical metallorganic CVD stainless steel reactor, specifically developed for the deposition of magnetic films, either singled or multilayered [5–6]. The reactor had computer controlled switching of gases for abrupt transients during deposition of multilayered structures. It also employed two independent precursor lines and four separate gas delivery lines for maintaining inert, (He or Ar), reductive (H_2) or oxidizing (O_2) atmosphere. Prior to reactor's entrance heat traced lines were used. The Co films were deposited from a cobalt carbonyl precursor onto a SiO_2 substrate. The cobalt carbonyl precursor was introduced to the reactor as an aerosol mixture, formed by the dissolution of cobalt

* Corresponding author. Tel.: +30 2107724046; fax: +30 2107723323.
E-mail addresses: elikoum@chemeng.ntua.gr (E.P. Koumoulos), vmarkakis@chemeng.ntua.gr (V. Markakis), vasiatsik@yahoo.gr (V.P. Tsikourkitoudi), charitidis@chemeng.ntua.gr (C.A. Charitidis), nickpapss@yahoo.gr (N. Papadopoulos), eh@metal.ntua.gr (E. Hristoforou).

http://dx.doi.org/10.1016/j.triboint.2014.09.018
0301-679X/

carbonyl into dichloromethane, 0.1 M concentrated. In a typical experiment a liquid (solution) flow of 7 g/h was mixed with a hydrogen gas flow of 0.05 l/min at 27 °C. The mixture (aerosol) was then introduced to the reactor, the temperature of which had been adjusted to 140 °C; further details are reported elsewhere [6].

As far as the deposition of the Co_3O_4 is concerned, the substrate (Si) was loaded and the reactor was purged with an argon flow of 0.75 l/h, while the susceptor was heated to the desired temperature (450 °C). Then a solid inclusion complex (placed in a specialized glass reservoir) of β-cyclodextrin with CoI_2 was sublimed at 115 °C, and the vapors were introduced into the reactor with the aid of a constant O_2 flow of 50 ml/min; further details are reported elsewhere [6]. The thickness of the produced Co and Co_3O_4 films ranged ~120–150 nm.

X-ray diffraction (XRD) tests were conducted using a Siemens D5000 diffractometer with nickel-filtered CuKα1 radiation (1.5405 Å), at 40 kV and 30 mA.

The nanoindentation and nanotribological tests in this work were performed using a nanomechanical test instrument equipped with a Berkovich tip (120 nm tip radius) allowing the application of loads from 1 to 30,000 μN. In all depth-sensing tests, a total of 10 indents were averaged to determine the mean *H* and *E* values for statistical purposes, with a spacing of 50 μm (~45% relative humidity, 23 °C). The above instrument is equipped with a scanning probe microscope (SPM), in which the sharp tip moves in a raster scan pattern across a sample surface using a three-axis piezo positioner.

The scratch tests performed in this work included three main segments. Firstly, a pre-scratch scan under a very low load (0.2 μN) was carried out. Then, the indenter scraped the sample under a ramp loading from an initial load of 0.2 μN to a maximum value of 500 μN at the end of the scratch. The scratch path was 10 μm and the tip velocity 0.2 μm/s. Finally, a post-scratch was carried under a low load (2 μN). The applied load during the initial scratch and post-scratch was very low in order to avoid any damage or permanent deformation of the films. In all scratch tests, a total of 5 scratches were averaged for statistical purposes, with a spacing of 10 μm (~45% relative humidity, 23 °C).

3. Results and discussion

3.1. X-ray diffraction/scanning electron microscopy

Cobalt oxide thin film was deposited in the form of Co_3O_4. Surprisingly, no phases corresponding to oxides of divalent cobalt were detected (Fig. 1a). Intermediate phases of cobalt silicides (Si content 59.67% w/w) were detected, probably due to the relatively high deposition temperature, which allowed diffusion of Si out from the substrate. Discrete peaks corresponding to typical Si angles of diffraction were detected (Fig. 1b), but this was, to some extent, attributed to the film's low thickness, which has been proven by AFM and MFM measurements (presented elsewhere [6]). The presence of peaks corresponding to Si angles can be attributed to the free from deposition wafer area that is left for many reasons, one of which is to directly measure the thickness of

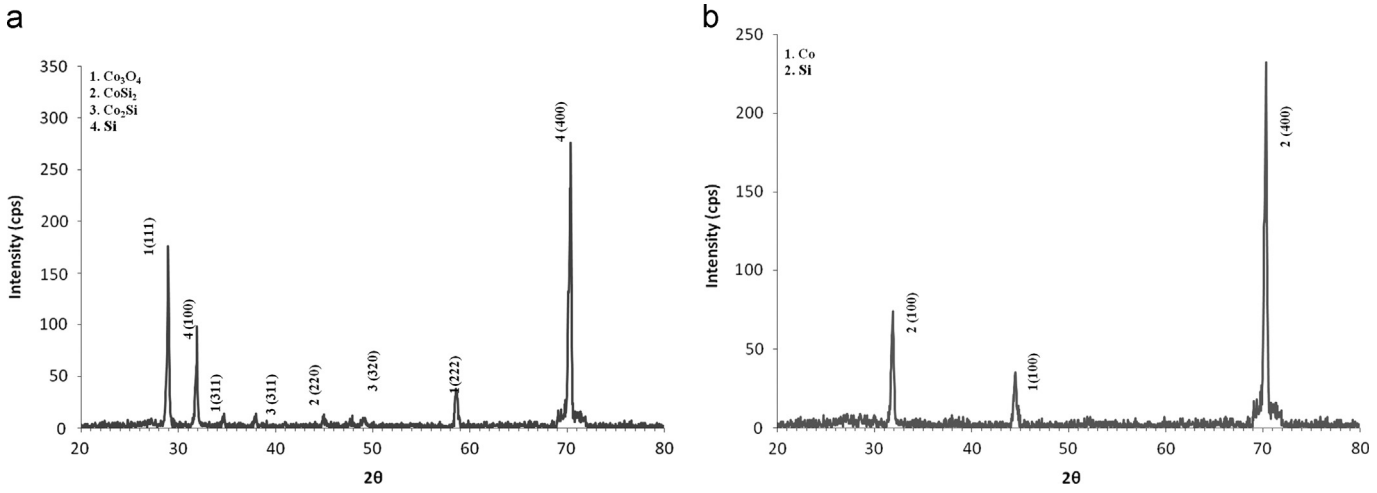

Fig. 1. X-ray diffraction of (a) Co_3O_4 and (b) Co thin films, respectively.

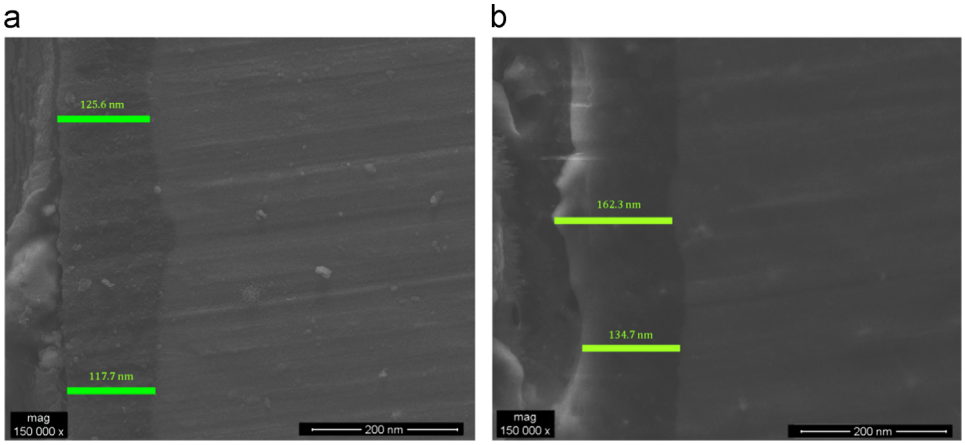

Fig. 2. Cross section images of (a) Co_3O_4 and (b) Co thin films, respectively.

the thin film. The cross section images of both thin films were determined by scanning electron microscopy (SEM) using a PHILIPS Quanta Inspect (FEI Company) microscope with W (tungsten) filament 25 KV(Fig. 2).

3.2. Load–displacement curves

It is important to evaluate the nanomechanical response in the overall tribological characterization of materials, as the contact between surfaces is usually initiated by the contact between surface asperities with contact areas only a few tens of square nanometers. In the present work, the load–unload curves of the probed materials are presented in Fig. 3 (comparison for applied loads of 500 and 1000 μN). Co_3O_4 thin film exhibits higher resistance to applied load (i.e. higher applied load values are needed in order to reach the same displacement). In the case of Co, greater plasticity is revealed, i.e. energy stored at the material after the indentation is over (total integration of curve area). The nanomechanical properties of the thin films, i.e. *H* and *E*, are presented elsewhere [7] and are in good agreement with similar measurements of the literature [8–9]. Cobalt thin film exhibit local changes (discontinuities), i.e. changes in the slope, referred as pop-ins and elbows in the loading and in the unloading curve, respectively [7]. During the pop-in, the indenter tip penetrates in the sample without an increase in the applied load. The first pop-in in each sample reveals the onset of plasticity, i.e. the first point at which plastic yield occurs. The onset of plasticity occurs at ~10 nm for each thin film. In this stage, the nanoindenter can be approximated as spherical and the experimental data deviate from the fully elastic curve. For lower loads than the load where the onset of plasticity occurs, reversibility of the indentations performed is observed. The pop-ins indicate a redistribution of material around the indentation site [7].

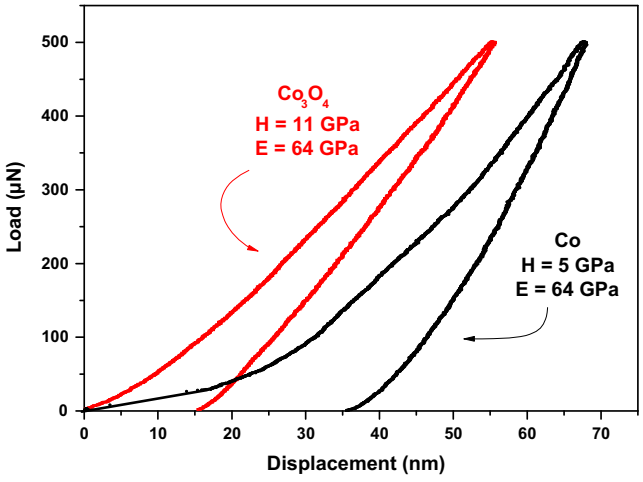

Fig. 3. Load–unload curves of Co (black) and Co_3O_4 (red) thin films (applied load of 500 μN) (For interpretation of the references to color in this figure legend, the reader is referred to the web version of this article.).

In Fig. 4, SPM images of Co and Co_3O_4 thin films are presented for applied loads of 2500 and 5000 μN; the indents are noted in black circle.

3.3. Wear analysis

The *H*/*E* ratio is of significant interest in tribology, as it can be used as a ranking parameter for materials in terms of wear. This ratio multiplied by a geometric factor is the "plasticity index", which is a valuable measure for the determination of the limit of elastic behavior in a surface contact (describes the deformation properties of rough surfaces) [10]. Fig. 5 shows the *H*/*E* ratio as a function of the displacement of the indenter. The Co_3O_4 thin film exhibits higher resistance to wear in comparison to the Co thin film.

A high H/E^* value means a reduced contact pressure, because the applied load is distributed over a larger area. A high *H*/*E* ratio is related to a high elastic strain prior to the plastic deformation, while it has long been known that, in a tribo-contact event between rough surfaces, purely elastic contact is desired for wear reduction [7].

Adhesion relation of a coating with a substrate is confirmed by using the Tresca's yield criterion and Tabor's relation, according to which, the load at the onset of yielding is proportional to H^3/E^2. The term H^3/E^2 combines *H* and *E* values of a material and describes the amount of elasticity exhibited by the film. In particular, high (low) values of H^3/E^2 indicate a highly elastic (plastic) behavior of the film under contact events (Fig. 6) [10,11]. The transition of film behavior due to the interface is evidenced, in a slightly lower displacement when compared with total film thickness (< 150 nm).

It is known that many of the mechanisms of film failure begin with or directly involve plastic deformation. Consequently, a particular concern in the usefulness of thin films as protective overcoat materials in hard disk and/or wear-resistant applications is that these films must be highly resistant to plastic deformation during contact events. The film has to undergo a high proportion of elastic deformation occurring when indenting, resulting in high values of *H* (which reflect the small amounts of plastic deformation occurring) (Figs. 3, 5); cobalt oxide thin film exhibit such behavior.

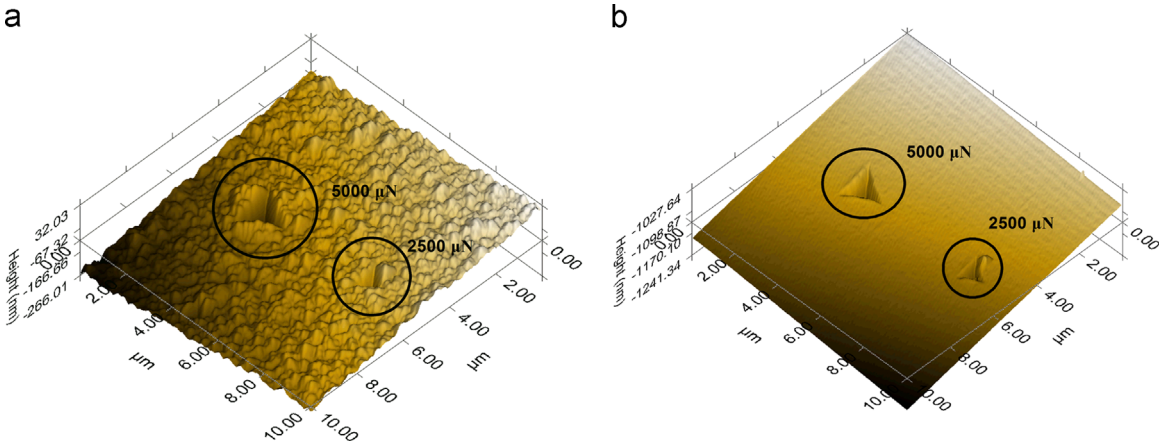

Fig. 4. 3D SPM image of indents (2500 and 5000 μN) on (a) Co and (b) Co_3O_4 thin film (image size 10×10 μm^2).

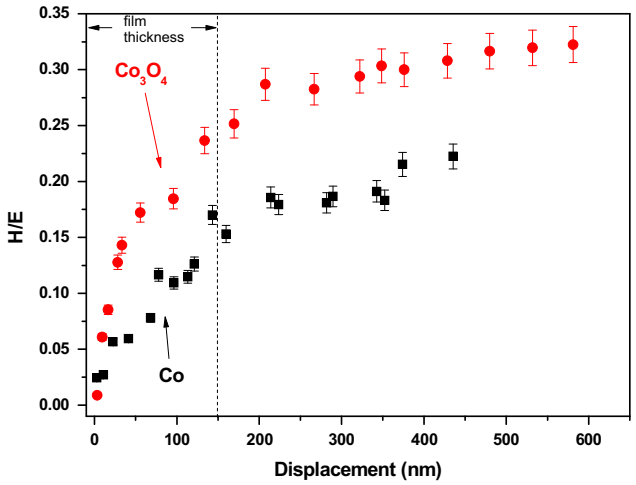

Fig. 5. Hardness to modulus ratio (resistance to wear) as a function of the displacement of the indenter for both thin films.

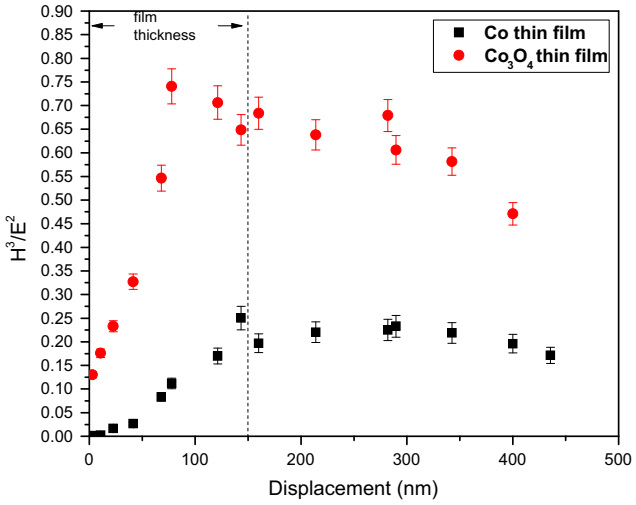

Fig. 6. H^3/E^2 as a function of the displacement of the indenter for both thin films.

3.4. Nanoscratch analysis

In Fig. 7, the coefficient of friction of the two thin films is presented in accordance to the scratch path. The coefficient of friction is the ratio of the lateral forces to the normal forces and can be expressed as the sum of adhesive and plowing friction coefficient. The Co_3O_4 thin film exhibits lower coefficient of friction compared to the Co thin film (low wear, in line with H/E and H^3/E^2).

In Fig. 8, nanoscratch depth profiles are presented for maximum normal load of 500 μN. The scratch scan curve corresponds to tip penetration profile during testing and the post-scratch curve corresponds to the final profile of the surface after scratching (i.e. plastic deformation of the probed film). The difference between scratch and post-scratch curve determines the elastic recovery of the films. The statistical error for the scratch depths is less than 10 nm, while the displacement resolution of the nano-indenter used in this work is better than 0.04 nm, making it possible to compare the scratch depths of different films. As it can be observed in Fig. 7, the deformation of the films is mainly plastic all over the scratch path. As far as the Co thin film is concerned, fluctuations during scratch can be observed indicating possible failure of the film. The increase in displacement during post-scratch can be attributed to a late recovery of deformation of the

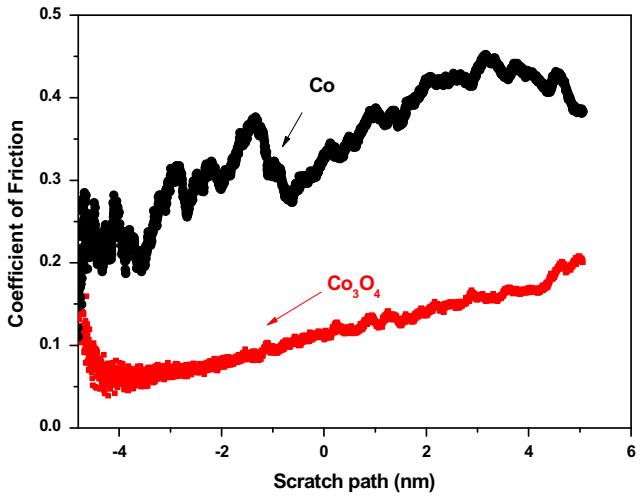

Fig. 7. Coefficient of friction for both thin films.

thin film in comparison to the substrate, a fact that induces shear stresses along the interface causing spallation of the film [11–12]. No sharp deviation is observed in the scratch curve of the Co_3O_4 thin film. Thus, the film has not been peeled off during load scratch process. However, a low increase in the deformation displacement can be observed, indicating a critical load (L_{cL}=150 μN) for the delamination of the film, caused by high compressive stresses. The load values, corresponding to the point where the Co_3O_4 thin film fails during post-scratch, are almost equal to 150 and 290 μN. The absence of fluctuations in the post scan curve for a scratch depth larger than 20 nm implies that the film does not delaminate after unloading, showing good adhesion to the substrate despite the relative high stress values and there is no cracks generation, material removal and debris. These events show that during scratching, plastic deformation successively occurs with increasing normal load due to the high elastic deformation, and film does not delaminate up to the normal load of 290 mN. In Fig. 9, SPM images of the scratches for both thin films are presented (AFM images are presented elsewhere [13]).

The Co_3O_4 films were uniformly grain distributed with, however enlarged grains, probably due to high deposition temperature [7]. The mean surface roughness (RMS) deviation of the films deposited at 450 °C was of the order of 5.5 nm, with the mean height being around 17.5 nm. On the contrary, the Co films originating from $Co_2(CO)_8$ presented an extremely smooth surface with a mean surface roughness around 2 nm and an average height of about 12.5 nm.

It should be noted that friction anisotropy is actually a phenomenon with two degrees of freedom since one can vary either the relative orientations of the crystal lattices or the direction of shearing with respect to the crystal lattices. In literature, the shearing direction is fixed with respect to one surface lattice and rotation of the crystal lattices with respect to one another (this experiment could reveal the possible effects of surface lattice commensurability) [14]. Rotating the shearing direction while maintaining the relative surface lattice orientations is an equally challenging experiment in nanoscale (already performed in macroscale).

4. Conclusions

In the present study, nanoindentation and nanoscratch techniques are utilized in order to investigate the nanomechanical (i.e. H and E) and nanotribological properties of CVD Co and Co_3O_4 thin films, which are widely used in applications for innovative

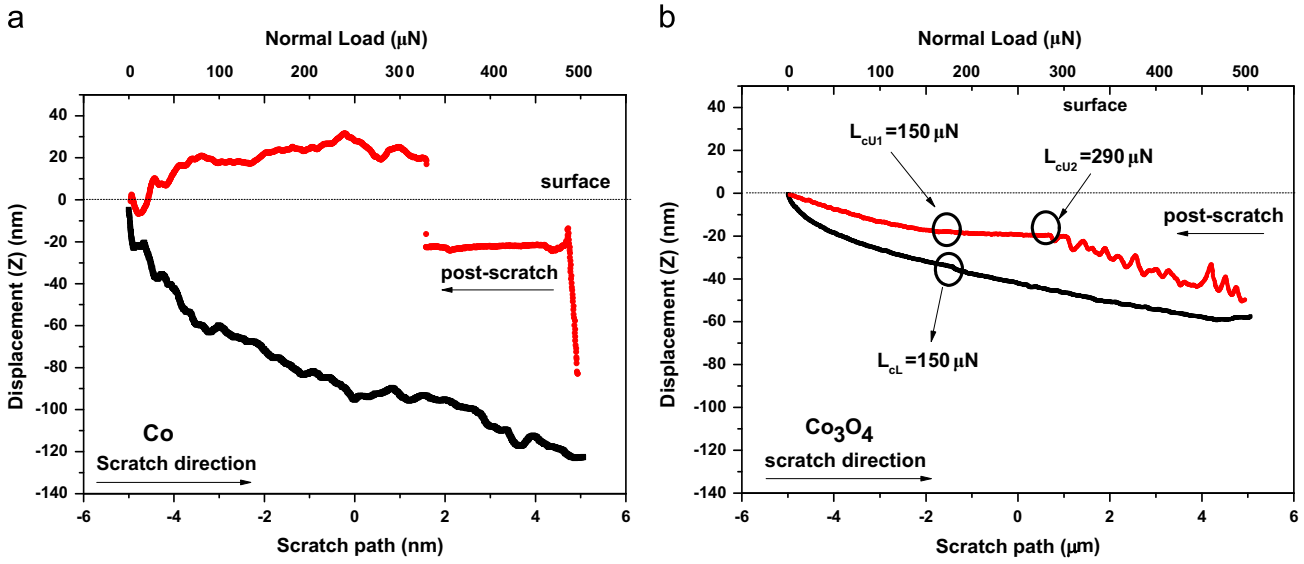

Fig. 8. Nanoscratch depth profile for (a) Co and (b) Co_3O_4 thin film, tested with ramping normal load 0.2–500 μN.

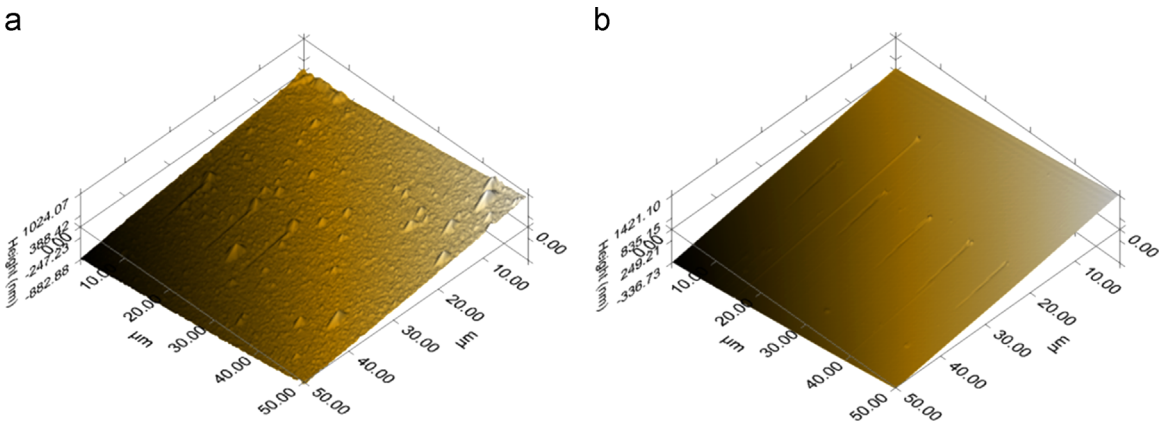

Fig. 9. SPM images of the scratch tracks (10 μm) for Co thin film (a) and Co_3O_4 thin film (b).

sensing and data storage devices due to their useful properties. The *H* and *E* values are in good agreement with similar measurements in the literature. A wear analysis based on the *H*/*E* ratio has been also performed. The Co_3O_4 thin film exhibits higher resistance to wear in comparison to the Co thin film, a fact that is confirmed by the nanoscratch analysis showing lower coefficient of friction for the Co_3O_4 thin film compared to the Co thin film. Furthermore, nanoscratch depth profiles have been performed for maximum normal load of 500 μN. The deformation of the films is mainly plastic all over the scratch path. For the Co thin film, an increase in displacement during post-scratch is observed which can be attributed to shear stresses that induce a late recovery of deformation of the thin film in comparison to the substrate. A critical load of 150 μN can cause a limited delamination of the Co_3O_4 thin film. The load values, corresponding to the point where the Co_3O_4 thin film fails during post-scratch, are around 150 and 290 μN.

Acknowledgments

The authors wish to acknowledge NTUA funded project for basic research PEVE-NTUA-2010/65187900 and Alexandros S. Onassis Public Benefit Foundation for the support of this work.

References

[1] Koumoulos EP, Charitidis CA, Papageorgiou DP, Papathanasiou AG, Boudouvis AG. Nanomechanical and nanotribological properties of hydrophobic fluorocarbon dielectric coating on tetraethoxysilane for electrowetting applications. Surf Coat Technol 2012;206(19–20):3823–31.
[2] Mane AU, Shalini K, Shivashankar SA. Cobalt oxide thin films prepared by metalorganic chemical vapor deposition from cobalt acetylacetonate. Physique 2001;IV 11:3–63.
[3] Papadopoulos ND, Illekova E, Karayanni HS, Hristoforou E. Synthesis and characterization of cobalt precursors for the growth of magnetic thin films by the MOCVD method. Optoelectron Adv Mater 2008;10:1098–102;
Wöllenstein J, Burgmair M, Plescher G, Sulima T, Hildenbrand J, Böttner H, et al. Cobalt oxide based gas sensors on silicon substrate for operation at low temperatures. Sens Actuators B 2003;93(2003):442–8.
[4] Ando M, Kobayashi T, Iijima S, Haruta MJ. Optical recognition of CO and H_2 by use of gas-sensitive Au–Co_3O_4 composite films. Mater Chem 1997;7:1779–83.
[5] Papadopoulos ND, Tsakiridis PE, Hristoforou E. Structural and electrical properties of undoped SnO_2 films developed by a low cost CVD technique with two different methods: comparative study. Optoelectron Adv Mater 2005;7:2693–706.
[6] Papadopoulos N, Karayianni C-S, Tsakiridis P, Sarantopoulou E, Hristoforou E. Effects of MOCVD thin cobalt films' structure and surface characteristics on their magnetic behavior. Chem Vap Depos 2011;17:211–20.
[7] Tsikourkitoudi VP, Koumoulos EP, Papadopoulos N, Charitidis CA. Growth, structural and mechanical characterization and reliability of chemical vapor deposited Co and Co_3O_4 thin films as candidate materials for sensing applications. Key Eng Mater 2011;495:108–11.
[8] Graça S, Colaço R, Vilar R. Indentation size effect in nickel and cobalt laser clad coatings. Surf Coat Technol 2007;202:538–48.

[9] Chen Y-T, Jian SR. The structural, magnetic and nanomechanical properties of hexagonal Co thin films. Alloys Compd 2009;481:365–8.
[10] Leyland A, Matthews A. On the significance of *H*/*E* ratio in wear control: a nanocomposite coating approach to oprimised tribological behavior. Wear 2000;246:1–11.
[11] Bull SJ. Failure mode maps in the thin film scratch adhesion test. Tribol Int 1997;30:491–8.
[12] Charitidis C, Logothetidis S, Gioti M. A comparative study of the nanoscratching behavior of amorphous carbon films grown under various deposition conditions. Surf Coat Technol 2001;125:201–6.
[13] Tsikourkitoudi VP, Koumoulos EP, Papadopoulos N, Hristoforou E, Growth Charitidis CA. Structural and mechanical characterization and reliability of chemical vapor deposited Co and Co_3O_4 thin films as candidate materials for sensing applications. J Optoelectron Adv Mater 2012;14(1):169–75.
[14] Gellman AJ, Ko JS. The current status of tribological surface science. Tribol Lett 2001;10(1–2):39–44.

Materials Research Bulletin 49 (2014) 552–559

Contents lists available at ScienceDirect

Materials Research Bulletin

journal homepage: www.elsevier.com/locate/matresbu

Nanocomposite NiO:Au hydrogen sensors with high sensitivity and low operating temperature

M. Kandyla [a,*], C. Chatzimanolis-Moustakas [a,b], E.P. Koumoulos [b], C. Charitidis [b], M. Kompitsas [a]

[a] National Hellenic Research Foundation, Theoretical and Physical Chemistry Institute, 48 Vasileos Constantinou Avenue, 11635 Athens, Greece
[b] National Technical University of Athens, School of Chemical Engineering, 9 Heroon Polytechniou Street, 15780 Zografou, Greece

ARTICLE INFO

Article history:
Received 2 May 2013
Received in revised form 31 July 2013
Accepted 29 September 2013
Available online 8 October 2013

Keywords:
A. Composites
A. Oxides
B. Sputtering
B. Laser deposition
D. Electrochemical properties

ABSTRACT

We present results on the development of nanocomposite NiO:Au thin-film hydrogen sensors, which are able to detect hydrogen concentrations as low as 2 ppm in air, operating at low temperatures in the range 125–150 °C. Thin NiO films were sputter-deposited on oxidized silicon substrates. The structural, morphological, and nanomechanical properties of the films were investigated with respect to post-deposition annealing. Au nanoparticles were added on the NiO surface via pulsed laser deposition and the films were tested as hydrogen sensors before and after Au deposition. The performance of the NiO films as hydrogen sensors improved significantly in the presence of Au nanoparticles on the surface. The detection limit (lowest detectable hydrogen concentration) decreased by two orders of magnitude, while the response time also decreased by a factor of three.

1. Introduction

Hydrogen is widely used in the chemical, petroleum, and metallurgical industries, as well as in power station cooling. Furthermore, the use of hydrogen finds increasing interest lately, due to its projection as the clean fuel of the future and as an important potential energy source. In addition to hydrogen fuel cells, which are already employed in specialized applications, hydrogen is expected to be mass produced and distributed in the near future for passenger vehicles and aircrafts, as well as a city gas. Dangers associated with hydrogen include high permeability through many materials, flammability (lowest explosion limit is 40,000 ppm in air), and lack of odor, taste, and color, which renders it undetectable by human senses [1]. Therefore, smart hydrogen sensors with high sensitivity and low power consumption are essential in order to achieve safe and efficient processing of hydrogen on a massive scale.

Gas sensor technologies vary depending on the mechanism of operation, such as resistive, electrochemical, catalytic, optical, and mechanical, among others. Each technology presents important advantages and certain disadvantages, depending on the application. Resistive gas sensors detect changes in the electrical resistance of a material in the presence of an analyte gas [1,2]. The advantages of resistive gas sensors include low cost, high sensitivity, and wide operating temperature range. Metal-oxide thin films have been successfully employed as resistive sensors due to their electrical response in the presence of a reducing or oxidizing gas. Metal oxides such as SnO_2 [3], ZnO [4], and TiO_2 [5], among others, have shown very good hydrogen sensing properties, such as high sensitivity, fast response, and long-term stability, combined with low-cost and flexible production, as well as simplicity in their use. One of the drawbacks of metal-oxide sensors, is that they have to be heated during operation in order to promote the reaction with the analyte gas. In general, the operating temperature of such sensors ranges between 180 and 450 °C [1], increasing the power consumption of the devices.

The advent of nanotechnology provides new structures and materials for gas sensing applications. Metal-oxide nanorods, nanowires, nanobelts, and nanodiscs [6–9], core–shell nanostructures [10], heterojunction nanofibers [11], and carbon nanotubes [12] are some examples of novel hydrogen nanosenors. New types of materials such as organic–inorganic hybrids [13] and graphene [14] have also been used recently for hydrogen sensing. The advantages of nanostructures include large active surface area, high charge carrier mobility, high sensitivity, and low fabrication costs.

Residual stresses may be developed during the micro/nano fabrication process of sensor devices, which can seriously affect

* Corresponding author. Tel.: +30 210 7273826; fax: +30 210 7273794.
E-mail address: kandyla@eie.gr (M. Kandyla).

0025-5408/$ – see front matter © 2013 Elsevier Ltd. All rights reserved.
http://dx.doi.org/10.1016/j.materresbull.2013.09.044

their operating performance and reliability, as they can cause rupture and/or delamination of thin films and nanostructures [15]. The mechanical and tribological behavior of sensing devices is of critical importance in determining long-term stability and reliability. Good maintenance of the mechanical and tribological properties of sensors can significantly impact their commercialization. Nanoindentation is a useful tool for the control of stresses for successful and reliable sensor operation. The variation of the nanomechanical/nanotribological response of sensors, as determined by nanoindentation, should be kept within a narrow range of values.

In this work, we present results on the fabrication of resistive nanocomposite NiO:Au hydrogen sensors, which are able to detect hydrogen concentrations as low as 2 ppm in air, operating at temperatures in the range 125–150 °C. Additionally, the structural, morphological, and nanomechanical properties of the sensors are investigated with respect to post-fabrication annealing. Even though NiO is a widely employed metal oxide, with excellent chemical stability [16], ease of fabrication, and applications ranging from electrochromism [17] to fuel cells [18], its use as a gas sensor material is limited. This is because NiO is a p-type semiconductor due to nickel vacancies [19], contrary to most other metal oxides, which are n-type semiconductors due to oxygen vacancies. It has been shown that n-type materials present higher response to analyte gases than p-type materials because surface effects dominate the resistive behavior of the former [20]. The most promising results reported so far for resistive NiO hydrogen sensors include the detection of concentrations down to 500 ppm, operating at the 300–650 °C temperature range, by thin NiO films [21,22]. Also, NiO films with thin Pt overlayers or embedded Au nanoparticles have been tested as resistive hydrogen sensors, detecting concentrations of 300–500 ppm while operating at lower temperatures, in the 150–420 °C range, due to the promoting role of the metallic elements [23,24]. Pure NiO films have been shown to operate at 125 °C for higher hydrogen concentrations of 3000 ppm [25]. Films of hollow NiO nano-hemispheres were employed as hydrogen sensors, detecting 200 ppm of hydrogen at 300–400 °C [26]. By employing NiO films with Au nanoparticles on the surface, we are able to detect two orders of magnitude lower hydrogen concentrations at lower operating temperatures, compared with concentrations and temperatures found in the literature, therefore improving the detection limit and reducing the power consumption of the devices. Thus, NiO performance is now comparable to the performance of n-type metal-oxide sensors, making NiO an attractive material for hydrogen sensing. Even though previous works in this field mainly employ embedded metallic nanoparticles in the bulk of the sensor film, the results presented in this paper are obtained with a very small amount of Au nanoparticles, which exist only on the sensor surface.

2. Materials and methods

Thin NiO films were deposited by DC reactive magnetron sputtering from a nickel target (76 mm diameter, 99.95% purity) on oxidized silicon substrates kept at room temperature. A mixture of oxygen and argon flows was used, controlled by mass flow controllers. The total gas pressure was kept at 0.6 Pa and the oxygen partial pressure was kept at 0.18 Pa. A sputtering power of 600 W was used. To investigate the effect of annealing, some samples were post-annealed at 400–600 °C for 1 h in nitrogen (annealed samples), while others were used for measurements without annealing (as-deposited samples).

Au nanoparticles were deposited on the NiO surface by pulsed laser deposition. The deposition took place in a vacuum chamber evacuated to a pressure of 10^{-5} mbar. Au targets were irradiated for 60 s by a Q-switched Nd:YAG laser system (9 ns pulse duration, 10 Hz repetition rate), operating at 355 nm. The NiO–Au target distance was 50 mm and the NiO samples were kept at 100 °C during Au deposition.

The surface morphology of the samples was investigated with the aid of a Philips Quanta Inspect Scanning Electron Microscope (SEM), equipped with an Energy Dispersive Spectrometer (EDS). A Theta D5000 X-ray diffractometer (XRD) with Cu K_α radiation was employed for structural characterization.

Nanoindentation measurements were performed on the NiO samples with a Hysitron Tribolab Nanomechanical Test Instrument, which allows the application of loads from 1 to 30,000 μN on the surface of the sample and records the displacement of the surface as a function of the applied load with high load resolution (1 nN) and high displacement resolution. The obtained curve is called load–displacement curve. The nanomechanical test instrument is equipped with a Scanning Probe Microscope, in which a sharp probe tip moves in a raster scan pattern across the sample surface using a three-axis piezo positioner. For each sample, a total of 10 indents with a spacing of 50 μm in a clean area environment with 45% humidity and 23 °C ambient temperature were averaged to determine the sample's mean hardness, H, and Young's modulus, E. In order for the test instrument to operate under closed loop load or displacement control, a feedback control option was used. All nanoindentation measurements were performed with the standard three-sided pyramidal Berkovich probe, with an average radius of curvature of about 100 nm [27], 40 s loading and unloading time, and 3 s of holding time, to avoid residual viscoelasticity [28,29]. Prior to indentation, the area function of the indenter tip was measured in fused silica, a standard material for this purpose [30].

Based on the half-space elastic deformation theory, H and E values for the NiO samples can be extracted from the experimental data (load–displacement curves) using the Oliver–Pharr method [31]. The derived expressions for calculating the elastic modulus, E, from indentation experiments are based on Sneddon's [32,33] elastic contact theory:

$$E = \frac{S\sqrt{\pi}}{2\beta\sqrt{A}}, \tag{1}$$

where S is the unloading stiffness (equal to the slope of the load–displacement curve at the beginning of unloading), A is the projected contact area between the tip and the substrate, and β is a constant that depends on the geometry of the indenter ($\beta = 1.167$ for a Berkovich tip [31]). The nanoindentation hardness, H, is given by:

$$H = \frac{P_m}{A}, \tag{2}$$

where P_m is the peak (maximum) applied load and the projected contact area, A, is calculated as:

$$A(h_c) = 24.5\,h_c^2 + \alpha_1\,h_c + \alpha_{1/2}\,h_c^{1/2} + \cdots + \alpha_{1/16}\,h_c^{1/16}, \tag{3}$$

where

$$\alpha_1 = -1.2396 \times 10^4, \quad \alpha_{1/2} = 8.0499 \times 10^5, \quad \alpha_{1/4} = -7.2931 \times 10^6, \quad \alpha_{1/8} = 1.7166 \times 10^7, \quad \alpha_{1/16} = -1.068 \times 10^7 \tag{4}$$

and

$$h_c = h_m - \varepsilon\,\frac{P_m}{S_m} \tag{5}$$

where h_m is the total penetration displacement of the indenter at peak load, P_m, and ε is an indenter geometry constant, equal to 0.75 for a Berkovich indenter [30,31].

The NiO samples were tested as resistive hydrogen sensors in a home-built sensor setup, before and after Au deposition. During measurements, the samples were heated inside an aluminum chamber and their temperature was continuously recorded by a thermocouple. A flow of hydrogen, controlled by a flowmeter, was allowed in the chamber, which was filled with air at atmospheric pressure. The hydrogen concentration in air was calculated from the hydrogen partial pressure in the chamber, measured by an MKS Baratron gauge. In order to achieve low hydrogen concentrations, to the single ppm level, hydrogen was mixed with dry nitrogen in a premixing chamber, thus achieving dilution factors below 10^{-2}. With a constant bias voltage of 1 V, the current through the samples was recorded in real time by a Keithley 485 picoammeter. The sensor response, S, was calculated by:

$$S = \frac{R_g - R_0}{R_0}, \quad (6)$$

where R_g is the electric resistance of the sample in the presence of hydrogen and R_0 is the resistance of the sample in air.

3. Results and discussion

3.1. Structural properties

Fig. 1a shows X-ray diffractograms of an as-deposited NiO film and of NiO films annealed at 400, 500, and 600 °C after sputtering. The curves have been vertically shifted for clarity. We observe that the as-deposited film is amorphous, as it does not present any diffraction peaks, while annealing induces partial crystallization in the material. With increasing annealing temperature, the films become more and more crystalline, as indicated by the intensity of the XRD peaks. The amorphous phase is reduced as the annealing temperature increases, since more energy is supplied for crystallite growth, thus resulting in an improvement of the crystallinity of the films. There are three common peaks in the diffractograms of the annealed films, at $2\theta = 37.4°$, 43.3°, and 63°. Even though the cubic phase of NiO leads to diffraction planes at the same positions as the rhombohedral phase of NiO, making it difficult to distinguish between the two phases from XRD data, NiO films deposited with similar conditions to those employed in this work were found to be rhombohedral [34]. Therefore, we attribute the XRD peaks to crystallization of the films at the (1 0 1), (0 1 2), and (1 1 0) orientations of the rhombohedral phase, respectively. The average size of the NiO grains is estimated from the Scherrer equation at 15–20 nm. A weak peak at 56.1°, which appears only for the film annealed at 500 °C, is most probably created by the (3 1 1) plane of the silicon substrate [35], since there is no known XRD peak at 56.1° for either the cubic or the rhombohedral phase of NiO.

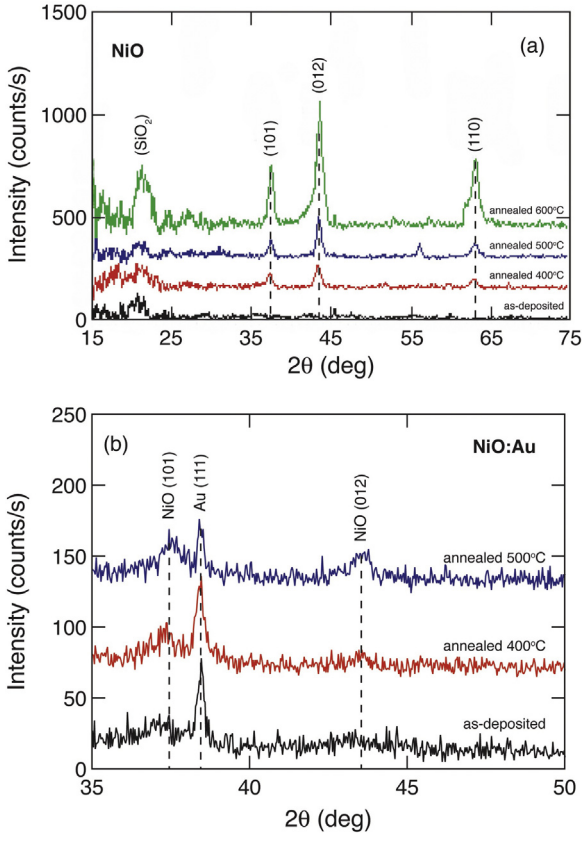

Fig. 1. X-ray diffractograms of (a) as-deposited and annealed (at 400, 500, and 600 °C) NiO films and (b) NiO films with Au nanoparticles.

Fig. 1b shows X-ray diffractograms of the NiO samples after the deposition of Au nanoparticles, where the curves have been again vertically shifted for clarity. The film annealed at 600 °C was not employed as a hydrogen sensor, therefore we did not deposit Au nanoparticles on this sample. The NiO peaks corresponding to the (1 0 1) and (0 1 2) orientations are still present and a new peak appears at $2\theta = 38.4°$, which represents the (1 1 1) plane of the cubic phase of Au. From the Scherrer equation we estimate the average size of Au nanoparticles to be 65–77 nm. Even though in Fig. 1a the (0 1 2) NiO orientation peak is more intense than the (1 0 1) orientation peak, the opposite is true after Au deposition for both films annealed at 400 °C and 500 °C, as we can see in Fig. 1b. Given the very small thickness of the NiO films, which is approximately 10 nm as we show below in Section 3.2, we attribute this effect to compressive stress induced by the deposition of Au, which creates a small change in the structural properties of the films.

3.2. Surface morphology and composition

Fig. 2a shows an SEM image of a NiO film, before Au deposition, in side view. From this image we measure the thickness of the film to be 10 nm. All NiO films employed in this work have the same thickness. Fig. 2b–d show SEM images of the as-deposited NiO film and films annealed at 400 and 500 °C, after Au deposition. From the XRD data, presented in Section 3.1, we estimate the average grain size of NiO to be 15–20 nm and the average size of Au particles at 65–77 nm. Even though it is not possible to resolve these features with the SEM magnification employed in Fig. 2b–d, these images provide a view of the surface morphology of the sensor films. The μm-size clusters that appear in Fig. 2b–d are probably particulates from the target material (Ni), which form on the surface of the NiO films during deposition, as it is often the case with sputtering.

Fig. 3 shows the EDS spectrum of the NiO film annealed at 400 °C, after Au deposition. We observe the presence of Ni and Au peaks, as well as the presence of a Si peak, originating from the substrate on which the NiO samples were deposited. Because the NiO films are only 10 nm thick, the magnitude of the Ni and Au peaks is much lower than the magnitude of the Si peak. Similar EDS spectra were recorded for the other NiO films after Au deposition.

3.3. Nanomechanical properties

Load–displacement curves, obtained by nanoindentation, are shown in Fig. 4 for the as-deposited NiO film, as well as for NiO films annealed at 400 and 500 °C. From these curves and Eqs. (1)–(5), the hardness, H, and elastic modulus, E, of the films are calculated and plotted in Fig. 5. These hardness and modulus values are not absolute values, since the films are so thin (~10 nm) that substrate effects can become important. However, based on

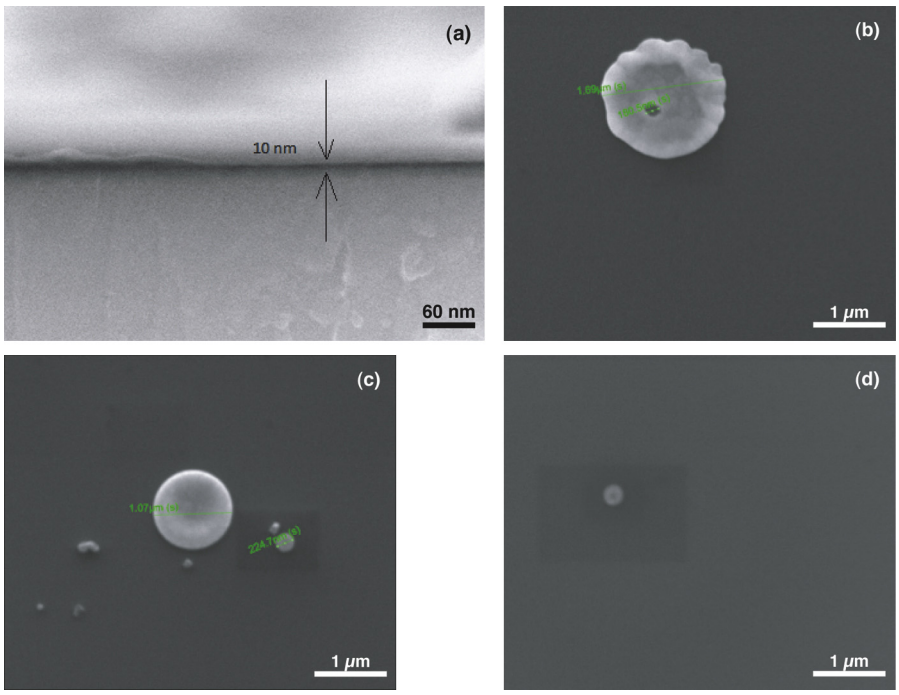

Fig. 2. SEM images of (a) a NiO film before Au deposition in side view, (b) as-deposited NiO, (c) NiO annealed at 400 °C, and (d) NiO annealed at 500 °C. (b)–(d) Images were obtained after Au deposition.

the fact that all parameters are kept identical for all three NiO films (e.g., indenter tip roundness, applied force protocol, substrate material, thickness) a direct comparison of the nanomechanical integrity of these thin film-substrate systems is possible. We observe the hardness of the NiO films decreases after annealing at 400 °C, while annealing at 500 °C induces the opposite effect. Also, the NiO film annealed at 400 °C shows increased elastic modulus, compared with the as-deposited and annealed at 500 °C samples. We note that even though the XRD data in Fig. 1 indicate gradual crystallization of the films upon annealing, they are not sufficient to predict the nanomechanical properties of the films. Indeed, from Fig. 1a we deduce a monotonic relation between annealing temperature and crystallinity, which does not follow for the hardness and elastic modulus. Therefore, nanoindentation provides complementary information for determining the optimum annealing temperature for thin-film sensors.

The resistance of the films to wear and their elasticity are determined by the ratios H/E and H^3/E^2, respectively, which are presented in Fig. 6. The ratio of hardness/elastic modulus, H/E, is of significant interest in tribology. High ratio of hardness to elastic modulus is indicative of good wear resistance in a disparate range of materials, such as ceramics, metals, and polymers [36]. As we can see in Fig. 6, the NiO film annealed at 500 °C shows enhanced resistance to wear, as indicated by H/E, as well as high elastic behavior under contact, as indicated by H^3/E^2. On the contrary, the NiO film annealed at 400 °C shows reduced resistance to wear and plastic behavior, compared with the as-deposited film. These results, combined with the results on hardness and elastic modulus, indicate that the nanomechanical properties of sputtered NiO films can be controlled by careful selection of the post-deposition annealing temperature.

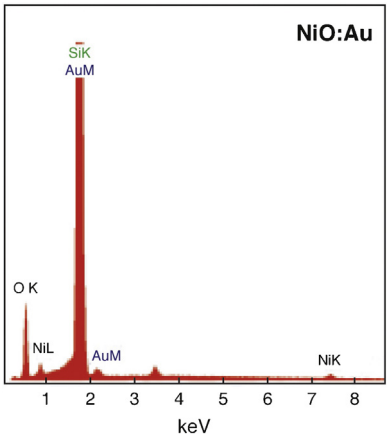

Fig. 3. EDS spectrum of the NiO film annealed at 400 °C, after Au deposition.

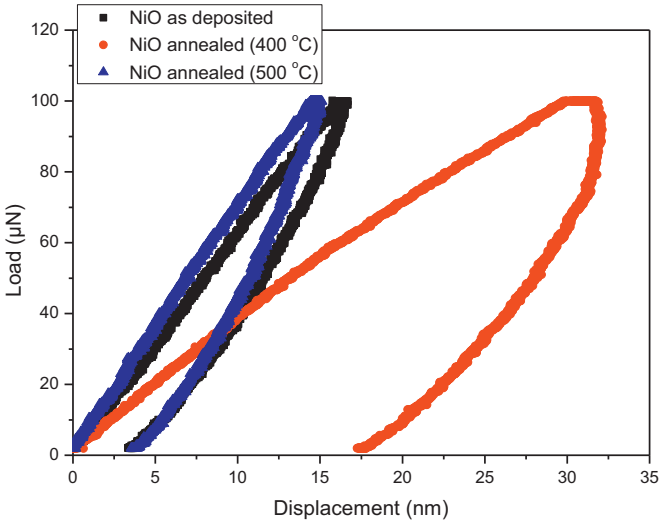

Fig. 4. Load–displacement curves for as-deposited NiO film and NiO films annealed at 400 and 500 °C.

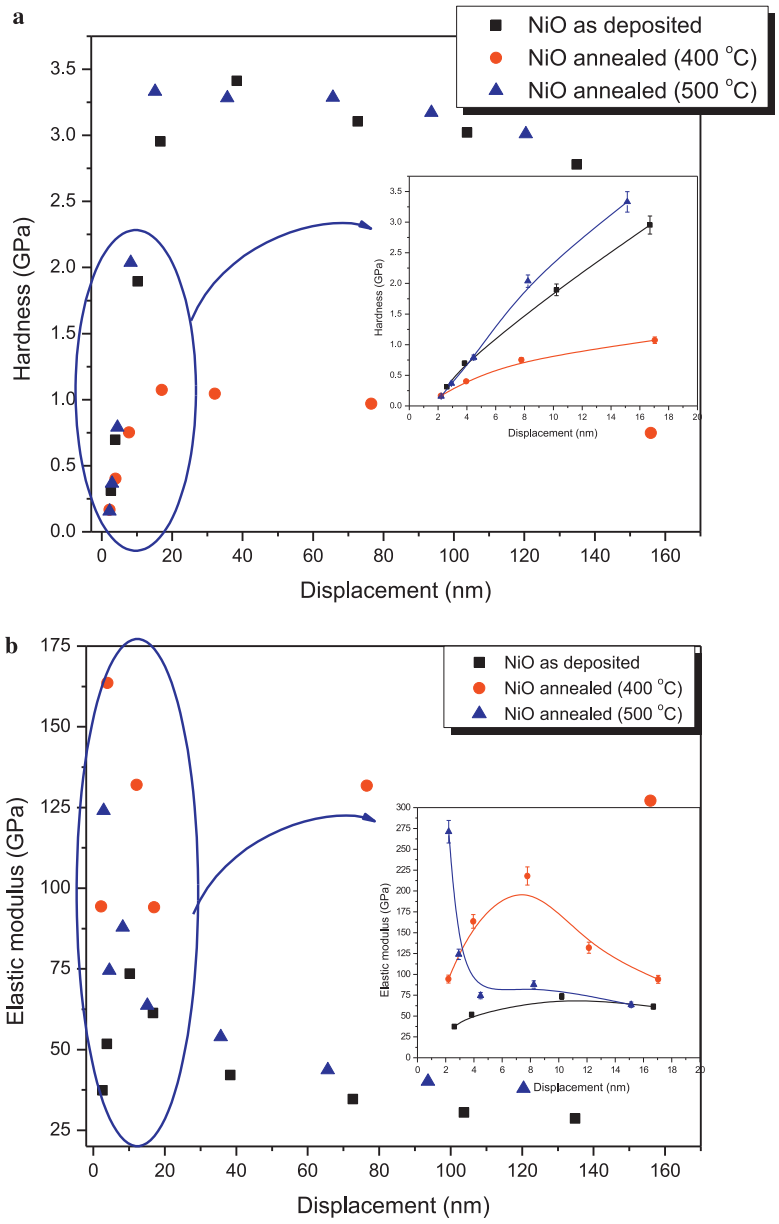

Fig. 5. (a) Hardness and (b) elastic modulus of the as-deposited NiO film and NiO films annealed at 400 and 500 °C, as a function of the displacement.

3.4. Hydrogen sensing

Fig. 7 shows response curves for hydrogen sensing in air for the NiO sample annealed at 400 °C, before and after deposition of Au nanoparticles. The response S is calculated according to Eq. (6). Because NiO is a p-type semiconductor, its electric resistance increases in the presence of hydrogen, which is a reducing gas [23,37]. This increase is due to the reaction of hydrogen with oxygen, which is adsorbed on the surface of NiO, and the subsequent release of H_2O vapor and free electrons, which recombine with the holes inside the material. Because the holes are the majority charge carriers in NiO, the reduction in the number of holes results in a resistance increase. Fig. 7a shows the response of the NiO sample to hydrogen before Au nanoparticle deposition on the surface, while Fig. 7b shows the response of the sample after Au deposition. Both curves were taken at 125 °C operating temperature, which is one of the lowest operating temperatures for NiO sensors reported in the literature. We observe that the deposition of Au nanoparticles allows for the detection of two orders of magnitude lower hydrogen concentrations compared to the pure NiO sample. Additionally, the response time of the sensor (defined as the time interval between 10% and 90% of the total signal change) decreased from ~15 min to ~5 min after Au deposition. Overall, the performance of the sensor is significantly improved by the presence of Au nanoparticles on the surface.

The NiO films were tested as hydrogen sensors for three different operating temperatures (125 °C, 130 °C, and 150 °C) and various hydrogen concentrations, before and after Au deposition. The results are summarized in Fig. 8, which shows the maximum response, S, for each temperature and hydrogen concentration combination for the NiO sample annealed at 400 °C. The response of the sensor increases with increasing operating temperature, because the adsorption–desorption kinetics, which affect the sensor performance, depend on the operating temperature [38,39]. For the same reason, higher operating temperature allows for the detection of lower hydrogen concentrations, as shown in Fig. 8a. On the other hand, it is

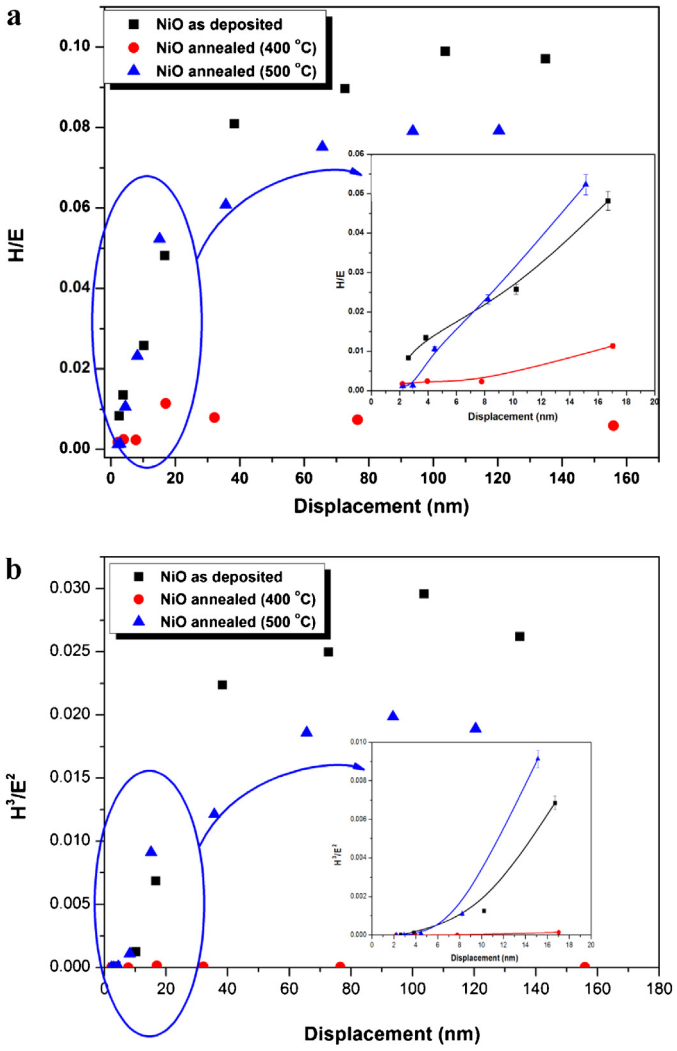

Fig. 6. Correlation of (a) H/E and (b) H^3/E^2 with displacement.

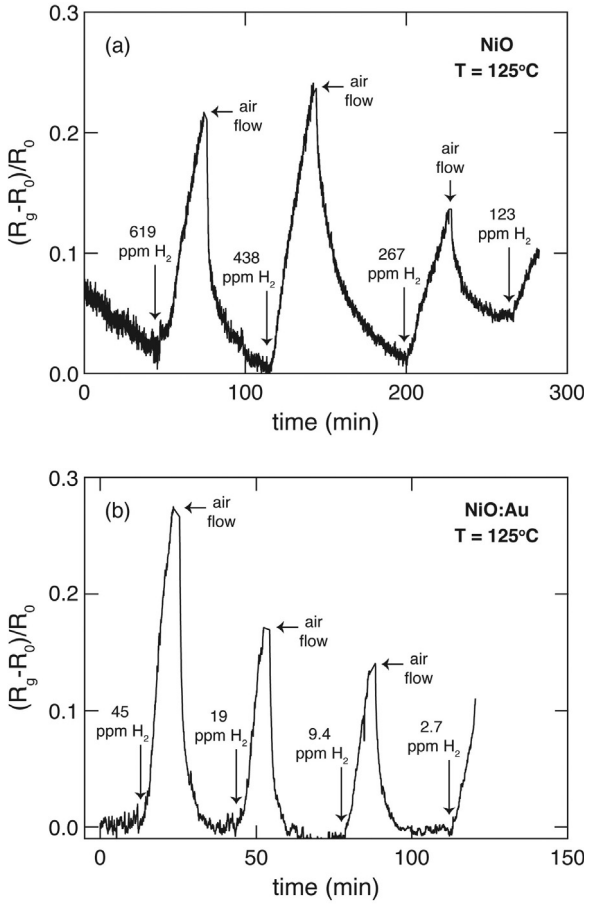

Fig. 7. Hydrogen sensing in air under dynamic flow conditions obtained with the NiO film annealed at 400 °C (a) before and (b) after Au deposition.

known that if the temperature is too high, the oxidation reaction of the analyte gas (here hydrogen) proceeds so rapidly before the gas reaches the sensor surface that the gas concentration seen by the sensor decreases significantly and the sensitivity of the sensor decreases as well [37,40]. Additionally, for high temperatures the desorption rate of hydrogen from the sensor surface becomes significant and competes with hydrogen sensing [25].

Clearly, in this work we are below the critical temperature for hydrogen and the response of the sensor improves with the temperature increase. Finding the optimum operating temperature for the detection of hydrogen is beyond the scope of this paper, which concentrates mainly on the development of highly efficient, low-power sensors. Comparing Fig. 8a and b we note that the deposition of Au nanoparticles on NiO improved the sensor performance for all temperatures. Table 1 lists the detection limit (lowest detectable hydrogen concentration) for each temperature with and without Au on the NiO surface. The presence of Au nanoparticles allowed for the detection of 1–2

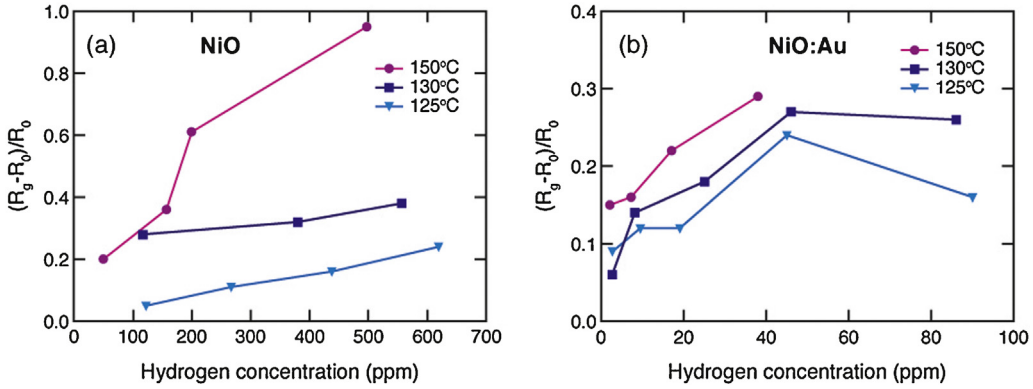

Fig. 8. Summary of sensing results for different operating temperatures and hydrogen concentrations in air, obtained (a) before and (b) after the deposition of Au nanoparticles on NiO annealed at 400 °C.

Table 1
Hydrogen detection limit achieved with NiO before and after Au deposition, for various operating temperatures.

Temperature (°C)	Detection limit (ppm)	
	Without Au	With Au
125	123	2.7
130	117	2.6
150	50	2

orders of magnitude lower hydrogen concentrations, pushing the sensor detection limit to the few-ppm level.

Au nanoparticles act as catalysts, lowering the energy barrier for dissociation of hydrogen and adsorbed oxygen molecules to atomic species in their vicinity [37,41]. Therefore, highly activated atomic hydrogen and oxygen is produced and interact with each other more efficiently, resulting in a detectable change in the electric resistance of NiO even for very low hydrogen concentrations. In the presence of Au nanoparticles, oxygen is not only adsorbed on the NiO surface but also on the surface of the nanoparticles. The interaction of these oxygen species with hydrogen produces additional free electrons in the nanoparticles, which exchange charge carriers with the NiO grains, in order to maintain neutrality. Therefore, additional free electrons are injected from the Au nanoparticles to NiO and contribute to the increase of the electric resistance of the material in the presence of hydrogen. As a result, the Au nanoparticles act not only as catalysts but also they increase the effective sensor area significantly. The combination of the above mechanisms leads to the observed orders of magnitude improvement of the sensor performance in the presence of Au nanoparticles.

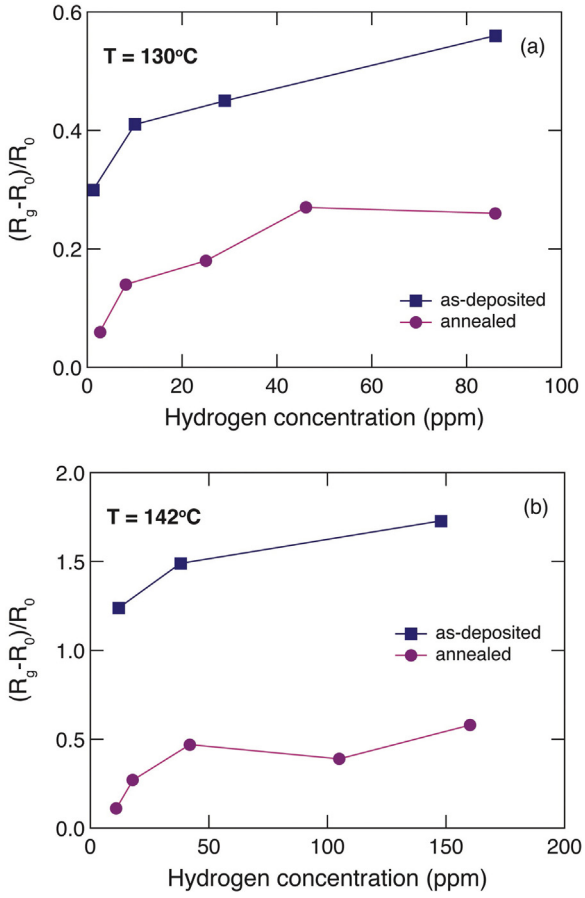

Fig. 9. Sensor response of as-deposited and annealed at 400 °C NiO films after Au deposition, at (a) 130 °C and (b) 142 °C operating temperatures.

The effect of post-deposition annealing on sensor performance was studied by comparing the response of the as-deposited NiO film with the film annealed at 400 °C. Au nanoparticles were deposited on both NiO films with identical conditions and the samples were subsequently tested as hydrogen sensors. The results are shown in Fig. 9 for two different operating temperatures. We observe that both samples were able to detect equally low hydrogen concentrations (down to a few ppm), however for both temperatures the as-deposited sample shows increased response compared to the annealed sample. The gas sensing performance of metal oxides depends on various parameters, including grain size, defects, and oxygen-adsorption properties. Annealing can induce an increase in grain size due to agglomeration, which reduces the porosity and active surface area of the film, deteriorating the sensing performance. Additionally, annealing affects the defect density of the sensing material. As mentioned in the introduction, NiO is a conductor due to the presence of lattice vacancies. During the sensing process, hydrogen interacts not only with the adsorbed oxygen on the surface of NiO, but also with the defect states of the film [39]. Annealing of the NiO samples improves their quality and decreases the defect density, therefore their performance as sensors declines. Similar effects have been observed in ZnO sensors, where sensitivity was found to be proportional to defect density [38,42] and annealing had a detrimental effect on sensitivity [39].

4. Conclusions

We have presented data on the performance of nanocomposite NiO:Au thin films as hydrogen sensors. NiO films were sputter-deposited on oxidized silicon substrates and Au nanoparticles were subsequently added on the NiO surface via pulsed laser deposition. The as-deposited NiO samples were amorphous and started crystallizing with post-deposition annealing. The Au nanoparticles were found to be crystalline directly after deposition. Depending on the annealing temperature, the hardness, resistance to wear, and elasticity of the films increased or decreased compared to the as-deposited samples. This indicates that the nanomechnical properties of the films, which are essential for their long-term stability and reliability, which in turn affect their potential for commercialization, can be controlled by post-deposition annealing. The performance of the NiO films as hydrogen sensors improved significantly in the presence of Au nanoparticles on the surface. The detection limit decreased by two orders of magnitude, while the response time also decreased by a factor of three. Hydrogen concentrations in air as low as 2 ppm were detected after Au deposition. These results were obtained for operating temperatures at the lower end of what is reported in the literature. In order to improve gas selectivity, it is also possible to operate these sensors at higher temperatures, optimized for hydrogen detection. Au nanoparticles act as catalysts and also increase the effective sensor area, resulting in significant improvement of the NiO sensing performance. Even though post-deposition annealing was found to improve the crystallinity of the NiO films, it proved detrimental for their sensing properties because it decreases the active surface area and/or the density of defects, which act as hydrogen absorption sites. NiO:Au nanocomposites are promising hydrogen sensor devices, satisfying the need for high sensitivity and low power consumption, which will allow them to ensure the safe and efficient processing of hydrogen on a massive scale.

Acknowledgement

We would like to thank Professor I. Hotovy for the preparation of NiO samples by DC sputtering and XRD measurements.

References

[1] T. Hubert, L. Boon-Brett, G. Black, U. Banach, Sens. Actuators B 157 (2011) 329–352.
[2] M. Kandyla, C. Pandis, S. Chatzandroulis, P. Pissis, I. Zergioti, Appl. Phys. A 110 (2013) 623–628.
[3] Y.-H. Choi, S.-H. Hong, Sens. Actuators B 125 (2007) 504–509.
[4] N. Al-Hardan, M.J. Abdullah, A.A. Aziz, Appl. Surf. Sci. 255 (2009) 7794–7797.
[5] A.Z. Sadek, J.G. Partridge, D.G. McCulloch, Y.X. Li, X.F. Yu, W. Wlodarski, et al. Thin Solid Films 518 (2009) 1294–1298.
[6] O. Lupan, G. Chai, L. Chow, Microelectron. J. 38 (2007) 1211–1216.
[7] L.L. Fields, J.P. Zheng, Y. Cheng, P. Xiong, Appl. Phys. Lett. 88 (2006) 263102.
[8] J.M. Baik, M.H. Kim, C. Larson, C.T. Yavuz, G.D. Stucky, A.M. Wodtke, et al. Nano Lett. 9 (2009) 3980–3984.
[9] A. Wei, L. Pan, W. Huang, Mater. Sci. Eng. B 176 (2011) 1409–1421.
[10] N. Singh, A. Ponzoni, R.K. Gupta, P.S. Lee, E. Comini, Sens. Actuators B 160 (2011) 1346–1351.
[11] Z. Wang, Z. Li, J. Sun, H. Zhang, W. Wang, W. Zheng, et al. J. Phys. Chem. C 114 (2010) 6100–6105.
[12] W. Wongwiriyapan, Y. Okabayashi, S. Minami, K. Itabashi, T. Ueda, R. Shimazaki, et al. Nanotechnology 22 (2011) 055501.
[13] L. Renard, H. Elhamzaoui, B. Jousseaume, T. Toupance, G. Laurent, F. Ribot, et al. Chem. Commun. 47 (2011) 1464–1466.
[14] W. Wu, Z. Liu, L.A. Jauregui, Q. Yu, R. Pillai, H. Cao, et al. Sens. Actuators B 150 (2010) 296–300.
[15] V.P. Tsikourkitoudi, E.P. Koumoulos, N. Papadopoulos, E. Hristoforou, C.A. Charitidis, J. Optoelectron. Adv. Mater. 14 (2012) 169–175.
[16] H. Kumagai, M. Matsumoto, K. Toyoda, M. Obara, J. Mater. Sci. Lett. 15 (1996) 1081–1083.
[17] Z. Jiao, M. Wu, Z. Qin, H. Xu, Nanotechnology 14 (2003) 458.
[18] X. Chen, N.J. Wu, L. Smith, A. Ignatiev, Appl. Phys. Lett. 84 (2004) 2700.
[19] D. Adler, J. Feinleib, Phys. Rev. B 2 (1970) 3112–3134.
[20] N. Barsan, C. Simion, T. Heine, S. Pokhrel, U. Weimar, J. Electroceram. 25 (2010) 11–19.
[21] H. Gu, Z. Wang, Y. Hu, Sensors 12 (2012) 5517–5550.
[22] H. Steinebach, S. Kannan, L. Rieth, F. Solzbacher, Sens. Actuators B 151 (2010) 162–168.
[23] I. Hotovy, J. Huran, P. Siciliano, S. Capone, L. Spiess, V. Rehacek, Sens. Actuators B 103 (2004) 300–311.
[24] E.D. Gaspera, M. Guglielmi, A. Martucci, L. Giancaterini, C. Cantalini, Sens. Actuators B 164 (2012) 54–63.
[25] A.M. Soleimanpour, Y. Hou, A.H. Jayatissa, Sens. Actuators B 182 (2013) 125–133.
[26] N.G. Cho, I.-S. Hwang, H.-G. Kim, J.-H. Lee, I.-D. Kim, Sens. Actuators B 155 (2011) 366–371.
[27] C.A. Charitidis, Int. J. Refract. Met. Hard Mater. 28 (2010) 51–70.
[28] G. Feng, A.H.W. Ngan, J. Mater. Res. 17 (2002) 660–668.
[29] H. Bei, E.P. George, J.L. Hay, G.M. Pharr, Phys. Rev. Lett. 95 (2005) 045501.
[30] M. Troyon, L. Huang, Surf. Coat. Technol. 201 (2006) 1613–1619.
[31] W.C. Oliver, G.M. Pharr, J. Mater. Res. 7 (1992) 1564–1583.
[32] I.N. Sneddon, Math. Proc. Camb. Philos. Soc. 44 (1948) 492–507.
[33] R.B. King, T.C. O'Sullivan, Int. J. Solids Struct. 23 (1987) 581–597.
[34] I. Hotovy, J. Huran, L. Spiess, J. Mater. Sci. 39 (2004) 2609–2612.
[35] G.B. Tong, S.A. Rahman, Solid State Sci. Technol. 12 (2004) 47–52.
[36] A. Leyland, A. Matthews, Surf. Coat. Technol. 177 (2004) 317–324.
[37] S.R. Morisson, Sens. Actuators 12 (1987) 425–440.
[38] M.-W. Ahn, K.-S. Park, J.-H. Heo, J.G. Park, D.W. Kim, K.J. Choi, et al. Appl. Phys. Lett. 93 (2008) 263103.
[39] O. Lupan, V.V. Ursaki, G. Chai, L. Chow, G.A. Emelchenko, I.M. Tiginyanu, et al. Sens. Actuators B 144 (2010) 56–66.
[40] N. Yamazoe, Y. Kurokawa, T. Seiyama, Sens. Actuators 4 (1983) 283–289.
[41] T. Korotcenkov, L.B. Gulina, B.K. Cho, S.H. Han, V.P. Tolstoy, Mater. Chem. Phys. 128 (2011) 433–441.
[42] L. Liao, H.B. Lu, J.C. Li, C. Liu, D.J. Fu, Y.L. Liu, Appl. Phys. Lett. 91 (2007) 173110.

Key Engineering Materials Vol. 495 (2012) pp 108-111
Online available since 2011/Nov/15 at www.scientific.net

doi:10.4028/www.scientific.net/KEM.495.108

Growth, Structural and Mechanical Characterization and Reliability of Chemical Vapor Deposited Co and Co_3O_4 Thin Films as Candidate Materials for Sensing Applications

Vasiliki P. Tsikourkitoudi[1, a], Elias P. Koumoulos[1, b], Nikolaos Papadopoulos[2,c], and Costas A. Charitidis[1, *d]

[1]National Technical University of Athens, School of Chemical Engineering, 9 Heroon Polytechniou Str., Zografos, Athens, Greece GR-157 80

[2]National Technical University of Athens, School of Mining Engineering and Metallurgy, 9 Heroon Polytechniou Str., Zografos, Athens, Greece GR-157 80

[a]vasiatsik@yahoo.gr, [b]elikoum@yahoo.gr, [c]nickpapss@yahoo.gr, *[d]charitidis@chemeng.ntua.gr

Keywords: Chemical Vapor Deposition, Co thin films, Co_3O_4 thin films, Nanoindentation, Nanomechanical Properties

Abstract. The adhesion and mechanical stability of thin film coatings on substrates is increasingly becoming a key issue in device reliability as magnetic and storage technology driven products demand smaller, thinner and more complex functional coatings. In the present study, chemical vapor deposited Co and Co_3O_4 thin films on SiO_2 and Si substrates are produced, respectively. Chemical vapor deposition is the most widely used deposition technique which produces thin films well adherent to the substrate. Co and Co_3O_4 thin films can be used in innovative applications such as magnetic sensors, data storage devices and protective layers. The produced thin films are characterized using nanoindentation technique and their nanomechanical properties (hardness and elastic modulus) are obtained. Finally, an evaluation of the reliability of each thin film (wear analysis) is performed using the hardness to elastic modulus ratio in correlation to the ratio of irreversible work to total work for a complete loading-unloading procedure.

Introduction

Experimental and theoretical studies of the properties of metal thin films on semiconductive surfaces have been stimulated by their fundamental and practical importance in the field of surface science, materials research and technology [1, 2]. In the recent years, the deposition of Co on Si substrates has attracted special interest, as Co thin films can be used in innovative magnetic devices in microelectronics, allowing their incorporation in Si technology and rendering them as candidate materials for sensing and data storage applications. Co_3O_4 thin films are also promising candidates due to useful properties, such as high catalytic activity at low cost [3], antiferromagnetism [4] and electrochromism [5] and have been considered for uses as magnetic detectors, counter electrodes, humidity or oxygen optical sensors [6], solar-selective absorbers and protective layers [7].

Chemical vapor deposition remains the most widely used deposition technique in many fields, especially for depositing thin films of electronic materials. It is capable of producing highly densed films with good adhesion to the substrate [8].

However, to our best knowledge, little research has been performed on the mechanical properties of Co and Co_3O_4 thin films for sensing applications. Thus, the mechanical characterization of Co and Co_3O_4 thin films is worth being studied and is prerequisite in order to be used as structural/functional elements in devices applications. The mechanical behavior of magnetic and storage devices is important in understanding reliability issues and concerns; mechanical and tribological aspects are of critical importance in determining long-term stability of such devices. Recently, nanoindentation has proven to be a powerful technique in providing information on mechanical properties (hardness, H, and elastic modulus, E) of thin films, based on analysis of load-displacement curves. Nanoindentation has attracted increasing interest, since allows a reliable characterization contrary to traditional methods i.e. micro hardness and tensile test [9].

Experimental

The films were grown in a vertical, cylindrical MOCVD stainless steel reactor, specifically developed for the deposition of magnetic films, either singled or multilayered. The reactor had computer controlled switching of gases for abrupt transients during deposition of multilayered structures. It also employed two independent precursor lines and four separate gas delivery lines for maintaining inert, (He or Ar), reductive (H_2) or oxidizing (O_2) atmosphere. Prior to reactor's entrance heat traced lines were used.

The Co films were deposited from a cobalt carbonyl precursor. The latter was introduced to the reactor as an aerosol mixture, formed by the dissolution of cobalt carbonyl into dichloromethane, 0.1 M concentrated. In a typical experiment a liquid (solution) flow of 7 g/h was mixed with a hydrogen gas flow of 0.05 l/min at 27 ^{O}C. The mixture (aerosol) was then introduced to the reactor, the temperature of which had been adjusted to 140 ^{O}C.

The nanoindentation tests in this work were performed using a nanomechanical test instrument, equipped with a Berkovich tip (120 nm tip radius) which allows the application of loads from 1 to 10000 μN. In all depth-sensing tests, a total of 10 indents were averaged to determine the mean *H* and *E* values for statistical purposes, with a spacing of 50 μm (~45% relative humidity, 23°C).

Results and Discussion

Magnetic properties. The magnetic responses of both Co_3O_4 and Co films under an externally applied magnetic field are presented in Fig 1. It was found that the easy axis of magnetization was the films' plane. The anisotropy field was found around 480 kA/m and 800 kA/m, respectively. Large anisotropy fields were recorded, especially for the Co films produced by $Co_2(CO)_8$. The coercive field along the hard axis magnetization was below the sensitivity limits of our magnetometer.

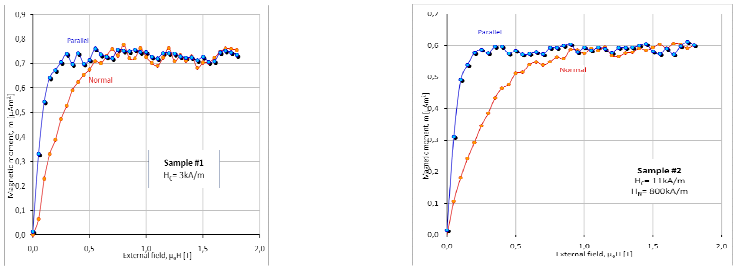

Fig. 1 Magnetic responses of both Co_3O_4 and Co films under an externally applied magnetic field

Nanomechanical Properties. At each imposed displacement, the true indentation *E* and the *H* can be deduced from the curves [10]. The graphs in Figs. 2a & 2b show the mean value of the *H* and *E* measurements as a function of the imposed displacement (the trend of the curvatures is similar for all samples). As the indentation displacement increases below 100 nm, a small increase of the *H* values is observed (Fig. 2a). This increase is probably a combination of either thin film nanomechanical properties, real effect of a native oxide at the surface and an artifact of the shape of the indenter tip for shallow displacements [9, 11-12]. As far as the *E* values are concerned (Fig. 2b), they are almost identical for both thin films.

a **b**

Fig. 2 Hardness (a) and Elastic modulus (b) values as a function of the displacement of the indenter.

The obtained results for H and E values are in good agreement with similar measurements presented in the literature, as presented in Table 1.

Table 1. Hardness and Elastic Modulus values of Co thin films as presented in the literature and this work.

***H* (GPa)**	***E* (GPa)**	**Displacement (nm)**	**Reference**
between 8 and 10	not mentioned	~150	[13]
4.25	85.15	-	[14]
8.65	54.97	150	this work

Hardness to Modulus Ratio – Wear Analysis. The total work created by the indenter (W_{tot}) which causes elastoplastic deformation at a maximum displacement and the work transferred by the sample to the indenter during unloading (W_u), have been examined. It was found that a remarkable correlation exists between the ratio of irreversible work to total work for a complete loading-unloading procedure, $(W_{tot}-W_u)/W_{tot}$, and the H/E^* term [15] is given below (Eq. 1):

$$\frac{H}{E^*} = \Pi_\theta \frac{(W_{tot} - W_u)}{W_{tot}}, \quad (1)$$

where $E^*=E/(1-\nu^2)$. The subscript, θ, denotes a possible dependence on indenter angle. Fig. 3 shows that for a given indenter angle, there is an approximate linear relationship between H/E^* and $(W_{tot}-W_u)/W_{tot}$. The Co_3O_4 thin film exhibits higher resistance to wear, compared with Co thin film. Nanoscratch testing of the samples revealed identical behaviour (Co_3O_4 thin film presented lower coefficient of friction). Thus, the material used in each application should be carefully chosen, depending on the demands of the application. Consequently, the value H/E^* may be obtained from the measurement of W_u and W_{tot}, which can be calculated from simple numerical integration based on load and displacement measurements.

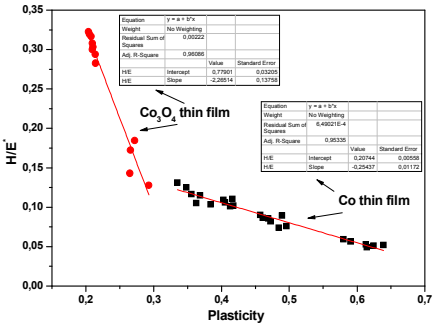

Fig. 3 Linear correlation of H/E^* and $(W_{tot}-W_u)/W_{tot}$ for both thin films.

The ratio H/E^* is of significant interest in tribology. This ratio multiplied by a geometric factor is the 'plasticity index' which describes the deformation properties of rough surfaces [16]. Furthermore, both H and E^* may be obtained using the above correlation together with a well-known relationship between E, contact area, and initial unloading slope [15, 17].

Conclusions

Chemical vapor deposited Co and Co_3O_4 thin films on SiO_2 and Si, respectively, are produced and characterized using nanoindentation technique. Co_3O_4 thin film exhibits higher resistance to applied load. In the case of Co, greater plasticity is revealed, i.e. energy stored at the material after indentation. The nanomechanical properties (H and E) for displacement 150 nm obtained (H=8.65 GPa & E=54.97 GPa,) are in good agreement with the literature. Finally, the wear analysis performed, using the H/E^* ratio in correlation to the $(W_{tot}-W_u)/W_{tot}$ term, revealed higher resistance to wear for Co_3O_4 thin film than Co thin film.

Acknowledgements

The authors wish to acknowledge NTUA funded project for basic research PEVE-NTUA-2010/65187900 for the support of this work.

References

[1] M.O. Aboelfotoh, A.D. Marwick and J.L. Freeouf: Phys. Rev. B.: Condens. Matter. Vol. 49 (1994), p. 10753; E. D. Gaspera, A. Martucci, and M. Post: Sens. Let. 9 (2011), p. 600

[2] A.E. Dolbak, B.Z. Olshanetsky and S.A. Teys: Surf. Sci. Vol. 373 (1997), p. 43; E. D. Gaspera, A. Martucci, M. Yaacob, J. Ou, K. Kalantar-Zadeh, and W. Wlodarski: Sens. Let. 9 (2011), p. 595

[3] M.J. Pollard, B.A. Weinstock, T.E. Bitterwolf, P.R. Griffiths, A.P. Newbery and J.B. Paine: J. Catal. Vol. 254 (2008), p. 218.

[4] Y. Ikedo, J. Sugiyama, H. Nozaki, H. Itahara, J.H. Brewer, E.J. Ansaldo, G.D. Morris, D. Andreica and A. Amato: Phys. Rev. B: Condens. Matter. Vol. 75 (2007), p. 054424.

[5] C.G. Granqvist: Handbook of Inorganic Electrochromic Materials (Elsevier, Amsterdam 1995).

[6] M. Ando, T. Kobayashi, S. Iijima and M.J. Haruta: Mater. Chem. Vol. 7 (1997), p. 1779.

[7] A.U. Mane, K. Shalini and S.A. Shivashankar: J. Phys. IV Vol. 11 (2001), p. Pr3-63.

[8] N.D. Papadopoulos, P.E. Tsakiridis and E. Hristoforou: J Optoelectron. Adv. M. Vol. 7 (2005), p. 2693.

[9] E.P. Koumoulos, C.A. Charitidis, N.M. Daniolos and D.I. Pantelis: Mater Sci Eng B (2011), in Press, Corrected Proof, doi:10.1016/j.mseb.2011.01.015.

[10] W.C. Oliver and G.M. Pharr: J. Mater. Res. Vol. 7 (1992). p. 1564.

[11] Y. Liu and A.H.W. Ngan: Scripta Mater. Vol. 44 (2001), p. 237.

[12] S. Lucas and J. Chevallier: Surf. Coat. Tech. Vol. 65 (1994), p. 128.

[13] S. Graça, R. Colaço and R. Vilar: Surf. Coat. Tech. Vol. 202 (2007), p. 538.

[14] Y.-T. Chen and S.R. Jian: J. Alloy Compd. Vol. 481 (2009), p. 365.

[15] Y.-T. Chen and C.-M. Cheng: Appl. Phys. Lett. Vol. 73 (1998), p. 614.

[16] J.A. Greenwood and J.B.P.Williamson: Proc. Roy. Soc. Lond.. Ser. A, Mathem. Phys. Sci. Vol. 295 (1966), p. 300.

[17] C.-M. Cheng and Y.-T. Chen: Appl. Phys. Lett. Vol. 71 (1997), p. 2623.

Materials and Applications for Sensors and Transducers
10.4028/www.scientific.net/KEM.495

Growth, Structural and Mechanical Characterization and Reliability of Chemical Vapor Deposited Co and Co₃O₄ Thin Films as Candidate Materials for Sensing Applications

10.4028/www.scientific.net/KEM.495.108

Growth, structural and mechanical characterization and reliability of chemical vapor deposited Co and Co_3O_4 thin films as candidate materials for sensing applications

V. P. TSIKOURKITOUDI, E. P. KOUMOULOS, N. PAPADOPOULOS[a], E. HRISTOFOROU[a], C. A. CHARITIDIS[*]
National Technical University of Athens, School of Chemical Engineering, 9 Heroon Polytechniou Str., Zografos, Athens, Greece GR-157 80
[a]*National Technical University of Athens, School of Mining Engineering and Metallurgy, 9 Heroon Polytechniou Str., Zografos, Athens, Greece GR-157 80*

The adhesion and mechanical stability of thin film coatings on substrates is increasingly becoming a key issue in device reliability as magnetic and storage technology driven products demand smaller, thinner and more complex functional coatings. In the present study, chemical vapor deposited Co and Co_3O_4 thin films on SiO_2 and Si substrates are produced, respectively. Chemical vapor deposition is the most widely used deposition technique which produces thin films well adherent to the substrate. Co and Co_3O_4 thin films can be used in innovative applications such as magnetic sensors, data storage devices and protective layers. The surface topography of the produced thin films is investigated with Atomic Force Microscopy and the mechanical behavior of them is evaluated. The produced thin films are also characterized using nanoindentation technique. Typical load-displacement curves are obtained and the local changes observed are explained. The nanomechanical properties (hardness and elastic modulus) of the thin films are obtained with Oliver & Pharr model. Finally, an evaluation of the reliability of each thin film (wear analysis) is performed using the hardness to elastic modulus ratio in correlation to the ratio of irreversible work to total work for a complete loading-unloading procedure.

(Received January 25, 2012; accepted February 20, 2012)

Keywords: Chemical Vapor Deposition, Co thin films, Co_3O_4 thin films, Nanoindentation, Nanomechanical Properties

1. Introduction

Experimental and theoretical studies of the properties of metal thin films on semiconductive surfaces have been stimulated by their fundamental and practical importance in the field of surface science, materials research and technology [1, 2]. In the recent years, the deposition of Co on Si substrates has attracted special interest, as Co thin films can be used in innovative magnetic devices in microelectronics, allowing their incorporation in Si technology and rendering them as candidate materials for sensing and data storage applications. Co_3O_4 thin films are also promising candidates due to useful properties, such as high catalytic activity at low cost [3], antiferromagnetism [4] and electrochromism [5] and have been considered for uses as magnetic detectors, counter electrodes, humidity or oxygen optical sensors [6], solar-selective absorbers and protective layers [7].

Chemical vapor deposition remains the most widely used deposition technique in many fields, especially for depositing thin films of electronic materials. It is capable of producing highly dense films with good adhesion to the substrate [8].

To our best knowledge, little research has been performed on the mechanical properties of Co and Co_3O_4 thin films for sensing applications. Thus, the mechanical characterization of Co and Co_3O_4 thin films is worth being studied and is prerequisite in order that the aforementioned thin films to be used as structural/functional elements in devices applications. The mechanical behavior of magnetic and storage devices is important in understanding reliability issues and concerns; mechanical and tribological aspects are of critical importance in determining long-term stability of such devices. Creep behavior is also another important issue which affects the reliability of the aforementioned devices [9]. Since many magnetic and sensing devices are often composed of multiple layers of thin films, the development of residual intrinsic stresses is possible during the microfabrication process. Such stresses are generated due to crystal dislocations, grain boundary interactions, excess vacancies or phase transformations and can provoke rupture and/or delamination of the thin film layer affecting the long-term stability and reliability of the aforementioned devices. For this reason, an appropriate control of intrinsic stresses is needed in order to ensure the commercialization and reliable operation of magnetic and sensing devices. Recently, nanoindentation has proven to be a powerful technique in providing information on mechanical properties (hardness, H, and elastic modulus, E) of thin films, based on analysis of load-displacement curves. Nanoindentation has attracted increasing interest, since allows a reliable characterization contrary to traditional methods i.e. micro hardness and

tensile test [10]. The shape of the load-displacement curves differ from one material to another and these differences usually indicate different mechanical properties. Significant interest has been shown on possible local changes, such as discontinuities and perturbations, observed on the load-displacement curves, as they may be a signal of physical events beneath the indenter, characterized by absorb or release of energy [11]. Such local changes may indicate the aforementioned causes of the generation of intrinsic stresses.

In the present research study, the surface topography of chemical vapor deposited Co and Co_3O_4 thin films is investigated through Atomic Force Microscopy (AFM) analysis and their magnetic behavior is evaluated. Furthermore, the nanomechanical properties of the aforementioned thin films are obtained through nanoindentation technique. An analysis of the local changes observed on the load-displacement curves of Co and Co_3O_4 thin films is also among the scopes of the present study. Finally, an analysis based on the H/E^* ratio is performed in order to estimate the wear resistance of the thin films.

2. Experimental

The films were grown in a vertical, cylindrical MOCVD stainless steel reactor [12], specifically developed for the deposition of magnetic films, either singled or multilayered. The reactor had computer controlled switching of gases for abrupt transients during deposition of multilayered structures. It also employed two independent precursor lines and four separate gas delivery lines for maintaining inert, (He or Ar), reductive (H_2) or oxidizing (O_2) atmosphere. Prior to reactor's entrance heat traced lines were used.

The substrates were positioned onto a stainless steel block, with three 4' recessed pockets. The three zone resistance heating was controlled by Ch-Al thermocouples embedded at the block's bottom surface with PID controllers. Two rotary vane pumps in-line connected were used for reactor's evacuation down to a base pressure of 10^{-4} mbar and process pumping accurately controlled by a manual throttle valve.

Silicon and blanket silicon dioxide were used as substrates. These were ex situ cleaned by a 30-sec Piranha etch solution, and then by a subsequent acetone and methanol rinse. Finally, they were washed with double-distilled water followed by drying in a high purity Ar atmosphere. In the case of the silicon substrates an additional first step was employed. These were dipped for 1 min in a 10% solution of HF acid and were immediately rinsed by double-distilled water.

The Co films were deposited from a cobalt carbonyl precursor. The latter was introduced to the reactor as an aerosol mixture, formed by the dissolution of cobalt carbonyl into dichloromethane, 0.1 M concentrated. In a typical experiment a liquid (solution) flow of 7 g/h was mixed with a hydrogen gas flow of 0.05 l/min at 27 ^oC. The mixture (aerosol) was then introduced to the reactor, the temperature of which had been adjusted to 140 ^oC.

In a typical experiment of Co_3O_4 deposition [13] the substrates were loaded and the reactor was purged with an argon flow of 0.75 l/h, while the susceptor was heated to the desired temperature (450 ^oC). Then a solid inclusion complex (placed in a specialized glass reservoir) of β-cyclodextrin with CoI_2 was sublimed at 115 ^oC [14], and the vapors were introduced into the reactor with the aid of a constant O_2 flow of 50 ml/min.

The thickness of the produced films is 150 nm.

AFM was used to provide additional information regarding films' surface topography and geometrical complexity. Imaging of the surface morphology was performed using a 'Quesant – Qscope 250'. The AFM was equipped with a 40 μm Dual PZT scanner. High-resolution images were obtained at different areas at the maximum scanning rate of 6 Hz and with 600 X 600 pixels resolution. All AFM images were acquired in ambient conditions at the intermittent contact mode. The scanned surfaces were also characterized by the surface roughness histograms. The magnetic response data were obtained by vibrating sample magnetometry with the aid of a VSM 155 Princeton Applied Research (2T). An external magnetic field was applied either parallel or normal to the film's surface.

The nanoindentation tests in this work were performed using a nanomechanical test instrument, equipped with a Berkovich tip (120 nm tip radius) which allows the application of loads from 1 to 10000 μN. The instrument is capable of recording penetration displacements as a function of applied loads with a high load resolution (1 nN) and a high displacement resolution (0.04 nm). The above instrument is equipped with a Scanning Probe Microscope (SPM), in which the sharp probe tip moves in a raster scan pattern across a sample surface using a three-axis piezo positioner. In all depth-sensing tests, a total of 10 indents were averaged to determine the mean H and E values for statistical purposes, with a spacing of 50 μm (~45% relative humidity, 23°C). Prior to indentation, the area function of the indenter tip was calibrated in a fused silica, a standard material for this purpose.

3. Results and discussion

Surface Topography. The Co_3O_4 films were uniformly grain distributed with, however enlarged grains (Fig. 1a), probably due to high deposition temperature. As was proved by histogram analysis (Fig. 1b) the mean surface roughness (RMS) deviation of the films deposited at 450 ^oC was of the order of 5.5 nm, with the mean height being around 17.5 nm. On the contrary, the Co films originating from $Co_2(CO)_8$ presented an extremely smooth surface (Fig. 2a) with a mean surface roughness around 2 nm and an average height of about 12.5 nm, as was revealed by histogram analysis (Fig. 2b).

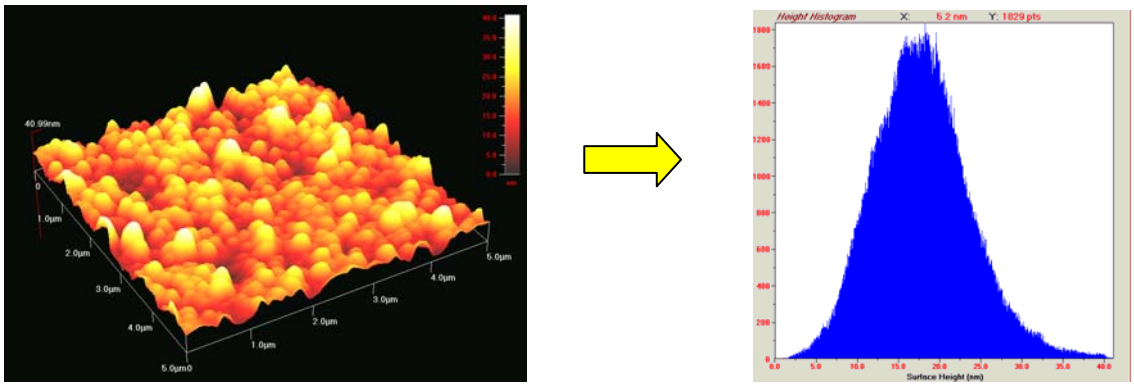

a b

Fig. 1. AFM (a) and histogram analysis (b) of Co_3O_4 thin films, respectively.

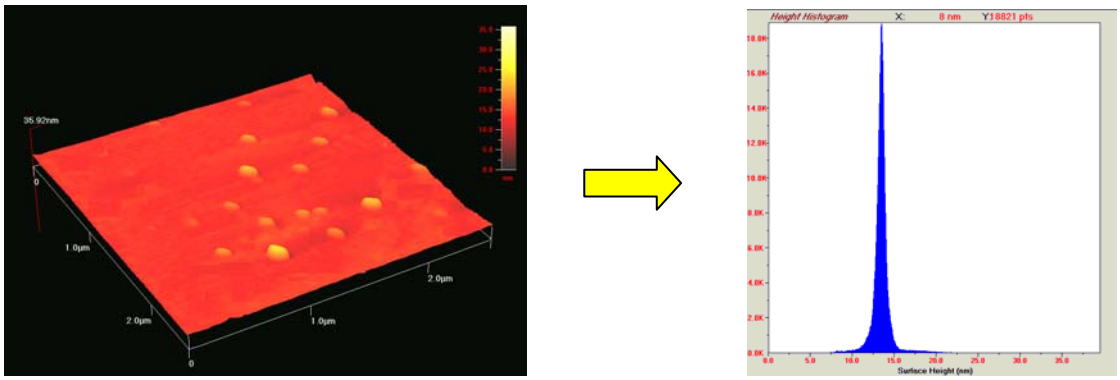

a b

Fig. 2. AFM (a) and histogram analysis (b) of Co thin films, respectively.

Magnetic properties. The magnetic responses of both Co_3O_4 and Co films under an externally applied magnetic field are presented in Fig. 3 (a-b). It was found that the easy axis of magnetization was the films' plane. The anisotropy field was found around 480 kA/m and 800 kA/m, respectively. Large anisotropy fields were recorded, especially for the Co films produced by $Co_2(CO)_8$. The coercive field along the hard axis magnetization was below the sensitivity limits of our magnetometer.

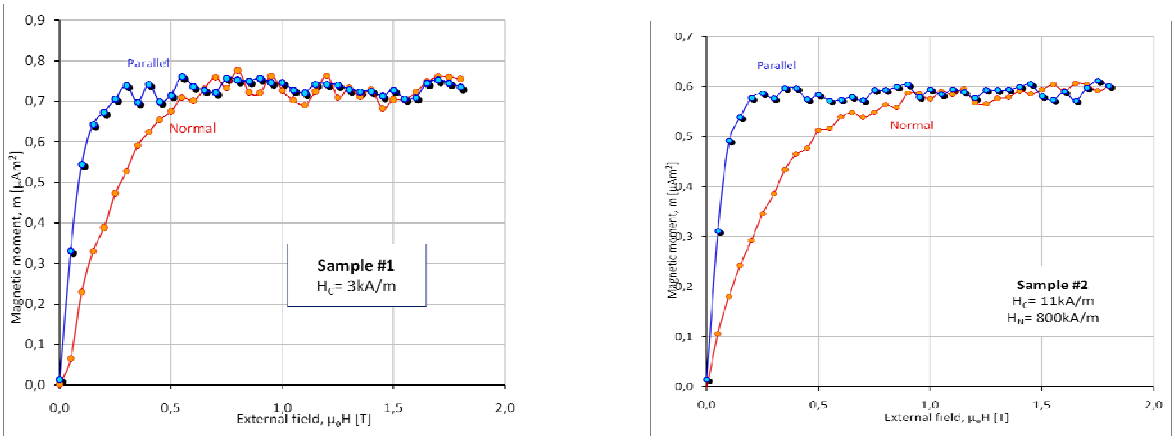

a b

Fig. 3. Magnetic responses of Co_3O_4 (a) and Co (b) thin films, respectively.

Load-displacement Curves. The loading-unloading curves of the probed materials are presented in Fig. 4 (a-b) (comparison for applied loads of 500 and 1000 μN). Co_3O_4 thin film exhibits higher resistance to applied load, i.e. higher applied load values are needed in order to reach the same displacement (higher values of hardness). In the case of Co, greater plasticity is revealed, i.e. energy stored at the material after the indentation is over (total integration of curve area).

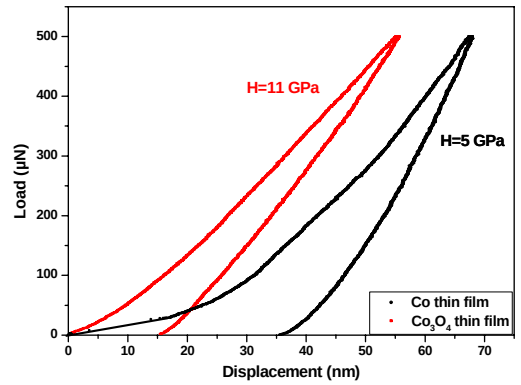

a

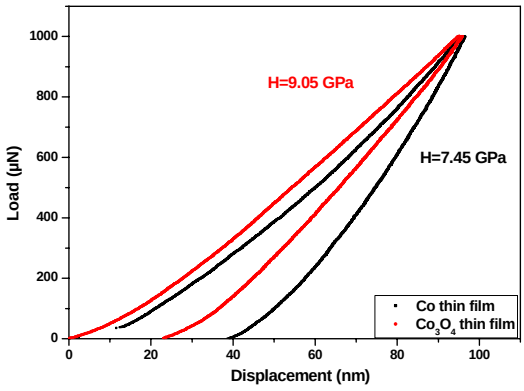

b

Fig. 4. Loading-unloading curves of Co and Co_3O_4 thin films (applied loads 500(a) & 1000(b) μN).

In Fig. 5 (a-b), typical load-displacement curves of Co and Co_3O_4 thin films are presented showing local changes (discontinuities), i.e. changes in the slope, referred as pop-ins and elbows in the loading and in the unloading curve, respectively. During the pop-in, the indenter tip penetrates in the sample without an increase in the applied load. The first pop-in in each sample reveals the onset of plasticity, i.e. the first point at which plastic yield occurs. The onset of plasticity occurs at ~10 nm for each thin film. In this stage, the nanoindenter can be approximated as spherical and the experimental data deviate from the fully elastic curve. For lower loads than the load where the onset of plasticity occurs, reversibility of the indentations performed is observed. The pop-ins indicate a redistribution of material around the indentation site (activity of atoms beneath the indenter). This is observed when a dislocation source is activated (first pop-in), is moving and multiplying (for pop-ins observed at higher loads) [11]. Several studies [15] propose that phase transformation and formation of cracks at the interface between the thin film and the interface may also contribute to pop-ins. As it is obvious from the representative load-displacement curves presented in Fig. 5(a-b), a large number pop-ins appear during nanoindentation of Co thin film.

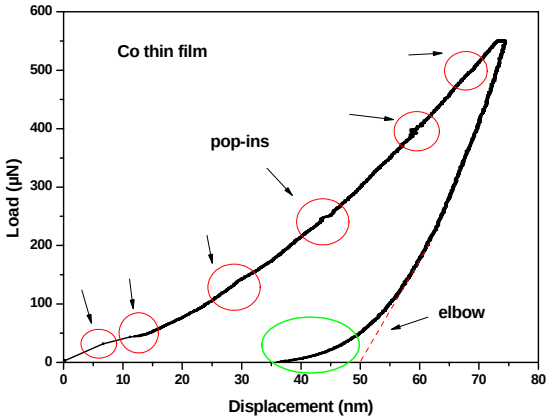

a

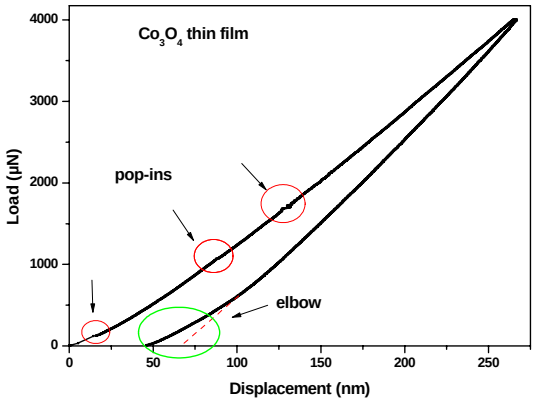

b

Fig. 5. Typical load-displacement curves of Co (a) and Co_3O_4 (b) thin films showing pop-ins and elbow.

Apart from the pop-ins in the loading curve, a change in slope ("elbow") is also observed in the unloading curves of Fig. 5 (a-b) (green circles). This linear unloading observed as an elbow may indicate the buckling of the thin film in order that the exerted compressive load is relieved. For this reason, the buckled material may rise and push back on the indenter [16]. The elbow can also be associated with phase transformations [17].

Nanomechanical Properties. At each imposed displacement, the true indentation E and the H can be deduced from the curves using the Oliver & Pharr model (*O&P*) [18], which calculates the contact area between the indenter tip and the sample using the tangent of the upper

part (30%) of the unloading curve, which is considered to be linear, along with the known area function. In *O&P* model, the derived expressions for calculating the elastic modulus from indentation experiments are based on Sneddon's elastic contact theory [19] (Equation 1):

$$E_r = \frac{S\sqrt{\pi}}{2\beta\sqrt{A_c}} \quad (1)$$

where S is the unloading stiffness (initial slope of the unloading load-displacement curve at the maximum displacement), A_c is the projected contact area between the tip and the substrate and β is a constant that depends on the geometry of the indenter (β =1.167 for Berkovich tip). Conventional nanoindentation hardness refers to the mean contact pressure, which depends on the geometry of the indenter (Eq. 2):

$$H_c = \frac{F}{A} \quad (2)$$

The graphs in Figs.6a & 6b show the mean value of the H and E measurements as a function of the imposed displacement (the trend of the curvatures is similar for all samples). As the indentation displacement increases below 100 nm, a small increase of the H values is observed (Fig. 6a). This increase is probably a combination of either thin film nanomechanical properties, real effect of a native oxide at the surface and an artifact of the shape of the indenter tip for shallow displacements [10, 20-21]. As far as the E values are concerned (Fig. 6b), they are similar for the two thin films. The obtained results for H and E values are in good agreement with similar measurements presented in the literature, as presented in Table 1.

Table 1. Hardness and Elastic Modulus values of Co thin films as presented in the literature and this work..

***H* (GPa)**	***E* (GPa)**	**Displacement (nm)**	**Reference**
between 8 and 10	not mentioned	~150	[22]
4.25	85.15	-	[23]
8.65	54.97	150	this work

Instant hardness analysis. According to contact mechanics, the instant hardness (measured at maximum displacement) during loading can be calculated as a function of the displacement or load. As shown in Figure 7, Co_3O_4 thin film exhibits enhanced resistance (with almost twice the hardness in 40 nm of displacement, arrow-noted) to deformation (instant hardness) compared to Co thin film, for identical loading rate. It is reported that the instant hardness changes over a wide range of the indentation loads tested [24]. Considering that hardness is defined as the material's resistance to plastic deformation loaded by an indenter, it is determined by the average contact pressure when the material responds plastically. When the material exhibits plastic hardening behavior, the contact pressure will change with the indentation applied load [25]. After the transition from elastic to plastic deformation, no hardening is shown in Fig. 7, revealing that H remains unchanged (also shown in Fig. 6)

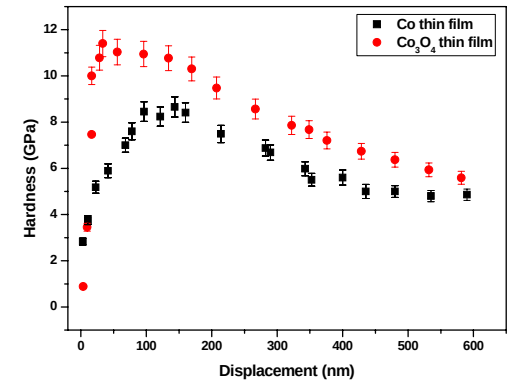

a

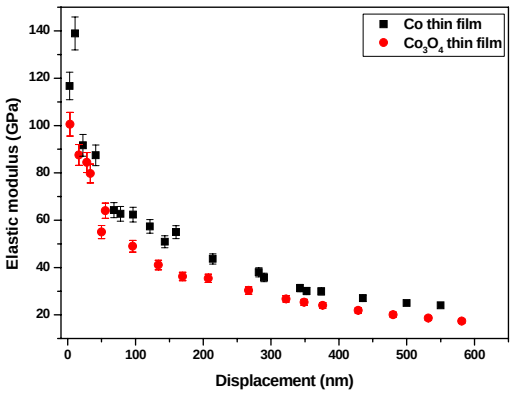

b

Fig. 6. Hardness (a) and elastic modulus (b) values as a function of the displacement of the indenter.

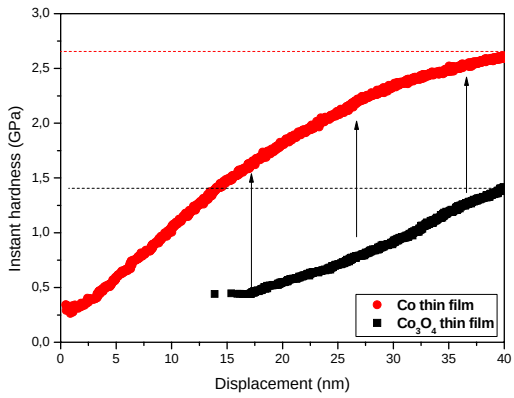

Fig.7. The instant hardness as a function of displacement both Co_3O_4 and Co thin films (extracted from Fig.4a).

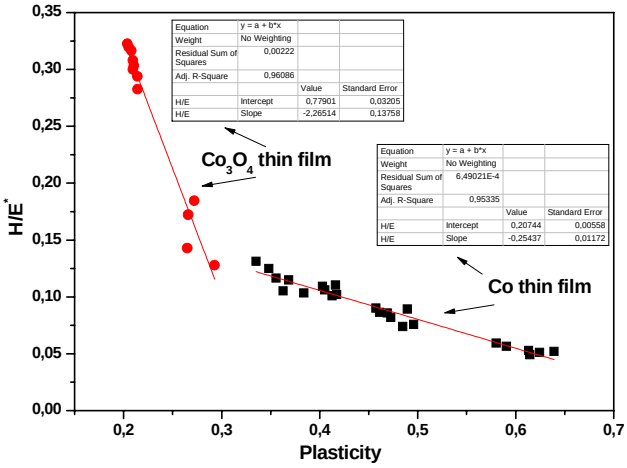

Fig. 8. Linear correlation of H/E and $(W_{tot}-W_u)/W_{tot}$ for both Co_3O_4 and Co thin films.*

Hardness to Modulus Ratio–Wear Analysis. The total work created by the indenter (W_{tot}) which causes elastoplastic deformation at a maximum displacement and the work transferred by the sample to the indenter during unloading (W_u), have been examined. It was found that a remarkable correlation exists between the ratio of irreversible work to total work for a complete loading-unloading procedure, $(W_{tot}-W_u)/W_{tot}$, and the H/E^* term [25] is given below (Eq. 3):

$$\frac{H}{E^*} = \Pi_\theta \frac{\left(W_{tot} - W_u\right)}{W_{tot}}, \qquad (3)$$

where $E^*=E/(1-\nu^2)$. The subscript, θ, denotes a possible dependence on indenter angle. Fig. 8 shows that for a given indenter angle, there is an approximate linear relationship between H/E^* and $(W_{tot}-W_u)/W_{tot}$. The Co_3O_4 thin film exhibits higher resistance to wear, compared with Co thin film. Nanoscratch testing of the samples revealed identical behaviour (Co_3O_4 thin film presented lower coefficient of friction). Thus, the material used in each application should be carefully chosen, depending on the demands of the application. Consequently, the value H/E^* may be obtained from the measurement of W_u and W_{tot}, which can be calculated from simple numerical integration based on load and displacement measurements.

The H/E^* ratio is of significant interest in tribology. This ratio multiplied by a geometric factor is the 'plasticity index' which describes the deformation properties of rough surfaces [26]. The correlation provides an alternative method for measuring H/E^* on micro- and nano- scale for both metals and ceramics. Furthermore, both H and E^* may be obtained using the above correlation together with a well-known relationship between E, contact area, and initial unloading slope [25, 27].

4. Conclusions

Chemical vapor deposited Co and Co_3O_4 thin films on SiO_2 and Si, respectively, were produced and characterized. The AFM analysis revealed that the Co_3O_4 films are uniformly grain distributed with enlarged grains (mean roughness ~17.5 nm), whereas the Co films originating from $Co_2(CO)_8$ presented an extremely smooth surface (mean surface roughness ~2 nm). As far as the magnetic responses of both Co_3O_4 and Co films under an externally applied magnetic field, it was found that the easy axis of magnetization was the films' plane. The anisotropy field was found around 480 kA/m and 800 kA/m, respectively. The load-displacement curves obtained from the nanoindentation technique showed that the Co_3O_4 thin film exhibited higher resistance to applied load (i.e. higher applied load values are needed in order to reach the same displacement. In the case of Co, greater plasticity was revealed, i.e. energy stored at the material after the indentation was over. An investigation of the local changes presented on the load-displacement curves was performed, revealing that the onset of plasticity for both thin films was at ~10 nm. Furthermore, it was found that the Co_3O_4 thin film was more resistant and stable under the exertion of load. The nanomechanical properties (H and E) for displacement 150 nm (H=8.65 GPa & E=54.97 GPa,) were found to be in good agreement with the literature. Finally, a wear analysis was performed using the H/E^* ratio in correlation to the $(W_{tot}-W_u)/W_{tot}$ term. The Co_3O_4 thin film exhibited higher resistance to wear, compared with Co thin film. Thus, depending on the demands of the application, the material used should be carefully chosen.

Acknowledgements

The authors wish to acknowledge NTUA funded project for basic research PEVE-NTUA-2010/65187900 and Alexandros S. Onassis Public Benefit Foundation for the support of this work.

References

[1] M.O. Aboelfotoh, A.D. Marwick, J.L. Freeouf, Phys. Rev. B., Condens. Matter. **49**, 10753 (1994)
[2] A.E. Dolbak, B.Z. Olshanetsky, S.A. Teys, Surf. Sci. **373**, 43 (1997),
[3] M.J. Pollard, B.A. Weinstock, T.E. Bitterwolf, P.R. Griffiths, A.P. Newbery and J.B. Paine, J. Catal. **254**, 218 (2008).
[4] Y. Ikedo, J. Sugiyama, H. Nozaki, H. Itahara, J.H. Brewer, E.J. Ansaldo, G.D. Morris, D. Andreica A. Amato, Phys. Rev. B: Condens. Matter. **75**, 054424 (2007).
[5] C. G. Granqvist, Handbook of Inorganic Electrochromic Materials (Elsevier, Amsterdam 1995).

[6] M. Ando, T. Kobayashi, S. Iijima and M.J. Haruta, Mater. Chem. **7**, 1779 (1997).
[7] A.U. Mane, K. Shalini and S.A. Shivashankar, J. Phys. IV, **11**, Pr3-63 (2001).
[8] N.D. Papadopoulos, P.E. Tsakiridis, E. Hristoforou, J. Optoelectron. Adv. Mater. **7**, 2693 (2005).
[9] R. Vladoiu, C.P .Lungu, I. Mustata, V. Bursikova, J. Bursik, J. Optoelectron. Adv. Mater. **9**, 1087 (2007)
[10] E.P. Koumoulos, C.A. Charitidis, N.M. Daniolos, D.I. Pantelis, Mater Sci Eng B **176**, 1585 (2011).
[11] C.A. Schuh, Materials Today **9**, 32 (2006).
[12] N.D. Papadopoulos, H.S. Karayianni, P.E. Tsakiridis, E. Sarantopoulou and E. Hristoforou, Chem. Vap. Deposition (2011), In Press.
[13] N.D. Papadopoulos, H.S. Karayianni, P.E. Tsakiridis, M. Perraki, E. Sarantopoulou and E. Hristoforou, J. Electrochem. Soc. **158**, 5 (2011); N.D. Papadopoulos, E. Illekova, H.S. Karayanni, E. Hristoforou, J. Optoelectron. Adv. Mater. **10,** 1098 (2008).
[14] N.D. Papadopoulos, H.S. Karayianni, P.E. Tsakiridis, M. Perraki, E. Hristoforou, Appl. Organomet. Chem. **24,** 112 (2010).
[15] T.H. Fang, W.J. Chang, C.M. Lin, Microelectron. Eng. **77,** 389 (2005).
[16] S.J. Bull, J. Phys. D: Appl. Phys. **38**, R393 (2005).
[17] V. Domnich, Y. Gogotsi, Rev. Adv. Mater. Sci. **3**, 1 (2002).
[18] W.C. Oliver, G.M. Pharr, J. Mater. Res. **7**, 1564 (1992); J. Menčik, L. Beneš, J. Optoelectron. Adv. Mater. **10**, 3288 (2008).
[19] I.N. Sneddon, Proc. Cambridge Phil. Soc. **44**, 492 (1948).
[20] Y. Liu, A.H.W. Ngan, Scripta Mater. **44**, 237 (2001).
[21] S. Lucas, J. Chevallier, Surf. Coat. Tech. **65**, 128 (1994).
[22] S. Graça, R. Colaço, R. Vilar, Surf. Coat. Tech. **202**, 538 (2007).
[23] Y.-T. Chen, S.R. Jian, J. Alloy Compd. **481**, 365 (2009).
[24] L. Chang and L. Zhang, Mat. Sci. Eng. A, **506**, 125 (2009).
[25] Y.-T. Chen, C.-M. Cheng, Appl. Phys. Lett. **73**, 614 (1998).
[26] J.A. Greenwood, J.B.P. Williamson, Proc. Roy. Soc. Lond., Ser. A, Mathem. Phys. Sci. **295**, 300 (1966).
[27] C.-M. Cheng, Y.-T. Chen, Appl. Phys. Lett. **71**, 2623 (1997).

*Corresponding author: charitidis@chemeng.ntua.gr

ppap.201500023C

Full Paper

O_2 plasma deep reactive ion etching with simultaneous nanotexturing of Cyclo olefin polymer (COP) in a high-density plasma reactor is performed. COP surfaces are coated with thin hydrophobic films to form surfaces of enhanced hydrophobicity and superhydrophobicity. To determine the effect of the plasma treatment on surface mechanical behavior and the adhesion of coatings onto nanotextured substrates, nanoindentation and nanoscratch are performed.

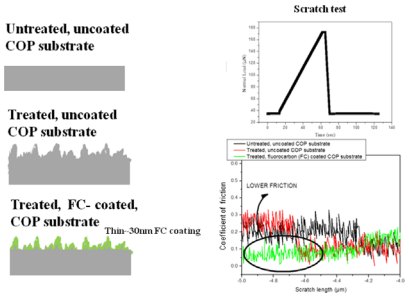

Nanoscale Mechanical and Tribological Properties of Plasma Nanotextured COP Surfaces with Hydrophobic Coatings

D. A. Dragatogiannis, E. Koumoulos, K. Ellinas, A. Tserepi, E. Gogolides, C. A. Charitidis*

Plasma Process. Polym. **2015,** *12,* 000–000

Early View Publication; these are NOT the final page numbers, use DOI for citation !!

ppap.201500023

Nanoscale Mechanical and Tribological Properties of Plasma Nanotextured COP Surfaces with Hydrophobic Coatings

Dimitrios A. Dragatogiannis, Elias Koumoulos, Kosmas Ellinas, Angeliki Tserepi, E. Gogolides, Costas A. Charitidis*

Cyclo olefin polymer (COP) surfaces, treated in oxygen plasmas under highly anisotropic conditions to favor roughness formation, are coated with thin hydrophobic films to form surfaces of enhanced hydrophobicity and superhydrophobicity. As hydrophobic coatings, plasma-deposited fluorocarbon (FC) thin films or spin-coated TEFLON AF1600 films are implemented. In this work, nanoindentation and nanoscratch experiments have been employed to elucidate the effect of plasma treatment on the mechanical behavior and tribological performance of the synthesized materials, taking into account viscoelastic effects. The data are evaluated to assess the wear behavior of such surfaces as a first guide to their practical applications. It is shown that short-time plasma treatment (<4 min) slightly changes mechanical, tribological, and wear properties of plasma-nanotextured COP, as compared to untreated COP. The nanoscratch experiments performed provide insight into the tribological properties of coated and uncoated, treated and untreated COP, in terms of coefficient of friction, applied normal load, and penetration depth. The difference between the normal displacement during scratch and post-scratch corresponds to the elastic recovery of the materials, being an index of the adhesion strength of the thin hydrophobic films on the COP substrate. The plasma deposited thin hydrophobic layer on the polymeric surfaces (untreated and treated) presents good adhesion, while the mechanical properties are greatly influenced by the substrate; it is also found that it effectively protects the polymeric surfaces, reducing plastic deformation.

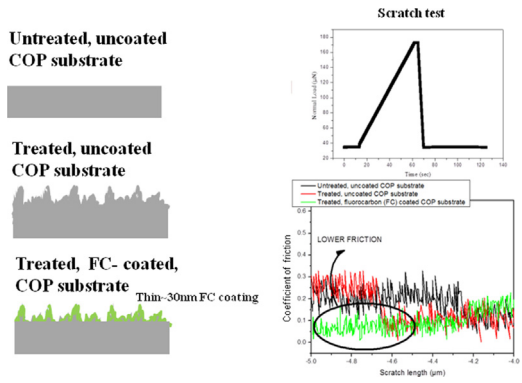

1. Introduction

Polymers are used as structural materials in various biomedical applications, including implants and instruments for minimally invasive surgical procedures;[1] in addition, the need for practical low-cost and disposable microfluidic chips for (bio) analytical applications has shifted attention toward optically transparent polymers such as (PMMA), polystyrene (PS), and cycloolefin polymer (COP), which offer good biomedical compatibility among other advantages.[2] In almost all such applications,

D. A. Dragatogiannis, E. Koumoulos, Prof. C. A. Charitidis
School of Chemical Engineering, National Technical University of Athens, 9 Heroon, Polytechniou St., Zografos, 157 80 Athens, Greece
E-mail: charitidis@chemeng.ntua.gr
K. Ellinas, Dr. A. Tserepi, Dr. E. Gogolides
Institute of Nanoscience and Nanotechnology, NCSR "Demokritos", 153 10 Aghia Paraskevi, Attiki, Greece

material performance depends on its surface properties; for example, effective catheterization requires that biochemical and tribological properties of the polymer surface are to be preserved during operation. Surface treatments of biopolymers resulting in low friction and good hemocompatibility, which is essential for preventing vessel clotting and thrombosis, are of high importance in intravenous procedures.[1]

Random nanotexturing of polymeric surfaces with pillar-like micro-nanostructures can be achieved with several technologies, such as plasma processing,[3,4] replication from Si moulds,[5] and ultra-short pulsed-laser irradiation.[6] In particular, short plasma nanotexturing modifies the chemistry and the topography of the polymeric surface without affecting the bulk properties, creates nanoscale surface roughness (nanotexture) and is used for controlling the optical, wetting, and flow properties, as well as biomolecule adsorption and cell adhesion on such surfaces.[7] This surface treatment is used in polymer-based microdevices, for flow control of micro-/nanofilters,[8] flexible electronics, and bio-MEMS.[9–11] The O_2 plasma modification of a PMMA surface results in high aspect ratio (HAR) topography with pillar-like structures.[12–15] The plasma treated surface acquires superhydrophilicity mainly due to −OH and −COOH groups on the surface after its exposure to O_2 plasma.[14,16]

To produce superhydrophobic surfaces, a thin hydrophobic film is deposited in order to tailor the surface properties, for example, a C_4F_8 plasma deposited thin fluorocarbon film (hereafter abbreviated as FC) or a spin-coated TEFLON AF1600.[14,17,18] Clearly, the aging of such surfaces, which can be damaged by impact or simply rubbing,[19] as well as their wear and chemical degradation, are major limitations to the successful application of superhydrophobic surfaces for various applications. Recent studies have focused on capillary forces,[20] abrasion resistance by sand blasting,[21] mechanical robustness to environmental and UV radiation.[22,23]

However, little work has been reported on the investigation of mechanical durability, mechanical stability, and wear resistance of random and ordered micro/nanotextured or/and structured surfaces by nano, micro-indentation and nano, micro-scratch tests.[24,25] The application of these techniques will give an insight into the deformation mechanisms associated with mechanical damage of the surface features and loss of superhydrophobicity, which is the main drawback for many practical applications.[25]

Also as reported by Dyett et al.,[25] the mechanical durability of these systems is frequently overlooked.

In our previous work, we have showed that plasma nanotextured PMMA surfaces for short etching times are mechanically stable against capillary forces, showing antireflective and superhydrophilic/superhydrophobic behavior, while long-time plasma treatments lead to nanoporous-filament-like PMMA surfaces, which can be mechanically stabilized by water immersion and drying.[15] Such treated PMMA, PEEK, and PDMS surfaces were also characterized as scratch resistant and superamphiphobic by means of an optimized nanoscratch protocol or compression tests.[15] In addition, adhesion strength of a plasma-deposited fluorocarbon and a spin-coated fluoropolymer on top of TEOS was investigated by Koumoulos et al.[26]

While most of the early work has been performed using polymers such as PMMA, little work has been done in two specific cyclic olefin materials: cyclic olefin polymer (COP) and cyclic olefin copolymer (COC).[27] These engineering plastics possess high optical clarity, even into the deep-UV range, low water absorption and, compared to other polymers, an exceptionally high resistance to organic solvents,[27] favorable properties for implementation of this polymeric material as substrate in microfluidics fabrication.

In continuation of our previous studies regarding wear resistance, mechanical properties and scratch resistivity of plasma nanotextured polymeric surfaces, we report the mechanical and tribological properties of nanotextured COP surfaces investigated by nanoindentation and nanoscratching tests.[8,15,26] Through these tests, hardness (H), reduced modulus (Er), and the coefficient of friction (CoF) were measured for both coated and uncoated COP substrates. The effects of nanotexturing on load–unload curves, plastic deformation, and adhesion have been investigated. Nanoscratching results are evaluated to estimate the wear resistance of the nanotextured surfaces, and the adhesion of the two hydrophobic coatings on the COP surfaces: plasma-deposited FC film and spin-coated Teflon AF film.

2. Materials and Methods

2.1. Materials

COP wafers having 1.5 mm thickness and 115 mm in diameter were purchased from microfluidics ChipShop GmbH, and were cut in pieces and thoroughly cleaned in iso-propyl-alcohol (IPA) and in de-ionized (DI) water prior to plasma processing.

Teflon AF 1600 is a copolymer of Poly[4,5-difluoro-2,2-bis(trifluoromethyl)-1,3-dioxole-*co*-tetrafluoroethylene] diluted at Fluorinert Fluid FC-77 solvent and then spun on the top of the substrate (~30 nm). After the spinning process, the sample is baked in air, at 95 °C for 10 min.

2.2. Plasma Processing

2.2.1. Plasma Nanotexturing

O_2 plasma deep reactive ion etching with simultaneous nanotexturing of the polymer for 4 min was performed

DOI: 10.1002/ppap.201500023

using a high-density plasma reactor (Helicon plasma reactor, Micromachining Etching Tool, MET, from Adixen-Alcatel). The system is equipped with a high density helicon antenna plasma source working at 13.56 MHz, a magnetically confined diffusion chamber and a load-lock. A detailed description of the plasma system is given in previous work.[28] The processing conditions used were 1900 W, 100 sccm O_2, 0.75 Pa, 15 °C, and bias voltage −100 V.

Using these conditions anisotropic etching is performed, the COP surface is nanotextured and roughness formation is favored. This nanotexture has been already used to produce robust superhydrophobic surfaces on PMMA, PEEK, and PDMS.[13,18] We note that this nanotexture is dual scale, comprising approximately 200 and 50 nm wide columnar structures during the first minutes of treatment that grows into the microscale after several minutes of treatment. For details about the formation of the nanotexture, please refer to our previous work.[14] In Figure 1, the nanotexture produced on COP after 4 min exposure to the plasma conditions described above is shown (treated (T) samples). The same nanotexture and thus the same wettability is observed in samples that are processed under the same conditions on different days.

2.2.2. Plasma Fluorocarbon Deposition

A thin fluorocarbon film deposition using C_4F_8 gas in a similar high-density plasma reactor (described above) at conditions 900 W, 0 V, 5.33 Pa C_4F_8, leading to a deposition rate of 30 nm min^{-1} was used (fluorocarbon coated (FC) and uncoated (UC) samples).[28] The deposition rate of the hydrophobic plasma coating is 30 nm min^{-1} and the duration of the deposition step 40 s, thus we consider that a very thin 20 nm thick FC layer is deposited on the surface. For this reason, no morphology change is observed after the FC deposition.

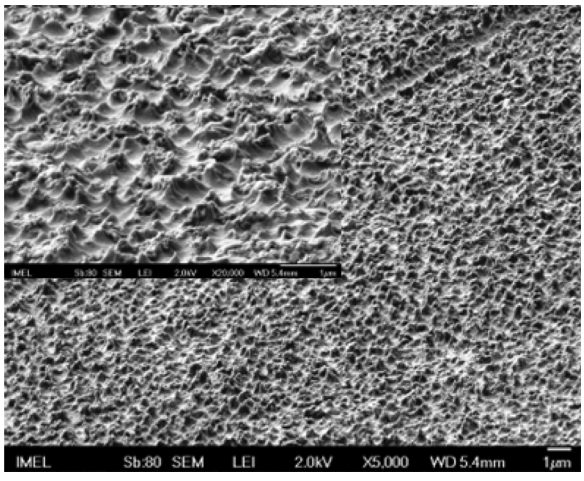

Figure 1. SEM image of 4 min T/COP surface. A higher magnification (×20 000) image is given as insert.

2.2.3. Teflon AF1600 Deposition

One weight percent Teflon AF 1600 solution was spin coated at 7 000 rpm for 30 s and baked at 95 °C for 10 min. This resulted in a conformal thin film with an approximate thickness of 30 nm (Teflon coated (TC) samples and UC samples).

2.3. Nanoindentation Experiments

The indentation tests were performed using a Hysitron-TriboLab nanomechanical test instrument. A three-sided pyramidal Berkovich diamond indenter (radius of ∼120 nm) was used for the experiments. Tip radius is calculated prior to each experimental procedure, following a calibration process. Experiments were performed in a clean area environment with ∼45% humidity and 23 °C ambient temperature.[29] In all depth-sensing tests, a total of five indents are averaged to determine the mean hardness (H) and elastic modulus (E) values for statistical purposes, with a spacing of 50 μm. The analysis of depth-sensing nanoindentation is unfortunately complicated by the presence of surface roughness due to challenges in determining the contact area between the indenter and the surface.[30] Also, the properties of a textured coated substrate will depend on its fabrication, and for inducing suoerhydrophobicity, generation of surface roughness is necessary. The surface exhibits multiscale roughness on similar scale to the indentation tip, discontinuities within the structures, and non-uniformity between surface features (anisotropic plasma etching). Such variation in contact area between the tip and the surface leads to high scatter in calculated material properties.[25] An increase in the number of indents and in the size of probing area would result in mean values more representative of the microstructure and the surface topography as a whole, with an improvement in the accuracy of the mean values but still with a high scatter in the calculated properties. However, the total number of measurements (five for each depth or load) is large enough considering that in the case of depth control protocol the measurements had been conducted at several depths from 20 to 50 nm (a total number of measurements approximately ∼100). For statistical analysis and to ensure reproducibility, measurements were obtained from different surface regions of each sample and several substrates coated with FC films were prepared under identical plasma conditions.

Nanoindentation tests were performed under two protocols: (a) load and (b) displacement control (see Figure 2). In the first case, load–unload curves were extracted at several applied loads, ranging from 100 to

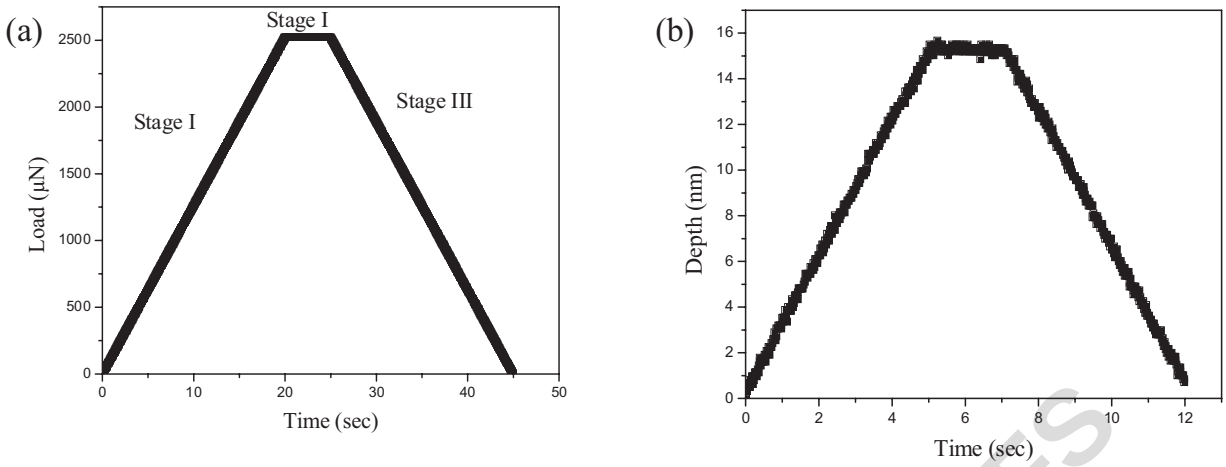

Figure 2. Representative (a) load versus time curve and (b) depth versus time curve during the load-control experiment.

4 000 μN, in order to study the effect of the treatment processes on the mechanical properties of the substrate. The duration of loading and unloading segments of the performed indentation tests have a course of 20 s, and holding time at the maximum load is 5 s. In the second case, load–unload curves were extracted at several applied displacements from 5 to 50 nm, in order to elucidate the effect of treatment process on the surface, quantify the substrate effect in the response, and study the coating-substrate mechanical behavior. The first experiment at high loads is probing the bulk region. The second is probing the top surface, i.e., the coating and the nanotexture.

2.4. Nanoscratch Experiments

The nanoscratching tests performed in this work include three main segments, namely pre-scan, scratch, and post-scan (Figure 3). In each experiment, a pre-scan was performed under very low load (1 μN). Then, the indenter scraped the sample and scratches of 10 μm length were generated. The normal applied loads used in this work were 50 and 140 μN. Finally, a post-scan under the same load as the pre-scan (1 μN) was conducted to obtain a post-scratch image of the sample. For each scratch experiment performed for a given load, three measurements were obtained from different regions of the samples with a spacing of 50 μm. In each scratch test, the coefficient of friction was calculated as the average of all friction coefficient data acquired in the sliding distance range of 0–10 μm.

Elastic modulus values can be extracted from the experimental data (load–displacement curves),[31] using the half-space elastic deformation theory with Sneddon's elastic contact theory for unloading between a conical

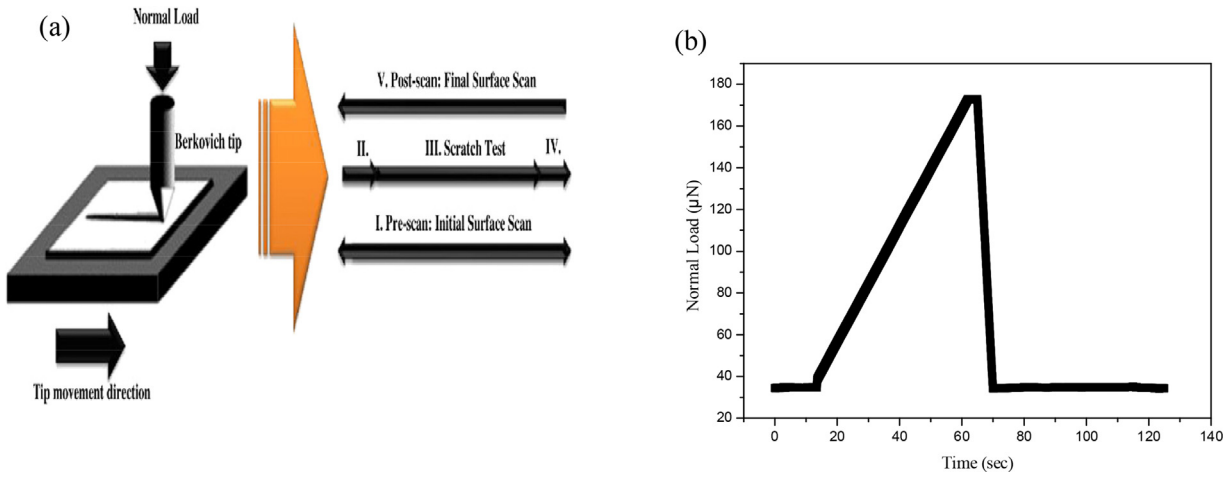

Figure 3. (a) Representative scheme of scratch segments and (b) scratch load protocol.[26]

DOI: 10.1002/ppap.201500023

indenter and the contact surface.[32] The derived expressions are presented below:

$$E_r = \frac{S\sqrt{\pi}}{2\beta\sqrt{A_c}} \quad (1)$$

where A_c is the projected contact area between the tip and the substrate, and β is a constant that depends on the geometry of the indenter ($\beta = 1.167$ for Berkovich tip). This relation was originally employed for the unloading stage during indentation of a conical tip into the contact surface, but also holds true for indentations with Berkovich and spherical tips. The reduced modulus is related to the material modulus E by the relation:

$$\frac{1}{E_r} = \frac{1-\nu_i{}^2}{E_i} + \frac{1-\nu_s{}^2}{E_s} \quad (2)$$

where ν is the Poisson ratio of the material and the subscript i refers to the properties of the indenter. An inherent weakness of this method is the prerequisite pre-estimation of the Poisson ratio of the tested material. Conventional nanoindentation hardness refers to the mean contact pressure and is also known as contact hardness, H_c, which is actually dependent upon the geometry of the indenter.

$$H_c = \frac{F}{A_c} \quad (3)$$

where,

$$A_c = A(h_c) = 24,5h_c{}^2 + a_1h_c + a_{1/2}h_c^{1/2} + \ldots + a_{1/16}h_c^{1/16} \quad (4)$$

and

$$h_c = h_m - \varepsilon\frac{P_m}{S_m} \quad (5)$$

where h_c is the contact depth and ε is an indenter geometry constant, equal to 0.75 for Berkovich and spherical indenter.[31]

2.5. Stiffness Correction

The Oliver and Pharr method is based on the assumption that the initial slope of the unloading load–displacement response is elastic, regardless of the fact that the contact might be visco-elastic or visco-plastic. For viscoelastic effects to be properly taken into account, a correction of the Oliver and Pharr method has been proposed. This correction is applied to the slope of the unloading segment of the load–displacement curves.[33] Ngan et al.[34–36] showed that the tip displacement rate (creep rate $\dot{h}_h$), loading rate (relaxation rate) at the end of the loading cycle, hold stage (Figure 2, Stages II and III) prior to unloading, as well as the unloading rate P_u have to be taken into consideration during the computation of the mechanical properties.[33] As a result, in order to take into account time dependent deformation and viscoelastic effects, the elastic stiffness S_e was calculated from the expression:[36,37]

$$\frac{1}{S_e} = \frac{1}{S} - \frac{\dot{h}_h}{\dot{P}_u} \quad (6)$$

As proposed by Cheng and Komvopoulos[1] for the study of similar plasma treated mechanical systems, the depth data of untreated and plasma-treated samples during the hold period was found to be of the form

$$h = h_0 + Ct^{1/2} \quad (7)$$

where t is the hold time, h_0 is the indentation depth at the start of the hold period ($t = 0$), and C is a constant intrinsic of the viscoelastic behavior of the material surface.

Substituting Eq. (6) into (7) gives:

$$\frac{1}{S_e} = \frac{1}{S} - \frac{C}{2t_0^{1/2}\dot{P}_u} \quad (8)$$

where t_0 is the hold period.

3. Results and Discussion

3.1. Nanomechanical Properties of Plasma-Treated and Untreated Samples

Load and unload curves, of the UT/FC and T/FC samples, for the two protocols applied, are presented in Figures 4 and 5. Comparison of the UT/FC and T/FC samples, for identical displacement, under the same load control protocol, reveals higher resistance to the applied load for the UT/FC sample, since higher load was required to reach the same displacement (Figure 4a and b). In addition, the same behavior is reported for small depths using the depth control protocol (Figure 5b). UT/FC sample revealed elastoplastic behavior (Figure 5a), while T/FC sample revealed a full plastic behavior (Figure 5b). Furthermore, negative loads are observed for the unloading curve of the T/FC samples (Figure 5b), indicating adhesive forces (the respective area under the 0 axis indicates the work of adhesion) between the tip and sample surface during unloading, before retraction of the tip. The slope change which is recorded at the first portion of the loading curves for the treated samples can be attributed to the surface roughness. Increasing the plasma treatment duration leads to an increase in surface roughness; slope changes are more

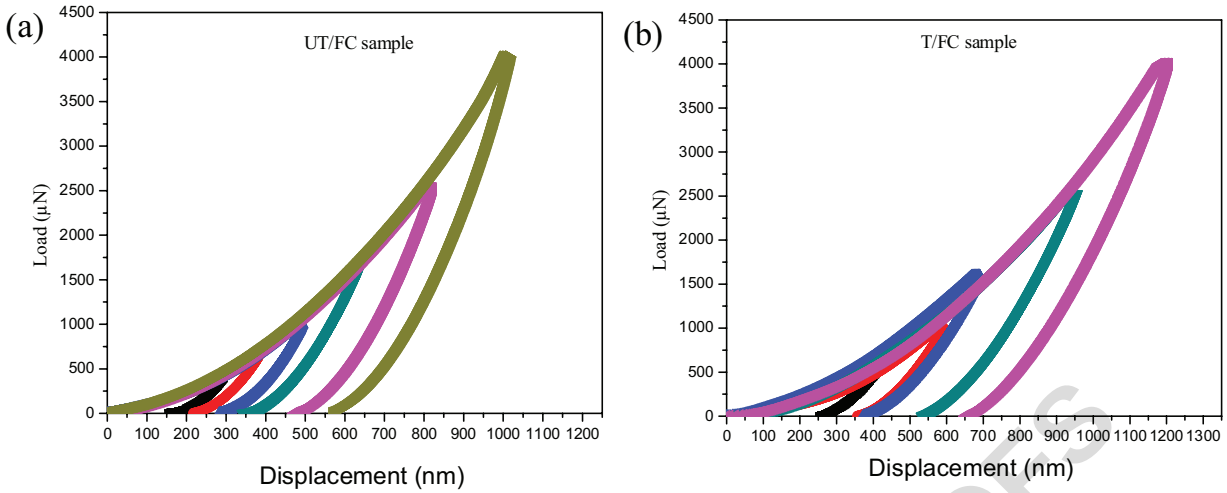

Figure 4. Nanoindentation load–unload curves of plasma deposited FC films on (a) untreated COP substrate and (b) 4 min textured COP substrate at different maximum depths (load control protocol).

pronounced, as has been previously revealed in similar studies on plasma treated PMMA.[38]

For small depths, UT/FC sample (Figure 5a), exhibited repeatable load–displacement behavior, since the two curves at the same maximum load showed exactly the same path. Also, note that the loading curves in this case are almost identical, for all peak load experiments. Considering that each indentation was performed at a different area of the coating surface, this repeatability implies uniform mechanical behavior over the whole surface area, indicating also good deposition of the FC coating on the COP substrate. These characteristics explain the narrow error bars of the elastic modulus and hardness of the UT/FC sample. Such uniform and consistent micromechanical properties are expected from materials that also have superior tribological performance.[39]

In the case of the T/FC sample, load–displacement curves vary significantly between indentations up to a certain depth, and the slopes of the loading curves differ significantly at the zero contact point. This implies that the mechanical deformation, hereby represented by the load–displacement curves, at the first stage of nanoindentations of the T/FC sample differ from surface location to location due to roughness spatial variation (Figure 1). In addition to this, the slope of the loading curve does not increase smoothly and a slope alterations can be observed

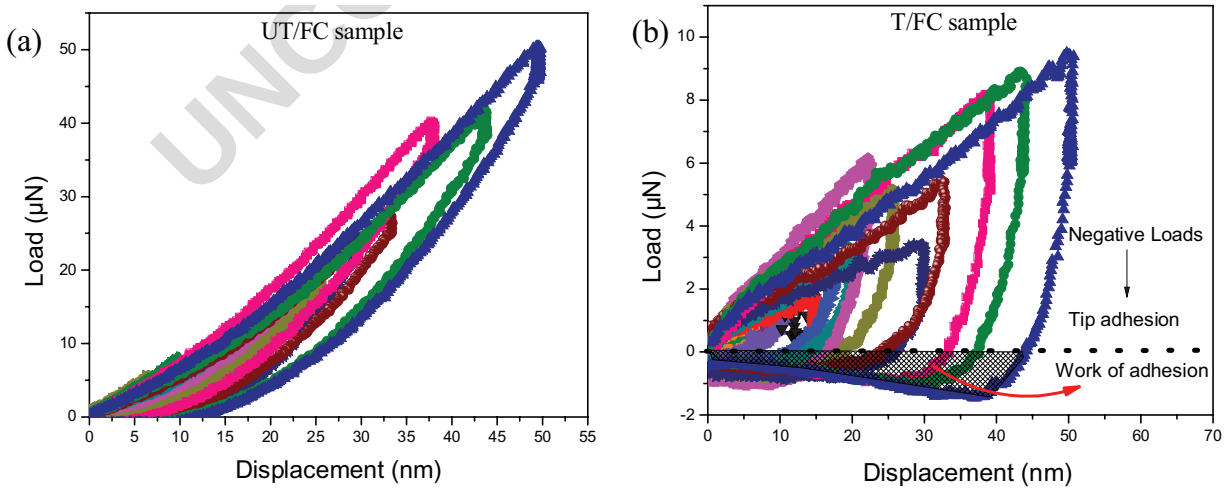

Figure 5. Nanoindentation load–unload curves (for small depths) of plasma deposited FC films on (a) untreated and (b) 4 min textured COP substrate at different maximum depths (depth control protocol).

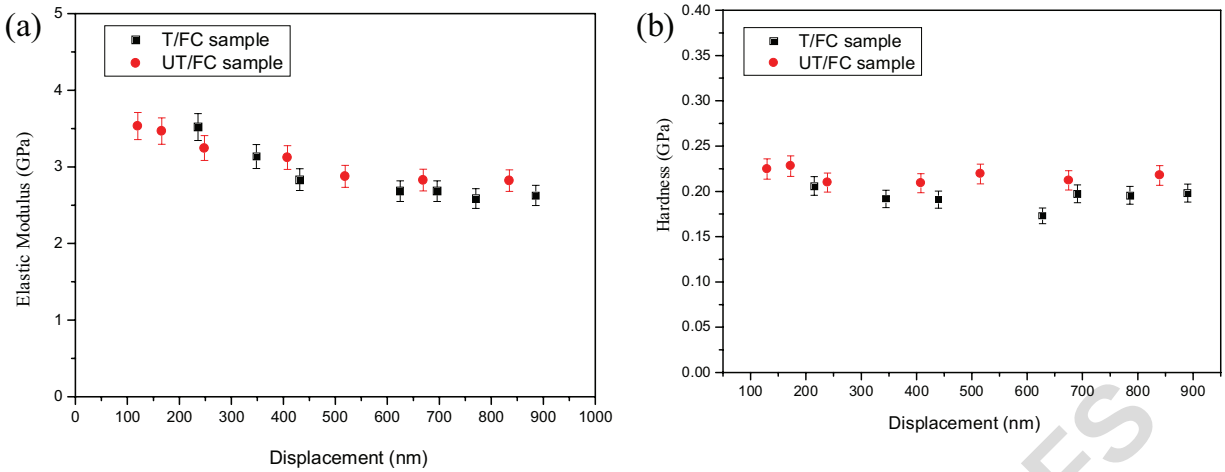

Figure 6. (a) Reduced modulus and (b) hardness curves varying with depth of plasma-deposited FC films on 4 min textured and untreated COP substrates.

at some depths, denoting that the nanostructures are not uniform. This behavior has been discussed in previous work,[39] in the case of polytetrafluoroethylene (PTFE)—and polyetheretherketone (PEEK)—based coating, where the mechanical behavior of the samples was successfully correlated with their microstructure, wear performance, and scanning electron imaging results. Also, as is depicted in Figure 5a and b, the indenter penetrates at approximately the same indentation depth by applying lower loads for treated COP than untreated. For penetration depths smaller than the roughness height, the tip is probing nanotextured COP coated with fluorocarbon and air in between pillars. In the case of T/FC samples, as shown in Figure 5b, a decrease in the unloading slope upon the retraction of the tip can be observed, one that can be attributed to the significant decrease in the contact area caused by the separation of the tip from the flattened pillars. Furthermore, the negative loads recorded during the retraction of the tip from the sample show the interaction between the coated texture with the tip supporting the reversible deformation of the remaining pillars.

3.2. Hardness and Reduced Modulus of Plasma-Treated and Untreated Samples

In Figure 6a and b, the E_r and H values of samples are presented as a function of indentation depth (under load control protocol). The E_r and H values were used to characterize the extent of penetration due to the surface

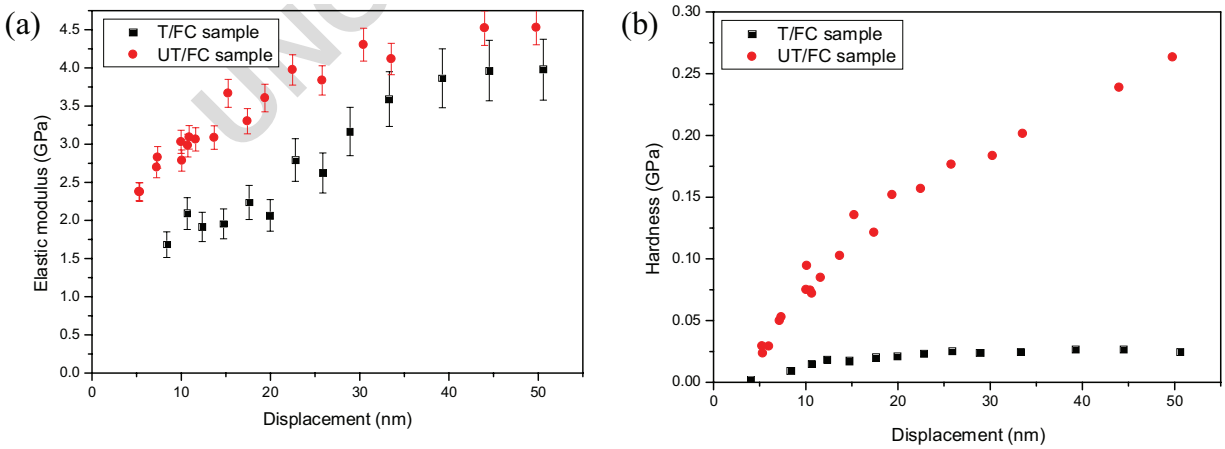

Figure 7. (a) Reduced modulus and (b) hardness curves varying with depth of plasma deposited FC film on (i) 4 min textured and (ii) untreated COP substrate.

modification.[40] Both coated and uncoated, untreated and treated COP samples exhibited almost equal values of E_r and H, for indentation depths over ~300 nm, with plain value reported also by other researchers.[41] This finding shows that no significant changes to the elasticity or hardness of the COP composite coatings are observed at values higher than 300 nm. On the other hand, an increase in E_r values at depth of ~20 to 50 nm was observed for the T/FC and UT/FC samples (Figure 7). In the case of T/FC sample, the H values were determined. In addition, E_r and H values for UT/FC sample are measured to be higher than those of T/FC sample near the surface (50 nm). Although some authors,[40] propose that such softening is due to hydrogen bonded network formed by the presence hydrophilic functional groups on the surface, in this case the material is nanotextured, and thus the surface is not smooth. The probe is sitting on nanotexture coated with fluorocarbon and air in between those pillars. Therefore the E and H are bound to be smaller. The maximum depth of surface modification appears to be approximately 100 nm in all cases. Any changes to the elasticity or hardness of the COP surface are observed at values less than 100 nm. Since the thickness of the FC plasma deposited film is almost ~30 nm, the alteration of the E_r and H values could not be clearly discerned by nanoindentation, due to the unmodified bulk. Interestingly, it can be observed that the hardness of T/FC sample, as depicted by depth profile presented in Figure 7b, is significantly lower than that of the untreated COP. This behavior can be attributed to the modification of the surface due to plasma processing. Previous studies in the literature reported that softening and decreased elasticity of the surface are the dominant trends observed following solvent exposure.[40] The nanoindentation data give an indication of the effects of both the surface modification as well as the bond strength of the FC coating onto COP substrates.[40] The softening observed is due to the fact that the top surface of the samples consists of nanotexture and air, the pillars being coated of course with FC. The FC coating is not deposited on a flat bulk material but it is sitting on the nanotexture profile. The tip is probing a "composite" interface of FC coated "forest" pillars. There is a decrease in the contact area by nanotexturing, which in turn, reduces the contact stiffness.

3.3. Viscoelastic Properties in the Bulk Region

Figure 8 shows the variation of the viscoelastic constant C with maximum indentation load for UT/UC and the T/FC sample. As expected, the effect of viscoelasticity on the contact stiffness of each material system increases with the maximum load in all cases. The almost identical C values suggest that structural modification due to plasma treatment was confined to the outermost surface layer of the

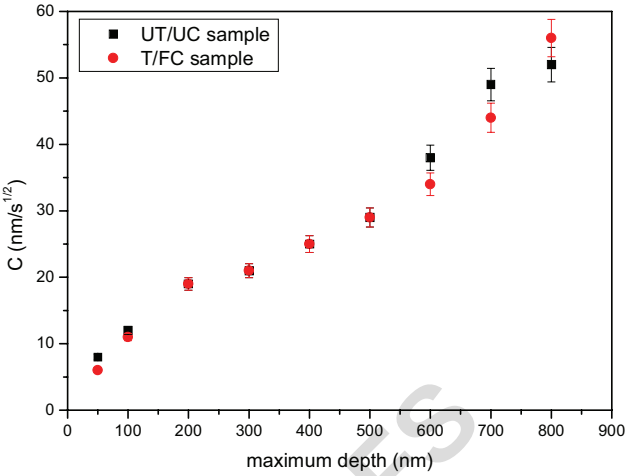

Figure 8. Viscoelastic constant C of untreated-uncoated COP and treated-coated COP.

COP substrate (thickness ~100 nm), implying that plasma treatment did not alter the viscoelastic behavior of the bulk material.[1]

3.4. Wear Resistance Analysis Based on H/E and H^3/E^2 Ratios

The material property H can be interpreted in a number of ways. Within this work, hardness is considered to be a measure of the material's (coated pillars in the case of T/FC or FC coating on the substrate in the case of U/FC) capacity to resist permanent deformation from an opposing load. From definition of the term, hardness is an ideal trait for surface structures. However, for rationalizing wear behavior, it has

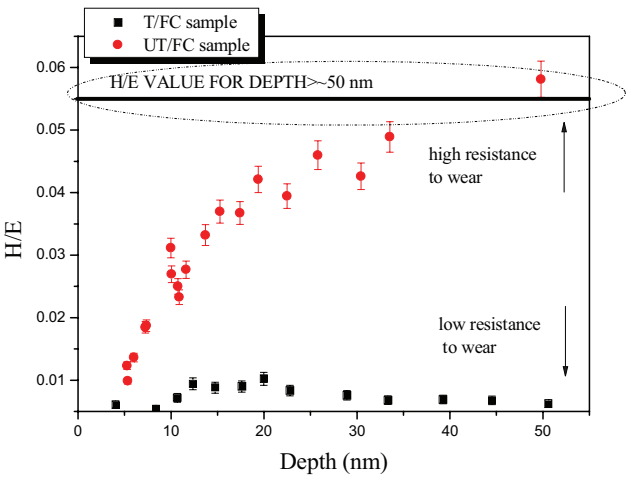

Figure 9. Hardness to modulus ratio for textured-FC coated COP and untreated-FC coated COP.

DOI: 10.1002/ppap.201500023

been reported that the ratios H/E and H^3/E^2 may be more relevant.

H/E and H^3/E^2 indexes are of significant interest in tribology and surface engineering. Hardness to elastic modulus ratio (H/E) is referred to as the "plasticity index," and is considered to be a valuable measure in determining the limit of elastic behavior in surface contact, thus is important for the avoidance of wear. A high ratio of H/E is indicative of good wear resistance in a disparate range of materials.[42] Higher stresses are expected for high ratio values of H/E, hard materials, and high stress concentrations develop toward the indenter tip, whereas in the case of low ratio values H/E, soft materials, the stresses are lower and are distributed more evenly across the cross-section of the material.[43] In Figure 9, the change of H/E slope reveals the strengthening of composite coating with increasing displacement. Adhesion relation of a coating with a substrate is confirmed by using the Tresca's yield criterion and Tabor's relation, according to which, the load at the onset of yielding is proportional to H^3/E^2. The term H^3/E^2 combines H and E values of a material and describes the amount of elasticity exhibited by the film. In particular, high (low) values of H^3/E^2 indicate a highly elastic (plastic) behavior of the film under contact events.[30,42] It is clearly demonstrated by the results shown in Figure 9 that the treated COP sample exhibits higher plastic deformation at the same loading condition than the untreated sample. The plastic deformation in the case of the treated samples starts at lower loads, a fact that is also confirmed by load–unload curves (Figure 5a and b).

Untreated COP sample showed high ratios of H/E, H^3/E^2, and an increasing trend with increasing depth as it is presented in Figures 9 and 10. In the case of treated COP sample, the H/E and H^3/E^2 ratios are significantly lower due to the plasma nanotexturing. What appears to be more important than the averaged property values in Figures 9 and 10 is the relative size of the error bars which is much higher for the treated sample (higher variability). Furthermore, the treated COP sample showed three orders of magnitude lower ratio H^3/E^2 values than the untreated sample.

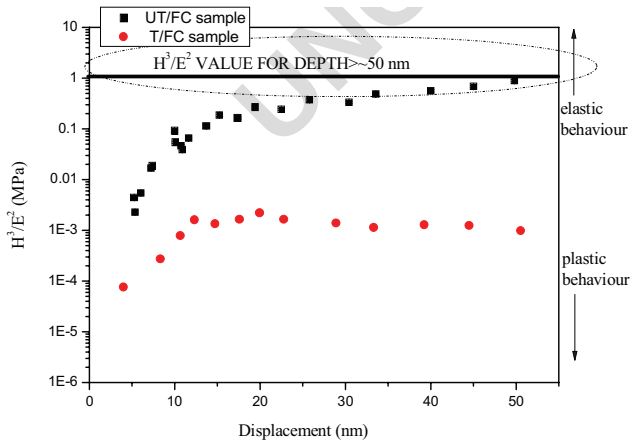

Figure 10. H^3/E^2 ratio for untreated-FC coated COP and textured-FC coated COP.

3.5. Nanotribological Properties of Plasma-Treated and Untreated Samples

Scratch tests provide useful information about the tribological performance of organic polymers under different conditions.[44,45] Specifically, nanoscratch tests enable the determination of coefficient of friction (CoF), which is the ratio of tangential force to normal force, the evaluation of wear resistance and the adhesion of coating into the bulk substrate. An estimation of the residual scratch ditch and the extent of immediate recovery can be obtained by comparing the pre-scratch with the post-scratch curve profiles. Additionally, the plastic deformation of all samples after each test (post-scratch segment) can also be studied using nanoscratch tests. However, since polymers are characterized by large elastic recovery and complex rheological behavior, the extrapolation of conclusions is far more complicated than in the case of metals.[45] Depth of scratches was measured in situ for all samples by scanning the topography of the film before and after the scratch (Figures 11–13) using an increasing normal load. The applied scratch protocol is shown in Figure 3b above, in section 2.4. The pre-scratch curve corresponds to the profile of the initial surface, the scratch curve corresponds to the tip penetration profile during testing and finally, the post-scratch curve corresponds to the final profile of the surface after scratching. During the post-scratch segment, the tip moves across the scratch path under very low load (<5 μN). In this way, the post-scan curve represents the residual depth of scratch trace after unloading, i.e., the plastic deformation of the probed film. The difference between scratch and post-scratch curves corresponds to the elastic recovery of the bulk substrate.

In Figure 11a, the surface morphologies of the scratches of the UT/UC sample under 140 μN and the corresponding initial and residual scratch profiles are displayed. The onset of the non-elastic behavior for the UT/UC sample occurs after 6 μm scratch length (corresponding force L_y of 120 μN), but in the case of treated samples earlier, after 1 μm scratch length. Comparing the profiles, the recovered scratch path of the treated sample presents the same residual final depth at ~150 nm. The morphology of the untreated sample is more uniform instead of treated sample which presents a rough residual surface with heights and valleys. The exhibited fluctuations in CoF correspond to higher wear deformation.

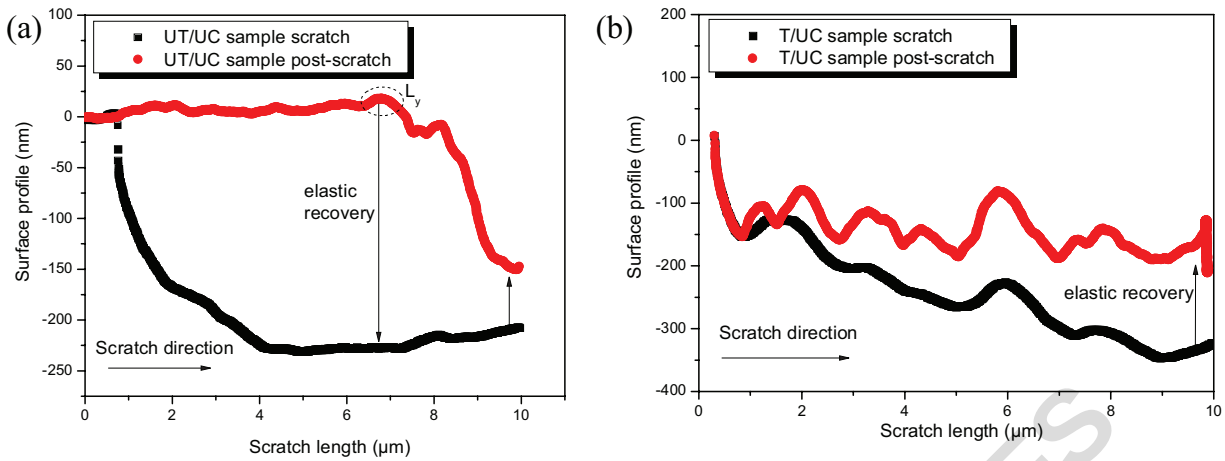

Figure 11. Nanoscratch depth profiles of the (a) uncoated, untreated COP sample and (b) uncoated, treated COP sample with applied maximum normal load of 140 μN.

In Figure 12a, the surface morphologies of the scratches of the UT/FC sample under 140 μN and the corresponding initial and residual scratch profiles are displayed. In Figure 12b, the surface morphologies of the scratches of the Teflon AF-coated, treated COP sample under 140 μN and the corresponding initial and residual scratch profiles are displayed. As observed from Figure 12a, the depth of the scratch path during loading is reversed after a certain value of scratch length for the untreated COP substrates. This possibly indicates that material is accumulated in front of the tip, as the tip moves, and is a clear evidence of poor adhesion of the FC plasma-deposited film on the untreated substrates. Comparing the profiles (Figure 12a and b), between FC plasma-deposited and Teflon AF-spin coated samples, a more uniform deformation with depth during scratch is observed in the case of Teflon AF-spin coated COP samples which is an indication of better adhesion of the coating to the substrate and a more uniform microstructure through the thickness. As reported by Yeo and Polycarpou,[39] the Teflon AF-spin coated sample can maintain its consistent frictional performance regardless of the removal of material wear with sliding.

In Figure 13a, the surface morphologies of the scratches of the T/FC sample under 140 μN and the corresponding initial and residual scratch profiles are displayed. In Figure 13b, the surface morphologies of the scratches of the Teflon AF-coated, treated COP sample under 140 μN, and the corresponding initial and residual scratch profiles are

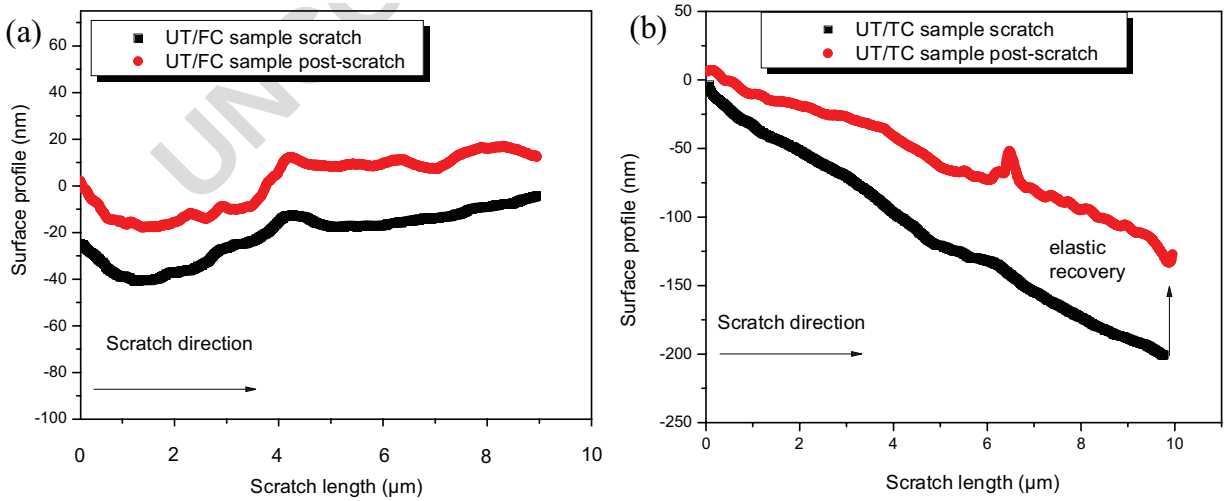

Figure 12. Nanoscratch depth profiles of (a) plasma-deposited FC and (b) Teflon AF-coated, untreated COP samples, with applied maximum normal load of 140 μN.

DOI: 10.1002/ppap.201500023

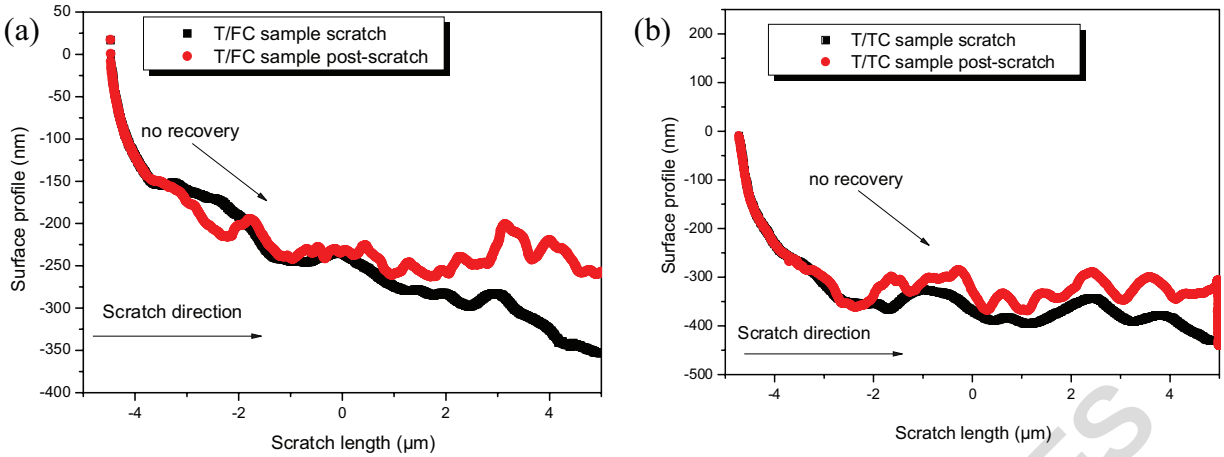

Figure 13. Nanoscratch depth profiles of the (a) plasma-deposited FC and (b) Teflon AF-coated, treated COP samples with applied maximum normal load of 140 μN.

displayed. The arrows in the figures represent the sliding direction of the indenter tip.

As stated above, the CoF is an important property that is measured through a scratch test, during which two mechanisms prevail: adhesion and ploughing.[46] The main factors that affect the overall coefficient of friction evolution during a scratch test are: the material type, the sliding speed and the lubricating conditions. In this study, scratch tests were performed in order to evaluate changes in CoF values before and after plasma treatment, with plasma-deposited FC and spin-coated Teflon AF coatings. Coefficient of friction values for the treated coated samples are found to be decreased compared to other samples; this indicates a higher wear resistant behavior compared to other samples. This result is in contrast with the H/E and H^3/E^2 measured ratios (see above), where treated samples present lower H/E values than plain samples; higher H/E values indicate higher wear resistance.[47]

The coefficient of friction values of FC-coated, treated COP samples are expected to be as low as the values reported in the literature (0.05–0.25).[48–50] Figure 14b shows that FC coated, treated samples exhibit almost 50% lower CoF compared to the uncoated, treated samples at the early stage of scratch experiment. Similarly, Teflon AF-coated, treated samples exhibit lower CoF compared again to the uncoated samples. This difference in friction characteristics can be related to differences in the FC film composition and structure compared to Teflon AF. As indicated, the CoF is

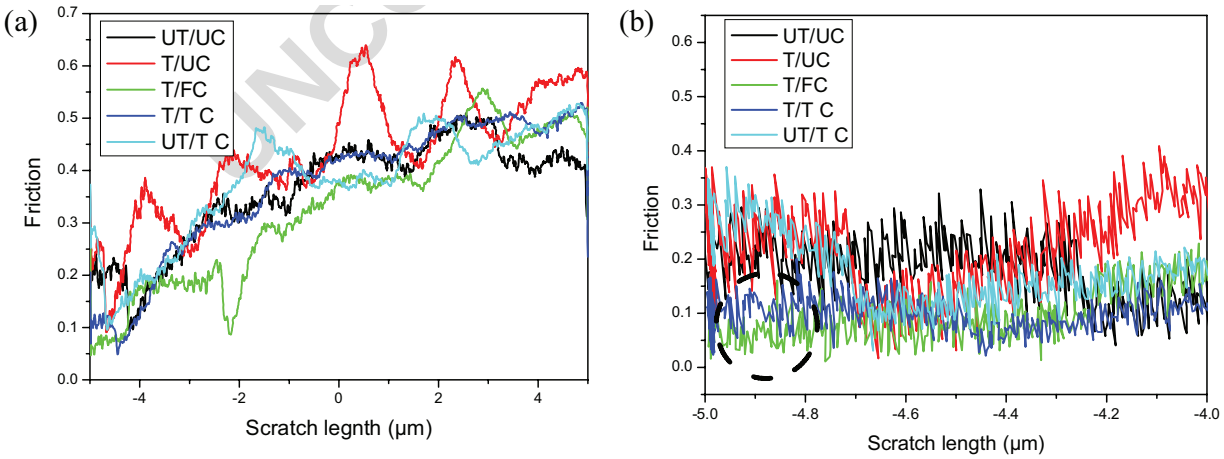

Figure 14. (a) Coefficient of friction curve as a function of scratch path, for all samples measured, and (b) at the early stage of scratch experiment where the surface is probed. The application of FC and Teflon-AF coatings on COP textured substrates results in lower CoF values.

decreased due to the plasma treatment of samples. Again, in all cases CoF decreases when either one of the hydrophobic coatings is applied on the treated surface.

4. Conclusions

The nanomechanical and tribological properties of plasma textured, coated, and uncoated COP polymeric substrates were measured using nanoindentation and nanoscratching tests. Hardness and reduced modulus were assessed, together with quantification of wear resistance, plastic deformation, and the coefficient of friction of the samples. The differences in the mechanical behavior between the coatings could be explained by the coatings' nano/micro-structure. Based on the experiments and the microstructure of the samples, the following conclusions could be drawn:

a) In the case of T/FC samples, the slopes of the loading curves differ significantly at the zero contact point, the slope of the loading curve does not increase smoothly (as in U/FC), denoting possible heterogeneity of the nanostructures and roughness spatial variation due to anisotropic plasma etching, and variation of contact area with increasing depth.
b) This implies also that the mechanical deformation, as represented by the load–displacement curves at the first stage of nanoindentations of the T/FC sample, differs in relation to the surface location, due to roughness spatial variation caused by the anisotropic plasma etching.
c) Another difference between untreated and treated samples is that the slope of the loading curve of the nanotextured surface is lower than that of the untreated surface. This can be related to the decrease in the contact area by nanotexturing, which in turn, reduces the contact stiffness.
d) Comparison of FC coated, treated and untreated, COP for identical displacement, under load control protocol, revealed greater resistance to the applied load for the untreated sample. It was found that the FC-coated, untreated COP exhibited very repeatable load–displacement behavior, indicating a uniform structure. Instead, the FC-coated treated COP samples presented displacement behavior which was quite variable.
e) FC-coated, untreated COP samples exhibited elasto-plastic behavior, whereas, treated samples revealed a plastic behavior.
f) Negative loads were observed for the unloading curve of the treated samples, indicating adhesive forces between the tip and sample surface.
g) The plasma deposited thin (30 nm) FC film on the COP substrates showed better adhesion for treated samples compared to untreated samples.
h) Coefficient of friction values for treated coated (both FC and Teflon AF) samples were found to be decreased compared to untreated uncoated COP.
i) Teflon AF coating showed lower CoF compared to the plasma-deposited FC.

Recent works highlight a correlation between the mechanical properties (nanoindentation) of coatings with their tribological performance (nanoscratching). In this work, notable differences between the nanoindentation responses and nanoscratching properties of the samples are reported. Additionally, untreated samples showed higher H/E ratios and higher coefficient of friction than the treated samples. This study revealed that the adhesion strength was increased in the case of treated substrates for both coatings tested. The adhesion strength between the coatings and the substrate could only be elucidated in a qualitative way by nanoscratching experiments.

Acknowledgements: This research was supported by the Project "THALIS-DESIgn and fabrication of Robust super-hyDROPhobic/philic surfaces and their application in therealization of "smart" microfluidic valves" funded by the Hellenic and European Regional Development Funds (ERDF) under the Hellenic National Strategic Reference Framework (NSRF) 2007–2013. Financial support for author D.A. Dragatogiannis through a PhD scholarship granted by Research Committee of the National Technical University of Athens (NTUA) is also gratefully acknowledged.

Received: February 8, 2015; Revised: April 29, 2015; Accepted: May 3, 2015;DOI: 10.1002/ppap.201500023

Keywords: cycloolefin polymer; hydrophobic coatings; nanoscale characterization; plasma treatment

[1] Q. Cheng, K. Komvopoulos, *J. Phys. D Appl. Phys.* **2012**, *45*, 095401.
[2] C. De Marco, S. M. Eaton, M. Levi, G. Cerullo, S. Turri, R. Osellame, *Langmuir* **2011**, *27*, 8391.
[3] F. Palumbo, R. Di Mundo, D. Cappelluti, R. d'Agostino, *Plasma Process Polym.* **2011**, *8*, 118.
[4] A. D. Tserepi, M. E. Vlachopoulou, E. Gogolides, *Nanotechnology* **2006**, *17*, 3977.
[5] L. Sainiemi, V. Jokinen, A. Shah, M. Shpak, S. Aura, P. Suvanto, S. Franssila, *Adv. Mater.* **2011**, *23*, 122.
[6] H. Pazokian, A. Selimis, J. Barzin, S. Jelvani, M. Mollabashi, C. Fotakis, E. Stratakis, *J. Micromech. Microeng.* **2012**, *22*, 035001.
[7] E. Gogolides, M. Vlachopoulou, K. Tsougeni, N. Vourdas, A. Tserepi, *Int. J. Nanomanuf.* **2010**, *6*, 152.
[8] K. Ellinas, A. Tserepi, E. Gogolides, *Microfluidics and Nanofluidics* **2014**, *17*, 489.
[9] B. Bhushan, *J. Vac. Sci. Technol. B* **2003**, *21*, 2262.
[10] J. H. Park, S. H. Lee, K. H. Choi, H. S. Noh, J. W. Lee, S. J. Pearton, *Thin Solid Films* **2010**, *518*, 6465.

[11] M. Palacio, B. Bhushan, N. Ferrell, D. Hansford, *Sensors Actuators A* **2007**, *135*, 637.
[12] U. Cvelbar, N. Krstulovic, S. Milosevic, M. Mozetic, *Vacuum* **2007**, *82*, 224.
[13] N. Vourdas, A. Tserepi, E. Gogolides, *Nanotechnology* **2007**, *18*, 125304.
[14] K. Tsougeni, N. Vourdas, A. Tserepi, E. Gogolides, *Langmuir* **2009**, *25*, 11748.
[15] K. Ellinas, S. P. Pujari, D. A. Dragatogiannis, C. A. Charitidis, A. Tserepi, H. Zuilhof, E. Gogolides, *Appl. Mater. Interfac.* **2014**, *6*, 6510.
[16] A. Vesel, M. Mozetic, *Vacuum* **2012**, *86*, 634.
[17] K. Tsougeni, A. Tserepi, G. Boulousis, V. Constantoudis, E. Gogolides, *Japan. J. Appl. Phys.* **2007**, *46*, 744.
[18] K. Ellinas, A. Tserepi, E. Gogolides, *Langmuir* **2011**, *27*, 3960.
[19] M. Callies, D. Quere, *Soft Matter* **2005**, *1*, 55.
[20] D. Chandra, S. Yang, *Acc. Chem. Res.* **2010**, *43*, 1080.
[21] C. H. Su, Y. Q. Xu, F. Gong, F. S. Wang, C. F. Li, *Soft Matter* **2010**, *6*, 6068.
[22] J. Zimmermann, F. A. Reifler, U. Schrade, G. R. J. Artus, S. Seeger, *Colloids Surf. A* **2007**, *302*, 234.
[23] Y. Xiu, D. W. Hess, C. P. Wong, *J. Colloid Interface Sci.* **2008**, *326*, 465.
[24] N. Satyanarayana, K. H. Lau, S. K. Sinha, *Appl. Phys. Lett.* **2008**, *93*, 261906.
[25] B. P. Dyett, A. H. Wu, R. N. Lamb, *ACS Appl. Mat. and Inter.* **2014**, *6*, 18380.
[26] E. P. Koumoulos, C. A. Charitidis, D. P. Papageorgiou, A. G. Papathanasiou, A. G. Boudouvis, *Surf. Coat. Techn.* **2012**, *206*, 3823.
[27] M. Kitsara, J. Ducrée, *J. of Micromech. Microeng.* **2013**, *23*, 033001.
[28] P. Bayiati, A. Tserepi, E. Gogolides, K. Misiakos, *J. Vacuum Sci. Tech. A* **2004**, *22*, 1546.
[29] C. A. Charitidis, *Int. J. Refract. Met. Hard Mater.* **2010**, *28*, 51.
[30] A. C. Fischer-Cripps, *Nanoindentation*, Springer, New York **2011**.
[31] W. C. Oliver, G. M. Pharr, *J. Mater. Res.* **1992**, *7*, 1564.
[32] I. N. Sneddon, *Proc. Camb. Philos. Soc.* **1948**, *44*, 492.
[33] U. D. Cakmak, T. Schöberl, Z. Major, *Meccanica* **2012**, *47*, 707.
[34] A. H. W. Ngan, H. T. Wang, B. Tang, K. Y. Sze, *Int. J. Solids Struct.* **2004**, *42*, 1831.
[35] A. Jäger, R. Lackner, J. Eberhardsteiner, *Meccanica* **2007**, *42*, 293.
[36] B. Tang, A. H. W. Ngan, *J. Mater. Res.* **2003**, *18*, 1141.
[37] J. Zhou, K. Komvopoulos, *J. Appl. Phys.* **2006**, *100*, 114329.
[38] A. Skarmoutsou, C. A. Charitidis, A. K. Gnanappa, A. Tserepi, E. Gogolides, *Nanotechnology* **2012**, *23*, 505711.
[39] S. M. Yeo, A. A. Polycarpou, *Trib. Int.* **2013**, *60*, 198.
[40] L. Brown, T. Koerner, J. H. Horton, R. D. Oleschuk, *Lab on a Chip* **2006**, *6*, 66.
[41] M. Olek, K. Kempa, S. Jurga, M. Giersig, *Langmuir* **2005**, *21*, 3146.
[42] A. Leyland, A. Matthews, *Surf. Coat. Technol.* **2004**, *177*, 317.
[43] Y. T. Cheng, C. M. Cheng, *Surf. Coat. Technol.* **2000**, *133*, 417.
[44] S. K. Sinha, D. B. Lim, *Wear* **2006**, *260*, 751.
[45] E. Felder, J. L. Bucaille, *Trib. Int.* **2006**, *39*, 70.
[46] M. Mansha, C. Gauthier, P. Gerard, R. Schirrer, *Wear* **2011**, *271*, 671.
[47] T. L. Oberle, *J. Metrol.* **1951**, *3*, 438.
[48] B. Bhushan, B. K. Gupta, *Handbook of Tribology: Materials, Coatings and Surface Treatments*, McGraw-Hill, New York **1991**.
[49] J. K. Lancaster, in *Friction and Wear, in Polymer Science*, Vol. 2, A. D. Jenkins, Ed. Amsterdam, North-Holland, **1972**, pp. 959–1046.
[50] E. Santner, H. Czichos, *Tribol. Int.* **1989**, *22*, 104.
[51] W. F. Mousa, M. Kobayashi, S. Shinzato, N. Neo, S. Yoshihara, T. Nakamura, *Biomaterials* **2000**, *21*, 2137.
[52] R. P. Gandhiraman, C. Volcke, V. Gubala, C. Doyle, L. Basabe-Desmonts, C. Dotzler, M. F. Toney, M. Iacono, R. I. Nooney, S. Daniels, B. James, D. E. Williams, *J. Mater. Chem.* **2010**, *20*, 4116.
[53] R. P. Gandhiraman, V. Gubala, C. C. O'Mahony, Th. Cummins, J. Raj, A. Eltayeb, C. Doyle, B. James, S. Daniels, D. E. Williams, *Vacuum* **2012**, *86*, 547.

Q1: Author: Please check suitability of suggested short title.
Q2: Author: Please confirm that given names (red) and surnames/family names (green) have been identified correctly.
Q3: Author: Please spell out the first name of Dr. E. Gogolides.
Q4: Author: Please shorten summary text to 700 characters maximum.
Q5: Author: References have been renumbered to follow the sequential order. Please check.
Q6: Author: Please provide the publisher name in Ref. 49.
Q7: Author: Please cite Refs. 51, 52, and 53 in the text.

Plasma Processes and Polymers

Editorial office:
Wiley-VCH
Plasma Processes and Polymers
Boschstrasse 12, 69469 Weinheim
Germany

Tel.: +49 (0) 6201 606 – 581 or 238
Fax: +49 (0) 6201 606 – 510
E-mail: plasma@wiley-vch.de

Reprint Order Form 2015

Short DOI: ppap._____

Please send me and bill me for

☐ no. of **Reprints** via ☐ airmail (+ 25 Euro) ☐ surface mail

Please send me and bill me for a

☐ **high-resolution PDF file** (330 Euro).

My e-mail address:

_____

Please note: It is not permitted to present the PDF file on the internet or on company homepages

Information regarding VAT
Please note that from German sales tax point of view, the charge for **Reprints, Issues or Posters** is considered as **"supply of goods"** and therefore, in general, such delivery is a subject to German sales tax. However, this regulation has no impact on customers located outside of the European Union. Deliveries to customers outside the Community are automatically tax-exempt. Deliveries within the Community to institutional customers outside of Germany are exempted from the German tax (VAT) only if the customer provides the supplier with his/her VAT number. The VAT number (value added tax identification number) is a tax registration number used in the countries of the European Union to identify corporate entities doing business there. It starts with a country code (e.g. FR for France, GB for Great Britain) and follows by numbers.

Mail reprints / posters to:

_____
_____
_____
_____
_____

Invoice address:

_____
_____
_____
_____
_____

VAT no.: _____
(Institutes / companies in EU countries only)

Purchase Order No.: _____

Credit Card Payment:

VISA, MasterCard, AMERICAN EXPRESS
Please use the Credit Card Token Generator located at the website below to create a token for secure payment. The token will be used instead of your credit card number.

Credit Card Token Generator:
https://www.wiley-vch.de/editorial_production/index.php

Please transfer your token number to the space below.

Credit Card Token Number

Cover Posters

Posters are available of all the published covers and frontispieces in two sizes

☐ DinA2 42 x 60 cm/ 17 x 24in (one copy: **39 Euro**)

☐ DinA1 60 x 84 cm/ 24 x 33in (one copy: **49 Euro**)

Postage for shipping posters overseas by airmail:
+ 25 Euro

Postage for shipping posters within Europe by surface mail:
+ 15 Euro

Price list for reprints (The prices include mailing and handling charges. All Wiley-VCH prices are exclusive of VAT)

No. of pages	Price (in Euro) for orders of 50 copies	100 copies	150 copies	200 copies	300 copies	500 copies
1-4	345	395	425	445	548	752
5-8	490	573	608	636	784	1077
9-12	640	739	786	824	1016	1396
13-16	780	900	958	1004	1237	1701
17-20	930	1070	1138	1196	1489	2022
for every additional 4 pages	147	169	175	188	231	315

★ **Special Offer** ★ If you order 200 or more reprints you will get a PDF file for half price.

Wiley-VCH Verlag GmbH & Co. KGaA; Location of the Company: Weinheim;
Chairman of the Supervisory Board: Stephen Michael Smith,
Trade Register: Mannheim, HRB 432833, General Partner: John Wiley & Sons GmbH,
Location: Weinheim, Trade Register Mannheim, HRB 432296,
Managing Directors: Dr. Jon Walmsley, Sabine Steinbach

WILEY-VCH

WILEY-BLACKWELL

USING e-ANNOTATION TOOLS FOR ELECTRONIC PROOF CORRECTION

Required software to e-Annotate PDFs: Adobe Acrobat Professional or Adobe Reader (version 7.0 or above). (Note that this document uses screenshots from Adobe Reader X)
The latest version of Acrobat Reader can be downloaded for free at: http://get.adobe.com/uk/reader/

Once you have Acrobat Reader open on your computer, click on the Comment tab at the right of the toolbar:

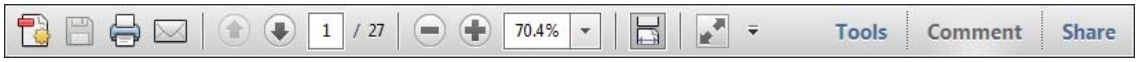

This will open up a panel down the right side of the document. The majority of tools you will use for annotating your proof will be in the Annotations section, pictured opposite. We've picked out some of these tools below:

1. Replace (Ins) Tool – for replacing text.

Strikes a line through text and opens up a text box where replacement text can be entered.

How to use it

- Highlight a word or sentence.
- Click on the Replace (Ins) icon in the Annotations section.
- Type the replacement text into the blue box that appears.

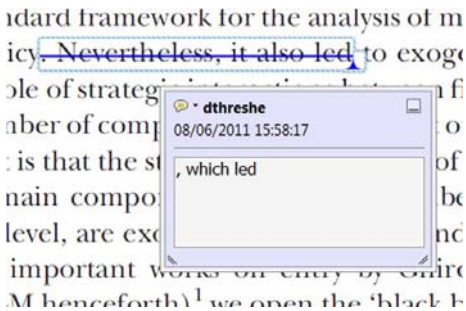

2. Strikethrough (Del) Tool – for deleting text.

Strikes a red line through text that is to be deleted.

How to use it

- Highlight a word or sentence.
- Click on the Strikethrough (Del) icon in the Annotations section.

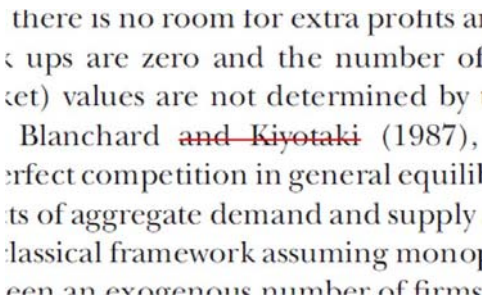

3. Add note to text Tool – for highlighting a section to be changed to bold or italic.

Highlights text in yellow and opens up a text box where comments can be entered.

How to use it

- Highlight the relevant section of text.
- Click on the Add note to text icon in the Annotations section.
- Type instruction on what should be changed regarding the text into the yellow box that appears.

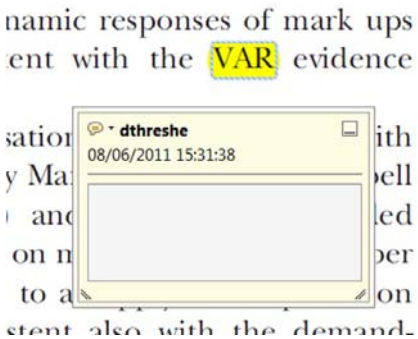

4. Add sticky note Tool – for making notes at specific points in the text.

Marks a point in the proof where a comment needs to be highlighted.

How to use it

- Click on the Add sticky note icon in the Annotations section.
- Click at the point in the proof where the comment should be inserted.
- Type the comment into the yellow box that appears.

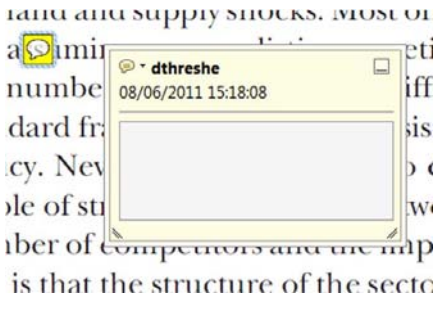

USING e-ANNOTATION TOOLS FOR ELECTRONIC PROOF CORRECTION

5. Attach File Tool – for inserting large amounts of text or replacement figures.

Inserts an icon linking to the attached file in the appropriate pace in the text.

How to use it

- Click on the Attach File icon in the Annotations section.
- Click on the proof to where you'd like the attached file to be linked.
- Select the file to be attached from your computer or network.
- Select the colour and type of icon that will appear in the proof. Click OK.

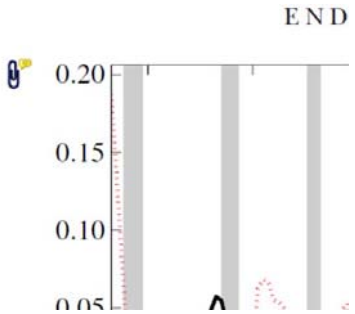

6. Add stamp Tool – for approving a proof if no corrections are required.

Inserts a selected stamp onto an appropriate place in the proof.

How to use it

- Click on the Add stamp icon in the Annotations section.
- Select the stamp you want to use. (The Approved stamp is usually available directly in the menu that appears).
- Click on the proof where you'd like the stamp to appear. (Where a proof is to be approved as it is, this would normally be on the first page).

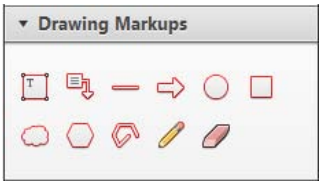

7. Drawing Markups Tools – for drawing shapes, lines and freeform annotations on proofs and commenting on these marks.

Allows shapes, lines and freeform annotations to be drawn on proofs and for comment to be made on these marks..

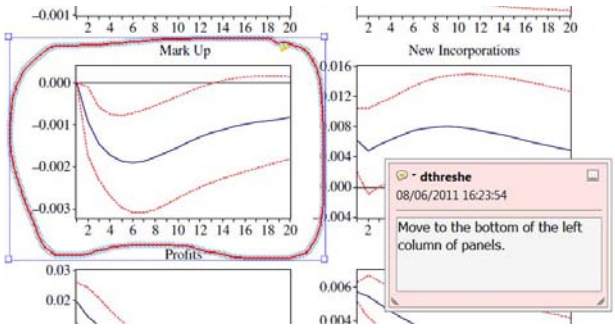

How to use it

- Click on one of the shapes in the Drawing Markups section.
- Click on the proof at the relevant point and draw the selected shape with the cursor.
- To add a comment to the drawn shape, move the cursor over the shape until an arrowhead appears.
- Double click on the shape and type any text in the red box that appears.

For further information on how to annotate proofs, click on the Help menu to reveal a list of further options:

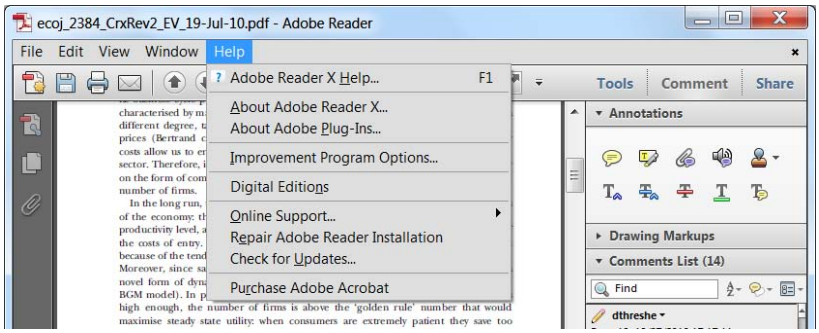

Surface & Coatings Technology 206 (2012) 3823–3831

Contents lists available at SciVerse ScienceDirect

Surface & Coatings Technology

journal homepage: www.elsevier.com/locate/surfcoat

Nanomechanical and nanotribological properties of hydrophobic fluorocarbon dielectric coating on tetraethoxysilane for electrowetting applications

Elias P. Koumoulos, Costas A. Charitidis *, Dimitrios P. Papageorgiou, Athanasios G. Papathanasiou, Andreas G. Boudouvis

National Technical University of Athens, School of Chemical Engineering, 9 Heroon, Polytechniou st., Zografos, Athens, GR-157 80, Greece

ARTICLE INFO

Article history:
Received 27 August 2011
Accepted in revised form 16 January 2012
Available online 26 January 2012

Keywords:
Multilayer
Thin coating
Fluorocarbon
Nanoindentation
Nanoscratch
Mechanical integrity

ABSTRACT

Low voltage electrowetting (EW) systems are typically made of stacks of an insulating dielectric layer underneath a hydrophobic top coating. Of importance here is the strength of adhesion of the coating on the dielectric, investigated through nanoidentation and nanoscratch testing. Improvement of the adhesion strength of the hydrophobic top coating to the main dielectric was attempted through a fluorocarbon interlayer and the stack exhibited improved adhesion strength proven by nanoscratch testing. The difference between the scratch and post-scratch curve corresponds to the elastic recovery of the films, making nanoscratch testing a reliable technique for defining the elastic and plastic regions of thin coatings. The friction mechanisms in accordance with applied load were determined. Additionally, nanoindentation measurements were performed in order to define the hardness and the elastic modulus of the multilayer structure (thickness of layers of few nm). Moreover, the elastic recovery of the stack was investigated and the residual imprints were revealed through SPM imaging. Nanoscratch can be used for a plethora of tests, where a single scratch is useful for critical load, film adhesion and mar studies. Nanoscratch data, coupled with in-situ images, provide detailed information concerning a material's behaviour under simultaneous normal and lateral stresses. The purpose of this work is to investigate the mechanical integrity of an EW device design i.e. contribution of each layer of the stack to the total mechanical integrity. This design is advantageous since it exhibits resistance to dielectric breakdown, higher contact angle modulation range and improved reliability in multiple EW tests.

1. Introduction

Electrowetting (EW) on dielectric is used to enhance the wettability of a dielectric solid substrate by a conductive liquid, by the application of an electric field [1]. The application of external electric fields induces variations of the contact angle of aqueous solutions on insulating surfaces such as polymers, glass, oxides and other dielectrics. An oil ambient electrowetting can provide more than 100° of contact angle modulation reversibly, with fast actuation speeds of the order of milliseconds [2]. As a result, electrowetting is promising for a number of applications such as lab-on-chip devices [3–6], liquid lenses [7,8], electronic displays [9–11] and "smart" microbatteries [12], to name a few. For all these applications it is desirable to use low voltages to induce contact angle changes, through either reduction of the dielectric thickness or the use of ionic surfactants [13]. However, frequent onset of dielectric failure (most commonly; electrolysis) is induced on thin dielectrics at high applied voltages. Consequently, improving the EW aspects that cause device failure, is in quest.

For evaluating the interfacial adhesion strength of thin films, a number of metrology tools have been developed [14–29]. Among them, peel, pull, and bulge tests are only suitable for film stacks with weak interfacial adhesion strengths and often fail to obtain accurate data [25]. The interfacial fracture toughness can be also obtained by a modified edge-lift test [25]. However, significant errors always occur during sample preparation and the determination of delamination. More generally, a four-point bending test is applied to determine the adhesion energy, but the procedures for sample preparation are very complicated [24–27]. Nanoindentation and nanoscratch tests have been widely applied for the measurement of mechanical properties of thin films [28,29].

Nanoscratch testing is a widely used characterization technique for analysis of both thin films and bulk materials. Nanoscratch provides the capability to investigate modes of deformation and fracture that are not possible using standard indentation measurements and is performed by applying a normal load in a controlled fashion while measuring the force required moving the tip laterally across the sample. Many different types of tests can be performed, varying the normal loading profile and lateral displacement pattern. The damage incurred from the test is then typically observed using optical or Scanning Probe Microscopy (SPM) imaging (in-situ SPM imaging of the sample with nanometer resolution for immediate feedback of

* Corresponding author. Tel.: +30 2107724046; fax: +30 2107722339.
E-mail address: charitidis@chemeng.ntua.gr (C.A. Charitidis).

0257-8972/$ – see front matter © 2012 Elsevier B.V. All rights reserved.
doi:10.1016/j.surfcoat.2012.01.034

the test results). Nanoscratch can be used for such a plethora of tests, where a single scratch with a ramped normal load is useful for critical load, film adhesion and mar studies, to name a few. Nanoscratch data, in conjunction with in-situ images, provide a wealth of information concerning a material's behaviour under simultaneous normal and lateral stresses. In the scratch test, a diamond tip is drawn over the film surface under progressively increasing normal load until the film is detached from the substrate. The critical load corresponding to the failure can provide qualitative nature of the scratch resistance or adhesion strength of the film, but it is difficult to extract adhesion strength quantitatively; the critical load depends not only on adhesion strength but also on several intrinsic (testing conditions such as loading rate, scratching speed, and indenter shape) and extrinsic factors (film–substrate system i.e. material properties, friction coefficient, and physical dimensions) [30]. Various models have been developed to obtain cohesive strength of the film and adhesive strength between the film and the substrate via conventional indentation procedure; yet there is no standard methodology for the quantitative assessment [31–34].

In this work, a multi-layered hydrophobic top coating is investigated. The stack consists of a plasma-deposited fluorocarbon and a spin-coated fluoropolymer on top of TEOS. Electrowetting tests on this sandwich-like top coating showed resistance to dielectric breakdown, reversible EW behaviour and improved adhesion strength, compared to other FP coatings tested [34]. The adhesion strength (adhesion to the substrate) was qualitatively assessed through nanoscratch tests. Aiming to realize reliable and robust EW devices, we investigate the mechanical integrity of an EW device design i.e. the contribution of each individual thin layer consisting the stack to the total mechanical integrity.

2. Experimental

Hydrophobic dielectric stacks commonly used in electrowetting experiments, consist of a main dielectric and a hydrophobic top coating. Tetraethoxysilane oxide is deposited via Chemical Vapor Deposition (CVD) on phosphorus-doped Si wafers and is used as the main dielectric; followed by a spin coated layer of hydrophobic Teflon® amorphous fluoropolymer.

In this work, on top of TEOS oxide, an alternative hydrophobic top coating is introduced. A thin plasma FC film (30 nm) is deposited as an adhesion promoter layer for the commercial Teflon® AF 1600 [34]. Teflon® AF (30 nm) is then spin coated on the plasma FC film. After spinning, the sample is baked in air at 95 °C for 5 min. The result is a sandwich-like hydrophobic coating, hereafter called composite coating, which consists of a thin plasma-deposited FC layer and a thin spin coated Teflon® layer. Verification of the thickness of the oxide and the top coating layers was performed with a spectroscopic ellipsometer (accuracy in the measured thickness ± 0.5 nm).

Nanoindentation testing was performed with a nanomechanical test instrument, which allows the application of loads from 1 to 30,000 μN and records the displacement as a function of applied loads with a high load resolution (1 nN) and a high displacement resolution. The nanomechanical test instrument employed in this study is equipped with a Scanning Probe Microscope (SPM), in which a sharp probe tip moves in a raster scan pattern across a sample surface using a three-axis piezo positioner. In all depth-sensing tests a total of 10 indents are averaged to determine the mean hardness (H) and elastic modulus (E) values for statistical purposes, with a spacing of 50 μm, in a clean area environment with 45% humidity and 23 °C ambient temperature. In order to operate under closed loop load or displacement control, feedback control option was used. All nanoindentation measurements have been performed with the standard three-sided pyramidal Berkovich probe, with an average radius of curvature of about 100 nm [35], with 40 s loading and unloading segment time separately and 3 s of holding time, to avoid residual viscoelasticity [36]. Prior to indentation, the area function of the indenter tip was measured in a fused silica, a standard material for this purpose [37].

Based on the half-space elastic deformation theory, H and E values can be extracted from the experimental data (load displacement curves) using the Oliver–Pharr (O&P) method [38], in which derived expressions for calculating the elastic modulus from indentation experiments are based on Sneddon's [39] elastic contact theory:

$$E_r = \frac{S\sqrt{\pi}}{2\beta\sqrt{A_c}} \tag{1}$$

where S is the unloading stiffness (initial slope of the unloading load–displacement curve at the maximum displacement of penetration (or peak load)), A_c is the projected contact area between the tip and the substrate and β is a constant that depends on the geometry of the indenter ($\beta = 1.167$ for Berkovich tip [39]). Conventional nanoindentation hardness refers to the mean contact pressure; this hardness, which is the contact hardness (H_c) is actually dependent upon the geometry of the indenter (Eqs. (2)–(4)).

$$H_c = F/A \tag{2}$$

where,

$$A(h_c) = 24,5{h_c}^2 + a_1 h_c + a_{1/2}{h_c}^{1/2} + \ldots + a_{1/16}{h_c}^{1/16} \tag{3}$$

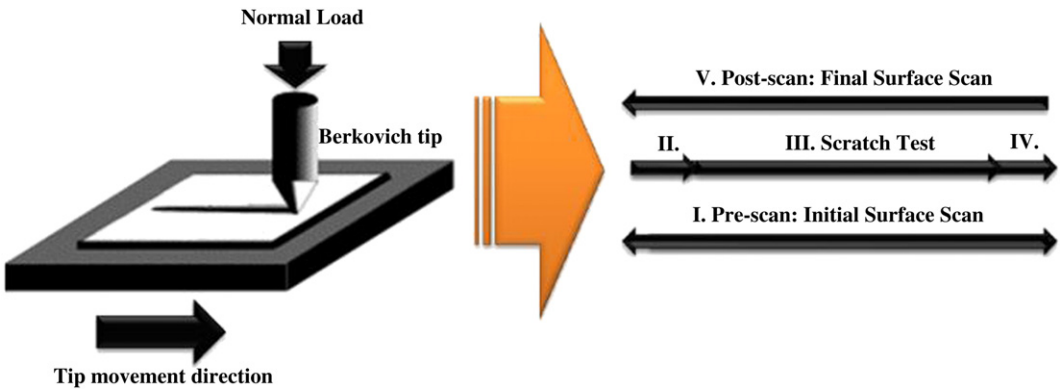

Fig. 1. Representative schematic of nanoscratch segments.

Table 1
Hardness and elastic modulus values for individual materials (Teflon®, FC and TEOS) consisting the multilayer structure.

	Hardness (GPa)	Elastic modulus (GPa)
Teflon® [40]	0.6	2.3
Teflon® [41]	0.025	1.2
Teflon® [42]	0.2	–
Teflon® [43]	0.05	1
TEOS [44]	8	75
plasma FC [43]	1	15

and

$$h_c = h_m - \varepsilon \frac{P_m}{S_m} \quad (4)$$

where h_m is the total penetration displacement of the indenter at peak load, P_m is the peak load at the indenter displacement h_m, and ε is an indenter geometry constant, equal to 0.75 for Berkovich indenter [18,38].

The scratch tests performed in this work included three main segments, namely pre-scan, scratch and post-scan (Fig. 1). Firstly, a pre-scan under a very small load (1 μN) was carried out. Then, the indenter scraped the sample under a certain force and scratch would be generated. The normal applied loads used in this work were 50, 150 and 300 μN. The length of the scratches was 10 μm. Finally, a post-scan under the same load as the pre-scan was conducted to get an image of sample after scratch. An estimation of the residual scratch ditch and the extent of immediate recovery can be obtained by comparing the pre-scratch with the post-scratch image profiles.

3. Results and discussion

3.1. Nanoindentation tests

Hardness and elastic modulus values for individual materials (Teflon®, FC and TEOS) comprising the multilayer structure are presented in Table 1.

The loading–unloading curves of the composite and Teflon® coatings on TEOS are presented in Fig. 2. In all comparative measurements reported hereafter the thickness of the composite and Teflon coatings is identical and equal to 60 nm. Comparison of both samples for identical displacement, (e.g. ~35 nm and ~65 nm), reveals greater resistance to applied load for the composite coating, as higher load is required in order to reach the same displacement as for Teflon® on TEOS (Fig. 2 a, b).

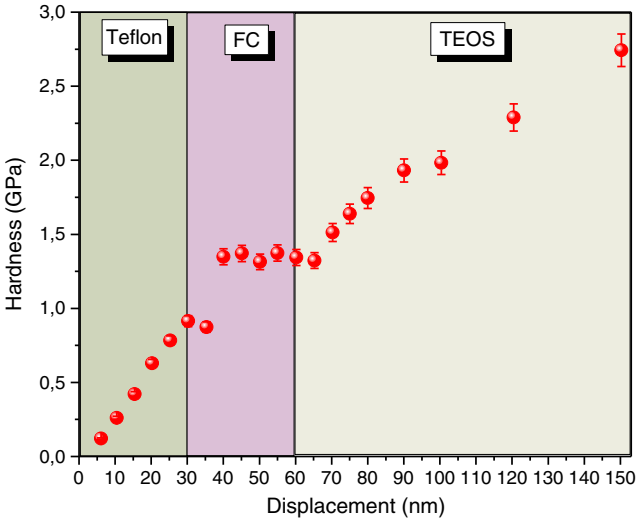

Fig. 3. Hardness vs. displacement for the composite coating on TEOS.

At the beginning of load application, the top Teflon® layer was slightly pressed, and the curves ascended smoothly. As the indentation proceeded, some of the applied load transferred to plasma FC, and shear stresses began to accumulate at the interfaces between the Teflon® film and plasma FC layer due to strain mismatch. At the applied load of 150 μN (indentation depth ~ 35 nm), sufficient shear stresses higher than the interfacial adhesion strength was expected to accumulate, and the interfaces delaminated which was expected to induce a stress release and result in the curve deviations, although no obvious film buckling was recognized from the surface morphology of the film stack at the indented region after nanoindentation test (Fig. 2).

Hardness and elastic modulus values vs. displacement are presented in Figs. 3 and 4, respectively. Nanomechanical behavior of each film consisting the composite coating is obvious (Fig. 5); however, significant substrate effects exist in case of composite coating. In Fig. 3 hardness increases with displacement in teflon and TEOS layer, but remains constant in FC layer. In most of the cases the nanomechanical integrity (e.g. H, E) of a top layer (30 nm Teflon in our case) depends on the material of the layer underneath. A general rule of thumb when testing thin films is to test only the first 10–20% of the film thickness to avoid substrate effect on measurements. In our case, the

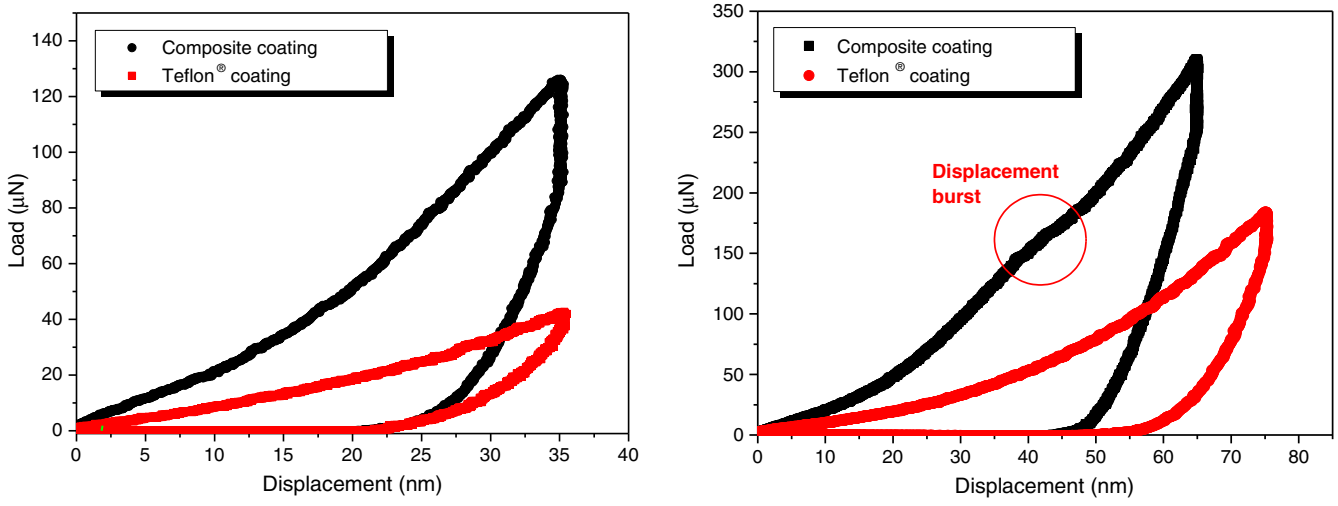

Fig. 2. Comparison of loading–unloading curves of composite and Teflon® coatings on TEOS for two different displacements.

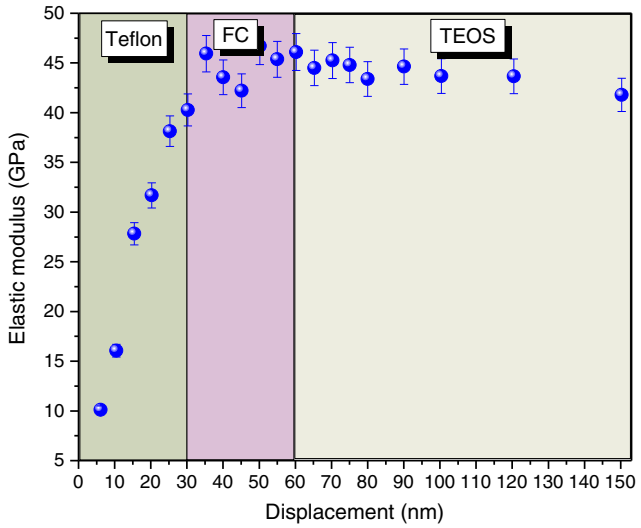

Fig. 4. Elastic modulus vs. displacement for the composite coating on TEOS.

higher percentage of thickness (>20%), the more significant substrate effect occurs [19]. Hardness has always been defined as an engineering parameter, representative of elasto-plastic deformations under a compressive load, not directly related to the atomistic or molecular built-up of the material; while elastic modulus is calculated from the unloading part (first linear section, as regarded by elasticity principles). Thus, elastic modulus is rather influenced by the recovery of the structure, in addition to the fact that both properties are calculated in separate sections of experiment. In Fig. 4 elastic modulus increases with displacement in teflon layer but remains constant in TEOS and FC layers.

3.2. Wear resistance study—H/E and H^3/E^2 ratios

The H/E ratio is of significant interest in tribology. Higher stresses are expected in high H/E, hard materials, and high stress concentrations develop towards the indenter tip, whereas in the case of low H/E, soft materials, the stresses are lower and are distributed more evenly across the cross-section of the material [45,46]. The high ratio of H/E is indicative of the good wear resistance in a disparate range of materials [46]: ceramic, metallic and polymeric (e.g. c-BN, tool steel and nylon, respectively), which

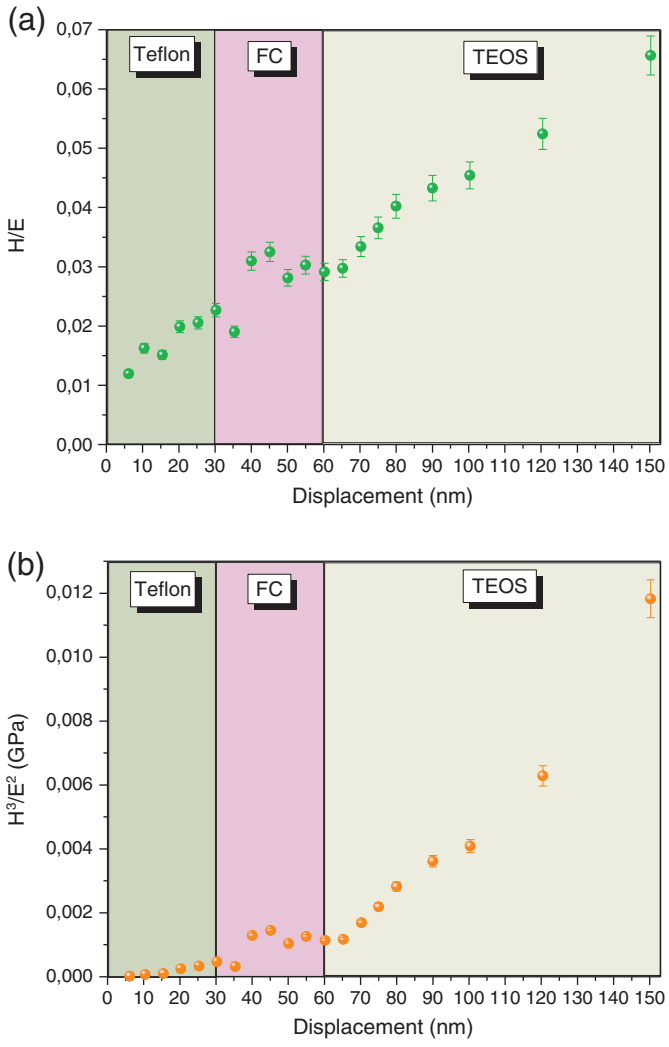

Fig. 6. (a) Hardness to modulus ratio and (b) H^3/E^2 for the composite coating.

are equally effective in resisting attrition for their particular intended application. In Fig. 6a, the change of H/E slope reveals the strengthening of composite coating with increasing displacement. Adhesion relation of a coating with a substrate is confirmed

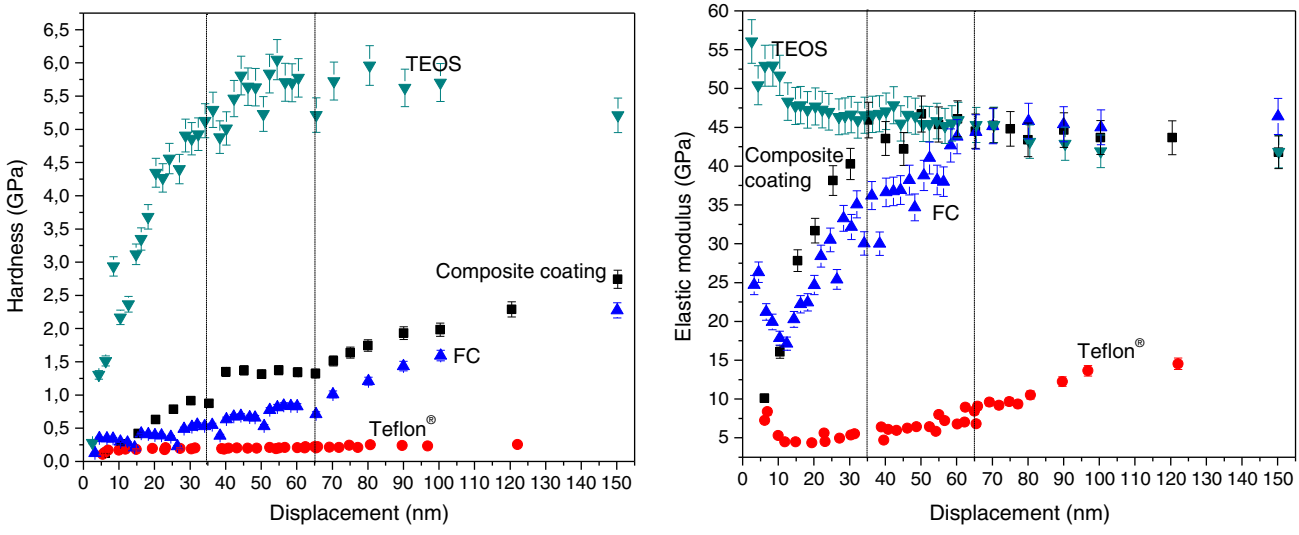

Fig. 5. Hardness and elastic modulus vs. displacement for composite coating and FC, Teflon® and plain TEOS.

by using the Tresca's yield criterion and Tabor's relation, according to which, the load at the onset of yielding is proportional to H^3/E^2. The term H^3/E^2 combines H and E values of a material and describes the amount of elasticity exhibited by the film. In particular, high (low) values of H^3/E^2 indicate a highly elastic (plastic) behaviour of the film under contact events [35,46].

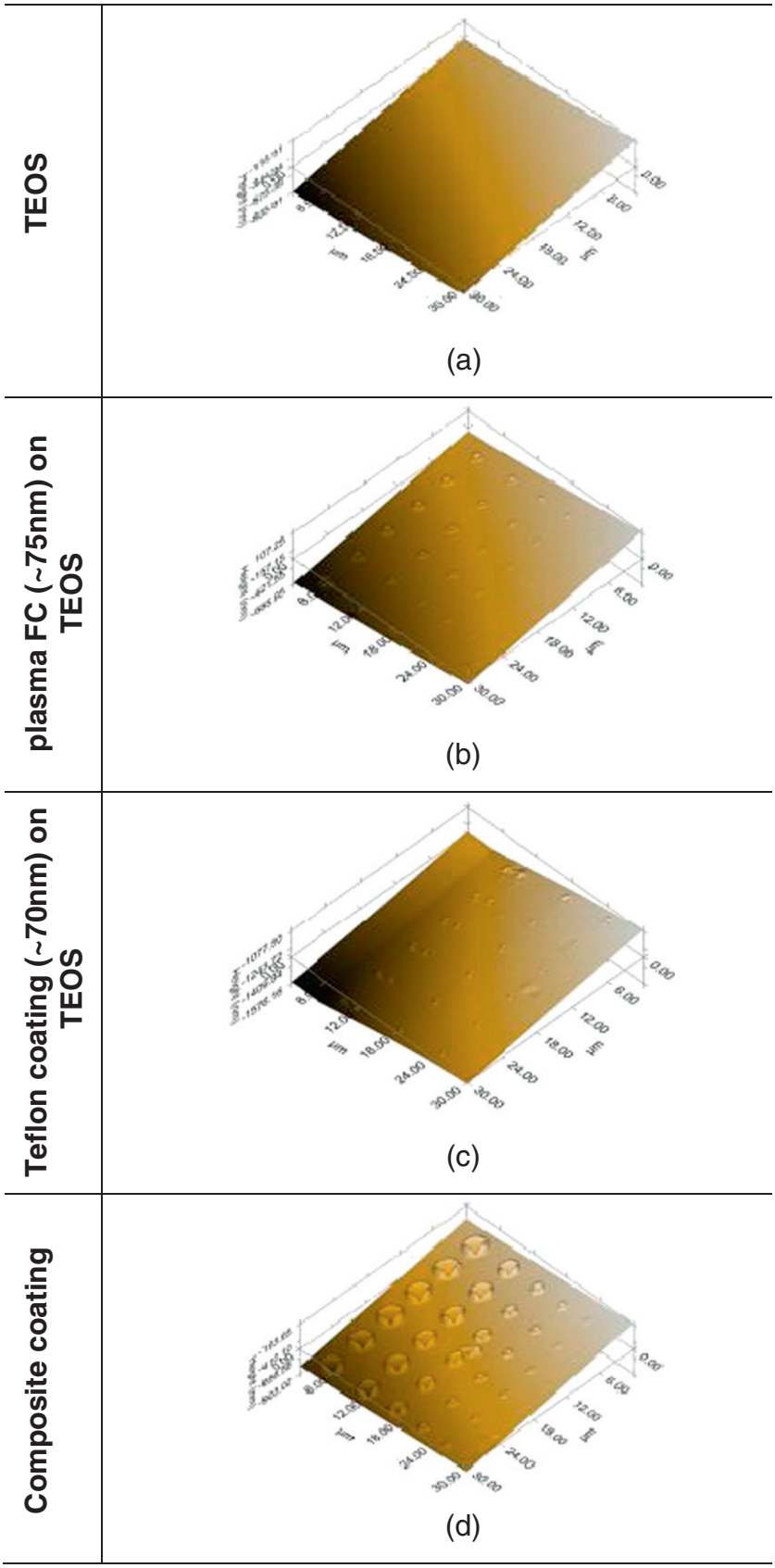

Fig. 7. SPM images for composite coating and FC, Teflon® and TEOS.

The composite coating exhibits higher plastic deformation at low displacement region (~0–60 nm), attributed to Teflon® and FC coating (Fig. 6b), while at ~150 nm the deformation is more elastic (TEOS region).

3.3. Pile-up/sink-in deformation mechanism

The contact area is influenced by the formation of pile-ups and sink-ins during the indentation process. To accurately measure the indentation contact area, pile-ups/sink-ins should be appropriately accounted for. The presence of creep during nanoindentation has an effect on pile-up, which results in incorrect measurement of the material properties. Fischer–Cripps observed this behavior, in case where the measured elastic modulus was much less than expected [47]. Rar et al. observed that the same material when allowed to creep for a long duration produced a higher value of pile-up/sink-in indicating a switch from an initial elastic sink-in to a plastic pile-up [48]. In Fig. 7 SPM images of nanoindentation imprint pattern for all samples are presented; significant pile-up deformation mechanism for the composite coating is observed.

In Fig. 8, the normalized pile-up/sink-in height h_c/h_m is plotted vs. displacement and the normalized hardness H/E. Higher stresses are expected in high H/E, hard materials, and high stress concentrations develop towards the indenter tip, whereas in case of low H/E, soft materials, the stresses are lower and are distributed more evenly across the cross-section of the material [47]. Rate sensitive materials experience less pile-up compared to rate insensitive materials due strain hardening. Cheng and Cheng reported a 22% pile-up for a work hardening exponent [49]. This is consistent with the fact that when h_c/h_m approaches 1 for small H/E, deformation is intimately dominated by pile-up [50,51]. On the other hand, when h_c/h_m approaches 0 for large H/E, it corresponds to purely elastic deformation and is apparently dominated by sink-in in a manner prescribed by Hertzian contact mechanics [52]. The composite coating exhibits a switch from pile-up to sink-in deformation in the interface of FC layer and TEOS (Fig. 9). In Fig. 10 SPM images of nanoindentation imprint in the composite coating are presented. The surface roughness is ~20 nm, and the pile-up effect around the imprint is also significant. The interface between top Teflon® layer and FC is noted with red circle.

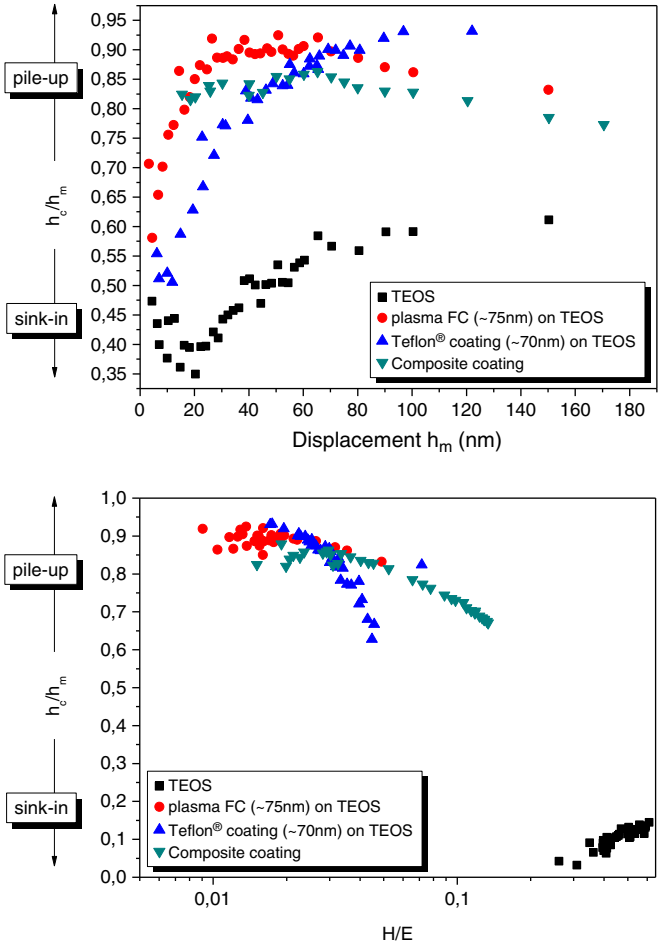

Fig. 8. Pile-up/sink-in deformation mechanisms investigation for composite coating and FC, Teflon® and TEOS samples.

3.4. Scratch tests

The prescan curve corresponds to the profile of the initial surface, scratch scan curve corresponds to the tip penetration profile during testing and finally, post scan curve corresponds to the final profile of the surface after scratching. In this way, the post scan curve represents the residual depth of scratch trace after unloading, i.e. the plastic deformation of the probed film. The difference between scratch and post scan curve corresponds to the elastic recovery of the films. The surface morphologies of the scratches of the two samples under 50 μN and the corresponding initial and residual scratch profiles are displayed in Fig. 11 (also shown in [34], Fig. 3). The arrows in the figure represent the sliding direction of the indenter tip. Comparing the profiles, the recovered scratch depth of the composite coating is close to ~30 nm, but just about ~15 nm for Teflon® coating on TEOS.

Additionally, the three stages in Fig. 11b corresponding to different mechanical behaviour could be attributed to the specific microstructure of the multilayer structure. More precisely, for normal loads lower than 18 μN (stage I), the penetration depth of the indenter did not exceed 30 nm and could be correlated to the mechanical response of the top layer (Teflon®). For normal loads higher than 18 μN and lower than 30 μN (stage II), the higher slope of the curve indicates that the underlying film was somewhat harder. Finally, for normal loads up to 50 μN (stage III), the slope of the curve was found similar to stage I.

As seen in the images in Fig. 12, there is a buildup of polymer material mostly on only one side of the scratch [53]. As the indenter moves along the surface, the displaced material forms a pile-up which accumulates on the sides of the scratch. A groove is formed which is roughly of the shape of a triangular prism. For the Berkovich tip, it should be noted that the orientation of the tip with respect to the scratch direction is very important. As the indenter scratches, total volume swiped by the indenter will depend on the projected

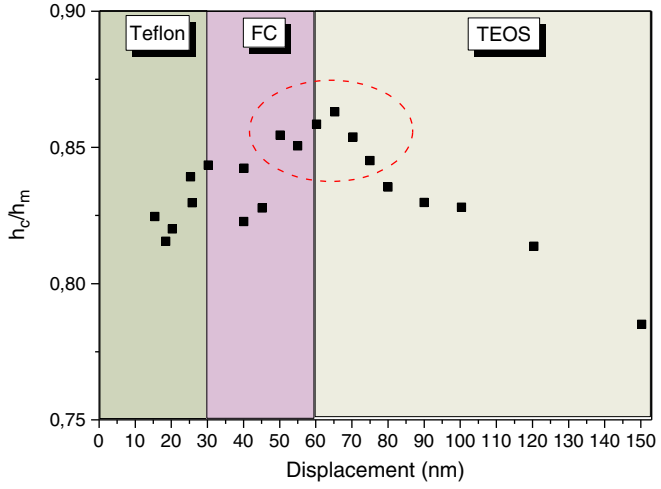

Fig. 9. Pile-up/sink-in deformation switch (in red dashed circle) for the composite coating.

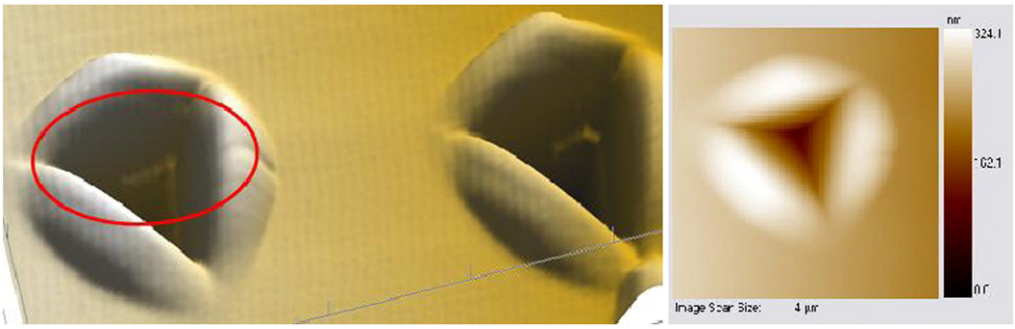

Fig. 10. SPM images of nanoindentation imprint in the composite coating.

area of the indenter along the scratch axis. These buildups are found on the same side of all scratches created, a fact that leads to the conclusion that the films were plastically deformed (buildup is most likely an accumulation of compressed materials).

When the scratch tip ploughs through the material ahead of it, the material will be either pushed forward or piled up sideways [54]. This phenomenon is usually observed for relatively ductile polymers, where ironing and plastic deformation take place readily. In addition to the surface friction between the substrate and the scratch tip, the material accumulated ahead of the tip.

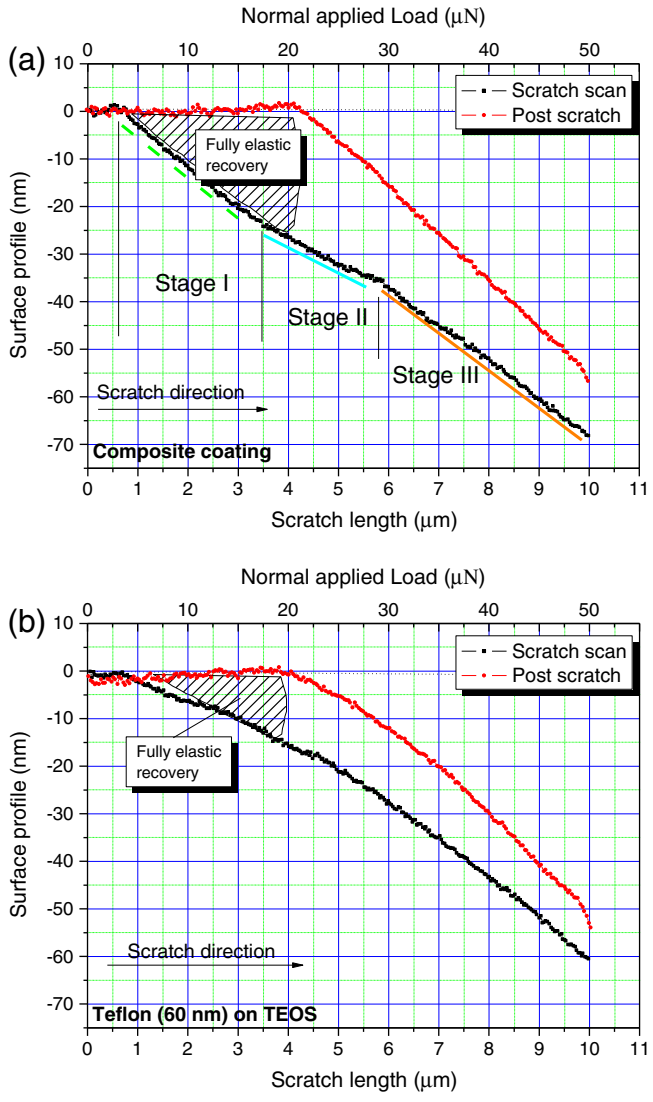

Fig. 11. Nanoscratch depth profiles of the two samples with applied load of 50 µN.

In Fig. 13, the scratch groove depth is given as a function of the applied normal load. It can be observed that the groove depth increases almost linearly with increasing load, as it is often reported in classical wear tests [55] and investigations in nanoscratching of similar multilayer geometries [56]. For the lowest applied load, both samples presented practically close behavior in the nanoscratch groove depth, but it increased as the normal load advanced [57]. It can be seen that the Teflon® coating on TEOS clearly appeared as the worst coating in terms of the nanoscratch resistance. On the other hand, the composite coating exhibited a more similar grooving resistance, exhibiting a lower groove depth at a load of 300 µN.

The friction coefficient (μ) is defined as the ratio of the tangential force to the normal force. These friction coefficients represent, in principle, the friction between the multilayers and diamond indenter. They can be viewed as dynamic, rather than static, friction coefficients. The increase of (μ) with normal load could be attributed to the increasing plastic deformation of the films which at the same time are worn out during testing.

The typical curve of friction coefficient values versus scratch length is shown in Fig. 14. In nanoscratch testing, it is generally observed that the lateral force does not linearly increase with the applied load. In other words, the apparent friction coefficient, defined as the ratio between the lateral force and the applied load, does not have a constant value. Comparison of simulations and experiments has shown that the non-linear behavior of the lateral force with the applied load may be mainly explained by the fact that the indenter is not perfectly sharp but has a rounded extremity [58]. The friction coefficient changes from 1 to 0.5 continuously at the beginning of scratching, which is corresponding to the loading stage. Then it keeps invariant at 0.5 for about 25 s during the steady scratching process. The average values of the steady stage are taken as the effective friction coefficient. These coefficient trends of both samples are quite similar, implying no significant differences between the two samples; however, there is a slight decrease of friction coefficient in the case of composite coating almost at the end of the scratch length.

For the composite coating, the friction coefficient decreases with increasing normal load to a minimum value (~0.4) corresponding to the initiation of scratching, regime I, then increases to a maximum value (~0.45), regime II, and, finally decreases (~0.3), regime III. The main friction mechanism in regime I was adhesion, while both adhesion and ploughing contribute to the friction coefficient in regimes II and III. For Teflon® coating on TEOS, the friction coefficient decreases with increasing normal load to a minimum value (~0.4) and remains constant, implying plastic flow is the dominant deformation mode. When a polymer undergoes extensive plastic deformation during scratching and the deformation is characterized by the ductile flow of the material around the indenter tip, a ploughing mechanism is encountered of the type seen with soft polymers. For Teflon® coating, the ploughing occurs without any evidence of discrete failure; it

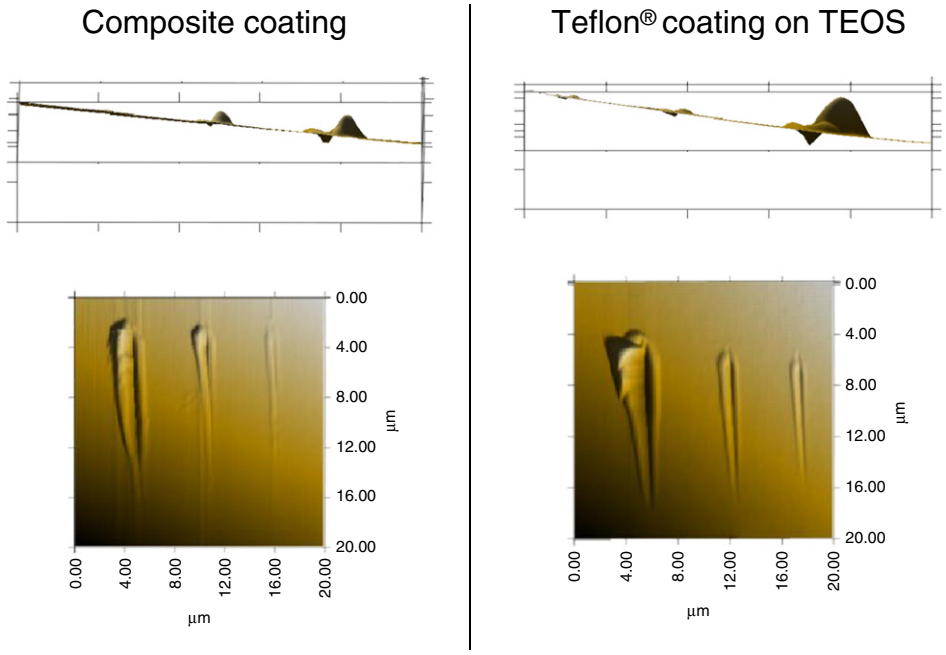

Fig. 12. SPM images of nanoscratch tests for applied load of 50, 100 and 300 µN.

is reported that this mechanism may be accompanied by a significant viscoelastic recovery at the rear of the contact and the formation of well-defined edges on the sides of the scratch grooves. It is appropriate, therefore, to term this type of deformation a viscoelastic–plastic ploughing, for the case of Teflon® coating. The composite coating showed higher elastic recovery than Teflon® coating on TEOS under the same normal load, implying that sustain higher scratch induced stresses.

As the load reaches a certain film value, the vertical depth of the scratch abruptly increases. This load is usually termed as the critical load (L_c). The adhesion strength to substrates, coating cracking, delamination and brittle fracture caused by scratch testing can be sensitively detected and characterized by the L_c at which any of the coating failures occurred [59] (introducing resistance against the tip movement [60]).

In Fig. 15 (also shown in [34], Fig. 5) normal load is plotted along with lateral displacement, since the tip scratches the surface under progressively increasing normal load and along the predefined path. The load at which a sudden rise in scratch length is investigated is the critical load. As denoted by the arrow, lateral displacement (or normal load) burst is observed at ~5.5 µm of scratch length that corresponds to an abrupt change in normal load at ~150 µN, proving weakening of strength (heterogeneity) [34,61].

4. Conclusions

In this work the adhesion strength of hydrophobic dielectric coatings for electrowetting applications, was investigated. Through nanoindentation testing, sufficient shear stresses higher than the interfacial adhesion strength were expected to accumulate. The interfaces delaminated inducing a stress release and resulting in the curve deviations, although no obvious film buckling was recognized from the surface morphology of the film stack at the indented region after nanoindentation test.

Nanoscrach testing was conducted to examine the mechanical interlayer properties of the proposed hydrophobic dielectric stack.

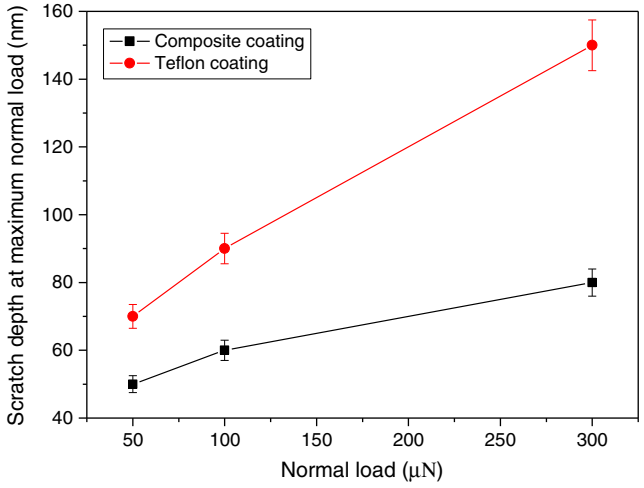

Fig. 13. Variation of nanoscratch groove depth against normal load for composite and Teflon® coatings on TEOS.

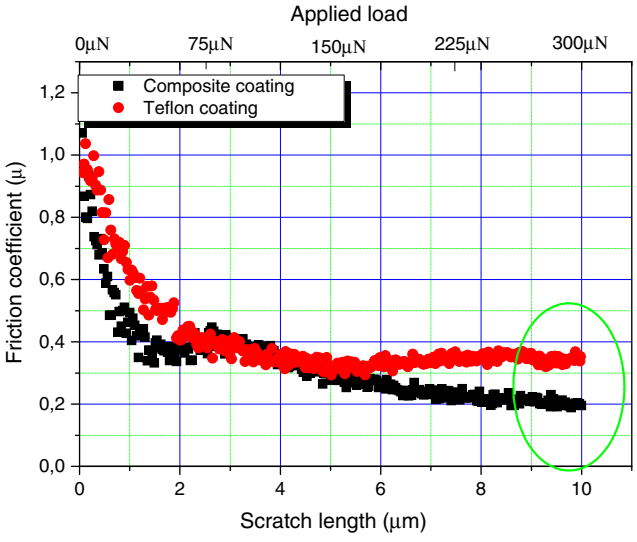

Fig. 14. Representative curves of friction coefficient values vs. scratch length for composite and Teflon® coatings on TEOS.

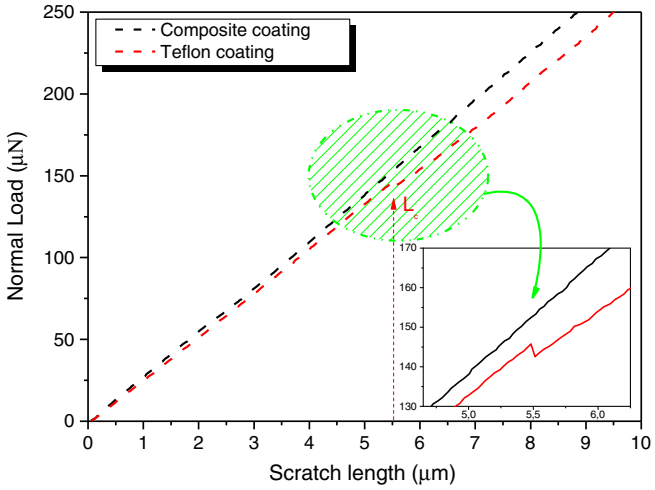

Fig. 15. Typical curve of friction coefficient values vs. scratch length for composite coating and Teflon® 60 nm on TEOS.

In terms of adhesion strength to TEOS substrate the sandwich-like hydrophobic top coating is superior to Teflon® coating. Comparing the scratch profiles, the recovered scratch depth of the composite coating on TEOS is close to ~30 nm, but just about ~15 nm for Teflon® coating on TEOS.

The change of H/E slope reveals the strengthening of composite coating with increasing displacement, while the composite coating exhibits higher plastic deformation at low displacement region (~0–60 nm), attributed to Teflon® and FC coating (at ~150 nm the deformation is more elastic (TEOS region)). The composite coating exhibits a switch from pile-up to sink-in deformation in the interface of FC layer and TEOS. Comparing the scratch profiles, the recovered scratch depth of the composite coating is close to ~30 nm, but just about ~15 nm for Teflon® coating on TEOS. A buildup of polymer material on only one side of the scratch was revealed through SPM imaging, and the coefficient of friction along with scratch mechanisms were investigated and discussed.

Acknowledgements

Authors D.P. Papageorgiou, A.G. Papathanasiou and A.G. Boudouvis kindly acknowledge the financial support of the European Research Council (ERC), through a Starting Grant (Grant agreement no. [240710]). The authors thank Drs. E. Gogolides and A. Tserepi at the Institute of Microelectronics, NCSR 'Demokritos', for their expert advice in plasma processing.

References

[1] M. Vallet, M. Vallade, B. Berge, Eur. Phys. J. B 11 (1999) 583.
[2] F. Mugele, Soft Matter 5 (2009) 3377.
[3] I. Barbulovic-Nad, H. Yang, P.S. Park, A.R. Wheeler, Lab. Chip 8 (2008) 519.
[4] B. Fair, Microfluid. Nanofluid. 3 (2007) 245.
[5] E.M. Miller, A.R. Wheeler, Anal. Bioanal. Chem. 393 (2009) 419.
[6] H. Moon, A.R. Wheeler, R.L. Garrell, J.A. Loo, C.J. Kim, Lab. Chip 6 (2006) 1213.
[7] B. Berge, J. Peseux, Eur. Phys. J. E 3 (2000) 159.
[8] S. Kuiper, B.H.W. Hendriks, Appl. Phys. Lett. 85 (2004) 1128.
[9] R.A. Hayes, B.J. Feenstra, Natural 425 (2003) 383.
[10] J. Heikenfeld, K. Zhou, E. Kreit, B. Raj, S. Yang, B. Sun, A. Milarcik, L. Clapp, R. Schwartz, Nat. Photonics 3 (2009) 292.
[11] K. Zhou, J. Heikenfeld, K.A. Dean, E.M. Howard, M.R. Johnson, Micromech. Microeng. 19 (2009) 1.
[12] V.A. Lifton, J.A. Taylor, B. Vyas, P. Kolodner, R. Cirelli, N. Basavanhally, A. Papazian, R. Frahm, S. Simon, T. Krupenkin, Appl. Phys. Lett. 93 (2008) 1.
[13] S. Berry, J. Kedzierski, B. Abedian, Colloid Interface Sci. 303 (2006) 517.
[14] S.Y. Chang, H.L. Chang, Y.C. Lu, S.M. Jang, S.J. Lin, M.S. Liang, Thin Solid Films 460 (2004) 167.
[15] A.A. Volinsky, N.R. Moody, W.W. Gerberich, Acta Mater. 50 (2002) 441.
[16] Q. Ma, Mater. Res. 12 (1997) 840.
[17] R.H. Dauskardt, M. Lane, Q. Ma, N. Krishna, Eng. Fract. Mech. 61 (1998) 141.
[18] W.C. Oliver, G.M. Pharr, Mater. Res. 7 (1992) 1564.
[19] A.C. Fischer-Cripps, Nanoindentation, Springer-Verlag, New York, 2002.
[20] A. Gouldstone, H.J. Koh, K.Y. Zeng, A.E. Giannakopoulos, S. Suresh, Acta Mater. 48 (2000) 2277.
[21] S.Y. Chang, T.Q. Chang, Y.S. Lee, J. Electrochem. Soc. 152 (2005) 657.
[22] A.A. Volinsky, J.B. Vella, W.W. Gerberich, Thin Solid Films 429 (2003) 201.
[23] T. Dharma Raju, K. Nakasa, M. Kato, Acta Mater. 51 (2003) 457.
[24] S.J. Bull, J. Phys. D 38 (2005) 393.
[25] J. Malzbender, J.M.J. den Toonder, A.R. Balkenende, G. de With, Mater. Sci. Eng. 36 (2002) 47.
[26] S.J. Bull, D.S. Rickerby, Surf. Coat. Technol. 42 (1990) 151.
[27] S.J. Bull, Surf. Coat. Technol. 50 (1991) 25.
[28] S. Benayoun, L.B. Fouilland-Paillé, J.J. Hantzpergue, Thin Solid Films 352 (1999) 156.
[29] J.H. Lee, W.M. Kim, T.S. Lee, M.K. Chung, B.K. Cheong, S.G. Kim, Surf. Coat. Technol. 133–134 (2000) 220.
[30] D.J. Morris, R.F. Cook, Mater. Res. Soc. Symp. Proc. 766 (2003) E9.3.
[31] R.F. Cook, D.J. Morris, J. Thurn, Mater. Res. Soc. Symp. Proc. 795 (2004) U.4.1.
[32] J. Malzbender, G. de With, J. Non-Cryst. Solids 265 (2000) 51.
[33] J. Malzbender, G. de With, J.M.J. den Toonder, Thin Solid Films 366 (2000) 139.
[34] D.P. Papageorgiou, E.P. Koumoulos, C.A. Charitidis, A.G. Boudouvis, A.G. Papathanasiou, J. Adhesion Sci. Technol. (2011), doi:10.1163/156856111X600226.
[35] C.A. Charitidis, Int. J. Refract. Met. Hard Mater 28 (2010) 51.
[36] G. Feng, A.H.W. Ngan, Mater. Res. 17 (2002) 660.
[37] H. Bei, E.P. George, J.L. Hay, G.M. Pharr, Phys. Rev. Lett. 95 (2005) 1.
[38] M. Troyon, L. Huang, Surf. Coat. Technol. 201 (2006) 1613.
[39] I.N. Sneddon, Proc. Camb. Philos. Soc. 44 (1948) 492;
R.B. King, Int. J. Solids Struct. 23 (1987) 1657.
[40] J. Wang, H.K. Kim, F.G. Shi, B. Zhao, T.G. Nieh, Thin Solid Films 377–378 (2000) 413.
[41] X. Li, B. Bhushan, Mater. Charact. 48 (2002) 11.
[42] T.Y. Zhang, W.H. Xu, M.H. Zhao, Acta Mater. 52 (2004) 57.
[43] G. Tang, X. Ma, M. Sun, X. Li, Carbon 43 (2005) 345.
[44] F. Chen, B. Li, T.D. Sullivan, C.L. Gonzalez, C.D. Muzzy, H.K. Lee, M.D. Levy, M.W. Dashiell, J. Kolodzey, J. Vac. Sci. Technol., B 18 (2000) 2826.
[45] Y.T. Cheng, C.M. Cheng, Surf. Coat. Technol. 133–134 (2000) 417.
[46] A. Leyland, A. Matthews, Surf. Coat. Technol. 177–178 (2004) 317.
[47] A.C. Fischer-Cripps, Mater. Sci. Eng., A 385 (2004) 74.
[48] A. Rar, S. Sohn, W.C. Oliver, D.L. Goldsby, T.E. Tullis, G.M. Pharr, Mater. Res. Soc. (2005) Boston. MA. USA.
[49] Y.T. Cheng, C.M. Cheng, Philos. Mag. Lett. 78 (1998) 115.
[50] R. Hill, B. Storakers, A.B. Zdunek, Math. Phys. Sci. 423 (1989) 301.
[51] S. Biwa, B. Storakers, J. Mech. Phys. Solids 43 (1995) 1303.
[52] H. Hertz, (1896). Miscellaneous Papers by H. Hertz, Macmillan.
[53] H.Y. Nie, M.J. Walzak, N.S. McIntyre, Appl. Surf. Sci. 253 (2006) 2320.
[54] H. Jiang, R. Browning, A. Moyse, H.J. Sue, Appl. Surf. Sci. 254 (2008) 4494.
[55] J.F. Archard, Appl. Phys. 241 (1953) 891.
[56] J.W. Lee, J.G. Duh, Surf. Coat. Technol. 188–189 (2004) 655.
[57] A.A.C. Recco, C.C. Viafara, A. Sinatora, A.P. Tschiptschin, Wear 267 (2009) 1146.
[58] S. Lafaye, M. Troyon, Wear 261 (2006) 905.
[59] X. Zhang, L. Hu, D. Sun, Acta Mater. 54 (2006) 5469.
[60] G.T. Lim, J.N. Reddy, H.J. Sue, ACS Symp. Ser. 912 (2005) 166.
[61] B.R. Kim, M.J. Ko, Thin Solid Films 517 (2009) 3216.

VSP *J. Adhesion Sci. Technol. (2011)* DOI:10.1163/156856111X600226

Journal of ADHESION SCIENCE and TECHNOLOGY
brill.nl/jast

Evaluating the Robustness of Top Coatings Comprising Plasma-Deposited Fluorocarbons in Electrowetting Systems

Dimitrios P. Papageorgiou, Elias P. Koumoulos, Costas A. Charitidis, Andreas G. Boudouvis and Athanasios G. Papathanasiou *

School of Chemical Engineering, National Technical University of Athens, GR-15780 Athens, Greece

Abstract

Thin dielectric stacks comprising a main insulating layer and a hydrophobic top coating are commonly used in low voltage electrowetting systems. However, in most cases, thin dielectrics fail to endure persistent electrowetting testing at high voltages, namely beyond the saturation onset, as electrolysis indicates dielectric failure. Careful sample inspection via optical microscopy revealed possible local delamination of the top coating under high electric fields. Thus, improvement in the adhesion strength of the hydrophobic top coating to the main dielectric is attempted through a plasma-deposited fluorocarbon interlayer. Interestingly enough the proposed dielectric stack exhibited (a) resistance to dielectric breakdown, (b) higher contact angle modulation range and (c) electrowetting cycle reversibility. Appearance of electrolysis in the saturation regime is inhibited, suggesting the use of this hydrophobic dielectric stack for the design of more efficient electrowetting systems. The possible causes of the improved performance are investigated by nanoscratch characterization.

Keywords

Electrowetting, plasma fluorocarbon deposition, hydrophobic coating, nanoscratch, adhesion strength

1. Introduction

Electrowetting (EW) deals with the enhancement of the wetting properties of solids by the modification of the electric charge density at a liquid/solid interface. Suitable application of external electric field induces variation of the contact angle of conductive liquids on insulating substrates such as polymers, glass and oxides. EW can provide more than 100° of contact angle modulation reversibly, especially in an oil ambient, with fast response to actuation in the order of milliseconds [1]. As a result, EW has been utilized for a number of technological applications such as lab-on-chip devices [2, 3], liquid lenses [4, 5], electronic displays [6, 7] and 'smart' microbatteries [8], to name a few. For all these applications it is desirable to use low voltages

* To whom correspondence should be addressed. Tel.: +30-2107723290; e-mail: pathan@chemeng.ntua.gr

 DOI:10.1163/156856111X600226

to induce contact angle changes, through either reduction of the dielectric thickness or the use of ionic surfactants [9]. However, indication of dielectric failure (most commonly electrolysis) is frequent, especially in cases of thin dielectrics. Consequently, improving the robustness of the dielectric is of great importance since it is related to the robustness of devices.

Electrowetting on dielectric (EWOD, usually called EW) can be realized when a conductive sessile drop sits on a hydrophobic dielectric on top of a conductive electrode [10]. The dependence of the contact angle, θ_V, on the applied voltage, V, is given by the Lippmann equation [11],

$$\cos\theta_V = \cos\theta_Y + \frac{1}{2\gamma} C V^2, \quad C = \varepsilon_0 \varepsilon_r / d, \tag{1}$$

where θ_Y is the Young's contact angle and γ is the liquid surface tension. C is the capacitance per unit area, d is the thickness of the dielectric with dielectric constant ε_r and ε_0 is the permittivity of vacuum. Lippmann equation demonstrates reliable predictions of θ_V at low voltages, however at high voltages experiments show that, beyond a critical voltage, V_s, the contact angle (CA) reaches a lower limit in contradiction to equation (1) which predicts complete wetting, i.e., $\theta_V = 0°$ at sufficiently high applied voltage. This phenomenon is widely known as CA saturation that limits the EW response to the applied voltage. Recent studies attribute the CA saturation to leakage current mechanisms, i.e., dielectric breakdown [12], dielectric charge trapping [13, 14] and air ionization [15] caused by the increased electric field strength in the vicinity of the three-phase contact line (TPL). Material breakdown at the onset of saturation coupled with the charge leakage propagating through the dielectric is of great research importance, as the understanding of the related mechanisms could lead to more efficient EW devices.

A usual choice for hydrophobic dielectric is stand-alone amorphous fluoropolymers (FPs). Stand-alone FPs inherently feature high porosity of the polymeric compound. The pores are considered to be conductive paths, which could lead more easily to dielectric breakdown in EW experiments especially when thin FP films are used. High porosity of the FP films is related to substantial charge injection; pore density affects charge injection which is related to limited EW response to the applied voltage. For this purpose, superior dielectrics in terms of insulation properties are used (e.g., SiO_2, Si_3N_4, tetraethoxysilane (TEOS)) which have lower porous density than FPs, thus dielectric breakdown is suppressed.

Since EW can only reduce CA, the chosen dielectric should be hydrophobic so as to achieve the highest CA modulation range possible. As a result, it is evident that a hydrophobic dielectric stack, namely a main insulating layer and a hydrophobic top coating, is requisite to attain high CA modulation and improved resistance to dielectric breakdown. This approach gives rise to separate optimization of the dielectrics and the hydrophobic coatings for the benefit of the EW response to the applied voltage.

In the case of dielectric optimization, stacked main dielectrics, such as SiO_2–Si_3N_4–SiO_2 (oxide–nitride–oxide (ONO)) have been investigated extensively for

use in integrated circuit memories. It was found that this type of structure exhibits higher breakdown field than the conventional single layer dielectrics (i.e., SiO_2, Si_3N_4). Tested ONO samples in our group [16] showed roughly 25% higher saturation voltage and almost 10° higher CA modulation, than the equivalent SiO_2 dielectric.

FPs as hydrophobic top coatings are an intriguing part of the hydrophobic dielectric investigated. In addition to the commercially available FPs (Teflon®, Cytop® and FluoroPel®), plasma-deposited fluorocarbons (FCs) were used as hydrophobic top coatings, which feature several distinct advantages [17]. Plasma technology is still under investigation for EW applications. Also self-assembled monolayers (SAMs) are used as hydrophobic coatings, however, the CA electrowetting irreversibility limits SAMs applicability in devices [18].

The main objective of this study was to improve the performance of the hydrophobic dielectric in terms of resistance to dielectric breakdown in EW tests and provide an estimation of the top coating adhesion strength to the oxide substrates tested.

Experiments in our group showed that a possible cause of EW degraded response might be the inadequate adhesion of the hydrophobic top coating to the main insulating substrate, coupled with the high porosity of the top coating material. Usually during EW sample testing, for applied voltages higher than V_s (saturation voltage), bubbles rise inside the liquid drop signaling electrolysis and ultimately sample failure. Detailed post inspection of the sample surface showed that the top coating starts to fail, in the form of random surface micro-cracks. Moreover, in some cases local delamination of the top coating from the substrate was noticeable. To study the potential of improving the adhesion strength of the top coating to the substrate and to reduce the porosity aspects of the hydrophobic dielectric, a plasma-deposited FC layer was implemented [19, 20]. EW experiments were conducted on this proposed hydrophobic dielectric stack as well as qualitative evaluation of the top coating adhesion to the main dielectric was attempted through nanoscratch tests.

Nanoscratch testing is a versatile tool for analysis of the mechanical properties of thin films and bulk materials. In scratch tests, a diamond stylus is drawn over the film surface under progressively increasing normal load (NL) until the film is detached from the substrate.

Single scratches with a ramped NL are useful for critical load (L_c), film adhesion and mar studies. The critical load (L_c), corresponding to film delamination, can provide a measure of the scratch resistance or adhesion strength of the film, but it is difficult to extract adhesion strength quantitatively since the critical load depends not only on adhesion strength but also on several intrinsic and extrinsic factors. While the intrinsic factors are related to the test conditions such as loading rate, scratching speed and indenter shape, the extrinsic parameters are connected to film–substrate system such as material properties, friction coefficient and physical dimensions [21]. That is why, all adhesion measurement techniques (including scratch test) are generally considered to measure what is called ‘practical adhesion’

[22]. Though various models have been developed to obtain cohesive strength of the film and adhesion strength between the film and the substrate via conventional indentation procedure, there is no standard methodology for quantitative assessment.

Reported herein is a sandwich-like hydrophobic top coating comprising a plasma-deposited fluorocarbon and a spin-coated fluoropolymer on top of TEOS. EW tests on this proposed composite top coating showed resistance to dielectric breakdown, reversible EW behavior and improved adhesion strength, compared to other FP coatings tested. Comparison of the adhesion strength (adhesion to the substrate) between the composite coating and FP coatings commonly used in EW experiments was qualitatively assessed through nanoscratch tests. Our objective was to estimate whether the interlayer mechanical properties were a key factor in EW device design.

2. Materials and Methods

Various hydrophobic dielectric stacks were fabricated on phosphorus-doped Si wafers which were also used as ground electrodes (resistivity, 1–10 Ω/cm). The hydrophobic dielectric stacks consisted of a main dielectric and a hydrophobic top coating. SiO_2 or TEOS were used as the main dielectrics. Commercial amorphous fluoropolymers (AFs) such as Asahi Cytop® 809M, Teflon® AF 1600, and plasma-deposited fluorocarbons (FCs) were used as hydrophobic top coatings.

The adhesion strength of Teflon® to various substrates is most commonly improved with the use of silanes. As a result, fluorosilanes are used as primers for the Teflon® AF [23] and, in particular, perfluorooctyltriethoxysilane solution is spin-coated onto the oxide layer and the coated wafers are heated at 95°C for 15 min. Teflon® AF is then spun on top of the fluorosilane layer.

Asahi Cytop® 809M, as a commercial AF alternative, is diluted in perfluorohexene and spun on top of SiO_2 (35 nm thick Cytop®). A special process sequence, in an oven, is needed for the Cytop® to adhere well to the oxide surface.

In this work, on top of TEOS, an alternative hydrophobic top coating was used. A thin plasma FC film (30–100 nm) was deposited as an adhesion promoter layer for the commercial Teflon® AF [19]. Teflon® AF (30–60 nm) was diluted in Fluorinert® Fluid FC-77 solvent, and then spin-coated on the plasma FC film. After spinning, the sample was baked in air at 95°C for 5 min.

Verification of the thicknesses of the oxide and the top coating layers was performed with a spectroscopic ellipsometer model M2000 from J. A. Woolam Co. (accuracy in the measured thickness ±0.5 nm).

AC Electrowetting (2.3 kHz sine wave) measurements are conducted in oil ambient. The samples are immersed in a completely transparent poly(methyl methacrylate) (PMMA) oblong tank filled with 99+% pure dodecane. The sessile droplet consists of 0.1% sodium dodecyl sulfate (SDS) in 0.1 N NaCl (conductivity ≈ 11.22 mS/cm).

Measurements of the dependence of the CA on the applied voltage were performed in an in-house built EW experimental setup, previously described in Papathanasiou *et al.* [16]. Real time image processing software, that was developed in-house, was used to analyze the drop shape. The method is described in [16] and the accuracy is of the order of $\pm 1.5°$.

The surface of the hydrophobic top coatings was inspected in detail with an optical microscope (Zeiss AX10 Imager.A1m). Immediately after the EW experiments the sessile drop was removed from the sample for optical characterization of the drop's footprint.

Nanoscratch testing was performed with Hysitron TriboLab® Nanomechanical Test Instrument, which allows the application of loads from 1 to 10 000 μN and records the displacement dependence on applied load with high load (1 nN) and high displacement (0.04 nm) resolution. The TriboLab® employed in this study is equipped with a Scanning Probe Microscope (SPM), in which a sharp probe tip moves in a raster scan pattern across the sample surface using a three-axis piezo positioner. All nanoscratch measurements were performed with the standard three-sided pyramidal Berkovich probe, with an average radius of curvature of about 100 nm, in a clean area environment with 45% humidity and 23°C ambient temperature [24].

The scratch tests performed in this work included three main segments. Firstly, a pre-scratch scan under a very small load (1 μN) was carried out. Then, the indenter scraped the sample under a certain force and a scratch was generated. The normal applied loads (NL) used in this work were 50–300 μN. The length of the scratches was 10 μm. Finally, a post-scratch test under the same NL as the pre-scratch test was conducted to obtain the image of the surface after scratch. An estimation of the residual scratch ditch and the extent of immediate recovery can be obtained by comparing the pre-scratch with the post-scratch image profiles.

3. Results and Discussion

3.1. Electrowetting on Composite Hydrophobic Coating

In this work we focused on the investigation of adequate coupling in terms of interlayer adhesion strength and chemical affinity of the hydrophobic dielectric used in EW experiments, namely the main insulating layer (TEOS) and the hydrophobic top coating. There are a number of known issues (i.e., dielectric charging, electrolysis) related to hydrophobic dielectrics in EW systems, which can either suppress the CA modulation range or cause sample failure. The investigation of the CA modulation at voltages $V > V_s$ is limited by the fact that dielectric breakdown is most likely to occur. Bubbles rise inside the liquid drop indicating electrolysis and ultimately sample failure. Detailed post inspection of the top coating (Teflon®) showed that under high electric fields it could possibly locally delaminate from the substrate. This observation led to a thorough investigation of alternatives to enhance the adhesion between the hydrophobic top coating (Teflon®) and the main dielectric (TEOS).

The adhesion of Teflon® to substrates (e.g., silicon, glass) depends primarily on physical interaction since it has no reactive chemical groups for chemical bonding [19]. Fluorosilanes, that were originally used in our group to promote adhesion between Teflon® coating and TEOS, proved to be inadequate for investigating the electrowetting CA modulation at voltages higher than V_s. Electrolysis was still present during the experiments in the saturation regime (at V_s and beyond). Our study showed that the adhesion of Teflon® AF to TEOS could be improved by the use of a thin plasma-deposited FC layer. Plasma-deposited FC films are known to adhere well to oxide surfaces due to an oxyfluoride interface layer on which a Teflon-like ($1 < F/C < 2$) layer grows (F/C stands for 'fluorocarbon ratio') [25]. It is the chemical affinity of the plasma-deposited FC to Teflon® that improves the overall bondability of Teflon® AF to the oxide substrate. The result is a sandwich-like hydrophobic coating, hereafter called 'Composite Coating', which consists of a thin plasma-deposited FC layer and a thin spin-coated Teflon® film.

In Fig. 1, EW experiments on the tested samples are presented. The EW tests were performed in dodecane ambient as follows: The applied voltage was increased from 0 V in increments of 2.5 V up to the critical voltage, namely V_s, where CA saturation sets on. Then the voltage was turned off and the sessile droplet rested back in its initial shape. This will be from now on referred to as an EW cycle. Moreover, robustness verification in terms of dielectric breakdown prevention was performed. For this purpose, composite coated samples were compared to Teflon® coated ones with respect to the CA dependence on applied voltage up to $2.5V_s$.

Usually, EW experimental data are presented up to the saturation limit, and compared with the predictions of the Young–Lippmann equation. In rare cases and for relatively thick hydrophobic dielectrics, experimental data for applied voltages $V > V_s$ are presented [26]. In this work three samples were tested at applied voltages apparently beyond the saturation. The samples consist of TEOS as the main dielectric (with thicknesses of 180 and 821 nm) and on top of it the following hydrophobic top coatings were fabricated: Two composite coatings (with thicknesses of 58 and 174 nm) and one Teflon® coating (52 nm thick).

As expected, the experimental data are in close agreement with the predictions of Young–Lippmann equation (dashed lines in Fig. 1(a) and (b)) up to the onset of saturation. In Fig. 1(a), samples of equal TEOS thicknesses and different types of top coatings (composite and Teflon® coatings) are compared, in terms of CA dependence on the applied voltage. For an applied voltage of 15 V, the contact angle modulation is 110° (from ≈160° to ≈50°) for both samples. However, the EW tests show that the Teflon® coated sample failed at about $1.4V_s$ (see arrow in Fig. 1(a)), as bubbles start to emerge from the sample surface. In contrast, the composite coating sample shows a CA of 37° at 44.2 V and a consequent maximum CA modulation of ≈125°.

The robustness of this composite coating sample was tested at high voltages, up to $2.5V_s$. We did not notice any sample failure indication (e.g., electrolysis) during this test, however, CA modulation gradually decreases from a maximum of 125° to

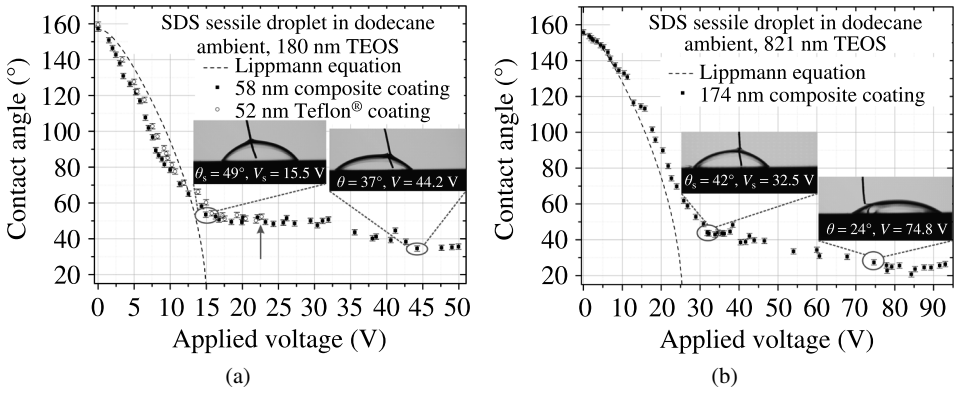

Figure 1. Contact angle dependence on the applied voltage, (a) comparison between the composite and Teflon® coatings, (b) for the composite coating.

110°. This gradual loss of performance is evident up to the fourth EW cycle and thereafter CA modulation range remains constant for at least up to thirty cycles.

In Fig. 1(b), the performance of a composite coated sample is shown in terms of maximum CA modulation. For an applied voltage of 74.8 V the maximum contact angle modulation is ≈130°. Wetting enhancement of 130° can be achieved at $2.5V_s$, without material failure. Material failure is also not evident at least up to thirty EW cycles. Similarly, CA modulation decreased to 115° during this EW test. Gradual decrease in maximum CA modulation range is observed in all composite coated samples tested at high voltages. Possibly charge trapping in the hydrophobic dielectric suppresses the wetting enhancement during the EW cycle sequence [14]. It should be mentioned that CA hysteresis (difference between the advancing and the receding CA) was ≈5°.

3.2. Optical Microscopy Characterization of the Hydrophobic Top Coatings

The surface of the hydrophobic coating was inspected by optical microscopy, immediately after the EW tests. The objective here was to examine the footprint, namely the effect of the EW test on the surface of the coating, of the electrowetted sessile drop for different hydrophobic top coatings. Optical observation was focused in the vicinity of TPL, because the electric field strength is expected to reach very high values, thus greater surface damage is expected [27].

The samples were carefully inspected after the following EW experimental procedure: The applied voltage was increased stepwise up to $2.5V_s$ and was held constant for about 30 s at each EW experiment. Then the voltage is turned off and the above cycle is repeated at least up to thirty times. The sessile drop is then removed and the sample surface is inspected with optical microscopy. The specifications of each tested sample featuring 300 nm TEOS as the main dielectric are presented in Table 1.

Three samples that consist of different hydrophobic top coatings were fabricated (see Table 1). The first sample (sample S1) that features only plasma-deposited FC

Table 1.
Specifications of the samples inspected

Sample	Coating	Coating thickness (nm)	In air	In dodecane (SDS droplet)	
			Static CA hysteresis (°)	EWOD hysteresis (°)	Saturation voltage, V_s (V)
S1	Plasma FC	60	42 ± 2.5	—	18 ± 1
S2	Teflon®	60	11 ± 2.5	5 ± 2.5	17.8 ± 1
S3	Composite	60	12 ± 2.5	5 ± 2.5	17.3 ± 1

coating on top of TEOS shows resistance to dielectric breakdown. However, upon voltage removal, the sessile drop does not recede to its initial shape and stays at its advanced wetting state. Static CA hysteresis of the sessile drop is 42°, which indicates high EW irreversibility [28]. Since it was not possible to perform reversible EW cycles due to high hysteresis, application of voltage for a long time was decided to test the robustness of the sample at high voltages. Our experiments showed that even if a voltage of the order of $2.5V_s$ was applied for 5 min, there was no sign of electrolysis. The microscopy inspection of the sample surface shows noticeable damage (Fig. 2(a)); however, material breakdown is not evident in the EW test. Clearly in the vicinity of the TPL there is a narrow band ($\approx$80 μm) that suggests that this portion of the surface is mostly affected. The stressed area looks like a ring with a narrow band at the edge, formed by the fully advanced wetting state of the drop. Although we observe these random formations, there is no macroscopic indication of material damage (i.e., electrolysis) that usually happens on Teflon® coating which will be discussed below.

The second sample (sample S2), with Teflon® AF as hydrophobic coating, appears highly affected (Fig. 2(b)) at the edge of the ring and on the inside of it. At applied voltage $\approx 1.7V_s$, bubbles started to rise inside the liquid drop indicating electrolysis. The narrow band at the edge of the ring is clearly visible in this sample ($\approx$75 μm). Inside the ring, random tree-like formations possibly indicate the presence of extended surface cracks. Similarly, Cytop® as hydrophobic top coating failed at applied voltage $\approx 1.4V_s$. Detailed inspection of the surface reveals that Cytop® coating exhibits a ripple-like topography which can be possibly attributed to material structure different from the Teflon® coating, however, there is no significant damage or crack formation to report. Comparison of Fig. 2(a) and (b) shows that the corresponding materials, namely plasma FC and Teflon® AF, behave differently under high electric fields.

The third sample tested (sample S3) features the proposed composite hydrophobic top coating (Fig. 2(c)). This coating combines the advantages of the previous top coatings as it shows resistance to sample failure and reversibility in EW tests. The footprint of the drop is more uniform and the ring in the vicinity of the TPL is still evident in all tested samples, with a narrow band of $\approx$50 μm. It should be

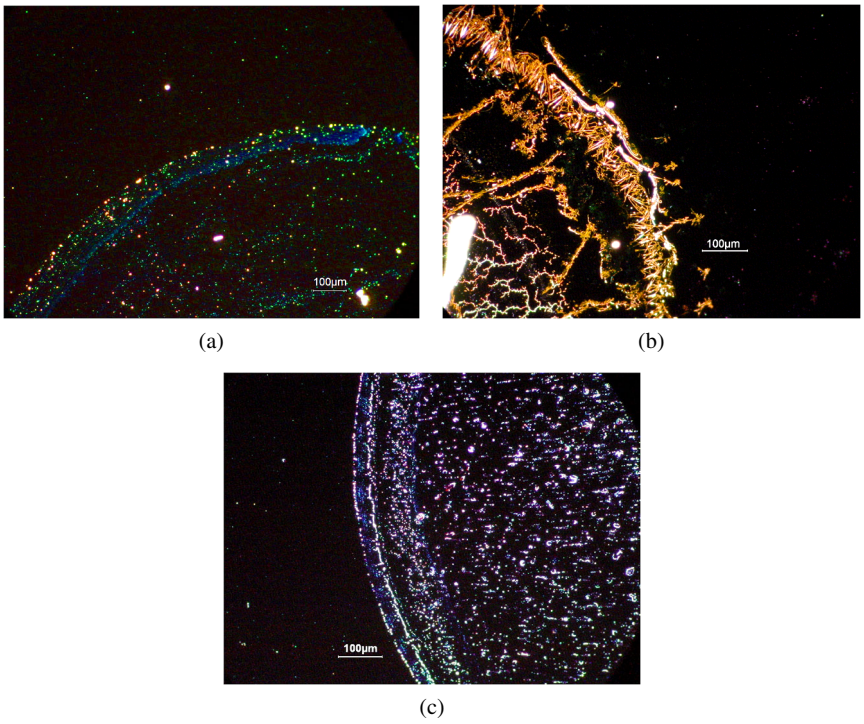

Figure 2. The effect of the EW tests on sample surfaces for (a) plasma FC coating, (b) Teflon® coating and (c) composite coating.

mentioned that the sample remains fully functional at least up to thirty EW cycles. The inspection of the surface revealed the absence of dendritic patterns seen in sample S2, although the upper layer is the same, i.e., Teflon® AF.

It should be noted that when electrolysis occurs, bubbles are localized in the vicinity of the TPL, confirming the high electric field strength in this region. The plasma-deposited FC interlayer might have a twofold advantage: on the one hand reduced void density between the hydrophobic coating and TEOS through better adhesion and on the other hand inhibition of local charge trapping in the overall hydrophobic top coating through reduced porosity. In the following section we focus on the interlayer mechanical properties of the hydrophobic dielectric to estimate the contribution of these factors to the overall EW system performance.

3.3. Nanoscratch Tests

Nanoscratch tests can provide a measure of the scratch resistance of the hydrophobic dielectric. Initially, nanoindentation tests were conducted to determine the hardness and elastic modulus of hydrophobic dielectric layers. The corresponding values for each layer were used to determine the sequence parameters for the following scratch tests, i.e., applied normal load (NL), scratch length, tip velocity. Two samples were tested. Sample S3 consists of 300 nm TEOS and 60 nm composite

top coating, namely, 30 nm spin-coated Teflon® on top of 30 nm plasma-deposited FC; sample S2 consists of 300 nm TEOS and 60 nm spin-coated Teflon®.

The pre-scratch scan curve corresponds to the profile of the initial flat surface, scratch scan curve corresponds to the tip penetration profile during testing and, finally, post-scratch scan curve corresponds to the final profile of the surface after scratching (1 μN). The post-scratch curve represents the residual depth of scratch trace after unloading, i.e., the plastic deformation of the probed film. The statistical error in the scratch depths is less than 10 nm, while the displacement resolution of the nanoindenter used in scratch testing is better than 0.1 nm, thus making possible to compare the scratch depths of different films.

The difference between the scratch and post-scratch curves corresponds to the elastic recovery of the films, making nanoscratch testing a reliable technique for defining the elastic and plastic regions of thin coatings. The surface profiles of the scratches of the two samples under 50 μN NL and the subsequent initial (scratch scan) and residual (post-scratch scan) scratch depth profiles are presented in Fig. 3.

The three regimes in Fig. 3(a) (I, II, III) are defined by the different slopes of the scratch scan curve. In detail, for sample S3 (Fig. 3(a)) and for NL lower than 18 μN (regime I), the penetration depth of the indenter did not exceed 30 nm. This fact could be correlated to the mechanical response of the top layer (Teflon®) and the underlying plasma FC layer of the composite coating. For sample S2 (Fig. 3(b)) and for NL lower than 18 μN the penetration depth of the indenter was ≈20 nm which is solely attributed to the mechanical properties of the Teflon® coating. For NL higher than 18 μN and up to 30 μN (regime II), the lower slope of the curve indicates that the plasma FC layer contributes to the overall scratch resistance of the composite coating to the applied NL [29]. Moreover, from the structural material viewpoint, the plasma FC interlayer is expected to be more resistant to the NL than the Teflon® AF. The structure (–C–C–) that these polymers are consisted of is

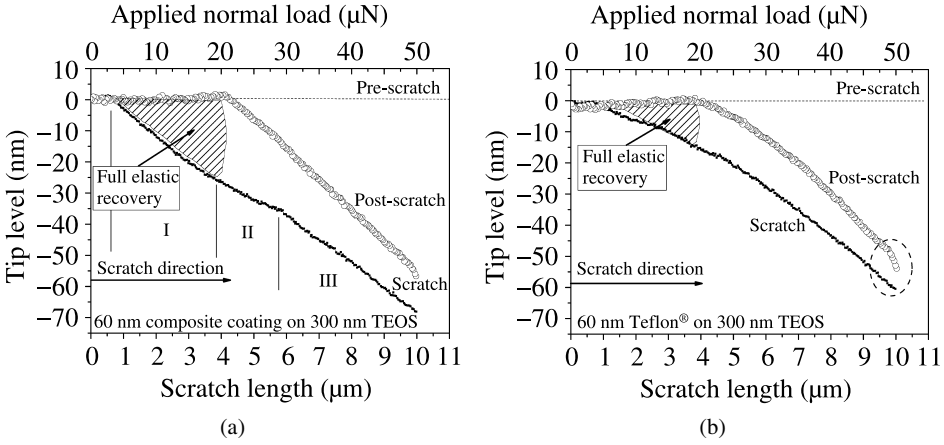

Figure 3. Scratch profiles for the (a) composite coating sample (sample S3) and (b) Teflon® coating (sample S2) on top of TEOS, with applied NL of 50 μN.

related to material hardness [30]. Chemical characterization of the plasma FC films through composition (XPS) analysis has shown that the plasma-deposited F/C ratio is 1.5 [31], whereas the F/C ratio of Teflon is 2. Hence, plasma-deposited FC is more crosslinked than the Teflon® AF (more (–C–C–) bonds per volume). As a result, it is not surprising that the plasma-deposited FC appears to be more resistant to the NL.

Comparing the surface profiles in Fig. 3(a) and (b), up to 20 μN of applied NL, the recovered scratch depth of the sample S3 is close to 30 nm, whereas the recovered scratch depth of the sample S2 is about 15 nm (hatched areas in Fig. 3(a) and (b)). The higher elastic recovery under the same NL suggests that the composite coating can sustain higher scratch induced stresses (higher scratch resistance, i.e., improved adhesion strength) than the Teflon® coating [29]. After NL ≈30 μN (regime III) both samples exhibited elastoplastic behaviour, with sample S2 exhibiting almost full plastic behavior (convergence of the initial and the residual scratch profiles) in the last few nanometers of displacement (indicated in Fig. 3(b) with a dashed circle).

In Fig. 4 the surface profiles of the two scratched samples are shown. As seen in Fig. 4(a) and (b), there is a buildup of polymer material mostly on one side of the scratch [32]. These buildups are found in all scratches created, which shows that the films were plastically deformed and that the buildup was most likely an accumulation of compressed materials.

When a moving scratch tip ploughs through the coating, the material will be either pushed forward or piled-up sideways ahead of the tip; material's pile-up on the sides of the indenter suggests plastic deformation of the film over an undeformable substrate [33, 34]. This phenomenon is usually observed for relatively ductile polymers, where plastic deformation is evident on applied strains [35]. In Fig. 4(c) cross-sectional scratch profiles (*via* SPM imaging at maximum load) of samples S3 and S2 at 50, 150 and 300 μN of applied NL are presented.

At high nanoscratch loads (300 μN) for the Teflon® coated sample (sample S2), the polymeric material accumulated on the sides of the tip which is apparent from Fig. 4(b) and (c). The result, shown in Fig. 4(b), is an indication of coating failure, which resulted in a blister sample damage (indicated by the circle in Fig. 4(b)). The displacement of the removed material on the sides of the scratch indicates that scratching caused mainly plastic deformation. This type of deformation of coating is possibly attributed to buckling and delamination effects, observed in the coating when it is subjected to scratch test. Significant pile-up of the material due to diamond tip scratching reveals wear and debris. In the case of the composite coating sample (sample S3) the ploughing by the tip does not create similar accumulation pattern (Fig. 4(a) and (c)), and consequently coating failure is suppressed. It should be noted though that sample S2 exhibited earlier accumulation of material. Larger plastic deformation in the case of sample S2 compared to sample S3 is evident by the residual depths, since in both cases the total penetration depth is almost identical.

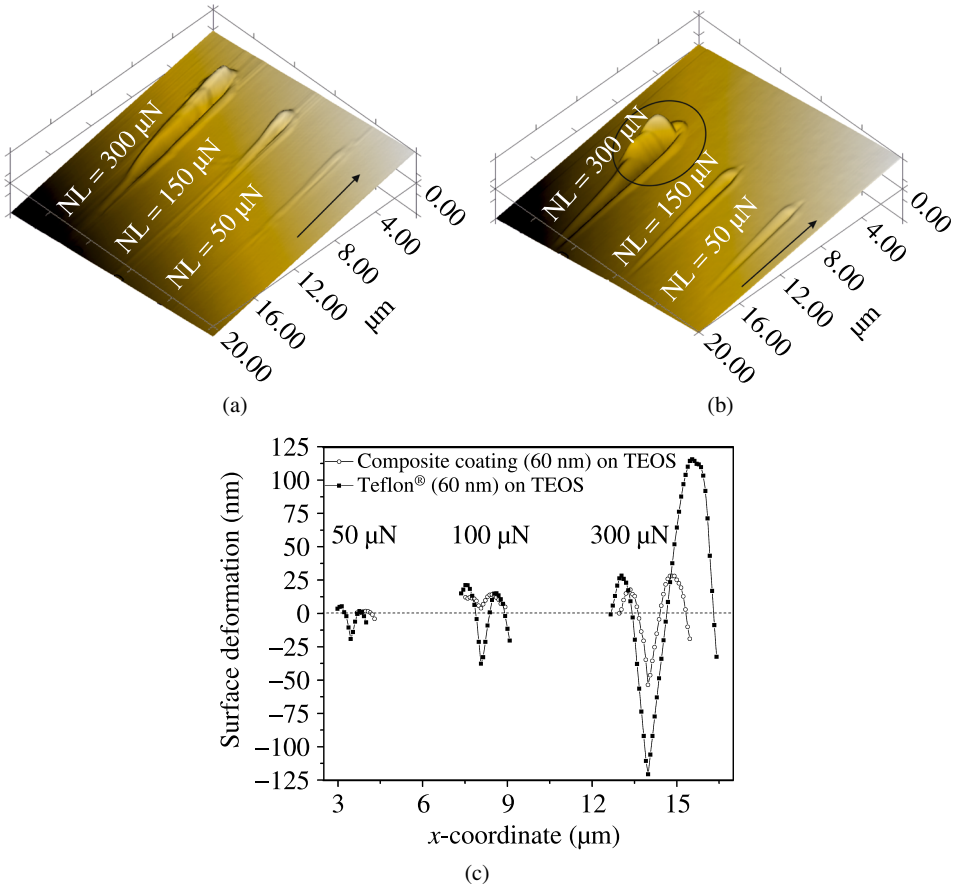

Figure 4. Scratched surface profiles: SPM images at 50, 100 and 300 μN of applied NL for (a) composite coating sample (sample S3), (b) Teflon® coated sample (sample S2). (c) Cross-sectional shapes at maximum applied NL of 50, 100 and 300 μN, i.e., at the end of scratch. Pointing arrow defines the scratch direction of the tip. (Zero level on the vertical axis corresponds to the level of the unscratched flat surface.)

In every Teflon® coated sample tested by nanoscratching, we observed an abrupt change in NL at a certain scratch depth (ranging from 68 to 76 nm). This abrupt change is attributed to a discontinuity in certain mechanical properties (e.g., elastic modulus) between Teflon® and TEOS which is related to the adhesion between the two and consequently an observed abrupt change in applied NL. Since this abrupt change was never observed in the case of the composite coating sample, it is suggested that plasma-deposited FC smooths out the aforementioned discontinuity between TEOS and the hydrophobic top coating (Teflon®), resulting in better EW performance.

In Fig. 5, applied NL dependences on scratch depth and length are presented. The tip scratches the surface under progressively increasing NL and along a pre-defined path. As denoted by the arrow, an abrupt change in NL is observed only when

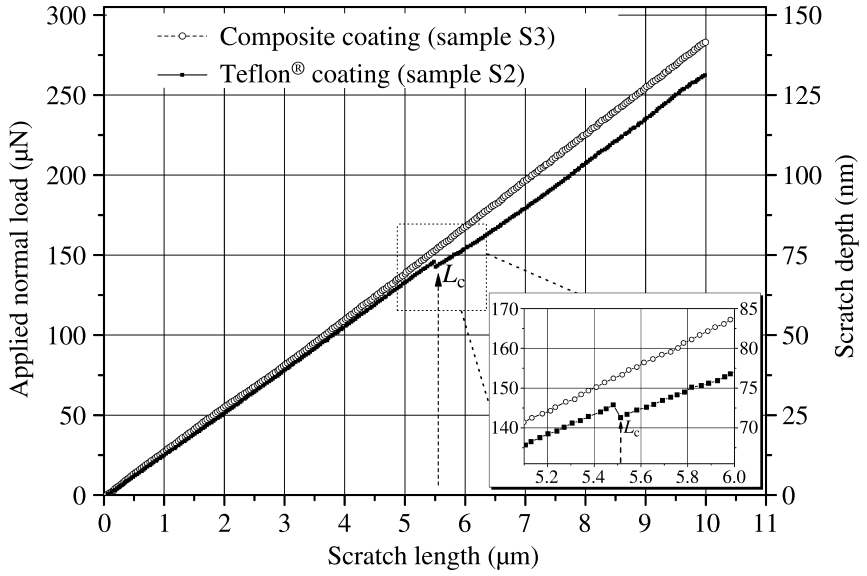

Figure 5. Applied normal load dependences on the scratch length and scratch depth for samples S3 and S2. The arrow indicates the onset of critical load. The inset is a magnification of the area depicted by the dashed line.

Teflon® coating is used, which is indicative of strength weakening due to material heterogeneity [21, 29, 36]; this occurs at a critical scratch length of ≈5.5 μm and NL ≈ 150 μN.

The scratch depth variation (see Fig. 5), indicates that the NL abrupt change sets in when the tip penetration is close to the Teflon®/TEOS interface (sample S2). The corresponding critical load is usually denoted as L_c. The existence of an L_c is an indication of failure in terms of coating cracking, delamination or brittle fracture caused by scratch testing [37]. High elasticity in combination with low hardness of the Teflon® top coating mostly favors delamination and not coating cracking or brittle fracture. Moreover, the Teflon® coating of the tested sample is approximately 60 nm thick which is close to the scratch depth value where the critical load appears. This strain mismatch evident by the abrupt change in the applied NL induces film delamination, and is not observed in the case of the composite coating. We suspect that the interlayer of plasma FC suitably bonds the oxide substrate and the spin-coated Teflon® layer, therefore the corresponding nanoscratch curve in Fig. 5 is smoother for the composite coating.

4. Conclusions

In this work the effect of plasma-deposited fluorocarbons, as structural layers of the top coating, on EW performance was investigated. A sandwich-like hydrophobic top coating was fabricated, here called composite coating, comprising a thin plasma-deposited FC layer and a thin spin-coated Teflon® layer. This sam-

ple showed resistance to dielectric breakdown, improved CA modulation and reversibility for at least up to thirty EW cycles, at applied voltages apparently beyond the saturation. Optical microscopy inspection revealed absence of dendritic patterns usually observed in Teflon® coatings. Nanoscrach testing was conducted to further investigate the interlayer mechanical properties of the proposed hydrophobic dielectric stack. Nanoscratch measurements showed improved adhesion strength of the composite coating to the oxide substrate compared to the equivalent Teflon® coating sample, confirming the observed improved robustness in EW tests.

Acknowledgements

The research leading to these results received funding from the European Research Council under the European Community's Seventh Framework Programme (FP7/2007-2013)/ERC Grant agreement No. (240710). The authors wish to thank Drs E. Gogolides and A. Tserepi at the Institute of Microelectronics, NCSR 'Demokritos', for their expert advice in plasma-deposited fluorocarbon films and cleanroom processing. The authors also wish to thank Drs Panagiota Petrou and Sotirios Kakabakos from the Institute of Radioisotopes and Radiodiagnostic Products of NCSR 'Demokritos' for providing access to their optical microscope. The authors would like to thank Prof. T. Krupenkin and Dr J. Ashley Taylor of the University of Wisconsin–Madison for kindly providing samples with Cytop® hydrophobic top coating.

References

1. F. Mugele, *Soft Matter* **5**, 3377 (2009).
2. R. B. Fair, *Microfluid Nanofluid* **3**, 245 (2007).
3. E. M. Miller and A. R. Wheeler, *Anal. Bioanal. Chem.* **393**, 419 (2009).
4. B. Berge and J. Peseux, *Eur. Phys. J. E* **3**, 159 (2000).
5. S. Kuiper and B. H. W. Hendriks, *Appl. Phys. Lett.* **85**, 1128 (2004).
6. R. A. Hayes and B. J. Feenstra, *Nature* **425**, 383 (2003).
7. J. Heikenfeld, K. Zhou, E. Kreit, B. Raj, S. Yang, B. Sun, A. Milarcik, L. Clapp and R. Schwartz, *Nature Photonics* **3**, 292 (2009).
8. V. A. Lifton, J. A. Taylor, B. Vyas, P. Kolodner, R. Cirelli, N. Basavanhally, A. Papazian, R. Frahm, S. Simon and T. Krupenkin, *Appl. Phys. Lett.* **93**, 043112 (2008).
9. S. Berry, J. Kedzierski and B. Abedian, *J. Colloid Interface Sci.* **303**, 517 (2006).
10. E. Seyrat and R. A. Hayes, *J. Appl. Phys.* **90**, 1383 (2001).
11. C. Quilliet and B. Berge, *Curr. Opin. Colloid Interface Sci.* **6**, 34 (2001).
12. A. G. Papathanasiou and A. G. Boudouvis, *Appl. Phys. Lett.* **86**, 164102 (2005).
13. A. I. Drygiannakis, A. G. Papathanasiou and A. G. Boudouvis, *Langmuir* **25**, 147 (2009).
14. H. J. J. Verheijen and M. W. J. Prins, *Langmuir* **15**, 6616 (1999).
15. M. Vallet, M. Vallade and B. Berge, *Eur. Phys. J. B* **11**, 583 (1999).
16. A. G. Papathanasiou, A. T. Papaioannou and A. G. Boudouvis, *J. Appl. Phys.* **103**, 034901 (2008).
17. P. Bayiati, A. Tserepi, P. S. Petrou, S. E. Kakabakos, K. Misiakos and E. Gogolides, *J. Appl. Phys.* **101**, 103306 (2007).

18. H. Moon, S. K. Cho, R. L. Garrell and C. J. Kim, *J. Appl. Phys.* **92**, 4080 (2002).
19. A. Datta, I. Y. Eom, A. Dhar, P. Kuban, R. Manor, I. Ahmad, S. Gangopadhyay, T. Dallas, M. Holtz, F. Temkin and P. K. Dasgupta, *IEEE Sensors J.* **3**, 788 (2003).
20. K. Takahashi, T. Mitamura, K. Ono, Y. Setsuhara, A. Itoh and K. Tachibana, *Appl. Phys. Lett.* **82**, 2476 (2003).
21. B. R. Kim and M. J. Ko, *Thin Solid Films* **517**, 3216 (2009).
22. K. L. Mittal, in: *Adhesion Measurement of Films and Coatings*, K. L. Mittal (Ed.), pp. 1–13. VSP, Utrecht (1995).
23. DuPont, Teflon® AF Amorphous Fluoropolymer, Product Information (2006).
24. C. A. Charitidis, *Int. J. Ref. Met. Hard Mater.* **28**, 51 (2010).
25. A. Tserepi, in: *Plasma Processes and Polymers*, R. D'Agostino (Ed.), p. 51. Wiley-VCH, Weinheim (2005).
26. M. Paneru, C. Priest, R. Sedev and J. Ralston, *J. Phys. Chem. C* **114**, 8383 (2010).
27. F. Mugele and J. C. Baret, *J. Phys.: Condens. Matter* **17**, R705 (2005).
28. P. Bayiati, A. Tserepi, D. Goustouridis, K. Misiakos and E. Gogolides, in: *Proceedings of the 1st Europ. Conf. on Microfluidics*, Bologna, Italy (2008).
29. Y. Liu, T. Zhang, G. Zhang, X. Niu, Z. Song, G. Min, Y. Lin, J. Zhang, W. Zhou, J. Zhang, J. Chu, Y. Wan and S. Feng, *Jpn. J. Appl. Phys.* **48**, 101601 (2009).
30. A. Itoh, A. Inokuchi, S. Yasuda, A. Teramoto, T. Goto, M. Hirayama and T. Ohmi, *Jpn. J. Appl. Phys.* **47**, 2515 (2008).
31. P. Bayiati, A. Tserepi, P. S. Petrou, K. Misiakos, S. E. Kakabakos, E. Gogolides and C. Cardinaud, *Microelectron. Eng.* **84**, 1677 (2007).
32. H. Nie, M. Walzak and N. McIntyre, *Appl. Surface Sci.* **253**, 2320 (2006).
33. H. Jiang, R. Browning and H. J. Sue, *Polymer* **50**, 4056 (2009).
34. B. Bhushan (Ed.), *Scanning Probe Microscopy in Nanoscience and Nanotechnology*. Springer, New York (2009).
35. J. A. Sauer and K. D. Pae, *Colloid Polym. Sci.* **252**, 680 (1974).
36. J. Ye, N. Kojima, K. Ueoka, J. Shimanuki, T. Nasuno and S. Ogawa, *J. Appl. Phys.* **95**, 3704 (2004).
37. X. W. Zhang, L. J. Hu and D. Z. Sun, *Acta Mater.* **54**, 5469 (2006).

Thin Solid Films 526 (2012) 168–175

Contents lists available at SciVerse ScienceDirect

Thin Solid Films

journal homepage: www.elsevier.com/locate/tsf

Structural and nanomechanical properties of a zeolite membrane measured using nanoindentation

C.A. Charitidis [a,*], E.P. Koumoulos [a], V. Nikolakis [b,c], D.A. Dragatogiannis [a]

[a] School of Chemical Engineering, Department of Materials, Science and Engineering, National Technical University of Athens, Zografou Campus, 15780 Athens, Greece
[b] Foundation for Research and Technology Hellas, Institute of Chemical Engineering Sciences, P.O. Box 1414, GR-26504 Patras, Greece
[c] Catalysis Center for Energy Innovation, Department of Chemical & Biomolecular Engineering, University of Delaware, Newark DE19716, USA

ARTICLE INFO

Article history:
Received 27 October 2011
Received in revised form 15 October 2012
Accepted 16 October 2012
Available online 23 October 2012

Keywords:
Nanoindentation
Zeolite membrane
Hardness
Modulus
Creep
Deformation
Pile-up/sink-in

ABSTRACT

Knowledge of the elastic constants of zeolite films is of great practical interest, due to its main applications. The structural and nanomechanical properties of a faujasite-type zeolite film have been measured using nanoindentation. The hardness and elastic moduli of the film are estimated from creep and non-creep nanoindentation measurements. The deformation mechanism was analyzed using a pile-up/sink-in analysis, revealing a switch of dominant deformation mechanism at ~250 nm of displacement. Wear analysis (hardness to elastic modulus ratio) provided information about the structural integrity and mechanical reliability of the film. Hardness and elastic modulus values were found to decrease with increasing penetration depth. In particular, the elastic modulus decreased from ~60 GPa (at displacement of 20–30 nm) to ~7 GPa (at displacement of 200 nm), and the hardness from ~8 GPa (at displacement of 20–30 nm) to ~0.8 GPa (at displacement of 500 nm).

1. Introduction

Zeolites are crystalline, microporous materials that are formed by corner linked aluminosilicate tetrahedral frameworks. They have channel and cages with dimensions similar to those of several industrially important molecules. As a result they are widely used in catalysis, in ion exchange and in gas separations. Zeolites are also used as cracking catalysts and water softening additives for detergents. During the last decades, there has been an increasing interest in developing novel zeolite based applications. Most efforts focused on the synthesis of permselective zeolite membranes for the separation of gas or liquid mixtures [1–4]. However, there has been a considerable amount of work toward the development of other types of applications such as modified electrodes [5], optical devices [6], films of low dielectric constant for the replacement of dense silica in the semiconductor industry [7] and gas sensors [8]. A solid knowledge of the zeolite crystal and film mechanical properties would be of great help in the design of engineering applications (especially in the case of permselective membranes, gas sensors, and low dielectric constant films) [7,9,10] as well as for the performance improvements in traditional zeolite based applications (i.e., zeolite catalysts) [11–13]. For example, several recent publications in the field of zeolite membranes have mentioned that the enhancement or loss of the membrane permselective performance might be attributed to changes of the zeolite polycrystalline film mechanical properties as a result of the adsorption of gas or vapor molecules [14,15]. Finally, a prerequisite for the utilization of zeolite layers as low dielectric constant films in the semiconductor industry is their ability to withstand the chemical and mechanical conditions encountered during the fabrication processes [7]. Thus, knowledge of the elastic constants of zeolite films is of great practical interest.

The knowledge of the mechanical properties of zeolites is scarce [7,9,11–13,16–20] mainly because of the difficulty of measuring these properties [12]. The elastic modulus (frequently also referred as Young modulus) of zeolites can be measured using either mechanical (nanoindentation, microdeformation, or three point bending) [11–13,19–21] or spectroscopic methods (Brilllouin or Synchrotron X-ray spectroscopy) [10,18,22]. Unfortunately, the mechanical methods often require samples having sizes of at least several millimeters that are much larger than the usual maximum size of the synthetic zeolite crystals (100–200 μm). In the case of spectroscopic techniques, the experimental procedures and the analysis of the data are rather complicated.

Wang et al. [21,23] measured the Young's modulus of a ~200 μm Zeolite Socony Mobil (ZSM)-5, (structure type MFI — mordenite framework inverted) zeolite single crystal using a homemade microdeformation tester. Lin et al. [12,24] measured the hardness (H) and elastic modulus (E) of zeolites (ferrierite (FER) and sodalite (SOD)) of smaller sizes than ZSM-5 by nanoindentation experiments.

* Corresponding author.
E-mail address: charitidis@chemeng.ntua.gr (C.A. Charitidis).

0040-6090/$ – see front matter © 2012 Elsevier B.V. All rights reserved.
http://dx.doi.org/10.1016/j.tsf.2012.10.021

Afterward, Brabec et al. [11] measured H and E of zeolite silicalite-1 crystal twins from depth sensing indentations using Berkovich tip in 2006. In the same year, Lethbridge et al. [25] had a typical indentation experiment, in which they measured Young's modulus of the zeolite single-crystal natrolite, and comparison with dynamic studies and simulations. In 2006, Niu et al. [26] determined bilinear elastic–plastic constitutive relation of zeolite crystals FER and SOD. The mechanical properties of several types of zeolites reported in the literature through various techniques are presented in Table 1, revealing the high range of H and E values for each case.

During nanoindentation, the applied load can be controlled at a constant value, whereas the penetration of the indenter tip into the sample surface is continuously recorded. This is often called constant-load indentation creep test, and it has been widely used to study the time-dependent properties of crystalline materials. The nanoindentation creep consists of two stages, transient (primary creep) and steady state (secondary creep) [35]. The stress exponent, n, of the steady-state creep can be derived from the constant load indentation tests [36–40]. In a nanoindentation creep experiment, the tip is pushed into the surface at a constant loading (or displacement) rate of indentation until a prefixed load or penetration displacement is reached, then the load (or displacement) is held constant while the indenter continues to creep into the material. With the indenter tip held fixed at that load (or displacement), the material beneath the indenter tip continues to deform in time and finally the indenter tip is retracted from the material. Creep within a specimen occurs during the hold time of the loading phase of nanoindentation testing and manifests itself as a change of indentation displacement with the load, kept constant. It is postulated that the stress fields in the material underneath the indenter develop a chemical potential gradient that lead to a thermally activated diffusional flux of atoms moving from below the indenter to the surface and along the interface between the indenter and the specimen, even under an elastic contact [41,42].

In this work, a study concerning the structural and nanomechanical properties of faujasite-type zeolite in sodium form (NaX FAU) film using nanoindentation is presented. In particular, the H and E of the film are estimated from creep and non-creep nanoindentation measurements and are compared with values measured using different experimental methods. Furthermore, a pile-up/sink-in analysis was performed, in order to investigate the deformation mechanism during nanoindentation; structural integrity and mechanical reliability were investigated through wear analysis using the H to E ratio (high H to E ratio gives greater coating flexibility with lower chance of cracking during substrate torsion and bending).

2. Experimental details

Faujasite membranes were synthesized on the polished surface of homemade porous α-Al_2O_3 disks (diameter: 14 mm; thickness: 2 mm; mean pore size: 150–200 nm and porosity: ~0.4) using the seeded growth method. The disks were prepared by pressing commercial α-Al_2O_3 powder (Baiwkowski CR-1) and heating for 3 h at 1200 °C and 30 °C at 1100 °C. The disks were further polished on one side using sand paper (grit sizes 320 and 600) before depositing the zeolite seed layers. Prior to hydrothermal treatment, commercial faujasite NaY (Aldrich) crystals were deposited on the support using a dip-casting technique. The size of these crystals was between ~700 nm and ~2 μm. The seeded supports were dried in the air and were then placed in polypropylene bottles. The membranes were synthesized in polypropylene bottles at 85 °C using a gel with molar composition of $4.17Na_2O/1.0Al_2O_3/5$ TEA (triethanolamine)/$1.87SiO_2/460H_2O$. It was prepared by adding tetraethylorthosilicate (TEOS 98%, Aldrich) in a NaOH and triethanol ammine (TEA, 95% Aldrich) solution at room temperature, under stirring. The mixture was stirred until a clear mixture was obtained which indicated the completion of the TEOS hydrolysis. A second solution was prepared by dissolving aluminum foil (Al 99.8%, 0.05 mm thick, Aldrich) in a NaOH solution. The second solution was then slowly added to the silica mixture under stirring. The duration of the synthesis was 120 h. During that time the deposited crystals grow and form a continuous film on the surface of the support. Additional details about the preparation of the synthesis gel can be found in [43–45]. After hydrothermal growth, the membranes were thoroughly washed several times with hot distilled water and were then calcined in air at 420 °C (heating rate 2 °C.min^{-1}) for 6 h. Powder X-ray diffraction (XRD) patterns were obtained using a Bruker D-8 ADVANCE diffractometer equipped with a LynxEye position sensitive detector and a CuKa X-ray source (40 kV, 40 mA).

Scanning Electron Microscopy (SEM) images of the top views of the films were acquired using a LEO-SUPRA 35VP Field Emission Scanning Electron Microscope operated at 20 kV in the variable pressure mode.

Nanoindentation testing was performed with a Hysitron Tribolab Nanomechanical Test Instrument, which allows the application of

Table 1
Nanomechanical properties of several types of zeolites reported in the literature.

Type	H (GPa)	E (GPa)	H/E	Method
NaX FAU [27]	–	41	–	–
NaX FAU [28]		50	–	–
NaX FAU [29]	–	30	–	Computational
NaX FAU [18]	–	38		Synchrotron X–ray
NaX FAU film [30]	–	37.5	–	Magnetoelastic ribbon
FER [12]	1	10	0.1	Nanoindentation
Silicalite-1 [31]	0.43–1.18	6.3–15.8	0.068–0.075	AFM
MFI (monoclinic) [7]	–	53.9	–	
Chabazite (CHA) (monoclinic) [7]	–	48.9	–	Nanoindentation
FER (orthorhombic) [7]	7.2	49.4	0.146	
Pure silica ZSM-11 (MEL) films [19]	0.36–1.22	10.1–17.6	0.036–0.069	Nanoindentation
Silicalite-1 crystal twins (as synth.) [11]	2.4	38.3	0.072	Nanoindentation
Silicalite-1 crystal twins (calc.) [11]	4.0	38.7	0.109	
MFI single crystal (as synth.) [32]	7.2	57.4	0.125	
Seeded-growth MFI film (calc.) [32]	4.3	43.4	0.099	
Seeded-growth MFI film (as-synthesized) [32]	5.5	45	0.122	Nanoindentation
MFI [21]		4		Microdeformation
CHA [7]		48.9 ± 1.2		Nanoindentation
Zeolitic imidazolate framework (ZIF) ($Zn(Im)_2$) [33]	1	8.5	–	
($LiB(Im)_4$) [33]	0.1	3	–	Nanoindentation
Natrolite (NAT) [22]		77.9		Brillouin spectroscopy
Analcime (ANA) [22]		81.5		
NAT [22]		85 ± 5		Three point bend
Linde type A (LTA) [34]		103 ± 42		Compression

loads from 1 to 30,000 μN and records the displacement as a function of applied loads with a high load resolution (1 nN) and a high displacement resolution. The nanomechanical test instrument employed in this study is equipped with a Scanning Probe Microscope, in which a sharp probe tip moves in a raster scan pattern across a sample surface using a three-axis piezo positioner. In all depth-sensing tests a total of 10 indents are averaged to determine the mean H and E values for statistical purposes, with a spacing of 50 μm, in a clean area environment with 45% humidity and at 23 °C. In order to operate under closed loop load or displacement control, feedback control option was used. All nanoindentation measurements have been performed with the standard three-sided pyramidal Berkovich probe, with an average radius of curvature of about 100 nm [46], with 40 s loading and unloading segment time separately and 3 s of holding time, to avoid residual viscoelasticity [47,48]. Prior to indentation, the area function of the indenter tip was measured in a fused silica, a standard material for this purpose [49].

Based on the half-space elastic deformation theory, H and E values can be extracted from the experimental data (load displacement curves) using the Oliver–Pharr method [50]. The derived expressions for calculating the elastic modulus from indentation experiments are based on Sneddon's [51] elastic contact theory:

$$E_r = \frac{S\sqrt{\pi}}{2\beta\sqrt{A_c}} \tag{1}$$

where S is the unloading stiffness (initial slope of the unloading load–displacement curve at the maximum displacement of penetration (or peak load)), A_c is the projected contact area between the tip and the substrate and β is a constant that depends on the geometry of the indenter (β = 1.167 for Berkovich tip [50]). Conventional nanoindentation H refers to the mean contact pressure; this H, which is the contact hardness (H_c) is actually dependent upon the geometry of the indenter (Eqs. (2)–(4)).

$$H_c = \frac{F}{A} \tag{2}$$

where,

$$A(h_c) = 24.5h_c^2 + a_1h_c + a_{1/2}h_c^{1/2} + \ldots + a_{1/16}h_c^{1/16} \tag{3}$$

where $a_1 = -1.2396\times10^4$, $a_{1/2} = 8.0499\times10^5$, $a_{1/4} = -7.2931\times10^6$, $a_{1/8} = 1.7166\times10^7$, $a_{1/16} = -1.068\times10^7$ and

$$h_c = h_m - \varepsilon\frac{P_m}{S_m} \tag{4}$$

where h_m is the total penetration displacement of the indenter at peak load, P_m is the peak load at the indenter displacement h_m, and ε is an indenter geometry constant, equal to 0.75 for Berkovich indenter [49,50].

3. Results and discussion

3.1. Structural characterization

The XRD pattern of the film is shown in Fig. 1a. Most of the reflections shown correspond to those of zeolite FAU. However there are a few reflections (denoted with the symbol A in the figure) that correspond to those of zeolite LTA. The relative intensities of the peaks of the two zeolites indicate that the film is comprised primarily by FAU type crystals. The LTA might be either part of the film or impurities that co-crystallized in the bulk and deposited on the surface of the film (i.e. white cubes shown on Fig. 1b). The reflection of alumina support is also seen at ~25.66° (denoted with *).

The SEM images showed that a continuous polycrystalline zeolite film (without visible cracks) has been formed on the α-Al_2O_3 support.

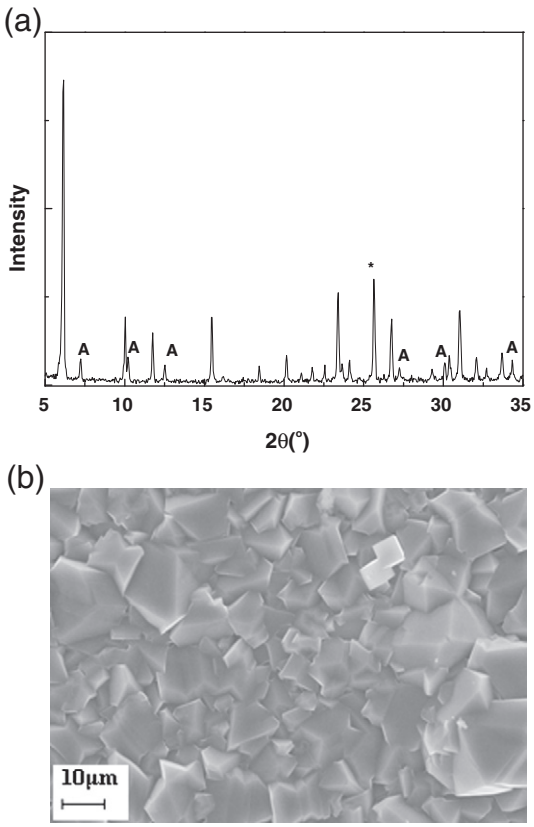

Fig. 1. a) XRD pattern and b) SEM image of the zeolite film.

On the low magnification images the scattered precipitation of crystals formed in the synthesis gel was revealed.

3.2. Nanomechanical properties

In the case of creep experiment, loading and unloading times were identical (5 s), while creep time was set to 30 s (40 and 3 s for conventional nanoindentation testing, respectively).

Hardness and E values were found to deviate at surface region (~0–100 nm), probably due to roundness of the tip and Indentation Size Effect (ISE), tending to reach a constant value of 0.5 and 5 GPa, respectively (Fig. 2). The reasons for the wide range in H and E values obtained from these nanoindentation measurements are currently unknown, but it is likely due to a combination of factors, including the polycrystallinity of the film, the grain boundaries of which may affect the compression tests and the presence of some small crystals remaining on the surface, which will behave differently than a crystal fully imbedded in the film. Furthermore, in a previous work using FAU films with magnetoelastic sensors E was estimated ~37.5 GPa [30]. This value is significantly different than that of ~5 GPa measured at high displacements. This discrepancy might be attributed to the magnitude of displacement of the magnetoelastic ribbons. Based on the magnetostriction coefficient of metglas the maximum displacement of these ribbons is expected to be less than 100 nm. In that region of displacement nanoindentation measurements also indicate that E of the film is between ~10 and 60 GPa. However, the accuracy of E measurement using nanoindentation depends on the projected area of indentation.

The measurements are expected to be accurate if the indentation samples have a sufficiently large area in order to give an adequate representation to all the constituent phases of a material, regardless of its porosity or possible artifacts. Thus, according to Eqs. (1) and (2) the increased values of E at low displacements might occur due to reduced contact area due to surface roughness. An alternative

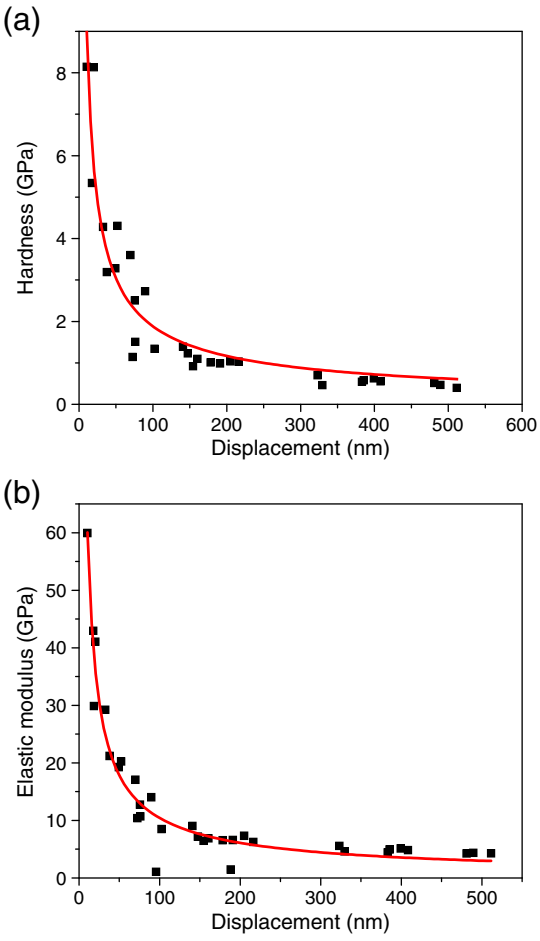

Fig. 2. Hardness and elastic modulus of the zeolite film as a function of the displacement.

way to measure E more accurately is the ultrasonic method, which is directly relates to the elastic property and density of the material.

In the case of very low contact area between the indenter and the sample, very high stresses can be developed. The high hydrostatic pressure exerted by the surrounding material allows plastic deformation at room temperature when conventional mechanical testing only leads to fracture. It is revealed that some materials exhibit ISE, which shows an increase in H with decreasing applied load [52]. Apparently, the existence of ISE may hamper the accurate measurement of H value, and is often attributed to experimental artifact, a consequence of inadequate measurement capability or presence of oxides on the surface [53]. Other possible explanations include indenter-specimen friction [54], and changing dislocation density for shallow indents due to the presence, for instance, of geometrically necessary dislocations [55]. The Berkovich indenter generates dislocations organized in a quite complex way during a nanoindentation test. As a result, even for very low deformations [56], it is difficult to formulate the stress field generated, even during an elastic deformation, as well as its modeling. Most of the dislocations stay generally confined around the residual imprint in a dense structure [57–59] with many dislocation interactions [60].

For describing the ISE we used the empirical equation in the Meyer's law [61,62], which uses a correlation technique between the applied indentation test load and the resultant indentation size using a simple power law, $P_{max} = Ch_c^n$, where C and n are constants derived directly from curve fitting of the experimental data. In particular, the exponent n, sometimes referred to as the Meyer index, is usually considered as a measure of ISE. Compared to the definition of the apparent hardness, no ISE would be observed for $n = 2$ [61,62].

The nanoindentation data for the material examined in the present study was plotted in Fig. 3. The data showed clear power-law relationship,

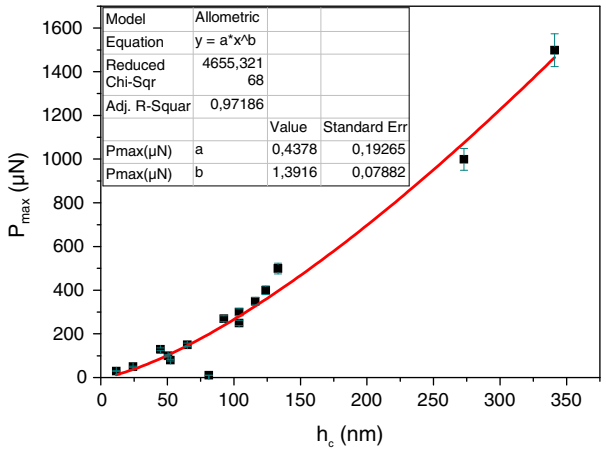

Fig. 3. Plot of P_{max} versus h_c according to the Meyer's law.

implying that the traditional Meyer's law was suitable for describing the nanoindentation data. Through power-law fitting analysis, the values of the parameters C and n were 0.4378 and 1.3916, respectively. The calculated n values pointed out higher apparent nanohardness values at lower loads, in other words, the presence of an ISE.

3.3. Creep analysis—comparison of nanomechanical properties

In Fig. 4, the penetration of the indenter tip into the sample surface (i.e. creep displacement) during the peak load holding against the holding time is presented, for each experiment. The magnitude of the total creep displacement during the peak load holding is strongly load dependent, i.e. larger peak load causes larger penetration. The creep displacement increases but at a decreasing rate, and it becomes almost linear with regard to the holding time (an initial sharp rise in creep displacement in the early part of the creep segment, followed by a region showing a smaller rate of increase in creep displacement). H and E (Fig. 5) values exhibit almost a similar behavior; enhanced nanomechanical properties in the surface region (noted in colored area) while decreasing with increasing displacement.

3.4. Stress exponent (steady-state creep)

Following Johnson's expanding cavity model [63] and the calculation of Bower [64], a self-similar stress/strain field can be assumed underneath a self-similar indenter. We further assume that steady-state

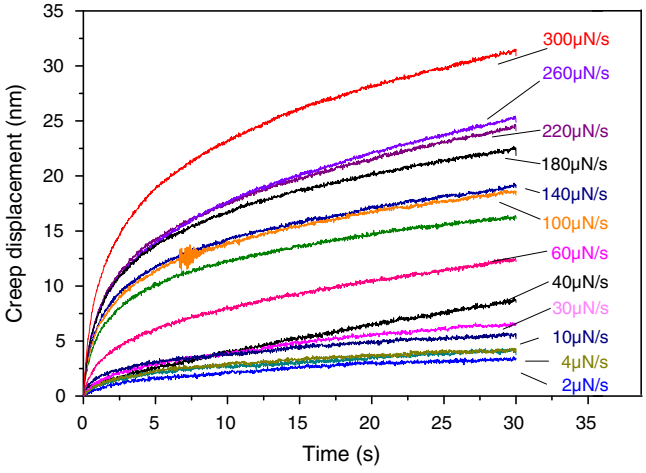

Fig. 4. Comparison of the creep curves (displacement axis was reset to show only the creep displacement, and time was reset to zero at the beginning of the hold period to facilitate comparison).

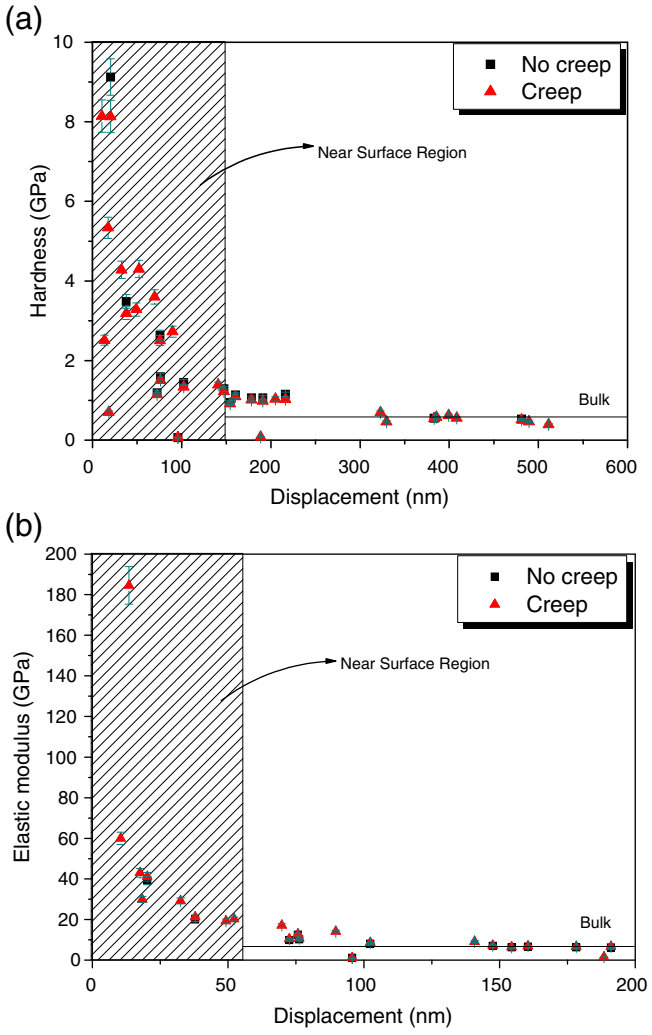

Fig. 5. Hardness and elastic modulus of the zeolite film as a function of displacement for creep measurement.

creep has been accomplished during the creep holding and use the following procedure to derive the stress exponent n, as defined in the conventional power-law creep (Eq. (5)) [63,65]:

$$\dot{\varepsilon} = A\sigma^{n} \tag{5}$$

where $\dot{\varepsilon}$ is the strain rate, σ is the applied stress, and A is a temperature-dependent material constant. The stress exponent that often provides a useful indication on the creep mechanisms involved can then be derived as $n = \frac{\partial(\ln\dot{\varepsilon})}{\partial(\ln\sigma)}$.

In indentation, the strain-rate and stress can be written following the scaling relations:

$$\dot{\varepsilon} \propto \frac{\dot{h}}{h}, \sigma \propto \frac{P}{24.5h^2} \tag{6}$$

where P is the applied load, h is the instantaneous indentation displacement, and the displacement rate is $\dot{h} = \frac{dh}{dt}$ [62], which can be obtained by fitting the creep displacement holding time curve at a constant load using an empirical equation [63]:

$$h(t) = h_0 + a(t - t_0)^b + kt, \tag{7}$$

where h_0, a, b, t_0 and k are fitting constants that vary, depending on each creep time–displacement curve. Feng and Ngan [66,67] applied

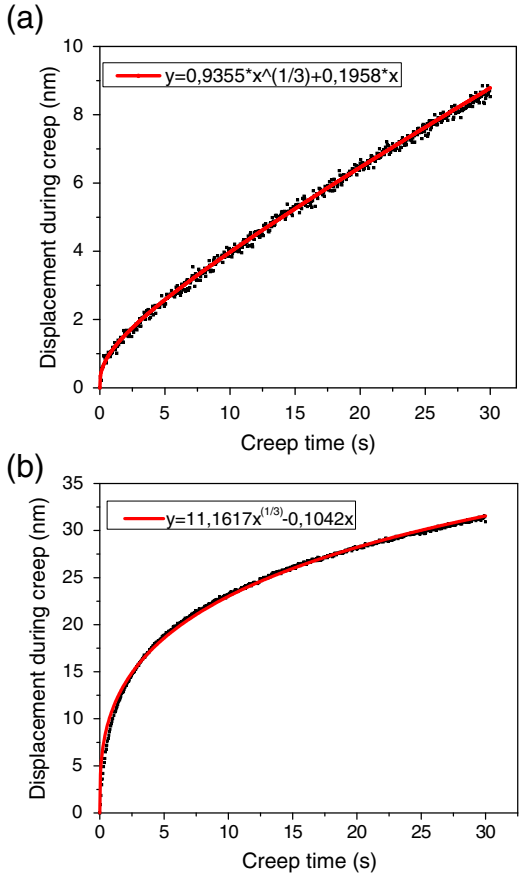

Fig. 6. Displacement-creep time for 5 and 1500 μN of maximum applied load.

a Maxwell two-element model to the creep displacement at maximum load in a conventional load–displacement response and determined an equivalent expression for the contact stiffness that included the creep rate expressed as a displacement over time. The h is obtained by fitting the displacement–time (h–t) curve by the following empirical law (for b equal to 1/3):

$$y = \alpha x^{1/3} + kx + c \tag{8}$$

where a, k and c are fitting constants that vary, depending on each creep time–displacement curve.

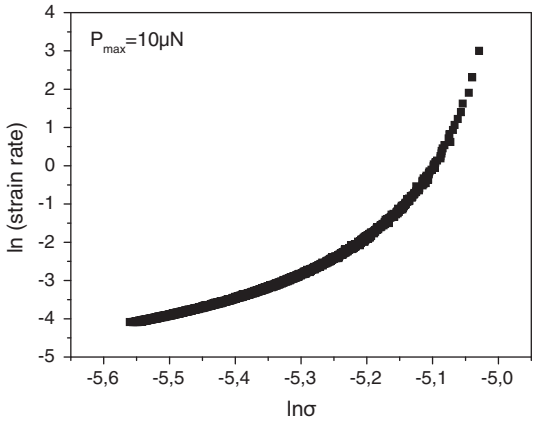

Fig. 7. The corresponding ln (strain rate) as a function of ln (stress) for a representative applied load of 10 μN.

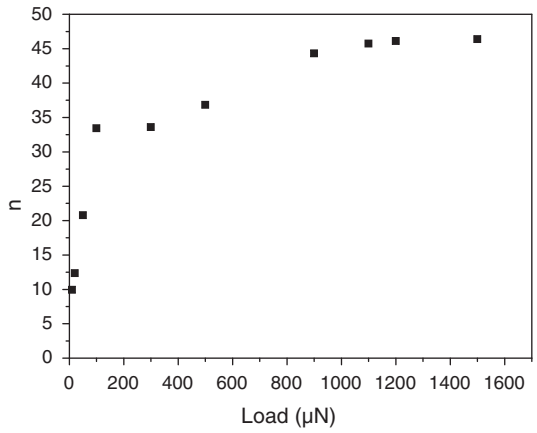

Fig. 8. Steady state stress exponent (n) dependence upon the indentation at the maximum loads ranging from 0 to 1600 μN, for a constant loading time of 5 s.

Fig. 6 shows that this law fits very well the results obtained through the creep experiment. The ln (strain rate) versus ln (stress) relation of the zeolite is presented in Fig. 7. The slope of this curve lowers rapidly with the holding time (i.e., where the stress decreases) and then gradually becomes constant at the end of the holding period. This constant value at the left of the curve, which corresponds to the end of the holding period, was taken to be the stress exponent n for the peak load.

Fig. 8 shows the variation of the stress exponent with the holding load at different indentation loading rates in zeolite sample. It can be seen that the stress exponent exhibits a strong dependence upon the indentation loading rate. The loading rate dependence of the stress exponent values of the tested samples may suggest a difference in the deformation mechanism during creep [68].

Nanoindentation creep is segregated from conventional uniaxial creep since the volume of materials involved is expanding during the creep holding, resulting in a continuous contribution of transient effect during the creep holding (especially at the beginning of holding where the transient effect can be dominant). In the case of a conventional uniaxial creep test, the material involved is limited within the gauge length of the sample [69,70]. The stress exponent measured from an indentation creep test shall not be equalized with that derived from the uniaxial tension/compression creep, since heterogeneous stress/strain field occurs underneath the nanoindenter in contrast to the generally uniform stress/strain field in a uniaxial creep test. The deformation mechanisms are different in that dislocation motion and/or atomic diffusion are the main deformation mechanisms for crystalline materials creep [71], while shear banding is the deformation mechanism in metallic glassy alloys [72].

3.5. Pile-up/sink-in deformation — wear analysis

An important feature of indentation experiments is that the material around the contact area tends to deform upwards (pile-up) or downwards (sink-in) with respect to the indented surface plane. The occurrence of such pile-up and sink-in patterns is usually interpreted in terms of the strain-hardening behavior of the indented material [72–75]. According to these studies the surface around indents tends to pile-up against the indenter in cases where the indented sample is heavily pre-strained with only little reserves for further work-hardening or has generally a low strain-hardening potential. On the other hand, when the sample is fully annealed and has a high strain-hardening potential, the surface around indents tends to sink-in e.g. [72–75]. The reason for this relationship between strain hardening behavior and displacement patterns is plausible: well-annealed soft metals which exhibit a high strain-hardening rate tend to show far off field plasticity yielding a large lateral smear out of the plastic out-of-plane displacement field. Rapid strain-hardening in the immediate vicinity of the indenter tip will cause plastic deformation to occur gradually further away from the contact region, causing the material to be displaced far away from the indentation entailing sink-in patterns. In contrast, strain-hardened materials as well as alloys and metallic glasses which exhibit a low (residual) strain-hardening rate will reveal a stronger localization of the plastic zone, creating a local pile-up instead of a sink-in displacement pattern around the indent.

Good knowledge of the deformation zone around an indent is of considerable importance for nanoindentation testing because the shape of the out-of-plane displacement zone determines the actual contact area between the indenter and the specimen. Sink-in patterns reduce and pile-up patterns increase the contact area. These differences in the surface deformation mode affect the quantitative analysis of the hardness measurements. Not taking the piling-up or sinking-in into account in micro- and nano-indentation hardness tests can result in significant errors when extracting hardness values from the experimental data [72,73].

The contact area is influenced by the formation of pile-ups and sink-ins during the indentation process. To accurately measure the indentation contact area, pile-ups/sink-ins should be appropriately accounted for. The presence of creep during nanoindentation has an effect on pile-up, which results in incorrect measurement of the material properties. Fischer-Cripps observed this behavior, in case where the measured elastic modulus was much less than expected [76]. Rar et al. observed that the same material when allowed to creep for a

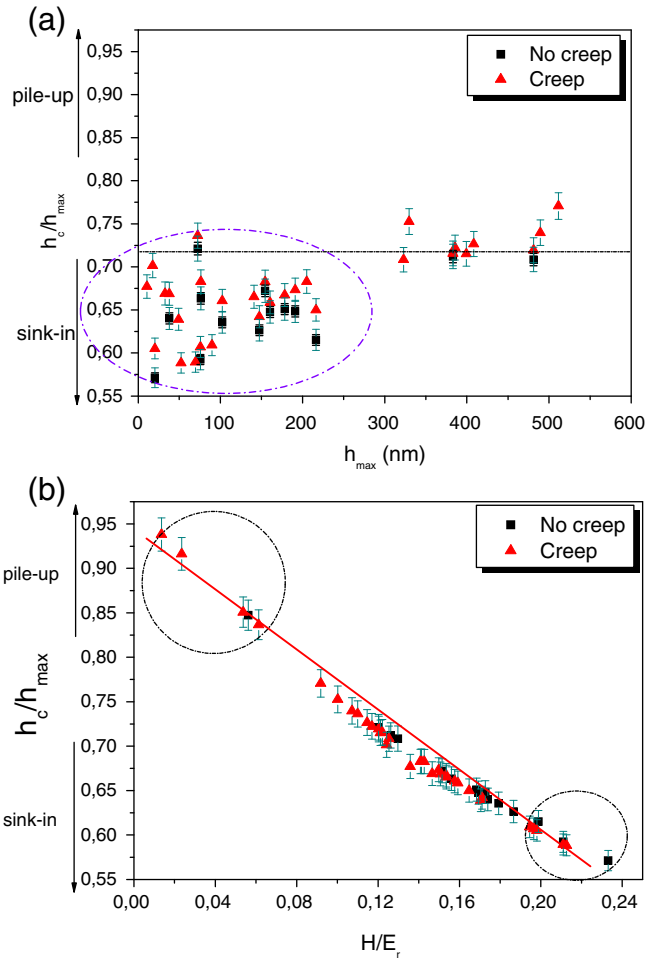

Fig. 9. Investigation of pile-up/sink-in deformation mechanism and linear correlation of h_c/h and displacement for the zeolite membrane.

long duration produced a higher value of pile-up/sink-in indicating a switch from an initial elastic sink-in to a plastic pile-up [77].

In Fig. 9, the normalized pile-up/sink-in height h_c/h is plotted vs. displacement and the normalized hardness H/E. Rate sensitive materials experience less pile-up compared to rate insensitive materials due to strain hardening. For rate insensitive materials, Cheng and Cheng reported a 22% pile-up and only sink-in was detected when the work hardening exponent reached 0.5 [78]. This is consistent with the fact that when h_c/h approaches 1 for small H/E, deformation is intimately dominated by pile-up [79,80]. On the other hand, when h_c/h approaches 0 for large H/E, it corresponds to purely elastic deformation and is apparently dominated by sink-in in a manner prescribed by Hertzian contact mechanics [81].

The ratio of H to E is of significant interest in tribology. Higher stresses are expected in the case of high H/E (hard materials) and high stress concentrations to develop towards the indenter tip, whereas in the case of low H/E (soft materials) the stresses are lower and are distributed more evenly across the cross-section of the material [76,82,83]. The high ratio H/E is indicative of the good wear resistance in a disparate range of materials [83]: ceramic, metallic and polymeric (e.g. c-BN, tool steel and nylon, respectively), which are equally effective in resisting attrition for their particular intended application. In Fig. 10a, the change of H/E slope reveals a slight decrease in wear resistance with increasing displacement.

Adhesion relation of a coating with a substrate is confirmed by using the Tresca's yield criterion and Tabor's relation, according to which, the load at the onset of yielding is proportional to H^3/E^2. The term H^3/E^2 combines H and E values of a material and describes the amount of elasticity exhibited by the film. In particular, high (low) values of H^3/E^2 indicate a highly elastic (plastic) behavior of the film under contact events (Fig. 10b) [48,84].

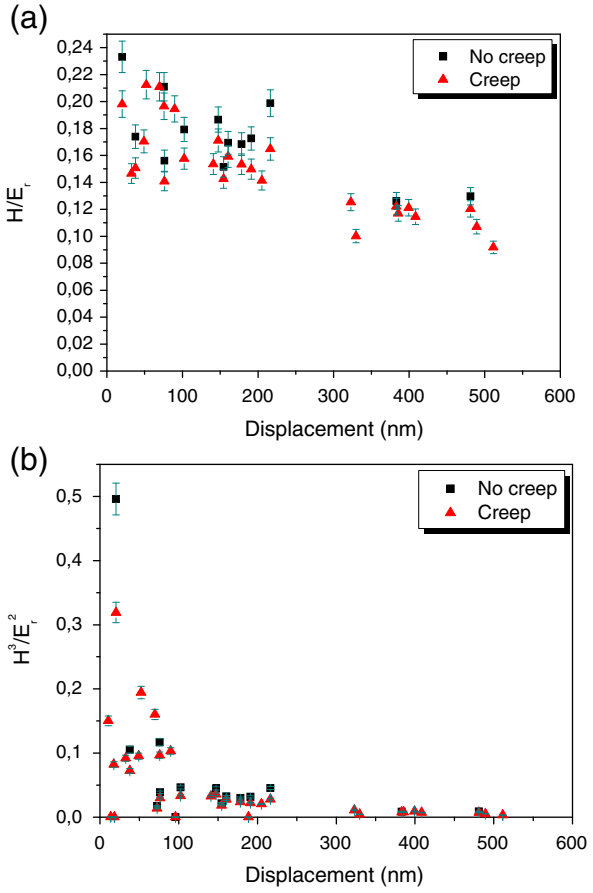

Fig. 10. Correlation of H/E (almost linear) and H^3/E^2 with displacement.

4. Conclusions

In this work, faujasite membranes were synthesized and characterized through XRD, SEM and nanoindentation. Hardness and elastic modulus values were found to decrease with increasing penetration depth; this slight decrease in the first few nm of displacement can be attributed to Indentation Size Effect. In the surface region hardness and elastic modulus values were 2.75 GPa and 12.5 GPa respectively, while for greater displacements they reached 1 GPa and 4.5 GPa, respectively. The creep investigation revealed that in the surface region hardness and elastic modulus values were 8 GPa and 60 GPa respectively, while for greater displacements they reached 0.8 GPa and 7 GPa, respectively. Hardness to elastic modulus ratio decreases as displacement increases, reaching a constant value of ~0.13 after ~400 nm of displacement, while in creep investigation the ratio reaches a constant value of ~0.12 after ~330 nm of displacement. Tresca yield criterion (H^3/E_r^2 as a function of displacement) revealed almost the same behavior. For Berkovich indenter and low displacement region (<200 nm), the h_c/h_{max} ratio diverge from unity, revealing that deformation is mainly dominated by sink-in (confirmed also by h_c/h_{max} and H/E_r correlation). The deformation mechanism switches and is dominated by pile-up for greater displacements. Creep investigation revealed that the lower the loading rate, the narrower the transient creep stage is (reaching earlier the steady-state creep stage). This could be attributed to the strain rate; using low loading rate, the period of reaching the maximum applied load is greater, thus creep may exist even in the loading part prior to hold time. Additionally, the strain field (distribution) below the indenter due to compression under various loading rates may be different, resulting in various creep behaviors.

Acknowledgements

V.N. acknowledges the financial support from the Catalysis Center for Energy Innovation, an Energy Frontier Research Center funded by the U.S. Department of Energy, Office of Science, Office of Basic Energy Sciences under Award No. DE-SC0001004.

References

[1] J. Caro, M. Noack, P. Kolsch, R. Schafer, Microporous Mesoporous Mater. 38 (2000) 3.
[2] A. Julbe, Stud. Surf. Sci. Catal. 157 (2005) 135.
[3] A. Tavolaro, E. Drioli, Adv. Mater. 975 (1999) 11.
[4] T. Bein, S. Mintova, Stud. Surf. Sci. Catal. 157 (2005) 263.
[5] A. Walcarius, Anal. Chim. Acta 384 (1999) 1.
[6] G. Schulz-Ekloff, D. Wohrle, B. van Dufel, R.A. Schoonheydt, Microporous Mesoporous Mater. 51 (2002) 91.
[7] Z. Li, M.C. Johnson, M. Sun, E.T. Ryan, D.J. Earl, W. Maichen, J.I. Martin, S. Li, C.M. Lew, J. Wang, M.W. Deem, M.E. Davis, Y. Yan, Angew. Chem. Int. Ed. 45 (2006) 6329.
[8] X.W. Xu, J. Wang, Y.C. Long, Sensors 6 (2006) 1751.
[9] H.K. Jeong, Z. Lai, M. Tsapatsis, J.C. Hanson, Microporous Mesoporous Mater. 84 (2002) 332.
[10] M. Lassinantti Gualtieri, C. Andersson, F. Jareman, J. Hedlund, A.F. Gualtieri, M. Leoni, C.J. Meneghini, Membr. Sci. 290 (2007) 95.
[11] L. Brabecc, P. Bohac, M. Stranyanek, R. Ctvrtlik, M. Kocirik, Microporous Mesoporous Mater. 956 (2006) 226.
[12] J. Lin, X.F. Shu, J.X. Dong, Mater. Lett. 59 (2005) 1595.
[13] T. Baimpos, V. Nikolakis, D. Kouzoudis, J. Memb. Sci. 130 (2012) 390–391.
[14] J. O'Brien-Abraham, M. Kanezashi, Y.S. Lin, Microporous Mesoporous Mater. 105 (2007) 140.
[15] M. Yu, T.J. Amundsen, M. Hong, J.L. Falconer, R.D. Noble, J. Membr. Sci. 298 (2007) 182.
[16] J. Dong, Y.S. Lin, M.Z.-C. Hu, R.A. Peascoe, E.A. Payzant, Microporous Mesoporous Mater. 34 (2000) 241.
[17] E.R. Geus, H. Bekkum, Zeolites 15 (1995) 333.
[18] M. Colligan, P.M. Forster, A.K. Cheetham, Y. Lee, T. Vogt, J.A. Hriljac, J. Am. Chem. Soc. 126 (2004) 12015.
[19] M. Johnson, Z. Li, J. Wang, Y. Yan, Thin Solid Films 515 (2007) 3164.
[20] R. Astala, S.M. Auerbach, P.A. Monson, J. Phys. Chem. B 108 (2004) 9208.
[21] Z. Wang, J. Lambros, R.F. Lobo, J. Mater. Sci. 37 (2002) 2491.
[22] C. Sanchez-Valle, S.V. Sinogeikin, Z.A.D. Lethbridge, R.I. Walton, C.W. Smith, K.E. Evans, J. Appl. Phys. 98 (2005) 053508.
[23] Z. Wang, R.F. Lobo, J. Lambros, Microporous Mesoporous Mater. 57 (2003) 1.
[24] J. Lin, X.F. Shu, J.X. Dong, Stud. Surf. Sci. Catal. 158 (2005) 231.

[25] Z.A.D. Lethbridge, J.J. Williams, R.I. Walton, C.W. Smith, R.M. Hooper, K.E. Evans, Acta Mater. 54 (2006) 2533.
[26] X.Y. Niu, J. Lin, X.F. Shu, Acta Mech. Solida Sin. 27 (2006) 394.
[27] C.R.A. Catlow, C.M. Freeman, M.S. Islam, R.A. Jackson, M. Leslie, S.M. Tomlinson, Philos. Mag. 58 (1988) 123.
[28] N.A. Ramsahye, R.G. Bell, J. Phys. Chem. B 109 (2005) 4738.
[29] P.G. Krokidas, E.D. Skouras, V. Nikolakis, V.N. Burganos, J. Phys. Chem. C 114 (2010) 22441.
[30] Th. Baimpos, I.G. Giannakopoulos, V. Nikolakis, D. Kouzoudis, Chem. Mater. 20 (2008) 1470.
[31] S. Eslava, C. Kirschhock, S. Aldea, M. Baklanov, F. Iacopi, K. Maex, J. Martens, Microporous Mesoporous Mater. 458 (2009) 118.
[32] M. Johnson, J. Wang, Z. Li, C. Lew, Y. Yan, Mater. Sci. Eng., A 456 (2007) 58.
[33] T.D. Bennett, J.C. Tan, S.A. Moggach, R. Galvelis, C. Mellot-Draznieks, B.A. Reisner, A. Thirumurugan, D.R. Allan, A.K. Cheetham, Chem. Eur. J. 16 (2010) 10684.
[34] S.-C. Kim, N.R. Keskar, A.V. McCormick, J.R. Chelikowsky, H.T. Davis, J. Chem. Phys. 102 (1995) 8656.
[35] C.-C. Huang, M.-K. Wei, S. Lee, Int. J. Plas. 27 (2011) 1093.
[36] M.J. Mayo, W.D. Nix, Acta Metall. 36 (1988) 2183.
[37] C.A. Charitidis, E.P. Koumoulos, V.P. Tsikourkitoudi, S.P. Vasilakos, P.A. Tarantili, Nanost. Pol. Nanocomp. 7 (2011) 32.
[38] W.B. Li, R. Warren, Acta Metall. 41 (1993) 3065.
[39] C.A. Charitidis, D.A. Dragatogiannis, E.P. Koumoulos, I.A. Kartsonakis, Mater. Sci. Eng. A 540 (2012) 226.
[40] Q. Wang, T. Liu, A. Gao, C. Zhang, C. Wang, J. He, Scr. Mater. 56 (2007) 1087.
[41] H. Pelletier, J. Krier, A. Cornet, P.J. Mille, Thin Solid Films 379 (2000) 147.
[42] S. Mandal, S. Kose, A. Frank, A.A. Elmustafa, Int. J. Surf. Sci. Eng. 2 (2008) 41.
[43] I.G. Giannakopoulos, V. Nikolakis, Ind. Eng. Chem. Res. 44 (2005) 226.
[44] V. Nikolakis, G. Xomeritakis, A. Abibi, M. Dickson, M. Tsapatsis, D.G. Vlachos, Membr. Sci. 184 (2001) 209.
[45] I.G. Giannakopoulos, K. Kalambaliki, V. Dracopoulos, V. Nikolakis, Stud. Surf. Sci. Catal. 158 A (2005) 137.
[46] C.A. Charitidis, Refract. Met. Hard Mater. 28 (2010) 70.
[47] G. Feng, A.H.W. Ngan, Mater. Res. 17 (2002) 660.
[48] H. Bei, E.P. George, J.L. Hay, G.M. Pharr, Phys. Rev. Lett. 95 (2005) 045501.
[49] M. Troyon, L. Huang, Surf. Coat. Technol. 201 (2006) 1613.
[50] W.C. Oliver, G.M. Pharr, Mater. Res. 7 (1992) 1564.
[51] I.N. Sneddon, Proc. Camb. Philos. Soc. 44 (1948) 492;
R.B. King, Int. J. Solids Struct. 23 (1987) 1657;
R. Rodriguez, I. Gutierrez, Mater. Sci. Eng., A 361 (2003) 377.
[52] L.E. Samuels, in: ASTM STP American Soc. Test. Mater., Philadelphia, PA, 889, 1986, p. 5.
[53] H. Li, A. Ghosh, Y.H. Han, R.C. Bradt, J. Mater. Res. 8 (1993) 1028.
[54] Q. Ma, D.R. Clarke, J. Mater. Res. 104 (1995) 853.
[55] Y. Gaillard, C. Tromas, J. Woirgard, Acta Mater. 54 (2006) 1409.
[56] H.S. Leipner, D. Lorenz, A. Zecker, H. Lei, P. Grau, Physica B 308 (2001) 446.
[57] Y.L. Chiu, A.H.W. Ngan, Acta Mater. 50 (2002) 1599.
[58] Y. Gaillard, C. Tromas, J. Woirgard, Philos. Mag. Lett. 83 (2003) 553.
[59] C. Tromas, Y. Gaillard, in: Encyclopedia Mater. Sci. TechnElsevier Science, Amsterdam, 2004, p. 1.
[60] E. Meyer, Phys. Z. 9 (1908) 66.
[61] U. Kolemen, J. Alloys Compd. 425 (2006) 429.
[62] O. Sahin, O. Uzun, U. Kolemen, N. Ucar, Mater. Charact. 58 (2007) 197.
[63] K.L. Johnson, in: first ed., Contact MechanicsCambridge University Press, Cambridge, 1985.
[64] A.F. Bower, N.A. Fleck, A. Needleman, N. Ogbonna, Proc. R. Soc. London, Ser. A 441 (1993) 97.
[65] B.N. Lucas, W.C. Oliver, Metall. Mater. Trans. A 30 (1999) 601.
[66] H. Li, A.H.W. Ngan, J. Mater. Res. 19 (2004) 513;
G. Feng, A.H.W. Ngan, J. Mater. Res. 17 (2002) 660.
[67] A.H.W. Ngan, B. Tang, J. Mater. Res. 17 (2002) 2604.
[68] J. Lapin, J. Intermet. 14 (2006) 115.
[69] C.A. Charitidis, E.P. Koumoulos, V.P. Tsikourkitoudi, D.A. Dragatogiannis, G. Lolas, Plast. Rub. Comp. Macrom. 41 (2012) 94.
[70] C.A. Charitidis, D.A. Dragatogiannis, E.P. Koumoulos, A study on time dependent properties of aluminum alloy by nanoindentation technique, Int. J. Struct. Integr., in press.
[71] C.A. Schuh, T.G. Nieh, Acta Mater. 51 (2003) 87.
[72] G.M. Pharr, W.C. Oliver, F.R. Brotzen, J. Mater. Res. 7 (1992) 1564.
[73] W.D. Nix, Mater. Sci. Eng., A 234–236 (1997) 37.
[74] M.M. Chaudhri, M. Winter, J. Phys. D Appl Phys. 21 (1988) 370.
[75] J. Alcala, A.C. Barone, M. Anglada, Acta Mater. 48 (2000) 3451.
[76] A.C. Fischer-Cripps, Mater. Sci. Eng., A 385 (2004) 74.
[77] A. Rar, S. Sohn, W.C. Oliver, D.L. Goldsby, T.E. Tullis, G.M. Pharr, Mater. Res. Soc. Symp. Proc. 841 (2005) 119.
[78] Y.T. Cheng, C.M. Cheng, Philos. Mag. Lett. 78 (1998) 115.
[79] R. Hill, B. Storakers, A.B. Zdunek, Math. Phys. Sci. 423 (1989) 301.
[80] S. Biwa, B. Storakers, Mech. Phys. Solids 43 (1995) 1303.
[81] H. Hertz, Miscellaneous Papers, H. Hertz, Macmillan, 1896.
[82] Y.T. Cheng, C.M. Cheng, Surf. Coat. Technol. 133 (2000) 417.
[83] A. Leyland, A. Matthews, Surf. Coat. Technol. 177 (2004) 317.
[84] A. Leyland, A. Matthews, Nanostruct. Sci. Technol. 12 (2006) 511.